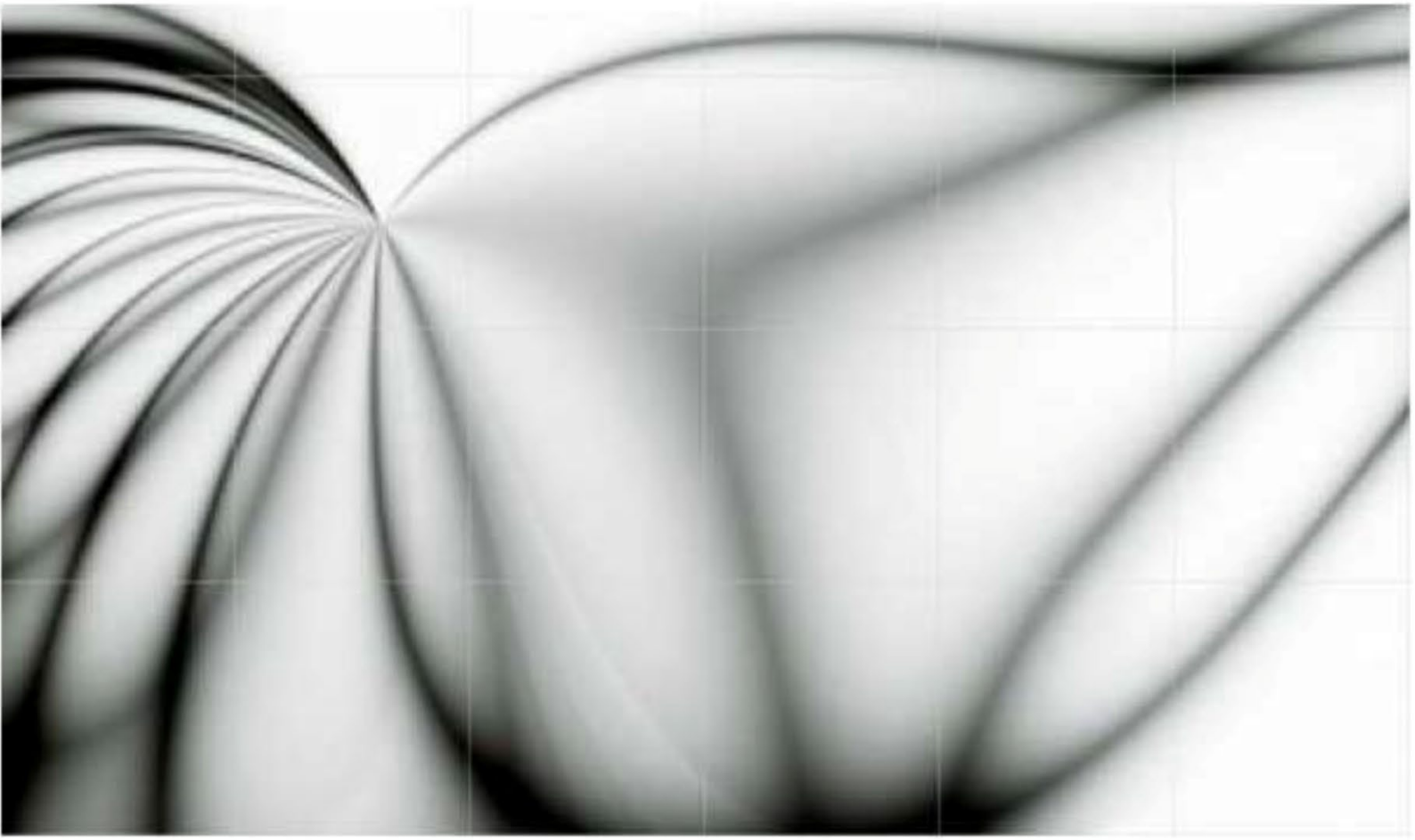
IJOCTA
An International Journal of Optimization and Control: Theories & Applications
2010

ISSN: 2146-0957
eISSN: 2146-5703
Volume 15 · Issue 3
July 2025

An International Journal of Optimization and Control:

Theories & Applications



ACCSCIENCE PUBLISHING



ACCSCIENCE PUBLISHING

An International Journal of Optimization and Control: Theories & Applications

Print ISSN: 2146-0957
Online ISSN: 2146-5703

An International Journal of Optimization and Control: Theories & Applications is a scientific, peer-reviewed, open-access journal that publishes original research papers and review articles of high scientific value in all areas of applied mathematics, optimization and control. It aims to focus on multi/inter-disciplinary research into the development and analysis of new methods for the numerical solution of real-world applications in engineering and applied sciences. The basic fields of this journal cover mathematical modeling, computational methodologies and (meta)heuristic algorithms in optimization, control theory and their applications. Note that new methodologies for solving recent optimization problems in operations research must conduct a comprehensive computational study and/or case study to show their applicability and practical relevance.



About the Publisher

AccScience Publishing is a publishing company based in Singapore. We publish a range of high-quality, open-access, peer-reviewed journals and books from a broad spectrum of disciplines.

Contact Us

Managing Editor
ijocta.office@accscience.sg

AccScience Publishing
9 Raffles Place, Republic Plaza 1 #06-00 Singapore 048619.

Volume 15 • Issue 3• July 2025
ISSN 2146-0957 (print) ISSN 2146-5703 (online)

An International Journal of Optimization and Control: Theories & Applications

Editor-in-Chief
Ramazan Yaman
Istanbul Atlas University, Turkey

ACCSCIENCE PUBLISHING

Access Science Without Barriers

Full issue copyright © 2025 AccScience Publishing
All rights reserved. Without permission in writing from the publisher, this full issue publication in its entirety may not be reproduced or transmitted for commercial purposes in any form or by any means, electronic or mechanical, including photocopying, recording, or any information storage and retrieval system. Permissions may be sought from ijocta.office@accscience.sg.

Article copyright © Respective Author(s)
See articles for copyright year. All articles in this full issue publication are open-access. There are no restrictions in the distribution and reproduction of individual articles, provided the original work is properly cited. However, permission to reuse copyrighted materials of an article for commercial purposes is applicable if the article is licensed under Creative Commons Attribution-NonCommercial. Check the specific license before reusing.

An International Journal of Optimization and Control: Theories & Applications
ISSN: 2146-0957 (print)
ISSN: 2146-5703 (online)

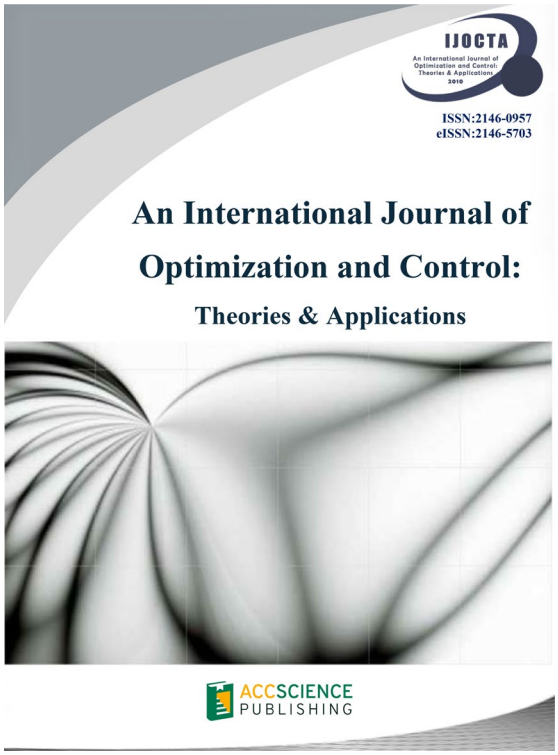
Editorial and Production Credits

Publisher: AccScience Publishing
Managing Editor: Hayley Man
Production Editor: Samyuktha Balakrishnan
Article Layout and Typeset: Sinjore Technologies (India)

For all advertising queries, contact ijocta.office@accscience.sg.

Supplementary file

Supplementary files of articles can be obtained at https://accscience.com/journal/IJOCTA/15/3.



Disclaimer

AccScience Publishing is not liable to the statements, perspectives, and opinions contained in the publications. The appearance of advertisements in the journal shall not be construed as a warranty, endorsement, or approval of the products or services advertised and/or the safety thereof. AccScience Publishing disclaims responsibility for any injury to persons or property resulting from any ideas or products referred to in the publications or advertisements. AccScience Publishing remains neutral with regard to jurisdictional claims in published maps and institutional affiliations.

IJOCTA
An International Journal of Optimization and Control: Theories & Applications
2010

https://accscience.com/journal/IJOCTA
ijocta.office@accscience.sg

An International Journal of Optimization and Control: Theories & Applications

Volume 15 • Issue 3
July 2025

Publisher:
AccScience Publishing
9 Raffles Place, Republic Plaza 1 #06-00
Singapore 048619

Print ISSN: 2146-0957
Online ISSN: 2146-5703

Editor-in-Chief:
Prof. Dr. Ramazan YAMAN

IJOCTA is an international, quarterly, and peer-reviewed journal indexed/ abstracted by:
- Emerging Sources Citation Index (ESCI)
- Scopus - Applied Mathematics
- Scopus - Control and Optimization
- Zentralblatt MATH
- ProQuest - Electronics & Communications Abstracts
- Proquest - Computer & Information Systems Abstracts
- Proquest - Mechanical & Transportation Eng. Abstracts
- EBSCOHost
- MathSciNet
- TR Dizin - Ulakbim (Science Database)
- Directory of Open Access Journals (DOAJ)

Editor-in-Chief
YAMAN, Ramazan - Istanbul Atlas University / Türkiye

Associate Editors
EVIRGEN, Firat - Balikesir University, Türkiye
KUCUKKOC, Ibrahim - Balikesir University / Türkiye
OZDEMIR, Necati - Balikesir University / Türkiye

Editorial Board Members
AGARWAL, Ravi P. - Texas A&M University Kingsville / USA
AGHABABA, Mohammad P. - Urmai University of Tech. / Iran
ATANGANA, A. - University of the Free State / South Africa
AVCI, Derya - Balikesir University / Türkiye
AYAZ, Fatma - Gazi University / Türkiye
BAGIROV, Adil - University of Ballarat / Australia
BALEANU, Dumitru I. - Lebanese American University / Lebanon
BOHNER, Martin - Missouri University of Science and Technology / USA
CAKICI, Eray – IBM Deutschland GmbH / Germany
CHEN, YangQuan - University of California Merced / USA
DAGLI, Cihan H. - Missouri University of Science and Technology / USA
DAI, Liming - University of Regina / Canada
BATTINI, Daria - Universita degli Studi di Padova / Italy
DAVIM, J. Paulo - University of Aveiro/ Portugal
DEMIRTAS, M. - Balikesir University / Türkiye
GÜRBÜZ, Burcu - Johannes Gutenberg-University Mainz / Germany
HAMMOUCH, Zakia - Moulay Ismail University / Morocco
HRISTOV, Jordan - University of Chemical Technology and Metallurgy / Bulgaria
JAJARMI, Amin - University of Bojnord / Iran
N. JANARDHANAN, Mukund - University of Warwick / United Kingdom
JONRINALDI, J. - Universitas Andalas, Padang / Indonesia
KARAOĞLAN, Aslan Deniz - Balikesir University / Türkiye
KATALINIĆ, Branko - Vienna University of Technology / Austria
NANE, Erkan - Auburn University / USA
PAKSOY, Turan – Necmettin Erbakan University / Türkiye
SHUKLA, Anurag – Rajkiya Engineering College Kannauj/ India
SULAIMAN, Shamsuddeen - Universiti Putra Malaysia / Malaysia
SUTIKNO, Tole - Universitas Ahmad Dahlan / Indonesia
TABUCANON, Mario T. - Asian Institute of Technology / Thailand
TEO, Kok Lay - Curtin University / Australia
MARTINEZ, Antonio J. Torija - University of Salford / UK
TRUJILLO, Juan J. - Universidad de La Laguna / Spain
WANG, Qing - Durham University / UK
WEBER, Gerhard Wilhelm - Poznan University of Technology / Poland
XU, Hongkun - National Sun Yat-Sen University / Taiwan (China)
YAMAN, Gulsen - Balikesir University / Turkey
ZAKRZHEVSKY, Mikhail V. - Riga Technical University / Latvia
ZHANG, David Z. - University of Exeter / UK
EROĞLU, Beyza Billur İskender - Balikesir University / Turkey

ACCSCIENCE PUBLISHING

crossref

We Use Plagiarism Detection iThenticate Learn More »

An International Journal of Optimization and Control: Theories & Applications

ACCSCIENCE PUBLISHING

Volume 15 | Issue 3 |
July 2025 | Page 379 – 548 |

IJOCTA
An International Journal of Optimization and Control: Theories & Applications
2010

CONTENTS

RESEARCH ARTICLES

379 Improving the performance of a chaotic nonlinear system of fractional-order brushless direct current electric motor using fractional-order sliding mode control

Amin Kaveh, Mohammad Vahedi, Majid Gandomkar

396 Using infinitesimal symmetries for determining the first Maxwell time of geometric control problem on SH (2)

Soukaina Ezzeroual, Brahim Sadik

407 Modeling and analysis of the dynamics of an excessive gambling problem with modified fractional operator

Mulualem Aychluh, D.L. Suthar, Clemente Cesarano, S.D. Purohit

426 Predefined-time fractional-order terminal SMC for robot dynamics

Saim Ahmed, Ahmad Taher Azar

435 FPGA design and implementation of fuzzy learning control: Application on DC motor position control

Mohand Achour Touat , Hocine Khati , Arezki Fekik , Ahmad Taher Azar , Hand Talem , Rabah Mellah, Saim Ahmed

449 Computational aspects of the crop field segmentation problem based on anisotropic active contour model

Ciro D'Apice, Umberto De Maio, Peter I. Kogut, Rosanna Manzo

464 Application of Jumarie-Stancu Collocation Series Method and Multi-Step Generalized Differential Transform Method to fractional glucose-insulin

Sayed Saber, Brahim Dridi, Abdullah Alahmari, Mohammed Messaoudi

483 Trajectory controllability of integro-differential system of fractional orders in Hilbert spaces

Urvashi Arora, Sachin Singh, V. Vijayakumar, Anurag Shukla

493 Investigate the solution of an initial Hilfer fractional value problem

Amol D. Khandagale, Arif S. Bagwan, Sabri T. M. Thabet, Imed Kedim

503 A novel ninth-order root-finding algorithm for nonlinear equations with implementations in various software tools

Srinivasarao Thota , Amir Naseem , Thumati Gopi , Kashireddy Sai NandanReddy , Padarthi Sai Kousik , Thulasi Bikku , Shanmugasundaram Palanisamy

517 Proportional integral derivative plus control for nonlinear discrete-time state-dependent parameter: Industrial applications

E. M. Shaban

535 A numerical method for solving distributed-order multi-term time-fractional telegraph equations involving Caputo and Riesz fractional derivatives

Safar Irandoust Pakchin, Mohammad Hossein Derakhshan, Shahram Rezapour

An International Journal of Optimization and Control: Theories & Applications
ISSN: 2146-0957 eISSN: 2146-5703
Vol.15, No.3, pp.379-395 (2025)
https://doi.org/10.36922/ijocta.8407

RESEARCH ARTICLE

Improving the performance of a chaotic nonlinear system of fractional-order brushless direct current electric motor using fractional-order sliding mode control

Amin Kaveh[1], Mohammad Vahedi[2*], and Majid Gandomkar[1]

[1]Department of Electrical Engineering, College of Technical, Islamic Azad University, Saveh, Iran
[2]Department of Mechanical Engineering, College of Technical, Islamic Azad University, Saveh, Iran
Amin.kaveh@iau.ac.ir, Mo.Vahedi@iau.ac.ir, majid.gandomkar@iau.ac.ir

ARTICLE INFO

Article History:
Received: January 14, 2025
Revised: March 7, 2025
Accepted: March 24, 2025
Published Online: April 22, 2025

Keywords:
Brushless direct current motor
Fractional-order sliding mode control Chaos
Lyapunov stability
Robust control

AMS Classification 2010:
34A08, 26A33, 34H10, 93C10

ABSTRACT

Brushless direct current (BLDC) motors are widely used in industrial applications due to their high efficiency and reliability. However, these motors exhibit inherent nonlinear and chaotic behavior, which can degrade performance and cause instability under certain operating conditions. This paper proposes a fractional-order sliding mode controller (FO-SMC) for robust chaos suppression and improved stability in BLDC motor systems to address this issue. The proposed controller leverages fractional-order calculus to enhance robustness, mitigate chattering, and provide better disturbance rejection than conventional control approaches. A comprehensive Lyapunov-based stability analysis is conducted to ensure finite-time convergence and system stability under parameter uncertainties and external disturbances. The effectiveness of the proposed FO-SMC is evaluated through extensive numerical simulations, comparing its performance against the integer-order sliding mode control method. The results demonstrate that FOS-MC significantly outperforms traditional controllers regarding settling time, overshoot reduction, and robustness to external perturbations. Additionally, the study explores the practical feasibility of implementing the proposed control strategy in real-time applications using Grunwald–Letnikov fractional derivatives, which enable efficient numerical approximation and digital implementation in field-programmable gate array-based and microcontroller-driven control systems. The findings confirm that FOS-MC provides a highly adaptive and resilient solution for stabilizing BLDC motors, making it a strong candidate for advanced industrial automation and high-performance motor control applications.

(cc) BY

1. Introduction

Nowadays, vehicles are increasingly being equipped with permanent magnet synchronous motors. One of the most widely used motors in industrial applications is the brushless direct current (BLDC) motor, which is particularly favored in the automotive industry due to its sensorless operation. These motors provide maximum torque at a standstill, and their torque decreases linearly with increasing speed. However, due to the square wave shape of the current and the commutation action between the phases, they exhibit torque ripple, which can impact their performance. Various techniques have been developed to minimize torque ripple in BLDC motors.[1–4]

By examining the performance of different electric motors, it is evident that conventional DC

*Corresponding Author

motors offer high efficiency but require a commutator and brushes, which demand regular maintenance. To overcome this limitation, BLDC motors have been introduced. These motors consist of a permanent magnet rotor and a stator winding similar to traditional motors, but unlike conventional DC motors, they do not require brushes for commutation, as this is managed electronically. The inverter plays the role of the commutator, making these motors more efficient and reliable.[1–4]

The BLDC motors offer several technical advantages over traditional DC and induction motors, including a simple control system, minimal need for sensors, long lifespan, low maintenance, a favorable torque-speed characteristic, fast dynamic response, high efficiency, noiseless operation, and a wide speed range. These features make BLDC motors preferred for applications requiring high efficiency, low noise, and precise control. Given these benefits, BLDC motors are widely used in high-power and high-torque applications with space limitations, where their compact size, efficiency, and torque-speed characteristics make them ideal. A novel sensorless control scheme proposes a terminal sliding mode observer to replace mechanical sensors and improve speed estimation in interior permanent magnet synchronous motors, ensuring observer stability.[5]

Fractional calculus is increasingly being applied in various fields because it can provide more accurate modeling of real systems, which often exhibit fractional-order dynamics. Chaos theory is one of the key areas where fractional calculus plays a crucial role. Chaotic systems are highly sensitive to initial conditions, and disorganized behavior emerges when phase plane trajectories are globally bounded but locally unstable. It is well established that chaos does not occur in nonlinear continuous-time systems of order less than three. Typically, chaotic systems are modeled using three coupled differential equations that include fractional-order derivatives.[6] Recent studies have demonstrated the effectiveness of fractional-order sliding mode controllers (FO-SMCs) in suppressing chaotic oscillations while improving system stability. For instance, Li et al. proposed a circulating current controller for modular multilevel converters, integrating fractional-order calculus to enhance response speed and minimize chattering.[7]

The existence of chaos in motor systems was first reported by Kuroe in 1989.[8,9] The first mathematical model analyzing chaos and bifurcation in permanent magnet synchronous motors was developed by Shahzad.[10] In recent years, BLDC motors have been increasingly adopted in automotive, aerospace, robotics, household appliances, medical devices, food and chemical processing, electric vehicles, and computer peripherals due to their high efficiency, long lifespan, and good speed-torque characteristics.[11,12] The chaotic behavior of BLDC motors was initially identified by Hemati,[13] and such behavior is undesirable in engineering applications because it can degrade system performance.[8] Consequently, numerous studies have been conducted on chaos control in BLDC systems[14,15] and the synchronization of chaotic BLDC motors.[16] Chaos in BLDC motors leads to oscillations, acoustic noise, mechanical vibrations, and increased electrical energy consumption, ultimately reducing motor lifespan. Thus, studying and controlling chaos is critical for improving motor design and performance.[14–19]

Since the 1970s, researchers have extensively studied the dynamic characteristics of electric motors, focusing on startup issues, speed control, and oscillations. These challenges, particularly low-speed oscillations in controlled-speed motors, are closely related to chaos in nonlinear systems. The mathematical models for multivariable BLDC motors are highly nonlinear and strongly coupled, leading to complex dynamical behaviors. Advances in permanent magnet materials have further increased the use of BLDC motors in servo systems, high-performance drives, and household appliances.[8]

Various control methodologies have been proposed for chaos mitigation in BLDC systems, including proportional-integral-derivative (PID) control, fractional-order PID (FOPID) control, and sliding mode control (SMC). While FOPID controllers enhance conventional PID strategies by incorporating fractional-order terms for improved flexibility and disturbance rejection, their computational complexity necessitates advanced optimization techniques such as particle swarm optimization or genetic algorithms for parameter tuning. SMC, particularly in its fractional-order form (FO-SMC), has emerged as a more promising alternative due to its robustness against parameter uncertainties, finite-time convergence, and reduced chattering.[20]

To comprehensively address the reviewers' concerns, this study also evaluates the potential integration of interval type-2 (IT2) fuzzy logic control (FLC) with FO-SMC for BLDC motor

control. IT2 FLC introduces a footprint of uncertainty, enhancing adaptability to nonlinearities and external disturbances compared to type-1 FLC.[21] This method has demonstrated superior performance in uncertain and nonlinear systems, particularly in real-world BLDC motor applications where parameter variations are inevitable.[22]

Despite its adaptability, IT2 FLC exhibits significantly higher computational complexity than conventional SMC and FO-SMC strategies, making it less practical for high-speed BLDC motor control. In contrast, FO-SMC leverages fractional calculus to incorporate memory effects, enabling smoother control actions and superior robustness without additional fuzzy tuning. Although IT2 FLC provides an adaptive framework, it lacks the finite-time convergence guarantees of FO-SMC, making the latter more suitable for high-precision motor control. However, a hybrid approach combining IT2 FLC and FO-SMC may offer a promising avenue for future research, merging the strengths of both methodologies.[23]

Furthermore, while widely used, traditional PID controllers struggle with parameter uncertainties and external disturbances in BLDC motors.[24] FOPID controllers improve upon PID by offering better tuning flexibility and disturbance rejection capabilities.[22] However, they still exhibit computational complexity and may fail to suppress chaotic oscillations[23] completely. To address these challenges, SMC and FO-SMC were developed as robust control alternatives. While SMC provides strong disturbance rejection and finite-time convergence, it suffers from chattering, potentially leading to mechanical wear in BLDC motors.[25] FO-SMC mitigates this issue by incorporating fractional calculus, achieving smoother control actions, enhanced robustness, and minimal chattering.[26] Simulation results confirm that FO-SMC outperforms PID, FOPID, and conventional SMC in reducing steady-state error, improving transient response, and minimizing control effort.

Recent research has also explored the hardware implementation of advanced control techniques using field-programmable gate arrays (FPGA). Huerta-Moro et al.[24] demonstrated that FPGA-based SMC and PID controllers for DC-DC buck converters significantly improved response time and reduced overshoot, suggesting their potential for real-time chaos suppression in BLDC motors. These findings reinforce the importance of integrating advanced controllers with efficient hardware platforms.

This study aims to design a FO-SMC to suppress chaotic behavior in a BLDC motor system. A suitable sliding surface is designed to stabilize the system, minimize oscillations, and improve adaptability under external disturbances and parameter uncertainties. The results demonstrate the superior performance of FO-SMC in mitigating chaos while ensuring system stability and efficiency.

2. Mathematical modeling and chaos analysis

2.1. Brushless direct current electric motor system and assumptions

In this study, the dynamic characteristics of a BLDC motor were analyzed to establish a robust control strategy (Figure 1). First, the mathematical model of the system is formulated, which is essential for investigating the bifurcation and chaos analysis. The system's equilibrium points and stability properties are subsequently determined to provide insights into its nonlinear dynamics.



Figure 1. Schematic of a brushless direct current motor[25]

A BLDC motor is powered by a DC electric source and differs from traditional DC motors by employing a closed-loop electronic controller instead of mechanical brushes. This controller converts the incoming DC current into motor coils that generate magnetic fields, enabling smooth and precise rotation. Unlike conventional

DC motors that rely on mechanical commutators, BLDC motors offer several advantages, including a higher torque-to-weight ratio, improved efficiency, greater torque output per watt, increased reliability, reduced noise, and extended lifespan due to the elimination of brush and commutator wear. Additionally, removing ionizing sparks reduces electromagnetic interference, making BLDC motors ideal for precision applications. Their efficiency is notably superior in no-load and low-load regions, primarily due to the absence of friction losses associated with brushes.[26,27]

This study makes the following key assumptions to ensure a realistic and practical evaluation of the FO-SMC for BLDC motors:

- Bounded motor parameter uncertainty: The motor parameters (resistance, inductance, and back electromotive force coefficients) are assumed to be within a reasonable uncertainty range, aligning with manufacturer-provided tolerances. This ensures feasibility without assuming unrealistic, completely unknown parameters.
- Fractional-order dynamics for accuracy: Since BLDC motors exhibit memory-dependent behaviors, fractional-order modeling provides a more precise representation than integer-order models, ensuring better energy dissipation and hereditary effects.
- Bounded external disturbances and load variations: Practical disturbances like friction and load torque changes are naturally bounded. Assuming finite limits ensures the stability of the FO-SMC, as real-world controllers cannot compensate for unbounded disturbances.
- Grunwald–Letnikov (GL) definition for fractional derivatives: The GL method is chosen for fractional derivative computations due to its computational efficiency, direct discrete approximation, and real-time feasibility, making it widely used in electromechanical systems.
- Negligible sensor noise and quantization effects: High-precision sensors and the inherent robustness of FO-SMC minimize the impact of sensor noise, making detailed noise modeling unnecessary for this study.

The dynamic equations of a BLDC electric motor are given in the following Equation (1)[26,27]:

$$\begin{cases} \frac{di_d}{dt} = \frac{1}{L_d}\left[v_d - Ri_d + \omega L_q i_q\right] \\ \frac{di_q}{dt} = \frac{1}{L_d}\left[v_q - Ri_q - \omega L_d i_d - \omega\psi_r\right] \\ \frac{d\omega}{dt} = \frac{1}{J}\left[n_p\psi_r i_q + n_p(L_d - L_q) i_d i_q - T_L - \beta\omega\right] \end{cases} \tag{1}$$

where $(v_d,\ i_d)$ and $(v_q,\ i_q)$ are the d-q voltage and current of the electric motor, L_q and L_d are the stator inductances, and R is the stator resistance. ψ_r, β, and J are the fixed magnetic flux, friction coefficient, and polar moment of inertia. The number of pairs of poles is represented by n_p. T_L is the external load torque, and ω is the rotor angular velocity. Based on an agreement, Equation (1) is simplified using the following transformations.[26]

Assuming $T = \begin{bmatrix} bk & 0 & 0 \\ 0 & k & 0 \\ 0 & 0 & R/L_q \end{bmatrix}$, where $b = L_q/L_d$, $k = \frac{\beta R}{L_q n_q \psi_r}$, a $\gamma = \frac{\psi_r}{kL_q}$, $\sigma = \frac{\beta\ L_q}{R\ J}$, $u_d = \frac{v_d}{R\ k}$, $u_q = \frac{v_q}{R\ k}$, $v = \frac{n_p b\ L_q^2 k^2((L_d - L_q))}{J\ R^2}$, $\widetilde{T_L} = \frac{L_q^2\ T_L}{J\ R^2}$, and $t' = (R\ t)/L_q$. State variables are obtained as $(\widetilde{.}) = T^{-1}(.)$. Using these transformations, Equation (1) is obtained as the following set of dimensionless equations[26]:

$$\begin{cases} \frac{d\widetilde{i}_d}{dt'} = u_d - \mu\ \widetilde{i}_d + \widetilde{\omega}\widetilde{i}_q \\ \frac{di_q}{dt'} = u_q - \widetilde{i}_q - \widetilde{\omega}\widetilde{i}_d + \gamma\widetilde{\omega} \\ \frac{d\widetilde{\omega}}{dt} = \sigma\left[\widetilde{i}_q\left(\widetilde{i}_q - \widetilde{\omega}\right) + \widetilde{i}_d + \ v\ \widetilde{i}_d\widetilde{i}_q - \ \widetilde{T}_{\ L}\right] \end{cases} \tag{2}$$

such that σ, γ, μ, and v are the structural parameters of the dynamic system of the motor after transformations and are the d-q reference voltage and current of the electric motor. $\widetilde{T}_{\ L}$ is the load torque after transformation and $\widetilde{\omega}$ is the rotor angular velocity after transformation. Assuming $\widetilde{i}_{\ q} = \ x_1$, $\widetilde{i}_{\ d} = \ x_2$, and $\widetilde{\omega} = \ x_3$ are similar to the Lorentz system, the dynamic equations of the BLDC system are converted to the state space form:

$$\begin{cases} \dot{x}_1 = -\mu x_1 + x_2 x_3 + u_d \\ \dot{x}_2 = -x_2 - x_1 x_3 + \gamma x_3 + u_q \\ \dot{x}_3 = -\sigma(x_3 - x_2) - \tilde{T}_L + v x_1 x_2 \end{cases} \tag{3}$$

The fractional order form of such a system is as follows[16,28]:

$$\begin{cases} {}_0D_t^{q_1} x_1 = -\mu x_1 + x_2 x_3 + u_d \\ {}_0D_t^{q_2} x_2 = -x_2 - x_1 x_3 + \mu x_3 + u_q \\ {}_0D_t^{q_3} x_3 = -\sigma(x_3 - x_2) - \tilde{T}_L + v x_1 x_2 \end{cases} \tag{4}$$

It should be noted that considering fractional-order dynamics in many systems can significantly improve stability and increase accuracy in system behavior. The numerical solution of the fractional-order BLDC system is formulated using the GL fractional derivative, ensuring a more precise representation of the system's nonlinear dynamics. The governing fractional-order equations are expressed as follows:[5,6]

$$\begin{cases} x_1(t_k) = -\mu x_1(t_{k-1}) + x_2(t_{k-1})\, x_3(t_{k-1}) \\ \qquad\qquad +u_d(t_{k-1})\, h^{q_1} - \sum_{j=v}^{k} c_j^{(q_1)} x_1(t_{k-j}) \\ x_2(t_k) = -x_2(t_{k-1}) - x_1(t_k)\, x_3(t_{k-1}) \\ \qquad\qquad + \gamma\, x_3(t_{k-1}) + u_q(t_{k-1})\, h^{q_2} \\ \qquad\qquad - \sum_{j=v}^{k} c_j^{(q_2)} x_2(t_{k-j}) \\ x_3(t_k) = \sigma\, x_2(t_k) - x_3(t_{k-1}) - \widetilde{T}_L(t_{k-1}) \\ \qquad\qquad + v\, x_1(t_k)\, x_2(t_k)\, h^{q_3} - \sum_{j=v}^{k} c_j^{(q_3)} x_3(t_{k-j}) \end{cases} \tag{5}$$

where T_{sim} is the simulation time, $N = [T_{sim}/h]$, and $(x_1(0),\ x_2(0),\ x_3(0),)$ are the initial conditions. The numerical solution of the fractional-order BLDC system follows the GL definition, where the system's discrete representation depends on the total number of computational steps, denoted as N. This parameter is essential for ensuring numerical accuracy and stability. The estimation of N is based on the total simulation time T_{sim} and the chosen time step, defined as $N = T_{sim}/h$. The selection of h plays a crucial role in balancing accuracy and computational efficiency as a smaller h improves precision but increases the computational load, whereas a larger h reduces complexity but may lead to numerical errors or instability in chaotic systems.

The time step should be chosen carefully to maintain stability in fractional-order systems. A smaller step size ensures better differentiation accuracy but can significantly slow down computations, while a larger step size may result in approximation errors. Moreover, the memory effect in fractional calculus requires a sufficient number of computational steps to capture the long-term system behavior properly. To avoid numerical divergence, the stability constraints and eigenvalues of the system must be analyzed, ensuring that the selected h allows proper system convergence.

The binomial coefficients $c_j^{(q)}$ are computed using the GL definition [6]:

$$(c_j^{(q)} = (-1)^j \binom{q}{j} = (-1)^j \frac{\Gamma(q+1)}{\Gamma(j+1)\Gamma(q-j+1)}) \tag{6}$$

where $\Gamma(n) = \int_0^\infty t^{n-1} e^{-t} dt$, is the Gamma function. The GL definition is a fundamental approach for defining fractional derivatives and integrals. The fractional derivative of order n for a function *f(t)* using this method is expressed as[6]:

$$(\frac{d^n}{dt^n} f(t) = \lim_{h\to 0} h^{-j} \sum_{j=0}^{n} (-1)^j \binom{n}{j} f(t-jh)) \tag{7}$$

This approach provides a discretized representation of fractional derivatives, making it computationally efficient for numerical simulations. It is particularly suitable for systems with memory effects and is widely used in electrical and mechanical applications, including BLDC motors. The GL approach provides a powerful framework for modeling fractional-order systems, particularly those with memory effects and long-range dependencies. Utilizing direct discretization eliminates the need for complex transformations, making it an efficient and straightforward method for numerical implementation. Moreover, its ability to capture hereditary system properties ensures accurate dynamic modeling, particularly in applications such as BLDC motors, where precise control over chaotic behavior is essential. Additionally, its computational stability makes it ideal for real-time control applications, reinforcing its superiority over other fractional-order numerical techniques. These advantages make the GL method preferred for solving fractional-order differential equations, ensuring theoretical rigor and practical feasibility in control design.

Since we are interested in the chaotic dynamics of the system, we need to focus on the equilibrium points and parameter ranges where we observe chaos. To obtain the fixed points of the system (3), we examine it for $\mu = 1$ and $v = 0$ under no-load conditions ($u_d = u_q = \widetilde{T}_L = 0$) :[3,8]

$$\begin{cases} \dot{x}_1 = -x_1 + x_2 x_3 \\ \dot{x}_2 = -x_2 - x_1 x_3 + \gamma x_3 \\ \dot{x}_3 = -\sigma(x_3 - x_2) \end{cases} \tag{8}$$

Therefore, we have the following in equation :

$$\dot{x}_1 = 0, \begin{cases} x_1 = 0 \\ x_1 = x_2 x_3 \end{cases} \tag{9}$$

$$\dot{x}_2 = 0, \begin{cases} x_2 = 0 \\ x_2 = x_3(\gamma - x_1) \end{cases} \tag{10}$$

$$\dot{x}_3 = 0, \begin{cases} x_3 = 0 \\ x_2 = x_3 \end{cases} \tag{11}$$

By solving Equations (2.1)–(11), three fixed points are obtained. We derive these equilibrium points and discuss their local behavior.

2.2. Bifurcation and chaos in the brushless direct current system

Hopf bifurcation occurs when the corresponding Jacobian matrix has a pair of pure imaginary poles and other eigenvalues of the real part are non-zero. Here, for the BLDC system, the Hopf bifurcation and its chaotic behavior under no-load condition ($\boldsymbol{u_d = u_q = \widetilde{T}_L = 0}$) are investigated. By examining Equations (2.1)–Equation (11), it is clear that $\boldsymbol{E_1 = (0, 0, 0)}$ is the first equilibrium point. And with $\boldsymbol{\gamma > 1}$, two other nontrivial equilibria are $\boldsymbol{E_2 = (\ \gamma -1,\ \sqrt{\gamma-1},\ \sqrt{\gamma-1})}$ and $\boldsymbol{E_3 = (\ \gamma -1,\ -\sqrt{\gamma-1},\ -\sqrt{\gamma-1})}$. A simple analysis shows that if $\boldsymbol{0 < \gamma < 1}$, the original equilibrium point is stable, and it loses its stability for $\boldsymbol{\gamma = 1}$ and creates two unreal equilibrium points that are initially stable. By linearizing the system, we obtain the Jacobian matrix to discuss the local behavior of its equilibrium points. The Jacobian matrix of the system is as follows [26]:

$$J = \begin{bmatrix} -1 & x_3 & x_2 \\ -x_3 & -1 & -x_1+\gamma \\ 0 & \sigma & -\sigma \end{bmatrix} \tag{12}$$

which has eigenvalues obtained by the roots of the following equation:

$$\begin{aligned} D(\lambda) \ &= \ \lambda^3 + (2+\sigma)\lambda^2 + (\sigma+\gamma)\lambda \\ &\quad +2\sigma(\gamma-1) = 0 \end{aligned} \tag{13}$$

When checked at non-origin equilibrium points (nontrivial equilibria), Since the two nontrivial equilibria are symmetric, their stability must be the same. For the bifurcation of two nontrivial equilibria, that is, the parameter values for which $\lambda = 0$ or $\lambda = j\omega$, is the solution of Equation (13). With $\lambda = 0$, we have $\gamma = 1$, which results in the bifurcation that was discussed. With $\lambda = j\omega$ and setting the real and imaginary parts equal to each other, we have the following:

$$\begin{cases} -\omega^3 + (\sigma+\gamma)\omega = 0 \\ -(2+\sigma)\omega^2 + 2\sigma(\gamma-1) = 0 \end{cases} \tag{14}$$

where $\omega^2 = \frac{2\sigma(\gamma-1)}{2+\sigma} = \sigma+\gamma$. By sorting the value of γ at which Hopf bifurcation occurs is obtained. For $\omega^2 > 0$, at this value of γ, that is:

$$\gamma_h = \frac{\sigma(\sigma+4)}{\sigma-2} \tag{15}$$

Which always holds for $\sigma > 2$. Therefore, the eigenvalues would be:

$$\omega^2 = \frac{2\sigma(\sigma+1)}{\sigma-2} > 0 \tag{16}$$

Therefore, the eigenvalues will be as follows:

$$\lambda_1 = -(\sigma+2), \quad \lambda_{2,3} = \pm j\sqrt{\frac{2\sigma(\sigma+1)}{\sigma-2}} \tag{17}$$

Therefore, $\gamma = \gamma_h$ corresponds to a Hopf bifurcation point of the system and for values close to $\gamma \neq \gamma_h$, the equilibria are surrounded by the limit cycle, and for $\gamma > \gamma_h$, all three equilibria would be unstable. System (8) does not change under $(x, y, z) \Leftrightarrow (x, -y, -z)$; thus, it can be said that it is symmetric regarding the y and z axes, and if $\nabla V = \frac{\partial}{\partial x}\left(\frac{dx}{dt}\right) + \frac{\partial}{\partial y}\left(\frac{dx}{dt}\right) + \frac{\partial}{\partial z}\left(\frac{dx}{dt}\right) = -(\sigma+2) < 0$, this system is convergent.

As mentioned before, if $\gamma \leq 1$, $E_1 = (0, 0, 0)$ is the only equilibrium point. When the system parameters change, we might expect BLDC to demonstrate stable, limited cycle, and chaotic behaviors.

As can be seen in Figure 2, $\widetilde{i_d} = x_2$ is stable for γ with initial values, but as γ increases, it tends toward chaos and instability. Because it varies a little around the original equilibrium point, but with increasing γ it goes toward chaos (irregular oscillations) and then instability. The same thing applies to the variables $\widetilde{i_q} = x_1$ and $\widetilde{\omega} = x_3$. In other words, it can be said that the parameter γ has a completely influential parameter in the system's stability, instability, and chaos.

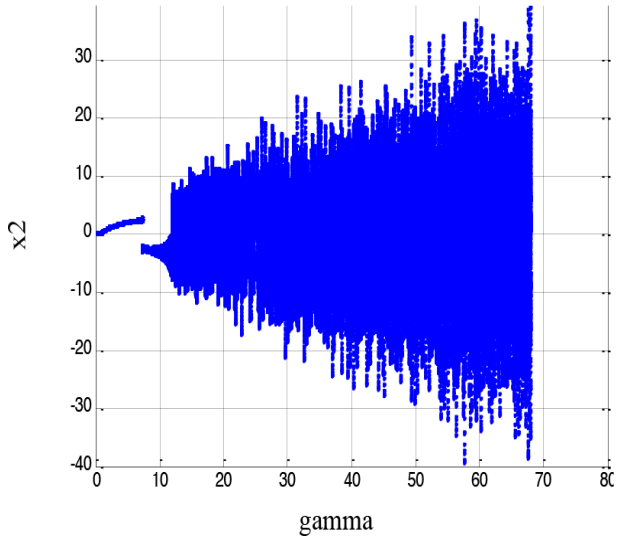


Figure 2. Bifurcation by changing γ and $\sigma = 5.4$

3. Control strategy for chaos suppression

This study considers the following assumptions to ensure the accurate modeling and practical feasibility of the proposed FO-SMC for the BLDC system.

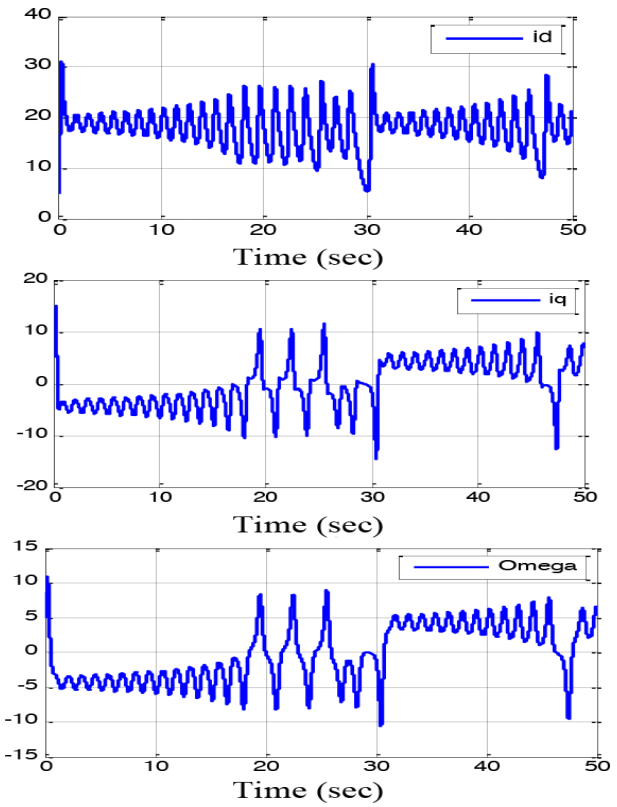


Figure 3. State variables $x_1(t)$, $x_2(t)$ and $x_3(t)$ of the fractional-order brushless direct current system without a control signal

Firstly, we analyze the FO-BLDC system under the no-load condition ($u_d = u_q = \widetilde{T}_L = 0$) and $v = 0$ in the form of Equation (4). We represent the parameter vector as $(\mu, \gamma, and\ \sigma) = (1,\ 20,\ and\ 5.46)$ and consider the system in homogeneous orders as $q_1 = q_2 = q_3 = 0.995$. To perform differentiation at the fractional order of 0.995, we can either first take the integral of the desired variable to the order of 0.005 and then take the first derivative of the result (Riemann–Liouville definition) or first take the first derivative of the function and then perform fractional-order integration of 0.005 (Caputo definition). If we do not apply any control input to the system $u(t) = 0$, it will exhibit chaotic behavior. For $T_{sim} = 50$ sec, a constant time step of $h = 0.005$, and initial conditions $(x_1(0),\ x_2(0),\ x_3(0)) = (0,\ 0, 0)$, the system will behave chaotically. With the above conditions, the state variables of the fractional-order BLDC system without a control signal are shown in Figure 3.

Furthermore, Figures 4 and 5 present the chaotic state trajectories of the FO-BLDC system without a control signal.

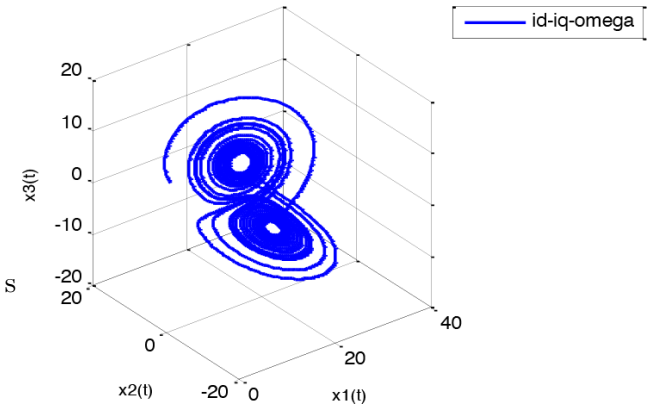


Figure 4. The chaotic state trajectories of the fractional-order brushless direct current system without control signals are represented by i_d, i_q, and ω

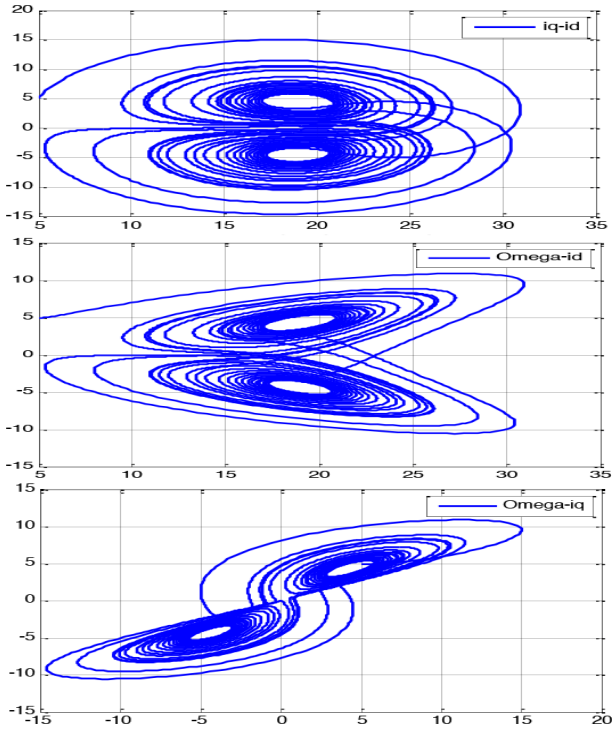


Figure 5. The chaotic state trajectories of the fractional-order brushless direct current system without a control signal are represented by $i_q - i_d$, $Omega - i_d$ and $Omega - i_q$

Based on this analysis, the points E_2 and E_3 represent unstable equilibrium points that satisfy the stability condition for chaotic behavior, while the point E_1 is a stable equilibrium point associated with two limit cycles.

Furthermore, when comparing the chaotic attractors of the fractional-order and conventional BLDC systems, we observe a larger stability region (attraction region) for the fractional-order system compared to the conventional one. For

instance, at a sampling time of $h = 0.005$, the fractional-order system reaches a stable equilibrium point. On the other hand, for a sampling time of $h = 0.05$, the conventional system becomes unstable from the sampling time, as illustrated in Figure 6.

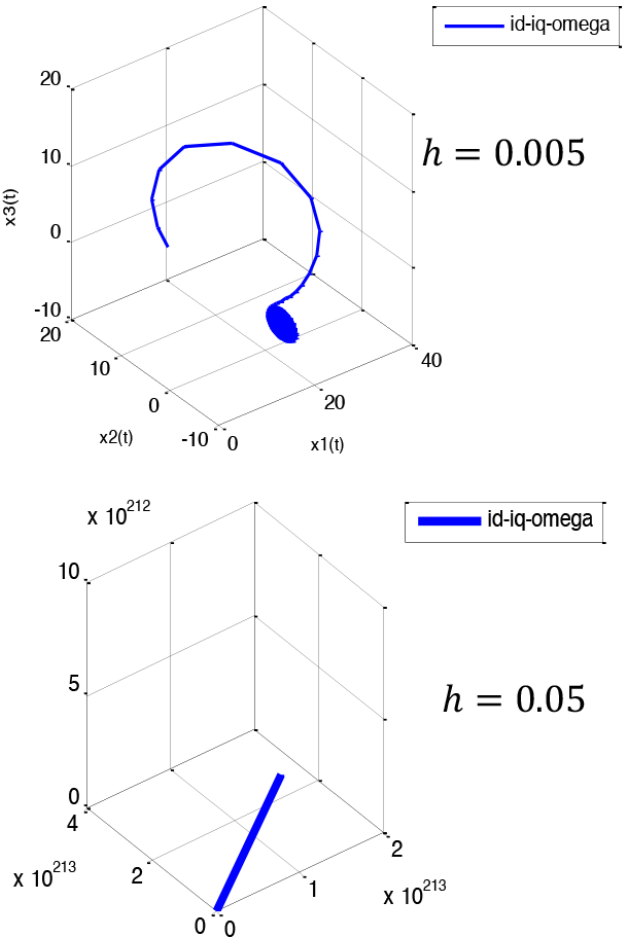


Figure 6. The chaotic state trajectories of the fractional order brushless direct current system without a control signal with $h = 0.005$ and $h = 0.05$

3.1. The fractional-order brushless direct current system with control input

We know that the fractional-order equation is represented by the following relationship:

$$\begin{cases} {}_0D_t^{q_1} x_1 = -x_1 + x_2 x_3 \\ {}_0D_t^{q_2} x_2 = -x_2 - x_1 x_3 + \mu x_3 \\ {}_0D_t^{q_3} x_3 = -\sigma(x_3 - x_2) \end{cases} \tag{18}$$

According to the no-load conditions and the characteristics of this section, using the trial and error method or drawing the bifurcation diagram, it can be seen that the system is unstable for $0 < q_1 = q_2 = q_3 = q < 0.6$ and $\vee\, q > 1.1$ conditions and when $0.6 < q < 0.98$ converges to one of the two equilibrium points of $E_2 \vee E_3$, and for $0.99 < q < 1.1$, chaotic behavior is generated. Therefore, to stabilize this section, we consider the variable $q = 0.995$.

Considering that the controlled system is an order-fractional system, the desired sliding surface must also have an order-fractional form. We define the sliding surface such that $S \to 0$ corresponds to $x_2 \to 0$; therefore, according to the fractional-order system in Equation (18), we define the slip surface in the form of Equation (19) [29]:

$$S = D_t^{q_2 - 1} x_2(t) \tag{19}$$

According to Equation (18), if $x_2 \to 0$, then $x_1 \to 0$ and $x_3 \to 0$, which transforms the problem into a regulation problem.

3.2. Control input design

Next, the control input u is defined as follows:[4–6]

$$u = u_{\text{eq}} + u_N \tag{20}$$

as u_{eq} is the equivalent control component, which keeps the states on the sliding surface. u_N is the switching component that directs the states to the sliding surface. u_N is primarily responsible for stabilizing the system and is designed using the Lyapunov stability criterion.

$$\begin{aligned} \dot{S}(x) &= \frac{\partial S}{\partial X} \cdot \dot{X}(t) \\ &= \frac{\partial S}{\partial X} \left[f(t,x) + B(t,x)(u_{\text{eq}} + u_N) \right] \\ &= \frac{\partial S}{\partial X} \left[f(t,x) + B(t,x)(u_{\text{eq}} + u_N) \right] \\ &= \frac{\partial S}{\partial X} \left[f(t,x) + B(t,x) u_{\text{eq}} \right] + \frac{\partial S}{\partial X} B(t,x) u_N \\ &= \frac{\partial S}{\partial X} B(t,x) u_N \end{aligned} \tag{21}$$

if we assume that $\frac{\partial S}{\partial X} B(t,x) = I$, where I is the identity matrix, then we have $\dot{S}(x) = u_N$, which satisfies this condition sufficiently.

The condition for the existence of sliding mode (condition $S_i \dot{S}_i < 0$) is given by $S \neq 0$. In the following, we will describe two important and commonly used cases in this article for the discontinuous control section:

(a) Relay with constant gain:

$$u_{i_N} = \begin{cases} -\alpha_i \, Sign(S_i(x)), & S_i(x) \neq 0,\ \alpha_i > 0 \\ 0, & S_i(x) = 0 \end{cases} \tag{22}$$

where the *sign* function is meant. It is observed that choosing this option for the discontinuous

part of the control system satisfies the sliding mode condition because:

$$S_i\dot{S}_i = -\alpha_i S_i(x)\, Sign(S_i(x)) < 0, \quad S_i(x) \neq 0 \tag{23}$$

(b) Linear continuous feedback:

By choosing $u_{i_N}(x) = -\beta_i\ S_i(x)$ where ($\beta_i > 0$) as the discontinuous function, the sufficient condition for sliding mode according to the following equation is satisfied. In more general cases, the discontinuous part of the control system can be considered as a combination of the first and second cases.

$$S_i\dot{S}_i = -\beta_i S_i^2(x) < 0 \tag{24}$$

(c) Combination of the relay with a constant gain and linear continuous feedback

In general, the discontinuous control component can be considered as a combination of the first and second modes:

$$u_{i_N} = \begin{cases} -\alpha_i \,\mathrm{Sign}(S_i(x)) - \beta_i S_i(x), & S_i(x) \neq 0,\ \alpha_i > 0,\ \beta_i > 0 \\ 0, & S_i(x) = 0 \end{cases} \tag{25}$$

With this choice, the sufficient condition for the discontinuous part of the control is satisfied because

$$S_i\dot{S}_i = -\alpha_i S_i(x)\, Sign(S_i(x)) - \beta_i S_i^2(x) < 0, \quad S_i(x) \neq 0 \tag{26}$$

Now, we denote the location of the control input in the fractional-order chaotic system:

$$\begin{cases} {}_0D_t^{q_1} x_1 = -x_1 + x_2 x_3 \\ {}_0D_t^{q_2} x_2 = -x_2 - x_1 x_3 + \gamma x_3 + u(t) \\ {}_0D_t^{q_3} x_3 = -\sigma(x_3 - x_2) \end{cases} \tag{27}$$

which $u(t)$ is the same as the combined control input. Since the sliding surface equation is defined based on the state variables according to Equation (19), the system converges to the desired state on the sliding surface.

The following equations hold on the sliding surface:

$$\begin{cases} S = 0 \\ \dot{S} = 0 \end{cases} \tag{28}$$

To obtain the equivalent control law, it suffices to substitute $\dot{S} = 0$:

$$\dot{S} =_0 D_t^{q_2} x_2 = -x_2 - x_1 x_3 + \gamma x_3 + u_{\mathrm{eq}}(t) = 0 \tag{29}$$

The equivalent control law $u_{eq}(t)$ is obtained as follows:

$$u_{\mathrm{eq}}(t) = -\left(-x_2 - x_1 x_3 + \gamma x_3\right) \tag{30}$$

Now, considering the Lyapunov candidate function as a positive definite function, we have the following:

$$V = \tfrac{1}{2} S^2 > 0 \tag{31}$$

For asymptotic stability, the derivative of this function must be negative definite:

$$\dot{V} = S\dot{S} < 0 \tag{32}$$

This is a proposed candidate for the switching control law to satisfy Equation (32), and based on Equation (23), it is given by:

$$u_N = -\beta\, Sign(S(x)) - \alpha\, S(x) \tag{33}$$

where α and β are positive real values. By combining Equations (30) and (33) and substituting into Equation (20), the general sliding mode control law for regulating the state variables of a typical BLDC system is obtained:

$$u(t) = x_2 + x_1 x_3 - \gamma x_3 - \beta\, Sign(S(x)) - \alpha\, S(x) \tag{34}$$

4. Simulation and comparative analysis

4.1. Numerical implementation of the proposed controller

Considering the parameter vector in the form of homogeneous orders $(\boldsymbol{\mu, \gamma, \sigma}) = \mathbf{(1,\ 20,\ 5.46)}$, we model the system as $\boldsymbol{q_1 = q_2 = q_3 = 0.995}$ and $\boldsymbol{T_{sim} = 50}$ **sec**. We set the time constant $\boldsymbol{h = 0.005}$ and initial conditions as $(\boldsymbol{x_1(0), x_2(0), x_3(0)}) = \mathbf{(5,\ 5, 5)}$. With the switching gain $\boldsymbol{k = 5}$ and based on the sliding mode control input, we design a relation (32) and implement it in MATLAB software. By plotting the phase trajectories $(\dot{\boldsymbol{x}} - \boldsymbol{x})$ for the reference currents $(\boldsymbol{d} - \boldsymbol{q})$ of the electric motor and the rotor angular speed $(\boldsymbol{\omega})$ in both uncontrolled and controlled states, we illustrate the system behavior in a single diagram. Similarly, we plot the previously separately drawn parametric diagrams for uncontrolled and controlled states.[28]

Figure 7 shows that the state variables and their rates of change have converged well to the zero set point. This indicates that the FO-SMC has effectively regulated the state variables of the BLDC system to the desired zero set point.

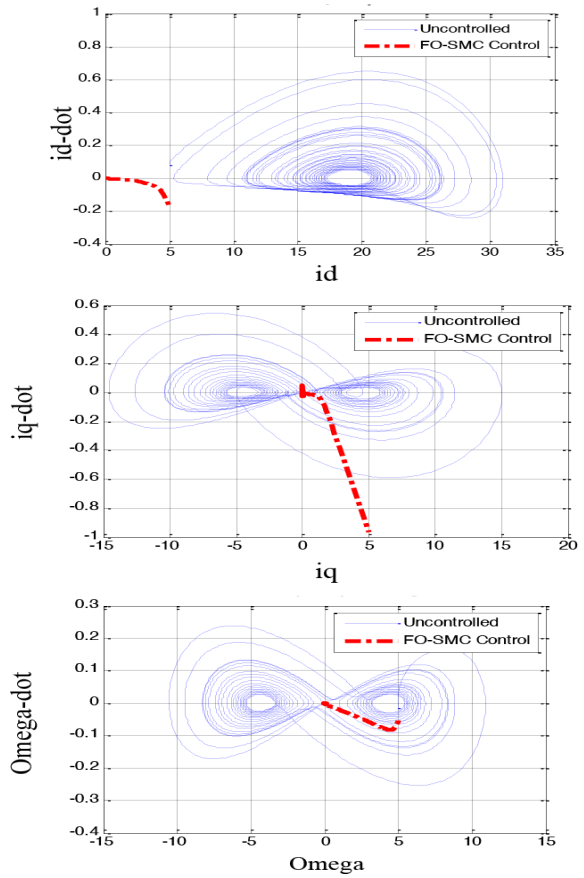


Figure 7. Phase plane diagram of state x_1, x_2, and x_3
Abbreviation: FO-SMC, fractional-order sliding mode controllers

Similar to before, we consider the system in the form of homogeneous orders with respect to the parameter vector $(\mu,\ \gamma,\ \sigma) = (1,\ 20,\ 5.46)$, we model the system as $q_1 = q_2 = q_3 = 0.995$ and $T_{sim} = 6\ sec.$ The time constant is $h = 0.005$, and the initial conditions are defined as $(x_1(0),\ x_2(0), x_3(0)) = (5,\ 5, 5)$. With the switching gain $k = 5$, we design relation (34) based on the sliding mode control input using the signum function and implement it in MATLAB software to plot the state trajectories, rates of change of the states, control input, and the sliding surface of the proposed method. We then compare the proposed method with conventional sliding mode control, which is applied to the system with the standard derivative, to determine the advantages of the proposed method.

Based on Figure 8, it can be observed that in the conventional sliding mode control strategy, the current i_d experiences a large overshoot at the beginning of the time, which may lead the system to saturation. On the other hand, based on this figure, it can be seen that the current i_q exhibits frequency oscillations over time in the conventional SMC strategy, which lowers the system performance, while the proposed method is completely smooth.

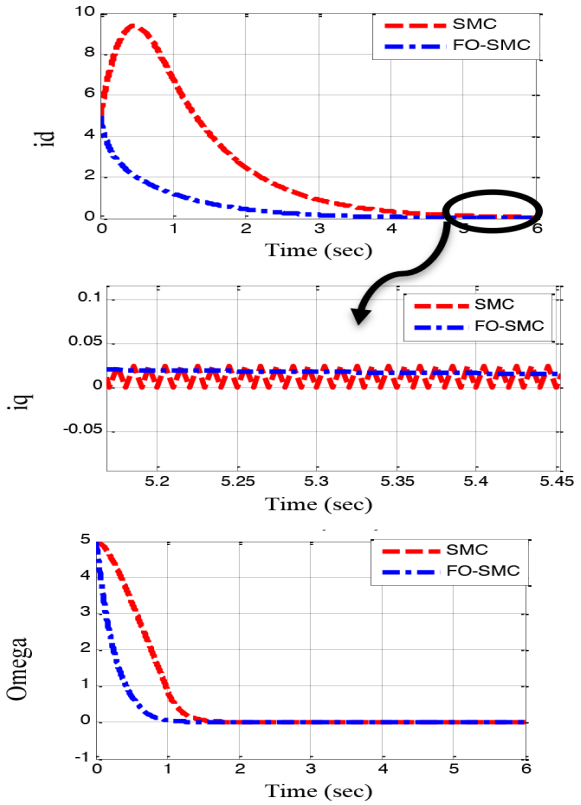


Figure 8. State trajectories regulation of i_d, i_q and Omega variables in the fractional-order brushless direct current system using the FO-SMC signal
Abbreviations: FO-SMC, fractional-order sliding mode controllers; SMC, sliding mode controller

As shown in Figure 9, the superiority of the proposed method is somewhat evident. Based on this figure, it is apparent that the proposed FO-SMC strategy for the FO-BLDC system requires much higher initial energy control, but this range limitation can be addressed by implementing a limiter if necessary.

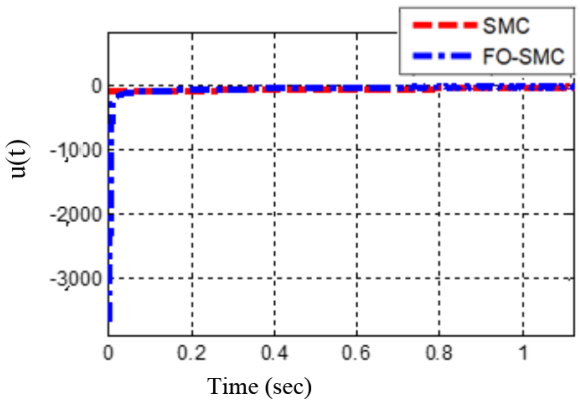


Figure 9. Control effort for state regulation of chaotic fractional-order BLDC system
Abbreviations: BLDC, brushless direct control; FO-SMC, fractional-order sliding mode controllers; SMC, sliding mode controller

Figure 10 illustrates the sliding surface used for state regulation of a chaotic FO-BLDC system. In this paper, the sliding surface is used to regulate the state of the BLDC system, which is known to exhibit chaotic behavior under certain conditions. By carefully designing the sliding surface, it is possible to control the system's dynamics and suppress chaotic behavior, leading to more predictable and stable operation. This is particularly important for practical applications of BLDC systems, where precise control over motor behavior is essential.

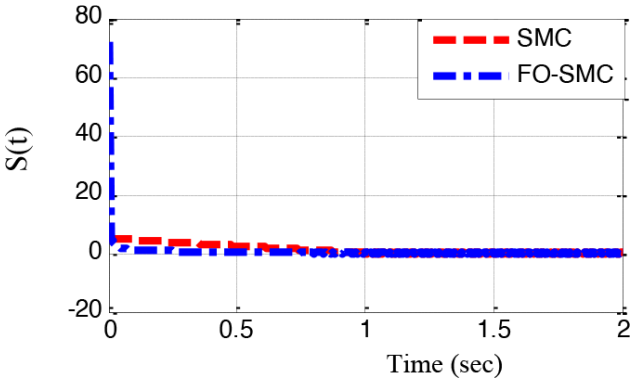


Figure 10. Sliding surface for state regulation of chaotic fractional-order BLDC system
Abbreviations: BLDC, Brushless direct control; FO-SMC, Fractional-order sliding mode controllers; SMC, Sliding mode controller

In Figure 11, which depicts the state rate trajectories of variable i_q, high-frequency oscillations can be observed in the rate of change of the second state variable when using the SMC method. However, this issue does not appear in the proposed method. The state rate trajectories of the variable i_q are important indicators of the behavior of the BLDC system, and the presence of high-frequency oscillations can negatively impact the system's performance and stability. The proposed method appears to provide a more effective means of regulating the state rates, resulting in smoother and more stable behavior of the BLDC system.

The analysis of Figures 10 and 11 demonstrates the effectiveness of the proposed FO-SMC in stabilizing the chaotic BLDC system while mitigating the adverse effects of external disturbances and parameter uncertainties. The sliding surface in Figure 10 ensures convergence of the state of the system by satisfying the Lyapunov stability criterion, thereby suppressing chaotic oscillations and enhancing the robustness. Compared to conventional SMC, the fractional-order approach significantly reduces high-frequency oscillations and chattering, leading to a smoother and more stable system response.

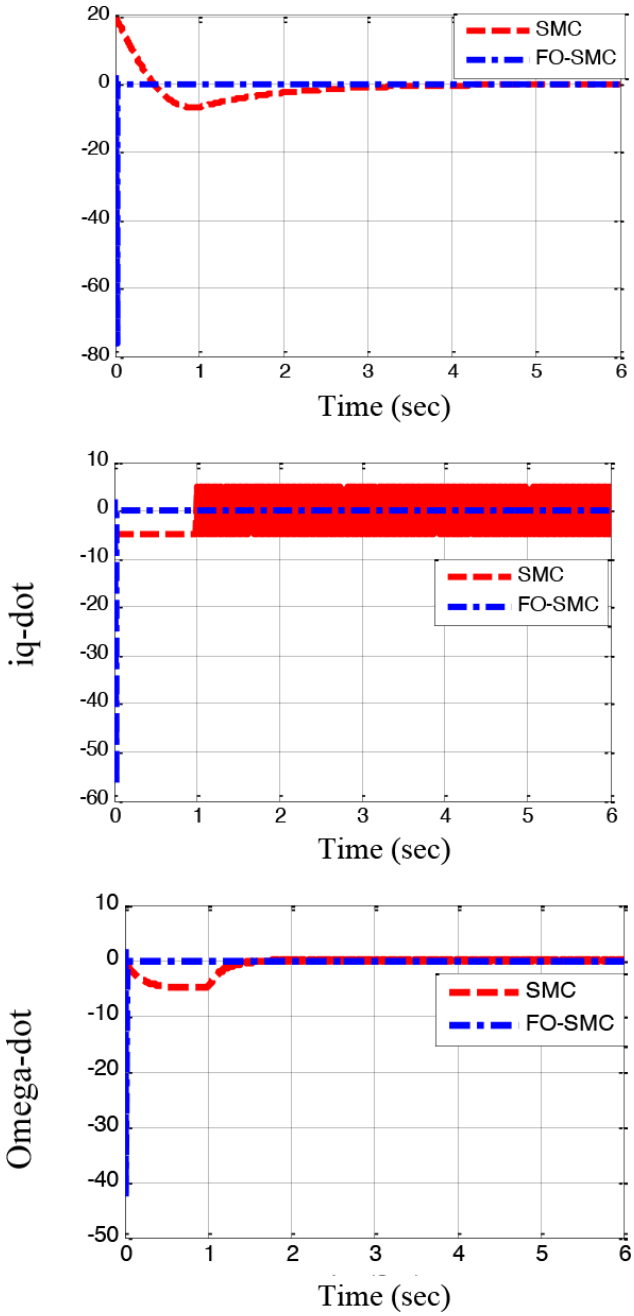


Figure 11. State rate trajectories regulation of variables i_d , i_q, and Omega in a fractional-order BLDC system using a fractional-order sliding mode control signal
Abbreviations: BLDC, brushless direct control; FO-SMC, fractional-order sliding mode controllers; SMC, Sliding mode controller

Additionally, Figure 8 highlights the improved regulation of state rate trajectories, showing that the FO-SMC strategy effectively minimizes fluctuations ini_d , i_q and *Omega*. This reduction in oscillations enhances the overall performance of the BLDC system by preventing excessive energy consumption and mechanical wear. Moreover, the method strongly resists uncertainties and external perturbations, ensuring reliable operation under practical conditions. These results confirm

that the proposed FO-SMC strategy outperforms conventional SMC, offering superior stability, robustness, and adaptability in controlling chaotic FO-BLDC systems.

To evaluate the performance of the controllers used in this paper, we use the following error metrics, which are the average sum of absolute errors:

$$\begin{cases} E_x = \dfrac{1}{T}\displaystyle\int_{T_0}^{T} \left(|e_{x_1}| + |e_{x_2}| + |e_{x_3}|\right) dt \\ E_{x-dot} = \dfrac{1}{T}\displaystyle\int_{T_0}^{T} \left(|e_{x_1-dot}| + |e_{x_2-dot}| + |e_{x_3-dot}|\right) dt \end{cases} \tag{35}$$

where $e_{x_1} = x_{1d} - x_1$, $e_{x_1-dot} = \dot{x}_{1d} - \dot{x}_1$, and $T = T_s.t_f$.

In Table 1, which presents the quantitative comparison of these two control methods, it can be observed that by calculating the average sum of absolute errors, the state regulation errors are somewhat close to each other, but there is a significant difference in the rate of change of state regulation errors, indicating the advantage and value of the proposed FO-SMC method.

4.2. Performance evaluation under parameter uncertainties and external disturbances

The FO-BLDC system with uncertainties and external disturbances is represented by Equation (36):

$$\begin{cases} {}_0D_t^{q_1} x_1 = -x_1 + x_2 x_3 \\ {}_0D_t^{q_2} x_2 = -x_2 - x_1 x_3 + \gamma x_3 + u(t) + \Delta g(x_1, x_2, x_3) + d(t) \\ {}_0D_t^{q_3} x_3 = -\sigma(x_3 - x_2) \end{cases} \tag{36}$$

where $\Delta g\,(x_1, x_2, x_3)$ refers to parameter uncertainties, and $d(t)$ refers to external disturbances. We aimed to observe the behavior and resistance of the system in response to these changes by applying them as inputs to the system. Moreover, these sentences are considered as the following equations:[10]

$$\begin{cases} \Delta g(x_1, x_2, x_3) = 10.75 \sin\left(10 x_1(t) \cos\left(3 x_2(t) \cos(\pi x_3(t)\right)\right) \\ d(t) = 5.25 \cos(2 x_2(t)) + 8.5 \sin(3t) \end{cases} \tag{37}$$

Now, similar to before, we consider the parameter vector as $(\mu,\ \gamma,\ \sigma) = (1,\ 20,\ 5.46)$, the homogeneous orders of the system as $q_1 = q_2 = q_3 = 0.995$, and $T_{sim} = 6$ sec. The time constant is $h = 0.005$, and the initial conditions as $(x_1(0),\ x_2(0), x_3(0)) = (5,\ 5, 5)$. A switching gain of $k = 5$ is used, and relation (32) is designed using the sign function based on the sliding mode control input. Its implementation in MATLAB software is used to plot the state paths, the state change rate, the control input, and the sliding surface of the proposed method. A comparison is made with normal sliding mode control, which is naturally applied to the normal derivative system, to determine the advantages of the proposed method.

Observing Figure 12, it becomes apparent that the conventional sliding mode strategy results in a significant overshoot in the current i_d at the beginning of the period, which may cause the system to become saturated. Additionally, it can be observed that the current i_q in the conventional sliding mode strategy exhibits irregular, frequency-based oscillations over time, which reduces the system's overall performance quality. In contrast, the proposed method results in a completely smooth behavior. Therefore, the performance of the proposed method is more desirable. Furthermore, the Omega plot indicates that the superiority of the proposed method is evident, as it exhibits better convergence speed and fewer oscillations.

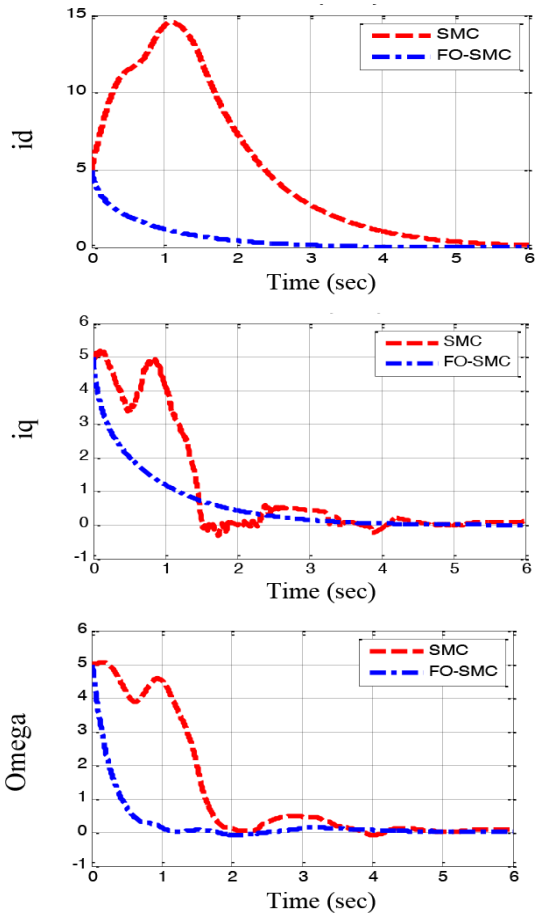


Figure 12. State trajectories regulation of i_d, i_q, and Omega variables in fractional-order BLDC system using FO-SMC signal in the presence of parameter uncertainties and external disturbances
Abbreviations: BLDC, brushless direct control; FO-SMC, fractional-order sliding mode controllers; SMC, sliding mode controller

Table 1. The average sum of absolute errors for state and rate of change of state regulation for fractional-order sliding mode control and conventional sliding mode control

The average sum of absolute errors.	**State regulation error** (E_x)	**Rate of change of state regulation error** (E_{x-dot})
SMC	7.2701	9.2106
FO-SMC	3.4487	0.1598

Abbreviations: FO-SMC, fractional-order sliding mode controllers; SMC, sliding mode controller.

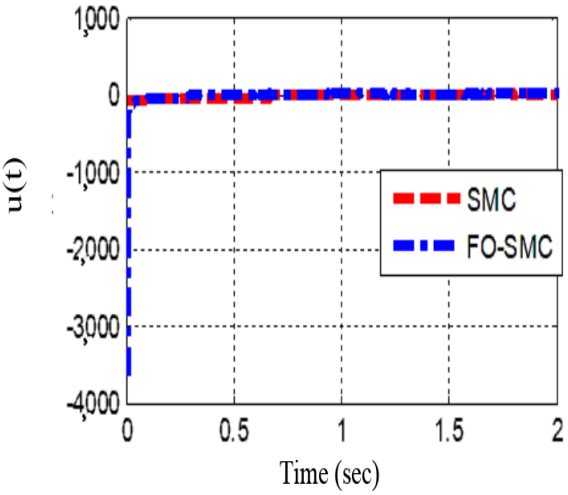


Figure 13. Effort for state regulation of fractional-order chaotic BLDC system in the presence of parameter uncertainties and external disturbances Abbreviations: BLDC, brushless direct control; FO-SMC, fractional-order sliding mode controllers; SMC, sliding mode controller

According to Figure 13, it is clear that the proposed FO-SMC method for the FO-BLDC system requires higher initial energy for control, which, of course, imposes limitations on this method. However, if necessary, this limitation can be constrained by using a limiter on the energy.

Figure 14 illustrates the behavior of the sliding surface in the presence of parametric uncertainties and external disturbances, emphasizing the robustness of the proposed FO-SMC. The sliding surface is a crucial element in control theory, playing a key role in stabilizing the chaotic FO-BLDC system under uncertain conditions. Unlike conventional SMC, which suffers from significant fluctuations and delayed convergence in the presence of uncertainties, the fractional-order sliding surface effectively reduces oscillations and accelerates state stabilization. This enhanced performance is due to the memory effect of fractional calculus, which improves system adaptability and ensures smoother control actions. By mitigating instability and enhancing robustness, the FO-SMC approach provides a more stable and efficient control strategy, making it highly suitable for real-world applications where uncertainties and disturbances are inevitable.

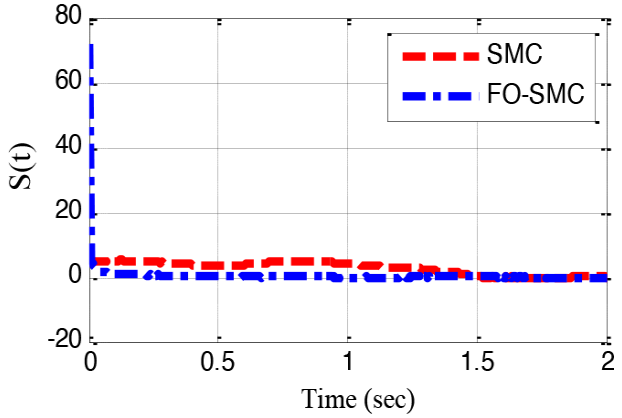


Figure 14. Sliding surface for state regulation of a fractional-order chaotic BLDC system in the presence of parameter uncertainties and external disturbances Abbreviations: BLDC, brushless direct control; FO-SMC, fractional-order sliding mode controllers; SMC, sliding mode controller

As seen in Figure 15, the proposed method achieves negligible convergence time and convergence error, unlike the conventional SMC method, in which the convergence of the sliding surface is undesirable. This highlights the superiority of the proposed method in providing more stable and predictable control of the BLDC system, even in the presence of parameter uncertainties and external disturbances. This figure illustrates the state rate trajectories of a BLDC system under the sliding mode control method and the proposed method. In the sliding mode control method, significant oscillations are observed in the rate of change of the first state variable $(i_d - dot)$, which can negatively affect the current regulation of the system. However, this issue is not present in the proposed method. In addition, as shown in this figure, high-frequency oscillations and significant changes in the amplitude of the rate of change of the second state variable $(i_q - dot)$ occur generated under the SMC method, which can be destructive for the current regulation of the system. However, these issues are not present in the proposed method. Furthermore, it is observed that relatively high-amplitude

oscillations with significant changes in the rate of change of the third state variable($Omega - dot$) over time occur under the sliding mode control method, which can be destructive for the frequency regulation of the system. However, these issues are not present in the proposed method. These observations highlight the superiority of the proposed method in regulating the state rates of the BLDC system with smoother and more stable behavior compared to the sliding mode control method.

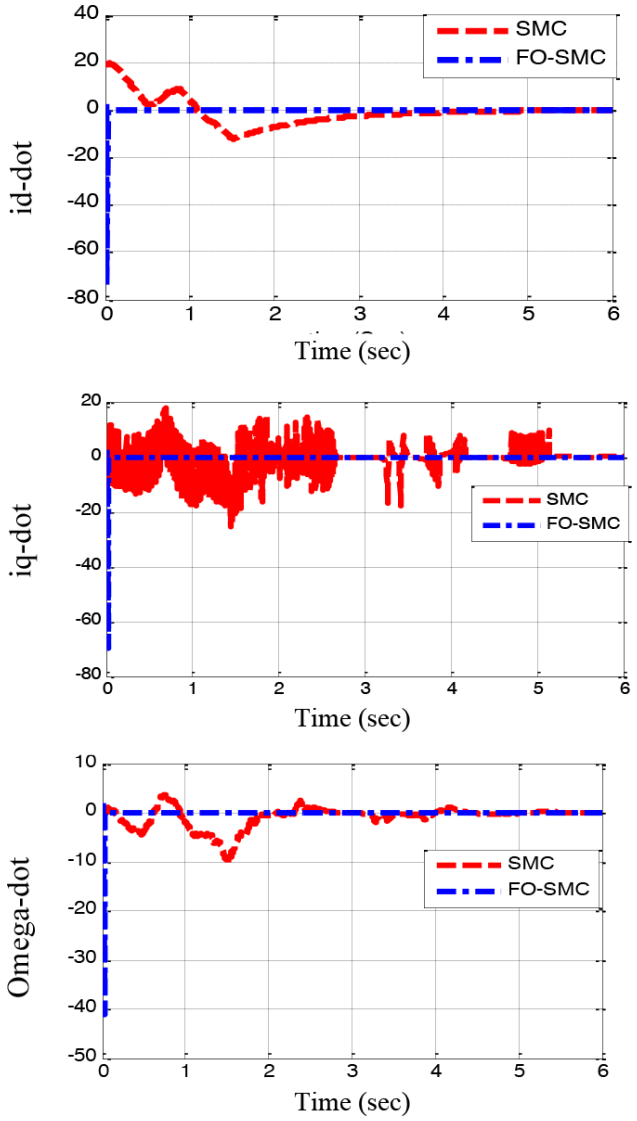


Figure 15. State rate trajectory regulation of variables i_d , i_q, and $Omega$ in the FO-BLDC system using the FO-SMC signal in the presence of parameter uncertainties and external disturbances. Abbreviations: BLDC, brushless direct control; FO-SMC, fractional-order sliding mode controllers; SMC, Sliding mode controller

In Table 2, which presents the quantitative comparison of these two control methods in the presence of parameter uncertainties and external disturbances, it is observed that the average sum of absolute error values indicates a significant increase in the state regulation error in the conventional SMC method compared to Table 1, while this increase is only 0.05 in the proposed method. In the section on the rate of change in the state regulation error, the state regulation error value in the conventional SMC method has increased by one unit compared to Table 1, while this increase is only 0.007 in the proposed method. This demonstrates the significant advantage and resistance of the proposed FO-SMC method compared to the already robust conventional sliding mode method, which is itself preferable to, for example, the PID method.

In general, the superiority of SMC over PID and FO-SMC over FOPID in controlling chaotic BLDC motor systems can be justified based on several critical performance factors. SMC provides robust control under parameter uncertainties and external disturbances, ensuring stable operation where PID controllers require continuous tuning and struggle with nonlinearities inherent in BLDC motors. Additionally, SMC guarantees finite-time convergence, whereas PID controllers only achieve asymptotic stability, often resulting in longer settling times and susceptibility to steady-state errors.

On the other hand, FO-SMC further improves upon SMC by reducing the chattering effect, which is a major issue in conventional sliding mode controllers. The fractional-order nature of FO-SMC introduces memory effects, offering greater flexibility in parameter tuning and enhanced adaptability to system variations. This results in a smoother control action and improved dynamic response compared to FOPID, which, despite its fractional-order terms, still relies on PID-based tuning strategies that can be computationally expensive and sensitive to high-frequency oscillations.

The comparative analysis confirms that FO-SMC is the most effective approach for chaotic BLDC motor control, as it provides higher stability, faster response times, and greater resilience to uncertainties compared to the other methods. These advantages make FO-SMC a superior choice for real-world BLDC applications requiring precise control, reduced energy consumption, and improved system reliability.

The simulation results presented in Figures 12 and 13 demonstrate the superiority of FO-SMC over conventional SMC in handling uncertainties. The conventional SMC exhibits significant overshoot and irregular oscillations in the controlled variables id, iq, and Omega, which

Table 2. The average sum of absolute errors for state and rate of change of state regulation for fractional-order sliding mode control and conventional sliding mode control in the presence of parameter uncertainties and external disturbances

The average sum of absolute errors.	**State regulation error** (E_x)	**Rate of change of state regulation error** (E_{x-dot})
SMC	7.2701	9.2106
FO-SMC	3.4487	0.1598

Abbreviations: FO-SMC, fractional-order sliding mode controllers; SMC, sliding mode controller.

may lead to performance degradation and excessive energy consumption. Conversely, FO-SMC achieves a more stable state trajectory, effectively suppressing oscillations and ensuring faster convergence to the desired operating point. This is attributed to the fractional-order terms, which introduce an additional degree of freedom, enabling the controller to adapt dynamically to variations in system parameters.

Additionally, Figures 14 and 15 further validate the enhanced stability and robustness of FO-SMC in regulating the sliding surface and state rate trajectories under uncertain conditions. The sliding surface in FO-SMC converges significantly faster than conventional SMC, ensuring improved tracking accuracy and predictable system behavior. Moreover, Table 2 quantitatively confirms the advantage of FO-SMC, with a notable reduction in the state regulation error (from 7.2701 in SMC to 3.4487 in FO-SMC) and a drastic decrease in the rate of change of state regulation error (from 9.2106 in SMC to 0.1598 in FO-SMC). These results highlight the robustness of the FO-SMC, proving that it reduces steady-state error, and ensure smoother transient response and lower energy consumption in the presence of disturbances.

5. Conclusion

One of the key challenges in nonlinear control systems, particularly in BLDC motors, is their susceptibility to parameter uncertainties and external disturbances. Traditional SMC techniques, while offering strong robustness, tend to suffer from high-frequency oscillations (chattering) and degraded performance when exposed to uncertainties. In contrast, FO-SMC leverages the memory effect of fractional calculus to provide a smoother control response while maintaining strong disturbance rejection capabilities. In this study, a FO-SMC was designed to regulate the chaotic behavior of a FO-BLDC system. The system was effectively driven toward its equilibrium point by carefully selecting an appropriate sliding surface and a suitable control input, mitigating chaotic oscillations.

Sliding mode control is widely recognized for its robustness against uncertainties and external disturbances, making it a preferred choice for nonlinear systems. However, a major drawback of conventional SMC is the chattering phenomenon, particularly in high-speed dynamic systems. Our analysis revealed that while SMC successfully stabilized the system in finite time, it also introduced significant fluctuations in x_1 and x_1-dot states. To address this limitation, FO-SMC was implemented, leading to a smoother system response and reduced state oscillations. Additionally, FO-SMC improved system adaptability and enhanced resistance to uncertainties and disturbances.

The superiority of FO-SMC over conventional SMC was demonstrated through both qualitative (graphical) and quantitative (Tables 1 and 2) comparisons. The key advantages of the proposed approach are summarized as follows:

- Fractional-order integration enhances stability: Transforming the system into a fractional-order framework inherently introduces a fractional-order integration operation, which helps reduce system errors and improves stability.
- Innovative hybrid control strategy: Unlike conventional methods, the proposed FO-SMC approach integrates a linear continuous term alongside relay control (as described in Equation (32)), resulting in smoother control behavior and significantly reducing chattering effects.
- Improved adaptability and robustness: Leveraging fractional-order dynamics in the controller significantly enhances the system's adaptability while increasing its resilience to parameter uncertainties and external disturbances.

These findings highlight the effectiveness of fractional-order control methodologies in suppressing chaotic behaviors, ensuring smooth operation, and enhancing the robustness of nonlinear systems. The proposed FO-SMC framework

presents a viable solution for improving stability, efficiency, and control precision in practical BLDC motor applications.

Acknowledgments

None.

Funding

None.

Conflict of interest

The authors declare they have no competing interests.

Author contributions

Conceptualization: Amin Kaveh, Mohammad Vahedi
Formal analysis: Mohammad Vahedi, Majid Gandomkar
Investigation: Amin Kaveh
Methodology: Mohammad Vahedi
Writing – original draft: Amin Kaveh
Writing – review & editing: Mohammad Vahedi, Majid Gandomkar

Availability of data

All data is presented in this paper.

References

1. Xia C. *Permanent Magnet Brushless DC Motor Drives and Controls*. John Wiley & Sons; 2012.
2. Jabbar MA, Phyu HN, Liu Z, Bi C. Modeling and numerical simulation of a brushless permanent-magnet DC motor in dynamic conditions by time-stepping technique. *IEEE Trans Ind Appl.* 2004;40(3):763-770. https://doi.org/10.1109/TIA.2004.826330.
3. Qi G. Energy cycle of brushless DC motor chaotic system. *Appl Math Model.* 2017;51:686-697. https://doi.org/10.1016/j.apm.2017.06.001.
4. Utkin VI. *Sliding Modes in Control and Optimization*. Springer; 1992.
5. DeCarlo RA, Zak SH, Matthews GP. Variable structure control of nonlinear multivariable systems: a tutorial. *Proc IEEE.* 1998;76(3):212-232. https://doi.org/10.1109/5.2070.
6. Zhou P, Bai R, Zheng JM. Stabilization of a fractional-order Chaotic brushless DC Motor via a Single Input. *Nonlinear Dyn.* 2015;(82):519-525. https://doi.org/10.1007/s11071-015-2452-2.
7. Li S, Li P, Zheng Z, Huang T. Fractional order sliding mode control for circulating current suppressing of MMC. *Electr Eng.* 2023;105(6):3791-3800. https://doi.org/10.1007/s00202-023-01902-7.
8. Petras I. *Fractional-Order Nonlinear Systems: Modeling, Analysis, and Simulation*. Springer; 2011.
9. Hilfer R. *Applications of Fractional Calculus in Physics*. World Scientific Pub. Co.; 2000.
10. Shahzad M. Chaos control in three dimensional cancer model by state space exact linearization based on Lie Algebra. *Int J Eng Technol.* 2016;4(33):1-11. https://doi.org/10.14419/ijet.v4i3.6129.
11. Xue G, Lin F, Qin B. Adaptive neural network control of chaotic fractional order permanent magnet synchronous motors using backstepping technique. *Front Phys.* 2020;8:12. https://doi.org/10.3389/fphy.2020.
12. Ge Z, Lin G. The complete, lag and anticipated synchronization of a BLDCM chaotic system. *Chaos, Solitons & Fractals.* 2007;34:740-764. https://doi.org/10.1016/j.chaos.2006.05.057.
13. Hemati N. Strange attractors in brushless DC motors. *IEEE Trans Circuits Syst I Fundam Theory Appl.* 1994;41(1):40-45. https://doi.org/10.1109/81.265867.
14. Ye S, Chau KT. Chaotization of DC motors for industrial mixing. *IEEE Trans Ind Electron.* 2007;54:2024-2032. https://doi.org/10.1109/TIE.2007.903252.
15. Reyes R, Cruz C, Nakano-Miyatake M, Perez-Meana H. Digital video watermarking in DWT domain using chaotic mixtures. *IEEE Lat Am Trans.* 2010;8:304-310. https://doi.org/10.1109/TLA.2010.5438444.
16. Rajagopal K, Vaidhyanathan S, Karthikeyan A, Duraisamy P. Dynamic analysis and chaos suppression in a fractional order brushless DC motor. *Electr Eng.* 2016;99:721-733. https://doi.org/10.1007/978-3-319-32273-5_2.
17. Sun LX, Lu S, Wen ZG, Li YF. Analysis of chaotic motion mechanism of permanent magnet synchronous motors. *Electr Mach Control.* 2019;23(3):97-104. https://doi.org/10.16383/j.aemc.2019.3.001.
18. Wu S, Zhang JA. Terminal sliding mode observer based robust backstepping sensorless speed control for interior permanent magnet synchronous motor. *Int J Control Autom Syst.* 2018;16(6):2743-2753. https://doi.org/10.1007/s12555-016-0782-x.
19. Tang C, Bai L, Zhang G, Yang J, Li T. Robust guaranteed cost control of PMSM chaotic system with uncertain parameters. *J Eng Sci Technol Rev.* 2020;13(3):181-190. https://doi.org/10.25103/jestr.133.01.
20. Yu X, Zhang C. Robust fractional-order PID control for chaotic systems. *Nonlinear Dyn.* 2021;103(2):1123-1140. http://dx.doi.org/10.2139/ssrn.5162779.
21. Kumar R, Singh M. Comparative study of PID, FOPID, and sliding mode control for uncertain systems. *IEEE Access.* 2020;8: 76523-76535. https://doi.org/10.31763/ijrcs.v5i1.1764.

22. Mendel JM. *Uncertain Rule-Based Fuzzy Logic Systems: Introduction and New Directions.* Springer; 2017. https://doi.org/10.1109/MCI.2007.357196.
23. El-Bardini M, El-Nagar AM. Interval Type-2 Fuzzy Control Design for Uncertain Nonlinear Systems. *ISA Trans.* 2014; 53(3):732-743. https://doi.org/10.1016/j.isatra.2014.02.007.
24. Huerta-Moro S, Tavizón-Aldama JD, Tlelo-Cuautle E. FPGA implementation of sliding mode control and proportional-integral-derivative controllers for a DC–DC buck converter. *Technologies.* 2024;12(10):184. https://doi.org/10.3390/technologies12100184.
25. Roy P, Ray S, Bhattacharya S. Control of chaos in brushless DC motor design of adaptive controller following back-stepping method. In: *International Conference on Control, Instrumentation, Energy & Communication (CIEC)* ; 2014. https://doi.org/10.1109/CIEC.2014.107.
26. Patra A, Chakrabarty K, Nag T. Control of Chaos in BLDC Motor Drive. In: *Proceedings of IEEE, Applied Signal Processing Conference (ASPCON)*; 2018. https://doi.org/10.1109/ASPCON.2018.8605733.
27. Yaz M, Cetin E. Brushless Direct Current Motor Design and Analysis. *COJ Electronics & Communications*; 2021. https://doi.org/10.31031/COJEC.2021.05.000602.
28. Hung JY, Gao W, Hung JC. Variable structure control: a survey. *Procs of the IEEE.* 1993;40(1):2-20. https://doi.org/10.1109/5.210201.
29. Xue G, Lin F, Qin B. Adaptive neural network control of chaotic fractional order permanent magnet synchronous motors using backstepping technique. *Front Phys.* 2020;8. https://doi.org/10.3389/fphy.2020.00062.

Amin Kaveh *received his Bachelor's degree in Electrical Engineering and Telecommunications from the Islamic Azad University, Najaf Abad Branch in Iran, in 2006 and his Master's degree from Khomeini Shahr University in Iran in 2012. He has been a Ph.D. candidate in Electrical Engineering and Control at the Islamic Azad University, Saveh Branch in Iran, since 2015. Currently, he is working as a researcher in the field of control engineering, focusing on nonlinear system control.*
http://orcid.org/0009-0000-6720-2510

Mohammad Vahedi *received his Bachelor's degree from Amirkabir University of Technology in Iran in 2004 and his Master's degree from Shiraz University in Iran in 2007. He then obtained his Ph.D. in Mechanical Engineering from Iran University of Science and Technology in 2014. He is currently an assistant professor and faculty member at the Islamic Azad University in Iran. His research interests include control of nonlinear systems, robotics, and intelligent control.*
http://orcid.org/0000-0003-1834-8577

Majid Gandomkar *is an Associated Professor in the University of Islamic Azad University, Saveh, Iran.*
https://orcid.org/0000-0001-6199-1483

An International Journal of Optimization and Control: Theories & Applications
(https://accscience.com/journal/ijocta)



This work is licensed under a Creative Commons Attribution 4.0 International License. The authors retain ownership of the copyright for their article, but they allow anyone to download, reuse, reprint, modify, distribute, and/or copy articles in IJOCTA, so long as the original authors and source are credited. To see the complete license contents, please visit http://creativecommons.org/licenses/by/4.0/.

An International Journal of Optimization and Control: Theories & Applications
ISSN: 2146-0957 eISSN: 2146-5703
Vol.15, No.3, pp.396-406 (2025)
https://doi.org/10.36922/IJOCTA025090036

RESEARCH ARTICLE

Using infinitesimal symmetries for determining the first Maxwell time of geometric control problem on SH(2)

Soukaina Ezzeroual* and Brahim Sadik

Department of Mathematics, Cadi Ayyad University, Faculty of Sciences Semlalia, Marrakesh, Morocco
s.ezzeroual.ced@uca.ac.ma, sadik@uca.ac.ma

ARTICLE INFO

Article History:
Received: February 25, 2025
Revised: April 1, 2025
Accepted: April 14, 2025
Published Online: April 29, 2025

Keywords:
Geometric control theory
Lie algebra
Maxwell time
Special hyperbolic group
Sub-Riemannian geometry

AMS Classification 2010:
93C85; 17B66; 53C17; 22E60; 53C22

ABSTRACT

In this work, we utilize infinitesimal symmetries to compute Maxwell points which play a crucial role in studying sub-Riemannian control problems. By examining the infinitesimal symmetries of the geometric control problem on the SH(2) group, particularly through its Lie algebraic structure, we identify invariant quantities and constraints that streamline the Maxwell point computation.

CC BY

1. Introduction

Describing locally optimal trajectories is crucial in dynamical systems, control theory, robotics, and other areas where precise motion control is necessary. In Sachkov,[1] Moiseev and Sachkov,[2] Sachkov,[3] several optimal control problems are investigated to determine optimal solutions and analyze the optimality of geodesics, specifically focusing on the first Maxwell time, which indicates how long a geodesic trajectory remains optimal. For more details on sub-riemannian geometry and geometric control theory, we refer the reader to Sachkov[1] and Agrachev et al.[4]

An optimal control problem concerns finding controls that steer the studied system from one state to another while minimizing certain quantities, often related to energy or time. A simple and interesting example is the geometric control problem on the Lie group SH(2) that involves controlling a system whose state space is the special Euclidean group in two dimensions. In Butt,[5] the author makes significant contributions to this problem by presenting optimal solutions derived using Pontryagin's maximum principle (PMP). Additionally, the author analyzes the discrete symmetries of this problem to understand the optimality of geodesics.

Infinitesimal symmetries are transformations that leave the fundamental equations of a system invariant. They are also powerful tools for studying problems in theoretical physics and dynamic systems, providing insight into conserved quantities and invariant structures within a system. By studying the Lie algebra of these symmetries, we can often derive conserved quantities that serve in the computation of some properties of some control systems.

In this work, we extend the analysis presented in Butt[5] by considering a control problem primarily addressed through geometric methods. We build upon both algebraic and geometric techniques Gallier and Quaintance[6] to further investigate this problem. First, we compute the infinitesimal symmetries of the sub-Riemannian problem and then apply these results to the geometric control problem on the Lie group SH(2), whose

*Corresponding Author

Lie algebra is non-nilpotent and solvable. Rather than relying on nilpotent approximations, which have been used in previous works by Hrdina and Zalabov´,[7] we directly compute the infinitesimal symmetries. This approach enhances the accuracy of calculating the first Maxwell time and avoids potential errors associated with nilpotent approximations.

Additionally, in Agrachev and Barilari,[8] the authors classify all sub-Riemannian structures on three-dimensional Lie groups using basic differential invariants. Our study, therefore, highlights the significance of the sub-Riemannian problem on the SH(2) group, as it plays a crucial role in the broader context of three-dimensional Lie groups. We focus on the motion of a unicycle, a classical problem in geometric mechanics. These concepts can also be adjusted for use in other nonholonomic mechanical systems; see Jean,[9] Hill and Nurowski,[10] Hermans,[11] Bloch.[12]

Moreover, deep learning techniques (see Mao et al.,[13] Peng et al.[14]) have shown their potential in optimizing complex dynamical systems. Such approaches could offer new perspectives for the analysis of sub-Riemannian structures and optimal control problems.

Sub-Riemannian geodesics are generally not optimal at all times. Each geodesic has a specific point where it ceases to be optimal. At this stage, the role of the infinitesimal symmetries of our problem on the group SH(2) becomes crucial. Using the Lie algebra of symmetries, we identify transformations that map a given geodesic to another geodesic. We show that there is a subgroup of symmetries isomorphic to the group SO(1, 2). Using this action, we determine the set of Maxwell points and, subsequently, the first Maxwell time corresponding to our infinitesimal symmetries. All of this is detailed in Section 4 of our main results.

2. Preliminaries on geometric control theory

In this section, we give some preliminaries on geometric control theory. For more details on the subject, see Agrachev et al.[4]

2.1. Controllability of control affine systems

A control affine system on a manifold M is any differential system of the form

$$\frac{dx}{dt} = X_0(x) + \sum_{i=1}^{m} u_i(t) X_i(x), \qquad (1)$$

where $X_0, X_1, \ldots, X_m$ are smooth vector fields on M and $u_i(t)$ are control inputs. Further details on control affine systems can be found in Jurdjevic.[15] Let $\mathcal{F}$ be a family of smooth vector fields on M, then the Lie algebra generated by $\mathcal{F}$ is the smallest Lie algebra that contains $\mathcal{F}$. It is obtained by considering all linear combinations of elements of $\mathcal{F}$, taking all Lie brackets of these, considering all linear combinations of these, and continuing so on. It will be denoted by $Lie(\mathcal{F})$ and its evaluation at any point $q \in M$ will be denoted by $Lie_q(\mathcal{F})$. The following result gives a necessary and sufficient condition for a driftless control affine system to be controllable.

Proposition 1. *(Jurdjevic[15]) The control affine system* $\frac{dx}{dt} = \sum_{i=1}^{m} u_i X_i(x)$ *with* $u = (u_1, \ldots, u_m) \in \mathbb{R}^m$ *is controllable if and only if* $Lie_q\mathcal{F} = T_qM$*, for all* $q \in M$.[1]

2.2. Sub-Riemannian problem and optimal solutions

Consider a sub-Riemannian manifold (M, Δ, g), where M is an n-dimensional smooth manifold, Δ is a smooth distribution of rank $k \leq n$, and g is a Riemannian metric on Δ; see Sachkov[1] for more details. The sub-Riemannian length of an admissible curve $\gamma(t)$, defined on $[0, t_1]$, is given by:

$$\ell(\gamma) = \int_0^{t_1} \sqrt{g_{\gamma(t)}(\dot\gamma(t), \dot\gamma(t))}\, dt.$$

Given two points q_0 and q_1 of M, the sub-Riemannian distance between q_0 and q_1 is stated by

$$d(q_0, q_1) = \inf\{\ell(\gamma) \mid \gamma \text{ admissible}, \\ \gamma(0) = q_0, \gamma(t_1) = q_1\}.$$

A sub-Riemannian problem is a control problem on a sub-Riemannian manifold (M, Δ, g) where one seek for admissible curves γ that satisfy the property $\ell(\gamma) = d(q(0), q(t_1))$. Suppose there exists a family of smooth vector fields $X_1, \ldots, X_k$ that forms an orthonormal frame on (Δ, g), i.e. $\forall q \in M$, $\Delta_q = span\{X_1(q), \ldots, X_k(q)\}$ and $g_q(X_i(q), X_j(q)) = \delta_{ij}$. Thus, sub-Riemannian minimizers (or optimal solutions) are the solutions of the following optimal control problem on M:

$$\dot x = \sum_{i=1}^{k} u_i X_i(x), \quad u = (u_1, ..., u_k) \in \mathbb{R}^k, \quad (2)$$

$$x(0) = q_0, \quad x(t_1) = q_1, \quad (3)$$

$$\ell = \int_0^{t_1} (\sum_{i=1}^{k} u_i^2)^{1/2} dt \longrightarrow \min. \quad (4)$$

[1]Here T_qM denotes the tangent space to M at the point q

If we add the condition $\sum_{i=1}^{k} u_i^2 \leq 1$, the system given by equations Equations(2)-(4), becomes:

$$\begin{aligned} &\dot{x} = \sum_{i=1}^{k} u_i X_i(x), \quad \sum_{i=1}^{k} u_i^2 \leq 1, \\ &x(0) = q_0, \quad x(t_1) = q_1, \\ &t_1 \to \min . \end{aligned} \tag{5}$$

By Filipov's theorem,[1] the existence of optimal solutions for the optimal control problem Equation (5), is guaranteed.

The Pontryagin Maximum Principle[4] provides necessary conditions for the optimality of trajectory solutions of sub-Riemannian control problems. Following this principle, we first compute trajectories, called extremals, of a dynamic system in the cotangent bundle of the variety M. Then the projections of the extremals on the state space M constitute the optimal solutions and are called geodesics. A point $\gamma(t_1)$ is called a Maxwell point along a geodesic γ if there exists another geodesic $\widetilde{\gamma} \not\equiv \gamma$ such that $\gamma(t_1) = \widetilde{\gamma}(t_1)$. This means that there exists a geodesic $\widehat{\gamma}$ coming to the point $q_1 = \gamma(t_1)$ earlier than γ.

3. Computing infinitesimal symmetries of a sub-Riemannian problem

Let (M, Δ, g) be a sub-Riemannian manifold, where M is endowed with a Lie group structure of dimension n that is left-invariant. This means that

$$\begin{aligned} \Delta_{ab} &= L_{a*}\Delta_b, \\ g_b(v, w) &= g_{ab}(L_{a*}v, L_{a*}w), \quad \forall a, b \in M. \end{aligned}$$

where L_{a*} denotes the differential of the left translation by a. We consider the sub-Riemannian system Equations(2)-(4) on the Lie group (M, Δ, g) and we assume it is controllable. Then $Lie_q\Delta = T_qM$ for every $q \in M$. Therefore,

$$\begin{aligned} Lie_q(\Delta) = \text{span}\{&X_1(q), \ldots, X_k(q), \\ &X_{k+1}(q), \ldots, X_n(q)\} \end{aligned} \tag{6}$$

for all $q \in M$, where Δ is given by the vector fields $X_1, \ldots, X_k$ and $X_{k+1}, \ldots, X_n \in Lie(\Delta)$. Furthermore, suppose the problem admits optimal solutions.

Definition 1. *(Agrachev and Barilari.[16]) Let M be a $2m+1$ dimensional manifold. A sub-Riemannian structure on M is said to be contact if Δ is a contact distribution, i.e. $\Delta = \ker\omega$, where $\omega \in \Lambda^1 M$ satisfies $(\bigwedge^m d\omega) \wedge \omega \neq 0$.*

By reference to Olver,[17] which provides us with an important result regarding the conditions that a symmetry vector must satisfy, we have that:

A vector v is a symmetry of our system if it satisfies the following two conditions:

$$\mathcal{L}_v(\Delta) \subset \Delta \quad \text{and} \quad \mathcal{L}_v(g) = 0. \tag{7}$$

where $\mathcal{L}$ denotes the Lie derivative. In what follows, we outline the necessary steps for computing the symmetry algebra of a system defined by Equations (2)-Eq.(4). We consider $\Delta = \{\Delta_q \subset T_qM \mid q \in M\}$, where $\Delta_q = \text{span}\{X_1(q), \ldots, X_k(q)\}$. Additionally, $\mathrm{g} = \sum_{\mathrm{i}=1}^{\mathrm{n}} \mathrm{a_i dq_i} \otimes \mathrm{dq_i}$, where a_i are some constants, represents a Riemannian metric such that $\mathrm{g(X_i, X_j)} = \delta_{\mathrm{ij}}$. Furtheremore, we suppose that Δ is a contact distribution, meaning that $\ker(\omega) = \Delta$, where $\omega \in \Lambda^1(M)$ is a 1-form in the manifold M. In terms of the local coordinates $q_1, \ldots, q_n$, the contact form can be written as $\omega = \sum_{i=1}^{n} e_i\, dq_i$, where e_i are scalar functions of the coordinates $q_1, \ldots, q_n$. An arbitrary vector field v can be expressed as $v = h_1(q_1, \ldots, q_n)X_1 + \ldots + h_n(q_1, \ldots, q_n)X_n$ and it is a symmetry vector if it satisfies the two preceding conditions Equation (7). We recall that in local coordinates, each X_j is of the form $X_j = \sum_{i=1}^{n} g_i^j \partial q_i$, where g_i^j are some scalar functions defined on M. Our approach begins by calculating $\mathcal{L}_v(X_1), \ldots, \mathcal{L}_v(X_k)$:

$$\begin{aligned} \mathcal{L}_v(X_j) &= [v, X_j] \\ &= [h_1X_1 + \ldots + h_nX_n, X_j] \\ &= -[X_j, h_1X_1 + \ldots + h_nX_n] \\ &= -h_1[X_j, X_1] - (X_jh_1)X_1 - \ldots \\ &- h_j[X_j, X_j] \\ &- (X_jh_j)X_j \quad - \ldots - h_n[X_j, X_n] \\ &- (X_jh_n)X_n \\ &= -h_1 \sum_{i=1}^{n} s_i \frac{\partial}{\partial q_i} - \left(\sum_{i=1}^{n} g_i^j \frac{\partial h_1}{\partial q_i}\right) \sum_{i=1}^{n} g_i^1 \frac{\partial}{\partial q_i} \\ &\quad - \ldots - \left(\sum_{i=1}^{n} g_i^j \frac{\partial h_j}{\partial q_i}\right) \sum_{i=1}^{n} g_i^j \frac{\partial}{\partial q_i} \\ &\quad - \ldots - h_n \sum_{i=1}^{n} t_i \frac{\partial}{\partial q_i} - \left(\sum_{i=1}^{n} g_i^j \frac{\partial h_n}{\partial q_i}\right) \\ &\quad \sum_{i=1}^{n} g_i^n \frac{\partial}{\partial q_i} \end{aligned}$$

where s_i and t_i are some scalar functions defined on M. Then, applying the condition $\omega(\mathcal{L}_v(X_j)) = 0$ yields an equation of the form:

$$\sum_{i \neq j}^{n} b_i h_i + \sum_{i=1}^{n} c_i \frac{\partial h_1}{\partial q_i} + \ldots + \sum_{i=1}^{n} d_i \frac{\partial h_n}{\partial q_i} = 0, \tag{8}$$

where b_i, c_i and d_i are some scalar functions. Extending the procedure to the all vector fields

$X_1, \ldots, X_k$, this yields a system of order k, consisting of equations of the form Equation (8).
Next, we compute the Lie derivative of g. We have:

$$\begin{aligned}\mathcal{L}_v(\mathrm{g}) &= \mathcal{L}_v\left(\sum_{i=1}^{n} a_i\, dq_i \otimes dq_i\right)\\ &= \sum_{i=1}^{n} a_i\, \mathcal{L}_v(dq_i \otimes dq_i)\\ &= \sum_{i=1}^{n} 2a_i\, dq_i\, \mathcal{L}_v(dq_i)\\ &= \sum_{i=1}^{n} 2a_i\, dq_i\ (i(v)\, d(dq_i) + d(i(v)\, dq_i))\\ &= \sum_{i=1}^{n} 2a_i\, dq_i\, d(i(v)\, dq_i)\\ &= \sum_{i=1}^{n} 2a_i\, dq_i\, d(dq_i(v))\end{aligned}$$

where $i(v)$, is the interior product. Condition $\mathcal{L}_v(\mathrm{g}) = 0$ provides a system of order $\frac{n(n+1)}{2}$, consisting of equations of the form:

$$\sum_{i=1}^{n} k_i h_i + \sum_{i=1}^{n} l_i \frac{\partial h_1}{\partial q_i} + \ldots + \sum_{i=1}^{n} r_i \frac{\partial h_n}{\partial q_i} = 0, \quad (9)$$

where k_i, l_i, and r_i are some scalar functions. Soving the system associated with Equations (8) and (9), we determine the functions h_i and, consequently, the generators v_i of our Lie algebra of symmetries. As a consequence, we can state the following result:

Proposition 2. *The infinitesimal symmetries of control system Equations (2)-(4) can be identified by calculating the flow associated with the vector field v_i at time s, denoted by $\gamma_i(s,t) = (q_1(s,t), \ldots, q_n(s,t))$. This flow is obtained by solving the system of differential equations:*

$$\frac{\partial \gamma_i(s,t)}{\partial s} = v_i(\gamma_i(s,t)), \quad \gamma_i(0,t) = (q_1(t), \ldots, q_n(t)).$$

4. Infinitesimal symmetries on SH(2) and the first Maxwell time

4.1. Geometric control problem on SH(2)

The motion of a unicycle on a hyperbolic plane can be described using the following driftless control system

$$\begin{cases} \dot{x} = u_1 \cosh z, \\ \dot{y} = u_1 \sinh z, \\ \dot{z} = u_2, \end{cases} \quad (10)$$

where u_1 is the translational velocity and u_2 is the angular velocity. The configuration and state manifold M of the system is three-dimensional, where, for any point $q = (x, y, z) \in M$, x and y are position variables and z is the angular orientation variable of the unicycle on the hyperbolic plane. A motion $m(x, y, z)$ on the configuration manifold M, parameterized by $x, y, z \in \mathbb{R}$, is a transformation that maps a point $\mathbf{a}(a_1, a_2)$ to a point $\mathbf{b}(b_1, b_2)$, such that:

$$\begin{aligned} b_1 &= a_1 \cosh z + a_2 \sinh z + x, \\ b_2 &= a_1 \sinh z + a_2 \cosh z + y. \end{aligned}$$

Composition of two motions $m_1(x_1, y_1, z_1)$ and $m_2(x_2, y_2, z_2)$ is another motion $m_3(x_3, y_3, z_3)$ given as:

$$m_3(x_3, y_3, z_3) = m_1(x_1, y_1, z_1).m_2(x_2, y_2, z_3)$$

where,

$$\begin{aligned} x_3 &= x_2 \cosh z_1 + y_2 \sinh z_1 + x_1, \\ y_3 &= x_2 \sinh z_1 + y_2 \cosh z_1 + y_1, \\ z_3 &= z_1 + z_2 \end{aligned}$$

The identity motion m_{Id} is given by $x = y = z = 0$, and inverse of a motion $m(x, y, z)$ is given by $m^{-1}(x^1, y^1, z^1)$ where,

$$\begin{aligned} x^1 &= -x \cosh z + y \sinh z, \\ y^1 &= x \sinh z - y \cosh z, \\ z^1 &= -z. \end{aligned}$$

The motions of the pseudo-Euclidean plane exhibit a group structure, with composition serving as the group operation. This group, known as the special hyperbolic group SH(2), also possesses a smooth manifold structure, which qualifies it as a Lie group. One can equivalently formulate problem Equation (10) as a sub-Riemannian problem on SH(2):

$$\begin{aligned} &\dot{q} = u_1 X_1(q) + u_2 X_2(q), \\ &q \in M = \mathrm{SH}(2), \quad u = (u_1, u_2) \in \mathbb{R}^2, \\ &q(0) = q_0 = m_{Id}, \quad q(t_1) = q_1, \\ &J = \frac{1}{2} \int_0^{t_1} \left(u_1^2 + u_2^2\right) dt \to \min \end{aligned} \quad (11)$$

where,

$$X_1 = \cosh z\, \partial_x + \sinh z\, \partial_y, \quad X_2 = \partial_z.$$

The problem under consideration is formulated on a sub-Riemannian manifold (M, Δ, g). Here, M represents the underlying smooth manifold, $\Delta = \mathrm{span}\{X_1, X_2\}$ denotes a distribution of rank 2, and g is a Riemannian metric defined on Δ such that $\mathrm{g}(\mathrm{X_i}, \mathrm{X_j}) = \delta_{\mathrm{ij}}$, explicitly $g = dx^2 - dy^2 + dz^2$. The vector fields X_1 and X_2, which span the distribution Δ, are left-invariant with respect to the group structure associated with M. One can see that the family

$\mathcal{F} = \{u_1X_1 + u_2X_2 | u = (u_1, u_2) \in \mathbb{R}^2\}$ is symmetric. Computing the vector field $X_3 = [X_1, X_2]$, we get $X_3 = [X_1, X_2] = -\sinh z\partial_x - \cosh z\partial_y$. Since X_1, X_2, and X_3 are linearly independent, we have

$$Lie_q(\mathcal{F}) = span(X_1(q), X_2(q), X_3(q)) = T_q(SH(2)),$$

for every point q. This implies that system Equation (11), is controllable. After transforming this system into an equivalent time-optimal problem with controls
$u_1^2 + u_2^2 \leqslant 1$, one can observe that

$$|u_1X_1 + u_2X_2| \leqslant c|q|, \quad q \in M.$$

This gives the inequality $|q(t)| \leqslant q_0 \exp(tc)$. Therefore, the attainable sets satisfy the following a priori bound:

$$\mathcal{A}_{q_0}(\leq t_1) \subset \{q \in M \mid |q| \leqslant q_0 \exp(t_1 c)\}.$$

Thus, according to Filipov's theorem ([1]), optimal controls exist.

4.2. Computing extremal trajectories

We begin by applying the Pontryagin Maximum Principle,[4] which allows to determine the extremal trajectories of system Equation(11). For this purpose, we define the functions $h_i(\lambda) = \langle \lambda, X_i \rangle \quad i = 1, 2, 3$, where $\lambda \in T^*M$. These functions (h_1, h_2, h_3), form a coordinate system on the fibers of T^*M. Consequently, we adopt the global coordinates (q, h_1, h_2, h_3) to describe the structure of T^*M. The Hamiltonian from the Pontryagin Maximum Principle (PMP) is given by:

$$h_u^v(\lambda) = \frac{\nu}{2}\left(u_1^2 + u_2^2\right) + u_1h_1(\lambda) + u_2h_2(\lambda),$$

where, $u = (u_1, u_2) \in \mathbb{R}^2$, and $v \in \{-1, 0\}$. Then the Pontryagin maximum principle[4] for the problem under consideration reads as follows.

Theorem 1. *([4]) Let $u(t)$ and $q(t), t \in [0, t_1]$, be an optimal control and the corresponding optimal trajectory in problem Equation (11). Then there exist a Lipschitzian curve $\lambda_t \in T^*M, \pi(\lambda_t) = q(t), t \in [0, t_1]$, and a number $v \in \{-1, 0\}$ for which the following conditions hold for almost all $t \in [0, t_1]$:*

$$\begin{aligned} \dot{\lambda}_t &= \vec{h}^v_{u(t)}(\lambda_t), \\ h^\nu_{u(t)}(\lambda_t) &= \max_{u \in \mathbb{R}^2} h^v_u(\lambda_t), \\ (v, \lambda_t) &\neq 0 \end{aligned} \tag{12}$$

Our analysis considers two distinct cases:

- Abnormal case

In this case $v = 0$. Thus, the Hamiltonian of PMP for the system takes the form:
$h_u(\lambda) = u_1h_1(\lambda) + u_2h_2(\lambda)$

$$\begin{aligned} \dot{h_1} &= \{h_u(\lambda), h_1\} \\ &= u_1\{h_1, h_1\} + u_2\{h_2, h_1\} \\ &= u_2h_3 \\ \dot{h_2} &= -u_1h_3 \end{aligned}$$

Then, Abnormal extremals satisfy the Hamiltonian system:

$$\begin{aligned} \dot{h_1} &= u_2h_3 \\ \dot{h_2} &= -u_1h_3 \\ \dot{q} &= u_1X_1 + u_2X_2 \end{aligned}$$

and the hypothesis $h_u(\lambda) \longrightarrow max$ implies

$$h_1(\lambda_t) = h_2(\lambda_t) = 0$$

Therefore, condition Equation (12) gives $h_3(\lambda_t) \neq 0$ and the first two equations of the Hamiltonian system yield $u_1(t) = u_2(t) = 0$. So, abnormal trajectories are constant.

- Normal case

The maximality condition

$$u_1h_1 + u_2h_2 - \tfrac{1}{2}(u_1^2 + u_2^2) \longrightarrow max$$

yields $u_1 = h_1$ and $u_2 = h_2$, and then the Hamiltonnianis $H = \frac{1}{2}(h_1^2 + h_2^2)$. Thus, we get the system:

$$\begin{aligned} \dot{h_1} &= h_2h_3 \\ \dot{h_2} &= -h_1h_3 \\ \dot{h_3} &= h_1h_2 \\ \dot{q} &= h_1X_1 + h_2X_2 \end{aligned}$$

and Hamiltonian system in the normal case is given by the equations:

$$\dot{h}_1 = h_2h_3, \quad \dot{h}_2 = -h_1h_3, \quad \dot{h}_3 = h_1h_2 \tag{13}$$

$$\dot{x} = h_1\cosh z, \quad \dot{y} = h_1\sinh z, \quad \dot{z} = h_2. \tag{14}$$

In this case, the initial covector λ lies on the initial cylinder defined by

$$C = T^*_{q_0}M \cap \{H(\lambda) = \frac{1}{2}\}.$$

This set can be explicitly described as

$$C = \{(h_1, h_2, h_3) \in \mathbb{R}^3 \mid h_1^2 + h_2^2 = 1\},$$

representing a cylinder in the cotangent space where the Hamiltonian takes the constant value $\frac{1}{2}$. We introduce the following change of variables:

$$h_1 = \cos(\alpha), \quad h_2 = \sin(\alpha).$$

With these coordinates, the vertical system Equation (13) satisfies the equations:

$$\dot{h}_3 = \frac{1}{2}\sin(2\alpha), \quad \dot{\alpha} = h_3.$$

Next, we introduce another change of variables:

$$\gamma = 2\alpha \in \mathbb{R}/4\pi\mathbb{Z}, \quad c = 2h_3 \in \mathbb{R}.$$

Finally, we obtain that the equation describing our vertical system corresponds to a mathematical pendulum given by:

$$\dot{\gamma} = c, \quad \dot{c} = -\sin(\gamma).$$

The total energy integral of the pendulum obtained is given as: $E = \frac{c^2}{2} - \cos(\gamma) = 2h_3^2 - h_1^2 + h_2^2$, according to this energy, the cylinder C can be decomposed in the following way. $C = \bigcup_{i=1}^{5} C_i$, where

$$\begin{aligned} C_1 &= \{\lambda \in C \mid E \in (-1, 1)\} \\ C_2 &= \{\lambda \in C \mid E \in (1, \infty)\} \\ C_3 &= \{\lambda \in C \mid E = 1, c \neq 0\} \\ C_4 &= \{\lambda \in C \mid E = -1\} \\ C_5 &= \{\lambda \in C \mid E = 1\} \end{aligned}$$

For a detailed derivation of the solutions to our system, refer to Butt([5]).

4.3. Infinitesimal symmetries

In this subsection, we compute the symmetry algebra of the control system Equation (11).

Proposition 3. *Infinitesimal symmetries of the control system Equation (11) form a Lie algebra generated (over $\mathbb{R}$) by the vector fields:*

$$\begin{aligned} v_1 &= -x\partial_y - y\partial_x - \partial_z, \\ v_2 &= \partial_x, \\ v_3 &= \partial_y. \end{aligned}$$

Proof. It is clear that Δ constitutes a contact distribution. Indeed, $\Delta = \ker(\omega)$, where $\omega = \cosh(z)dy - \sinh(z) \in \Lambda^1(M)$ and we have $d\omega \wedge \omega \neq 0$. Let $v = f_1(x, y, z)X_1 + f_2(x, y, z)X_2 + f_3(x, y, z)X_3$ be a vector field. The conditions $\omega(\mathcal{L}_v(X_1)) = 0$ and $\omega(\mathcal{L}_v(X_2)) = 0$, lead to the following system:

$$f_2 + \cosh z\frac{\partial f_3}{\partial x} + \sinh z\frac{\partial f_3}{\partial y} = 0, \tag{15}$$

$$f_1 - \frac{\partial f_3}{\partial z} = 0. \tag{16}$$

Moreover, the Lie derivative of the metric g has the form:

$$\begin{aligned} \mathcal{L}_v(\mathrm{g}) =& 2(\cosh z\frac{\partial f_1}{\partial x} - \sinh z\frac{\partial f_3}{\partial x})dx^2 \\ &+ 2(\cosh z\frac{\partial f_3}{\partial y} - \sinh z\frac{\partial f_1}{\partial y})dy^2 \\ &+ 2(\frac{\partial f_2}{\partial z})dz^2 \\ &+ (2\cosh z\frac{\partial f_1}{\partial y} - 2\sinh z\frac{\partial f_3}{\partial y} \\ &- 2\sinh z\frac{\partial f_1}{\partial x} + 2\cosh z\frac{\partial f_3}{\partial x})dxdy \\ &+ (2f_1\sinh z + 2\cosh z\frac{\partial f_1}{\partial z} - 2f_3\cosh z \\ &- 2\sinh z\frac{\partial f_3}{\partial z} + 2\frac{\partial f_2}{\partial x})dxdz \\ &+ (-2\sinh z\frac{\partial f_1}{\partial z} - 2f_1\cosh z \\ &+ 2\cosh z\frac{\partial f_3}{\partial z} + 2f_3\sinh z + 2\frac{\partial f_2}{\partial y})dzdy \end{aligned}$$

Now the relation $\mathcal{L}_v(\mathrm{g}) = 0$ implies:

$$\cosh z\frac{\partial f_1}{\partial x} - \sinh z\frac{\partial f_3}{\partial x} = 0, \tag{17}$$

$$\cosh z\frac{\partial f_3}{\partial y} - \sinh z\frac{\partial f_1}{\partial y} = 0, \tag{18}$$

$$\frac{\partial f_2}{\partial z} = 0, \tag{19}$$

and

$$\begin{aligned} 2\cosh z\frac{\partial f_1}{\partial y} - 2\sinh z\frac{\partial f_3}{\partial y} \\ -2\sinh z\frac{\partial f_1}{\partial x} + 2\cosh z\frac{\partial f_3}{\partial x} = 0, \end{aligned}$$

and

$$\begin{aligned} 2f_1\sinh z + 2\cosh z\frac{\partial f_1}{\partial z} - 2f_3\cosh z \\ -2\sinh z\frac{\partial f_3}{\partial z} + 2\frac{\partial f_2}{\partial x} = 0, \end{aligned}$$

and

$$\begin{aligned} -2\sinh z\frac{\partial f_1}{\partial z} - 2f_1\cosh z + 2\cosh z\frac{\partial f_3}{\partial z} \\ +2f_3\sinh z + 2\frac{\partial f_2}{\partial y} = 0. \end{aligned}$$

Using equation Equation (16), we have $f_1 = \frac{\partial f_3}{\partial z}$. By substituting f_1 into Equations (17) and (18), we obtain the following:

$$\begin{aligned} \cosh z\frac{\partial^2 f_3}{\partial z \partial x} - \sinh z\frac{\partial f_3}{\partial x} = 0, \\ \cosh z\frac{\partial f_3}{\partial y} - \sinh z\frac{\partial^2 f_3}{\partial z \partial y} = 0. \end{aligned} \tag{20}$$

Thus

$$\frac{\partial f_3}{\partial x} = c_1 \cosh z + f(x,y),$$
$$\frac{\partial f_3}{\partial y} = c_2 \sinh z + g(x,y).$$

By integrating Equations (17) and (18) with respect to x and y, respectively, we obtain:

$$\cosh z f_1 - \sinh z f_3 = 0,$$
$$\cosh z f_3 - \sinh z f_1 = 0.$$

Then we get:

$$\cosh z \frac{\partial f_3}{\partial z} - \sinh z f_3 = 0,$$
$$\cosh z f_3 - \sinh z \frac{\partial f_3}{\partial z} = 0.$$

Therefore, we deduce that :

$f_3 = c_1 x \cosh z + c_2 y \sinh z + c_3 \cosh z + c_4 \sinh z,$

$f_1 = c_1 x \sinh z + c_2 y \cosh z + c_3 \sinh z + c_4 \cosh z.$

Using Equation (15) we get $f_2 = -c_1$ and $c_2 = -c_1$. Hence, we obtain the following:

$f_1 = c_1 x \sinh z - c_1 y \cosh z + c_3 \sinh z + c_4 \cosh z$

$f_2 = -c_1$

$f_3 = c_1 x \cosh z - c_1 y \sinh z + c_3 \cosh z + c_4 \sinh z$

For $c_1 = 1$, $c_3 = c_4 = 0$, we find
$v_1 = -x\partial_y - y\partial_x - \partial_z$. □

Proposition 4. *The action of the flow of the infinitesimal transformation $v_1 = -x\partial_y - y\partial_x - \partial_z$, at the time s maps a geodesic with the initial condition $x(0) = y(0) = z(0) = 0$ to another geodesic.*

$$\begin{aligned} x &\mapsto x\cosh(s) - y\sinh(s), \\ y &\mapsto y\cosh(s) - x\sinh(s), \\ z &\mapsto z - s. \end{aligned} \tag{21}$$

4.4. First Maxwell time corresponding to infinitesimal symmetries

The transformation Equation (**??**) can be viewed as the result of composing two distinct motions: the first motion $m(x,y,z)$, which represents the geodesic under consideration, and a second motion $m(0,0,-s)$. Their combination results in a new motion $m(x',y',z')$, corresponding to a different geodesic, given by:

$$m(x',y',z') = m(0,0,-s) \cdot m(x,y,z)$$

The motion $m(0,0,-s)$ is a transformation in the hyperbolic plane, mapping each point (a_1,a_2) to another point (b_1,b_2), such that:

$$b_1 = a_1 \cosh s - a_2 \sinh s,$$
$$b_2 = a_2 \cosh s - a_1 \sinh s.$$

This motion can be represented in matrix form as follows:

$$N = \begin{pmatrix} \cosh(s) & -\sinh(s) & 0 \\ -\sinh(s) & \cosh(s) & 0 \\ 0 & 0 & 1 \end{pmatrix}$$

It is clear that the group generated by the matrix N is isomorphic to $\mathrm{SO}(1,2)$, the Lorentz group. Therefore, Proposition (4) yields the following result:

Corollary 1. *For each $R \in \mathrm{SO}(1,2)$, the map*

$$(x,y,z) \longmapsto R \cdot (x,y,z),$$

which represents a motion in the group M, maps geodesics starting at the origin to other geodesics. This map is defined by the composition of these two motions.

It can be noted that the set of fixed points of this action is:

$$\mathrm{S} = \{(0,0,\mathrm{z}) \quad |\mathrm{z} \in \mathbb{R}\}$$

Proposition 5. *The intersection of our geodesics with the set* S *provides the set of Maxwell points. Consequently, the following result is obtained:*

1. *If $\lambda \in C_1 \cup C_3 \cup C_4$, the geodesics do not intersect* S *for any $t > 0$.*
2. *If $\lambda \in C_2$, the set of Maxwell points is given by: $MAX = \{(0,0,z(4nk_0K) \quad k_0 \in (0,1)\}$*
3. *If $\lambda \in C_5$, the set of Maxwell points is given by: $MAX = \{(0,0,z(t)) \quad t > 0\}$*

Proof. (1) We begin with the case where $\lambda = (\varphi, k) \in C_1$, the geodesics intersect the set S if and only if: $x_t = y_t = 0$. Let $L_1 = x_t + y_t$, and $L_2 = x_t - y_t$, we then obtain the following expressions for L_1 and L_2:

$$L_1 = \omega\big((E(\varphi_t) - E(\varphi)) - k(sn(\varphi_t) - sn(\varphi))\big),$$
$$L_2 = \frac{1}{\omega(1-k^2)}\big((E(\varphi_t) - E(\varphi)) + k(sn(\varphi_t) - sn(\varphi))\big).$$

The equations $L_1 = 0$ and $L_2 = 0$ hold if and anly if $(E(\varphi_t) - E(\varphi)) = 0$. This condition cannot be satisfied for all $t > 0$. Therefore, the geodesics do not intersect the set S. In the case where $\lambda \in C_3$, we have $L_1 = \frac{1}{\omega}(\varphi_t - \varphi)$ and $L_2 = 2\omega(tanh(\varphi_t) - tanh(\varphi))$, since both equations cannot be obtained for each $t > 0$, this leads to our result. In the last case, it is clear that there is no intersection between our geodesic and S.

(2) If $\lambda \in C_2$. It is assumed that $L_1 = x_t + y_t$ and $L_2 = x_t - y_t$, which gives us the following expressions:

$$L_1 = \omega\Big(-(E(\psi_t) - E(\psi)) + k'^2(\psi_t - \psi) + k\big(sn(\psi_t) - sn(\psi)\big)\Big),$$

$$L_2 = \frac{1}{\omega(1-k^2)}\Big((E(\psi_t) - E(\psi)) - k'^2(\psi_t - \psi) + k\big(sn(\psi_t) - sn(\psi)\big)\Big).$$

We have $L_1 = 0$ and $L_2 = 0$. if and only if both equations, $h_1 = 2k(\big(sn(\psi_t) - sn(\psi)\big) = 0$ and $h_2 = (E(\psi_t) - E(\psi)) - k'^2(\psi_t - \psi) = 0$, hold. The equation $h_1 = 0$ holds exclusively when $t = 4nkK$ with $k \in (0,1)$. Here $K(k) = \int_0^{\pi/2} \frac{dt}{\sqrt{1-k^2\sin^2 t}}$, $k'^2 = 1 - k^2$, for these given values, it follows that $h_2(4nkK) = 4nE(k) - 4nk'^2K$. We subsequently take $g(k) = E(k) - k'^2K$ $k \in [0,1)$ we observe that its derivative $g'(k) = kK(k)$, indicating g increases on the interval $[0,1)$, with $g([0,1)) = [0,1)$. Therefore, there exists $k_0 \in (0,1)$ such that $g(k_0) = 0$. Since $z(4nk_0K) = 0$, the set of Maxwell points is reduced to $\{(0,0,0)\}$.

(3) If $\lambda \in C_5$ For each t, we have $x_t = 0$ and $y_t = 0$, with $z_t \neq 0$. Subsequently, for each strictly positive t, our geodesic intersects S. For more details on elliptic functions (see Olver[18])

□

Corollary 2. *The first Maxwell time T_1^{Max} where our geodesic loses optimality corresponding to this action is given as:*

$$\lambda \in C_1 \cup C_3 \cup C_4 \Longrightarrow T_1^{Max} = +\infty$$
$$\lambda \in C_2 \Longrightarrow T_1^{Max} = 4k_0K(k_0), \quad k_0 \in (0,1)$$
$$\lambda \in C_5 \Longrightarrow T_1^{Max} = t_0, \quad t_0 \neq 0$$

Proof. Whenever our geodesics do not intersect the set S they are optimal, and as a result $T_1^{Max} = +\infty$. In case 2, we assign the 1 to n to find the first Maxwell time. In case 5, there is always an intersection; consequently, our geodesic is no longer optimal. The first Maxwell time is a certain non-zero $t \neq 0$. □

Here, we include several figures and some numerical verification to better understand our method.

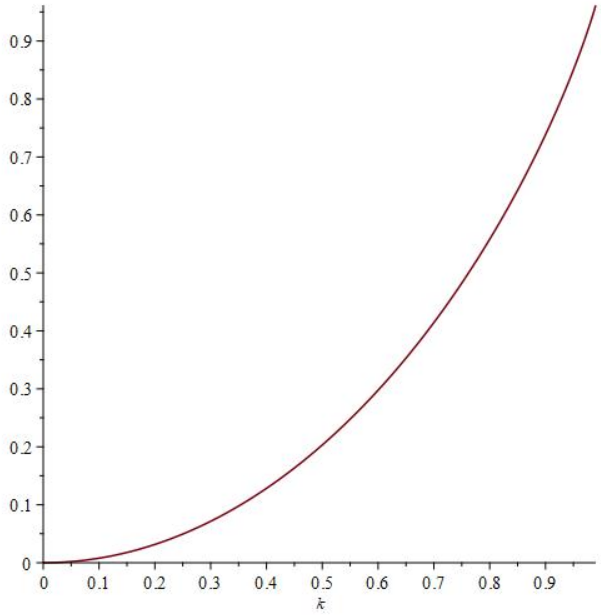


Figure 1. The graph of the function g

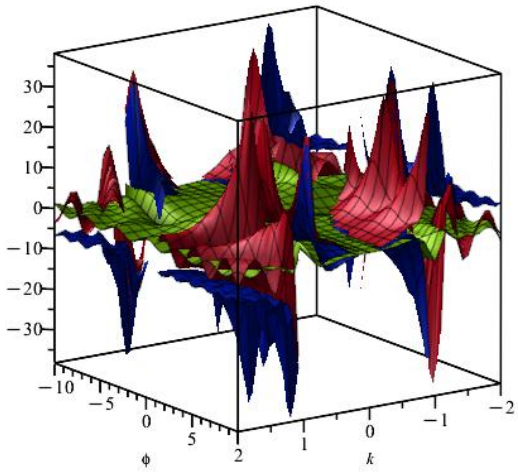


Figure 2. Local minimizer, in the case $\lambda = (\varphi, k) \in C_1$

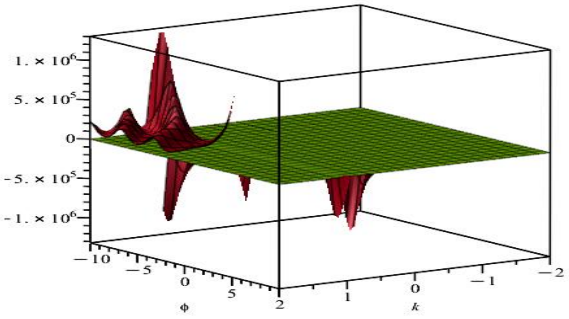


Figure 3. The trajectory's symmetric in the case $\lambda \in C_1$

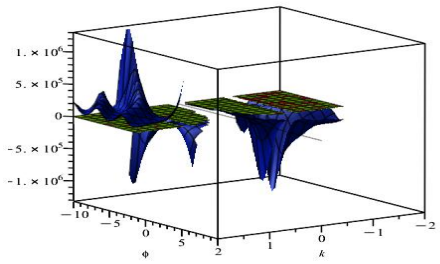


Figure 4. The trajectory $(x(t), y(t))$ and its symmetry, in the case $\lambda \in C_1$

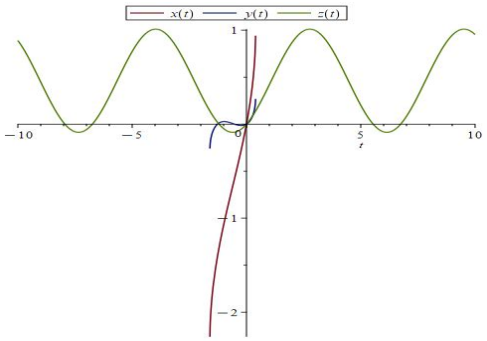


Figure 5. The local minimizer for numerical values, where $\lambda \in C_1$

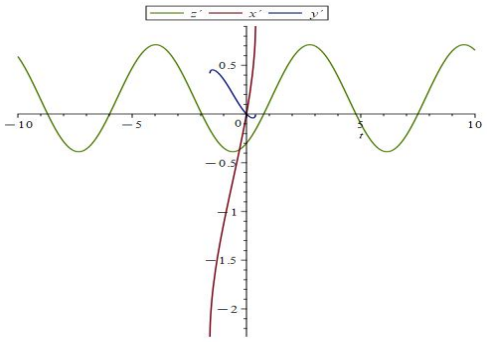


Figure 6. The trajectory's symmetric for numerical values, where $\lambda \in C_1$

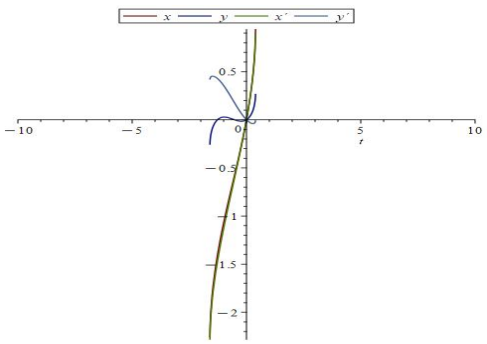


Figure 7. The trajectory $(x(t), y(t))$ and its symmetry for numerical values, where $\lambda \in C_1$

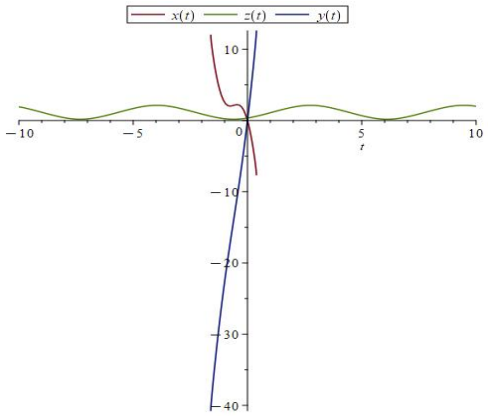


Figure 8. The local minimizer for numerical values, where $\lambda = (\varphi, k) \in C_2$

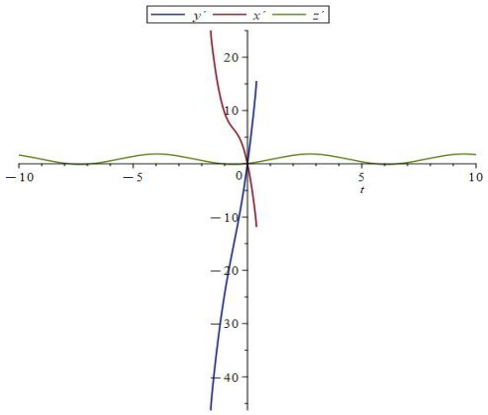


Figure 9. The trajectory's symmetric for numerical values, where $\lambda \in C_2$

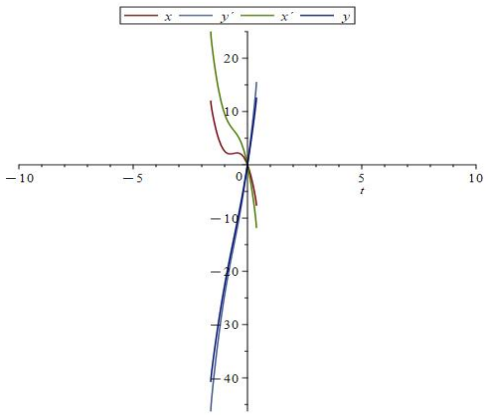


Figure 10. The trajectory and its symmetry for numerical value, where $\lambda \in C_2$

Table 1. Numerical verification of the Maxwell points

k_0	10^{-3}	10^{-12}	10^{-15}
$t = 4k_0K(k_0)$	6.283×10^{-3}	6.283×10^{-12}	6.283×10^{-15}
x_t	$-1.25\times10^{-5}-8.37\times10^{-9}i$	1.89×10^{-12}	2.03×10^{-15}
y_t	$-6.28\times10^{-3}-8.37\times10^{-6}i$	-6.43×10^{-12}	-6.44×10^{-15}

To simulate the dynamics of the system, we used the RK45 numerical integration method, which is an adaptive Runge-Kutta method of 4th

and 5th order. This method solves the differential equations governing the system while adjusting the time step based on the required precision. This approach was chosen for its robustness and efficiency in handling complex nonlinear systems. Using this method, we were able to obtain the trajectories and detect the moments when the trajectories come sufficiently close, thus identifying the Maxwell times.

Table 2. Maxwell times via numerical integration

Index	Maxwell Time (Numerical)
1	0.02013
2	0.0401
3	0.0201
4	0.0201
5	0.0401

The Figures 2, 3, and 4 illustrate the trajectory and its symmetry without numerical values, highlighting their intersections. Figures 5 and 6 introduce numerical parameters to visualize the trajectory and its symmetric counterpart, while Figure 7 confirms the absence of intersections for strictly positive times. In the second case, Figure 10 reveals an intersection closer to 0 with a minimized value of k_0. Numerically, Table 1 provides the Maxwell times for each k_0, whenever x_t and y_t approach 0, indicating an intersection between the trajectory and its symmetric counterpart which subsequently leads to a loss of optimality. Table 2 presents the Maxwell times obtained through numerical integration. Our method, which leverages both geometric and algebraic properties, allows us to determine the symmetry algebra of the system. This structure enables us to efficiently identify the points where the trajectory loses its optimality, while reducing computational costs. Moreover, by comparing the two tables, we observe that the Maxwell times in Table 1 are more precise and inferred compared to those obtained numerically.

5. Conclusion

In this work, we computed the infinitesimal symmetries of a sub-Riemannian problem under certain conditions. We then applied this approach to our sub-Riemannian problem on the special hyperbolic Lie group SH(2), where we determined the infinitesimal symmetries of the geometric control problem by leveraging the structure of the associated Lie algebra. This allowed us to identify the Maxwell points and, consequently, compute the first Maxwell time corresponding to these symmetries, which, in turn, enabled us to study the loss of optimality along a geodesic.

The methods used in this study could be particularly useful for analyzing other sub-Riemannian problems associated with a solvable Lie group. If the group is not solvable, one can proceed using the nilpotent approximation, which has been widely used in several works. An interesting direction for future research would be to explore how the methodology developed for SH(2) can be extended to higher-dimensional Lie groups or more complex distributions.

Moreover, the theoretical results obtained in this work have practical implications in robotics, control engineering, and physics. Many real-world systems, such as unicycle-type models, evolve in non-Euclidean spaces, making geometric approaches essential. In particular, determining Maxwell time enables real-time trajectory adjustments, optimizing efficiency and energy consumption in applications like mobile robotics. While this study focuses on the theoretical aspects, future work could include numerical experiments to further illustrate these benefits in concrete scenarios.

Acknowledgments

None.

Funding

None.

Conflict of interest

The authors declare that they have no conflict of interest regarding the publication of this article.

Author contributions

Conceptualization: All authors
Formal analysis: All authors
Methodology: All authors
Writing–original draft: All authors
Writing–review & editing: All authors

Availability of data

Not applicable.

Further disclosure

A preliminary summary of this work was presented at the International Conference on Mathematics and Decision, held at the UM6P Vanguard Center (UM6P, Rabat, December 17-20, 2024).

References

1. Sachkov Y. *Introduction to geometric control*. In: Springer Optimization and Its Applications. Moscow:URSS; 2019:192. https://doi.org/10.1007/978-3-031-02070-4
2. Moiseev I, Sachkov YL. Maxwell strata in sub-Riemannian problem on the group of motions of a plane. *ESAIM: COV* 2010; 16(2): 380–399. https://doi.org/10.1051/cocv/2009030
3. Sachkov YL. *Complete description of the Maxwell strata in the generalized Dido problem*. Sb. Math. 2006;197(6):901–950. https://doi.org/10.1070/SM2006v197n06ABEH003783
4. Agrachev AA, Barilari D, Boscain U. *A Comprehensive Introduction to Sub-Riemannian Geometry*. Cambridge University Press; 2019. https://doi.org/10.1017/9781108677325
5. Butt YA. *Sub-Riemannian Problem on Lie Group of Motions of Pseudo-Euclidean Plane*; 2015: 53–91. http://142.54.178.187:9060/xmlui/handle/123456789/1122
6. Gallier J, Quaintance J. *Notes on Differential Geometry and Lie Groups [Lecture Notes]*; 2016.
7. Hrdina J, Zalabová L. Local Geometric Control of a Certain Mechanism with the Growth Vector (4,7). *J Dyn Control Syst.*; 2020:26;199–216. https://doi.org/10.1007/s10883-019-09460-7
8. Agrachev AA, Barilari D. *Sub-Riemannian structures on 3D Lie groups*. J Dyn Control Syst. 2012;18(1):21–44. https://doi.org/10.1007/s10883-012-9133-8
9. Jean F. *Control of Nonholonomic Systems: From Sub-Riemannian Geometry to Motion Planning*. In: Springer Briefs in Mathematics. Springer; 2014.
10. Hill CD, Nurowski P. *A Car as Parabolic Geometry*; 2019. arXiv:1908.01169.
11. Hermans J. *A symmetric sphere rolling on a surface*. Nonlinearity 1995;8:1–23. https://doi.org/10.1088/0951-7715/8/4/003
12. Bloch AM. Nonholonomic Mechanics and Control. Springer; 2015. https://doi.org/10.1007/978-1-4939-3017-3
13. Mao Z, Kobayashi R, Nabae H, Suzumori K. *Multimodal strain sensing system for shape recognition of tensegrity structures by combining traditional regression and deep learning approaches*. IEEE Robot Automation Lett. 2024;9(11):1-6. https://doi.org/10.1109/LRA.2024.3469811
14. Peng Y, Yang X, Li D, et al. *Predicting flow status of a flexible rectifier using cognitive computing*. Exp Syst Appl. 2025;264: 125878. https://doi.org/10.1016/j.eswa.2024.125878
15. Jurdjevic V. *Optimal Control and Geometry: Integrable Systems*, Vol. 154. Cambridge University Press; 2016. https://doi.org/10.1017/CBO9781316286852
16. Agrachev A, Barilari D. *Sub-Riemannian Structures on 3D Lie Groups*. SISSA & MIAN; 2011. https://doi.org/10.48550/arXiv.1007.4970
17. Peter J.Olver, *Application of Lie Groups to Differential Equations*; 1993. https://doi.org/10.1007/978-1-4612-4350-2
18. Olver FWJ, Lozier DW, Boisvert RF, Clark CW. (2010). *NIST Handbook of Mathematical Functions*. National Institute of Standards and Technology, Cambridge University Press; 2010.
19. Bonnard B, Cots O. *Geometric numerical methods and results in the contrast imaging problem in nuclear magnetic resonance*. Math Models Methods Appl Sci. 2014;24(1):187–212. https://doi.org/10.1142/S0218202513500504

Soukaina Ezzeroual *is a PhD student in Mathematics at Cadi Ayyad University, Faculty of Sciences Semlalia. Her research focuses on sub-Riemannian geometry, optimal control, algebra, and analysis. She is conducting her research under the supervision of Professor Brahim Sadik. .*

https://orcid.org/0009-0003-4536-3892

Brahim Sadik *is a Professor-Researcher in Mathematics at Cadi Ayyad University, Faculty of Sciences Semlalia. His research focuses on Algebra, Analysis, and Applied Mathematics, and he has published several articles in these fields.*

https://orcid.org/0000-0002-3548-0265

This work is licensed under a Creative Commons Attribution 4.0 International License. The authors retain ownership of the copyright for their article, but they allow anyone to download, reuse, reprint, modify, distribute, and/or copy articles in IJOCTA, so long as the original authors and source are credited. To see the complete license contents, please visit http://creativecommons.org/licenses/by/4.0/.

An International Journal of Optimization and Control: Theories & Applications
ISSN: 2146-0957 eISSN: 2146-5703
Vol.15, No.3, pp.407-425 (2025)
https://doi.org/10.36922/ijocta.7096

RESEARCH ARTICLE

Modeling and analysis of the dynamics of an excessive gambling problem with modified fractional operator

Mulualem Aychluh[1], D.L. Suthar[2,3*], Clemente Cesarano[4], and S.D. Purohit[5]

[1]Department of Mathematics, Samara University, Samara, Afar, Ethiopia
[2]Department of Mathematics, Wollo University, Dessie, Ethiopia
[3]Department of Mathematics, Saveetha School of Engineering (SIMATS),Thandalam, Chennai, Tamil Nadu, India
[4]International Telematic University UNINETTUNO, Roma, Italy
[5]Rajasthan Technical University, Kota, Rajasthan, India
muleaychluh62@gmail.com, dlsuthar@gmail.com, c.cesarano@uninettuno.it, sunil a purohit@yahoo.com

ARTICLE INFO

Article History:
Received: December 6, 2024
Revised: April 7, 2025
Accepted: April 16, 2025
Published Online: May 5, 2025

Keywords:
Excessive gambling problem
Modified fractional operator
Numerical method
Fractional mathematical modeling

AMS Classification 2010:
26A33; 34A08; 35H15; 34K50
47H10; 60H10

ABSTRACT

This work introduces a fractional-order model of gambling addiction using the modified Atangana-Baleanu-Caputo operator. We establish solution existence/uniqueness, derive the reproduction number $\mathcal{R}_0$, and analyze stability. Numerical results demonstrate how fractional order v influences addiction dynamics. The model identifies key intervention parameters through sensitivity analysis. The optimal control strategy is proposed to reduce progression to addiction. These approaches provide new tools for understanding and managing problem gambling behaviors.

CC BY

1. Introduction

Games of chance have a long history dating back to Egyptian civilization.[1,2] Monetary rewards significantly contribute to popularity, as the primary objective of gambling is to generate financial rewards for lucky participants. These rewards enhance the appeal of chance-based games and act as psychological and biological factors in the development of gambling addiction in many individuals. Recently, gambling has grown into a rapidly expanding industry with millions of dollars in cash flows. The world focus on gambling has highlighted its uncontrolled distribution in modern society. There are several ways to gamble, ranging from state lotteries and sports betting (including predicting football matches) to more sophisticated casinos with slot machines, roulette wheels, and poker tables. Technology has diversified gambling options, enabling various electronic video gambling activities. Many people benefit from gambling, but many also incur unwanted losses. This can lead to a difficult way of life, as individuals may try to spend more money to recover from their losses. Every regular gambler encounters what is known as a "near-miss," a failure that appears extremely close to success. This often leads to repeated gambling, ultimately transforming gamblers into addicted ones. Surprisingly, most games have the lowest probability of winning. Anyone from any walk of life can lead to gambling addiction. Several factors, including social, biological, and cognitive-educational aspects, may contribute to the progression from gambling

*Corresponding Author

to problem gambling, which is a form of addiction. Problem gambling reflects a loss of control over gambling that persists despite often severe negative consequences.[3]

Gambling addiction occurs when gambling is the daily focus of participants. Skitch and Hodgins[3] defined problem gambling as a less judgmental way of describing a repetitive pattern of gambling that leads to serious destructive consequences and is beyond voluntary control. In recent decades, problem gambling has become a major public health issue. Problem gambling is a repetitive behavior, despite harm and negative consequences. It is an addictive behavior with high comorbidity with alcohol problems.[4] In the past two decades, the world community has gradually come to accept that addiction is a type of disease. Recently, gambling problems have been recognized as a major public health issue in modern society. The clinical definition of problem gambling was determined using the Diagnostic and Statistical Manual, 4th Edition, Test Revision (DSM-IV-TR) symptom checklist (American Psychiatric Association [APA]).[5] According to a study in Room et al.,[6] problem gambling leads to several social and psychological problems, including depression and alcohol and drug dependence. Research findings related to problem gambling suggest that this disorder is a real issue that needs to be addressed as a public health concern.

Over the last two decades, excessive gambling has been a primary subject of analysis and investigation in mathematics and statistics. Several mathematical models have been formulated to understand the dynamics of excessive gambling better. For example, Do and Lee[7] used a simple compartmental model to explore gambling dynamics by focusing on young people's gambling. In that study, the basic reproduction number was $\mathcal{R}_0 = 1.466$. The authors of Kong et al.[8] analyzed online gambling on scale-free networks. Shaffer and Korn[9] viewed problems associated with gambling as a socially transmitted disease. In Young and Tae,[10] Lee and Do examined the dynamics of gambling among older adults. The authors of ref.[11] investigated impulsivity trajectories and gambling in adolescence. The authors of ref.[12] focused on the reduction of attentional blink for gambling-related stimuli in problem gamblers. Brown et al.[13] investigated the differences between problem and non-problem gamblers in electronic machine games. Coping strategies in adolescents with gambling problems were the main study objective of the paper in Gupta et al.[14] The authors of Michalczuk et al.[15] studied pathological gamblers' impulsivity and cognitive distortions at the United Kingdom's national problem gambling clinic. Sharpe et al.[16] formulated a cognitive-behavioral model of problem gambling from a biopsychosocial perspective. An author in C$\breve{}$at$\breve{}$alin[17] provides a mathematician's advice for safe and rational gambling, one of which is "understanding your game."

Recently, mathematical models involving non-integer order derivatives have gained significant attention because they are more accurate and realistic than classical models.[18–20] An important question that led to the birth of fractional-order calculus in 1695 came from the letter L'Hopital sent to Leibniz. The Riemann and Liouville definition fails to explain the importance of starting conditions. The Caputo derivative addresses this problem, but when defined with a power-law kernel, it has a notable limitation owing to its singular nature.[21] The exponential decay kernel definition by Caputo and Fabrizio addressed the issue of singularity but introduced a locality problem. The first definition of a non-singular arbitrary order derivative by Caputo and Fabrizio significantly contributed to the concept of non-singular kernel fractional calculus. A novel fractional-order Caputo–Fabrizio operator, derived in 2015,[22] addresses several linear and nonlinear issues. The fractional operator is frequently used in various branches of mathematics and engineering. Many authors have applied this fractional operator to investigate the behavior of mathematical models (see[23] and references cited therein). Non-local and non-singular operators are key reasons why fractional calculus is becoming increasingly popular. A few years ago, significant efforts were made to find more interesting and novel non-singular arbitrary order derivatives based on kernels. Atangana and Baleanu studied a well-known non-singular derivative within the Mittag-Leffler kernel in 2016 and used it to solve various science and engineering problems.[24] This operator was recently updated.[25]

In recent years, many global issues have been modeled using arbitrary order calculus.[26] Motivated by the advancement of arbitrary order calculus, many authors have focused on studying the results of nonlinear differential equations with a fractional operator by developing various analytical, semi-analytical, and fully numerical techniques to find approximate solutions.

The primary reason for using non-integer order derivative models is that many systems exhibit memory, history, or non-local effects, which are challenging to model with

integer order derivatives. Recent studies have confirmed the effectiveness of the modified Atangana-Baleanu-Caputo (mABC) fractional derivative in solving linear and nonlinear problems, such as the linear time-fractional advection-diffusion equation,[27] the spread of the polio model including the vaccination effect,[28] the hepatitis C model,[29] novel solutions of fractional differential equations,[30] the fractional-order leukemia model[31] and the waterborne disease model.[32]

This study focuses on fractional modeling of the problem of excessive gambling using the mABC non-integer order derivative operator, which is a modified version of the Atangana-Baleanu-Caputo fractional derivative operator.

Systems of fractional differential equations are used to represent many real-life issues. Nonlinear problems can be successfully modeled using a system of arbitrary-order differential equations. However, finding analytical results for systems of ordinary differential equations involving nonlinear terms can be highly difficult, requiring approximation techniques to find numerical values.

Numerous numerical schemes have been created to obtain approximate results of non-integer order differential equations. Some of these methods include the fractional power series method,[33] exponential Galerkin method,[34] spectral collocation method, [35] and Galerkin finite element method.[36]

In the current study, we apply the Lagrange's interpolation approach based on the modified ABC derivative to approximate a novel model of excessive gambling problem.

The paper introduces a novel fractional-order model for gambling addiction problem using the modified ABC operator, addressing memory effects and non-local dynamics that classical models fail to capture. Key contributions include the derivation of the reproduction number $\mathcal{R}_0$ and stability analysis, sensitivity analysis to identify critical intervention parameters and optimal control strategies to manage gambling addiction. The study has some limitations, such as no demographic ageing and fixed parameters, no validation with real-world gambling addiction-reported data, and stochastic effects (e.g., sudden policy changes) may alter dynamics. The motivation for this study comes from the need to introduce a new mathematical model of gambling problems. The mABC operator was chosen for its non-singular kernel and ability to model memory effects, providing a more realistic representation of gambling addiction. The modified ABC fractional derivative operator is an acceptable option because of its ability to represent the dynamical systems effectively. Traditional models fail to capture memory effects and realistic transition dynamics. The modified ABC operator demonstrates superior performance in representing real-world problems. The study makes important contributions to the ongoing advancement of dynamical systems, particularly in gambling addiction.

The remainder of this paper is organized as follows. A definition of mABC fractional derivative and some of its basic properties are provided in Section 2. The fractional model for the problem of excessive gambling and its qualitative analysis are discussed in Section 3. The numerical scheme for approximating the proposed system is presented in Section 4. In Section 5, we discuss the results of numerical simulations. Finally, conclusion is presented.

2. Fundamental concepts

This section provides the most important definitions and properties applied throughout the study. It presents a clear overview of the modified ABC fractional calculus in the Caputo sense.

Definition 1. ([27–32]) *Let $m(t) \in L^1(0,T)$ be a function. The modified ABC derivative of $m(t)$ is defined as:*

$$ {}^{mABC}D^{\upsilon}_{0^+} m(t) = \frac{\mathcal{B}(\upsilon)}{1-\upsilon} \begin{bmatrix} m(t) - E_{\upsilon}\left(-\gamma_{\upsilon} t^{\upsilon}\right) m(0) \\ -\gamma_{\upsilon} \int_0^t (t-\eta)^{\upsilon-1} m(\eta) \\ \times E_{\upsilon,\ \upsilon}\left(-\gamma_{\upsilon}(t-\eta)^{\upsilon}\right) d\eta \end{bmatrix}. \tag{1} $$

where $\gamma_{\upsilon} = \dfrac{\upsilon}{1-\upsilon}$, $\upsilon \in (0,\ 1)$ is the order of derivative, and E_{υ} is the Mittag-Leffler function defined by:

$$ E_{\upsilon}(\chi) = \sum_{i=0}^{\infty} \frac{\chi^i}{\Gamma(\upsilon i + 1)}, \quad \chi \in \mathbb{C}, \tag{2} $$

and

$$ E_{\upsilon,\ \sigma}(\chi) = \sum_{i=0}^{\infty} \frac{\chi^i}{\Gamma(\upsilon i + \sigma)}, \quad \chi \in \mathbb{C}, \tag{3} $$

where $\upsilon \in (0,\ 1)$, $\mathcal{B}(\upsilon) = 1 - \upsilon + \dfrac{\upsilon}{\Gamma(\upsilon)}$ characterized as $\psi(0) = \psi(1) = 1$. The $\mathcal{L}$-transform of equation (1) is defined as:

$$\mathcal{L}\left[{}_0^{mABC}D_0^{\upsilon}m\left(t\right)\right]\left(\eta\right) = \frac{\mathcal{B}\left(\upsilon\right)}{1-\upsilon}\left[\frac{\eta^{\upsilon}\mathcal{L}\left\{m\left(t\right)\right\}\left(\eta\right)-\eta^{\upsilon-1}m\left(0\right)}{\eta^{\upsilon}+\gamma_{\upsilon}}\right]. \tag{4}$$

Definition 2. ([27–32]) *Let $m\left(t\right)\in L^1\left(0,\ T\right)$ be a function. The modified ABC integral is then express as follows:*

$$^{mAB}I_0^{\upsilon}m\left(t\right) = \frac{\psi\left(1-\upsilon\right)}{\mathcal{B}\left(\upsilon\right)}\left[m\left(t\right)-m\left(0\right)\right] + \gamma_{\upsilon}\left[{}^{RL}I_0^{\upsilon}\left(m\left(t\right)-m\left(0\right)\right)\right]. \tag{5}$$

where, the Riemann-Liouville integral operator is given by

$$^{RL}I^{\upsilon}m\left(t\right) = \frac{1}{\Gamma\left(\upsilon\right)}\int_0^t \frac{s\left(\eta\right)}{\left(t-\eta\right)^{1-\upsilon}}d\eta. \tag{6}$$

3. Model formulation

In this section, we consider a newly created model of excessive gambling based on modified ABC fractional differential equations. We focus on the NAMPR model, which addresses the problem of gambling within a population. This model comprises the following five types.

- **N:** The number of individuals who know nothing about gambling (non-gamblers).
- **A:** The number of individuals who are aware of the risks of gambling and gamble without problems but are exposed to problem gambling (no problem gamblers).
- **M:** The number of individuals who have minor symptoms of problem gambling and are at risk of addiction (minor-risk gamblers).
- **P:** The number of individuals who are addicted to gambling and gamble permanently (permanent gamblers).
- **R:** The number of individuals who have stopped or recovered from problem gambling (recovered gamblers).

The total population is computed as follows:

$$T(t) = N(t) + A(t) + M(t) + P(t) + R(t).$$

All parameters in the model are assumed to have values greater than zero and are defined as follows: all new recruits, assumed to have no awareness of the risks of gambling and never having gambled before, are recruited at a rate of Λ. An individual in stage N is not introduced to gambling, but contacts from gamblers urge them to gamble with no problems, leading them to transition to stage A at time t. This contact is modeled using a parameter α_1, which is directly related to the proportion of non-problem gamblers, minor risk gamblers, and excessive problem gamblers already participating in gambling activities.

$$\frac{\vartheta_1}{\alpha_1} = \frac{\gamma_1 A + \gamma_2 M + \gamma_3 P}{T}.$$

Individuals in stage A may transfer to stage R by stopping any gambling activities before addiction, measured using a parameter $\wp$, or they may develop minor symptoms of problem gambling. This step could be induced by the influence rate, measured in terms of the proportion of already existing problematic gambling stages: $\frac{\gamma_2 M + \gamma_3 P}{T}$ multiplied by a proportionality parameter α_2. Therefore, the overall problem gambling rate is:

$$\frac{\vartheta_2}{\alpha_2} = \frac{\gamma_2 M + \gamma_3 P}{T}.$$

There are three possible transition directions from stage M. Individuals in stage M may return to stage A by minimizing the frequency and intensity of their gambling, measured using a parameter λ, transfer to stage R by stopping gambling activities, denoted by the stopping rate ς, or transition to the excessive gambling problem stage. The latter step can be introduced by the influence rate, measured in terms of the proportion in the excessive gambling stage: $\frac{\gamma_3 P}{T}$ multiplied by a constant α_3. Therefore, the overall problem of the excessive gambling rate is: $\vartheta_3 = \alpha_3\frac{\gamma_3 P}{T}$.

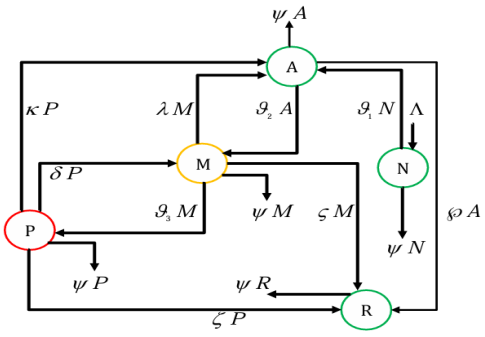


Figure 1. Problem gambling model flow diagram

There are also three possible transition directions from Stage P. Addicted gamblers may recover naturally or with the help of religion, social media awareness, school education, and professional help. When an addicted gambler returns to being a non-problem gambler, a transition to stage A occurs, modeled using κ. Individuals in the excessive problem gambling stage will either recover or stop all gambling activities, resulting in

a transition to stage R, modeled using the recovery parameter ζ. As the severity of the gambling problem decreases, an addicted problem gambler can transition to the minimum risk stage M at a rate δ. We assumed that recovered individuals would not return to the gambling activities and would never gamble again. The parameter ψ denotes the natural death rate. The model assumes no gambling problem-induced death and does not consider the age of gamblers. The approximate results of the gambling problem model using the modified ABC fractional operator are obtained using the Tofik-Atangana numerical scheme.

Figure 1 is a flow diagram of the gambling problem model, illustrating transitions between compartments and key parameters governing dynamics. In the modified ABC fractional operator, a model system of differential equations with positive initial conditions can be defined as follows:

$$\begin{cases} {}^{*}\mathcal{D}_t^{\upsilon} N(t) = \Phi_1(t) = \Lambda - \vartheta_1 N - \psi N, \\ {}^{*}\mathcal{D}_t^{\upsilon} A(t) = \Phi_2(t) = \vartheta_1 N + \lambda M + \kappa P \\ \qquad\qquad - (\wp + \vartheta_2 + \psi) A, \\ {}^{*}\mathcal{D}_t^{\upsilon} M(t) = \Phi_3(t) = \vartheta_2 A + \delta P \\ - (\lambda + \varsigma + \vartheta_3 + \psi) M, \\ {}^{*}\mathcal{D}_t^{\upsilon} P(t) = \Phi_4(t) = \vartheta_3 M - (\kappa + \delta + \zeta + \psi) P, \\ {}^{*}\mathcal{D}_t^{\upsilon} R(t) = \Phi_5(t) = \wp A + \varsigma M + \zeta P - \psi R. \end{cases} \tag{7}$$

where $*$ represents $mABC$. Equation (7) describes the rates of change for each compartment, incorporating fractional-order dynamics via the modified ABC operator. Parameters ϑ_1, ϑ_2 and ϑ_3 demonstrate model transitions influenced by problem gambler interactions.

3.1. Qualitative analysis

Here, we discuss the basic behaviors of model (7) such as solvability, existence and uniqueness, positivity, and boundedness of solutions. For $0 < t < T < +\infty$, system (7) can be written as follows:

$$ {}^{mABC}D_0^{\upsilon} m(t) = \Phi(t,\ m(t)), \tag{8}$$

with starting solution

$$m(0) = m_0, \tag{9}$$

where, the vector-valued functions $m : [0,\ +\infty) \to \mathbb{R}^5$ and $\Phi : \mathbb{R}^5 \to \mathbb{R}^5$ such that

$$m(t) = \begin{pmatrix} N(t) \\ A(t) \\ M(t) \\ P(t) \\ R(t) \end{pmatrix},$$

and

$$\Phi(m(t)) = \begin{pmatrix} \Phi_1(t) \\ \Phi_2(t) \\ \Phi_3(t) \\ \Phi_4(t) \\ \Phi_5(t) \end{pmatrix}.$$

Theorem 1. *The function Φ in (8) is Lipschitz continuous in η.*

Proof. For the state variable N, we have

$$\|\Phi_1(t,\ N) - \Phi_1(t,\ N_1)\|$$

$$= \left\| \alpha_1 \frac{\gamma_1 A + \gamma_2 M + \gamma_3 P}{T} + \psi \right\| \|N_1 - N\|.$$

Using triangular inequality, we have

$$\|\Phi_1(t,\ N) - \Phi_1(t,\ N_1)\| \le c\,\|N_1 - N\|.$$

where $c = \alpha_1 \dfrac{\gamma_1 \varrho_2 + \gamma_2 \varrho_3 + \gamma_3 \varrho_3}{T} + \psi$.

$$\begin{cases} \|N(t)\| = \sup_{t\in T} |N(t)| = \varrho_1, \\ \|A(t)\| = \sup_{t\in T} |A(t)| = \varrho_2, \\ \|M(t)\| = \sup_{t\in T} |M(t)| = \varrho_3, \\ \|P(t)\| = \sup_{t\in T} |P(t)| = \varrho_4, \\ \|R(t)\| = \sup_{t\in T} |R(t)| = \varrho_5. \end{cases}$$

Thus, $\Phi_1(t,\ N)$ satisfies the Lipschitz condition with the Lipschitz constant c. Moreover, if $0 \le c < 1$, then $\Phi_1(t,\ N)$ is a contraction. Similarly, we can show the existence of Lipschitz constants and the contraction principle for $\Phi_2(t)$, $\Phi_3(t)$, $\Phi_4(t)$, and $\Phi_5(t)$. Consequently, we have:

$$\|\Phi(t,\ m(t)) - \Phi(t,\ m_1(t))\|_{\infty} \le \eta_{\Phi} \|m - m_1\|_{\infty}. \tag{10}$$

and hence Φ is a Lipschitz continuous function.

Theorem 2. ***(Solvability)*** *The mABC fractional gambling model has at least one solution $m(t) \in C\left([0,\ \tau],\ \mathbb{R}_+^5\right)$.*

Proof. The mABC system is equivalent to:

$$m(t) - m_0 = {}^{mAB} I_0^{\upsilon} \Phi(t,\ m(t)). \tag{11}$$

Equation (11) has the following form:

$$m(t)-m_0=\frac{1-\upsilon}{\mathcal{B}(\upsilon)}\Phi(t,\ m(t))+\frac{\upsilon}{\mathcal{B}(\upsilon)\Gamma(\upsilon)}\int_0^t(t-s)^{\upsilon-1}\Phi(s,\ m((s))\,ds-\frac{1-\upsilon}{\mathcal{B}(\upsilon)}\Phi(0,\ m(0))\left(1+\frac{\gamma_\upsilon}{\Gamma(\upsilon+1)}t^\upsilon\right). \tag{12}$$

Define $T:\mathbb{C}\left([0,\ \tau],\ \mathbb{R}^5\right)\to\mathbb{C}\left([0,\ \tau],\ \mathbb{R}^5\right)$ as:

$$T[m](t)=m_0+\frac{1-\upsilon}{\mathcal{B}(\upsilon)}\Phi(t,\ m(t))+\frac{\upsilon}{\mathcal{B}(\upsilon)\Gamma(\upsilon)}\int_0^t(t-s)^{\upsilon-1}\Phi(s,\ m((s))\,ds-\frac{1-\upsilon}{\mathcal{B}(\upsilon)}\Phi(0,\ m(0))\left(1+\frac{\gamma_\upsilon}{\Gamma(\upsilon+1)}t^\upsilon\right). \tag{13}$$

Since Φ is continuous, and the modified ABC integral preserves continuity $\Rightarrow$ T is continuous. Next, we need to show that all possible solutions to the equation $m=\delta T[m]$ for $\delta\in[0,\ 1]$ are uniformly bounded in the space $C\left([0,\ \tau],\ \mathbb{R}^5_+\right)$. For $\delta\in[0,\ 1]$, the equation $m=\delta T[m]$ expands to:

$$m(t)=\delta m_0+\delta\left[\frac{1-\upsilon}{\mathcal{B}(\upsilon)}\Phi(t,\ m(t))+\frac{\upsilon}{\mathcal{B}(\upsilon)\Gamma(\upsilon)}\int_0^t(t-s)^{\upsilon-1}\Phi(s,\ m((s))\,ds-\frac{1-\upsilon}{\mathcal{B}(\upsilon)}\Phi(0,\ m(0))\left(1+\frac{\gamma_\upsilon}{\Gamma(\upsilon+1)}t^\upsilon\right)\right].$$

Taking the supremum norm of both sides, we have:

$$||m||\le\delta||m_0||+\delta\left[\frac{1-\upsilon}{\mathcal{B}(\upsilon)}||\Phi(t,\ m(t))||+\frac{\upsilon}{\mathcal{B}(\upsilon)\Gamma(\upsilon)}\int_0^t(t-s)^{\upsilon-1}||\Phi(s,\ m((s))||ds+\frac{1-\upsilon}{\mathcal{B}(\upsilon)}\Phi(0,\ m(0))\left(1+\frac{\gamma_\upsilon}{\Gamma(\upsilon+1)}t^\upsilon\right)\right].$$

Simplify the integral:

$$||m||\le\delta||m_0||+\delta\left[\frac{1-\upsilon}{\mathcal{B}(\upsilon)}||\Phi||+\frac{\tau^\upsilon}{\mathcal{B}(\upsilon)\Gamma(\upsilon)}||\Phi||+\frac{1-\upsilon}{\mathcal{B}(\upsilon)}\Phi_0\left(1+\frac{\gamma_\upsilon}{\Gamma(\upsilon+1)}\tau^\upsilon\right)\right].$$

Since $\delta\in(0,\ 1)$, we have:

$$||m||\le||m_0||+\frac{1-\upsilon}{\mathcal{B}(\upsilon)}\left[1+\frac{\tau^\upsilon}{(1-\upsilon)\Gamma(\upsilon)}\right]||\Phi||+\frac{1-\upsilon}{\mathcal{B}(\upsilon)}\Phi_0\left(1+\frac{\gamma_\upsilon}{\Gamma(\upsilon+1)}\tau^\upsilon\right).$$

Assume that

$$||\Phi||\le C_\Phi\left(1+||m||\right).$$

Then,

$$||m||\le||m_0||+\frac{1-\upsilon}{\mathcal{B}(\upsilon)}\left(1+\frac{\gamma_\upsilon}{\Gamma(\upsilon+1)}\tau^\upsilon\right)\times\left(\Phi_0+C_\Phi\left(1+||m||\right)\right).$$

Let

$$k=\frac{1-\upsilon}{\mathcal{B}(\upsilon)}\left(1+\frac{\gamma_\upsilon}{\Gamma(\upsilon+1)}\tau^\upsilon\right).$$

Then

$$||m||\le||m_0||+k\left(\Phi_0+C_\Phi\left(1+||m||\right)\right).$$

By rearranging this inequality, we obtain:

$$||m||\le\frac{||m_0||+k\Phi_0+kC_\Phi}{1-kC_\Phi}.$$

Therefore,

$$||m||\le M:=\frac{||m_0||+k\Phi_0+kC_\Phi}{1-kC_\Phi}.$$

This proves uniform boundedness.

Let $t_1,\ t_2\in[0,\ \tau]$. From the definition of T, we have:

$$T[m](t_2)-T[m](t_1)=\frac{1-\upsilon}{\mathcal{B}(\upsilon)}\left(\Phi(t_2,\ m(t_2))-\Phi(t_1,\ m(t_1))\right)+\frac{\upsilon}{\mathcal{B}(\upsilon)\Gamma(\upsilon)}(I_2-I_1)+\frac{\upsilon}{\mathcal{B}(\upsilon)\Gamma(\upsilon+1)}\Phi_0\left[t_1^\upsilon-t_2^\upsilon\right], \tag{14}$$

where

$$I_2-I_1=\int_{t_1}^{t_2}(t_2-s)^{\upsilon-1}\Phi(s,\ m((s))\,ds+\int_0^{t_1}\left((t_2-s)^{\upsilon-1}-(t_1-s)^{\upsilon-1}\right)\Phi(s,\ m((s))\,ds.$$

Since Φ is Lipschitz continuous in m and continuous in t, there exists η_Φ such that:

$$||\Phi(t_2,\ m(t_2))-\Phi(t_1,\ m(t_1))||\le\eta_\Phi\left(|t_2-t_1|+||m(t_2-m(t_1)||\right). \tag{15}$$

Using mean value theorem, there exists $\chi\in(t_1,\ t_2)$ such that

$$|\,(t_2-s)^{\upsilon-1}-(t_1-s)^{\upsilon-1}\,|=(\upsilon-1)(\chi-s)^{\upsilon-2}|t_2-t_1|,$$

and we have:

$$||I_2 - I_1|| \leq ||\Phi|| \left(\frac{(t_2 - t_1)^{\upsilon}}{\upsilon} + \tau^{\upsilon}(t_2 - t_1)^{\upsilon} \right). \tag{16}$$

From Equations (14) -(16), we have:

$$||T[m](t_2) - T[m](t_1)||$$

$$\leq \frac{1-\upsilon}{\psi(\upsilon)} \left(\eta_{\Phi} \left(|t_2 - t_1| + ||m(t_2 - m(t_1)|| \right) \right)$$

$$+ \frac{\upsilon}{\mathcal{B}(\upsilon)\Gamma(\upsilon)} ||\Phi|| \left(\frac{(t_2 - t_1)^{\upsilon}}{\upsilon} + \tau^{\upsilon}(t_2 - t_1)^{\upsilon} \right)$$

$$+ \frac{\upsilon}{\mathcal{B}(\upsilon)\Gamma(\upsilon+1)} \Phi_0 \left| t_2^{\upsilon} - t_1^{\upsilon} \right|.$$

For $\upsilon \in (0,\ 1)$ and $t_2 > t_1 > 0$, we have:

$$t_2^{\upsilon} = (t_1 + (t_2 - t_1))^{\upsilon} \leq t_1^{\upsilon} + (t_2 - t_1)^{\upsilon}$$

$$\Rightarrow |t_2^{\upsilon} - t_1^{\upsilon}| \leq (t_2 - t_1)^{\upsilon}.$$

Thus,

$$||T[m](t_2) - T[m](t_1)|| \leq c\,(t_2 - t_1)^{\upsilon},$$

where

$$c = \frac{1-\upsilon}{\psi(\upsilon)} \left(\eta_{\Phi} + \eta_{\Phi} k \right)$$

$$+ \frac{1}{\mathcal{B}(\upsilon)\Gamma(\upsilon)} \left(2 + \upsilon\tau^{\upsilon} \right) ||\Phi||.$$

Given $\epsilon > 0$, choose $\delta = (\epsilon/c)^{1/\upsilon}$ such that

$$|t_2 - t_2| < \delta \Rightarrow ||T[m](t_2) - T[m](t_1)|| < \epsilon.$$

This holds uniformly for all m, proving equicontinuity. Since T is continuous, compact, and the set $m = \delta T[m]$ is bounded, there exists at least one fixed point $m = \delta T[m]$ which solves the system.

3.1.1. Existence and uniqueness of the solution

As shown in Theorem 2, T is continuous, $m = \delta T[m],\ \delta \in (0,\ 1)$ is bounded uniformly, and T is equicontinuous. By Schaefer's theorem, T has a fixed point $\hat{m} = T[\hat{m}]$, which is a solution.

Theorem 3. *Assuming that the condition of Equation* (15) *is satisfied, there is a solution of the mABC fractional system given by Equation* (8).

Proof. Equation (10) confirms the Lipschitz condition of $\Phi(t,\ m(t))$. For $m_1, m_2 \in C([0,\tau],\ \mathbb{R}^5$, we have

$$||T[m_2](t) - T[m_1](t)|| \leq \frac{1-\upsilon}{\mathcal{B}(\upsilon)} \eta_{\Phi} ||m_2 - m_1||$$

$$+ \frac{\upsilon}{\mathcal{B}(\upsilon)\Gamma(\upsilon)} \eta_{\Phi} ||m_2 - m_1|| \frac{\tau^{\upsilon}}{\upsilon}$$

$$= \left(\frac{1-\upsilon}{\mathcal{B}(\upsilon)} + \frac{\upsilon}{\mathcal{B}(\upsilon)\Gamma(\upsilon+1)} \tau^{\upsilon} \right) \eta_{\Phi} ||m_2 - m_1||.$$

Define the contraction constant:

$$k(\tau) = \left(\frac{1-\upsilon}{\mathcal{B}(\upsilon)} + \frac{\upsilon}{\mathcal{B}(\upsilon)\Gamma(\upsilon+1)} \tau^{\upsilon} \right) \eta_{\Phi} < 1.$$

This is always possible since $\psi(\upsilon) = 1 - \upsilon + \frac{\upsilon}{\Gamma(\upsilon)} > 1 - \upsilon$:

$$\lim_{\tau \to 0^+} k(\tau) = \frac{1-\upsilon}{\mathcal{B}(\upsilon)} \eta_{\Phi} < 1$$

We assume that $\sup_{t \in [0,\ \tau]} |\Phi(t,\ m(0))| = \varrho$, $S_{\upsilon} = \left\{ m(t) \in \mathbb{C}\left([0,\ \tau],\ \mathbb{R}^5\right) : \|m(t)\| \right\} < \upsilon$. For $m(t) \in S_{\upsilon}$, and $t \in [0,\ \tau]$, we have

$$\|\Phi(t,\ m(t))\| = \|\Phi(t,\ m(t)) - \Phi_0 + \Phi_0\| \leq \eta_{\Phi}\upsilon + \varrho. \tag{17}$$

Furthermore, for $m \in \left\{ m \in \mathbb{C}\left([0,\ \tau],\ \mathbb{R}^5\right) \right\}$, we have

$$\|m(t)\| = \max \|Tm(t)\| \leq m_0 + \frac{1-\upsilon}{\mathcal{B}(\upsilon)} \left(\eta_{\Phi} \|m(t)\| + \varrho \right)$$

$$+ \frac{\upsilon}{\mathcal{B}(\upsilon)\Gamma(\upsilon)} \left(\eta_{\Phi} \|m(t)\| + \varrho \right) t^{\upsilon}$$

$$+ \frac{1-\upsilon}{\mathcal{B}(\upsilon)} \Phi_0 \left(1 + \frac{\gamma_{\upsilon}}{\Gamma(\upsilon+1)} t^{\upsilon} \right)$$

$$= \pi_1 + \pi_2 \|m(t)\|.$$

We have that

$$\pi_1 = m_0 + \frac{1-\upsilon}{\mathcal{B}(\upsilon)} \Phi_0 \left(1 + \frac{\gamma_{\upsilon}}{\Gamma(\upsilon+1)} t^{\upsilon} \right)$$

$$+ \left[\frac{1-\upsilon}{\mathcal{B}(\upsilon)} + \frac{\upsilon}{\mathcal{B}(\upsilon)\Gamma(\upsilon)} t^{\upsilon} \right] \varrho,$$

$$\pi_2 = \eta_{\Phi} \left[\frac{1-\upsilon}{\mathcal{B}(\upsilon)} + \frac{\upsilon}{\mathcal{B}(\upsilon)\Gamma(\upsilon)} t^{\upsilon} \right].$$

Thus,

$$\|m(t)\| \leq \frac{\pi_1}{1 - \pi_2}. \tag{18}$$

According to Leray-Schauder's alternative theorem, system (8) has a solution.

3.1.2. Positivity and boundedness of the result

Theorem 4. *The set of solutions of the system* (7) *with nonnegative initial conditions defined in the region* $\Omega = \{(N,\ A,\ M,\ P,\ R) \in \mathbb{R}_+^5 : 0 \leq N(t) + A(t) + M(t) + P(t) + R(t) :\ T(t) \leq \frac{\Lambda}{\psi}\}$ *is positively invariant.*

Proof. Differentiating the total population $T(t) = N(t) + A(t) + M(t) + P(t) + R(t)$ with respect to time and using equations in system (7), we obtain

$$ {}^{mABC}D_0^{\upsilon}T(t) \leq \Lambda - \psi T(t). \tag{19}$$

Applying the Laplace transform on two sides of the above inequality, we obtain:

$$\mathcal{L}\left\{{}^{mABC}D_0^{\upsilon}T(t);\ s\right\} \leq \frac{\Lambda}{s} - \psi\mathcal{L}\left\{T(t);\ s\right\}$$

$$\Rightarrow \frac{\mathcal{B}(\upsilon)\, s^{\upsilon}\mathcal{L}\left\{T(t);\ s\right\}}{\upsilon + (1-\upsilon)\, s^{\upsilon}} + \psi\mathcal{L}\left\{T(t);\ s\right\}$$
$$\leq \Lambda s^{\upsilon-(\upsilon+1)} + \frac{\mathcal{B}(\upsilon)\, T(0)\, s^{\upsilon-1}}{\upsilon + (1-\upsilon)\, s^{\upsilon}}.$$

Implies

$$\mathcal{L}\left\{T(t);\ s\right\} \leq \frac{\Lambda\upsilon}{\mathcal{B}(\upsilon) + (1-\upsilon)\,\psi} \times \frac{s^{\upsilon-(\upsilon+1)}}{s^{\upsilon} + \dfrac{\upsilon\psi}{\mathcal{B}(\upsilon) + (1-\upsilon)\,\psi}}$$
$$+ \left(\frac{\Lambda(1-\upsilon)}{\mathcal{B}(\upsilon) + (1-\upsilon)\,\psi} + \frac{\mathcal{B}(\upsilon)\, T(0)}{\mathcal{B}(\upsilon) + (1-\upsilon)\,\psi}\right) \times \frac{s^{\upsilon-1}}{s^{\upsilon} + \dfrac{\upsilon\psi}{\mathcal{B}(\upsilon) + (1-\upsilon)\,\psi}}.$$

Applying the inverse Laplace, we arrive at:

$$T(t) \leq \frac{\Lambda\upsilon}{\mathcal{B}(\upsilon) + (1-\upsilon)\,\psi} E_{\upsilon,\ \upsilon+1}\left(-\eta t^{\upsilon}\right) + \frac{1}{\mathcal{B}(\upsilon) + (1-\upsilon)\,\psi} \times \left(\Lambda(1-\upsilon) + \mathcal{B}(\upsilon)\, T(0)\right) E_{\upsilon,\ 1}\left(-\eta t^{\upsilon}\right), \tag{20}$$

where $\eta = \dfrac{\upsilon\psi}{\mathcal{B}(\upsilon) + (1-\upsilon)\,\mu}$ and $E_{\alpha,\ \beta}(.)$ is the Mittag-Leffler function of two parameters $\alpha > 0$ and $\beta > 0$ defined as:

$$E_{\alpha,\ \beta}(\chi) = \sum_{i=0}^{\infty} \frac{x^i}{\Gamma(\alpha i + \beta)},$$

whose Laplace transform is

$$\mathcal{L}\left\{\chi^{\beta-1}E_{\alpha,\ \beta}\left(\mp\eta\chi^{\alpha}\right);\ s\right\} = \frac{s^{\alpha-\beta}}{s^{\alpha} \pm \eta}$$

provided that $s > |\eta|^{1/\alpha}$. The Mittag-Leffler function satisfies

$$E_{\alpha,\ \beta}(\chi) = \frac{E_{\alpha,\ \beta-\alpha}(\chi)}{\chi} - \frac{1}{\chi\Gamma(\beta-\alpha)},$$

and for the case $\alpha = \upsilon,\ \beta = \upsilon + 1$ and $x = -\eta t^{\upsilon}$, we have

$$E_{\upsilon,\ \upsilon+1}\left(-\eta t^{\upsilon}\right) = \frac{1}{\eta t^{\upsilon}}\left(1 - E_{\upsilon,\ 1}\left(-\eta t^{\upsilon}\right)\right). \tag{21}$$

The Mittag-Leffeler function is bounded for all $t > 0$, possess an asymptotic behavior,[37] introducing the relation (21) in inequality (20), it is obvious that $T(t) \leq \dfrac{\Lambda}{\psi}$ as $t \to \infty$. Thus, $N(t)$ and all other variables of the system (7) are bounded in the region Ω.

Theorem 5. *If the set of initial conditions* $\{N(0) \geq 0,\ A(0) \geq 0,\ M(0) \geq 0,\ P(0) \geq 0,\ R(0) \geq 0\} \in \mathbb{R}_+^5$ *then, the solutions of* $N(t)$, $A(t)$, $M(t)$, $P(t)$, *and* $R(t)$ *are non-negative for all* $t \geq 0$.

Proof. Assume that all the state variables of the model are continuous. Consider the first equation of the system (7):

$$ {}^{mABC}D_0^{\upsilon}N(t) = \Lambda - \alpha_1 N\frac{\gamma_1 A + \gamma_2 M + \gamma_3 P}{T} - \psi N. \tag{22}$$

Since, all the solutions are bounded, let $\dfrac{\gamma_1 A + \gamma_2 M + \gamma_3 P}{T}$ is bounded by σ. Then,

$$ {}^{mABC}D_0^{\upsilon}N(t) \geq -aN, \tag{23}$$

where $a = \alpha_1\sigma + \psi$. Applying the Laplace transform in Eq. (23) and using Eq. (4), we have:

$$\frac{\mathcal{B}(\upsilon)}{1-\upsilon}\left[\frac{s^{\upsilon}\mathcal{L}\left\{N(t);\ s\right\} - N(0)\, s^{\upsilon-1}}{s^{\upsilon} + \dfrac{\upsilon}{1-\upsilon}}\right] \geq -a\mathcal{L}\left\{N(t)\right\}.$$

Further simplification gives:

$$\frac{\mathcal{B}(\upsilon)\, s^{\upsilon}\mathcal{L}\left\{N(t);\ s\right\}}{\upsilon + (1-\upsilon)\, s^{\upsilon}} - \frac{\mathcal{B}(\upsilon)\, N(0)\, s^{\upsilon-1}}{\upsilon + (1-\upsilon)\, s^{\upsilon}} \geq -a\mathcal{L}\left\{N(t)\right\}.$$

$$\left[\mathcal{B}(\upsilon)\, s^{\upsilon} + a\upsilon + a(1-\upsilon)\, s^{\upsilon}\right]\mathcal{L}\left\{N(t);\ s\right\} \geq \mathcal{B}(\upsilon)\, s^{\upsilon-1}N(0)$$

$$\mathcal{L}\left\{N(t);\ s\right\} \geq \frac{\mathcal{B}(\upsilon)\, N(0)}{\mathcal{B}(\upsilon) + a(1-\upsilon)} \frac{s^{\upsilon-1}}{s^{\upsilon} + \dfrac{a\upsilon}{\mathcal{B}(\upsilon) + a(1-\upsilon)}}.$$

Taking the inverse Laplace transform in the above inequality, we obtain:

$$N(t) \geq \frac{\mathcal{B}(\upsilon)\, N(0)}{\mathcal{B}(\upsilon) + a(1-\upsilon)} E_{\upsilon,\ 1}\left(\frac{-a\upsilon t^{\upsilon}}{\mathcal{B}(\upsilon) + a(1-\upsilon)}\right).$$

Since $E_{\upsilon,\ 1}\left(-\dfrac{a\upsilon}{\mathcal{B}(\upsilon) + a(1-\upsilon)}t^{\upsilon}\right) > 0$ and $N(0) > 0$, then $N(t) \geq 0$. In the same way,

it is easy to prove that the remaining state variables are non-negative for all $t > 0$. Therefore, the solutions of system (7) are non-negative for all $t \geq 0$.

3.2. Stability analysis of the model

In this section, the basic reproduction number and stability analyses of endemic and no problem gambling equilibrium points are discussed.

3.2.1. No problem gambling equilibrium point

To find the gambling problem-free equilibrium point of the model, we set the derivatives of all compartments to zero and assume that there are no individuals with gambling problem ($M = 0,\ P = 0$ and $R = 0$). The system reduces to:

$$\begin{cases} \Lambda - \alpha_1 N \dfrac{\gamma_1 A}{T} - \psi N = 0, \\ \\ \alpha_1 N \dfrac{\gamma_1 A}{T} - (\wp + \psi) A = 0. \end{cases} \tag{24}$$

Solving these equations yield:

$$E_0 = \left(s,\ \frac{\alpha_1\gamma_1 - \wp - \psi}{\wp + \psi} s,\ 0,\ 0,\ 0 \right).$$

where $s = \dfrac{\Lambda}{\alpha_1\gamma_1 - \wp}$ and $\alpha_1\gamma_1 > \wp$ to ensure positivity of N_0 and $\alpha_1\gamma_1 > \wp + \psi$ for positivity of A_0. This equilibrium represents a state where there are no individuals with gambling problems and the population consists only of non-gamblers (N) and non-problem gamblers (A).

3.2.2. The basic reproduction number

The basic reproduction number $\mathcal{R}_0$ is a critical threshold in epidemiological models, representing the average number of new "infections" (in this case, new problem gamblers) generated by a single addicted gambler in a fully susceptible population.

$$F = \begin{bmatrix} \alpha_2\gamma_2 q & \alpha_2\gamma_3 q \\ 0 & 0 \end{bmatrix}, \quad V = \begin{bmatrix} u & -\delta \\ 0 & v \end{bmatrix}$$

where

$$q = \frac{\alpha_1\gamma_1 - \wp - \psi}{\alpha_1\gamma_1},\ u = \lambda + \varsigma + \psi,$$
$$v = \kappa + \delta + \zeta + \psi.$$

Using the next-generation matrix method, the basic reproduction number of the proposed model is the dominant eigenvalue of FV^{-1}. Therefore,

$$\mathcal{R}_0 = \alpha_2\gamma_2 \frac{\alpha_1\gamma_1 - \wp - \psi}{\alpha_1\gamma_1(\lambda + \varsigma + \psi)}.$$

Theorem 6. *The gambling problem-free equilibrium point E_0 is locally asymptotically stable when $\mathcal{R}_0 < 1$ and unstable when $\mathcal{R}_0 > 1$.*

Proof. To prove the local stability, we consider the Jacobian matrix of the system (7) at E_0 as follows:

$$J(E_0) = \begin{bmatrix} a_{11} & a_{12} & a_{13} & a_{14} & 0 \\ a_{21} & 0 & a_{23} & a_{24} & 0 \\ 0 & 0 & a_{33} & a_{34} & 0 \\ 0 & 0 & 0 & a_{44} & 0 \\ 0 & a_{52} & a_{53} & a_{54} & a_{55} \end{bmatrix}, \tag{25}$$

where

$$a_{11} = -(\alpha_1\gamma_1 - \wp), \quad a_{12} = -(\wp + \psi)$$

$$a_{13} = -\gamma_2 \frac{\wp + \psi}{\gamma_1}, \quad a_{14} = -\gamma_3 \frac{\wp + \psi}{\gamma_1}$$

$$a_{21} = \alpha_1\gamma_1 - \wp - \psi,$$

$$a_{23} = \gamma_2 \frac{\wp + \psi}{\gamma_1} + \lambda - \alpha_2\gamma_2 \frac{\alpha_1\gamma_1 - \wp - \psi}{\alpha_1\gamma_1}$$

$$a_{24} = \gamma_3 \frac{\wp + \psi}{\gamma_1} + \kappa - \alpha_2\gamma_3 \frac{\alpha_1\gamma_1 - \wp - \psi}{\alpha_1\gamma_1},$$

$$a_{25} = 0, \quad a_{52} = \wp, \quad a_{53} = \varsigma, \quad a_{54} = \zeta$$

$$a_{33} = \left(\alpha_2\gamma_2 \frac{\alpha_1\gamma_1 - \wp - \psi}{\alpha_1\gamma_1} \right) - (\lambda + \varsigma + \psi)$$

$$a_{34} = \left(\alpha_2\gamma_3 \frac{\alpha_1\gamma_1 - \wp - \psi}{\alpha_1\gamma_1} \right) + \delta,$$

$$a_{44} = -(\kappa + \delta + \zeta + \psi), \quad a_{55} = -\psi$$

In this Jacobian matrix, three of the eigenvalues are negative, that is $m_1 = -\psi$, $m_2 = -(\kappa + \delta + \zeta + \psi)$ and $m_3 = -(\lambda + \varsigma + \psi)(1 - \mathcal{R}_0)$ for $\mathcal{R}_0 < 1$. The remaining eigenvalues can be obtained from the characteristic equation:

$$m^2 + d_1 m + d_2 = 0. \tag{26}$$

Since the coefficients $d_1 = \alpha_1\gamma_1 - \wp > 0$ for $\alpha_1\gamma_1 > \wp$ and $d_2 = (\wp + \psi)(\alpha_1\gamma_1 - \wp - \psi) > 0$ for $\alpha_1\gamma_1 > \wp + \psi$. The solutions of Equation (26) have negative real parts. Since the $Im(m_i = 0,\ i = 1,\ 2,\ 3,\ 4$, then clearly $|\arg(m_i)| = \pi > \dfrac{\upsilon\pi}{2},\ \upsilon \in (0, 1)$. According to the Matignon criterion,[38] the equilibrium point E_0 is stable when $\mathcal{R}_0 < 1$.

3.2.3. Endemic equilibrium point

Adjusting the model equation to zero and solve simultaneously, we get the endemic equilibrium point $E^* = (N^*,\ A^*,\ M^*,\ P^*,\ R^*)$. where

$$M^* = \frac{c\Lambda}{\alpha_3\gamma_3\psi}, \quad \text{where } c = \kappa + \delta + \zeta + \psi$$

$$A^* = \frac{\left(d + \alpha_3\gamma_3 P^*\right)\dfrac{c\Lambda}{\alpha_3\gamma_3\psi} - \delta P^*}{\alpha_2\left(\dfrac{c\gamma_2}{\alpha_3\gamma_3} + \dfrac{\psi\gamma_3}{\Lambda}P^*\right)}, \quad d = \varsigma + \lambda + \psi$$

$$N^* = \frac{\Lambda}{\alpha_1\dfrac{\gamma_1 A^* + \gamma_2 M^* + \gamma_3 P^*}{T^*} + \psi}$$

$$R^* = \frac{\wp A^* + \varsigma M^* + \zeta P^*}{\psi}$$

and we have the following quadratic equation for P^*

$$a_1 P^{*2} - a_2\left(1 - \frac{1}{\mathcal{R}_0}\right)P^* = 0,$$

where $a_1 = \dfrac{\psi\alpha_2\gamma_3^2}{\Lambda\gamma_2(\kappa + \delta + \zeta + \psi)}$ and $b = \dfrac{(\varsigma + \lambda + \psi)\alpha_1\gamma_1}{\alpha_2\gamma_2}$. Since $P^* \neq 0$, we have $P^* = \dfrac{a_2}{a_1}\left(1 - \dfrac{1}{\mathcal{R}_0}\right)$ and P^* is positive when $\mathcal{R}_0 > 1$.

Theorem 7. *The gambling problem-free equilibrium point E_0 is globally asymptotically stable if $\mathcal{R}_0 \leq 1$ and unstable if $\mathcal{R}_0 > 1$.*

Proof. Assume the Lyapunov function:

$$L(t) = M(t) + P(t).$$

Taking the modified ABC derivative both sides and using Equation (7), we have:

$$\begin{aligned} {}^*\mathcal{D}_t^{\upsilon} L(t) &= \alpha_2\frac{\gamma_2 M + \gamma_3 P}{T}A + \delta P \\ &-(\lambda + \varsigma + \alpha_3\frac{\gamma_3 P}{T} + \psi)M \\ &+\alpha_3\frac{\gamma_3 P}{T}M - (\kappa + \delta + \zeta + \psi)P \end{aligned}$$

At the gambling problem-free equilibrium point E_0, we have:

$$\begin{aligned} {}^*\mathcal{D}_t^{\upsilon} L(t) &= \alpha_2\gamma_2 M\frac{\alpha_1\gamma_1 - \wp - \psi}{\alpha_1\gamma_1} - (\lambda + \varsigma + \psi)M \\ &+\alpha_2\gamma_3 P\frac{\alpha_1\gamma_1 - \wp - \psi}{\alpha_1\gamma_1} - (\kappa + \zeta + \psi)P \\ &= (\Re 0 - 1)(\lambda + \varsigma + \psi)M \\ &+\left[\alpha_2\gamma_3\frac{\alpha_1\gamma_1 - \wp - \psi}{\alpha_1\gamma_1} - (\kappa + \zeta + \psi)\right]P \end{aligned}$$

All the model parameters are nonnegative; it follows that ${}^*\mathcal{D}_t^{\upsilon} L(t) \leq 0$ for $\mathcal{R}_0 < 1$ and $\alpha_2\gamma_3\dfrac{\alpha_1\gamma_1 - \wp - \psi}{\alpha_1\gamma_1} \leq (\kappa + \zeta + \psi)$. ${}^*\mathcal{D}_t^{\upsilon} L(t) = 0$ if and only if $M = P = 0$. Thus, by LaSalle's invariance principle, the gambling problem-free equilibrium point E_0 is globally asymptotically stable in a positively invariant region if $\mathcal{R}_0 \leq 1$.

4. Numerical method

In this section, we use an approximation technique for the system in (1). By applying the fundamental theorem of modified ABC fractional calculus, system (7) can be written as:

$$\begin{cases} m(t) - m(0) = \dfrac{1-\upsilon}{\mathcal{B}(\upsilon)}f(t,\ m(t)) \\ +\dfrac{\upsilon}{\mathcal{B}(\upsilon)\Gamma(\upsilon)}\int_0^t (t-\varsigma)^{\upsilon-1} f(\varsigma,\ m(\varsigma))\,d\varsigma \\ -\dfrac{1-\upsilon}{\mathcal{B}(\upsilon)}f(0,\ m(0))\left(1 + \dfrac{\gamma_{\upsilon}}{\Gamma(\upsilon+1)}t^{\upsilon}\right). \end{cases} \tag{27}$$

We are producing a numerical scheme for this system with the help of Lagrange's interpolation polynomials. Setting $t = t_{n+1}$, $n = 0, 1,\ 2,\ \ldots,\ M$ with $h = \dfrac{T}{M}$, we have:

$$\begin{cases} m_{n+1}(t) = m(0) + \dfrac{1-\upsilon}{\mathcal{B}(\upsilon)}f(t_n,\ m(t_n)) \\ +\dfrac{\upsilon}{\mathcal{B}(\upsilon)\Gamma(\upsilon)}\int_0^{t_{n+1}} (t_{n+1}-\varsigma)^{\upsilon-1} f(\varsigma,\ m(\varsigma))\,d\varsigma \\ -\dfrac{1-\upsilon}{\mathcal{B}(\upsilon)}f(0,\ m(0))\left(1 + \dfrac{\gamma_{\upsilon}}{\Gamma(\upsilon+1)}t_n^{\upsilon}\right). \end{cases} \tag{28}$$

or equivalently,

$$\begin{cases} m_{n+1}(t) = m(0) + \dfrac{1-\upsilon}{\mathcal{B}(\upsilon)} f(t_n,\ m(t_n)) \\ \\ +\dfrac{\upsilon}{\mathcal{B}(\upsilon)\Gamma(\upsilon)} \begin{pmatrix} \sum_{i=1}^{n} \int_{t_i}^{t_{i+1}} (t_{n+1}-\varsigma)^{\upsilon-1} \\ \\ \times f(\varsigma,\ m(\varsigma))\, d\varsigma \end{pmatrix} \\ \\ -\dfrac{1-\upsilon}{\mathcal{B}(\upsilon)} f(0,\ m(0)) \left(1 + \dfrac{\gamma_\upsilon}{\Gamma(\upsilon+1)} t_n^{\upsilon}\right). \end{cases} \tag{29}$$

The function $f(\varsigma,\ m(\varsigma))$ can be approximated over $(t_i,\ t_{i+1})$ using the Lagrange's interpolation polynomial as:

$$f(\varsigma,\ m(\varsigma)) = \begin{bmatrix} \dfrac{f(t_i,\ m(t_i))}{h}(t - t_{i-1}) \\ \\ -\dfrac{f(t_{i-1},\ m(t_{i-1}))}{h}(t - t_i) \end{bmatrix}$$

Substituting it into Equation (29), we obtain:

$$\begin{cases} m_{n+1}(t) = m(0) + \dfrac{1-\upsilon}{\mathcal{B}(\upsilon)} f(t_n,\ m(t_n)) \\ \\ +\dfrac{\upsilon}{\mathcal{B}(\upsilon)\Gamma(\upsilon)} \sum_{i=1}^{n} \begin{bmatrix} \dfrac{f(t_i,\ m(t_i))}{h} I_1 \\ \\ -\dfrac{f(t_{i-1},\ m(t_{i-1}))}{h} I_2 \end{bmatrix} \\ \\ -\dfrac{1-\upsilon}{\mathcal{B}(\upsilon)} f(0,\ m(0)) \left(1 + \dfrac{\gamma_\upsilon}{\Gamma(\upsilon+1)} t_n^{\upsilon}\right). \end{cases} \tag{30}$$

where $I_1 = \int_{t_i}^{t_{i+1}} (t_{n+1}-\varsigma)^{\upsilon-1}(\varsigma - t_{i-1})\, d\varsigma$ and $I_2 = \int_{t_i}^{t_{i+1}} (t_{n+1}-\varsigma)^{\upsilon-1}(\varsigma - t_i)\, d\varsigma$. Computing these integrals, we finally get the approximate solution as:

$$\begin{cases} m_{n+1}(t) = m(0) + \dfrac{1-\upsilon}{\mathcal{B}(\upsilon)} f(t_n,\ m(t_n)) \\ \\ +\dfrac{\upsilon}{\mathcal{B}(\upsilon)} \sum_{i=1}^{n} \begin{bmatrix} \dfrac{h^\upsilon f(t_i,\ m(t_i))}{\Gamma(\upsilon+2)}(A-B) \\ \\ -\dfrac{h^\upsilon f(t_{i-1},\ m(t_{i-1}))}{\Gamma(\upsilon+2)} \\ (C-D) \end{bmatrix} \\ \\ -\dfrac{1-\upsilon}{\mathcal{B}(\upsilon)} f(0,\ m(0)) \left(1 + \dfrac{\gamma_\upsilon}{\Gamma(\upsilon+1)} (nh)^{\upsilon}\right). \end{cases} \tag{31}$$

where

$$\begin{cases} A = (n-i+2+\upsilon)(n+1-i)^{\upsilon} \\ \\ B = (n-i+2+2\upsilon)(n-i)^{\upsilon} \\ \\ C = (n+1-i)^{\upsilon+1} \\ \\ D = (n-i+1+\upsilon)(n-i)^{\upsilon} \end{cases}$$

5. Graphical results and discussion

The graphical results validate the theoretical processes. The choice of the fractional order υ in the modified ABC fractional derivative, which is in the range (0, 1], is primarily owing to its mathematical consistency with integer-order derivatives. In this section, we implement the proposed technique to solve system (7) with the initial solutions and model parameters provided in Table 1. The approximate results were obtained using the numerical scheme presented in Section 4. Due to the lack of organized data on excessive gambling, no real data have been provided for our model results. Therefore, the approximate values are not estimated based on real data, and the results are obtained using assumed parameter values and initial conditions. The gambling problem-free equilibrium point exists when $\alpha_1\gamma_1 > \wp + \psi$. The fractional order υ influences transient dynamics but not equilibrium point stability. The basic reproduction number is then computed to be $\mathcal{R}_0 = 1.4826$ and unstable gambling problem-free equilibrium point is $E_0 = (2.7583,\ 15.6306,\ 0,\ 0,\ 0)$. $\mathcal{R}_0 > 1$ means that on average each problem gambler spreads addiction to more than 1 person. Interventions must reduce $\mathcal{R}_0$ below one. Some key strategies are to reduce transmission α_2 &γ_2, increase recovery rates, λ, & ς and raise awareness.

5.1. Optimal control analysis

We consider the system (7) by adding the control variable $c(t)$, which ranges from 0 to 1, where zero corresponds to the absence of application of any control mechanism, and one refers to the case where there is a fully controlled scenario. The intermediate values $c(t) \in (0,\ 1)$ quantify the effect of applying the intervention mechanisms. The control directly reduces the progression to addiction by a factor of $1 - c$. The control variable:

- Represents interventions like counseling, self-exclusion programs, and early treatment
- Reduces the transition rate from M to P.

Table 1. Value of the model parameters for equation (7)

Parameter	Value	Source	Parameter	Value	Source
N_0	200	Assumed	A_0	75	Assumed
M_0	42	Assumed	P_0	14	Assumed
R_0	0	Assumed	Λ	0.33	Calculated
α_1	0.7	[10]	λ	0.07	[10]
γ_1	0.2	Assumed	$\wp$	0.02	Assumed
γ_2	0.3	Assumed	ς	0.015	Assumed
γ_3	0.4	Assumed	κ	0.34	[10]
α_2	0.5	Assumed	δ	0.014	Assumed
α_3	0.2	Assumed	ζ	0.01	Assumed
ψ	0.001	Assumed			

The modified fractional-order system with mABC derivative:

$$\left.\begin{aligned}
&{}^{*}\mathcal{D}_t^{v} N(t) = \Lambda - \alpha_1 N \tfrac{\gamma_1 A+\gamma_2 M+\gamma_3 P}{T} - \psi N \\
&{}^{*}\mathcal{D}_t^{v} A(t) = \alpha_1 N \tfrac{\gamma_1 A+\gamma_2 M+\gamma_3 P}{T} + \lambda M + \kappa P \\
&\quad - \left(\wp + \alpha_2 \tfrac{\gamma_2 M+\gamma_3 P}{T} + \psi\right) A \\
&{}^{*}\mathcal{D}_t^{v} M(t) = \left(\alpha_2 \tfrac{\gamma_2 M+\gamma_3 P}{T}\right) A + \delta P \\
&\quad - \left[\lambda + \varsigma + (1-c)\alpha_3 \tfrac{\gamma_3 P}{T} + \psi\right] M \\
&{}^{*}\mathcal{D}_t^{v} P(t) = (1-c)\alpha_3 \tfrac{\gamma_3 P}{T} M - (\kappa + \delta + \zeta + \psi) P \\
&{}^{*}\mathcal{D}_t^{v} R(t) = \wp A + \varsigma M + \zeta P - \psi R
\end{aligned}\right\}$$

The main objective is to find the optimal control unit $c(t)$ such that the following control objective function is minimized:

$$J(u) = \int_0^T \left[A_1 M(t) + A_2 P(t) + \frac{1}{2} B c^2(t)\right] dt \tag{32}$$

where:

- $A_1, A_2 > 0$: Weights for at-risk and addicted populations.
- $B > 0$: Cost weight for control implementation.
- T: Final time

To solve the new system, we need to derive the necessary optimality conditions for the problem. To do this, we define the Hamiltonian function:

$$\begin{aligned}
H = {} & A_1 M(t) + A_2 P(t) + \frac{1}{2} B c^2(t) \\
& + d_N \left[\Lambda - \alpha_1 N \frac{\gamma_1 A + \gamma_2 M + \gamma_3 P}{T} - \psi N\right] \\
& + d_A \left[\alpha_1 N \frac{\gamma_1 A + \gamma_2 M + \gamma_3 P}{T} + \lambda M + \kappa P \right. \\
& \left. - \left(\wp + \alpha_2 \frac{\gamma_2 M + \gamma_3 P}{T} + \psi\right) A\right] \\
& + d_M \left[\alpha_2 \frac{\gamma_2 M + \gamma_3 P}{T} A + \delta P \right. \\
& \left. - \left[\lambda + \varsigma + (1-c)\alpha_3 \frac{\gamma_3 P}{T} + \psi\right] M\right] \\
& + d_P \left[(1-c)\alpha_3 \frac{\gamma_3 P}{T} M - (\kappa + \delta + \zeta + \psi) P\right] \\
& + d_R \left[\wp A + \varsigma M + \zeta P - \psi R\right]
\end{aligned} \tag{33}$$

where d_N, d_A, d_M, d_P and d_R are adjoint variables. To obtain the necessary optimality conditions:

$$\left.\begin{aligned}
&{}_0^{*}D_t^{v} \Phi_i(t) = \frac{\partial H}{\partial d_{\Phi_i}}(t) \\
&{}_0^{*}D_t^{v} d_{\Phi_i}(t) = -\frac{\partial H}{\partial \Phi_i}(t) \\
&\frac{\partial H}{\partial c}(t) = 0, \quad i = 1,\ 2,\ 3,\ 4,\ 5.
\end{aligned}\right\} \tag{34}$$

where $\Phi_1 = N(t)$, $\Phi_2 = A(t)$, $\Phi_3 = M(t)$, $\Phi_4 = P(t)$ and $\Phi_5 = R(t)$. The transversality conditions:

$$d_i(T) = 0, \quad i \in \{d_{\Phi_i}\}.$$

Accordingly, the optimal control $c*(t)$ of a new dynamic system, which minimizes the objective functional (32), is characterized by

$$c*(t) = \min\left(\max\left(0, \frac{\alpha_3 \frac{\gamma_3 P(t)}{T} M(t)(d_P(t) - d_M(t))}{B}\right),\ 1\right). \tag{35}$$

5.2. Sensitivity analysis

Performing a sensitivity analysis on the gambling model helps to identify which model parameters most significantly influence the system's behavior. Next, we calculate the normalized sensitivity index for $\mathcal{R}_0$ with respect to the model parameter p as:

$$S_p = \frac{p}{\mathcal{R}_0} \times \frac{\partial \mathcal{R}_0}{\partial p}.$$

The sensitive parameters and their sensitivity index are shown in Table 2.

Table 2. Sensitivity indices of $\mathcal{R}_0$

Parameter	Sensitivity index
α_1	$+0.1765$
α_2	$+1.0000$
γ_2	$+1.0000$
ψ	-0.0200
$\wp$	-0.1681
λ	-0.8140
ς	-0.1744
γ_1	$+0.1765$

Table 2 discusses the sensitivity of the basic reproduction number $\mathcal{R}_0$. The parameters α_1, α_2, γ_1 and γ_2 have positive imapcts, which means decreasing these parameters leads to a reduction in the value of $\mathcal{R}_0$ α_1 has a positive but relatively weak influence on $\mathcal{R}_0$. To reduce $\mathcal{R}_0$, prioritize decreasing the parameters α_2 and γ_2. The parameters $\wp$, λ, ς and ψ have negative imapcts, which means increasing these parameters leads to a reduction in the value of $\mathcal{R}_0$. For instance, a 42.8571% decrease (from 0.7 to 0.4) in α_1 decreases $\mathcal{R}_0$ by approximately 13.2402%. A 40% decrease (from 0.5 to 0.3) in α_2 decreases $\mathcal{R}_0$ by approximately 40%. A 33.3334% decrease (from 0.3 to 0.2) in γ_2 decreases $\mathcal{R}_0$ by approximately 33.3334%. Similarly, a 28.5714% increase (from 0.07 to 0.09) in λ decreases $\mathcal{R}_0$ by approximately 18.8722%.

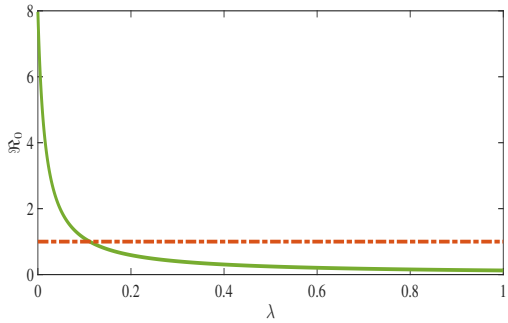


Figure 2. Effects of a parameter λ on the basic reproduction number $\mathcal{R}_0$

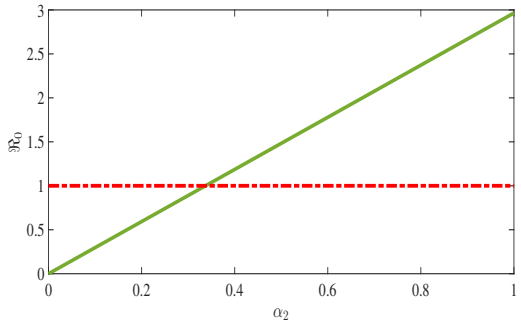


Figure 3. Effects of a parameter α_2 on the basic reproduction number $\mathcal{R}_0$

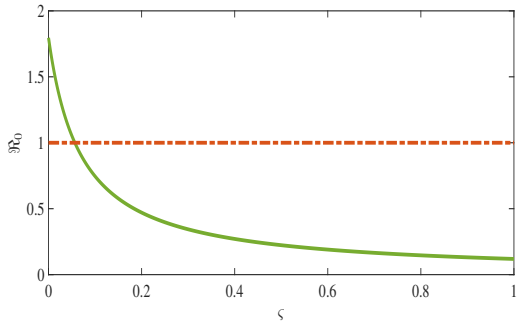


Figure 4. Effects of a parameter ς on the basic reproduction number $\mathcal{R}_0$

Figures 2-4 indicate the effects of senstive parameters on the basic reproduction number. To stabilize the gambling problem-free equilibrium point, limit interactions between aware individuals and problem gamblers and promote awareness of gambling risks.

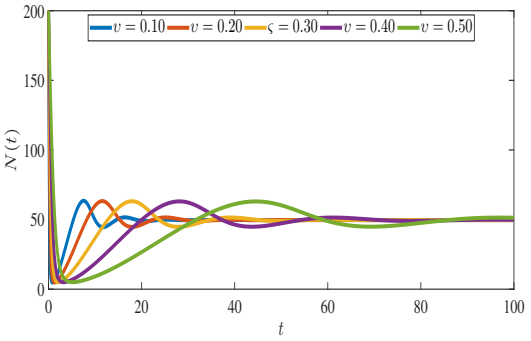


Figure 5. The approximate solutions of $N(t)$ with different fractional order values

In Figure 5, we plotted the approximate results of the system (7) using the numerical scheme presented in Section 4 for different fractional order values υ. The graph confirms that the order of fractional differential equations significantly affects the simulation of the system using the proposed scheme. A small change in the fractional order value can

have a significant impact on the system results.

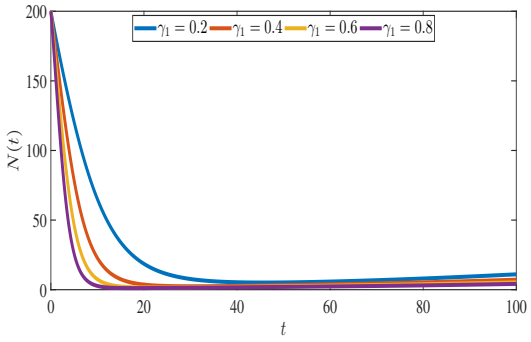


Figure 6. The approximate solutions of $N(t)$ with different values γ_1 when $\upsilon = 0.95$

Figure 6 examines how the parameter γ_1 (weight of non-problem gamblers A on no gamblers N) affects the solution $N(t)$ with time intervals. Higher γ_1 (e.g., $\gamma_1 = 0.8$) accelerates the decline of $N(t)$, as more individuals transition to start gambling. Conversely, lower γ_1 (e.g., $\gamma_1 = 0.2$) slows the decline, reducing recruitment into gambling activities. Public awareness campaigns (reducing γ_1) could slow gambling uptake.

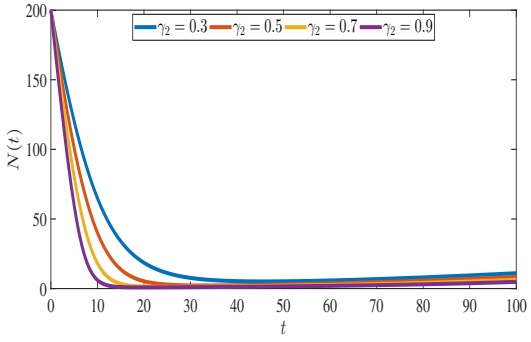


Figure 7. The approximate solutions of $N(t)$ with different values γ_2 when $\upsilon = 0.95$

Figure 7 tests the impact of γ_2, which is the influence of minor-risk gamblers. Early intervention for minor-risk gamblers may indirectly protect the new gamblers.

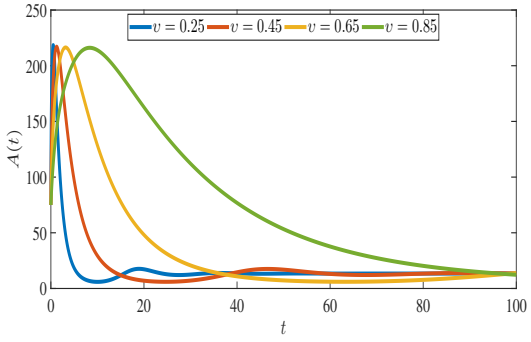


Figure 8. The approximate solutions of $A(t)$ with different fractional order values

Some non-problem gamblers may show interest in gambling frequently. For a few weeks, they will gamble with no problem but may show signs of addiction and will move to the addiction stage. Figures 8-9 confirm the behavior of no problem gamblers and minor-risk under varying fractional order values. Due to several factors, peaceful gambling can transition into excessive gambling activities.

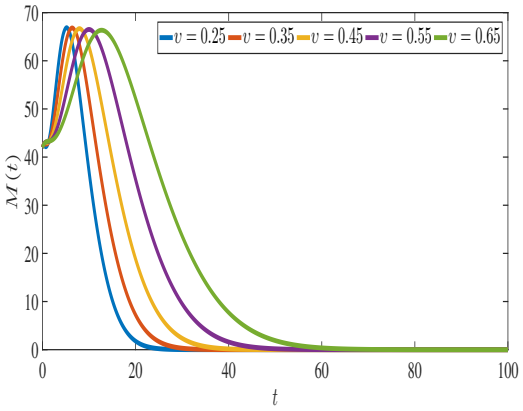


Figure 9. The approximate solutions of $M(t)$ with different fractional order values

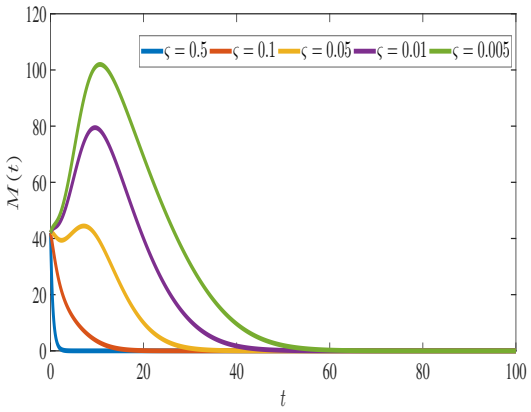


Figure 10. The approximate solutions of $M(t)$ with different values of recovery rate ς when $\upsilon = 0.5$

Figure 10 evaluates how the recovery rate ς (transition from M to R) affects $M(t)$. Higher recovery rate (e.g., $\varsigma = 0.5$) rapidly reduces $M(t)$, as more quit gambling. Lower recovery rate (e.g., $\varsigma = 0.005$) increases the risk of gambling in the population. Strengthening recovery programs (e.g., counseling, religion activities) reduces the risks of gamblers. Early decision to stop daily gambling is highly recommended, especially for young gamblers. Numerical results of the behavior of minor risk gamblers in relation to the recovery parameter ς are shown in Figure 10. It is clearly visible that as the recovery rate ς increases from 0.005 to 0.5, the number of individuals in the risk gambling stage decreases.

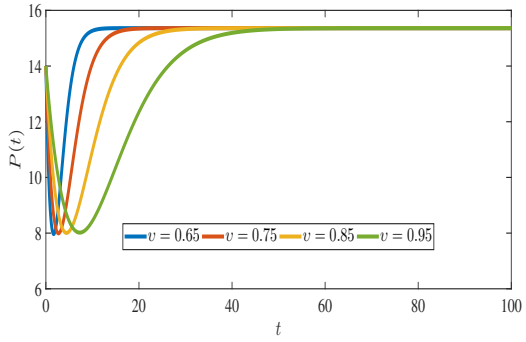


Figure 11. The approximate solutions of $P(t)$ with different fractional order values when $\mathcal{R}_0 > 1$

The large number of addicted gamblers can result from a daily focus on reward values. To reduce this number, individuals must focus on reducing their daily investment in gambling activities and return to their previous non-problematic stage. Figure 11 indicates the dynamics of addicted gamblers under different fractional order values. The graph is plotted when the basic reproduction number is greater than one.

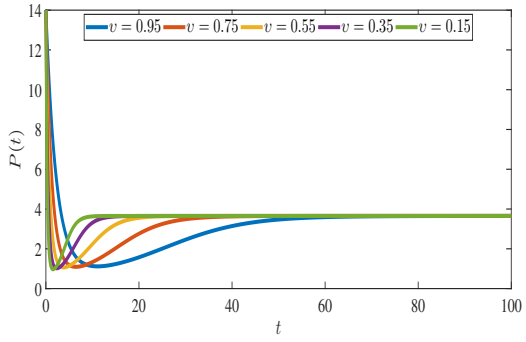


Figure 12. The approximate solutions of $P(t)$ with different fractional order values when $\mathcal{R}_0 < 1$

Figure 12 shows the behavior of addicted population with several fractional order υ when the basic reproduction number $\mathcal{R}_0 < 1$. Since $\mathcal{R}_0 < 1$, gambling problems will not persist (GPFE is stable).

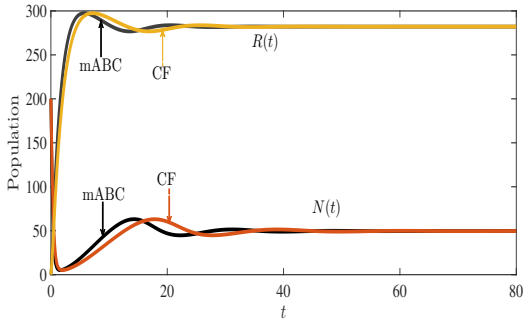


Figure 13. Solutions of the system (7) for Caputo–Fabrizio (CF) and mABC with $\upsilon = 0.35,\ \alpha_1 = 1$

Figure 13 depicts the solutions of $N(t)$ and $R(t)$ obtained by the CF and mABC approaches. The reader may see from these illustrations that our model solutions are found to be in good agreement under both fractional operators. Figure 14 shows the results of $A(t)$ and $M(t)$ obtained by the CF and mABC derivatives.

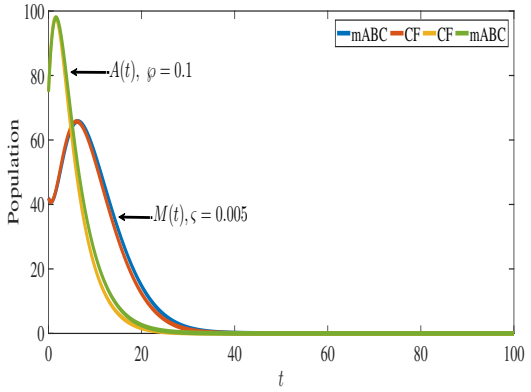


Figure 14. Solutions of the system 7 for C-F and mABC with $\upsilon = 0.70$

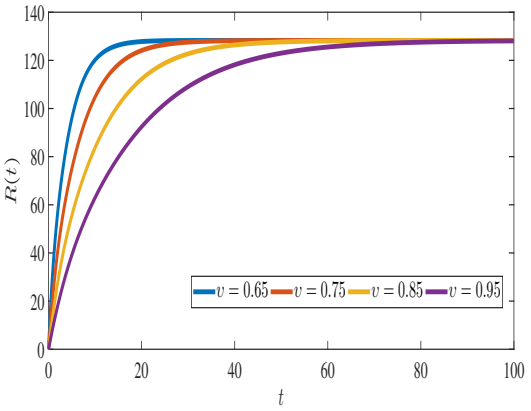


Figure 15. The approximate solutions of $R(t)$ with different fractional order values

Figure 15 demonstrates the dynamics of recovered individuals with different values of υ. Also, Figure 16 shows the effects of recovery rate ς.

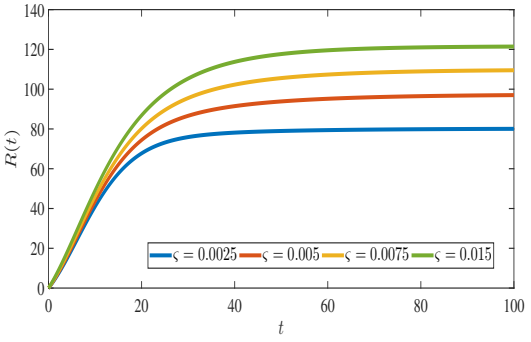


Figure 16. The approximate solutions of $R(t)$ with different values recovery rate ς when $\upsilon = 0.75$

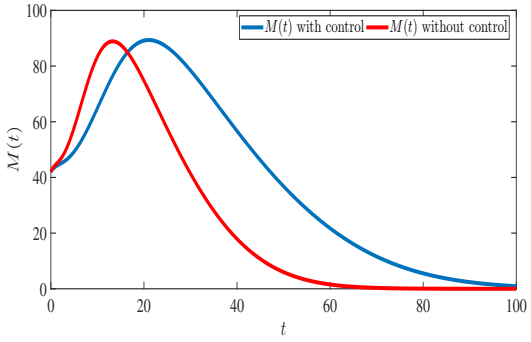


Figure 17. Minor risk infected population with control and without control

Figure 17 confirms the minor risk gamblers with and without the control measures, it can also be seen that when using the control measures, the minor risk population increases, this is due to the fact that the highly addicted population is reduced because of the control impact.

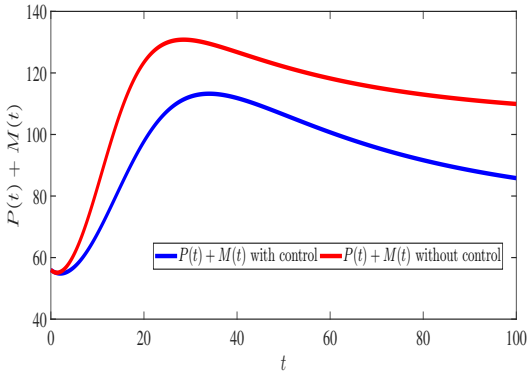


Figure 18. Total addicted population with control and without control

Figure 18 indicates the total addicted population with and without control strategy. From this figure, we confirmed that the total number of the addicted population is reduced due to the control strategy.

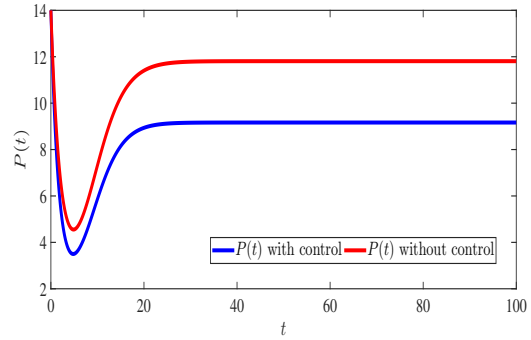


Figure 19. Permanent addicted population with control and without control

Figure 19 shows the highly addicted gamblers with and without the control measures, as we can see from the graph with control $c(t)$, the addicted population $P(t)$ reduces significantly. Interventions (e.g., counseling) reduce $P(t)$ by lowering $\mathcal{R}_0$ to less than unity.

6. Conclusion

In the present study, the problem of excessive gambling model has been investigated by one of the robust nonlocal fractional operator. The modified ABC fractional derivative operator is applied to present a system of differential equations, with approximate results achieved using numerical method. This study considers a deterministic problem gambling model under positive initial conditions, including non-negative model parameters. The fractional order is υ, and consideration was given to the dimensional consistency between the rest of the model parameters. As a result, several significant features of the proposed fractional version of the model have been documented, such as the model formulation, the existence/uniqueness of the solution, invariant region, stability analysis, and most importantly, the basic reproduction number. It should be noted that the fractional-type dynamical system under investigation comprehends the behavior of the model more correctly than the variant of the integer order. Figures 5-14 demonstrate how fractional order υ and sensitive parameters influence addiction dynamics, guiding targeted interventions. A comparative analysis between the fractional time derivative approach of mABC and CF models has been done. The comparisons are given in Figures 13-14. It is evident that these two operators are very effective for approximating fractional systems of differential equations, and the solutions are in good agreement under both derivatives. All the computations in the study were performed using MATLAB R2016a computational software. As a recommendation, the mathematical modeling of the problem of excessive gambling needs to be continued because of its significant social, economic, and political impacts. A better understanding of mathematical modeling research, including different factors of problem gambling, can inform policy-making and therapy for highly addicted individuals. Future work should incorporate stochastic effects and validate parameters based on confirmed real-world data, including different factors of gambling addiction.

Acknowledgments

None.

Funding

None.

Conflict of interest

The authors declare they have no competing interests.

Author contributions

Conceptualization: Mulualem Aychluh, D.L. Suthar
Formal analysis: S.D. Purohit
Investigation: Clemente Cesarano
Methodology: D.L. Suthar
Writing-original draft: Mulualem Aychluh, D.L. Suthar
Writing-review & editing: Clemente Cesarano, S.D. Purohit

Availability of data

Not applicable.

AI tools statement

All authors confirm that no AI tools were used in the preparation of this manuscript.

References

1. Reith G. The Age of Chance: Gambling and Western Culture. New York: Routledge; 1999.
2. Peter F, Nigel ET. The History of Problem Gambling. Springer: New York Heidelberg Dordrecht London; 2013 http://doi.org/10.1007/978-1-4614-6699-4
3. Skitch SA, Hodgins DC. (2004). Impulsivity, compulsivity and pathological gambling: an exploratory study of pathological gambling as an impulsivity-compulsivity spectrum disorder. *Int Gambl Stud.* 2004;4(2):175–88.
4. Zendle D, Meyer R, Over, H. (2019). Adolescents and loot boxes: links with problem gambling and motivations for purchase. R Soc Open Sci. 2019;6(6):190049. http://doi.org/10.1098/rsos.190049
5. American Psychiatric Association [APA]. Diagnostic and Statistical Manual of Mental Disorders (4th ed., text revision (DSM-IV-TR)). Washington, DC; 2000.
6. Room R, Turner NE, Ialomiteanu A. Community effects of the opening of the Niagara Casino: a first report. *Addiction.* 1999;94:1449–1466. http://doi.org/10.1046/j.1360-0443.1999.941014492.x
7. Do TS, Lee YS. A differential equation model for the dynamics of youth gambling. *Osong Public Health Res Perspect.* 2014;5(4):233-241.
8. Kong Y, Li T, Wang Y. (2021). Dynamics analysis of an online gambling spreading model on scale-free networks. *Adv Differ Equ.* 2021; 11(2021). https://doi.org/10.1186/s13662-020-03165-z
9. Shaffer HJ, Korn DA. Gambling and related mental disorders: a public health analysis. *Annu Rev Public Health.* 2002;23:171-212. https://doi.org/10.1146/annurev.publhealth.23.100901.140532
10. Young SL, Tae SD. A mathematical modeling approach to gambling among older adults. *Appl Math Comput.* 2013;221:403-410. https://doi.org/10.1016/j.amc.2013.05.075
11. Weiwei L, Grace PL, Asha G, et al. Impulsivity trajectories and gambling in adolescence among urban male youth. *Addiction.* 2013;108(4):780-788. https://doi.org/10.1111/add.12049
12. Brevers D, Cleeremans A, Tibboel H, et al. Reduced attentional blink for gambling-related stimuli in problem gamblers. *J Behav Ther Exp Psychiatry.* 2011;42(3):265–269. https://doi.org/10.1016/j.jbtep.2011.01.005
13. Brown SL, Rodda S, Phillips JG. Differences between problem and nonproblem gamblers in subjective arousal and affective valence amongst electronic gaming machine players. *Addict Behav.* 2004;29(9):1863–1867. https://doi.org/10.1016/j.addbeh.2004.03.030
14. Gupta R, Derevensky J, Marget N. Coping strategies employed by adolescents with gambling problems. *Child Adolesc Ment Health.* 2004;9(3): 115–120. https://doi.org/10.1111/j.1475-3588.2004.00092.x
15. Michalczuk R, Bowden-Jones H, Verdejo-García A, Clark L. Impulsivity and cognitive distortions in pathological gamblers attending the UK National Problem Gambling Clinic: a preliminary report. *Psychol Med.* 2011;41(12):2625–2635. https://doi.org/10.1017/s003329171100095x
16. Sharpe L. A reformulated cognitive-behavioral model of problem gambling: a biopsychosocial perspective. *Clin Psychol Rev.* 2002;22(1):1–25. doi: 10.1016/s0272-7358(00)00087-8
17. Cătălin B. Understanding Your Game: A Mathematician's Advice for Rational and Safe Gambling. PhilScience Press; 2022. ISBN 978-606-9735-00-8
18. Aychluh M, Suthar DL, Purohit SD. Analysis of the nonlinear Fitzhugh-Nagumo equation and its derivative based on the Rabotnov fractional exponential function. *Partial Diff Equat Appl Math.* 2024;11:100764. https://doi.org/10.1016/j.padiff.2024.100764
19. Ndolane S. Existence, uniqueness, and stability analysis results for the SIR epidemic model with a fractional operator. In: Mathematical Methods in Medical and Biological Sciences; 2025:267-278. https://doi.org/10.1016/B978-0-44-328814-2.00020-5

20. Suthar DL, Haile H, Mulualem A. Effect of vaccination on the transmission dynamics of COVID-19 in Ethiopia. *Results Phys.* 2022;32:105022 https://doi.org/10.1016/j.rinp.2021.105022
21. Baleanu D, Agarwal RP. Fractional calculus in the sky. *Adv Differ Equat.* 2021;117(2021):1-9. https://doi.org/10.1186/s13662-021-03270-7
22. Caputo M, Fabrizio M. A new definition of fractional derivative without singular kernel. *Prog Fract Differ Applicat.* 2015;1(2):73–85. http://dx.doi.org/10.12785/pfda/010201
23. Elvin JM, Sekson S, Sanoe K. A Caputo–Fabrizio fractional differential equation model for HIV/AIDS with treatment compartment. *Adv Diff Equat.* 2019;200(2019):1-20. https://doi.org/10.1186/s13662-019-2138-9
24. Atangana A, Baleanu D. New fractional derivatives with non-local and non-singular kernel: theory and applications to heat transfer model. *Thermal Sci.* 2016;20:763–769.
25. Al-Refai M, Baleanu D. On an extension of the operator with Mittag-Leffler kernel. *Fractals.* 2022;30(5):2240129. https://dx.doi.org/10.1142/S0218348X22501298
26. Ndolane S. SIR epidemic model with Mittag–Leffler fractional derivative Author links open overlay panel. *Chaos Sol Fractals.* 2020;137:109833. https://doi.org/10.1016/j.chaos.2020.109833
27. Zaid O. Numerical solutions of linear time-fractional advection-diffusion equations with modified Mittag-Leffler operator in a bounded domain. *Phys Scrip.* 2024;99(1):015205. https://doi.org/10.1088/1402-4896/ad0fd0
28. Matiur R, Mehmet Y, Muhammad A, Adnan S. Theoretical and numerical investigation of a modified ABC fractional operator for the spread of polio under the effect of vaccination. *AIMS Biophys.* 2024;11(1):97–120. https://doi.org/10.3934/biophy.2024007
29. Hasib K, Jehad A, Dumitru B, Ghada A, & Mutti-Ur R. Existence of solutions and a numerical scheme for a generalized hybrid class of n-coupled modified ABC-fractional differential equations with an application. *AIMS Math.* 2023;8(3):6609–6625. https://doi.org/10.3934/math.2023334
30. Odibat Z, Baleanu D. New solutions of the fractional differential equations with modified Mittag-Leffler kernel. *J Comput Nonlinear Dyn.* 2023;18(9):18091007. https://doi.org/10.1115/1.4062747
31. Khan H, Alzabut J, Alfwzan WF, Gulzar H. Nonlinear dynamics of a piecewise modified ABC fractional-Order leukemia model with symmetric numerical simulations. *Symmetry.* 2023;15(7):1338. https://doi.org/10.3390/sym15071338
32. Khan H, Alzabut J, Gulzar H. Existence of solutions for hybrid modified ABC-fractional differential equations with p-Laplacian operator and an application to a waterborne disease model. *Alexandria Eng J.* 2023;70:665–672. https://doi.org/10.1016/j.aej.2023.02.045
33. Aychluh M, & Ayalew M. The fractional power series method for solving the nonlinear Kuramoto-Sivashinsky equation. *Int J Appl Comput Math.* 2025;11(29):1-27. https://doi.org/10.1007/s40819-025-01850-9
34. Şuayip Y, Karaçayır M. An exponential Galerkin method for solutions of HIV infection model of CD4+ T-cells. *Comput Biol Chem.* 2017;67:205-212. https://doi.org/10.1016/j.compbiolchem.2016.12.006
35. Ayalew M, Mekash A, Aychluh M. Numerical approximation of space-fractional diffusion equation using Laguerre spectral collocation method. *Int J Math Ind.* 2025;2450029. https://doi.org/10.1142/S2661335224500291
36. Al-Omari A, Schuttler HB, Arnold J, Taha T. Solving nonlinear systems of first order ordinary differential equations using a Galerkin finite element method. *IEEE Access.* 2013;1(2013):408-417. https://doi.org/10.1109/ACCESS.2013.2269192
37. Baleanu, D, Fernandez A. On some new properties of fractional derivatives with Mittag-Leffler kernel. *Commun Nonlinear Sci Numer Simulat.* 2018;59:444–462. https://doi.org/10.1016/j.cnsns.2017.12.003
38. Matignon D. Stability results for fractional differential equations with applications to control processing. *Comput Eng Syst Appl Multi-conf.* 1996;2:963-968.

Mulualem Aychluh *is a mathematics lecturer at Samara University in Ethiopia. His specialties include mathematical modeling, numerical methods, special functions, and fractional calculus. He received his BSc from Jimma University (2013) and an MSc in Numerical Analysis from Wollo University (2022). With more than 7 years of academic and research experience, he specializes in chaos solitons, integral transforms, and advanced computational approaches. I also act as a reviewer of Mathematical Reviews/MathSciNet., the Zentralblatt MATH and a number of well-known journals.*
https://orcid.org/0000-0002-5295-1559

D.L. Suthar *is an Associate Professor, Department of Mathematics, College of Natural Science, at Wollo University, Dessie, Amhara Region, Ethiopia. I have acquired a full-time Ph.D. in Mathematics (Special Function) with 17 years of teaching experience and 20 years of research experience, including a Ph.D. program. In my supervision, 5 students have completed Ph. D. degree and 21 students completed M.Sc. Thesis. My research interests include Special functions, Fractional Calculus, Integral transforms, Basic Hypergeometric Series, Geometric Function Theory and*

Mathematical Physics. I had also organized a diverse range of workshops/conferences in the fields of mathematical sciences, engineering innovations and a number of seminars on mathematical discipline in order to enrich their knowledge and the skills of the student community. Apart from the above, I received the International Travel Grants from ICM (Brazil, Russia), and ICIAM (Spain, Japan) to attend International Conferences. I have published 224 research articles in national and international journals and 5 books for engineering students. I have played a role as author in the preparation of the Modules for Special Function, Tensor analysis, and Research Methodology. I wrote curriculum for establishing the Doctorate of Philosophy (PhD) in Analysis, and curriculum for establishing Master's Degree in Real Analysis, Algebra, Differential Equation, and Numerical Analysis. I have ample knowledge of mathematical application skills, such as MATLAB, Mathematica, Lingo, Maple, Latex. I am a lifetime member of the Indian Science Congress Association, the Society for Special Function Their Application, the Indian Mathematical Society and I also act as a reviewer of Mathematical Reviews/MathSciNet., the Zentralblatt MATH and a number of well-known journals.

http://orcid.org/0000-0001-9978-2177

Clemente Cesarano *is an Associate Professor of Numerical Analysis at the International Telematic University UNINETTUNO in Rome. He also holds the position of Vice Dean of the Faculty of Engineering and coordinates the university's Mathematics Section. Additionally, he directs master's programs in Project Management and Applied and Industrial Mathematics. Dr. Cesarano earned his degree in Mathematics from the University of Basilicata in 1996/97, graduating with honors. He pursued doctoral studies in Applied Mathematics at the University of Ulm in Germany and the Complutense University of Madrid in Spain, completing his Ph.D. with a thesis on generalized Hermite polynomials. His research interests encompass mathematical and numerical analysis, special functions, fractional calculus, and differential equations. He has authored numerous publications in these fields and serves on the editorial board of various scientific journals. Beyond his academic roles, Cesarano is affiliated with several research institutions, including the National Research Council (CNR) and the National Institute for Advanced Mathematics (INdAM). He is also an Honorary Fellow of the Australian Institute of High Energetic Materials. At UNINETTUNO, he plays a pivotal role in developing academic curricula, fostering international collaborations, and coordinating initiatives such as the "Education Without Borders" project, which supports refugee students.*

https://orcid.org/0000-0002-1694-7907

S.D. Purohit *is currently an Associate professor of Mathematics at Rajasthan Technical University, Kota. He did his M.Sc. and Ph.D. in Mathematics from Jai Narayan Vyas University, Jodhpur, India. He was awarded the University Gold Medal for being the topper in M.Sc. Mathematics and awarded Junior Research Fellowship and Senior Research Fellow of CSIR. Recently, he also did his Post Doctorate Fellowship at Lebanese American University, Beirut, Lebanon. He has 19 years of teaching and research experience. Since 2006 to 2014, he worked as assistant professor of mathematics at CTAE, Maharana Pratap University of Agriculture & Technology, Udaipur. Presently, he is Associate Dean, Academic Affairs; Associate Dean, Applied Sciences and Public Relation Officer at RTU, Kota. His research area includes Special Functions, Fractional Calculus, q-Calculus, Computational Mathematical Techniques, Mathematics Modelling, Geometric Function Theory, Integral Inequalities and Fluid Dynamics. Based on a study by Stanford University (USA) scientists, he was placed in the top 2% of scientists worldwide for both career-long and single-year impact in the field of applied mathematics. He has published 12 books, 10 book chapters and more than 260 research papers, in national and international esteemed journals. He is a reviewer for Mathematical Reviews, USA (AMS) and Zentralblatt MATH, Berlin since last 16 years. He is a member of the Editorial Board and guest editor for a number of international mathematical and interdisciplinary journals.*

https://orcid.org/0000-0002-1098-5961

This work is licensed under a Creative Commons Attribution 4.0 International License. The authors retain ownership of the copyright for their article, but they allow anyone to download, reuse, reprint, modify, distribute, and/or copy articles in IJOCTA, so long as the original authors and source are credited. To see the complete license contents, please visit http://creativecommons.org/licenses/by/4.0/.

An International Journal of Optimization and Control: Theories & Applications
ISSN: 2146-0957 eISSN: 2146-5703
Vol.15, No.3, pp.426-434 (2025)
https://doi.org/10.36922/IJOCTA025060020

RESEARCH ARTICLE

Predefined-time fractional-order terminal SMC for robot dynamics

Saim Ahmed[1,2*] and Ahmad Taher Azar[1,2]

[1]College of Computer and Information Sciences, Prince Sultan University, Riyadh, Saudi Arabia
[2]Automated Systems and Computing Lab (ASCL), Prince Sultan University, Riyadh, Saudi Arabia
sahmed@psu.edu.sa, aazar@psu.edu.sa

ARTICLE INFO

Article History:
Received: February 6, 2025
Revised: April 9, 2025
Accepted: April 17, 2025
Published Online: May 6, 2025

Keywords:
Predefined-time control,
Fractional-order SMC scheme
Robotic manipulator

AMS Classification 2010:
93D05; 93C95; 93C10; 70E60

ABSTRACT

This study presents an investigation into fractional-order predefined-time terminal sliding mode control (FoPtSMC) for robotic manipulators, particularly focusing on addressing uncertainties and external disturbances. The study introduces a new predefined-time fractional-order SMC method to ensure guaranteed predefined-time convergence and superior tracking performance. This approach also aims to mitigate control input chattering, a common issue in such systems. The Lyapunov analysis is used, and the study establishes the predefined time stability of the proposed closed system. Furthermore, the effectiveness of the proposed FoPtSMC technique is validated through computer simulations applied to a robotic manipulator system.

CC BY

1. Introduction

Precisely controlling robotic manipulators is crucial for automating tasks in various industries. However, it can be challenging due to their complex and unpredictable movements. Unknown disturbances and uncertainties can compromise precise motions and stable performance.[1] Traditional control methods rely on complex mathematical models to predict robot behavior and design control strategies. Real-world robots may behave differently due to manufacturing variations, resulting in unexpected behaviors or unmodeled dynamics that can significantly impact control performance, leading to errors, instability, or safety hazards.[2,3] This sensitivity to uncertainties underscores the increasing need for robust control approaches in robotics, which prioritize maintaining expected tracking performance and closed-loop stability even under unknown factors.[4]

The effectiveness of sliding mode control (SMC) in managing uncertainties and external disturbances has solidified its popularity in controlling complex systems, especially in the context of real-world robots with intricate dynamics that are difficult to model accurately.[5–9] Terminal Sliding Mode Control (TSM), an extension of SMC, provides the additional benefit of ensuring state convergence within a predetermined time frame, leading to enhanced precision and resilience for robots following a planned trajectory.[10,11] However, the literature suggests that TSM may demonstrate slower convergence compared to alternative methods.[12–14] Moreover, specific TSM implementations can present design complexities, necessitating careful attention.[15–18] Research endeavors have concentrated on enhancing the robustness and responsiveness of TSM.[19,20] One promising strategy is fractional-order SMC, which combines SMC with the fractional-order control scheme, offering several advantages.[21] Fractional-order SMC has the potential to enhance the system's response speed and path-following accuracy while reducing control jitters.[22] By having these advantages, fractional-order SMC emerges as a

*Corresponding Author

promising approach for precise and resilient control of robotic manipulators, particularly in scenarios involving uncertainties and disturbances.[23] Subsequent sections will examine further the theory of PtSMC, present simulation results demonstrating its effectiveness, and explore its implications for controlling robotic systems.

Finite-time control methods guarantee state convergence within a set timeframe, but the system's initial conditions can influence the speed of convergence.[24,25] Fixed-time SMC ensures convergence within a predefined time, independent of the initial state.[26] However, this bound may not always match real-world settling times, and achieving the desired performance can be challenging for certain systems due to design parameter dependencies. To address these limitations, predefined time control allows designers to specify a desired settling time bound in advance, offering greater flexibility and potentially faster convergence than fixed-time methods. Various predefined time control techniques have been developed for nonlinear systems, such as predefined time synchronization for chaotic systems using fast TSM controllers and predefined time parameters.[27] Another example is a unique sliding surface design based on a sigmoid function, ensuring robust predefined-time convergence for second-order nonlinear systems with matched disturbances.[28] This approach enables precise predefined-time contour tracking for robotic manipulators without requiring exact knowledge of the robot parameters.[29]

This study explores predefined-time convergence control for robotic manipulators in the presence of uncertainties and disturbances. To the best of the authors' knowledge, there is currently no literature on the fractional-order control with predefined-time SMC technique for robotic systems using the predefined-time lemma. Thus, we propose a predefined-time fractional-order sliding mode control (FoPtSMC) scheme, which offers the following:

(1) Enhanced trajectory tracking to obtain high performance by combining predefined-time SMC with a fractional-order control.
(2) Improved closed-loop system response through the use of fractional order.
(3) Uncertain dynamics are mitigated using the robust SMC scheme.
(4) Guarantee of predefined-time convergence of the closed-loop system through Lyapunov stability analysis.

This work is organized as follows: Section 2 consists of the preliminaries. Section 3 presents the robot model, control design of FoPtSMC, and stability investigations using Lyapunov theory. Section 4 includes simulations to validate our approach, and Section 5 discusses it. In the end, Section 6 provides a conclusion of this work.

2. Preliminaries

The important Lemmas are given in this section.

Lemma 1. For $P(t)$, the Lyapunov function with an initial value of $P(0)$, predefined stability is deduced by[29]

$$\dot{P}(t) \leq -d_1 P(t)^{1+\frac{h}{2}} - d_2 P(t)^{1-\frac{h}{2}}$$

where $d_i > 0$ and $0 < h < 1$. The predefined-time T can be obtained as

$$T = \frac{\pi}{h\sqrt{d_1 d_2}} \tag{1}$$

Lemma 2. We provide the significant inequalities for k_i as[30]

$$\begin{aligned} &\sum_{i=1}^{n} |k_i|^{1+h} \geq \left(\sum_{i=1}^{n} |k_i|^2\right)^{\frac{1+h}{2}}, \ when\ 0 < h < 1 \\ &\sum_{i=1}^{n} |k_i|^{h} \geq n^{1-h}\left(\sum_{i=1}^{n} |k_i|\right)^{h}, \ when\ h > 1. \end{aligned} \tag{2}$$

Definition 1: The fractional-order derivative with function $z(t) \in \mathfrak{R}$, we have

$$\mathcal{D}_t^{\varrho} z(t) = \frac{1}{\Gamma(1-\varrho)} \frac{d}{dt} \int_b^t \frac{z(\mathfrak{T})}{(t-\mathfrak{T})^{\varrho}} d\mathfrak{T}$$

where $0 \leq \varrho < 1$, we get the fractional derivative of signum function as[34]

$$\mathcal{D}_t^{\varrho} sign(z(t)) \begin{cases} > 0 & when\ \ z(t) > 0\ \ and\ \ t > 0 \\ < 0 & when\ \ z(t) < 0\ \ and\ \ t > 0\,. \end{cases}$$

3. Design of predefined-time control approach

The equation represents the robotic manipulator dynamics utilized in this study[30]:

$$m(x)\ddot{x} + c(x,\dot{x})\dot{x} + g(x) = v(t) + v_d + v_u \tag{3}$$

where $x, \dot{x}, \ddot{x} \in \mathfrak{R}^n$ is position, velocity, and acceleration, respectively. $m(x) \in \mathfrak{R}^{n\times n}$ is positive definite inertia matrix with the condition $0 < \bar{x}_1(m(x)) \leq \|m(x)\| \leq \bar{x}_2(m(x))$, where $\bar{x}_1$ and $\bar{x}_2$ expresses the min and max eigenvalues. $c(x,\dot{x}) \in \mathfrak{R}^{n\times n}$ denotes the coriolis and centripetal forces, $g(x) \in \mathfrak{R}^n$ represents the gravitational force vector. In addition, $v_u \in \mathfrak{R}^n$ are uncertain dynamics. $v(t) \in \mathfrak{R}^n$ denotes control

torque, and $v_d \in \Re^n$ is bounded external disturbances.

Equation (3) is provided as follows:

$$\ddot{x} = m^{-1}(x)(v(t) + v_d + v_u - c(x,\dot{x})\dot{x} - g(x)) \tag{4}$$

The tracking error is given as:

$$\ddot{\varepsilon} = m^{-1}(x)(v(t) + v_d + v_u - c(x,\dot{x})\dot{x} - g(x)) - \ddot{x}_d \tag{5}$$

where $\varepsilon = x - x_d$ is tracking error, and x_d is desired input.

This section examines the development of an innovative control strategy for perturbed robotic manipulators in the existence of uncertainty. First, it analyzes the key characteristics of the proposed predefined-time fractional-order sliding mode control (FoPtSMC) scheme.

3.1. Predefined-time based fractional-order sliding surface

In light of SMC's rapid convergence and robustness, researchers have explored various sliding surfaces to enhance control performance. The demonstrated ability of the recommended sliding surface to deliver precise predefined-time control for n-degree-of-freedom (DOF) robotic manipulators makes it particularly advantageous. Consequently, the proposed sliding surface is formulated as

$$\begin{aligned}\sigma(t) &= a_1|\varepsilon|^{1+\frac{\eta}{2}}sign(\varepsilon) + a_2|\varepsilon|^{1-\frac{\eta}{2}}sign(\varepsilon)\\ &+a_3\mathcal{D}^{\alpha}sign(\varepsilon) + \dot{\varepsilon}\end{aligned} \tag{6}$$

where sliding surface is represented by $\sigma(t) \in \Re^n$, $a_1, a_2, a_3 \in \Re^+$ are positive constants, and $0 < \eta < 1$.

Then, $\dot{\sigma}(t)$ can be obtained as

$$\begin{aligned}\dot{\sigma}(t) &= a_1(1+\tfrac{\eta}{2})|\varepsilon|^{\frac{\eta}{2}}\dot{\varepsilon} + a_2(1-\tfrac{\eta}{2})|\varepsilon|^{-\frac{\eta}{2}}\dot{\varepsilon}\\ &+a_3\mathcal{D}^{\alpha+1}sign(\varepsilon) + \ddot{\varepsilon}\end{aligned} \tag{7}$$

From (5) into (7) yields

$$\begin{aligned}\dot{\sigma}(t) &= a_1(1+\tfrac{\eta}{2})|\varepsilon|^{\frac{\eta}{2}}\dot{\varepsilon} + a_2(1-\tfrac{\eta}{2})|\varepsilon|^{-\frac{\eta}{2}}\dot{\varepsilon}\\ &+a_3\mathcal{D}^{\alpha+1}sign(\varepsilon) + m^{-1}(x)(v(t) + v_d + v_u\\ &-c(x,\dot{x})\dot{x} - g(x)) - \ddot{x}_d\end{aligned} \tag{8}$$

Equation (8) can be given as

$$\begin{aligned}\dot{\sigma}(t) &= a_1(1+\tfrac{\eta}{2})|\varepsilon|^{\frac{\eta}{2}}\dot{\varepsilon} + a_2(1-\tfrac{\eta}{2})|\varepsilon|^{-\frac{\eta}{2}}\dot{\varepsilon}\\ &+a_3\mathcal{D}^{\alpha+1}sign(\varepsilon) + m^{-1}(x)(v(t) - c(x,\dot{x})\dot{x} - g(x))\\ &+\wp(x,\dot{x},\ddot{x}) - \ddot{x}_d\end{aligned} \tag{9}$$

where $\wp(x,\dot{x},\ddot{x}) = m^{-1}(x)(v_u + v_d)$, it is bounded by $\|\wp(x,\dot{x},\ddot{x})\| \le \wp_1 + \wp_2\|x\| + \wp_3\|\dot{x}\|^2$, and $\wp_1, \wp_2$ and, $\wp_3 > 0$.

Using the provided sliding surface, we will now develop the FoPtSMC method for n-DOF robotic manipulators. This control law is designed to be resilient to disturbances and uncertainties.

3.2. Design of FoPtSMC scheme

The control law FoPtSMC is designed to ensure the robust operation of perturbed robotic manipulators under bounded uncertain dynamics:

$$v(t) = m(x)\begin{pmatrix} m^{-1}(x)(c(x,\dot{x})\dot{x} + g(x)) + \ddot{x}_d\\ -(\wp_1 + \wp_2\|x\| + \wp_3\|\dot{x}\|^2)sign(\sigma(t))\\ -a_1(1+\frac{\eta}{2})|\varepsilon|^{\frac{\eta}{2}}\dot{\varepsilon} - a_2(1+\frac{\eta}{2})|\varepsilon|^{-\frac{\eta}{2}}\dot{\varepsilon}\\ -a_3\mathcal{D}^{\alpha+1}sign(\varepsilon)\\ -b_1|\sigma(t)|^{1+\frac{\mu}{2}}sign(\sigma(t))\\ -b_2|\sigma(t)|^{1-\frac{\mu}{2}}sign(\sigma(t))\end{pmatrix} \tag{10}$$

where $|\varepsilon|^{-\frac{\eta}{2}} = 0$ if $\varepsilon = 0$, b_1, b_2 are positive constants, and $0 < \mu < 1$.

By substituting $v(t)$ into (9), $\dot{\sigma}(t)$ can be computed as

$$\begin{aligned}\dot{\sigma}(t) &= a_1(1+\tfrac{\eta}{2})|\varepsilon|^{\frac{\eta}{2}}\dot{\varepsilon} + a_2(1-\tfrac{\eta}{2})|\varepsilon|^{-\frac{\eta}{2}}\dot{\varepsilon}\\ &+a_3\mathcal{D}^{\alpha+1}sign(\varepsilon)\\ &+m^{-1}(x)\begin{pmatrix} m(x)\begin{pmatrix} m^{-1}(x)c(x,\dot{x})\dot{x}\\ +m^{-1}(x)g(x)\\ -(\wp_1 + \wp_2\|x\| + \wp_3\|\dot{x}\|^2)\\ \times sign(\sigma(t))\\ -a_1(1+\frac{\eta}{2})|\varepsilon|^{\frac{\eta}{2}}\dot{\varepsilon}\\ -a_2(1+\frac{\eta}{2})|\varepsilon|^{-\frac{\eta}{2}}\dot{\varepsilon}\\ -a_3\mathcal{D}^{\alpha+1}sign(\varepsilon) + \ddot{x}_d\\ -b_1|\sigma(t)|^{1+\frac{\mu}{2}}sign(\sigma(t))\\ -b_2|\sigma(t)|^{1-\frac{\mu}{2}}sign(\sigma(t))\end{pmatrix}\\ -c(x,\dot{x})\dot{x} - g(x)\end{pmatrix}\\ &+\wp(x,\dot{x},\ddot{x}) - \ddot{x}_d\end{aligned} \tag{11}$$

Simplifying (11), $\dot{\sigma}(t)$ is expressed as

$$\begin{aligned}\dot{\sigma}(t) &= -(\wp_1 + \wp_2\|x\| + \wp_3\|\dot{x}\|^2)sign(\sigma(t))\\ &+\wp(x,\dot{x},\ddot{x}) - b_1|\sigma(t)|^{1+\frac{\mu}{2}}sign(\sigma(t))\\ &-b_2|\sigma(t)|^{1-\frac{\mu}{2}}sign(\sigma(t))\end{aligned} \tag{12}$$

We have finalized the design of the control scheme and sliding surface, and we are now ready to move forward with the stability analysis. The complete proposed diagram is given in Figure 1.

3.3. Stability analysis

In this section, we conduct an analysis of the closed-loop system's stability using the Lyapunov theorem. Equation (3) is utilized to represent the system dynamics.

If $\sigma(t) = 0$ in (6), one has

$$\begin{aligned}\dot{\varepsilon} &= -a_1|\varepsilon|^{1+\frac{\eta}{2}}sign(\varepsilon) - a_2|\varepsilon|^{1-\frac{\eta}{2}}sign(\varepsilon)\\ &-a_3D^{\alpha}sign(\varepsilon)\end{aligned} \tag{13}$$

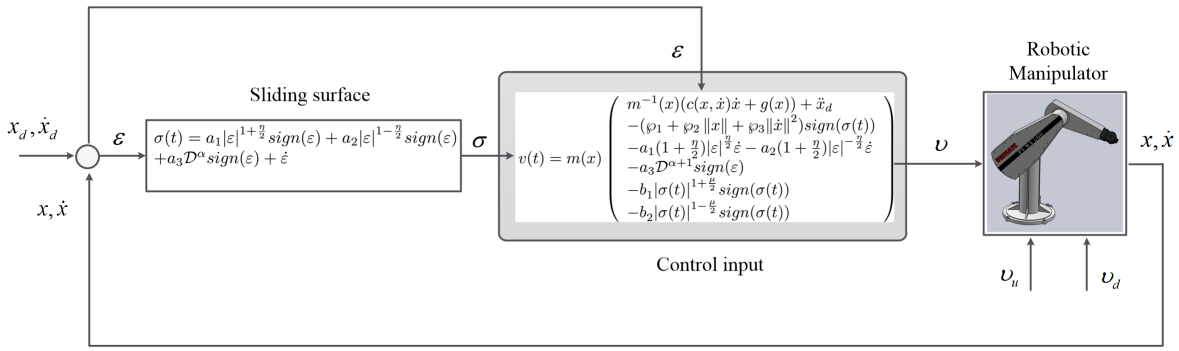


Figure 1. Proposed control model.[32]

We can obtain the stability of the tracking error by carefully selecting a Lyapunov function candidate:

$$P_1(t) = \frac{1}{2}\sum_{i=1}^{n} \varepsilon_i{}^2(t) \tag{14}$$

Then $\dot{P}_1(t)$ is calculated as

$$\dot{P}_1(t) = \sum_{i=1}^{n} \varepsilon_i(t)\dot{\varepsilon}_i(t) \tag{15}$$

Equation (13) substituted into (15), one obtains

$$\dot{P}_1(t) = \sum_{i=1}^{n} \varepsilon_i(t) \begin{pmatrix} -a_1|\varepsilon|^{1+\frac{\eta}{2}} sign(\varepsilon) \\ -a_2|\varepsilon|^{1-\frac{\eta}{2}} sign(\varepsilon) \\ -a_3\mathcal{D}^{\alpha} sign(\varepsilon) \end{pmatrix} \tag{16}$$

After simplification using Definition 1, the equation becomes:

$$\dot{P}_1(t) \leq -a_1\sum_{i=1}^{n}\left(|\varepsilon_i(t)|^2\right)^{\frac{4+\eta}{4}} - a_2\sum_{i=1}^{n}\left(|\varepsilon_i(t)|^2\right)^{\frac{4-\eta}{4}} \tag{17}$$

By using Lemma 2, we can express the previous equation more concisely

$$\begin{aligned} \dot{P}_1(t) \leq & -a_1 n^{-\frac{\eta}{4}}\left(\sum_{i=1}^{n}|\varepsilon_i(t)|^2\right)^{\frac{4+\eta}{4}} \\ & -a_2\left(\sum_{i=1}^{n}|\varepsilon_i(t)|^2\right)^{\frac{4-\eta}{4}} \end{aligned} \tag{18}$$

then Equation (18) can be expressed as

$$\begin{aligned} &\dot{P}_1(t) \leq -a_1 2^{\frac{4+\eta}{4}} n^{-\frac{\eta}{4}} P_1(t)^{\frac{4+\eta}{4}} - a_2 2^{\frac{4-\eta}{4}} P_1(t)^{\frac{4-\eta}{4}} \\ &= -a_1 2^{1+\frac{\eta}{4}} n^{-\frac{\eta}{4}} P_1(t)^{1+\frac{\eta}{4}} - a_2 2^{1-\frac{\eta}{4}} P_1(t)^{1-\frac{\eta}{4}} \end{aligned} \tag{19}$$

Utilizing Lemma 1, we can prove that the sliding surface defined in Equation (6) converges to zero within a specific time frame

$$T_1 = \frac{2\pi}{\eta\sqrt{2^{1+\frac{\eta}{4}}2^{1-\frac{\eta}{4}}n^{-\frac{\eta}{4}}a_1a_2}} = \frac{\pi}{\eta\sqrt{a_1a_2n^{-\frac{\eta}{4}}}} \tag{20}$$

Theorem 1: Using the n-DOF robotic manipulator model (3), designed sliding surface (6), and FoPtSMC control method (10) ensures the system trajectory converges to zero within a predefined time, under specified conditions for bounded uncertainties and disturbances.

Proof: We have selected the Lyapunov function candidate as shown below:

$$P_2(t) = \frac{1}{2}\sum_{i=1}^{n}\sigma_i^2(t) \tag{21}$$

The $\dot{P}_2(t)$ can be formulated as:

$$\dot{P}_2(t) = \sum_{i=1}^{n}\sigma_i(t)\dot{\sigma}_i(t) \tag{22}$$

Substituting Equation (12) into Equation (22), the following equation can be expressed as

$$\begin{aligned} \dot{P}_2(t) = & \sum_{i=1}^{n}\sigma_i(t) \\ & \times \begin{bmatrix} -(\wp_1 + \wp_2\|x\| + \wp_3\|\dot{x}\|^2)sign(\sigma(t)) \\ +\wp(x,\dot{x},\ddot{x}) - b_1|\sigma(t)|^{1+\frac{\mu}{2}} sign(\sigma(t)) \\ -b_2|\sigma(t)|^{1-\frac{\mu}{2}} sign(\sigma(t)) \end{bmatrix} \end{aligned} \tag{23}$$

Solving Equation (23) using Assumption 1

$$\dot{P}_2(t) \leq \sum_{i=1}^{n}\sigma_i(t)\begin{bmatrix} -b_1|\sigma(t)|^{1+\frac{\mu}{2}} sign(\sigma(t)) \\ -b_2|\sigma(t)|^{1-\frac{\mu}{2}} sign(\sigma(t)) \end{bmatrix} \tag{24}$$

It can be expressed as

$$\dot{P}_2(t) \leq -b_1\sum_{i=1}^{n}\left(|\sigma_i(t)|^2\right)^{\frac{4+\mu}{4}} - b_2\sum_{i=1}^{n}\left(|\sigma_i(t)|^2\right)^{\frac{4-\mu}{4}} \tag{25}$$

By Lemma 2, the following equation can be given as

$$\begin{aligned} \dot{P}_2(t) \leq & -b_2 n^{-\frac{\mu}{4}}\left(\sum_{i=1}^{n}|\sigma_i(t)|^2\right)^{\frac{4+\mu}{4}} \\ & -b_2\left(\sum_{i=1}^{n}|\sigma_i(t)|^2\right)^{\frac{4-\mu}{4}} \end{aligned} \tag{26}$$

Subsequently, we can derive Equation (26) as follows

$$\dot{P}_2(t) \leq -b_1 n^{-\frac{\mu}{4}} 2^{\frac{4+\mu}{4}} P_2(t)^{\frac{4+\mu}{4}} - b_2 2^{\frac{4-\mu}{4}} P_2(t)^{\frac{4-\mu}{4}} \tag{27}$$

This analysis confirms that the system trajectory converges to $\sigma(t)$ in predefined time, as provided

by Lemma 1:

$$T_2 = \frac{2\pi}{\mu\sqrt{b_1 b_2 n^{-\frac{\mu}{4}} 2^{1+\frac{\mu}{4}} 2^{1-\frac{\mu}{4}}}} = \frac{\pi}{\mu\sqrt{n^{-\frac{\mu}{4}} b_1 b_2}} \tag{28}$$

The total settling time can be calculated by including T_1 and T_2, validating the predefined-time convergence of the proposed method in alignment with the FoPtSMC scheme.

4. Simulation results

A simulation study evaluates the effectiveness of the proposed FoPtSMC scheme applied to a PUMA 3-DOF robotic manipulator with external disturbances. The study describes the manipulator's model parameters, and details of the robot's dynamics are taken from.[33] To validate the performance of the proposed method, it has been compared with a fractional-order finite-time SMC scheme,[31] and the simulations have been performed on the MATLAB/Simulink software. The desired trajectories and uncertain dynamics are provided as follows:

$$x_d = \begin{bmatrix} sin(t\pi/3) - 1 + cos(t\pi/5) \\ cos(t\pi/5 + (\pi/2)) + sin(t\pi/3) \\ sin(t\pi/5 + (\pi/2)) - 1 \end{bmatrix},$$

$$v_u = \begin{bmatrix} 0.5\dot{x}_1 + sin(3x_1) \\ 1.3\dot{x}_2 - 1.8sin(2x_2) \\ -0.1\dot{x}_3 - 0.5sin(x_3) \end{bmatrix},$$

$$v_d = \begin{bmatrix} 0.5sin(\dot{x}_1) \\ 1.1sin(\dot{x}_2) \\ 0.15sin(\dot{x}_3) \end{bmatrix}.$$

In addition, the appropriate parameters for the developed FoPtSMC scheme are given in Table 1.

Table 1. Proposed control parameters

Parameter	Value
a_1	6
a_2	6
a_3	0.0002
b_1	30
b_2	30
η	0.3
μ	0.1
α	0.01
$x_1(0)$	-0.2
$x_2(0)$	-0.2
$x_3(0)$	-0.2

The performance of the proposed FoPtSMC scheme is evaluated comprehensively, with a particular focus on handling uncertain system dynamics under disturbances, as depicted in Figures 2 - 4.

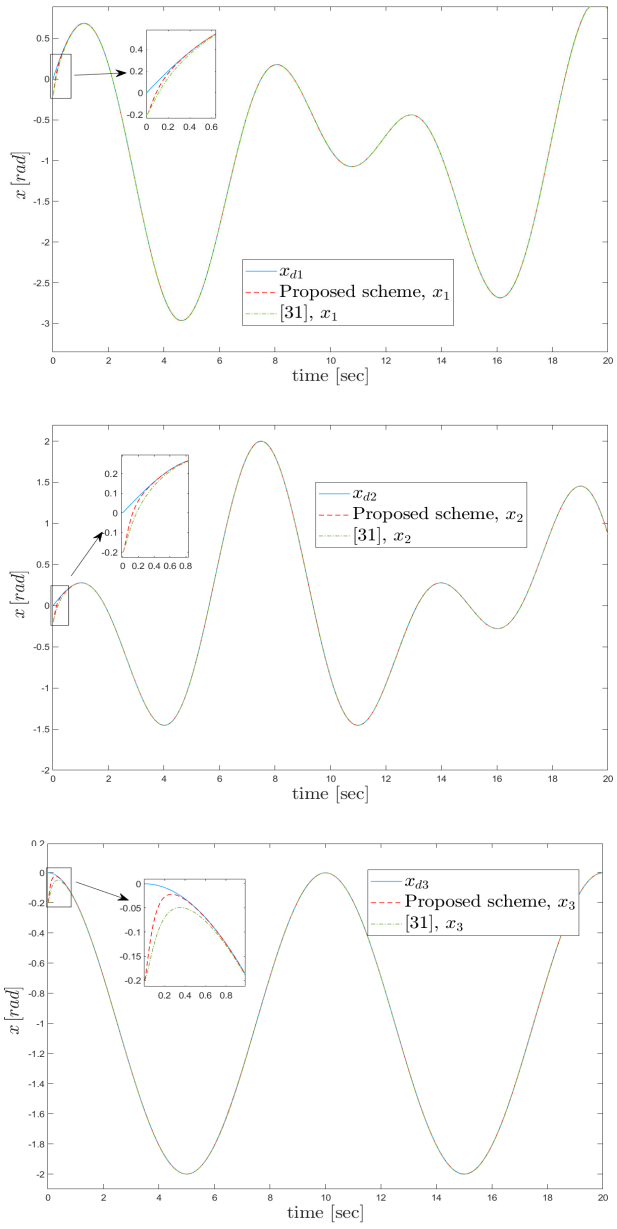


Figure 2. Position tracking under uncertain dynamics.

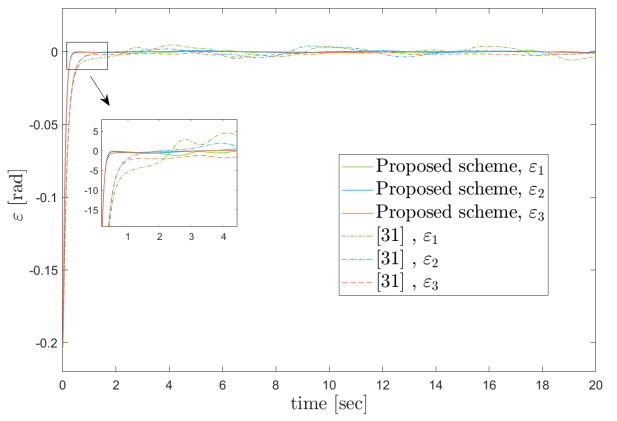


Figure 3. Tracking error under uncertain dynamics.

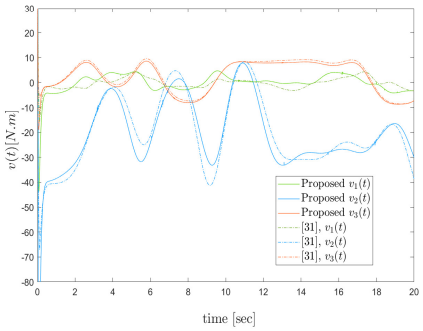


Figure 4. Control input under uncertain dynamics.

The expected performance of the FoPtSMC method under uncertain dynamics in comparison with[31] is effectively shown in Figures 2-4. Figure 2 showcases the proposed controller's precise ability to track the desired trajectory, while Figure 3 exhibits minimal tracking errors of the proposed scheme, affirming its effectiveness. Furthermore, Figure 4 illustrates the control inputs that guide the system state onto and maintain it on the desired surfaces to ensure the desired dynamics, indicating the proposed controller's robust performance in achieving accurate tracking. Additionally, the proposed method delivers smooth control torques. The comprehensive assessment presented in Figures 2-4 emphasizes the efficacy of the proposed FoPtSMC scheme in achieving precise position trajectory tracking under uncertain dynamics.

5. Discussion

The proposed FoPtSMC strategy has been designed to control nonlinear dynamical systems with bounded external disturbances. This research aims to improve tracking and transient characteristics while maintaining resilience in a closed-loop system. The FoPtSMC strategy is intended to ensure rapid sliding mode convergence within a specific time frame, and the Lyapunov technique was used to demonstrate stability.

The simulation findings show that the FoPtSMC technique effectively manages a second-order nonlinear dynamical robotic system under external perturbations. The graphical depictions in Figures 2-3 display the variables x_1, x_2, x_3, and the tracking error ε_1, ε_2, ε_3, demonstrating the successful control performance and the ability of the proposed system to reduce the tracking error to zero rapidly. Figure 4 depicts the control input, which has desirable qualities such as smoothness and acceptable tracking performance, successfully mitigating the effects of external disturbances. The simulation adequately illustrates and supports the theoretical analysis, emphasizing the FoPtSMC approach's advantages in increased responsiveness, lower tracking error, and greater control over nonlinear dynamics. This work thoroughly addresses the constraints of the proposed controller parameters and stability proofs. The FoPtSMC approach's proper parameters were carefully determined within designated ranges to obtain the overall system's stability and error convergence within a fixed time. The study underlines the need to select appropriate parameter values, such as $a_1, a_2, a_3 > 0$, $b_1, b_2 > 0$, $0 < \alpha, \mu, \eta < 1$, to achieve stability and convergence within a specific time period; thereby simplifying the process of picking acceptable values and increasing convergence speed.

In conclusion, the suggested FoPtSMC method has tremendous promise for increasing nonlinear systems' tracking capabilities and robustness, especially in the face of external disturbances. The work gives unique insights into the development and application of the FoPtSMC approach, with implications for a wide range of control engineering applications.

6. Conclusion

The research focuses on controlling the trajectory tracking of robotic manipulators in the presence of uncertainties and external disturbances. To address this issue, a predefined-time fractional-order sliding mode control (FoPtSMC) scheme is proposed. This scheme allows the system state to converge to the desired trajectory within a predefined time, thereby improving tracking performance. Simulations on a manipulator with uncertain dynamics confirm the effectiveness of FoPtSMC. It demonstrates faster response times, reduced tracking errors, and improved rejection of uncertainties and disturbances. Moreover, future work should look into unknown dynamics in nonlinear systems research, which will help advance our understanding and application of the FoPtSMC technique.

Acknowledgments

This paper is derived from a research grant funded by the Research, Development, and Innovation Authority (RDIA), Kingdom of Saudi Arabia, with grant number 13382-psu-2023- PSNU-R-3-1-EI-. This research is supported by Automated Systems and Computing Lab (ASCL), Prince Sultan University, Riyadh, Saudi Arabia. The authors would like to thank Prince Sultan University, Riyadh, Saudi Arabia for supporting this work.

Funding

This paper is funded by Prince Sultan University, Riyadh, Saudi Arabia. The authors would like to thank Prince Sultan University for paying the article processing fee for this paper.

Conflict of interest

The authors declare that the research was conducted in the absence of any commercial or financial relationships that could be construed as a potential conflict of interest.

Author contributions

Conceptualization: All authors
Formal analysis: All authors
Investigation: All authors
Methodology: All authors
Writing – original draft: Saim Ahmed
Writing – review & editing: All authors

Availability of data

The original contributions presented in the study are included in the article, further inquiries can be directed to the corresponding author.

References

1. Elhadidy MS, Abdalla WS, Abdelrahman AA, Elnaggar S, Elhosseini M. Assessing the accuracy and efficiency of kinematic analysis tools for sixdof industrial manipulators: The kuka robot case study. *AIMS Mathematics*.2024;9(6):13944–13979. https://doi.org/10.3934/math.2024678
2. Joseph SB, Dada EG, Abidemi A, Oyewola DO, Khammas BM. Metaheuristic algorithms for pid controller parameters tuning: Review, approaches and open problems. *Heliyon*.2022;8(5):1-29. https://doi.org/10.1016/j.heliyon.2022.e09399
3. Singh S, Azar AT, Ouannas A, Zhu Q, Zhang W, Na J. Sliding mode control technique for multi-switching synchronization of chaotic systems. *2017 9th International conference on modelling, identification and control (ICMIC)*. 2017;880–885. http://dx.doi.org/10.1109/ICMIC.2017.8321579
4. Thanh HLNN, Vu MT, Mung NX, Nguyen NP, Phuong NT. Perturbation observer-based robust control using a multiple sliding surfaces for nonlinear systems with influences of matched and unmatched uncertainties. *Mathematics*.2020;8(8):1371. https://doi.org/10.3390/math8081371
5. Li D, Slotine J-JE. On sliding control for multi-input multi-output nonlinear systems. *1987 American Control Conference*. 1987;874–879.
6. Almakhles D. The complex adaptive delta-modulator in sliding mode theory. *Entropy*. 2020;22(8):1-11. https://doi.org/10.3390/e22080814
7. Humaidi AJ, Ibraheem IK, Azar AT, Sadiq ME. A new adaptive synergetic control design for single link robot arm actuated by pneumatic muscles. *Entropy*. 2020;22(7):723. https://doi.org/10.3390/e22070723
8. Chiliveri VR, Kalpana R, Subramaniam U, Muhibbullah M, Padmavathi L. Novel reaching law based predictive sliding mode control for lateral motion control of in-wheel motor drive electric vehicle with delay estimation. *IET Intelligent Transport Systems*. 2024;18(5):872–888. https://doi.org/10.1049/itr2.12474
9. Elmorshedy MF, Selvam S, Mahajan SB, Almakhles D. Investigation of high-gain two-tier converter with pi and super-twisting sliding mode control. *ISA transactions*.2023;138:628–638. https://doi.org/10.1016/j.isatra.2023.03.020
10. Zhao D, Li S, Gao F. A new terminal sliding mode control for robotic manipulators. *IFAC Proceedings Volumes*. 2008;41(2):9888–9893. https://doi.org/10.3182/20080706-5-KR-1001.01673
11. Boukattaya M, Gassara H. Time-varying nonsingular terminal sliding mode control for uncertain second-order nonlinear systems with prespecified time. *International Journal of Adaptive Control and Signal Processing*. 2022;36(8):2017–2040. https://doi.org/10.1002/acs.3445
12. Feng Y, Yu X, Man Z. Non-singular terminal sliding mode control of rigid manipulators. *Automatica*. 2002;38(12):2159–2167. https://doi.org/10.1016/S0005-1098(02)00147-4
13. Souissi S, Boukattaya M. Time-varying nonsingular terminal sliding mode control of autonomous surface vehicle with predefined convergence time. Ocean Engineering. 2022;263:112264. https://doi.org/10.1016/j.oceaneng.2022.112264
14. Chen J, Zhang H, Tang Q, Zhang H. Adaptive fuzzy sliding mode control of the manipulator based on an improved super-twisting algorithm. *Proceedings of the Institution of Mechanical Engineers, Part C: Journal of Mechanical Engineering Science*. 2024;238(10):4294–4306. http://dx.doi.org/10.1177/09544062231214835
15. Yang L, Yang J. Nonsingular fast terminal sliding-mode control for nonlinear dynamical systems. *International Journal of Robust and Nonlinear Control*. 2011;21(16):1865–1879. http://dx.doi.org/10.1002/rnc.1666
16. Ton C, Petersen C. Continuous fixed-time sliding mode control for spacecraft with flexible appendages. *IFAC-PapersOnLine*. 2018;51(12):1–5. https://doi.org/10.3934/mbe.2022106
17. Chen J, Zhao C, Tang Q, Liu X, Wang Z, Tan C, Wu J, Long T. Low chattering trajectory

tracking control of non-singular fast terminal sliding mode based on disturbance observer. *International Journal of Control, Automation and Systems*. 2023;21(2):440–451. https://doi.org/10.1007/s12555-021-0604-0
18. Chen J, Tang Q, Zhao C, Zhang H. Adaptive sliding mode control for robotic manipulators with backlash. *Proceedings of the Institution of Mechanical Engineers, Part C: Journal of Mechanical Engineering Science*. 2023;237(24):5842–5852. http://dx.doi.org/10.1177/09544062231167555
19. Faraj MA, Maalej B, Derbel N. Design and analysis of nonsingular terminal super twisting sliding mode controller for lower limb rehabilitation exoskeleton contacting with ground. In State estimation and stabilization of nonlinear systems: Theory and applications. Springer. 2023;367–386. http://dx.doi.org/10.1007/978-3-031-37970-$3_1$9
20. Zaway I, Jallouli-Khlif R, Maalej B, Medhaffar H, Derbel N. From PD to fractional order PD controller used for gait rehabilitation. *2021 18th International Multi-Conference on Systems, Signals & Devices (SSD)*. 2021;948–953. http://dx.doi.org/10.1109/SSD52085.2021.9429318
21. Gokyildirim A, Calgan H, Demirtas M. Fractional-order sliding mode control of a 4d memristive chaotic system. *Journal of Vibration and Control*. 2024;30(7-8):1604–1620. http://dx.doi.org/10.1177/10775463231166187
22. Chen Z, Wang X, Cheng Y. Adaptive finite-time disturbance observerbased recursive fractional-order sliding mode control of redundantly actuated cable driving parallel robots under disturbances and input saturation. *Journal of Vibration and Control*. 2023;29(3-4):675–688. https://doi.org/10.1177/10775463211051460
23. Bingi K, Rajanarayan Prusty B, Pal Singh A. A review on fractionalorder modelling and control of robotic manipulators. *Fractal and Fractional*. 2023;7(1):77. https://doi.org/10.3390/fractalfract7010077
24. Mofid O, Amirkhani S, Din Su, Mobayen S, Vu MT, Assawinchaichote W. Finite-time convergence of perturbed nonlinear systems using adaptive barrier-function nonsingular sliding mode control with experimental validation. Journal of Vibration and Control. 2023;29(13-14):3326–3339. http://dx.doi.org/10.1177/10775463221094889
25. Rojsiraphisal T, Mobayen S, Asad JH, Vu MT, Chang A, Puangmalai J. Fast terminal sliding control of underactuated robotic systems based on disturbance observer with experimental validation. *Mathematics*. 2021;9(16):1935. http://dx.doi.org/10.3390/math9161935
26. Ahmed S, Azar AT, Ibraheem IK. Model-free scheme using time delay estimation with fixed-time fsmc for the nonlinear robot dynamics. *AIMS Mathematics*. 2024;9(4):9989–10009. https://doi.org/10.3934/math.2024489
27. Xue H, Liu X. A novel fast terminal sliding mode with predefined-time synchronization. *Chaos, Solitons & Fractals*. 2023;175:114049. http://dx.doi.org/10.1016/j.chaos.2023.114049
28. Mazhar N, Malik FM, Raza A, Khan R. Predefined-time control of nonlinear systems: A sigmoid function based sliding manifold design approach. *Alexandria Engineering Journal*. 2022;61(9): 6831–6841. http://dx.doi.org/10.1016/j.aej.2021.12.030
29. Mu˜noz-V´azquez AJ, S´anchez-Torres JD, Guti´errez-Alcal´a S, Jim´enez-Rodr´ıguez E, Loukianov AG. Predefined-time robust contour tracking of robotic manipulators. Journal of the Franklin Institute. 2019;356(5):2709–2722. http://dx.doi.org/10.1016/j.jfranklin.2019.01.041
30. Ahmed S, Azar AT. Enhanced tracking control for n-dof robotic manipulators: A fixed-time terminal sliding mode approach with time delay estimation. *Results in Engineering*. 2024;24:102904. http://dx.doi.org/10.1016/j.rineng.2024.102904
31. Nojavanzadeh D, Badamchizadeh M. Adaptive fractional-order nonsingular fast terminal sliding mode control for robot manipulators. *IET Control Theory Appl*. 2016;10(13):1565–1572. http://dx.doi.org/10.1049/iet-cta.2015.1218
32. Grabcad community. accessed: Mar. 17, 2013. [online] : Https://grabcad.com/library/robot-puma-560. (n.d.).
33. Armstrong B, Khatib O, Burdick J. The explicit dynamic model and inertial parameters of the puma 560 arm. Proceedings. *1986 IEEE international conference on robotics and automation*. 1986;3:510–518. https://doi.org/10.1109/ROBOT.1986.1087644
34. Yin C, Huang X, Chen Y, Dadras S, Zhong S-m, Cheng Y. Fractional-order exponential switching technique to enhance sliding mode control. *Appl Math Model*. 2017;44:705–726. https://doi.org/10.1016/j.apm.2017.02.034

Saim Ahmed *received his B.S degree in Electronics Engineering from Sir Syed University of Science and Technology, Karachi, Pakistan in 2009. He received his M.E degree in Industrial Control and Automation from Hamdard University, Karachi, Pakistan, in 2013. He completed his Ph.D. degree in control science and engineering from Nanjing University of Science and Technology, China in 2019. He has served as an Assistant Professor at the Department of Mechatronics, Shaheed Zulfikar Ali Bhutto Institute of Science and Technology, Karachi, Pakistan. He is currently working as a Postdoctoral Researcher at Prince Sultan University, Saudi Arabia. His research interests include the theory and applications of adaptive control, sliding mode control, time delay control, robotic exoskeleton and manipulators, nonlinearities and their compensation.*

https://orcid.org/0000-0002-2302-705X

Ahmad Taher Azar *is a full Professor at College of Computer and Information Sciences (CCIS), Prince Sultan University, Riyadh, Saudi Arabia. He is a leader of Automated Systems and Computing Lab (ASCL), Prince Sultan University, Saudi Arabia. He is currently an editor for IEEE Transactions on Fuzzy Systems, IEEE Systems Journal, IEEE Transactions on Neural Networks and Learning Systems, Springer's Human-centric Computing and Information Sciences, and Elsevier's Engineering Applications of Artificial Intelligence. Prof. Azar was named one of the top 2% of scientists in the world in Artificial Intelligence by Stanford University, based on single-year impact and career-long impact. These rankings were published by Stanford University in the PLOS journal and were based on the SCOPUS database. Prof. Azar has expertise in Artificial Intelligence, Control Theory and Applications, Robotics, Machine Learning, Computational Intelligence and dynamical system modeling. He has authored/co-authored over 500 research papers in prestigious peer-reviewed journals, book chapters, and conference proceedings.*

https://orcid.org/0000-0002-7869-6373

An International Journal of Optimization and Control: Theories & Applications
(https://accscience.com/journal/ijocta)



This work is licensed under a Creative Commons Attribution 4.0 International License. The authors retain ownership of the copyright for their article, but they allow anyone to download, reuse, reprint, modify, distribute, and/or copy articles in IJOCTA, so long as the original authors and source are credited. To see the complete license contents, please visit http://creativecommons.org/licenses/by/4.0/.

An International Journal of Optimization and Control: Theories & Applications
ISSN: 2146-0957 eISSN: 2146-5703
Vol.15, No.3, pp.435-448 (2025)
https://doi.org/10.36922/IJOCTA025070023

RESEARCH ARTICLE

FPGA design and implementation of fuzzy learning control: Application on DC motor position control

Mohand Achour Touat[1], Hocine Khati[1], Arezki Fekik[2,3], Ahmad Taher Azar[4,5], Hand Talem[1], Rabah Mellah[1] and Saim Ahmed[4,5*]

[1]Design and Drive of Production Systems Laboratory, Faculty of Electrical and Computing Engineering, University Mouloud Mammeri of Tizi-ouzou, Tizi-ouzou, Algeria
[2]Nantes University, Centrale Nantes, CNRS, LS2N, UMR 6004, Nantes, France
[3]Department of Electrical Engineering Faculty of Applied Sciences, University of Bouira, Bouira, Algeria
[4]College of Computer and Information Sciences, Prince Sultan University, Riyadh, Saudi Arabia
[5]Automated Systems and Computing Lab (ASCL), Prince Sultan University, Riyadh, Saudi Arabia
Mohand-achour.touat@ummto.dz, hocine.khati@ummto.dz, Arezki.Fekik@univ-nantes.fr, aazar@psu.edu.sa, talemhand2015@gmail.com, Rabah.mellah@ummto.dz, sahmed@psu.edu.sa

ARTICLE INFO

Article History:
Received: February 10, 2025
Revised: March 12, 2025
Accepted: March 27, 2025
Published Online: May 8, 2025

Keywords:
Learning fuzzy control
FPGA
HDL Coder
Adaptive control
FIL
Optimization

AMS Classification 2010:
26A33; 34A08; 35H15; 34K50 47H10; 60H10

ABSTRACT

This paper investigates the implementation of a Fuzzy Model Reference Learning Control (FMRLC) on a Zedboard Zynq-7000 FPGA. The proposed adaptive controller dynamically adjusts its knowledge base and incorporates a memory-based control mechanism to retain and utilize past results in recurring situations. The design and deployment of the controller were carried out using the MATLAB/Simulink environment and applied to the angular position control of a DC motor. Initially, the controller was tested using the FPGA-In-the-Loop (FIL) approach to assess its robustness against disturbances in simulation. Subsequently, it was experimentally validated for real-time motor position control. The results obtained in FIL simulations and experimental tests demonstrate high tracking accuracy and strong disturbance rejection. These findings underscore both the superiority of the proposed controller over the conventional PID controller and the effectiveness of the adopted design methodology.

CC BY

1. Introduction

In recent years, fuzzy logic applications have experienced significant growth across various domains, ranging from industrial applications such as medical instruments and robotics to consumer products like washing machines, cameras, and automobiles. Fuzzy logic, based on fuzzy set theory, offers a set of if-then rules, eliminating the need for complex differential equations. This approach provides a structured methodology for modeling, manipulating, and implementing human heuristic knowledge in control systems. Widely adopted in automatic control, fuzzy logic avoids intricate nonlinear equations while leveraging expert knowledge. However, experts cannot always anticipate uncertainties arising during system operation. To ensure safe system functionality and accurate trajectory tracking despite disturbances, it is crucial to automatically update human knowledge without operator intervention.

To address these challenges, various adaptive control algorithms have been introduced in the literature, including fuzzy adaptive control.[1–4]

*Corresponding Author

While adaptive control can update the knowledge base, it may yield inconsistent results for identical uncertainties or disturbances.[5–8] To overcome this limitation, learning adaptive control strategies have been proposed, equipping control mechanisms with memory. These methods ensure consistent results for recurrent situations, thereby reducing computation time.[9–12]

Although fuzzy controllers demonstrate excellent performance in simulation, their practical implementation demands high-performance control boards due to significant computational requirements. Field Programmable Gate Arrays (FPGAs) have emerged as a powerful solution in control applications,[13] enabling high sampling frequencies, parallel data processing, and low power consumption.[14] Their integration accelerates control algorithms, ensuring rapid convergence toward desired performance.[15] Several studies have explored FPGA-based control implementations. For instance, Huerta et al.[16] examined FPGA implementation of PID and sliding mode controllers for DC-DC buck converters. Wang et al.[17] developed a neural network-based PID controller for motion control systems. Similarly, Li et al.[18] investigated FPGA-accelerated predictive control for autonomous driving. Meghwal et al. [19] presented a robust fuzzy controller implemented on FPGA for matrix converter-based induction motor control, while Attafi et al.[20] focused on real-time FPGA implementation of robust control for wind energy conversion systems.

In this paper, a learning adaptive control strategy, namely the Fuzzy Model Reference Learning Control (FMRLC), is implemented on a Zedboard Zynq-7000 FPGA for DC motor position control. The proposed controller is first validated in a real-time simulation environment using the FPGA-in-the-Loop (FIL) approach, a technique widely employed in laboratories to assess prototype controllers under real operating conditions. Compared to conventional numerical simulations, FIL provides a more realistic validation by incorporating real-world factors such as noise, disturbances, and implementation challenges, which may not be accounted for in idealized simulations.

The proposed methodology leverages MATLAB/Simulink for controller design and FPGA implementation. Simulink, in conjunction with HDL Coder, enables direct FPGA deployment without requiring VHDL programming.[21] However, since floating-point data types in Simulink are not supported by all FPGA platforms, the Fixed-Point Tool is utilized to convert floating-point designs into fixed-point representations. This conversion optimizes FPGA hardware resource utilization and minimizes power consumption.

Several implementation works on FPGA based on fuzzy logic have been carried out. [22–31] In,[22,23] the implementation of a fuzzy controller on FPGA using the FIL technique on the MATLAB-Simulink environment is presented. The design, simulation, and FPGA implementation of a fuzzy controller to regulate the speed of a DC motor in real time is presented in.[27] In,[28] genetic and pipeline algorithms are implemented in FPGA to optimize fuzzy controller parameters. In ref., [29] an FPGA design approach with partial reconfiguration (PR) using a fuzzy controller is used to control an electromechanical system.

This study presents the implementation of an FMRLC-based position control strategy for a DC motor, incorporating a memory-based control mechanism to ensure consistent responses to recurring conditions, thereby reducing computational overhead. In the first phase, the fuzzy controller is designed in MATLAB/Simulink and implemented on a Zedboard Zynq-7000 FPGA using the FIL technique. In this setup, the FMRLC controller runs on the FPGA, while the remaining control system components operate within Simulink to assess performance and robustness under various disturbances. The second phase involves deploying the algorithm onto the FPGA board using HDL Coder's "IP Core Generation" technique for real-time implementation. This method allows direct integration of the control strategy onto the Zedboard by generating an IP block via Vivado software, eliminating the need for manual VHDL coding and significantly reducing development time. "IP Core Generation" automatically generates the VHDL code, compiles the bitstream programming file, and transfers it to the Zedboard.

The structure of this paper is as follows: Section 2 provides an overview of the FMRLC control strategy. Section 3 details the mathematical modeling of the DC motor in both theoretical and experimental contexts. Section 4 describes the design and FPGA implementation of the FMRLC controller. Section 5 presents simulation results in FIL mode along with experimental validation. Finally, the conclusions are summarized in Section 6.

2. Architecture of the control strategy

The Fuzzy Model Reference Learning Controller (FMRLC) is shown in Figure 1. As illustrated , it has three main parts as defined by[32]: Fuzzy Direct Controller (FC) synthesized to control the DC

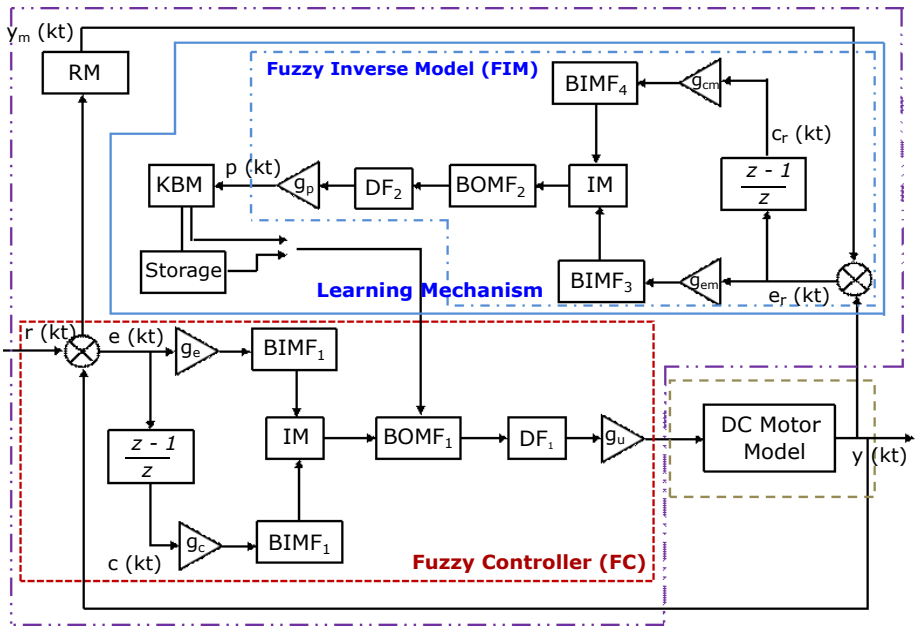


Figure 1. Block diagram of FMRLC

motor, the reference model (RM), and the learning mechanism. This last part is divided into two subparts: Knowledge Base Modifier (KBM) and Fuzzy Inverse Model (FIM). This control strategy is based on the Model Reference Adaptive Direct Control (MRAC). This method aims to synthesize a fuzzy controller, by adjusting its membership functions in order to reject different disturbances of the controlled system. The main parts of the FMRLC control scheme are detailed in Figure 1 and are described as follows:

2.1. Direct fuzzy logic controller

The Fuzzy Controller (FC) designed in this paper is to generate a control signal in order to force the output of the system to follow the assigned DC motor position reference signal; it has two inputs:

$$e\,(kt) = r\,(kt) - y\,(kt) \tag{1}$$

$$c\,(kt) = \frac{z-1}{z} e\,(kt) \tag{2}$$

$e\,(kt)$ defines the error between the position reference signal and the position output signal of the DC motor, $c\,(kt)$ constitutes the error change. These inputs are normalized by the mean of the scaling factors g_e and g_c that belong to the interval [-1 1]. The input membership functions of the error and its derivatives are introduced, respectively, in BIMF1 and BIMF2 with the number 5, while the output ones are given in the BOMF1 with the number 5. The inference mechanism (IM) used in this study is of Mamdani type based on the min-max inference method, and is expressed in the form of IF-THEN rules. Its rule base is summarized in Table 1. The membership functions are shown in Figure 2, with five fuzzy sets on the universe of discourse, with linguistic values, which are the following: Negative Big (NB), Negative (N), Zero (ZE), Positive (P), and Positive Big (PB).

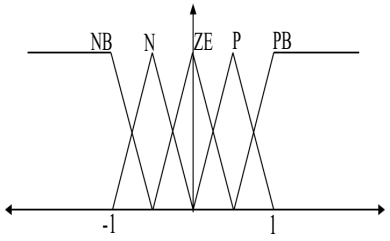


Figure 2. Membership functions

Table 1. Initial rule base of the fuzzy controller

		$c\,(kt)$	$c\,(kt)$	$c\,(kt)$	$c\,(kt)$	$c\,(kt)$
		-1	-0.5	0	0.5	1
$e\,(kt)$	-1	-1	-1	-1	-0.5	0
$e\,(kt)$	-0.5	-1	-1	-0.5	0	0.5
$e\,(kt)$	0	-1	-0.5	0	0.5	1
$e\,(kt)$	0.5	-0.5	0	0.5	1	1
$e\,(kt)$	1	0	0.5	1	1	1

The defuzzification part is introduced in DF1. In this case, the Center Of Gravity (COG) method is used. The output of FC constitutes the control signal $u\,(kt)$ and normalized to the same interval as the input with the scaling factor g_u. The dynamic model of the DC motor is approximated with the first-order model and represented in the Reference Model (RM).

The last part of the block diagram shown is the learning mechanism; this part modifies the knowledge base with respect to plant parametric disturbances. The latter modifications are made on the output membership functions in order to force the closed-loop system to behave like the reference model. According to Figure 1, the learning mechanism consists of following two parts: a fuzzy inverse model (FIM) and a knowledge base modifier (KBM). The fuzzy inverse model is based on the same inference mechanism as the fuzzy controller (FC). The inputs of the FIM are as follows:

$$e_r(kt) = y_m(kt) - y(kt) \tag{3}$$

$$c_r(kt) = \frac{z-1}{z} e_r(kt) \tag{4}$$

$e_r(kt)$ is the error between the output of the reference model and the plant output; $c_r(kt)$ is the error change. The output of this controller is the necessary changes in the plant inputs. Likewise to the fuzzy controller, the FIM shown in Figure 1 contains normalizing scaling factors, namely g_{em}, g_{cm} and g_p for each universe of discourse. It is important to notice that the selection of the normalizing gains can impact the overall performance of the system. For this reason, it is essential to use an optimization algorithm to compute these parameters. This is done by using the MATLAB/Simulink response optimization tool. The output of the FIM represents the variation of the FC's output membership function center. In order to get a better performance, modification of the FC rule base is performed by the knowledge base modifier (KBM).

2.2. Reference model

The reference model is chosen so that the system will have a rapid response. In this case, the choice is made for a model with the best dynamics ensured by conventional control under perfect conditions, i.e., no disturbances or parametric variations. This dynamic is approximated by the following first-order model:

$$R(s) = \frac{1}{1+\tau_m s} \tag{5}$$

Where τ_m is the time constant to be determined.

2.3. Learning mechanism

The learning mechanism adjusts the ground rules of the direct FC by exploiting information such as the output of the controlled system $y(kt)$ and that of the reference model and the already existing basis of the direct FC.

The output $p(kt)$at instant $(kt-t)$ represents the correction to be made to the command at instant in order to reduce the following error $e_r(kt)$. In other words, we force the FC to produce the desired command: $u(kt-t)+p(kt)$ necessary to cancel the tracking error $e_r(kt)$. So, the next time we encounter the same circumstances, the command will be the one that will reduce the tracking error.

3. Mathematical model of the DC motor

In order to be able to simulate and implement the closed-loop systems on the FPGA board, the mathematical model of the DC motor is required. The equivalent electric circuit of the DC motor armature and the diagram of the rotor are shown in Figure 3.

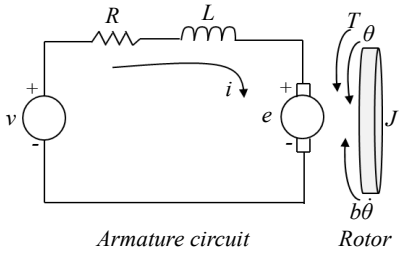


Figure 3. Electrical circuit of a DC motor

Let us take the input of the system the voltage source v applied to the motor armature, while the output is the position of the shaft θ.

Generally, the torque generated by the DC motor is proportional to the armature current and the magnetic fields. Suppose that the latter is constant; therefore, the torque T is proportional to the current of the armature i by a constant factor K_1:

$$T = K_1 i \tag{6}$$

The electromotive force E is proportional to the velocity of the shaft $\dot{\theta}$ by a constant factor K_2:

$$E = K_2 \dot{\theta} \tag{7}$$

The constants of the torque T and the electromotive force E are equal, i.e., $K_1 = K_2$. Therefore, we take $K_1 = K_2 = K$.

From the Figure 3, we have the following equations:

$$J\ddot{\theta} + b\dot{\theta} = Ki \tag{8}$$

$$L\frac{di}{dt} + Ri = v - K\dot{\theta} \tag{9}$$

By applying the Laplace transform to the above equations, we obtain :

$$(Js + b)\, s\theta(s) = KI(s) \tag{10}$$

$$(Js + b)\, I(s) = V(s) - Ks\theta(s) \tag{11}$$

From Equation (10) , the current formula is given by:

$$I(s) = \frac{(Js + b)\, s\theta(s)}{K} \tag{12}$$

From Equations (11) and (12), and considering that the output of the system is the angular position of the motor shaft $\theta(s)$, and the input of the system is the voltage of the armature $V(s)$, the transfer function of the DC motor is :

$$\frac{\theta(s)}{V(s)} = \frac{K}{s\left[(Ls + R)(Js + b) + K^2\right]} \tag{13}$$

Where :
J : Moment of inertia of the rotor
R : Electric resistance
L : Electric inductance
b : Motor viscous friction constant
However, in our case, the numerical values of the above constants are not available, so the calculation of the model of the DC motor must be done experimentally using the Zedboard FPGA.

The DC motor is considered as a black box. Its identification consists of applying a voltage V and obtaining the angular position θ of the motor. Based on these measurements, the MATLAB system identification toolbox[33] is used to calculate the parameters of the motor model.

During the identification process, it is discovered that the DC motor does not start within a range of voltage values. Knowing that the motor supply voltage is 12V, the dead zone of this motor is [-2.4V 2.4V]. The model obtained by the System Identification Toolbox is represented by the following discrete transfer function, with a sampling time of T_e=0.001 s.

$$\begin{aligned} G(z) = \frac{\theta(z)}{V(z)} &= \frac{b_0}{a_2 z^2 + a_1 z + a_0} \\ &= \frac{16.4}{z^2 + 0.6615z + 0.00041255} \end{aligned} \tag{14}$$

4. FPGA implementation

Before applying the controller to the experimental device, we must first test its behavior on the Zedboard Zynq-7000 FPGA using the FPGA-in-the-loop (FIL) simulation technique in the Simulink environment of MATLAB.

4.1. Fixed point data type

FPGA circuits generally support the following two types of data: fixed-point data and floating-point data. However, designs based on the fixed-point data type consume fewer hardware resources and less power, with shorter computation times.[34]

However, most complex algorithms have nonlinear functions that are not supported by the fixed-point data type. These functions must, therefore, be approximated by other linear functions, which negatively affects the accuracy of the computations. In this work, the design methodology adopted is based on MATLAB-Simulink software.

The fixed-point representation on MATLAB-Simulink used in this work is as follows: $fixdt(s, l, d)$. $fixdt$ creates a numerical type on Simulink describing a fixed point. s represents the sign bit, l the length of the binary word and d the length of its fractional part.

For example, $fixdt(1, 16, 8)$: Here, 16 represents the length of the signal in bits, 1 is the sign bit (signed in this case), and 8 is the length of the fractional part in bits. Details of the fixed-point representation in MATLAB-Simulink are given in Table 2.

Table 2. Fixed-point représentation in Simulink

$Datatypemode$	$Fixed-point:$ $binarypointscaling$
$Signedness$	$Signed$
$Wordlength$	16
$Fractionlength$	8

The control algorithm is developed in the Simulink environment as a double-precision floating-point model using blocks supported by the HDL Coder and then converted to a fixed-point model using the Fixed-Point Tool. This tool calculates the correct integer and fractional parts of each input/output block from the developed floating-point model, respecting the rules of fixed-point arithmetic and optimizing binary word lengths.

4.2. FPGA in the loop simulation

Before applying it to the motor control, the proposed algorithm must be simulated on the MATLAB-Simulink environment with the system in order to test its behavior during various robustness tests. The proposed controller is developed on Simulink with the blocks of HDL Coder and converted into a model with a fixed-point data type, then its VHDL code is generated, which is

finally implemented on the hardware (FPGA) and then tested on the Simulink environment through the FIL functionality.[21] In this study, the Xilinx Zedboard is used, which has a Zynq-7000 AP SoC XC7Z020-CLG484-1 FPGA.[35]

FIL mode simulation is performed for real-time DC motor position control. The generated VHDL code is executed in the target hardware to control the DC motor model synthesized in Simulink. The Zedbaord exchanges the send data of position and signal control in each sampling period with the Simulink environment via the JTAG communication protocol. The concept of FIL simulation is described in Figure 4.

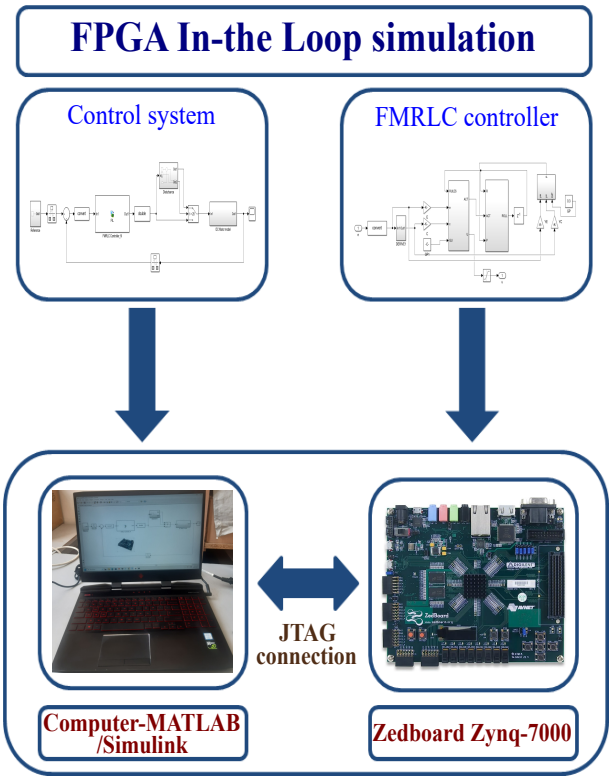


Figure 4. FPGA in-the loop diagram

4.3. Experimental implementation

4.3.1. Experimental setup

The control system consists of a 12 V DC motor (model DFRobot 28PA51G) equipped with a Hall Effect encoder and an adapter board for the encoder (FIT0324) Figure 5, which allows to recover the motor shaft position signal. The encoder can provide 675 pulses per revolution, with a maximum speed of 143 rpm. This motor is connected to an L298N (H-bridge) module, which will allow to change the speed and direction of the motor rotation.

The reference signal was generated by another encoder similar to the motor's. The controller, the two encoders, and the PWMs were programmed using Simulink blocks supported by HDL Coder. The encoder output was programmed as 16 bits, while the PWM input was programmed as 8 bits. The controller output was calculated using the Fixed-Point Tool by combining 16-bit integers and fractions to ensure accuracy. Figure 6 shows the control diagram developed in the Simulink environment.

This model was implemented via HDL Coder from Simulink, by "HDL Workflow Advisor" through the "IP Core Generation" functionality. This technique makes it possible to generate an IP block (Figure 7), whose target hardware is the zynq-7000 FPGA. Next, the VHDL code is generated from the IP block, which is then implemented on the Zedbaord as a bitstream programming file.

The implementation blocks obtained using the Vivado software are as follows:

The encoder block (Figure 8) has two logic inputs, A and B, representing the square-wave signals provided by the sensor, and a 16-bit integer output (int16) representing the position of the motor shaft (in pulses).

Figure 9 shows the PWM block, which includes an input u (the control signal) coded on 8 bits (unit8) and an output that is the DC motor supply voltage.

The FMRLC controller block (Figure 10) has an input e, which is the error between the desired position and the measured position, coded in fixed point on 16 bits ($fixdt(1,16,8)$) and an output u, which is the control signal, also coded in fixed point on 16 bits ($fixdt(1,16,6)$).

The PID controller block is shown in Figure 11, it has the position error e as an input and the control signal u as an output, both coded in fixed point to 16 bits (($fixdt(1,16,8)$) for e and ($fixdt(1,16,4)$) for u).

Details of the implementation of the PID and FMRLC controllers on the Zedboard FPGA are given in Table 3. These results are obtained in both cases using the 16-bit fixed-point data type.

The controller execution time depends on the controller complexity and the number of bits used for the signals. As can be seen, the PID has a lower propagation time than the FMRLC due to the large number of blocks it contains.

Table 3. Features of PID and FMRLC controller implementation on the Zedboard FPGA

Controller	Bits	Propagation	Maximum frequency
PID	16	14.14 (ns)	70.85 (MHz)
FMRLC	16	98.115 (ns)	10.19 (MHz)

4.3.2. FPGA resources

Despite the complexity of the algorithm, the use of the fixed-point tool allows to obtain an optimal

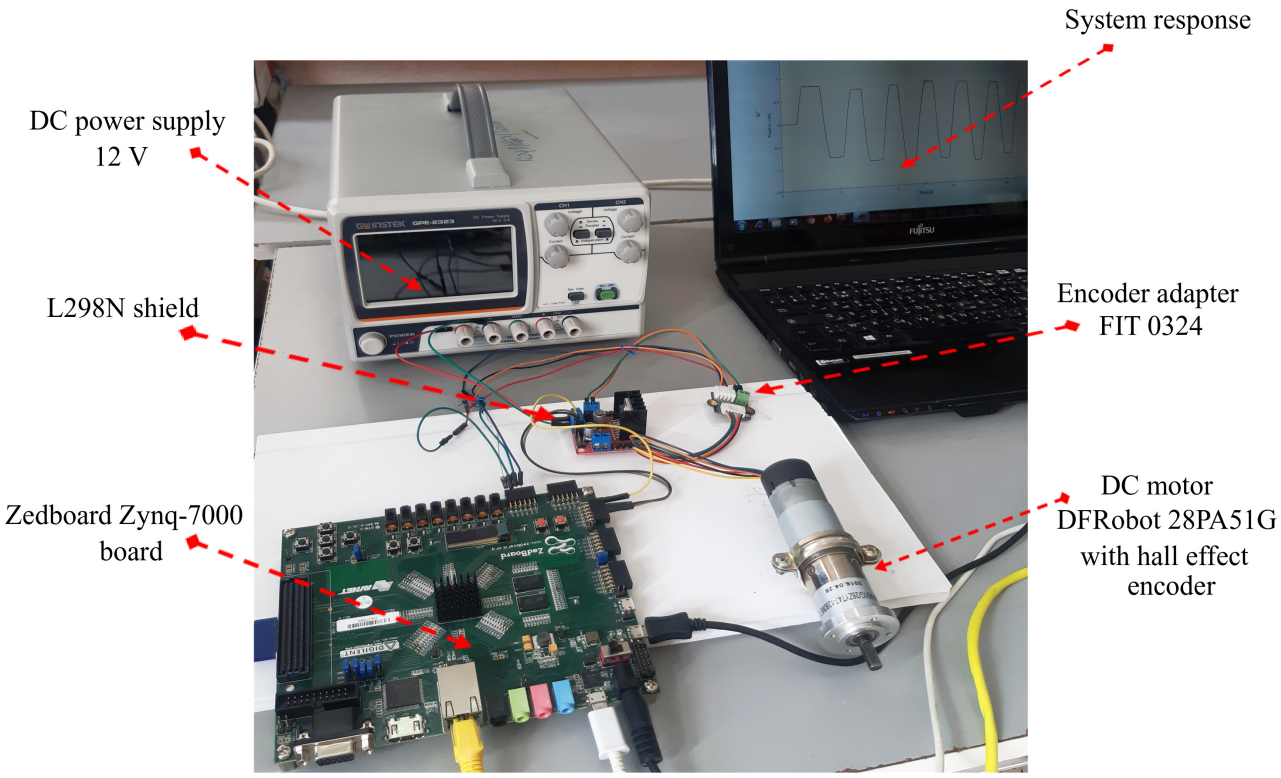


Figure 5. Experimental setup

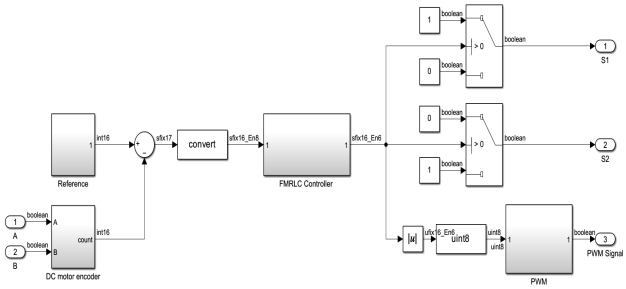


Figure 6. Control diagram in Simulink environment

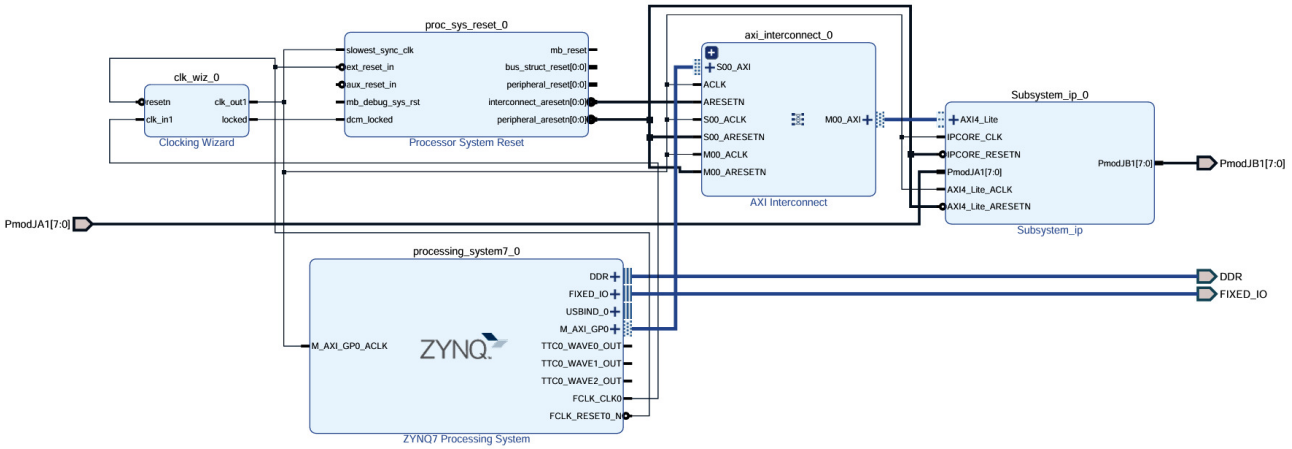


Figure 7. IP block of the realized design

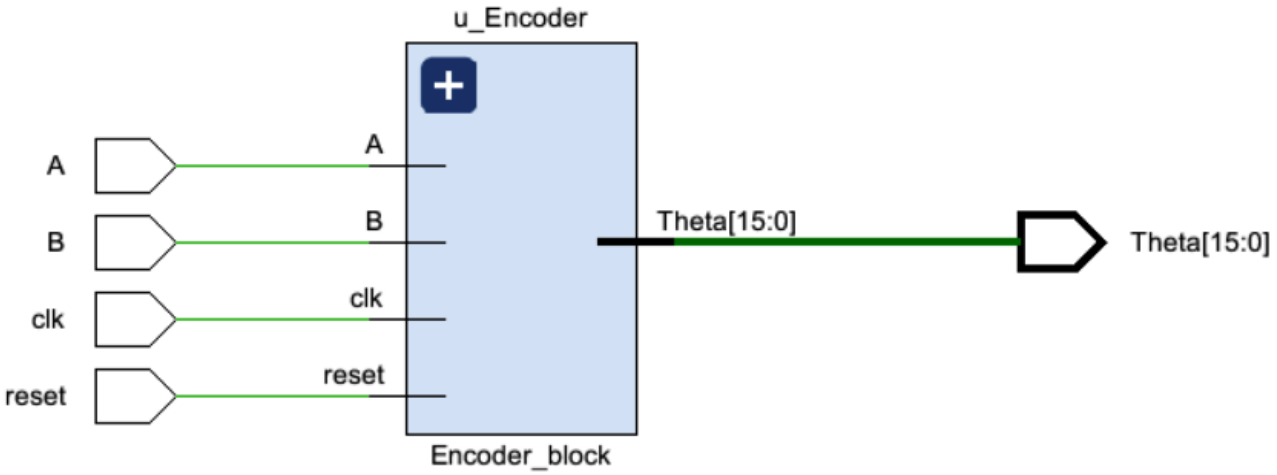


Figure 8. Encoder implementation block on FPGA

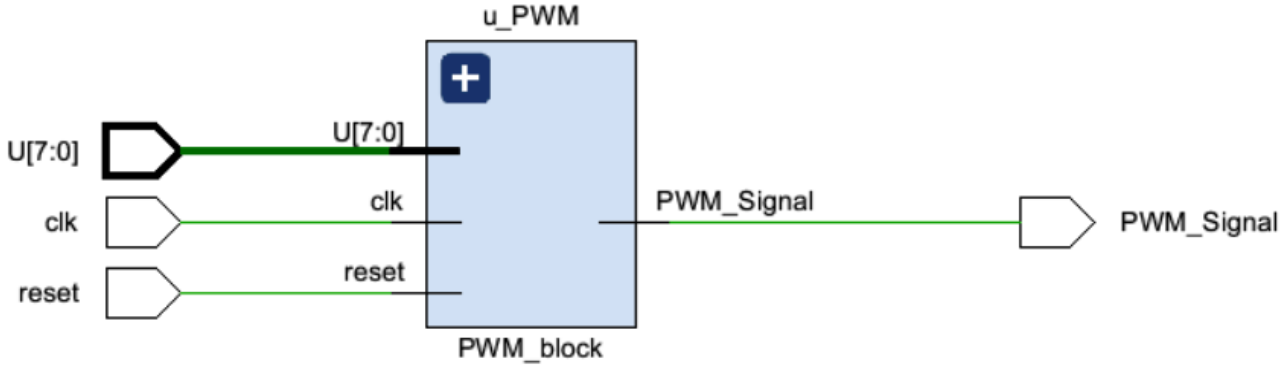


Figure 9. PWM implementation block on FPGA

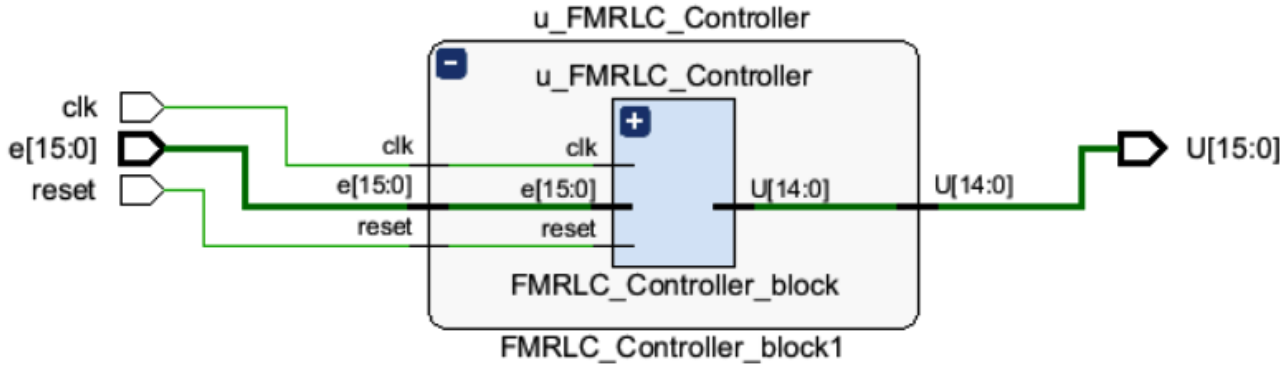


Figure 10. FMRLC implementation block on FPGA

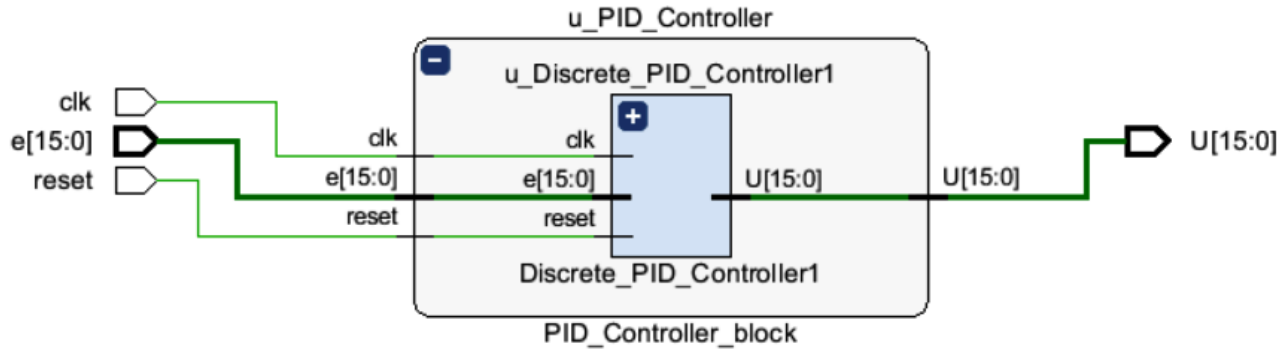


Figure 11. PID implementation block on FPGA

VHDL code in terms of computation time and resources consumed by the FPGA circuit.[36,37] Table 4 illustrates the hardware resources consumed when implementing the PID and FMRLC controllers on the Zedboard, using a sample rate of 1 MHz. As we can see, the FMRLC control consumed 12.68% of LUTs (Look Up Table), 0.47% of LUTRAMs (Memory LUT), 1.62% of FFs (Flip-Flop), 38.18% of DSPs (Digital Signal Processor), 6.00% of IOs (Input/Output), 6.38% of BUFGs (Global Buffer) and 25.00% of MMCMs (Mixed-Mode Clock Manager).

Table 4. FPGA resources consumption

Resource	Available	Utilization (PID)	Utilization (FMRLC)
LUT	53200	651(1.22%)	6801(12.68%)
LUTRAM	17400	39(0.22%)	81(0.47%)
FF	106400	664(0.62%)	1725(1.62%)
DSP	220	6(2.73%)	84(38.18%)
IO	200	12(6.00%)	12(6.00%)
BUFG	32	3(9.38%)	3(9.38%)
MMCM	4	1(25.00%)	1(25.00%)

5. Results

5.1. FIL simulation results

In this section, the results obtained by implementing the proposed algorithm with FPGA in the loop are presented in order to see the behavior of the proposed controller in case tracking with a sinusoidal reference. In this execution mode, the FMRLC controller is implemented and executed on the Zedboard with a sampling frequency of 1 kHz, while the rest of the control loop (DC motor model and reference) is executed in the Simulink environment (Figure 12).

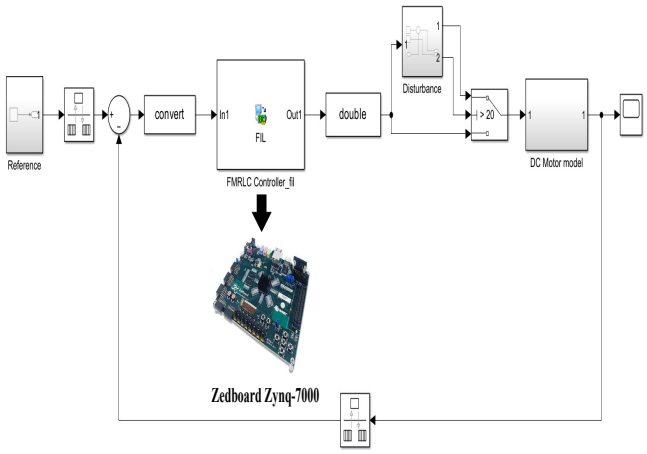


Figure 12. FMRLC controller implementation with FPGA In-the Loop

5.1.1. FIL simulation with parametric disturbances

In order to prove the efficiency and robustness of the proposed algorithm against parameter uncertainties, these parameters are varied in real-time simulation (see Table 5):

Table 5. DC motor model parameter variations

Time	t=8s	t=15s	t=23s	t=32s
Parameter	b_0	a_1	a_0	Dead zone
Value	10	2	2	[-3.1V 3.3V]

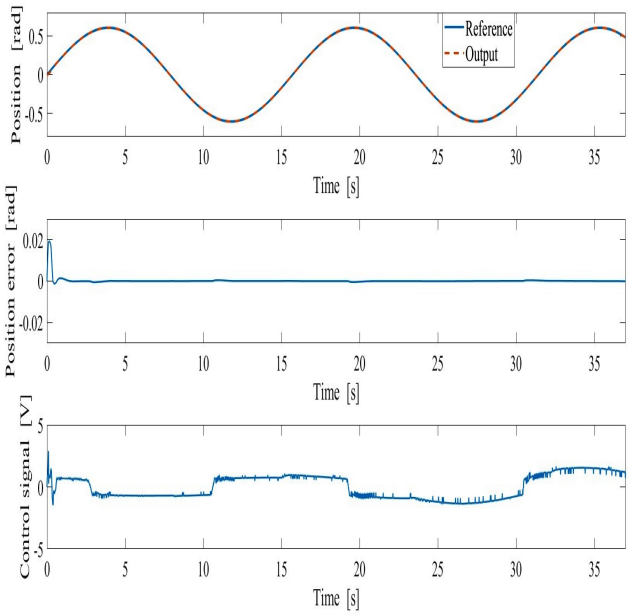


Figure 13. Simulation results of position tracking with parametric disturbances

The results obtained in Figure 13 show a good tracking of the reference changes with an error close to zero, despite the parametric variations made on the parameters of the motor model at times t = 8 s, t = 15 s, and t = 23 s, as well as the variation of the dead zone at time t = 32 s. The proposed controller is able to adapt to the dynamic variations of the system by modifying the parameters of the membership functions in a short time, thanks to the controller structure equipped with a learning mechanism with memory and to the high computational power of the FPGA.

5.1.2. FIL simulation with disturbances on the control

In this case, the robustness test is performed by injecting a disturbance at time t = 20s on the control signal provided by the FMRLC controller. The control signal provided by the Zedboard is 3.3 V, and the perturbation formula is (expressed in volts):

$$D(t) = 0.52sin(t) \tag{15}$$

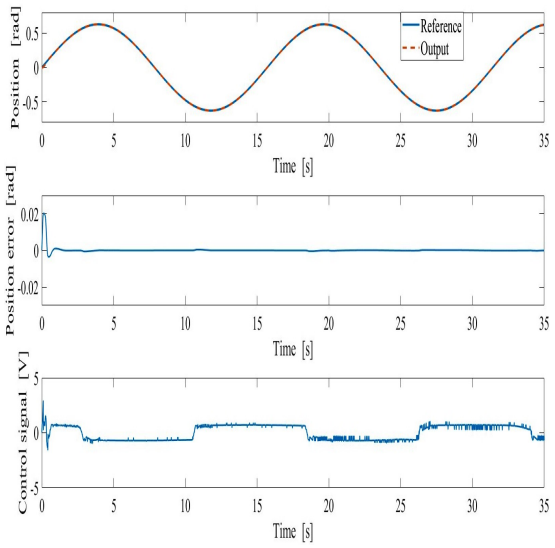


Figure 14. Simulation results of position tracking with disturbances on the control

According to the simulation results obtained in FIL mode (Figure 14), good tracking and good stability are observed. The proposed controller shows good robustness despite the disturbance injected into the control signal at time t = 20s. The FMRLC controller manages to adapt to the reference changes and rejects the applied disturbance.

5.2. Experimental results

In this part, the experimental results obtained during the position control of the DC motor using the Zedboard FPGA are presented. In order to verify the efficiency of the proposed algorithm, the results obtained with the FMRLC controller were compared with those obtained with the PID controller.

5.2.1. PID controller

The PID controller parameters were tuned using the PID Tuner tool in Simulink. The parameters obtained are as follows: P = 21, I = 1.9, and D = 15. The experimental results obtained with the PID controller are shown in Figures 15 and 16.

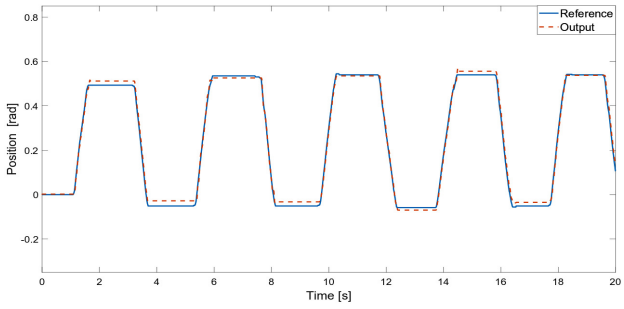


Figure 15. Experimental results of position tracking with PID controller

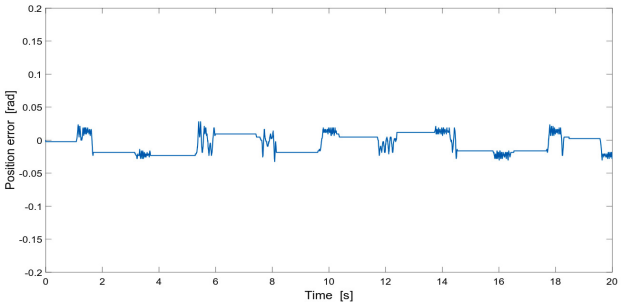


Figure 16. Position tracking error with PID controller

Figure 15 shows a test with a reference varying between 0.04 rad and 0.55 rad, generated by an encoder similar to that of the DC motor. As can be seen, the PID controller performs well, with a short response time that quickly converges to the desired reference signal. The tracking error is about ±0.03 rad, as shown in Figure 16.

5.2.2. FMRLC controller

Figures 17 and 18 show the experimental results obtained with the FMRLC controller.

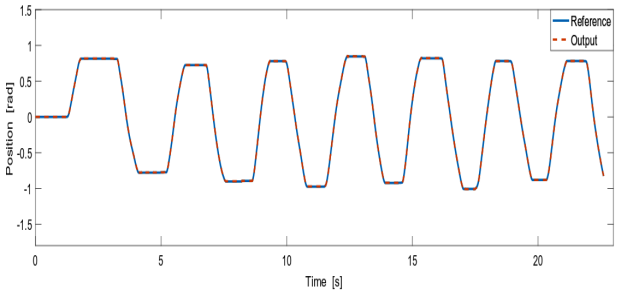


Figure 17. Experimental results of position tracking with FMRLC controller

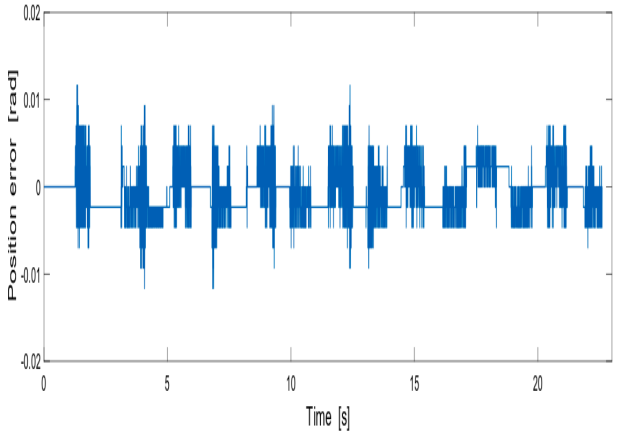


Figure 18. Position tracking error with FMRLC controller

The generated setpoint varies between −0.9 and 0.9. Excellent tracking can be seen here. The FMRLC controller closely tracks the reference signal with a very short response time, as shown in Figure 17. This is reflected in a tracking error of

about ±0.012. This error is practically inferior to that obtained with the PID controller, as shown in Figure 18.

The experimental results obtained show good position tracking and stability, with a lower error compared to the results of the PID controller. These results are explained on the one hand by the use of the knowledge base modifier, which modifies the membership functions in real time according to the DC motor dynamics, and on the other hand by the use of the Zedboard FPGA, which provides very short sampling times and parallel computation, accelerating the computation time to quickly converge to the desired performance.

6. Conclusion

This paper presents the implementation of a fuzzy logic controller FMRLC on a Zedboard FPGA to control the position of a DC motor. The idea was to implement a fuzzy controller with learning on an FPGA board. The use of this configurable circuit, which offers parallel data computation at a high operating frequency, aims at accelerating the computations, in particular the learning process, which requires a significant computation time to converge to the desired performance. The design and implementation of the controller were carried out using the MATLAB-Simulink environment. This methodology allows great design flexibility by using simple blocks on Simulink without resorting to low-level programming languages (VHDL/Verilog), thus reducing the design time of the algorithm. The fixed-point data type is used to optimize the use of hardware resources on the FPGA. This binary representation can affect the accuracy of calculations, but the design results in low power and resource consumption compared to floating-point based designs.[34]

The FMRLC controller was first tested using the FIL technique in Simulink, then implemented on the Zedboard and applied to the experimental device. The FIL simulation results showed good tracking performance and good robustness to disturbances. The experimental results showed the efficiency of the proposed controller compared to the conventional controller (PID), which can be explained by the controller adapting the parameters of the membership functions to each different situations. The design methodology used to implement the algorithm on the Zedboard FPGA board allowed to obtain a fast and accurate algorithm with an optimal consumption of hardware resources. The co-simulation results and the experimental results demonstrated the effectiveness of this design methodology.

Acknowledgments

This paper is derived from a research grant funded by the Research, Development, and Innovation Authority (RDIA), Kingdom of Saudi Arabia, with grant number 13382-psu-2023- PSNU-R-3-1-EI-. This research is supported by Automated Systems and Computing Lab (ASCL), Prince Sultan University, Riyadh, Saudi Arabia. The authors would like to thank Prince Sultan University, Riyadh, Saudi Arabia for supporting this work.

Fundings

This paper is funded by Prince Sultan University, Riyadh, Saudi Arabia. The authors would like to thank Prince Sultan University for paying the article processing fee for this paper.

Conflict of interest

The authors declare that have no conflict of interest.

Author contributions

Conceptualization: Mohand Achour Touat, Hocine Khati, Hand Talem, Ahmad Taher Azar
Formal analysis: Mohand Achour Touat, Arezki Fekik, Rabah Mellah, Ahmad Taher Azar, Saim Ahmed
Methodology: Mohand Achour Touat, Hocine Khati, Arezki Fekik, Ahmad Taher Azar
Writing – original draft: Mohand Achour Touat, Hocine Khati, Arezki Fekik, Ahmad Taher Azar, Saim Ahmed
Writing – review & editing: Arezki Fekik, Ahmad Taher Azar, Rabah Mellah, Saim Ahmed

Availability of data

The original contributions presented in the study are included in the article/supplementary material, further inquiries can be directed to the corresponding author/s.

References

1. Kemal U, Beyza Nur A. Adaptive MIMO fuzzy PID controller based on peak observer. *Int J Optim Control: Theor Appl.* 2023;13(2):139–150.
2. Masjudin, Alimuddin, Aisah SN, Wiryadinata R. Dc motor speed control based on fuzzy adaptive with fuzzy model reference learning control (fmrlc) algorithm. *In: 2020 2nd International Conference on Industrial Electrical and Electronics (ICIEE). IEEE*; 2020: 79-83.
3. Devashish J, Arifa A, Sanatan K, Debanjan R. Fuzzy-PID and interpolation: a novel synergetic approach to process control. *Int J Optim Control: Theor Appl.* 2024;14(4):355-364.

4. Fajrianto MR, Wahyudi W, Sudjadi S. Perancangan kontroler fuzzy model reference learning control (fmrlc) berbasis mikrokontroler atmega16 sebagai kendali motor brushless dc (bldc). *Transient: J Ilmiah Teknik Elektro*2017;6:597–604.
5. Saim A, Haoping W, Yang T. Fault tolerant control using fractional-order terminal sliding mode control for robotic manipulators. *Stud. Inform. Control.* 2018;27(1):55-64.
6. Saim A, Ahmad Taher A, Ibraheem KI. Nonlinear system controlled using novel adaptive fixed-time SMC. *AIMS Math* 2024;9(4):7895-7916.
7. Kopasakis G, Kopasakis G. Adaptive performance seeking control using fuzzy model reference learning control and positive gradient control. *In: 33rd Joint Propulsion Conference and Exhibit*; 1997: 3191.
8. Zhen L, Xu L. Fuzzy learning enhanced speed control of an indirect field-oriented induction machine drive. *IEEE Trans Control syst Technol.* 2000;8:270–278.
9. Mayhan P, Washington G. Fuzzy model reference learning control: a new control paradigm for smart structures. *Smart Mater struct.* 1998;7:874.
10. Layne JR, Passino KM, Yurkovich S. Fuzzy learning control for antiskid braking systems. *IEEE Trans Control Syst Technol.* 1993;1:122–129.
11. Reay D, Dunnigan M. Learning issues in model reference based fuzzy control. *IEEE Proc Control Theor Appl.*, 1997;144:605–611.
12. Duka AV, Oltean SE, Dulau M. Model reference adaptive control and fuzzy model reference learning control for the inverted pendulum. *comparative analysis. In: Proceedings of WSEAS International Conference on Dynamical Systems and Control*; 2005:168–173.
13. Monmasson E, Idkhajine L, Cirstea MN, Bahri I, Tisan A, Naouar MW. Fpgas in industrial control applications. *IEEE Trans Ind Informat* 2011;7:224-243.
14. Hace A, Franc M. Fpga implementation of sliding-mode control algorithm for scaled bilateral teleoperation. *IEEE Transac Ind Inform.* 2012;9:1291–1300.
15. Fekik A, Khati H, Azar AT, et al. FPGA in the loop implementation of the PUMA 560 robot based on backstepping control. *IET Control Theor Appl.* 2024;18(15): 1877-1891.
16. Huerta-Moro S, Tavizón-Aldama JD, Tlelo-Cuautle E. FPGA implementation of sliding mode control and proportional-integral-derivative controllers for a DC–DC buck converter. *Technol.* 2024;12(10):184.
17. Wang J, Li M, Jiang W, Huang Y, Lin R. A design of FPGA-based neural network PID controller for motion control system. *Sens.* 2022;22(3):889.
18. Li Y, Li SE, Jia X, Zeng S, Wang Y. FPGA accelerated model predictive control for autonomous driving. *J Intell Connect Vehicl.* 2022;5(2):63-71
19. Meghwal R, Yadav VK, Vardia M. Robust fuzzy controller design with FPGA implementation for matrix converter based induction motor drive. *e-Prime Adv Elect Eng Electron Energy* 2024;10:100752.
20. El Attafi A, El Alami H, Bossoufi B, et al. Robust control of a wind energy conversion system: FPGA real-time implementation. *Heliyon.* 2024; 10(15):e35712.
21. Chakravarty S. Technology and Engineering Applications of Simulink. *BoD–Books on Demand*; 2012.
22. Akkaya Ş, Üzgün HD, Akbati O. Fuzzy logic controller implementation with fpga in the loop simulation. *In: Proceedings of the 2017 International Conference on Mechatronics Systems and Control Engineering* ; 2017: 33-37.
23. Akbatı O, Üzgün HD, Akkaya S. Hardware-in-the-loop simulation and implementation of a fuzzy logic controller with fpga: case study of a magnetic levitation system. *Trans Instit Measure Control.*, 2019;41:2150-2159.
24. Deliparaschos K, Nenedakis F, Tzafestas SG. Design and implementation of a fast digital fuzzy logic controller using fpga technology. *J Intell Robot Syst.*, 2006;45:77-96.
25. Khati H, Mellah R, Talem H. Neuro-fuzzy control of a position-position teleoperation system using fpga, *In: 2019 24th International Conference on Methods and Models in Automation and Robotics (MMAR). IEEE*; 2019:64-69.
26. Khati H, Talem H, Mellah R, Bilek A. Neuro-fuzzy control of bilateral teleoperation system using fpga. *Iranian J Fuzzy Syst.* 2019;16:17-32.
27. Azzouz B, Hadjira B. Hardware/software codesign for intel ligent motor drive on an fpga, *In: 2020 2nd International Workshop on Human-Centric Smart Environments for Health and Well-being (IHSH). IEEE*; 2021; 227-232.
28. Lotfy A, Kaveh M, Mosavi M, Rahmati A. An enhanced fuzzy controller based on improved genetic algorithm for speed control of dc motors. *Analog Integr Circ Signal Process.* 2020;105:141-155.
29. Abdelkrim H, Othman SB, Saoud SB. Fpga implementation of self-reconfigurable fuzzy logic controller. *In: 2018 International Conference on Advanced Systems and Electric Technologies(IC ASET). IEEE*; 2018:151-156.
30. Moussa I, Khedher A. Real-time wte using flc implementation on fpga board: theoretical and experimental studies. *In: 2020 17th International Multi-Conference on Systems, Signals & Devices(SSD). IEEE*; 2020: 428-433.
31. Anand, M.S., Tyagi, B. (2012). Design and implementation of fuzzy controller on fpga. *Int J Intell Syst Applicat.* 2012; 10:35-42.
32. Layne JR, Passino KM. Fuzzy model reference learning control. *J Intell Fuzzy Syst.* 1996;4:33–47.
33. Ljung L. System Identification Tool-box: User's Guide. Citeseer; 1995.

34. Finnerty A, Ratigner H. Reduce power and cost by converting from floating point to fixed point. In: WP491 (v1. 0) ; 2017: 9-10.
35. Crockett LH, Elliot RA, Enderwitz MA. The Zynq Book Tutorials for Zybo and Zedboard. *Strathclyde Academic Media*; 2015.
36. Khati H, Fekik A, Azar AT, et al. Optimizing UAV stability and control with FPGA-based PID control system design. *In: 2024 International Conference on Control, Automation and Diagnosis (ICCAD). IEEE* ;2024:1-6.
37. Fekik A, Khati H, Azar AT, Hamida ML, Denoun H, & Kamal NA. FPGA-based performance evaluation of backstepping control and computed torque control for industrial robots. *Int J Automat Control.* 2025;19(1):101-132.

Mohand Achour Touat *was born in 1977. He earned his state engineer diploma in Automation in 2002 from Mouloud Mammeri University in Algeria. In 2005, he obtained a specialist diploma in Control Systems from the National Aviation University of Ukraine. He later received his PhD in Engineering Sciences, specializing in Computer-Aided Design. Currently, he is a lecturer in the Automation Department at Mouloud Mammeri University, where he has been the head of the department since 2016. His current research focuses on robuste control and artificial intelligence.*
https://orcid.org/0000-0002-5758-7653

Hocine Khati *obtained the Bachelor's and Master's degrees in Automation from Mouloud MAMMERI University of Tizi Ouzou (UMMTO), Algeria, in 2013 and 2015, respectively. In 2020, he obtained the Dotoral degree in Automatic Control from the same institution. He is currently an Associate Professor in the Automatic Department at UMMTO. His current research focuses on digital control, adaptive control, robotics, and artificial intelligence.*
https://orcid.org/0009-0004-5556-6308

Arezki Fekik *is a lecturer at Akli Mohand Oulhadj University in Bouira, Algeria. He currently works as a research engineer and is responsible for experimental testing and research in electrical systems control at the Laboratoire des Sciences Numériques de Nantes (LS2N), École Centrale de Nantes. He has published over 65 journal articles, conference papers, and book chapters in the fields of power electronics and its applications. His current research focuses on power electronics and its applications, such as wind turbines, photovoltaic systems, reliability, harmonics, microgrids, and variable speed drives.*
https://orcid.org/0000-0001-5053-1764

Ahmad Taher Azar *is a full Professor at College of Computer and Information Sciences (CCIS), Prince Sultan University, Riyadh, Saudi Arabia. He is a leader of Automated Systems and Computing Lab (ASCL), Prince Sultan University, Saudi Arabia. He is currently an editor for IEEE Transactions on Fuzzy Systems, IEEE Systems Journal, IEEE Transactions on Neural Networks and Learning Systems, Springer's Human-centric Computing and Information Sciences, and Elsevier's Engineering Applications of Artificial Intelligence. Prof. Azar was named one of the top 2% of scientists in the world in Artificial Intelligence by Stanford University, based on single-year impact and career-long impact. These rankings were published by Stanford University in the PLOS journal and were based on the SCOPUS database. Prof. Azar has expertise in Artificial Intelligence, Control Theory and Applications, Robotics, Machine Learning, Computational Intelligence and dynamical system modeling. He has authored/co-authored over 500 research papers in prestigious peer-reviewed journals, book chapters, and conference proceedings.*
https://orcid.org/0000-0002-7869-6373

Hand Talem *obtained his mechanical engineering degree in 2007 from the maritime school in Bousmail, Tipaza, Algeria, and his automatic engineering degree from the Université Mouloud MAMMERI de Tizi Ouzou (UMMTO), Algeria, in 2009. In 2010, he enrolled in the Magister en Automatique program at the same institution. He is currently the Chief Engineer at the Algerian shipping company CNAN. His current research interests include numerical control, adaptive control, robotics, and artificial intelligence.*
https://orcid.org/0009-0002-8483-7221

Rabah Mellah *received the Doctoral degrees in Automatic Control from USTHB University of Algeria in 2006. He is a professor at the Department of Automatic, UMMTO University, Tizi-Ouzou, Algeria. His research interests include nonlinear system, robotics, teleoperation, fuzzy logic and neural networks.*
https://orcid.org/0000-0003-2273-7532

Saim Ahmed *received his B.S degree in Electronics Engineering from Sir Syed University of Science and Technology, Karachi, Pakistan in 2009. He received his M.E degree in Industrial Control and Automation from Hamdard University, Karachi, Pakistan, in 2013. He completed his Ph.D. degree in control science and engineering from Nanjing University of Science and Technology, China in 2019. He has served as an Assistant Professor at the Department of Mechatronics, Shaheed Zulfikar Ali Bhutto Institute of Science and*

Technology, Karachi, Pakistan. He is currently working as a Postdoctoral Researcher at Prince Sultan University, Saudi Arabia. His research interests include the theory and applications of adaptive control, sliding mode control, time delay control, robotic exoskeleton and manipulators, nonlinearities and their compensation.

https://orcid.org/0000-0002-2302-705X

An International Journal of Optimization and Control: Theories & Applications
(https://accscience.com/journal/ijocta)



This work is licensed under a Creative Commons Attribution 4.0 International License. The authors retain ownership of the copyright for their article, but they allow anyone to download, reuse, reprint, modify, distribute, and/or copy articles in IJOCTA, so long as the original authors and source are credited. To see the complete license contents, please visit http://creativecommons.org/licenses/by/4.0/.

An International Journal of Optimization and Control: Theories & Applications
ISSN: 2146-0957 eISSN: 2146-5703
Vol.15, No.3, pp.449-463 (2025)
https://doi.org/10.36922/IJOCTA025060018

RESEARCH ARTICLE

Computational aspects of the crop field segmentation problem based on anisotropic active contour model

Ciro D'Apice[1], Umberto De Maio[2], Peter I. Kogut[3,4], and Rosanna Manzo[5*]

[1]Department of Management Innovation Systems, University of Salerno, Fisciano, Italy
[2]Department of Mathematics and Applications "R. Caccioppoli", University of Naples "Federico II", Naples, Italy
[3]Department of Differential Equations, Oles Honchar Dnipro National University, Dnipro, Ukraine
[4]EOS Data Analytics Ukraine, Dnipro, Ukraine
[5]Department of Political and Communication Sciences, University of Salerno, Fisciano, Italy
cdapice@unisa.it, udemaio@unina.it, p.kogut@i.ua, peter.kogut@eosda.com, rmanzo@unisa.it

ARTICLE INFO

Article History:
Received: February 4, 2025
1st revised: February 11, 2025
2nd revised: April 4, 2025
Accepted: April 11, 2025
Published Online: May 20, 2025

Keywords:
Segmentation problem
Piecewise smooth approximation
Optimality conditions
Active contour model
Euler-Lagrange equation

AMS Classification 2010:
26A33; 34A08; 35H15; 34K50

ABSTRACT

In this paper, we analyze the numerical aspects of the practical implementation of the generalized active contour model, that has been recently proposed in the literature, for extracting agricultural crop fields with a high level of inhomogeneity from satellite data. We also derive the corresponding Euler–Lagrange equation and discuss its relaxation method.

CC BY

1. Introduction

This paper deals with the numerical aspects of the implementation of the generalized active contour model, which has been recently proposed in,[1] for extracting agricultural crop fields with a high level of inhomogeneity from satellite data. These investigations have been justified by various applications, such as in satellite image segmentation under remote sensing of the Earth's surface. Fixed a field $\Omega \subset \mathbb{R}^2$, one of the fundamental problems in agriculture is to give a disjunctive decomposition into a finite quantity of nonempty subsets $\Omega = \Omega_1 \cup \Omega_2 \cup \cdots \cup \Omega_K \cup \Omega^*$ such that a distinctive value of some agricultural index (PVI, NDVI, LAI, etc.) could be associated to each of these subsets. The characteristic feature of the decomposition is that it has to be closely related to a given objective agricultural index $f : \Omega \to \mathbb{R}$. Namely, this decomposition has to inherit the following properties:

(a) $\{\Omega_i\}_{i=1}^K$ are open subsets of Ω with nonempty interior, whereas Ω^* stands for the boundaries between different Ω_j;
(b) within each Ω_i the objective agricultural index f varies smoothly and/or slowly;
(c) the function f cannot vary discontinuously inside each Ω_i;
(d) the decomposition is optimal in the following sense: the approximation of f by a piece-wise constant function $f^* : \Omega \to \mathbb{R}$ is such that the restrictions f^* to the pieces

*Corresponding Author

$\Omega_j,\ f^*|_{\Omega_j}$, are defined as

$$|f^*|_{\Omega_j}(x) = \langle f\rangle_{\Omega_j} := \frac{1}{|\Omega_j|}\int_{\Omega_j} f(s)\,ds, \quad \forall\, j = 1,\dots,K, \forall\, x \in \Omega_j,$$

and the 1-D Hausdorff measure of the set $\bigcup_{j=1}^{K} \partial\Omega_j$ should be as small as possible.

Hereinafter, the decomposition of Ω satisfying properties (a)–(d) is denoted with f-decomposition.

The role of the function $f : \Omega \to \mathbb{R}$ is explained by pointing out that after the f-decomposition the new objects $\{\Omega_j\}_{j=1}^{K}$ should have homogeneous values of f (see[2,3]). To characterize a measure of the variability of f in each subdomain Ω_j, one can calculate the coefficient of variation, that is, it is the ratio of the standard deviation of $f(x)$ within Ω_j to its mean $\langle f\rangle_{\Omega_j}$. Furthermore, if we consider applications in agriculture it might be reasonable to regard the NDVI-characteristic as the primary feature of the zone of interest Ω, that is, in this case, $f(x) = \mathrm{NDVI}(x)$ for all $x \in \Omega$. However, a thorough analysis of this issue shows that it is a difficult task to understand NDVI characteristics quantitatively over Ω. By presuming that the vegetation data generated from the NDVI is uniformly and smoothly distributed within the specific crop fields, numerous studies have restricted this interpretation.[4,5] If they attempt to use the NDVI on heterogeneous canopies, for example, plantations that have weeds, mixed soil, and various crop mixtures where the vegetation has varying NDVI characteristics because of spatial variability, this assumption is violated.

Accordingly, the data acquired in this manner is a valuable source of information that may be applied to the management of environmental resources.[6,7] Specifically, it enables us to determine the crop's health and find out whether there are trouble spots within the designated fields or areas where the crops require nutrients or water. A similar point of view is recommended as crucial in.[3,6] Some methods for assessing such characteristics have recently been proposed in.[8–10] The most stringent barrier to creating such a decomposition, however, is that these subdomains cannot include even minor portions of various fields with plausibly distinct crops, nor should they overlap or contain any fragments of field borders. Because of this, the segmentation challenge indicated above is fairly difficult.

Moreover, the principal distinguishing characteristic of f-decomposition is the impossibility to reduce it to the well-known settings of the segmentation problem (consult the model of Mumford-Shah[11] or the approaches proposed by[12–19] along with the others). We refer to the recent study[17] for an overview of the state of the art in this topic.

To sort out these issues, we involve an anisotropic specification of the standard active contour model. Apparently, the latter was first introduced in[20] to transform the image segmentation problem into a minimization problem in a suitable functional space, and it offered a fresh perspective on image segmentation, which was referred to as the focus and hot spot of analysis in.[21] The subject of image segmentation has seen the proposal of numerous good algorithms based on active contour models in recent years (we recommend that readers consult the latest publications[22–28] and the bibliography therein). However, their correct application to the NDVI-decomposition of agricultural fields remains an open problem nowadays.

The main idea, that was realized in the new setting of variational issue for the f-decomposition, is that we associate with a given objective function $f : \Omega \to \mathbb{R}$ the constrained optimization problem as follows:

$$J(c,\varphi) = T(c,\varphi) + \alpha\sum_{j=1}^{m}\int_{\Omega} |M^f D\chi_{\{\varphi(x)>l_j\}}| \to \inf_{\varphi\in\Xi}, \quad (1)$$

where $T : \mathbb{R}^{m+1} \times BV(\Omega) \to \mathbb{R}$ is a fidelity term, $\{l_0, l_1, \dots, l_{m+1}\}$ is a given collection of distinct level values, $\chi_{\{\varphi(x)>l_j\}}$ is the characteristic function of the set $\{x \in \Omega : \varphi(x) > l_j\}$, and the set of feasible solutions Ξ is defined as follows: $(c,\varphi) \in \Xi$ if and only if $(c,\varphi) \in \mathbb{R}^{m+1} \times BV(\Omega)$ and

$$l_0 \le \varphi(x) \le l_{m+1} \text{ a.e. in } \Omega,$$
$$c = (c_0, c_1, \dots, c_m),\ c_j \ge 0,\ j = 0,\dots,m.$$

As for the matrix-value function $M^f(\cdot) : \Omega \to \mathbb{R}^{2\times 2}$, it is the so-called anisotropic diffusion tensor that avoids the emergence of subdomains with f discontinuity zones or locations where this function has a tendency to change quickly.

Thus, the main idea, which we push forward, is that the segmentation problem should be given as a constrained minimization problem with a special anisotropic cost functional, where the "effect of anisotropy" we associate with the structure topology of f-distribution (see[29]). With that in mind, we utilize the main characteristic of the given function f — the normal unit vector field $\theta : \Omega \to \mathbb{R}^2$ to level sets of f. As a result,

we define $M^f(\cdot)$ as a parametrized square matrix function $M^f(x) = \left[I - \eta^2 \theta(x) \otimes \theta(x)\right]$ and demonstrate that the f-decomposition of the domain Ω relies heavily on this tensor (the technical details are explained in Section 2). As for the fidelity term $T(c, \varphi)$, we give its precise definition in Section 2. Its characteristic feature is the fact that instead of the standard Euclidean metric, we involve into consideration the Jeffrey divergency as a more stable metric with respect to outliers.

The outcomes of simulations using satellite photos of agricultural fields, where the area of high oscillatory edges (the crop locations' boundaries) is rather significant, support the advantage of including M^f in the final term of J_ε. We refer to Section 4 for further information.

Thus, if $(c^0, \varphi^0) \in \underset{(c,\varphi)\in\Xi}{\operatorname{Absmin}} J(c, \varphi)$, then

$$f^*|_{\Omega_j}(x) = c_j^0 := \frac{1}{|\Omega_j|} \int_{\Omega_j} f(s)\, ds, \quad \forall\, x \in \Omega_j, \quad \text{and} \quad \forall\, j = 0, \ldots, m.$$

is a piece-wise approximation of f and the corresponding f-decomposition takes the form

$$\begin{aligned}
\Omega_0 &= \left\{ x \in \Omega \,:\, \left(\varphi^0\right)_\rho (x) < l_1 \right\}, \\
\Omega_j &= \left\{ x \in \Omega \,:\, l_j < \left(\varphi^0\right)_\rho (x) < l_{j+1} \right\}, \\
& \quad j = 1, \ldots, m-1, \\
\Omega_m &= \left\{ x \in \Omega \,:\, \left(\varphi^0\right)_\rho (x) > l_m \right\}, \\
\Omega_* &= \bigcup_{j=1}^{m} \left\{ x \in \Omega \,:\, \left(\varphi^0\right)_\rho (x) = l_j \right\}.
\end{aligned}$$

Here, $\left(\varphi^0\right)_\rho \in C^\infty(\overline{\Omega})$ denotes a smooth approximation of $\varphi^0 \in BV(\Omega)$. Moreover, setting $\Omega = \Omega_i$, $i = 0, 1, \ldots, m$, while for a new pair of subdomains, the mean values of f continue to be distinct, we can iteratively carry on with the decomposition process.

The outline of the paper is as follows. In Section 2 we introduce the setting of the optimization problem for f-decomposition of Ω and discuss its main principle features. Section 3 is devoted to prove that, under some assumptions, the corresponding optimality system can be represented in the form of the Euler–Lagrange equation with the corresponding initial and boundary conditions. The aim of Section 4 is to describe the numerical scheme and a procedure to solve the Euler–Lagrange system numerically. Section 4 includes the outcomes of simulation using real-life satellite images, demonstrating that the proposed model exhibits accuracy and efficiency.

2. Statement of the piecewise-constant Mumford–Shah segmentation problem

Denote by Ω a bounded open subset of $\mathbb{R}^2$ with a Lipschitz boundary. Given a subset $E \subset \Omega$, let $|E|$ be its 2-dimensional Lebesgue measure $\mathcal{L}^2(E)$, $\overline{E}$ its closure, ∂E its boundary, and χ_E of E the characteristic function. The notation $u|_E$ denotes the restriction of a given function u to the set $E \subseteq \Omega$. Indicate the infinitely differentiable functions having compact support in Ω by $C_0^\infty(\Omega)$. Let $\mathcal{H}^k$ be the Hausdorff k-dimensional measure and $\mu \llcorner E$ the measure μ restricted to the set E.

Let $f : \Omega \to \mathbb{R}$ be a given objective function that can be interpreted as a gray-scale image such that a value $\gamma > 0$ exists satisfying

$$f(x) \geq \gamma > 0 \text{ a.e. in } \Omega, f \in L^\infty(\Omega). \tag{2}$$

The following statement for the f-decomposition of Ω in the framework of the Mumford–Shah segmentation problem has been recently proposed in[1]

$$\begin{aligned}
J(c, \varphi) = & \int_\Omega (f - c_0) \log\left(\frac{f}{c_0}\right) \chi_{\{\varphi(x) < l_1\}}\, dx \\
& + \sum_{j=1}^{m-1} \int_\Omega (f - c_j) \log\left(\frac{f}{c_j}\right) \\
& \qquad \times \left[\chi_{\{\varphi(x) > l_j\}} - \chi_{\{\varphi(x) > l_{j+1}\}}\right] dx \\
& + \int_\Omega (f - c_m) \log\left(\frac{f}{c_m}\right) \chi_{\{\varphi(x) > l_m\}}\, dx \\
& + \alpha \sum_{j=1}^{m} \int_\Omega |M^f D\chi_{\{\varphi(x) > l_j\}}| \to \inf_{\varphi \in \Xi},
\end{aligned} \tag{3}$$

where $\alpha > 0$ is a weight coefficient and feasible solutions are given by: $(c, \varphi) \in \Xi$ iff $(c, \varphi) \in \mathbb{R}^{m+1} \times BV(\Omega)$ and

$$\begin{aligned}
& l_0 \leq \varphi(x) \leq l_{m+1} \text{ a.e. in } \Omega, \\
& c = (c_0, c_1, \ldots, c_m),\ c_j \geq 0,\ j = 0, \ldots, m.
\end{aligned} \tag{4}$$

Here, $\{l_0, l_1, \ldots, l_{m+1}\}$ is a given collection of distinct level values, and $M^f(\cdot) \in C^\infty(\Omega; \mathbb{R}^{2\times 2})$ stands for the squared matrix such that

$$M^f(x) = \left[I - \eta^2 \theta(x) \otimes \theta(x)\right] \tag{5}$$

with

$$\theta(x) = \begin{cases} \nabla f_\sigma(x) |\nabla f_\sigma(x)|^{-1}, & \text{if } |\nabla f_\sigma(x)| \neq 0, \\ 0, & \text{otherwise,} \end{cases}$$

where the stated threshold, $\eta \in (0, 1)$, must be close enough to 1, $f_\sigma = \left(G_\sigma * f(\cdot)\right)(x) := \int_\Omega f(y) G_\sigma(x - y)\, dy$ is the convolution of f with

a Gaussian kernel, and

$$G_\sigma(x) = \frac{1}{\left(\sqrt{2\pi}\sigma\right)^2} \exp\left(-\frac{|x|^2}{2\sigma^2}\right), \quad \sigma > 0,$$

and $\sigma > 0$ is a tuned small positive value.

For the simplicity, we assume that the vector field $\theta \in C^\infty(\Omega;\mathbb{R}^2)$ vanishes along the boundary $\partial\Omega$, that is,

$$M^f(x) = I \quad \forall\, x \in \partial\Omega. \tag{6}$$

As for the total variation of the measure $M^f Du$, we define it by the rule

$$\begin{aligned} |M^f Du|(\Omega) &:= \int_\Omega |M^f Du| \\ &= \sup\Big\{ \int_\Omega u \operatorname{div}(M^f\varphi)\, dx \ : \ \varphi \in C_0^1(\Omega;\mathbb{R}^2), \\ &\qquad |\varphi(x)| \le 1 \ \forall\, x \in \Omega)\Big\}. \end{aligned} \tag{7}$$

Since the existence of minimizers to the problem (3)–(4) remains an open issue nowadays, according to,[1] the following family of two-parametric approximated problems should be used

$$\begin{aligned} J_{\varepsilon,\tau}(c,\varphi) &= \int_\Omega (f-c_0)\log\left(\frac{f}{c_0}\right)\left[\chi_{A_0^\tau}\right]_\varepsilon dx + \\ &\sum_{j=1}^{m-1}\int_\Omega (f-c_j)\log\left(\frac{f}{c_j}\right)\left(\left[\chi_{A_j^\tau}\right]_\varepsilon - \left[\chi_{A_{j+1}^\tau}\right]_\varepsilon\right) dx \\ &+ \int_\Omega (f-c_m)\log\left(\frac{f}{c_m}\right)\left[\chi_{A_m^\tau}\right]_\varepsilon dx \\ &+ \frac{1}{\varepsilon}\left[\|\Psi(l_0-\varphi)\|_{L^1(\Omega)} + \|\Psi(\varphi-l_{m+1})\|_{L^1(\Omega)}\right] \\ &+ \varepsilon|M_\varepsilon^f D\varphi|(\Omega) \\ &+ \alpha\sum_{j=1}^m \int_{\Omega_{2\varepsilon}} \left|M_\varepsilon^f D\left[\chi_{E_j^\tau}\right]_\varepsilon\right| \to \inf_{\varphi\in\Xi_\varepsilon}, \end{aligned} \tag{8}$$

where τ and ε are small parameters, which vary within strictly decreasing sequences of positive numbers converging to 0,

$$\left.\begin{aligned} A_0^\tau &= \{x\in\Omega : \varphi(x) \le l_1 - \tau\}, \\ A_j^\tau &= \{x\in\Omega : \varphi(x) \ge l_j + \tau\}, \\ E_j^\tau &= \{x\in\Omega : \varphi(x) \ge l_j - \tau\}, \\ j &= 1,\dots,m, \end{aligned}\right\} \tag{9}$$

$$\begin{aligned} \Omega_{2\varepsilon} &= \left\{x\in\mathbb{R}^2 : \operatorname{dist}(x,\Omega) \le 2\varepsilon\right\}, \\ M_\varepsilon^f(x) &= \left[I - (1-\varepsilon)^2\theta(x)\otimes\theta(x)\right], \end{aligned} \tag{10}$$

$$\Psi(z) = \left\{\begin{array}{ll} z^{2-\tau}, & \text{if } z \ge 0, \\ 0, & \text{if } z < 0, \end{array}\right\} \tag{11}$$

with a given exponent $\delta \in (1,2)$, and

$$\begin{aligned} \Xi_\varepsilon = \big\{&(c,\varphi) \in \mathbb{R}^{m+1}\times BV(\Omega) \ : \\ &c = (c_0,c_1,\dots,c_m),\ c_j \ge 0,\ j = 0,\dots,m\big\}. \end{aligned} \tag{12}$$

As for the functions $\left[\chi_{A_j^\tau}\right]_\varepsilon(\cdot), \left[\chi_{E_j^\tau}\right]_\varepsilon(\cdot) \in C^\infty(\mathbb{R})$, they have the following representations:

$$\begin{aligned} \left[\chi_{A_0^\tau}\right]_\varepsilon &= H_\varepsilon(l_1 - \tau - \varphi), \\ \left[\chi_{A_j^\tau}\right]_\varepsilon &= H_\varepsilon(\varphi - l_j - \tau),\ j = 1,\dots.m, \\ \left[\chi_{E_j^\tau}\right]_\varepsilon &= H_\varepsilon(\varphi - l_j + \tau),\ j = 1,\dots.m, \end{aligned}$$

where $H_\varepsilon(z) = [\eta_\varepsilon * H](z)$ stands for the smooth approximation of the Heaviside step function $H(z) = \left\{\begin{smallmatrix} 1,\ z\ge 0 \\ 0, z<0\end{smallmatrix}\right\}$ through the mollification. For the practical implementations, it would be enough to set

$$H_\varepsilon(z) = \left\{\begin{array}{ll} 0, & z < -\varepsilon, \\ \frac{z}{2\varepsilon} + \frac{1}{2}\left(1 + \frac{1}{\pi}\sin\frac{\pi z}{\varepsilon}\right), & -\varepsilon \le z \le \varepsilon, \\ 1, & z > \varepsilon. \end{array}\right. \tag{13}$$

Considering that the slope of $H_\varepsilon(z)$ is sufficiently near to $H(z)$, the Heaviside function for $\varepsilon > 0$ small enough, and that

$$\begin{aligned} &H_\varepsilon(\cdot) \in C^2_{loc}(\mathbb{R}), \\ &\|H(\cdot) - H_\varepsilon(\cdot)\|_{L^1(\mathbb{R})} = \varepsilon, \quad \forall\, \varepsilon > 0, \end{aligned} \tag{14}$$

the function $H_\varepsilon(\cdot)$ is seen as a $H(z)$ pointwise approximation.

The function $\delta_\varepsilon \in C_0^1(\mathbb{R})$ is defined, establishing

$$\begin{aligned} \delta_{1,\varepsilon}(z) &= \frac{dH_\varepsilon(z)}{dz} \\ &= \left\{\begin{array}{ll} 0, & |z| > \varepsilon, \\ \frac{1}{2\varepsilon}\left(1 + \cos\frac{\pi z}{\varepsilon}\right), & |z| \le \varepsilon, \end{array}\right. \quad \forall\, z \in \mathbb{R}, \end{aligned} \tag{15}$$

as an approximation of $\delta(z)$, that is, the Dirac function.

The following result has recently been established in:[1]

Theorem 1. *Let $f : \Omega \to \mathbb{R}$ be a given grayscale image satisfying properties* (2)*. Then, for each $\varepsilon \in (0,1)$ and $\tau > 0$ small enough, the constrained minimization problem* (8)–(12) *admits at least one solution. Moreover, if $(c^0_{\varepsilon,\tau}, \varphi^0_{\varepsilon,\tau}) \in \Xi_\varepsilon$ is a local minimizer to problem* (8)–(12)*, then*

$$c^0_{\varepsilon,\tau,0} = c_0(\varphi^0_{\varepsilon,\tau}) = \frac{\int_\Omega f H_\varepsilon(l_1 - \varphi^0_{\varepsilon,\tau} - \tau)\, dx}{\int_\Omega H_\varepsilon(l_1 - \varphi^0_{\varepsilon,\tau} - \tau)\, dx},$$

$$c^0_{\varepsilon,\tau,j} = c_j(\varphi^0_{\varepsilon,\tau}) = \frac{\int_\Omega f\left[H_\varepsilon(\varphi^0_{\varepsilon,\tau} - l_j - \tau) - H_\varepsilon(\varphi^0_{\varepsilon,\tau} - l_{j+1} - \tau)\right] dx}{\int_\Omega \left[H_\varepsilon(\varphi^0_{\varepsilon,\tau} - l_j - \tau) - H_\varepsilon(\varphi^0_{\varepsilon,\tau} - l_{j+1} - \tau)\right] dx},$$

$$c^0_{\varepsilon,\tau,m} = c_m(\varphi^0_{\varepsilon,\tau}) = \frac{\int_\Omega f H_\varepsilon(\varphi^0_{\varepsilon,\tau} - l_m - \tau)\,dx}{\int_\Omega H_\varepsilon(\varphi^0_{\varepsilon,\tau} - l_m - \tau)\,dx}, \tag{16}$$

and the pair $\varphi^0_{\varepsilon,\tau}$ *satisfies the following optimality condition*

$$\begin{aligned}
&-\int_\Omega \left(f - c^0_{\varepsilon,\tau,0}\right)\log\left(\frac{f}{c^0_{\varepsilon,\tau,0}}\right)\\
&\qquad\times \delta_\varepsilon(l_1 - \varphi^0_{\varepsilon,\tau} - \tau)[\varphi - \varphi^0_{\varepsilon,\tau}]\,dx\\
&\quad+\sum_{j=1}^{m-1}\int_\Omega \left(f - c^0_{\varepsilon,\tau,j}\right)\log\left(\frac{f}{c^0_{\varepsilon,\tau,j}}\right)\\
&\qquad\times \delta_\varepsilon(\varphi^0_{\varepsilon,\tau} - l_j - \tau)\\
&\qquad\times H_\varepsilon(-\varphi^0_{\varepsilon,\tau} + l_{j+1} + \tau)[\varphi - \varphi^0_{\varepsilon,\tau}]\,dx\\
&\quad-\sum_{j=1}^{m-1}\int_\Omega \left(f - c^0_{\varepsilon,\tau,j}\right)\log\left(\frac{f}{c^0_{\varepsilon,\tau,j}}\right)\\
&\qquad\times \delta_\varepsilon(-\varphi^0_{\varepsilon,\tau} + l_{j+1} + \tau)\\
&\qquad\times H_\varepsilon(\varphi^0_{\varepsilon,\tau} - l_j - \tau)[\varphi - \varphi^0_{\varepsilon,\tau}]\,dx\\
&\quad+\int_\Omega \left(f - c^0_{\varepsilon,\tau,m}\right)\log\left(\frac{f}{c^0_{\varepsilon,\tau,m}}\right)\\
&\qquad\times \delta_\varepsilon(\varphi^0_{\varepsilon,\tau} - l_m - \tau)[\varphi - \varphi^0_{\varepsilon,\tau}]\,dx\\
&\quad+\frac{1}{\varepsilon}\int_\Omega \left[\Psi'(\varphi^0_{\varepsilon,\tau} - l_{m+1}) - \Psi'(l_0 - \varphi^0_{\varepsilon,\tau})\right]\\
&\qquad\times [\varphi - \varphi^0_{\varepsilon,\tau}]\,dx\\
&\quad+ j_{\varepsilon,\tau}(\varphi) - j_{\varepsilon,\tau}\left(\varphi^0_{\varepsilon,\tau}\right) \geq 0, \quad \forall\,\varphi \in BV(\Omega),
\end{aligned} \tag{17}$$

where

$$\begin{aligned}
\Phi_\varepsilon(\varphi) &= \frac{1}{\varepsilon}\left[\|\Psi(l_0 - \varphi)\|_{L^1(\Omega)}\right.\\
&\qquad\left.+\|\Psi(\varphi - l_{m+1})\|_{L^1(\Omega)}\right],\\
j_{\varepsilon,\tau}(\varphi) &= \varepsilon|M^f_\varepsilon D\varphi|(\Omega)\\
&\qquad+\alpha\sum_{j=1}^{m}\int_{\Omega_{2\varepsilon}}\left|M^f_\varepsilon D\left[\chi_{E^\tau_j}\right]_\varepsilon\right|.
\end{aligned}$$

Moreover, we have the following result concerning the asymptotic behavior of the approximated problem (8)–(12) (for the technical details, we refer to[30,31]).

Theorem 2. *Let* $\tau \ll 1$ *be a given positive value. Let* $\left\{(c^0_{\varepsilon,\tau}, \varphi^0_{\varepsilon,\tau}) \in \Xi_\varepsilon\right\}_{\varepsilon\to 0}$ *be a sequence of optimal pairs to the approximated minimization problems* (8)–(12). *Assume that* $\left\{\varphi^0_{\varepsilon,\tau}\right\}_{\varepsilon>0}$ *is a bounded sequence in* $BV(\Omega)$, *and the relaxed problem*

$$J_\tau(c,\varphi) \to \inf_{\substack{(c,\varphi)\in\Xi\\ \varphi\in BV(\Omega)}} \tag{18}$$

has a nonempty set of minimizers for the given value $\tau > 0$. *Then there exists a pair* $(c^*_\tau, \varphi^*_\tau) \in \Xi$ *such that* $\varphi^*_\tau \in BV(\Omega)$ *and, up to a subsequence,*

$$\begin{aligned}
c^0_{\varepsilon,\tau} &\to c^*_\tau \ \ \textit{in}\ \ \mathbb{R}^{m+1} \ \ \textit{as}\ \varepsilon\to 0,\\
\varphi^0_{\varepsilon,\tau} &\to \varphi^*_\tau \ \ \textit{strongly in}\ \ L^1(\Omega),\\
M^f D\varphi^0_{\varepsilon,\tau} &\overset{*}{\rightharpoonup} M^f D\varphi^*_\tau \ \textit{weakly-*}\ \textit{in}\ \ \mathcal{M}(\Omega;\mathbb{R}^2),\\
\inf_{(c,\varphi)\in\Xi} J_\tau(c,\varphi) &= J_\tau(c^*_\tau,\varphi^*_\tau)\\
&= \lim_{\varepsilon\to 0} J_{\varepsilon,\tau}(c^0_{\varepsilon,\tau},\varphi^0_{\varepsilon,\tau}) = \lim_{\varepsilon\to 0}\inf_{(c,\varphi)\in\Xi_\varepsilon} J_{\varepsilon,\tau}(c,\varphi),
\end{aligned}$$

where the objective functional $J_\tau : \Xi \to \mathbb{R}$ *is defined as*

$$\begin{aligned}
J_\tau(c,\varphi) &= \int_\Omega (f - c_0)\log\left(\frac{f}{c_0}\right)\chi_{A^\tau_0}\,dx\\
&\quad+\sum_{j=1}^{m-1}\int_\Omega (f - c_j)\log\left(\frac{f}{c_j}\right)\left[\chi_{A^\tau_j} - \chi_{A^\tau_{j+1}}\right]\,dx\\
&\quad+\int_\Omega (f - c_m)\log\left(\frac{f}{c_m}\right)\chi_{A^\tau_m}\,dx\\
&\quad+\alpha\sum_{j=1}^{m}\int_\Omega |M^f D\chi_{E^\tau_j}|.
\end{aligned}$$

3. On representation of optimality system (17) in the form of Euler–Lagrange equation

In this section, we characterize the solution $(c^0_{\varepsilon,\tau}, \varphi^0_{\varepsilon,\tau})$ of the minimization problem (8)–(12) for given values $\varepsilon \in (0,1)$ and $\tau > 0$ deriving for that the equation satisfied by $(c^0_{\varepsilon,\tau}, \varphi^0_{\varepsilon,\tau})$. To do so, we decompose $J_{\varepsilon,\tau} : \Xi_\varepsilon \to \mathbb{R}$ as the sum of three functionals, that is,

$$J_{\varepsilon,\tau}(c,\varphi) = I_{\varepsilon,\tau}(c,\varphi) + \Phi_\varepsilon(\varphi) + \Lambda_{\varepsilon,\tau}(\varphi), \tag{19}$$

where $I_{\varepsilon,\tau} : \mathbb{R}^{m+1} \times L^2(\Omega) \to \mathbb{R}$ and $\Phi_\varepsilon : L^2(\Omega) \to \mathbb{R}$ are defined by the rules

$$\begin{aligned}
I_{\varepsilon,\tau}(c,\varphi) &= \int_\Omega (f - c_0)\log\left(\frac{f}{c_0}\right)\left[\chi_{A^\tau_0}\right]_\varepsilon\,dx\\
&\quad+\sum_{j=1}^{m-1}\int_\Omega (f - c_j)\log\left(\frac{f}{c_j}\right)\\
&\qquad\times\left(\left[\chi_{A^\tau_j}\right]_\varepsilon - \left[\chi_{A^\tau_{j+1}}\right]_\varepsilon\right)\,dx\\
&\quad+\int_\Omega (f - c_m)\log\left(\frac{f}{c_m}\right)\left[\chi_{A^\tau_m}\right]_\varepsilon\,dx,
\end{aligned} \tag{20}$$

$$\begin{aligned}
\Phi_\varepsilon(\varphi) &= \frac{1}{\varepsilon}\left[\|\Psi(l_0 - \varphi)\|_{L^1(\Omega)}\right.\\
&\qquad\left.+\|\Psi(\varphi - l_{m+1})\|_{L^1(\Omega)}\right],
\end{aligned} \tag{21}$$

and $\Lambda_{\varepsilon,\tau} : L^2(\Omega) \to \mathbb{R}$ is defined by

$$\begin{aligned}
\Lambda_{\varepsilon,\tau}(\varphi) &= \varepsilon|M^f_\varepsilon D\varphi|(\Omega)\\
&\quad+\alpha\sum_{j=1}^{m}\int_{\Omega_{2\varepsilon}}\left|M^f_\varepsilon D\left[\chi_{E^\tau_j}\right]_\varepsilon\right|,
\end{aligned} \tag{22}$$

if $\varphi \in BV(\Omega)$, and

$$\Lambda_{\varepsilon,\tau}(\varphi) = \infty, \text{ if } \varphi \in L^2(\Omega) \setminus BV(\Omega).$$

Taking into account the fact that $\Psi \in C^1_{loc}(\mathbb{R})$, it can be shown that

$$\Phi_\varepsilon\left(\varphi^0_{\varepsilon,\tau} + \lambda h\right) = \Phi_\varepsilon\left(\varphi^0_{\varepsilon,\tau}\right) + \lambda D_\varphi \Phi_\varepsilon\left(\varphi^0_{\varepsilon,\tau}\right)[h] + r(h,\lambda),$$

for any $h \in L^2(\Omega)$, where, as $\lambda \to 0, |r(h,\lambda)| = o(|\lambda|)$, and $D_\varphi\Phi_\varepsilon(\varphi^0_{\varepsilon,\tau}) : L^2(\Omega) \to \mathbb{R}$ is a linear continuous functional with the following representation:

$$D_\varphi \Phi_\varepsilon\left(\varphi^0_{\varepsilon,\tau}\right)[h] = \frac{1}{\varepsilon}\Big[- \int_\Omega \Psi'(l_0 - \varphi^0_{\varepsilon,\tau}) h\, dx + \int_\Omega \Psi'(\varphi^0_{\varepsilon,\tau} - l_{m+1}) h\, dx\Big]. \quad (23)$$

Here, $\Psi'(z) = \left\{ \begin{array}{ll} \delta z^{\delta-1}, & \text{if } z \geq 0, \\ 0, & \text{if } z < 0 \end{array} \right\}$.

We also observe that the right-hand side in (23) can be represented as follows:

$$\begin{aligned} &\frac{1}{\varepsilon}\int_\Omega \left[\Psi'(\varphi^0_{\varepsilon,\tau} - l_{m+1}) - \Psi'(l_0 - \varphi^0_{\varepsilon,\tau})\right][\varphi - \varphi^0_{\varepsilon,\tau}]\, dx \\ &= \frac{2-\tau}{\varepsilon}\int_\Omega [\varphi - \varphi^0_{\varepsilon,\tau}] \\ &\times \left\{ \begin{array}{ll} (\varphi^0_{\varepsilon,\tau} - l_{m+1})^{1-\tau}, & \text{if } \varphi^0_{\varepsilon,\tau} - l_{m+1} > 0, \\ 0, & \text{otherwise} \end{array} \right\} dx \\ &- \frac{2-\tau}{\varepsilon}\int_\Omega [\varphi - \varphi^0_{\varepsilon,\tau}] \\ &\times \left\{ \begin{array}{ll} (l_0 - \varphi^0_{\varepsilon,\tau})^{1-\tau}, & \text{if } l_0 - \varphi^0_{\varepsilon,\tau} > 0, \\ 0, & \text{otherwise} \end{array} \right\} dx. \end{aligned} \quad (24)$$

Since $(c^0_{\varepsilon,\tau}, \varphi^0_{\varepsilon,\tau})$ is an optimal pair to the approximated minimization problem (8)–(12), it follows from representation (19)–(22) that

$$J_{\varepsilon,\tau}(c^0_{\varepsilon,\tau}, \varphi) - J_{\varepsilon,\tau}(c^0_{\varepsilon,\tau}, \varphi^0_{\varepsilon,\tau}) \geq 0 \quad \forall\, \varphi \in L^2(\Omega). \quad (25)$$

Taking into account that, for each $\varphi \in BV(\Omega)$,

$$\begin{aligned} &\Lambda_{\varepsilon,\tau}(\varphi) - \Lambda_{\varepsilon,\tau}\left(\varphi^0_{\varepsilon,\tau}\right) \\ &= \int_\Omega \left(L(\varphi) - L(\varphi^0_{\varepsilon,\tau})\right)|M^f_\varepsilon D\varphi^0_{\varepsilon,\tau}| \\ &+ \int_\Omega L(\varphi)|M^f_\varepsilon D\varphi| - \int_\Omega L(\varphi)|M^f_\varepsilon D\varphi^0_{\varepsilon,\tau}| \end{aligned} \quad (26)$$

with

$$L(\varphi) = \left(\varepsilon + \alpha \sum_{j=1}^m \delta_\varepsilon(\varphi - l_j + \tau)\right), \quad (27)$$

and setting

$$\begin{aligned} V_1\left(\varphi^0_{\varepsilon,\tau}\right) &= -\left(f - c^0_{\varepsilon,\tau,0}\right)\log\left(\frac{f}{c^0_{\varepsilon,\tau,0}}\right) \\ &\times \delta_\varepsilon(l_1 - \varphi^0_{\varepsilon,\tau} - \tau) \\ &+ \sum_{j=1}^{m-1}\left(f - c^0_{\varepsilon,\tau,j}\right)\log\left(\frac{f}{c^0_{\varepsilon,\tau,j}}\right) \\ &\times \delta_\varepsilon(\varphi^0_{\varepsilon,\tau} - l_j - \tau) H_\varepsilon(-\varphi^0_{\varepsilon,\tau} + l_{j+1} + \tau) \\ &- \sum_{j=1}^{m-1}\left(f - c^0_{\varepsilon,\tau,j}\right)\log\left(\frac{f}{c^0_{\varepsilon,\tau,j}}\right) \\ &\times \delta_\varepsilon(-\varphi^0_{\varepsilon,\tau} + l_{j+1} + \tau) H_\varepsilon(\varphi^0_{\varepsilon,\tau} - l_j - \tau) \\ &+ \left(f - c^0_{\varepsilon,\tau,m}\right)\log\left(\frac{f}{c^0_{\varepsilon,\tau,m}}\right)\delta_\varepsilon(\varphi^0_{\varepsilon,\tau} - l_m - \tau) \\ &+ \Big[\left\{ \begin{array}{l} (\varphi^0_{\varepsilon,\tau} - l_{m+1})^{1-\tau}, \quad \text{if } \varphi^0_{\varepsilon,\tau} - l_{m+1} > 0, \\ 0, \text{ otherwise,} \end{array} \right\} \\ &- \left\{ \begin{array}{l} (l_0 - \varphi^0_{\varepsilon,\tau})^{1-\tau}, \text{if } l_0 - \varphi^0_{\varepsilon,\tau} > 0, \\ 0, \text{ otherwise,} \end{array} \right\}\Big]\frac{2-\tau}{\varepsilon}, \end{aligned} \quad (28)$$

$$\mathcal{J}(w,\varphi) = \left\{ \begin{array}{ll} \displaystyle\int_\Omega L(w)\,|M^f_\varepsilon D\varphi| & \text{if } \varphi \in BV(\Omega), \\ +\infty & \text{if } \varphi \in L^2(\Omega) \setminus BV(\Omega), \end{array} \right. \quad (29)$$

$$V_2\left(\varphi^0_{\varepsilon,\tau}\right) = \alpha \sum_{j=1}^m \delta'_\varepsilon(\varphi^0_{\varepsilon,\tau} - l_j + \tau), \quad (30)$$

we see that inequality (25) leads to the relation

$$\begin{aligned} &\int_\Omega V_1\left(\varphi^0_{\varepsilon,\tau}\right)\varphi\, dx + \int_\Omega V_2\left(\varphi^0_{\varepsilon,\tau}\right)\varphi\,|M^f_\varepsilon D\varphi^0_{\varepsilon,\tau}| \\ &+ \left[\mathcal{J}(w,\varphi) - \mathcal{J}(w,\varphi^0_{\varepsilon,\tau})\right]\Big|_{w=\varphi} \geq o(1)h, \\ &\forall\, \varphi \in L^2(\Omega), \end{aligned} \quad (31)$$

where $h = \varphi - \varphi^0_{\varepsilon,\tau}$, and $o(1) \to 0$ as $\|h\|_{L^2(\Omega)} \to 0$.

Hence,

$$-V_1\left(\varphi^0_{\varepsilon,\tau}\right) \in \left[\partial\left(\int_\Omega V_2\left(\varphi^0_{\varepsilon,\tau}\right)\varphi\,|M^f_\varepsilon D\varphi^0_{\varepsilon,\tau}| + \mathcal{J}(w,\varphi)\right)\right]\Big|_{w=\varphi^0_{\varepsilon,\tau}}.$$

Since

$$\begin{aligned} &\partial\left(\int_\Omega V_2\left(\varphi^0_{\varepsilon,\tau}\right)\varphi\,|M^f_\varepsilon D\varphi^0_{\varepsilon,\tau}| + \mathcal{J}(w,\varphi)\right) \\ &= \partial\left(\int_\Omega V_2\left(\varphi^0_{\varepsilon,\tau}\right)\varphi\,|M^f_\varepsilon D\varphi^0_{\varepsilon,\tau}|\right) + \partial\mathcal{J}(w,\varphi) \end{aligned}$$

by the Moreau–Rockafellar Theorem, it follows that the Euler–Lagrange equation for $\varphi^0_{\varepsilon,\tau}$ takes

the form

$$\partial\left(\int_\Omega V_2\left(\varphi^0_{\varepsilon,\tau}\right)\varphi\,|M^f_\varepsilon D\varphi^0_{\varepsilon,\tau}|\right)+ \partial\mathcal{J}(w,\varphi)|_{w=\varphi^0_{\varepsilon,\tau}}+V_1\left(\varphi^0_{\varepsilon,\tau}\right)\ni 0. \quad (32)$$

Following Anzellotti,[32] for an open bounded set with Lipschitz boundary $\Omega\subset\mathbb{R}^2$, we denote

$$X_2(\Omega)=\left\{z\in L^\infty(\Omega;\mathbb{R}^2)\,:\,\mathrm{div}(z)\in L^2(\Omega)\right\} \quad (33)$$

to give a correct interpretation of the Anzelotti pairing (z,Du) with $u\in BV(\Omega)$. In this case, if $u\in BV(\Omega)$ and $z\in X_2(\Omega)$, then for every test function $\psi\in C^\infty_0(\Omega)$, we have

$$\langle(z,Du),\psi\rangle:=-\int_\Omega u\,\mathrm{div}(\psi z)\,dx= -\int_\Omega u\psi\,\mathrm{div}(z)\,dx-\int_\Omega u(z,\nabla\psi)\,dx. \quad (34)$$

Arguing as in,[?Proposition 4.1.]Vese it can be shown that $\xi\in\partial\mathcal{J}(w,\varphi)|_{w=\varphi^0_{\varepsilon,\tau}}$ if and only if there exists a vector field $\boldsymbol{z}\in X_2(\Omega)$ (see (33)) such that the following conditions hold:

$$\|\boldsymbol{z}\|_{L^\infty(\Omega;\mathbb{R}^2)}\le 1,$$
$$\left(\boldsymbol{z},M^f_\varepsilon D\varphi^0_{\varepsilon,\tau}\right)=\left|M^f_\varepsilon D\varphi^0_{\varepsilon,\tau}\right| \quad \text{as measures},$$
$$-\mathrm{div}\left(L(\varphi^0_{\varepsilon,\tau})M^f_\varepsilon\boldsymbol{z}\right)=\xi \quad \text{in } \Omega,$$
$$\left[L(\varphi^0_{\varepsilon,\tau})M^f_\varepsilon\boldsymbol{z},\nu_\Omega\right]=0 \quad \text{a.e. on } \partial\Omega.$$

Then taking into account the Anzelotti representation (34) and the fact that

$$-\mathrm{div}\left(L(\varphi^0_{\varepsilon,\tau})M^f_\varepsilon\boldsymbol{z}\right) =-V_2\left(\varphi^0_{\varepsilon,\tau}\right)\left(M^f_\varepsilon D\varphi^0_{\varepsilon,\tau},\boldsymbol{z}\right) -L(\varphi^0_{\varepsilon,\tau})\,\mathrm{div}\left(M^f_\varepsilon\boldsymbol{z}\right) =-V_2\left(\varphi^0_{\varepsilon,\tau}\right)\left|M^f_\varepsilon D\varphi^0_{\varepsilon,\tau}\right|-L(\varphi^0_{\varepsilon,\tau})\,\mathrm{div}\left(M^f_\varepsilon\boldsymbol{z}\right)$$

we can finally rewrite (32) as follows

$$-L(\varphi^0_{\varepsilon,\tau})\,\mathrm{div}\left(M^f_\varepsilon\boldsymbol{z}\right)+V_1\left(\varphi^0_{\varepsilon,\tau}\right)\ni 0, \quad (35)$$
$$\left[L(\varphi^0_{\varepsilon,\tau})M^f_\varepsilon\boldsymbol{z},\nu_\Omega\right]=0 \quad \text{a.e. on } \partial\Omega, \quad (36)$$
$$\left(\boldsymbol{z},M^f_\varepsilon D\varphi^0_{\varepsilon,\tau}\right)=\left|M^f_\varepsilon D\varphi^0_{\varepsilon,\tau}\right|, \quad (37)$$
$$\|\boldsymbol{z}\|_{L^\infty(\Omega;\mathbb{R}^2)}\le 1. \quad (38)$$

If in addition $\varphi^0_{\varepsilon,\tau}$ is differentiable in the weak sense, then the Euler–Lagrange system (35)–(38) assumes the form of the following boundary value problem:

$$-L(\varphi^0_{\varepsilon,\tau})\,\mathrm{div}\left(M^f_\varepsilon\frac{M^f_\varepsilon\nabla\varphi^0_{\varepsilon,\tau}}{|M^f_\varepsilon\nabla\varphi^0_{\varepsilon,\tau}|}\right)+V_1\left(\varphi^0_{\varepsilon,\tau}\right)=0 \quad \text{in } \mathcal{D}'(\Omega), \quad (39)$$

$$\left(M^f_\varepsilon\frac{M^f_\varepsilon\nabla\varphi^0_{\varepsilon,\tau}}{|M^f_\varepsilon\nabla\varphi^0_{\varepsilon,\tau}|},\nu_\Omega\right)=0 \quad \text{a.e. on } \partial\Omega. \quad (40)$$

4. Numerical approximation of the optimality conditions

In this section, we briefly describe the numerical scheme and a procedure to solve the Euler–Lagrange system (39)–(40) numerically. Since for implementations, it is reasonable to define the solution of the problem (39)–(40) using a "gradient descent"strategy, denoted by S a given circle and by $d(x,S)$ the Euclidean distance of the point $x\in\Omega$ from the circle S, we suggest starting with the initial level function $\varphi_0\in C(\Omega)$ that can be defined as follows (see also the other variants in[19])

$$\varphi_0(x)=\begin{cases}+d(x,S), & x\in\text{inside}\,S,\\ 0, & x\in S,\\ -d(x,S), & x\in\text{outside}\,S.\end{cases} \quad (41)$$

Next, for numerical purposes, we calculate $u_{\varepsilon,\tau}$, the continuous approximation of the BV solution $\varphi^0_{\varepsilon,\tau}$, with $\varepsilon>0$ and $\tau>0$ small enough, as a solution of the problem

$$\frac{\partial\varphi}{\partial t}=L(\varphi)\,\mathrm{div}\left(M^f_\varepsilon\frac{M^f_\varepsilon\nabla\varphi}{|M^f_\varepsilon\nabla\varphi|}\right)-V_1(\varphi) \quad \text{in } (0,\infty)\times\Omega, \quad (42)$$

$$\left(M^f_\varepsilon\frac{M^f_\varepsilon\nabla\varphi}{|M^f_\varepsilon\nabla\varphi|},\nu_\Omega\right)=0 \text{ on } (0,\infty)\times\partial\Omega, \quad (43)$$

$$\varphi(0,\cdot)=\varphi_0(\cdot) \text{ in } \Omega. \quad (44)$$

The second point that we realize in this algorithm is to consider the adaptive version of the model (42)–(44). Following[19] and,[34] we substitute the multipliers $\delta_\varepsilon(-\varphi^0_{\varepsilon,\tau}+l_{j+1}+\tau)$ in the external force $V_1(\varphi)$ with 1. It has been recently shown in[34] that, in this way, the external force without $\delta_\varepsilon(-\varphi^0_{\varepsilon,\tau}+l_{j+1}+\tau)$ can take action on φ everywhere in Ω (not simply on the prescribed level sets of φ), and so can keep φ moving more quickly towards the desired segment edges. As a result, the adaptive version of the external force $V_1(\varphi)$ takes the form

$$\widehat{V}_1(\varphi)=-\left(f-c^0_{\varepsilon,\tau,0}\right)\log\left(\frac{f}{c^0_{\varepsilon,\tau,0}}\right)$$

$$+\left(f-c^0_{\varepsilon,\tau,m}\right)\log\left(\frac{f}{c^0_{\varepsilon,\tau,m}}\right)$$
$$+\sum_{j=1}^{m-1}\left(f-c^0_{\varepsilon,\tau,j}\right)\log\left(\frac{f}{c^0_{\varepsilon,\tau,j}}\right)$$
$$[H_\varepsilon(-\varphi+l_{j+1}+\tau)-H_\varepsilon(\varphi-l_j-\tau)]$$
$$+\frac{2-\tau}{\varepsilon}\left\{\begin{array}{l}(\varphi-l_{m+1})^{1-\tau},\quad \text{if } \varphi-l_{m+1}>0,\\ 0,\ \text{otherwise},\end{array}\right\}$$
$$-\frac{2-\tau}{\varepsilon}\left\{\begin{array}{ll}(l_0-\varphi)^{1-\tau}, & \text{if } l_0-\varphi>0,\\ 0, & \text{otherwise.}\end{array}\right\} \quad (45)$$

We also need to specify the boundary condition on $\partial\Omega$ associated with (43). To obtain a well-posed problem, we change the natural boundary condition (43) just slightly, namely

$$\left(M^f_\varepsilon\frac{M^f_\varepsilon\nabla\varphi}{\sqrt{\varepsilon^2+|M^f_\varepsilon\nabla\varphi|^2}},\nu_\Omega\right)=0 \quad \text{a.e. on } \partial\Omega.$$

Because the denominator $\sqrt{\varepsilon+|M^f_\varepsilon\nabla\varphi|^2}$ is strictly positive, the matrix function $M^f_\varepsilon(x)$ for each $x\in\Omega$ is symmetric, and the discrete gradients are bounded in the norm, we can pass to the following boundary condition instead of (43)

$$\left(M^f_\varepsilon\nabla\varphi, M^f_\varepsilon\nu_\Omega\right)=0 \quad \text{on } \partial\Omega, \qquad (46)$$

where ν_Ω is a unit normal to $\partial\Omega$. However, in view of the assumption (6), this condition can be rewritten as follows:

$$\frac{\partial\varphi}{\partial\nu_\Omega}=0 \quad \text{on } \partial\Omega.$$

Consequently, we obtain the subsequent problem for numerical simulation

$$\frac{\partial\varphi}{\partial t}=L(\varphi)\,\mathrm{div}\left(\frac{\left(M^f_\varepsilon\right)^2\nabla\varphi}{\sqrt{\varepsilon^2+|M^f_\varepsilon\nabla\varphi|^2}}\right)-\widehat{V}_1(\varphi)$$
$$\text{in } (0,\infty)\times\Omega, \qquad (47)$$
$$\frac{\partial\varphi}{\partial\nu_\Omega}=0 \quad \text{on } (0,\infty)\times\partial\Omega, \qquad (48)$$
$$\varphi(0,\cdot)=\varphi_0(\cdot) \quad \text{in } \Omega, \qquad (49)$$

where the functions $L(\varphi)$ and $\widehat{V}_1(\varphi)$ are defined by (27) and (45), respectively.

Quasi-linear partial differential equations can be solved in a variety of ways (for a list of methods, check the references[35,36]). Finite differences techniques and an explicit scheme of the forward Euler method are maybe the best choices because we are working with pixels in image processing. Let Δt be a time step size. Then setting

$$t=n\Delta t,\ n=0,1,2,\ldots,$$
$$x=i\ (1\le i\le N_x),\quad y=j\ (1\le j\le N_y),$$

where (x,y) stands for image pixel and $N_x\times N_y$ is the original image size at the grid G_H, we define the following discrete notations

$$\Delta^x_\pm\varphi^n_{ij}=\pm\left(\varphi^n_{i\pm1,j}-\varphi^n_{ij}\right),$$
$$\Delta^y_\pm\varphi^n_{ij}=\pm\left(\varphi^n_{i,j\pm1}-\varphi^n_{ij}\right),$$
$$m(a,b)=\mathrm{minmod}\,(a,b)=$$
$$\min\left(|a|,|b|\right)\frac{\mathrm{sgn}\,a+\mathrm{sgn}\,b}{2},$$

where $\varphi^n_{i,j}$ denotes the approximation of $\varphi_{k+1}(n\Delta t,i,j)$. Then, the numerical approximation of the principle components of the boundary value problem (47)–(49) takes the form

$$\left(\frac{\partial\varphi}{\partial t}\right)^n_{i,j}\approx\frac{\varphi^{n+1}_{i,j}-\varphi^n_{i,j}}{\Delta t},$$
$$\left(\mathrm{div}\left(\frac{\left(M^f_\varepsilon\right)^2\nabla\varphi}{\sqrt{\varepsilon^2+|M^f_\varepsilon\nabla\varphi|^2}}\right)\right)^n_{i,j}\approx$$
$$\Delta^x_-\left(X^n_{i,j}\right)+\Delta^y_-\left(Y^n_{i,j}\right),$$
$$X^n_{i,j}=aP^n_{i,j}+bQ^n_{i,j},\quad Y^n_{i,j}=bP^n_{i,j}+cQ^n_{i,j},$$
$$\left(\begin{array}{cc}a & b\\ b & c\end{array}\right)=\left(M^f_\varepsilon\right)^2,$$
$$P^n_{i,j}=\frac{\Delta^x_+\varphi^n_{i,j}}{\sqrt{\varepsilon^2+\left(\Delta^x_+\varphi^n_{i,j}\right)^2+\left(m\left(\Delta^y_+\varphi^n_{i,j},\Delta^y_-\varphi^n_{i,j}\right)\right)^2}},$$
$$Q^n_{i,j}=\frac{\Delta^y_+\varphi^n_{i,j}}{\sqrt{\varepsilon^2+\left(\Delta^y_+\varphi^n_{i,j}\right)^2+\left(m\left(\Delta^x_+\varphi^n_{i,j},\Delta^x_-\varphi^n_{i,j}\right)\right)^2}}.$$

As a result, utilizing the formulas given above, we arrive at the following numerical scheme associated with the initial boundary problem (47)–(49):

$$\varphi^{n+1}_{i,j}=\varphi^n_{i,j}+L(\varphi^n_{i,j})$$
$$\times\left(\Delta^x_-\left[X^n_{i,j}\right]+\Delta^y_-\left[Y^n_{i,j}\right]\right)\Delta t-\widehat{V}_1(\varphi^n_{l,j})\Delta t$$
$$\forall i=1,\ldots,N_x,\quad \forall j=1,\ldots,N_y,$$
$$\forall n=0,1,\ldots \qquad (50)$$

with the initial conditions

$$\varphi^0_{i,j}=(\varphi_0)_{i,j},$$
$$\forall i=1,\ldots,N_x,\quad \forall j=1,\ldots,N_y, \qquad (51)$$

and boundary conditions

$$\varphi^n_{0,j}=\varphi^n_{1,j},\quad \varphi^n_{N_x,j}=\varphi^n_{N_x-1,j},$$
$$v^n_{l,0}=v^n_{l,1},\quad \varphi^n_{l,N_y}=\varphi^n_{l,N_y-1}, \qquad (52)$$
$$\forall l=1,\ldots,N_x,\quad \forall j=1,\ldots,N_y.$$

Since the set-level function $\varphi(x)$ should be subjected by the constraints (see (4))

$$l_0 \le \varphi(x) \le l_{m+1} \text{ a.e. in } \Omega,$$

in practice this constraint can be incorporated by renormalizing $\varphi^n_{i,j}$ (when $\varphi^n_{i,j} < l_0$ or $\varphi^n_{i,j} > l_{m+1}$) after each time step. It means that we can omit the last two terms in the external force $\widehat{V}_1(\varphi)$ that emerge as the penalizing ones. As a result, we can modify the iteration procedure (50) as follows:

$$\begin{aligned}\varphi^{n+1}_{i,j} &= \varphi^n_{i,j} + L(\varphi^n_{i,j})\left(\Delta^x_-\left[X^n_{i,j}\right] + \Delta^y_-\left[Y^n_{i,j}\right]\right)\Delta t \\ &+ \left(f - c^0_{\varepsilon,\tau,0}\right)\log\left(\frac{f}{c^0_{\varepsilon,\tau,0}}\right) \\ &- \left(f - c^0_{\varepsilon,\tau,m}\right)\log\left(\frac{f}{c^0_{\varepsilon,\tau,m}}\right) \\ &- \sum_{j=1}^{m-1}\left(f - c^0_{\varepsilon,\tau,j}\right)\log\left(\frac{f}{c^0_{\varepsilon,\tau,j}}\right) \\ &\times \left[H_\varepsilon(-\varphi^n_{i,j} + l_{j+1} + \tau) - H_\varepsilon(\varphi^n_{i,j} - l_j - \tau)\right], \end{aligned} \tag{53}$$

$$\varphi^{n+1}_{i,j} = l_0 \quad \text{if} \quad \varphi^{n+1}_{i,j} < l_0, \tag{54}$$

$$\varphi^{n+1}_{i,j} = l_{m+1} \quad \text{if} \quad \varphi^{n+1}_{i,j} > l_{m+1}, \tag{55}$$

$$\forall i = 1,\dots,N_x, \quad \forall j = 1,\dots,N_y, \quad \forall n = 0,1,\dots$$

Taking into account the following estimates:

$$\left(M^f_\varepsilon\right)^2 \le I \quad \text{in the sense of quadratic forms,}$$

$$|P^n_{i,j}| \le \frac{1}{\varepsilon}|\Delta^x_+\varphi^n_{i,j}|, \quad |Q^n_{i,j}| \le \frac{1}{\varepsilon}|\Delta^y_+\varphi^n_{i,j}|,$$

$$L(\varphi^n_{i,j}) \le \varepsilon + \alpha\frac{m}{\varepsilon}$$

and arguing as in[?Chapter 28]Salgado, we can deduce the following stability conditions for the proposed approximation scheme

$$\Delta t\left(1 + \alpha\frac{m}{\varepsilon^2}\right) < \frac{1}{2}. \tag{56}$$

Therefore, the stability of the numerical scheme (51),(52),(53)–(55) depends critically on the parameter $\alpha > 0$ being chosen correctly. As for the stopping condition, it can be formalized as follows:

$$\max_{1\le i\le N_x}\max_{1\le j\le N_y}\left|\varphi^{n+1}_{i,j} - \varphi^n_{l,j}\right| \le \varepsilon.$$

Our next intention in this section is to discuss the algorithm for restoration and visualization of the level sets

$$S_j := \{x \in \Omega : \varphi(x) = l_j\}, \quad j = 1,2,\dots,m.$$

Definition 1. *Let $f : \Omega \to \mathbb{R}$ be a gray-scale image satisfying conditions (2). Let $\varphi^0_{\varepsilon,\tau} \in BV(\Omega)$ be a solution of the minimization problem (8)–(12) with $\varepsilon > 0$ and $\tau > 0$ small enough. Let $\left(\varphi^0_{\varepsilon,\tau}\right)_\rho \in C^\infty(\overline{\Omega})$ be the smoothed version as the convolution of the 2-D Gaussian kernel G_ρ and $\varphi^0_{\varepsilon,\tau}$. We say that the following decomposition*

$$\Omega = \Omega_0 \cup \Omega_1 \cup \dots \cup \Omega_m \cup \Omega_*$$

is quasi-optimal for the approximation of f by piecewise constant function $f_* : \Omega \to \mathbb{R}$ if

- *the restrictions $f_*|_{\Omega_j}$ are defined as*

$$f_*|_{\Omega_j} = c^0_{\varepsilon,\tau,j}, \quad j = 0,\dots,m,$$

where the constants $c^0_{\varepsilon,\tau,j}$ are given by (16);

- *the subdomains (or segments) $\{\Omega_j\}_{j=0}^m$ are related to the function $\varphi^0_{i,j}$ as follows*

$$\Omega_0 = \left\{x \in \Omega : \left(\varphi^0_{\varepsilon,\tau}\right)_\rho(x) < l_1\right\}, \tag{57}$$

$$\Omega_j = \left\{x \in \Omega : l_j < \left(\varphi^0_{\varepsilon,\tau}\right)_\rho(x) < l_{j+1}\right\}, \tag{58}$$

$$j = 1,\dots,m-1,$$

$$\Omega_m = \left\{x \in \Omega : \left(\varphi^0_{\varepsilon,\tau}\right)_\rho(x) > l_m\right\}; \tag{59}$$

- *Ω_* stands for the boundaries between different Ω_j, that is,*

$$\Omega_* = \bigcup_{j=1}^m \left\{x \in \Omega : \left(\varphi^0_{\varepsilon,\tau}\right)_\rho(x) = l_j\right\}.$$

As immediately follows from this definition, each segment Ω_j of the given f-decomposition can be associated with the corresponding coefficient of variation CV_j, $j = 0,\dots,m$. This coefficient is the measure that quantifies the degree of variability in the set of data by calculating the ratio of the standard deviation of $f(x)$ within Ω_j to its mean $f_*|_{\Omega_j}$, that is,

$$CV_j = \frac{\sqrt{\int_{\Omega_j}\left(f(x) - f_*|_{\Omega_j}(x)\right)^2 dx}}{f_*|_{\Omega_j}}$$

for all $j = 0,\dots,m$.

Thus, by this definition, the boundaries $\partial\Omega_j$ of the segments Ω_j can be defined as the corresponding level sets S_j. To identify these sets, we make use of the so-called marching squares method.[38,39] The main steps of this approach can be described as follows:

(1) Given an index $j \in \{1,\dots,m\}$ and a smoothed version $\left(\varphi^0_{\varepsilon,\tau}\right)_\rho \in C^\infty(\overline{\Omega})$ of the level set function $\varphi^0_{\varepsilon,\tau} \in BV(\Omega)$, create a binary image $\mathfrak{B}_j$ following the rule

$$\mathfrak{B}_j(x) = \begin{cases} 1, & \text{if } \left(\varphi^0_{\varepsilon,\tau}\right)_\rho(x) \ge l_j, \\ 0, & \text{if } \left(\varphi^0_{\varepsilon,\tau}\right)_\rho(x) < l_j, \end{cases} \quad \forall x \in \Omega.$$

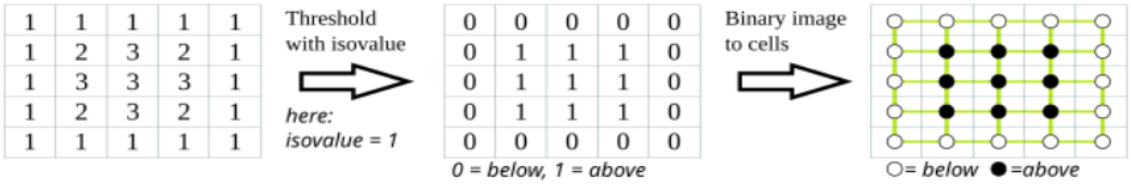
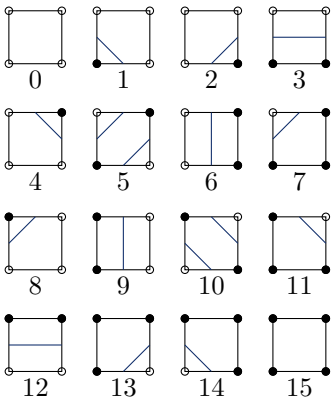


Figure 1. Binary image $\mathfrak{B}_j$ with $l_j = 1$

Then every 2×2 block of pixels in the binary image forms a contouring cell, so the whole image is represented by a grid of such cells (see Fig.1). In fact, just for illustration, this picture reflects the main actions that we have to do in order to find out a correct location of the level set $\left(\varphi^0_{\varepsilon,\tau}\right)_\rho(x) = 1.5$.

(2) Follow these steps for every cell in the contouring grid:

(a) To create a binary index, combine the 4 bits at the cell's corners: Using the bitwise OR and left-shift, go clockwise around the cell from the most significant bit at the top left to the least significant bit at the bottom left, adding the bit to the index. As indicated in the table below, the resulting 4-bit index has 16 potential values in the range $0 - 15$.



(b) Utilize the cell index to access a prebuilt lookup table with 16 entries that list the edges required to represent the cell.

(c) To determine the precise location of the contour line along the cell's edges, use linear interpolation between the initial field data values. (see Fig. 2).

5. Numerical Results

In this section, we dwell on two possible ways for the implementation of the proposed approach to domain decomposition. We call these ways just direct and adaptive segmentation procedures. The key point of the direct segmentation is the fact that the number $m+1$ of segments that must correspond to the homogeneity zones of a given function $f : \Omega \to \mathbb{R}$, should be prescribed a priori, provided the degree of variability of the original distribution $f : \Omega \to \mathbb{R}$ over Ω satisfies the condition

$$CV\left(f\big|_\Omega\right) = \frac{\sigma\left(f\big|_\Omega\right)}{\text{mean}\left(f\big|_\Omega\right)} \cdot 100\% > \delta_{\min},$$

where $\delta_{\min} > 0$ is a given threshold. Typically, a distribution f is considered homogeneous, especially in the agricultural application, if $CV(f\big|_\Omega) \leq 15\%$.

To illustrate the efficiency of the proposed model and the scheme of direct segmentation, we provided numerical experiences with images that the Sentinel-2 satellite has delivered. we used a 10 m/pixel image over the Dnipro region of Ukraine as input data (see the left panel in Figure 3).

With medium-sized fields of different shapes, this area exemplifies a typical agricultural landscape. The observed data suffer from noise and blurring, as can be seen from the image in Fig. 3 (also refer to the related histogram in Fig. 4).

Using the variational approach recently proposed in[40] (see also[7,8]), we implemented the deblurring and denoizing procedure as the first stage (see the right panel in Fig. 3). The smoothed picture histogram has a marked compactly localized spectrum, as shown in Figure 4. This spectrum could be regarded as a "good option"for its piecewise constant approximation.

Numerical simulations of f-decomposition following the scheme of the direct segmentation have been performed considering three different variants setting $f(x) = u_i(x)$, in Ω, where u_i with $i = 1, 2, 3$ stands for the intensity of the satellite image at the left panel of Figure 1 in red, blue, and green spectral channels, respectively. To define a segmentation in each of these channels, we applied the iteration procedure (51), (52), (53)–(55) to the corresponding function $f = u_i$ with

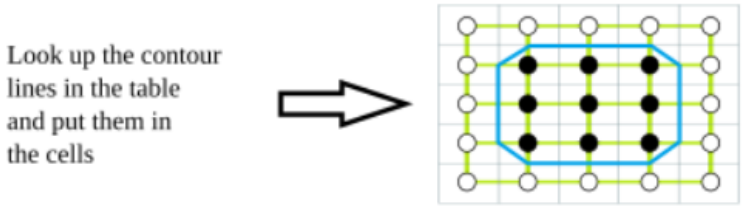


Figure 2. Variant of the contour lines in the cell



Figure 3. On the left: The original satellite photo. On the right: The photo after denoising

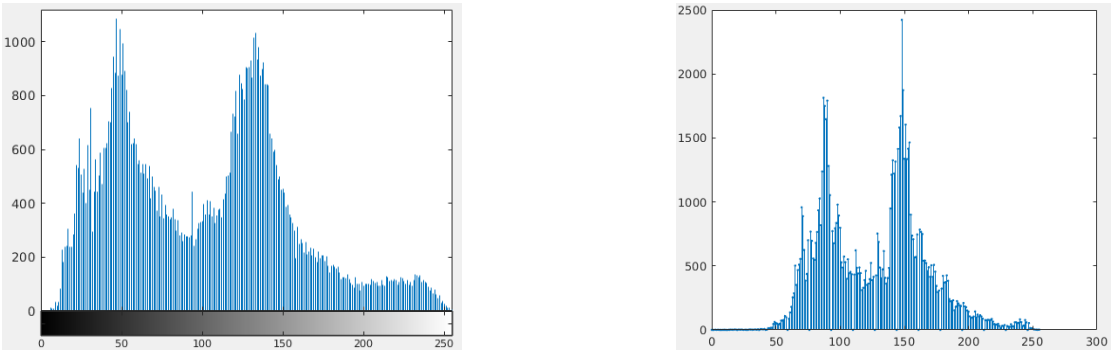


Figure 4. On the left: Histogram of the original image. On the right: Histogram of the smoothed data

the following setting

$$m = 3, \quad l_0 = -20000, \quad l_1 = -18000,$$
$$l_2 = -2000, \quad l_3 = 10000, \quad l_4 = 20000,$$
$$\sigma = 3, \quad \tau = 0.1, \quad \eta = 1 - \varepsilon,$$
$$\varepsilon = 0.01, \quad \Delta t = 0.05,$$

and $\varphi_0 \in C(\Omega)$ of (41), the initial level set function, was taken with S circle having radius 20 and center in the central point of Ω, and $d(x, S)$ the Euclidean distance between the point $x \in \Omega$ and S.

The parameter α is defined by the rule (56). Results of segmentation that have been obtained in this way, are depicted in Fig. 5–6. In fact, the given f-decomposition can be drilled down for each channel by iterative setting $\Omega = \Omega_i$, $i = 1, 2$, and so on. Regarding the procedure's stop-condition, it can be taken as follows:

$$\text{either} \quad \mathcal{L}^2(\Omega_i) < \delta_1 \quad \text{or} \quad CV\left(f\big|_{\Omega_i}\right) < \delta_2$$

for given $\delta_1, \delta_2 > 0$.

However, it should be emphasized that the main drawback of the direct approach to the segmentation procedure is the fact that the final result (the shape of the obtained segments, their area, and the corresponding coefficient of variation) crucially depends on the number of segments $m+1$ that we prescribe as an input characteristic. To circumvent this restriction, we make use of the adaptive approach. In this context, we do not fix a priori the number of segments, but instead, we decompose the interval $[l_0, l_{m+1}]$ into a uniform grid

$$l_0 < l_1 < l_2 < \cdots < l_{M-1} < l_M < l_{m+1}$$

with $l_j = l_0 + j\Delta l$, where the integer $M > 0$ satisfies the condition

$$\frac{|\Omega|}{M+1} \approx S^*.$$

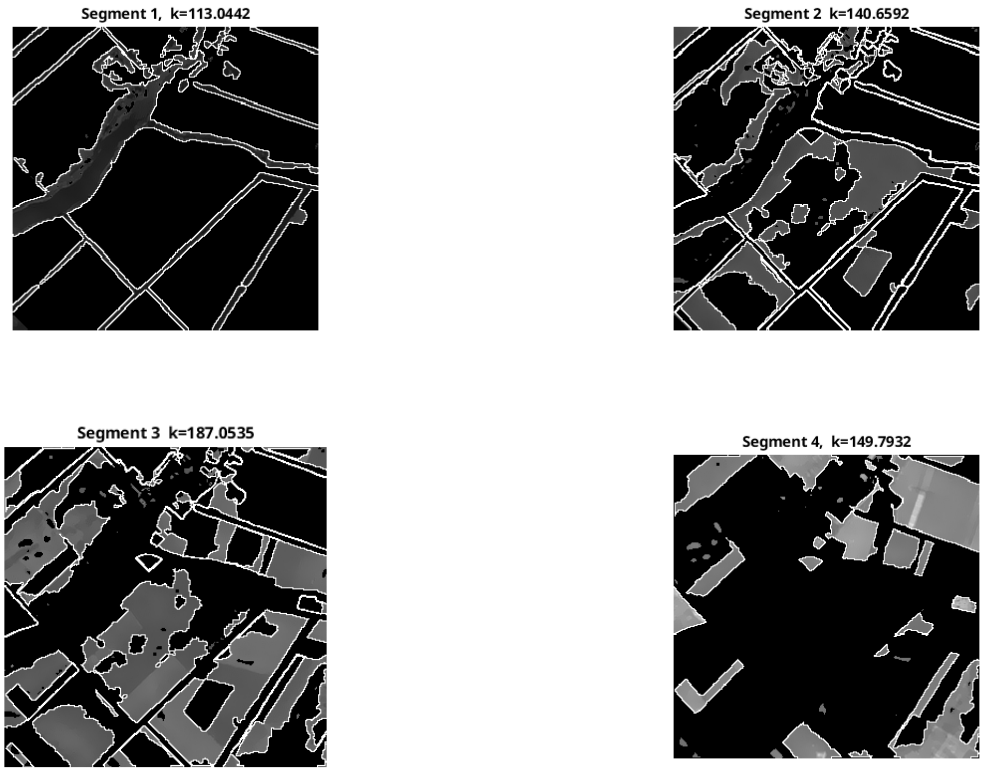


Figure 5. f-decomposition with $f(x) = u_{red}(x)$

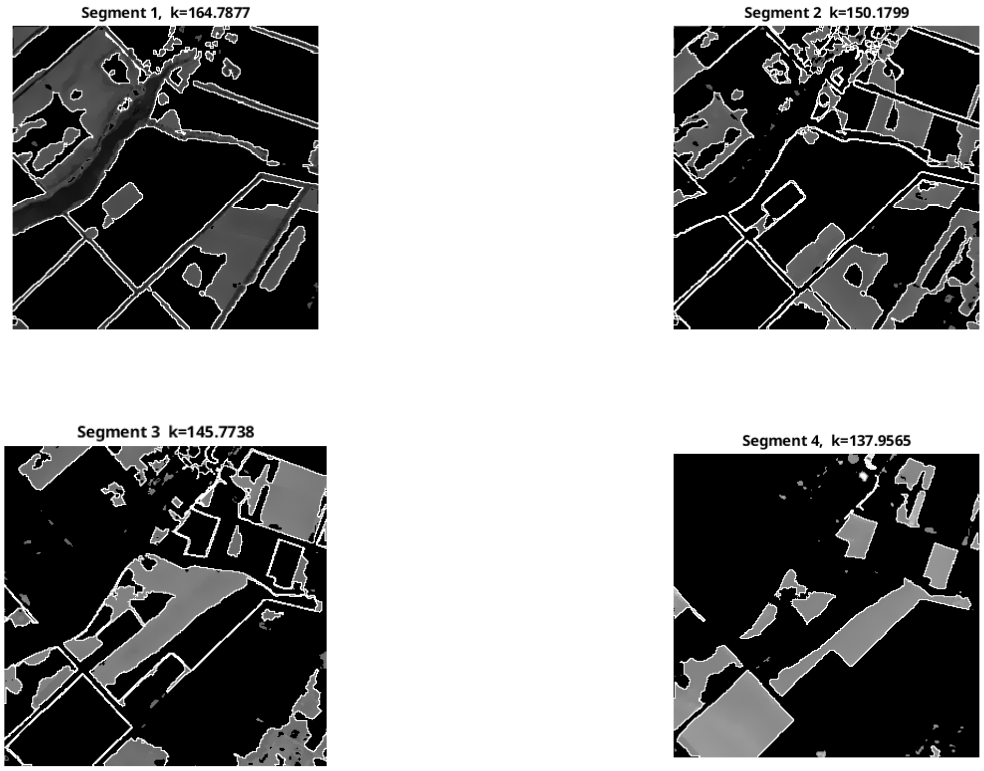


Figure 6. f-decomposition with $f(x) = u_{green}(x)$

Here, S^* stands for the area of a standard field in a given region.

After that we define the function $\varphi^0_{\varepsilon,\tau}$ as a solution of the problem (51), (52), (53)–(55) with the given collection $\{l_j\}_{j=1}^M$. Let $\{S_j\}_{j=0}^M$ be a set of the corresponding segments that we identify by the rules (57)–(59). Then we define the true segments as follows:

```
k=1;
True_Segment(k):=S_0;
for j=1:M
  if area(S_1)<0.10 S*
     combine{True_Segment(k),S_j};
  else
 k=k+1;
 True_Segment(k):=S_j;
end
Number_of_true_Segments:=k;
```

Here, the multiplier 0.10 emerges as a part of the field that can be neglected as a zone of inhomogeneity.

6. Conclusion

The generalized active contour model, proposed in,[1] to extract agricultural crop fields with a high degree of inhomogeneity from satellite data has been implemented. Setting an optimization problem, it was possible to achieve a disjunctive decomposition of a given field into a finite number of non-empty subsets, each of which could be associated with a unique value of an agricultural index. The Euler–Lagrange equation with the appropriate initial and boundary conditions has been used to express the corresponding optimality system under certain assumptions. A method for the numerical solution of the Euler–Lagrange system has been provided along with a numerical scheme. Using a direct approach to the segmentation technique and the new adaptive one, numerical simulations utilizing real-life satellite images have been conducted to show the accuracy and effectiveness of the proposed model.

Acknowledgments

None.

Funding

None.

Conflict of interest

The authors declare no conflict of interest.

Author contributions

Conceptualization: All authors
Formal analysis: All authors
Investigation: All authors
Methodology: All authors
Writing-original draft: All authors
Writing-review & editing: All authors

Availability of data

Not applicable.

References

1. D'Apice C., Kogut PI, Manzo R. On generalized active contour model in the anisotropic BV space and its application to satellite remote sensing of agricultural territory. *Netw Heterogen Media.* 2025;20(1): 113-142.
2. Mulla DJ. Twenty five years of remote sensing in precision agriculture: key advances and remaining knowledge gaps. *Biosyst Eng.* 2013; 114(4):358-371.
3. Xue J, Su B. Significant remote sensing vegetation indices: a review of developments and applications. *Hindawi J Sens.* 2017;2017:1-17. (Article ID 1353691)
4. Hnatushenko VV, Kogut PI, Uvarov M. Variational approach for rigid co-registration of optical/SAR satellite images in agricultural areas. *J Comput Appl Math.* 2022;400:15. Id 113742.
5. Khanenko P, Kogut PI, Uvarov M. On variational problem with nonstandard growth conditions for the restoration of clouds corrupted satellite images. In: *CEUR Workshop Proceedings, the 2nd International Workshop on Computational and Information Technologies for Risk-Informed Systems, CITRisk-2021*, September 16-17, 2021, Kherson, Ukraine, Vol. 3101; 2021: 6-25.
6. Ivanchuk N, Kogut PI, Martyniuk P. On generation of daily cloud free images at a high resolution level. In: M. Zgurovsky, N. Pankratova, eds. *System Analysis and Artificial Intelligence. Studies in Computational Intelligence*, Vol 1107. Cham: Springer; 2023: 203-232.
7. D'Apice C, Kogut PI, Manzo R. A two-level variational algorithm in the Sobolev-Orlicz space to predict daily surface reflectance at LANDSAT high spatial resolution and MODIS temporal frequency. *J Comput Appl Math.* 2023;434:115339.
8. D'Apice C, Kogut PI, Manzo R, Uvarov M. Variational model with nonstandard growth conditions for the restoration of satellite optical images using synthetic aperture radar. *Eur J Appl Math.* 2023; 34(1):77-105.
9. Hnatushenko VV, Kogut PI, & Uvarov MV. On satellite image Segmentation via piecewise constant approximation of selective smoothed target mapping. *Appl Math Comput.* 2021;389:125615.

10. Kogut PI, Kupenko OP, Uvarov NV. On increasing of resolution of satellite images via their fusion with imagery at higher resolution. *J Optimiz DiffEquat Appl.* 2021;29(1):54-78.
11. Mumford D, Shah J. Optimal approximation by piecewise smooth functions and associated variational problems. *Commun Pure Appl Math.* 1989;42(5):577-685.
12. Alvarez L, Lions PL, Morel J-M. Image selective smoothing and edge detection by nonlinear diffusion. II. *SIAM J Numer Anal.* 1992;9(3):845-866.
13. Caselles V, Kimmel R, Sapiro G. Geodesic active contours. *Int J Comput Vis.* 1997;22(1):61-79.
14. Chan T, Vese L. Active contours without edges. *IEEE Trans Image Process.* 2001;10(2):266-277.
15. Alvarez L, Guichard F, Lions PL, Morel J-M. Axioms and fundamental equations of image processing. *Arch Ration Mech Anal.* 1993;123(3):199-257.
16. Catté F, Coll T, Lions PL, J-M. Image selective smoothing and edge detection by nonlinear diffusion. I. *SIAM J Numer Anal.* 1992;29(1):182-193.
17. Yang C, Weng G, Chen Y. Active contour model based on local Kullback-Leibler divergence for fast image segmentation. *Eng Appl Artif Intell.* 2023;123:106472.
18. Han B, Wun Y. Active contour model for inhomogenous image segmentation based on Jeffreys divergence. *Pattern Recognit.* 2020;107: 1075202.
19. Yuan Y., He C. Adaptive active contours without edges. *Math Comput Modell.* 2012;55:1705-1721.
20. Kass M, Witkin A, Terzopoulos D. Snakes: active contour models. *Int J Comput Vis.* 1988;1(4):321-331.
21. Dai L, Ding J, Yang J. Inhomogeneity-embedded active contour for natural image segmentation. *Pattern Recognit.* 2015;48(8):2513-2529.
22. Chen Y, Wu L, Wang G, Weng G, Chen H. An active contour model for image segmentation using morphology and nonlinear Poisson's equation. *Optik.* 2023;287: 170997.
23. Fang L, Liang X, Xu C, Wang Q. Image segmentation using a novel dual active contour model. *Multimedia Tools Appl.* 2024;83(2):3707-724.
24. Ge P, Chen Y, Wang G, Weng G. An active contour model based on Jeffreys divergence and clustering technology for image segmentation. *J Vis Commun Image Represent.* 2024;99:104069.
25. Kon NA, Jumaat AK, Suhaizi MDA. Active contour models for boundary extraction with application to medical images with noise. *J Adv Res ApplSciEng Technol.* 2024;33(2):300-312.
26. Mazlin MS, Jumaat AK, Embong R. Partitioning intensity inhomogeneity colour images via Saliency-based active contour. *Int J Elect Comput Eng.* 2024;14(1):337-346.
27. Suryana ME, Rizki M, Irzal M, Aryani R. Solving wound perimeter detection with active contour model enhanced with interpolation. *AIP Conf Proc.* 2024;2982(1):060005.
28. Zhang M, Meng D, Pei Y, Wen J. Research on image segmentation method based on improved Snake model. *Multimedia Tools Appl.* 2024;83(5):13977-13994.
29. Ivanchuk N, Kogut PI, Kupenko O. Generalized active contour model in an anisotropic variable exponent Sobolev space. *J Optimiz Diff Equat Appl.* 2024;32(1):1-32.
30. Kogut PI, Kohut Ya, Parfinovych N. Solvability issues for some noncoercive and nonmonotone parabolic
equations arising in the image denoising problems. *J Optimiz Differ Equat Appl.* 2022;30(2):19-48.
31. Kogut PI, Kohut Y, Manzo R. Fictitious controls and approximation of anÂ optimal control problem for Perona-Malik equation. J Optimiz *Differ Equat Appl.* 2022;30(1):42-70.
32. Anzellotti G. Pairings between measures and bounded functions and compensated compactness. *Ann di Matematica Pura ed Appl.* 1983; 135(IV): 293-318.
33. Vese L. A study in the BV space of a denoising-deblurring variational problem. *Appl Math Optim.* 2001;44:131-161.
34. Ivanchuk N, Ivanchuk V. On PDE formulation of the relaxed version of generalized active contour model in anisotropic Sobolev space. *J Optimiz Differ Equat Applicat.* 2024; 32(2):118-136.
35. Aubert G, Kornprobst P. *Mathematical Problems in Image Processing: Partial Differential Equations and the Calculus of Variations*. New York: Springer; 2006: 147.
36. Karami F, Meskine D, Sadik K. A new nonlocal model for the restoration of textured images. *J Appl Anal Comput.* 2019;9(6):2070-2095.
37. Salgado AJ, Wise SM. *Classical Numerical Analysis: A Comprehensive Course*. Cambridge University Press; 2022.
38. Maple C. Geometric design and space planning using the marching squares and marching cube algorithms. In: *2003 International Conference on Geometric Modeling and Graphics*; 2003:90-95.
39. Mantz H, Jacobs K, Mecke K. Utilizing Minkowski functionals for image analysis: a marching square algorithm. *J Stat Mech: Theory Exp.* 2008;12:12015.
40. D'Apice C, Kogut PI, Kupenko O, Manzo R. On variational problem with nonstandard growth functional and its applications to image processing. *J Math Imaging Vis.* 2023;65(3): 472-491.

Ciro D'Apice *obtained the degree cum laude in Mathematics in 1991 and the PhD in Mathematics in 1997 at the University of Naples "Federico II." He is a Full Professor in Mathematical Analysis at Dipartimento di Scienze Aziendali-Management & Innovation Systems (DISA-MIS), University of Salerno. His research interests*

include the following: variational calculus, homogenization and optimal control; complex networks modeling: conservation laws and applications to traffic networks, telecommunication ones, and supply chains, queueing systems and networks; analytical aspects for the temporal and spatial behaviour of solutions of dynamic problems.
https://orcid.org/0000-0003-3194-3063

Umberto De Maio *is an Associate Professor at Dipartimento di Matematica e Applicazioni "R. Caccioppoli", Universitá degli Studi di Napoli Federico II. His research interests include the following: homogenization theory, control theory and asymptotic analysis. He has been the scientific leader of international and national research projects. He was awarded the National Scientific Qualification as a full professor. He has been a Member of several competition committees. He is the coordinator/promoter of Erasmus Exchanges with several international universities. He has been a member of the steering committee of the Double Master's Degree Program in Mathematical Analysis and Modelling. He has been on the organizing committee of several international conferences. He has participated in several national and international conferences. He has taught courses in Mathematical Analysis at several Italian universities. He has been a lecturer in several doctoral courses..*
https://orcid.org/0000-0001-7397-5237

Peter I. Kogut *is a Professor at the Department of Mathematical Analysis and Optimizations, Oles Honchar Dnipro National University, where his teaching focuses on variational methods in mathematical physics, optimal control theory for distributed systems, and nonlinear functional analysis. He received a Ph.D. degree in calculus of variations and optimal control theory in 1989 (Cybernetic Institute of National Academy of Science of Ukraine), and then the scientific degree of Doctor of Sciences in Math and Physics in 1998. In 1998 he was awarded the First Prize of the National Academy of Science for the research in homogenization theory of optimal control problems. He has over 200 journal publications in Mathematical Sciences and 2 books in mathematics that have been published by Birkhauser (2011) and Walter de Gruyter GmbH (2019). His major scientific results cover the different areas of optimization theory, optimal control problems for PDEs, image processing, asymptotic analysis, optimization in partially ordered spaces, and homogenization theory. .*
https://orcid.org/0000-0003-1593-0510

Rosanna Manzo *received a degree cum laude in Mathematics in 1996 and PhD in Information Engineering in 2007 at the University of Salerno. She is an Associate Professor in Mathematical Analysis at the Department of Political and Communication Sciences (DiSPC), University of Salerno. The research activity focuses on the following topics: fluid dynamic models for road networks, telecommunication networks, supply chains and blood flows; optimal control for hybrid systems; variational analysis and optimization in normed spaces; queueing systems and networks.*
https://orcid.org/00000-0002-3891-1825

An International Journal of Optimization and Control: Theories & Applications
(https://accscience.com/journal/ijocta)

This work is licensed under a Creative Commons Attribution 4.0 International License. The authors retain ownership of the copyright for their article, but they allow anyone to download, reuse, reprint, modify, distribute, and/or copy articles in IJOCTA, so long as the original authors and source are credited. To see the complete license contents, please visit http://creativecommons.org/licenses/by/4.0/.

An International Journal of Optimization and Control: Theories & Applications
ISSN: 2146-0957 eISSN: 2146-5703
Vol.15, No.3, pp.464-482 (2025)
https://doi.org/10.36922/IJOCTA025120054

RESEARCH ARTICLE

Application of Jumarie-Stancu Collocation Series Method and Multi-Step Generalized Differential Transform Method to fractional glucose-insulin

Sayed Saber[1,2*], Brahim Dridi[3], Abdullah Alahmari[3], and Mohammed Messaoudi[4]

[1]Department of Mathematics, Faculty of Science, Al-Baha University, Al-Baha, Saudi Arabia
[2]Department of Mathematics and Computer Science, Faculty of Science, Beni-Suef University, Egypt
[3]Department of Mathematics, Faculty of Sciences, Umm Al-Qura University, Saudi Arabia
[4]Department of Mathematics and Statistics, College of Science, Imam Mohammad Ibn Saud Islamic University (IMSIU), Riyadh, Saudi Arabia
Sayed011258@science.bsu.edu.eg, iodridi@uqu.edu.sa, aahmari@uqu.edu.sa, mmessaoudi@imamu.edu.sa

ARTICLE INFO

Article History:
Received: March 19, 2025
1st revised: April 20, 2025
2nd revised: April 24, 2025
Accepted: April 29, 2025
Published Online: May 20, 2025

Keywords:
Fractional calculus
Glucose-insulin model
Numerical methods
Chaos control
Numerical simulation
MSGDTM
JSCSM

AMS Classification:
46C05; 49J20; 93C20; 49K20; 34K05; 34A12; 26A33

ABSTRACT

This study applies the Multi-Step Generalized Differential Transform Method (MSGDTM) and the Jumarie-Stancu Collocation Series Method (JSCSM) to analyze a fractional-order Model (1). The model incorporates Caputo fractional derivatives to capture the nonlocal and memory-dependent characteristics of glucose-insulin interactions, considering physiological factors such as β-cell activity and external glucose intake. Stability analysis reveals bifurcations and chaotic attractors, demonstrating the system's sensitivity to fractional orders. Numerical simulations compare MSGDTM and JSCSM accuracy and efficiency, highlighting MSGDTM's superior convergence and lower approximation error. The results show that fractional-order modeling provides a more accurate framework for understanding glucose-insulin dynamics and predicting metabolic behavior. Furthermore, control mechanisms are introduced to mitigate chaos, offering potential strategies for managing diabetes. This work emphasizes the robustness of MSGDTM in solving complex fractional biological models. It provides insights into fractional calculus applications in biomedical research.

CC BY

1. Introduction

Insulin regulation is a cornerstone of human metabolic processes, with imbalances leading to diabetes mellitus, a chronic condition affecting millions worldwide. Understanding the glucose-insulin interaction is crucial for developing effective treatment strategies. Traditional integer-order models are widely used to describe these interactions; however, they often fail to capture the complex physiological memory and hereditary properties inherent in biological systems. To address this limitation, fractional-order differential equations (FDEs) have emerged as a powerful tool, incorporating memory effects and nonlocal dynamics that better represent real-world biological phenomena.

Fractional calculus, characterized by its nonlocal operators and ability to retain memory

*Corresponding Author

effects, provides a flexible and robust mathematical framework for modeling intricate biological systems.[1,2] Its growing significance spans various disciplines, including engineering,[3] plant epidemiology,[4] mathematical biology,[5] medicine,[6] psychology, and life sciences.[7] Additionally, it finds applications in viscoelasticity,[8] electromagnetic wave propagation,[9] quantum mechanics,[10] physics,[11-22] and diabetes modeling,[23-34] Computer virus, zoonotic disease.[35] A key focus of this study is to analyze system stability, bifurcation structures, and chaotic dynamics using tools such as phase portraits, Lyapunov exponents, and bifurcation diagrams.[36,37]

In order to mitigate chaotic fluctuations, a simple linear controller is introduced. Studies show that fractional-order models enhance glucose-insulin interactions, leading to improved diabetes management strategies.[38–40] This research integrates fractional calculus, chaos theory, and computational simulations to advance both theoretical and applied aspects of glucose-insulin regulation, emphasizing memory effects in biological processes, and paving the way for biomedical progress. This work delves into the intricate behavior and regulatory mechanisms of the proposed model, leveraging memory-dependent fractional derivatives to capture long-term physiological interactions. Using advanced computational methods, including the MSGDTM and the JSCSM, the study formulates and analyzes a time-dependent fractional-order model of glucose-insulin dynamics, incorporating the interplay between glucose levels, insulin secretion, and beta-cell activity. These numerical schemes effectively solve the complex fractional differential equations governing the system's behavior.[41-65] Tsai and Chen[44] introduced the Laplace-Adomian-Padé approximation method, while Zeng et al.[45] derived analytical approximations for FDEs. Additionally, Khan et al.[46] combined the LADM in prior studies; see also.[44,45,47,48] Analytical techniques for solving fractional differential equations include the ADM,[49] the LADM,[50] the ADM,[51] the HAM,[52] the MSGDTM,[53] the Galerkin finite element method,[54] the Legendre wavelets method,[55] the spectral collocation method,[56] and JSCSM.[66] This study contributes an improved variant of the generalized differential transform method (GDTM),[57-60] refined to enhance solution accuracy over extended time intervals. Traditional GDTM approaches are limited to short-term approximations due to small time steps. By contrast, MSGDTM extends solution validity over longer periods while maintaining high precision, outperforming conventional techniques.[61-73] Numerical comparisons indicate strong agreement between the MSGDTM solutions and those obtained via the classical Runge-Kutta method when the derivative order is set to one.

It was proposed by Ackerman et al. (1964) that a 2D linear differential equation could be used to represent glucose tolerance test data. The mathematical model proposed is as follows:

$$\begin{aligned}\dot{\hat{u}}(\iota) &= \mathrm{a}_1\hat{v}(\iota) - \mathrm{a}_2\hat{u}(\iota) + c_1,\\ \dot{\hat{v}}(\iota) &= -\mathrm{a}_3\hat{v}(\iota) - \mathrm{a}_4\hat{u}(\iota) + c_2 + I.\end{aligned}$$

In these equations, $\hat{u}$ and $\hat{v}$ denote insulin and glucose concentrations, respectively, and I indicates the rate at which blood glucose levels increase. Based on the Lotka-Volterra framework (Elsadany et al.,[Elsadany] Shabestari et al.[75] developed a model to analyze glucose-insulin relationships. In this model:[75]

$$\begin{aligned}{}^{\mathrm{C}}\mathscr{D}^{\alpha}_{0,\iota}\hat{u}(\iota) =& -\mathrm{a}_1\hat{u}(\iota) + \mathrm{a}_2\hat{u}(\iota)\hat{v}(\iota) + \mathrm{a}_3\hat{v}^2(\iota) + \mathrm{a}_4\\ & \hat{v}^3(\iota) + \mathrm{a}_5\hat{w}(\iota) + \mathrm{a}_6\hat{w}^2(\iota) + \mathrm{a}_7\hat{w}^3(\iota)\\ & + \mathrm{a}_{20},\\ {}^{\mathrm{C}}\mathscr{D}^{\alpha}_{0,\iota}\hat{v}(\iota) =& -\mathrm{a}_8\hat{u}(\iota)\hat{v}(\iota) - \mathrm{a}_9\hat{u}^2(\iota) - \mathrm{a}_{10}\hat{u}^3(\iota)\\ & + \mathrm{a}_{11}\hat{v}(\iota)(1-\hat{v}(\iota)) - \mathrm{a}_{12}\hat{w}(\iota) - \mathrm{a}_{13}\\ & \hat{w}^2(\iota) - \mathrm{a}_{14}\hat{w}^3(\iota) + \mathrm{a}_{21},\\ {}^{\mathrm{C}}\mathscr{D}^{\alpha}_{0,\iota}\hat{w}(\iota) =& \mathrm{a}_{15}\hat{v}(\iota) + \mathrm{a}_{16}\hat{v}^2(\iota) + \mathrm{a}_{17}\hat{v}^3(\iota)\\ & - \mathrm{a}_{18}\hat{w}(\iota) - \mathrm{a}_{19}\hat{v}(\iota)\hat{w}(\iota).\end{aligned} \tag{1}$$

The model parameters are defined as follows: a_1 represents the natural decay rate of insulin in the absence of glucose, while a_2 quantifies the influence of glucose on insulin stimulation and a_3 captures the acceleration of insulin production as glucose levels rise. The basal secretion of insulin from β-cells, independent of glucose, is governed by a_4, with a_5 accounting for a minor contribution to basal insulin release and a_6 serving as an adjustment factor in basal insulin dynamics. Parameter a_7 introduces a positive feedback component to insulin release from β-cells. Insulin's regulatory effect on glucose metabolism is modeled by a_8, whereas a_9 and a_{10} represent strong and secondary reductions in glucose concentration due to insulin activity. The increase in glucose from external sources or metabolism without insulin influence is described by a_{11}. Parameters

a_{12}, a_{13}, and a_{14} characterize the effects of β-cell-derived insulin on lowering glucose levels, including both negative modulation and auxiliary impacts. The dynamics of β-cell growth and decline are detailed by a_{15}, which captures activation due to glucose elevation; a_{16}, which accounts for inhibitory influences at higher glucose levels; and a_{17}, a supporting factor for glucose-driven β-cell expansion. The natural loss of β-cells over time is modeled by a_{18}, while a_{19} reflects a progressive decline in β-cell population. Lastly, a_{20} represents a constant term for external input or loss in glucose dynamics. a_{21} denotes the baseline rate of insulin synthesis under normal physiological conditions. Glucose-insulin fractional order is given by

$$\begin{aligned}
{}^{\mathrm{C}}\mathscr{D}^{\alpha}_{0,\iota}\hat{u}(\iota) =& -\mathrm{a}_1\hat{u}(\iota) + \mathrm{a}_2\hat{u}(\iota)\hat{v}(\iota) + \mathrm{a}_3\hat{v}^2(\iota) \\
&+ \mathrm{a}_4\hat{v}^3(\iota) + \mathrm{a}_5\hat{w}(\iota) + \mathrm{a}_6\hat{w}^2(\iota) \\
&+ \mathrm{a}_7\hat{w}^3(\iota) + \mathrm{a}_{20} - d_1(\hat{v}+\hat{w}), \\
{}^{\mathrm{C}}\mathscr{D}^{\alpha}_{0,\iota}\hat{v}(\iota) =& -\mathrm{a}_8\hat{u}(\iota)\hat{v}(\iota) - \mathrm{a}_9\hat{u}^2(\iota) - \mathrm{a}_{10}\hat{u}^3(\iota) \\
&+ \mathrm{a}_{11}\hat{v}(\iota)(1-\hat{v}(\iota)) - \mathrm{a}_{12}\hat{w}(\iota) \\
&- \mathrm{a}_{13}\hat{w}^2(\iota) - \mathrm{a}_{14}\hat{w}^3(\iota) + \mathrm{a}_{21}, \\
{}^{\mathrm{C}}\mathscr{D}^{\alpha}_{0,\iota}\hat{w}(\iota) =& \mathrm{a}_{15}\hat{v}(\iota) + \mathrm{a}_{16}\hat{v}^2(\iota) \\
&+ \mathrm{a}_{17}\hat{v}^3(\iota) - \mathrm{a}_{18}\hat{w}(\iota) \\
&- \mathrm{a}_{19}\hat{v}(\iota)\hat{w}(\iota) - d_2(\hat{u}+\hat{v}+\hat{w}).
\end{aligned} \tag{2}$$

Using Caputo derivatives, this study proposes and examines a Model (1). It focuses on assessing system stability, bifurcation patterns, and chaotic dynamics across fractional orders. In addition, the research evaluates how well the MSGDTM and the JSCSM solve fractional differential equations, emphasizing their computational efficiency and accuracy. Moreover, the study explores effective control strategies to suppress chaotic fluctuations and enhance glucose stability.

The remainder of this paper is organized as follows. Section 2 discusses fractional calculus and the Caputo derivative. MSGDTM and JSCSM are applied to the glucose-insulin model in Section 3, along with a comparison. Numerical simulations, bifurcation analyses, and stability results are presented in Section 4. In Section 5, we summarize key findings and discuss potential future research directions in fractional-order biomedical modeling.

2. Stability investigation

Equation (1) has the following Jacobian matrix:

$$J(\hat{u},\hat{v},\hat{w}) = \begin{pmatrix} -a_s\hat{v} - 2a_g\hat{u} - 3a_{10}\hat{u}^2 \\ 0 \\ \\ -a_1 + a_2\hat{v} \\ -a_8\hat{u} + a_{11}(1-2\hat{v}) \\ a_{15} + 2a_{16}\hat{v}_3a_{17}\hat{v}^2 - a_{19}\hat{w} \\ \\ a_2\hat{u} + 2a_3\hat{v} + 3a_4\hat{v} \\ -a_{12} - 2a_{13}\hat{w} - 3a_{14}\hat{w}^2 \\ -a_{18} - a_{19}\hat{v} \\ \\ a_5 + 2a_6\hat{w} + 3a_7\hat{w}^2 \end{pmatrix}$$

Following the approach in Shabestari et al. (2018), equilibrium points $E_1(0.805, 1.815, 1.319)$ and $E_2(0.624, 0.935, 0.877)$ are considered. The eigenvalues of system (1) at E_1 are $\Lambda_{1,2} = -1.7564 \pm 7.5090i$ and $\Lambda_3 = 1.3802$. For E_2, they are $\Lambda_{1,2} = 0.5262 \pm 2.3472i$ and $\Lambda_3 = -2.8372$. Define:

$$\Delta(\lambda) = \mathrm{diag}\left(\lambda^{M\alpha_1}, \lambda^{M\alpha_2}, \lambda^{M\alpha_3}\right) - J.$$

For linear systems to be asymptotically stable, the following must hold:

$$|\arg(\lambda)| > \frac{\pi}{2M}.$$

For instability at equilibrium points, the condition is:

$$\frac{\pi}{2M} - \min_j\{\arg(\Lambda_j)\} \geq 0,$$

where Λ_j are roots of $\det\left(\mathrm{diag}\left(\lambda^{Mq_x}, \lambda^{Mq_y}, \lambda^{Mq_z} - \boldsymbol{J}_{E_j}\right) = 0\right.$ for each equilibrium E_j $(i = 1, 2, 3)$.

$$\alpha < \frac{2}{\pi}\min_j|\arg(\Lambda_j)| \approx 0.86.$$

For chaotic attractors in the model (1), the following must be satisfied:

$$\frac{\pi}{2M} - \min_j\{|\arg(\Lambda_j)|\} \geq 0.$$

According to Table 1, the equilibrium points E_1 and E_2 behave as saddle points of index two.

Table 1 also presents the Kaplan-Yorke (KY) dimension for various fractional derivatives, computed as:

$$\dim(LE) = 2 + \frac{LE_1 + LE_2}{|LE_3|}.$$

Table 2 compares KY dimensions of different fractional derivatives, revealing that system (1)

possesses a relatively higher dimension of 2.09, indicating increased complexity.

3. Bifurcation diagrams

The parameter a_{16} could represent the system's response to stress or external factors affecting glucose regulation. a_{16} (-2 to 0) could represent the system's response to stress or external factors affecting glucose regulation. Bifurcations may indicate shifting glucose levels due to changing external conditions. Related dynamics is bifurcation in a_{16} shows external stressors affect glucose dynamics. In a bifurcated liver, a parameter a_{17} could describe the delay in insulin response, with bifurcations representing an oscillatory glucose response. a_{17} (0 to 1) may describe insulin response delay. As response times vary, bifurcations may indicate changes from stable glucose regulation to oscillatory or chaotic behavior. The bifurcation in a_{17} might be related to liver response delays. Insulin and other metabolic pathways might be represented by a_{18}. There might be interactions between insulin and other metabolic pathways in a_{18}. a_{18} bifurcations (-1 to 0) may indicate a change from stable to complex glucose dynamics. A bifurcation in a_{18} may give insight into glucose regulation. An indicator of insulin resistance might be a_{19}. There is a possibility that the rate at which insulin resistance develops can be represented by a_{19} (-1 to 0). The point of bifurcation could result in a transition from stable glucose regulation to instability as resistance increases as the point of bifurcation is reached. In the case of an increase in a_{19}, this could be a result of varying rates at which insulin resistance develops as a result of variable insulin resistance levels leading to a change in glucose stability. In the system (1), there might be a parameter called a_{20} that describes the strength of feedback mechanisms that exist. It might be possible to describe the strength of feedback mechanisms in the Model (1) by the parameter a_{20}. It is possible that bifurcations in a_{20} (-1 to 0) could indicate that glucose dynamics are changing from stable to complex due to changes in the strength of feedback. This could be attributed to the bifurcation of a_{20} indicating how variations in feedback strength can affect the stability of glucose levels. A parameter known as a_{21} is used as a potential indicator of how multi-factor influences glucose regulation in a system. In order to better understand how several factors act on the regulation of glucose, a_{21} (-1 to 0) might be a good indicator. Bifurcations could indicate transitions from stable to chaotic behavior as these factors vary. It is possible that the bifurcation in a_{21} could be a reflection of multiple influences that combine to affect glucose dynamics and stability overall. During the regulation of glucose and insulin dynamics within the human body, every parameter from a_1 to a_{21} is crucial. Diabetes requires understanding these bifurcations to predict and manage the complex dynamics of glucose regulation. Predicting and controlling critical transitions in complex systems, whether biological or physical, requires understanding bifurcation. Stability may shift to chaos or vice versa, affecting the stability and behavior of the system. By understanding these bifurcations, we can develop strategies for managing biological processes, designing stable physical systems, and preventing undesirable behaviors. Critical transitions can be predicted and controlled by understanding the bifurcation of parameters in complex systems. During these transitions, the system can go from stability to chaos or vice versa, affecting its behavior and stability significantly. By recognizing these bifurcations, we can design stable physical systems and prevent undesirable behaviors like chaotic oscillations.

4. Methods

4.1. Jumarie-Stancu collocation series method

We apply the JSCSM to approximate the solutions for $\hat{u}(t)$, $\hat{v}(t)$, and $\hat{w}(t)$ in the following steps.

Assume each function can be expanded as a series:

$$\hat{u}(t) = \Sigma_{n=0}^{\infty} a_n \iota^n,$$
$$\hat{v}(t) = \Sigma_{n=0}^{\infty} b_n \iota^n,$$
$$\hat{w}(t) = \Sigma_{n=0}^{\infty} c_n \iota^n,$$

where a_n, b_n, and c_n are coefficients to be determined for $\hat{u}$, $\hat{v}$, and $\hat{w}$, respectively.

Using the Jumarie fractional derivative, we approximate the fractional Caputo derivative ${}^{\mathtt{C}}\mathscr{D}_{0,\iota}^{\alpha}$ for each series term:

$${}^{\mathtt{C}}\mathscr{D}_{0,\iota}^{\alpha} \iota^n \approx \frac{\iota^{n-\alpha}}{\alpha(n+1)} \cdot \alpha(n+1-\alpha).$$

Then, each derivative can be represented as:

$${}^{\mathtt{C}}\mathscr{D}_{0,\iota}^{\alpha} \hat{u}(t) \approx \Sigma_{n=0}^{\infty} a_n \, {}^{\mathtt{C}}\mathscr{D}_{0,\iota}^{\alpha}(\iota^n),$$
$${}^{\mathtt{C}}\mathscr{D}_{0,\iota}^{\alpha} \hat{v}(t) \approx \Sigma_{n=0}^{\infty} b_n \, {}^{\mathtt{C}}\mathscr{D}_{0,\iota}^{\alpha}(\iota^n),$$
$${}^{\mathtt{C}}\mathscr{D}_{0,\iota}^{\alpha} \hat{w}(t) \approx \Sigma_{n=0}^{\infty} c_n \, {}^{\mathtt{C}}\mathscr{D}_{0,\iota}^{\alpha}(\iota^n).$$

Select collocation points $\{\iota_0, \iota_1, \ldots, \iota_m\}$ within the time interval of interest.

Substitute the series and fractional derivative approximations into each of the differential equations:

$$\Sigma_{n=0}^{\infty} a_n {}^{\mathtt{C}}\mathscr{D}_{0,\iota}^{\alpha}(\iota_j^n) = -a_1\hat{u}(\iota_j) + a_2\hat{u}(\iota_j)\hat{v}(\iota_j) + \cdots + a_{20},$$
$$\Sigma_{n=0}^{\infty} b_n {}^{\mathtt{C}}\mathscr{D}_{0,\iota}^{\alpha}(\iota_j^n) = -a_8\hat{u}(\iota_j)\hat{v}(\iota_j) - \cdots + a_{21},$$
$$\Sigma_{n=0}^{\infty} c_n {}^{\mathtt{C}}\mathscr{D}_{0,\iota}^{\alpha}(\iota_j^n) = a_{15}\hat{v}(\iota_j) + \cdots - a_{19}\hat{v}(\iota_j)\hat{w}(\iota_j),$$

where $j = 0, 1, \ldots, m$.

Based on the complexity of the algebraic system, the coefficients a_n, b_n, and c_n can be determined numerically or symbolically. Once the coefficients are determined, approximate solutions are constructed as:

$$\hat{u}(t) \approx \Sigma_{n=0}^{N} a_n \iota^n,$$
$$\hat{v}(t) \approx \Sigma_{n=0}^{N} b_n \iota^n,$$
$$\hat{w}(t) \approx \Sigma_{n=0}^{N} c_n \iota^n,$$

where N is the number of terms chosen based on the desired accuracy.

4.2. MSGDTM

Let the differential transforms of $\hat{u}(t)$, $\hat{v}(t)$, and $\hat{w}(t)$ be represented as $\hat{u}(\hat{k})$, $\hat{v}(\hat{k})$, and $\hat{w}(\hat{k})$, respectively. Assume the initial values satisfy $\hat{u}(0) = \hat{u}_0$, $\hat{v}(0) = \hat{v}_0$, and $\hat{w}(0) = \hat{w}_0$. The solution process begins with these initial conditions in the transformed domain at $k = 0$. Applying the recurrence relations derived earlier, we iteratively compute $\hat{u}(\hat{k}+1)$, $\hat{v}(\hat{k}+1)$, and $\hat{w}(\hat{k}+1)$ for each k up to the desired approximation order K. The approximate solutions in the original domain for $\hat{u}(t)$, $\hat{v}(t)$, and $\hat{w}(t)$ can then be reconstructed via the inverse differential transform. Using the MSGDTM methodology, partition the interval $[0, T]$ into M subintervals. To illustrate the approach, consider the system analyzed in:[63]-[67]

$$\begin{aligned}
\mathscr{D}_1^{\alpha} \upsilon_1(t) &= g_1(t, \upsilon_1, \upsilon_2, ..., \upsilon_n),\\
\mathscr{D}_2^{\alpha} \upsilon_2(t) &= g_2(t, \upsilon_1, \upsilon_2, ..., \upsilon_n),\\
&\vdots\\
\mathscr{D}_n^{\alpha} \upsilon_n(t) &= g_n(t, \upsilon_1, \upsilon_2, ..., \upsilon_n).
\end{aligned} \tag{3}$$

subject to

$$\upsilon_j(\iota_0) = d_j, \qquad i = 1, 2, ..., n, \tag{4}$$

The solution of the problem (3)-(4) is sought over the domain $[\iota_0, T]$. The kth-order approximation of the solution to this problem is:

$$\upsilon_j(t) = \sum_{j=0}^{K} \Gamma_j(\hat{k})(t - \iota_0)^{k\alpha_j}, \quad \iota \in [\iota_0, T],$$

where $\Gamma_j(\hat{k})$ satisfies

$$\frac{\alpha((\hat{k}+1)\alpha_j + 1)}{\alpha(k\alpha_j + 1)} \Gamma_j(\hat{k}+1) = g_j(k, \Gamma_1, \Gamma_2, ..., \Gamma_n),$$

and with initial conditions $\Gamma_j(0) = d_j$. The differential transform of $g_j(k, \Gamma_1, \Gamma_2, ..., \Gamma_n)$ corresponds to $g_j(t, \upsilon_1, \upsilon_2, ..., \upsilon_n)$ for $j = 1, 2, ..., n$. Partition the interval $[\iota_0, T]$ into M subintervals $[\iota_{m-1}, \iota_m]$, where $m = 1, 2, ..., M$, using a step size of $h = (T - \iota_0)/M$ and nodes $\iota_m = \iota_0 + mh$. The principles of MSGDTM are outlined below.

Initially, the MSGDTM method solves (3)-(4) on the first interval $[\iota_0, \iota_1]$, yielding the approximate solution $\upsilon_{i,1}(t)$ for $t \in [\iota_0, \iota_1]$. For $m \geq 2$, applying MSGDTM to (3)-(4) on $[\iota_{m-1}, \iota_m]$ uses the continuity condition $\upsilon_{i,m}(\iota_{m-1}) = \upsilon_{i,m-1}(\iota_{m-1})$. Repeating this process results in approximations $\upsilon_{i,m}(t)$ for all $m = 1, 2, ..., M$. The final approximation is defined as:

$$\upsilon_j(t) = \begin{cases} \upsilon_{i,1}(t) & \text{if } \iota \in [\iota_0, \iota_1],\\ \upsilon_{i,2}(t) & \text{if } \iota \in [\iota_1, \iota_2],\\ \vdots & \\ \upsilon_{i,M}(t) & \text{if } \iota \in [\iota_{M-1}, \iota_M]. \end{cases}$$

MSGDTM remains effective for all step sizes h. For system (1), the MSGDTM procedure yields:

$$\begin{aligned}
\hat{u}(\hat{k}+1) =& \frac{\alpha(\alpha k + 1)}{\alpha(\alpha(\hat{k}+1) + 1)} \Big(- b_1\hat{u}(\hat{k}) + b_2\hat{u}(\hat{k})\hat{v}(\hat{k}) + b_3\hat{v}^2(\hat{k})\\
&+ b_4\hat{v}^3(\hat{k}) + b_5\hat{w}(\hat{k}) + b_6\hat{w}^2(\hat{k})\\
&+ b_7\hat{w}^3(\hat{k}) + b_{20}\Big),\\
\hat{v}(\hat{k}+1) =& \frac{\alpha(\alpha k + 1)}{\alpha(\alpha(\hat{k}+1) + 1)} \Big(- b_8\hat{u}(\hat{k})\hat{v}(\hat{k}) - b_9\hat{u}^2(\hat{k}) - b_{10}\hat{u}^3(\hat{k})\\
&+ b_{11}\hat{v}(\hat{k})(1 - \hat{v}(\hat{k})) - b_{12}\hat{w}(\hat{k})\\
&- b_{13}\hat{w}^2(\hat{k}) - b_{14}\hat{w}^3(\hat{k}) + b_{21}\Big),\\
\hat{w}(\hat{k}+1) =& \frac{\alpha(\alpha k + 1)}{\alpha(\alpha(\hat{k}+1) + 1)} \Big(b_{15}\hat{v}(\hat{k}) + b_{16}\hat{v}^2(\hat{k}) + b_{17}\hat{v}^3(\hat{k})\\
&- b_{18}\hat{w}(\hat{k}) - b_{19}\hat{v}(\hat{k})\hat{w}(\hat{k})\Big).
\end{aligned}$$

The initial values: $\hat{u}(0) = d_1$, $\hat{v}(0) = d_2$, and $\hat{w}(0) = d_3$. Following is the differential transform

Table 1. Equilibrium points and their Eigenvalues

Equilibrium point and Eigenvalues	
$E_1(0.805, 1.815, 1.319)$	$\Lambda_{1,2} = -1.7564 \pm 7.5090i$, $\Lambda_3 = 1.3802$
$E_2(0.624, 0.935, 0.877)$	$\Lambda_{1,2} = 0.5262 \pm 2.3472i$, $\Lambda_3 = -2.8372$

Table 2. Lyapunov Exponents vs. α for Model (1)

α	LE1	LE2	LE3	dim(LE)
0.7	0.0182	-0.8429	-7.3948	1.88847
0.8	0.4326	-0.0034	-5.3810	2.079762
0.9	0.1163	-0.0685	-3.0441	2.01570
0.95	0.0529	-0.1489	-2.2316	1.956981
1.0	0.2045	-0.0038	-2.0108	2.099811

Table 3. Revised set of parameter values employed in this research, adapted from the model by Shabestari et al. [75]

a_1	2.04	a_2	0.10	a_3	1.09	a_4	-1.08
a_5	0.03	a_6	-0.06	a_7	2.01	a_8	0.22
a_9	-3.84	a_{10}	-1.20	a_{11}	0.30	a_{12}	1.37
a_{13}	-0.30	a_{14}	0.22	a_{15}	0.30	a_{16}	-1.35
a_{17}	0.50	a_{18}	-0.42	a_{19}	-0.15	a_{20}	-0.19
a_{21}	-0.56						

series solution for system (1):

$$\hat{u}(t) \simeq \sum_{k=0}^{K} \hat{U}(\hat{k})\iota^{\alpha k},$$
$$\hat{v}(t) \simeq \sum_{k=0}^{K} \hat{V}(\hat{k})\iota^{\alpha k},$$
$$\hat{w}(t) \simeq \sum_{k=0}^{K} \hat{W}(\hat{k})\iota^{\alpha k}.$$

For the MSGDTM approach, the series solution of system (1) is obtained similarly for $\hat{u}(t)$, $\hat{v}(t)$, and $\hat{w}(t)$.

4.3. MSGDTM and JSCSM error analysis

The approximation errors of the JSCSM and the MSGDTM when applied to the fractional glucose-insulin model are discussed here. The error is computed as the L_2-norm for the difference between the approximate solutions and a reference solution obtained using a high-accuracy numerical method.

For a given solution component $\hat{u}(t)$, the L_2-norm of the error is defined as:

$$\text{Error}(\hat{u}) = \sqrt{\frac{1}{M}\Sigma_{j=1}^{M}\big(\hat{u}_{\text{approx}}(\iota_j) - \hat{u}_{\text{ref}}(\iota_j)\big)^2},$$

where M is the total number of time points in the interval $[0, T]$, and $\hat{u}_{\text{approx}}(\iota_j)$ and $\hat{u}_{\text{ref}}(\iota_j)$ denote the approximate and reference solutions for the time point ι_j.

Similarly, the errors for $\hat{v}(t)$ and $\hat{w}(t)$ are defined. The total error is then given as:

$$\text{Total Error} = \sqrt{\text{Error}(\hat{u})^2 + \text{Error}(\hat{v})^2} + \sqrt{\text{Error}}(\hat{w})^2.$$

The procedure for error evaluation is the following:

(1) Compute $\hat{u}_{\text{JSCSM}}(t)$, $\hat{v}_{\text{JSCSM}}(t)$, and $\hat{w}_{\text{JSCSM}}(t)$ using JSCSM for a given truncation order N.
(2) Compute $\hat{u}_{\text{MSGDTM}}(t)$, $\hat{v}_{\text{MSGDTM}}(t)$, and $\hat{w}_{\text{MSGDTM}}(t)$ using MSGDTM for the same truncation order N.
(3) Compare both approximate solutions with a high-accuracy reference solution, $\hat{u}_{\text{ref}}(t)$, $\hat{v}_{\text{ref}}(t)$, and $\hat{w}_{\text{ref}}(t)$, obtained using a reliable numerical method such as the fractional Runge-Kutta method.
(4) Compute the L_2-norm for both methods.

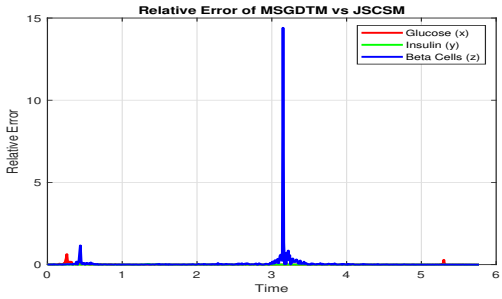
The approximation errors for JSCSM and MSGDTM are compared across different truncation orders ($N = 5, 10, 15$) in Table 4. The table highlights the superiority of MSGDTM in achieving lower errors for the same truncation order.

From Table 4, it is evident the following:

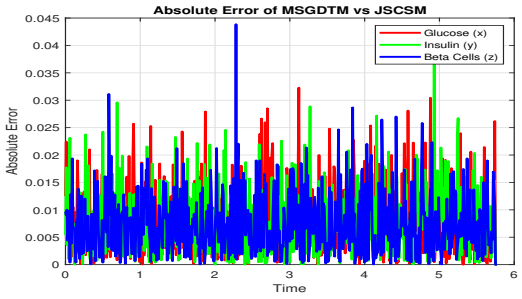
- Both JSCSM and MSGDTM achieve higher accuracy as the truncation order N increases.
- MSGDTM consistently outperforms JSCSM in terms of approximation accuracy, achieving lower errors for all truncation orders tested.

Table 4. Approximation errors for JSCSM and MSGDTM at different truncation orders

Truncation Order (N)	Error (JSCSM)	Error (MSGDTM)
5	3.21×10^{-2}	2.11×10^{-2}
10	1.47×10^{-2}	8.95×10^{-3}
15	7.63×10^{-3}	4.02×10^{-3}

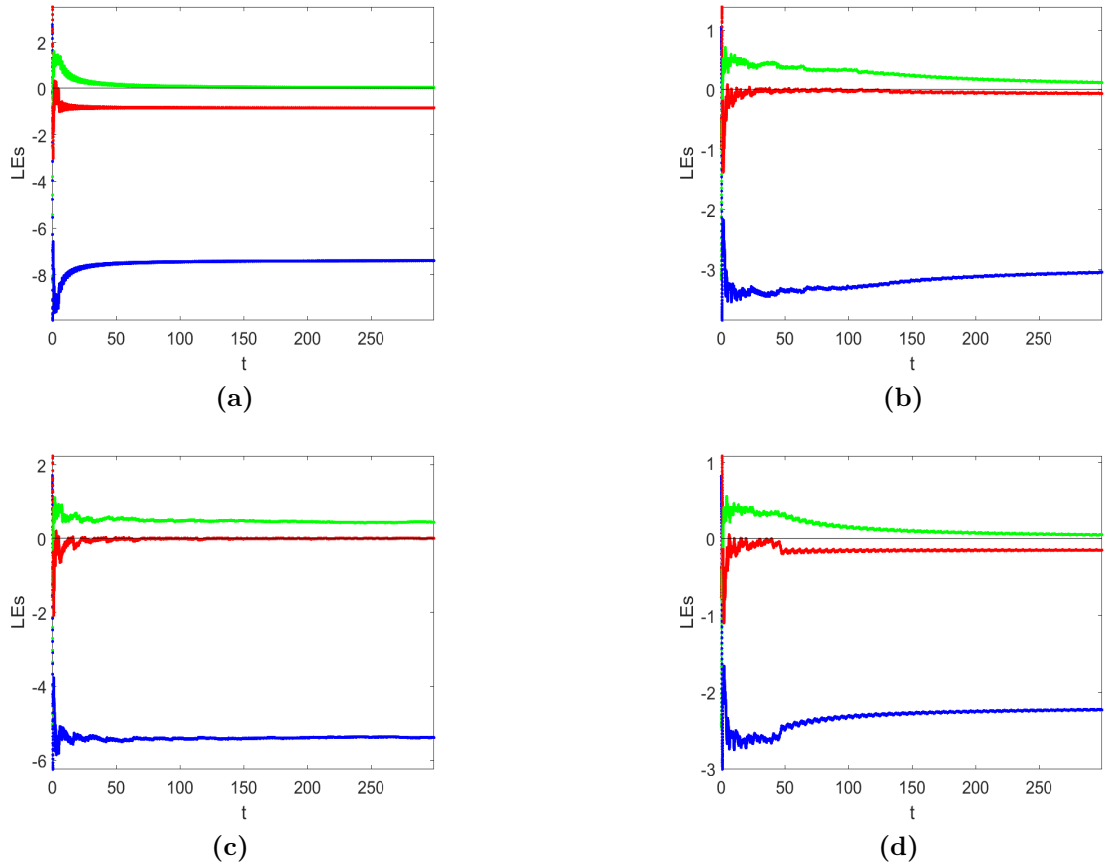


(g) Relative error of MSGDTM.



(h) Relative error of JSCSM

Figure 1. Relative error of MSGDTM versus JSCSM



(a) **(b)** **(c)** **(d)**

Figure 2. Lyapunov exponents for Model (1)

- The faster convergence of MSGDTM can be attributed to its efficient handling of fractional dynamics over subintervals.

This analysis demonstrates the effectiveness of both methods in solving fractional-order systems. While MSGDTM offers superior accuracy, JSCSM remains a computationally viable approach for moderate truncation orders.

5. Model simulation and control analysis

This section presents graphical representations of the Model (1) under varying fractional orders and control implementations. Figures 5 and 6 display the temporal progression of glucose ($\hat{u}$), insulin ($\hat{v}$), and beta-cell function ($\hat{w}$) for both

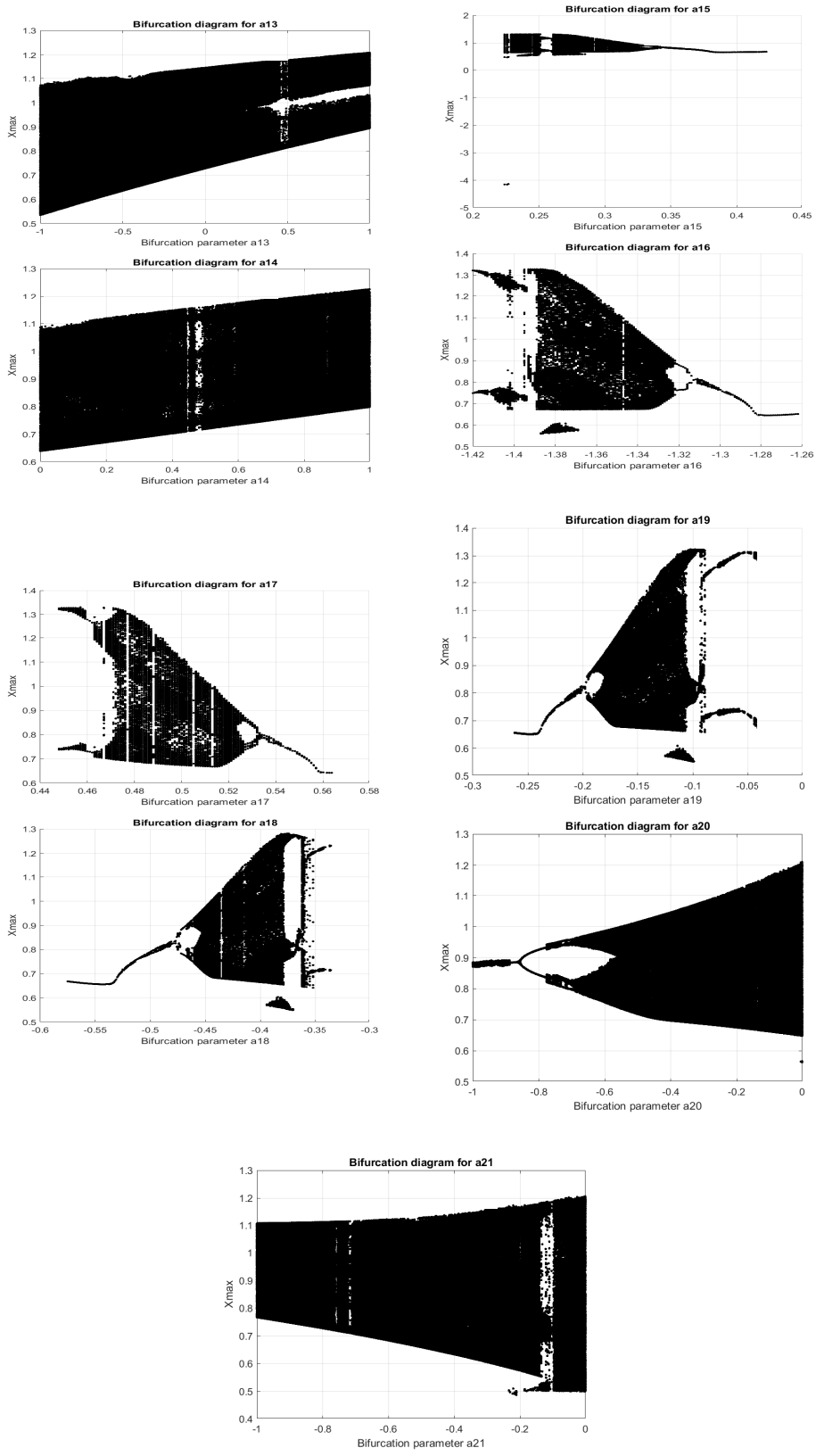


Figure 3. Model bifurcation (1)

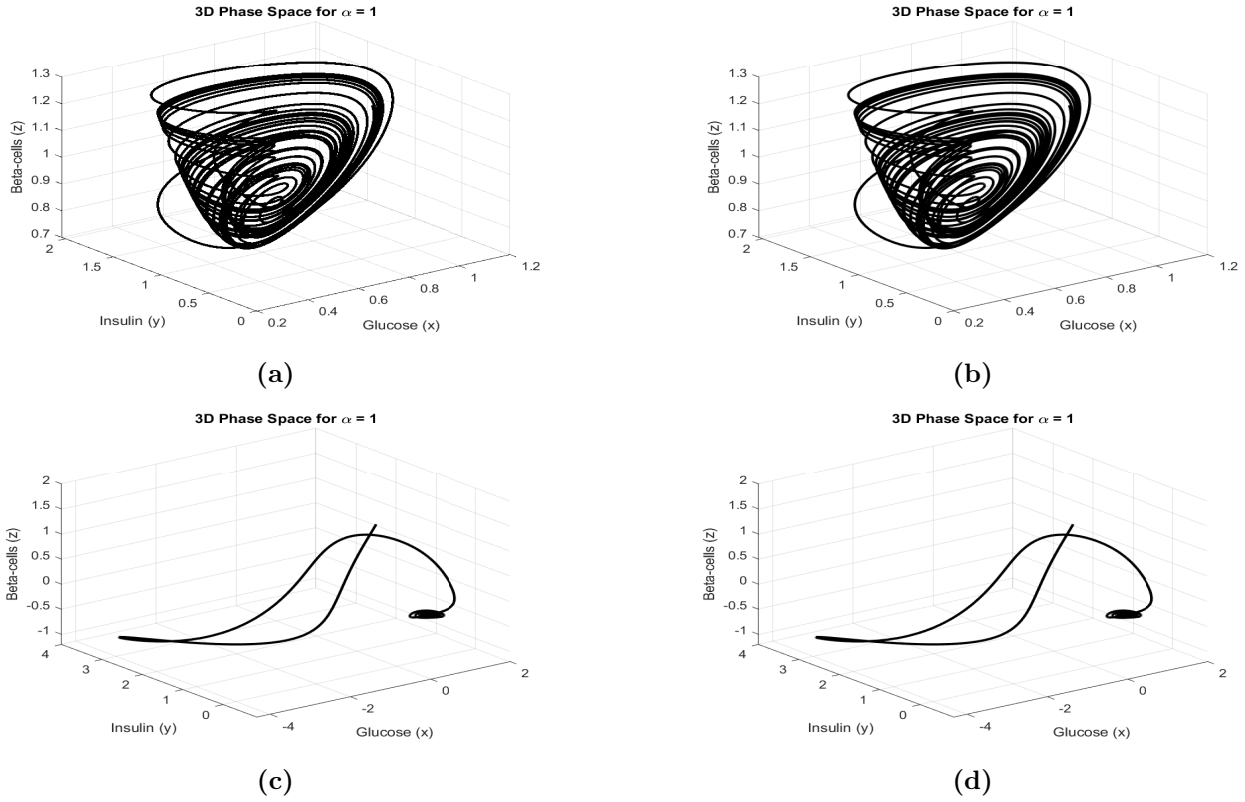


Figure 4. Compared between the 3D phases of (1) illustrated in (a), (b) and the controlled system (2) illustrated in (c), (d) under JSCSM and MSGDTM for $\alpha = 1$

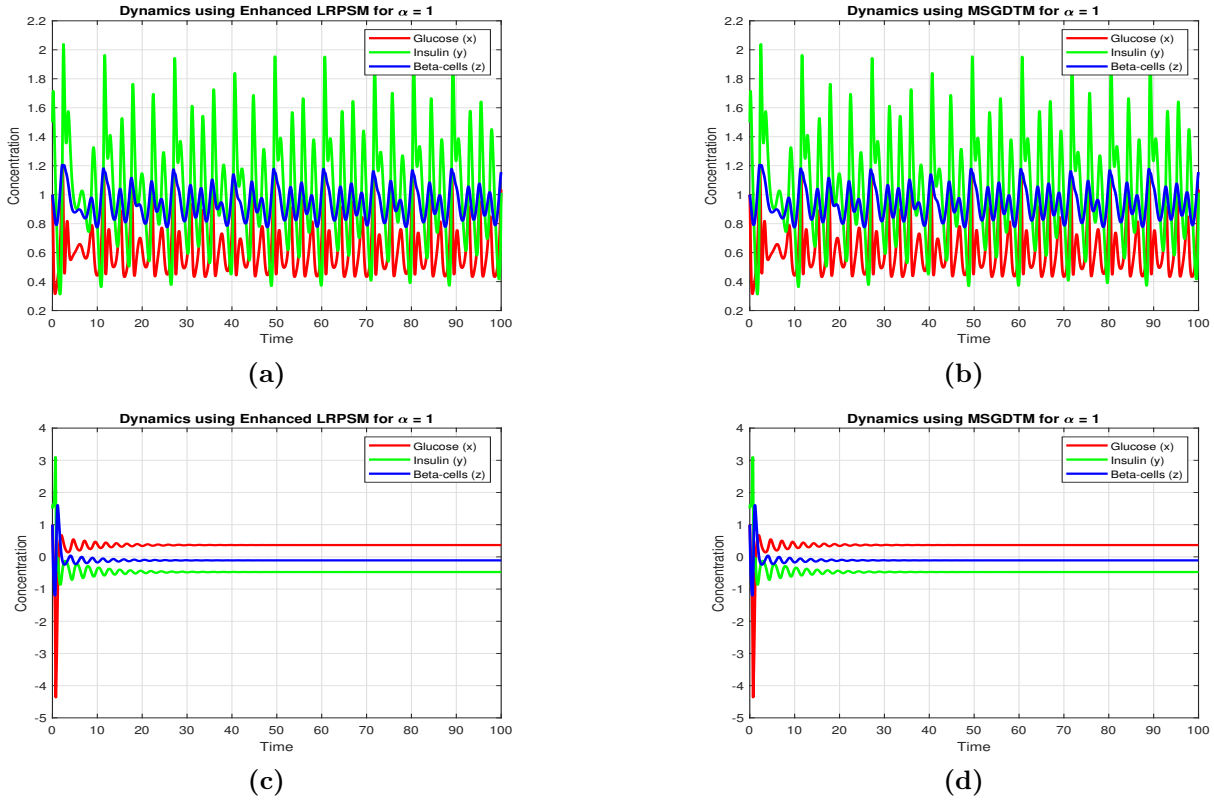


Figure 5. The time series of (1) shown in (a), (b) and the controlled system (2) shown in (c), (d) for $\alpha = 0.98$ under JSCSM and MSGDTM

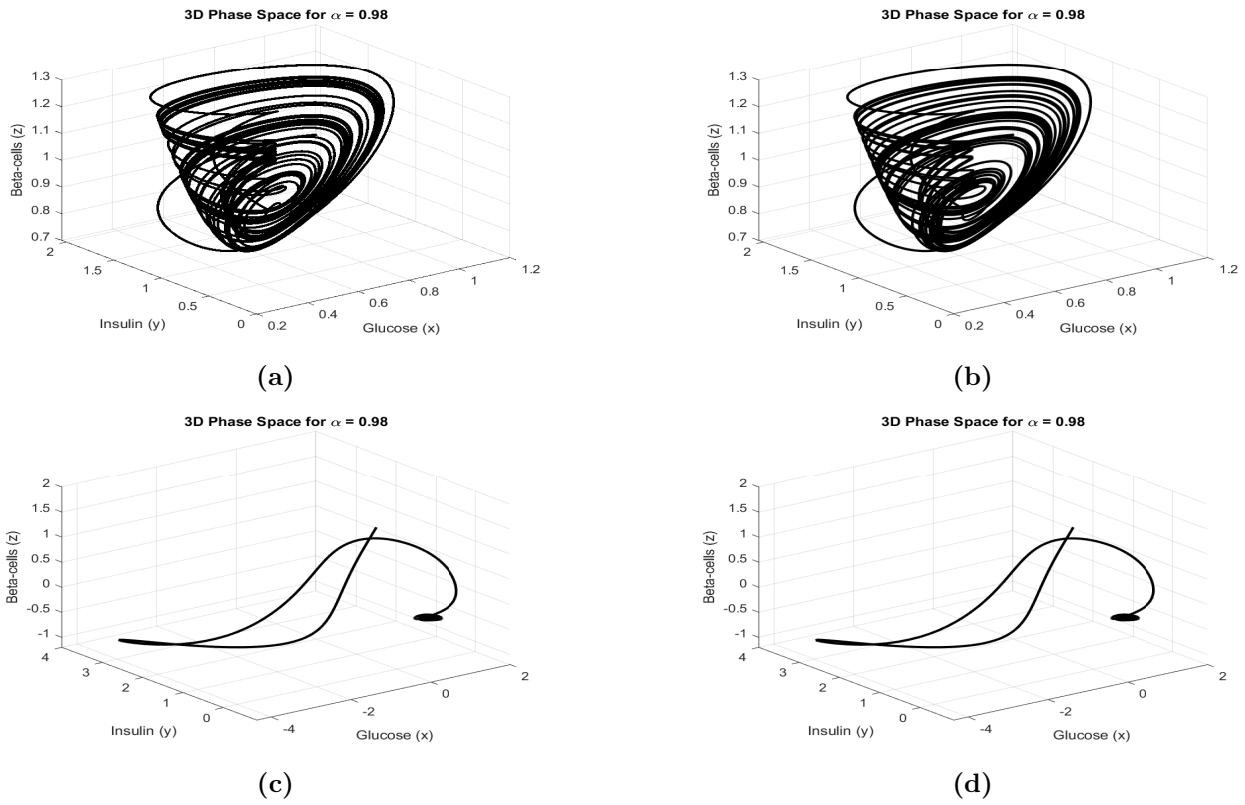


Figure 6. Compared between the 3D phases of (1) illustrated in (a), (b) and the controlled system (2) illustrated in (c), (d) under JSCSM and MSGDTM for $\alpha = 0.98$

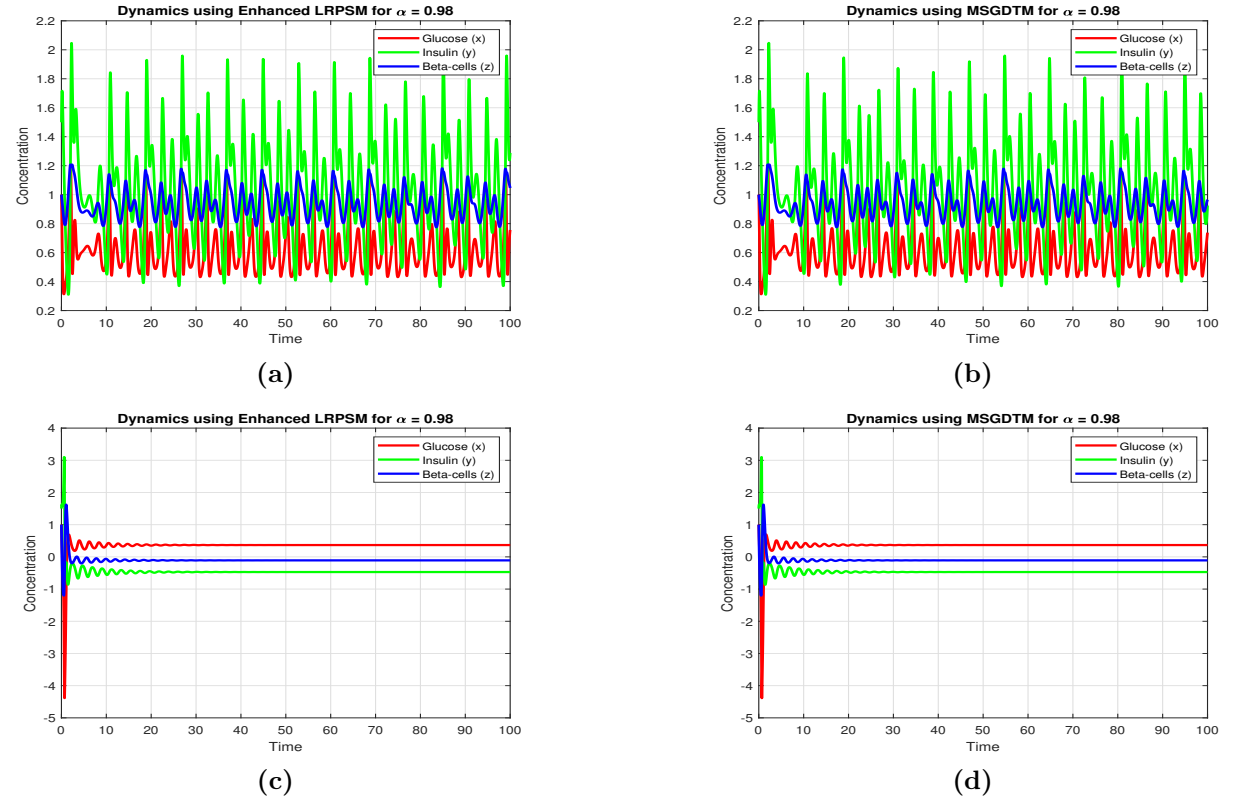


Figure 7. The time series of (1) shown in (a), (b) and the controlled system (2) shown in (c), (d) for $\alpha = 1$ under JSCSM and MSGDTM

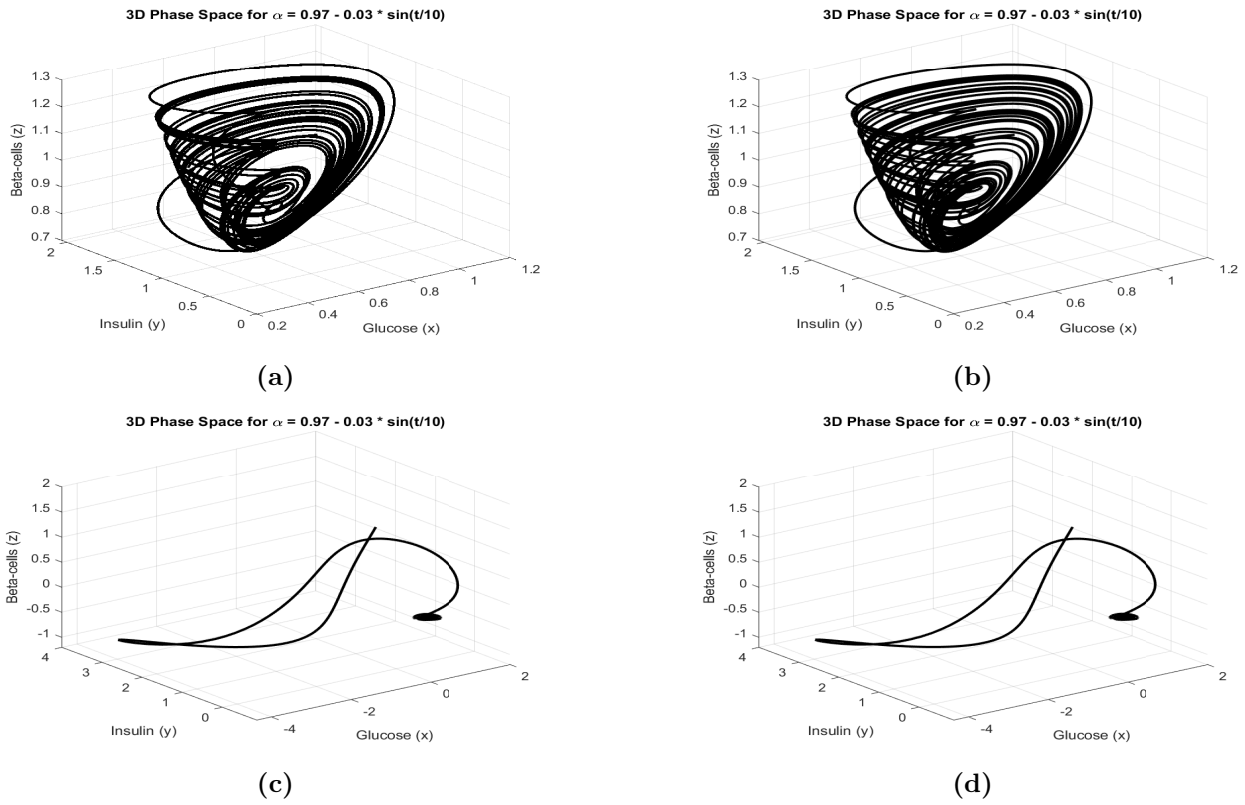


Figure 8. Compared between the 3D phases of (1) illustrated in (a), (b) and the controlled system (2) illustrated in (c), (d) under JSCSM and MSGDTM for $\alpha = 0.97 - 0.03 \times sin(t/10)$

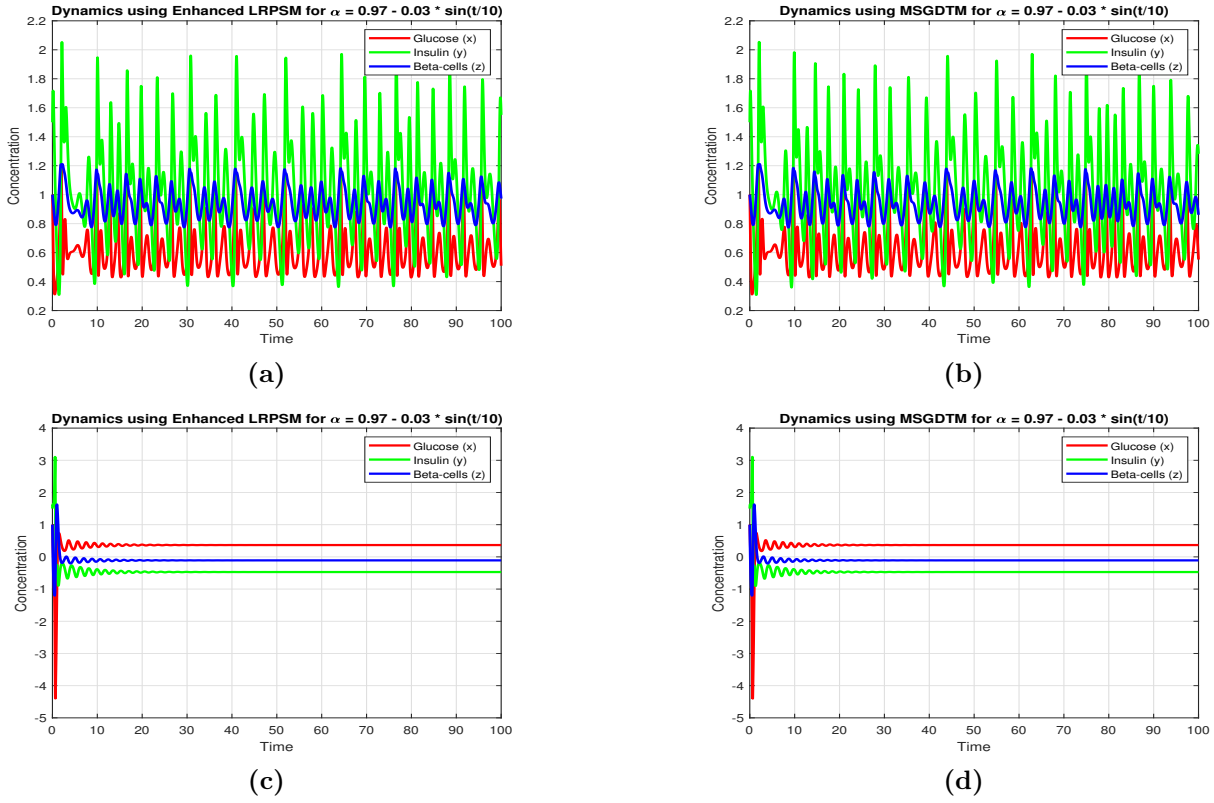


Figure 9. The time series of (1) shown in (a), (b) and the controlled system (2) shown in (c), (d) for $\alpha = 0.97 - 0.03 \times sin(t/10)$ under JSCSM and MSGDTM

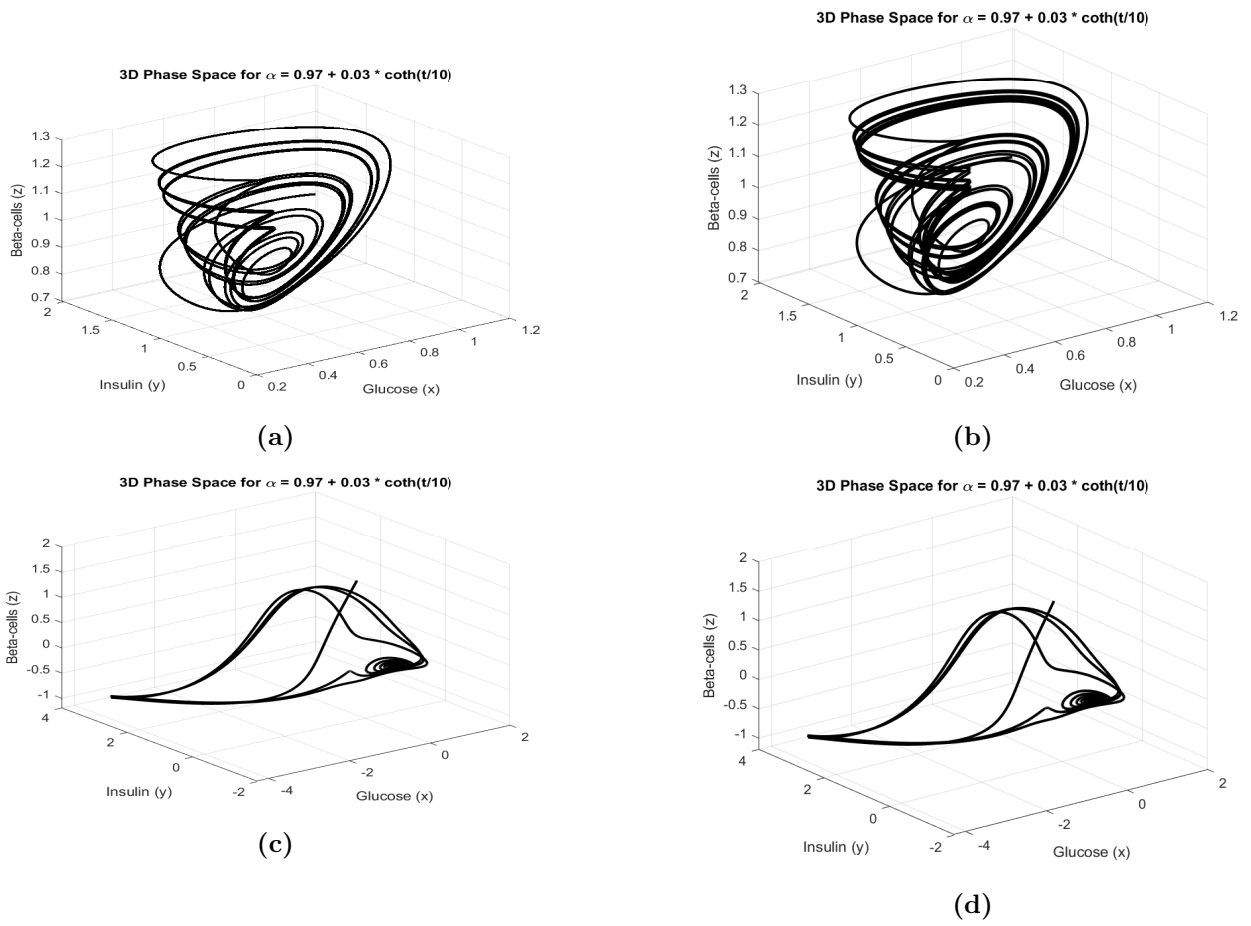


Figure 10. Compared between the 3D phases of (1) illustrated in (a), (b) and the controlled system (2) illustrated in (c), (d) under JSCSM and MSGDTM for $\alpha = 0.97 + 0.03 \times coth(t/10)$

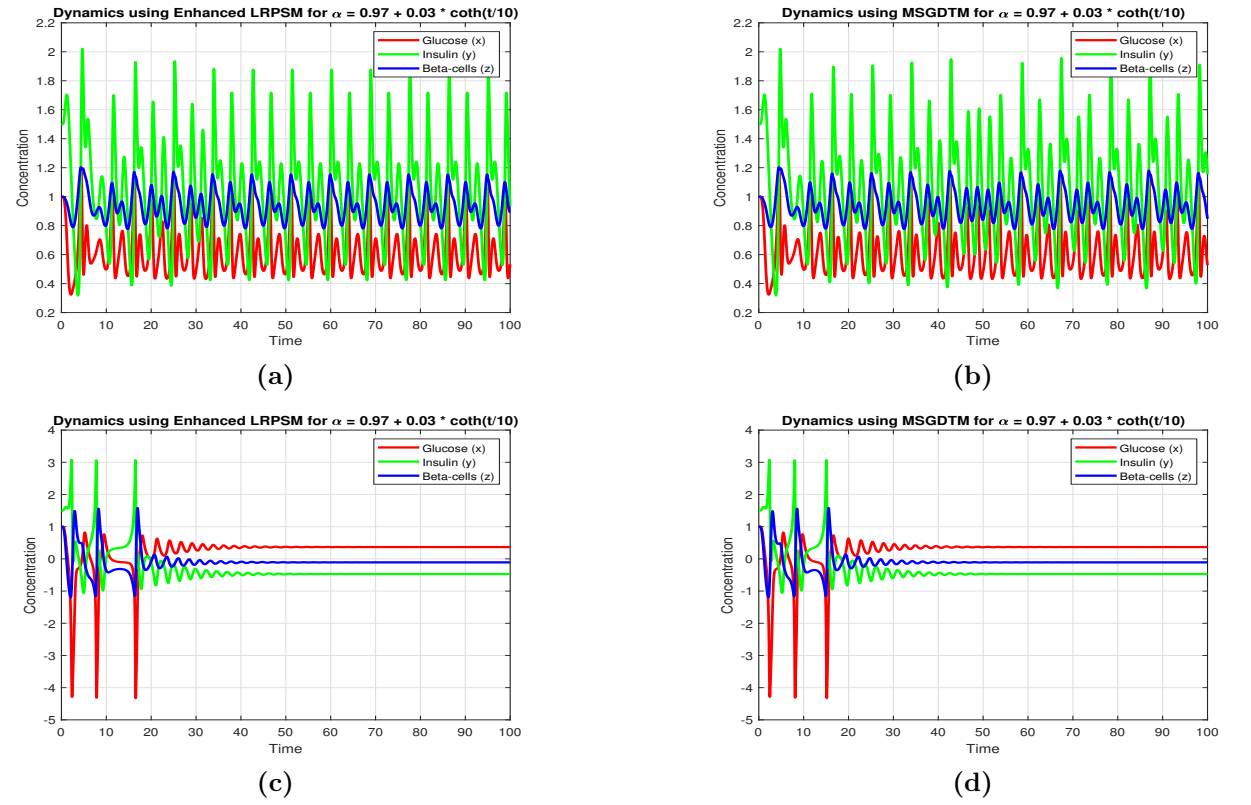


Figure 11. The time series of (1) shown in (a), (b) and the controlled system (2) shown in (c), (d) for $\alpha = 0.97 + 0.03 \times coth(t/10)$ under JSCSM and MSGDTM

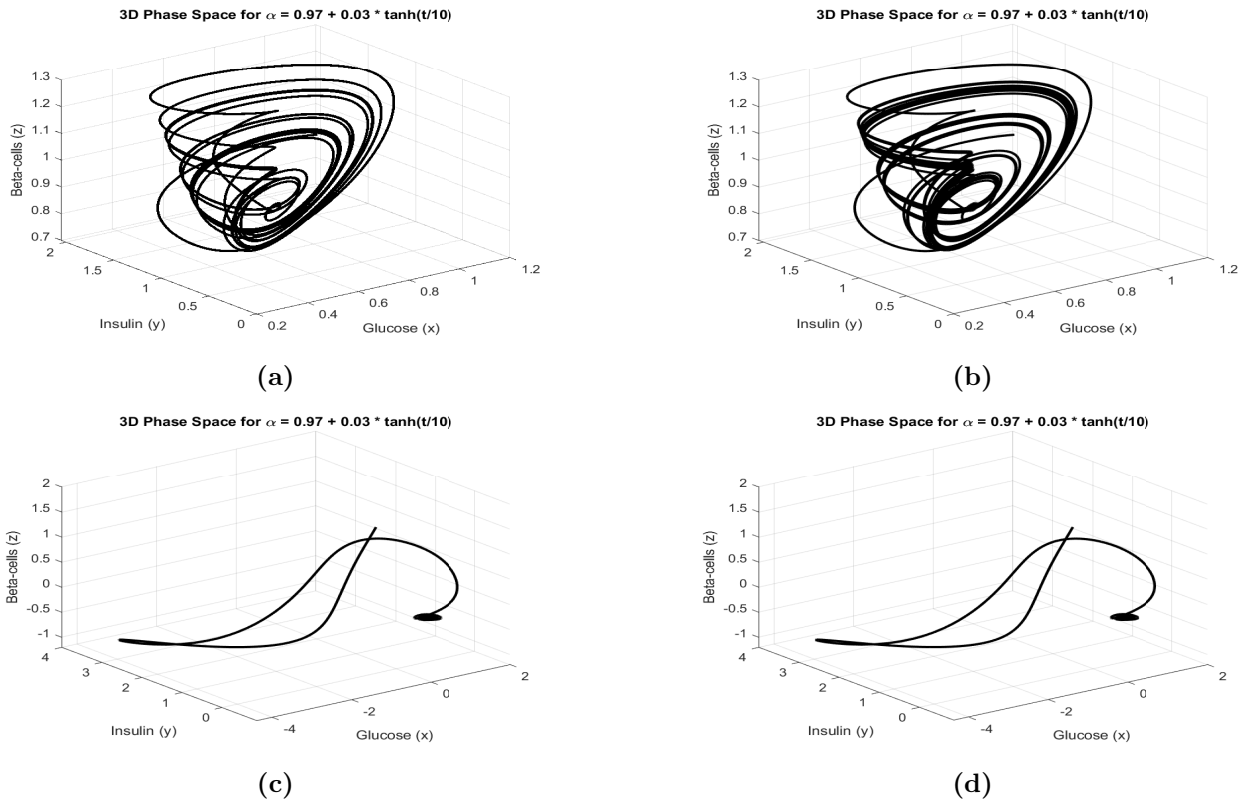


Figure 12. Compared between the 3D phases of (1) illustrated in (a), (b) and the controlled system (2) illustrated in (c), (d) under JSCSM and MSGDTM for $\alpha = 0.97 + 0.03 \times \tanh(t/10)$

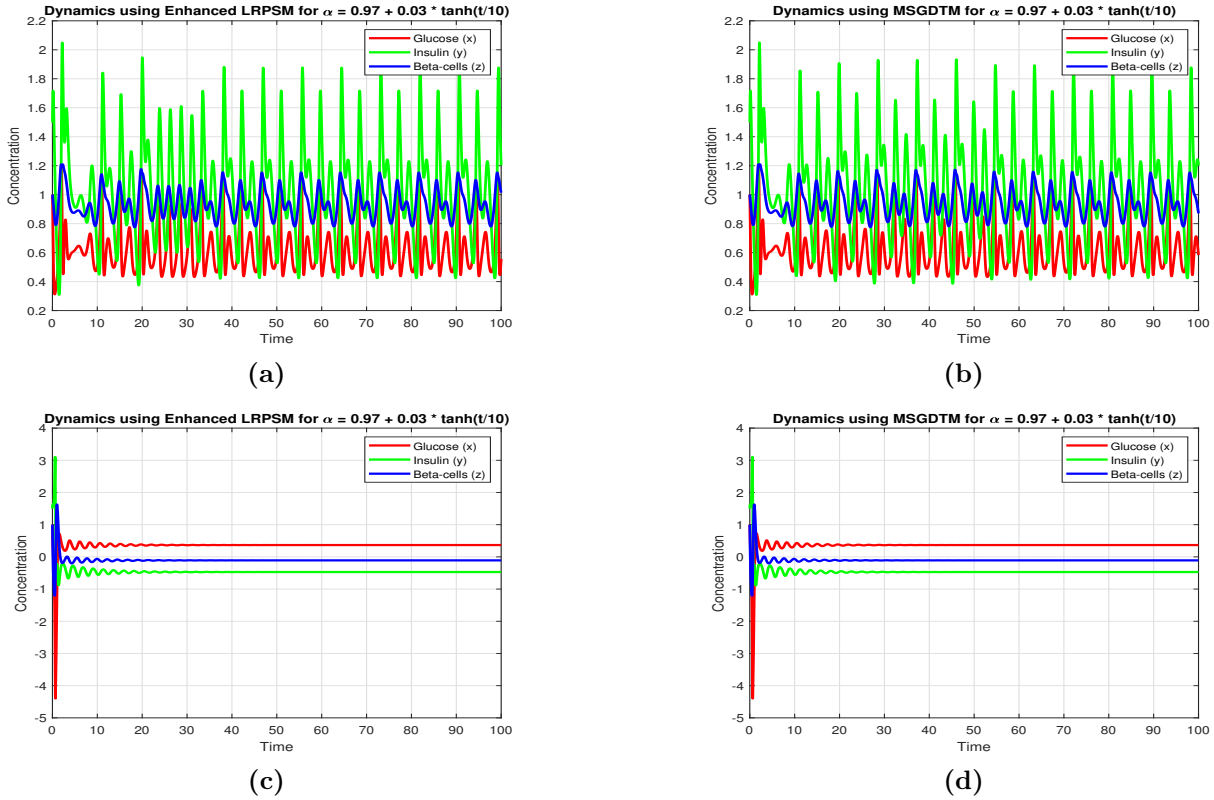


Figure 13. The time series of (1) shown in (a), (b) and the controlled system (2) shown in (c), (d) for $\alpha = 0.97 + 0.03 \times \tanh(t/10)$ under JSCSM and MSGDTM

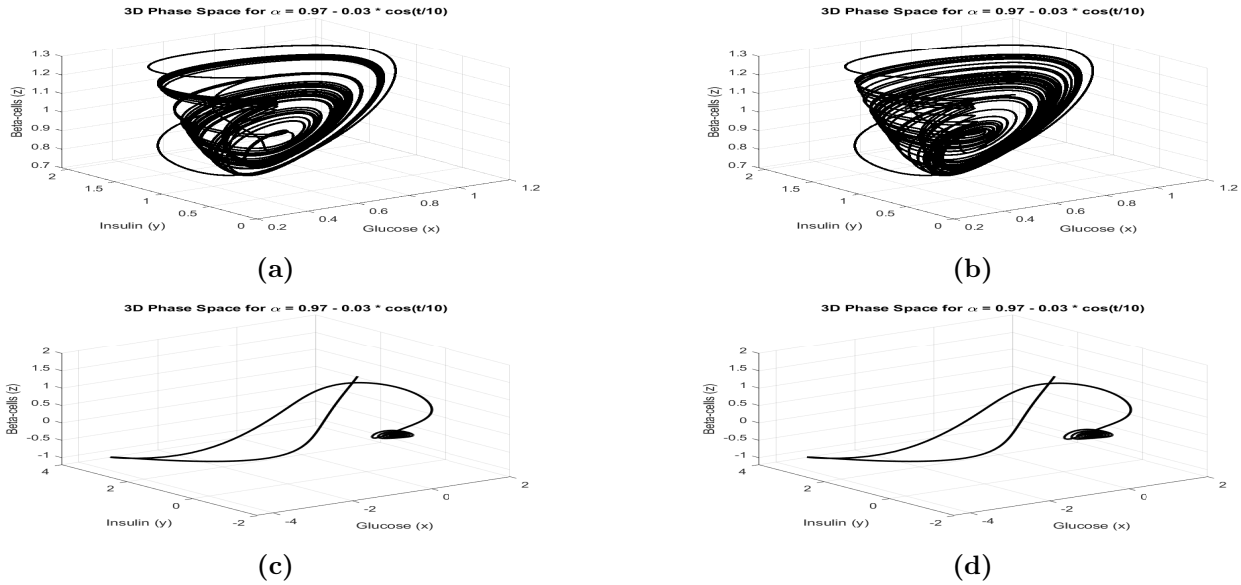


Figure 14. Compared between the 3D phases of (1) illustrated in (a), (b) and the controlled system (2) illustrated in (c), (d) under JSCSM and MSGDTM for $\alpha = 0.97 - 0.03 \times cos(t/10)$

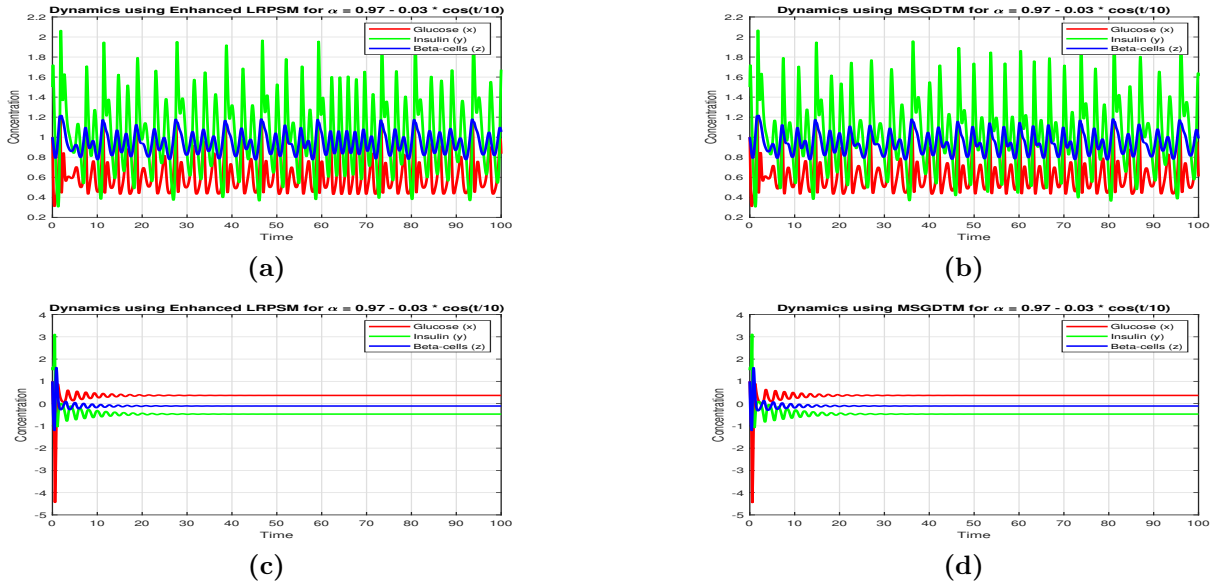


Figure 15. The time series of (1) shown in (a), (b) and the controlled system (2) shown in (c), (d) for $\alpha = 0.97 - 0.03 \times cos(t/10)$ under JSCSM and MSGDTM

uncontrolled and controlled scenarios at orders $\alpha = 1$ and $\alpha = 0.98$. In contrast, Figures 7 through 9 investigate more intricate fractional order variations, such as sinusoidal fluctuations ($\alpha = 0.97 - 0.03\sin(t/10)$), hyperbolic tangent adjustments ($\alpha = 0.97 + 0.03\tanh(t/10)$), and other time-dependent modifications. These visualizations reveal transitions between equilibrium, oscillatory dynamics, and chaotic behavior, underscoring the model's responsiveness to fractional order variations. Additionally, Figure 10 showcases a phase plane projection (xyz), providing a comparative visualization of system trajectories and attractor structures under different fractional orders and control strategies.

6. Discussion

This study presented a Model (1) to capture the memory-dependent and nonlinear behaviors inherent in metabolic control systems. Using the Caputo derivative framework, combined with two numerical schemes (MSGDTM and JSCSM), we explored how fractional-order dynamics and key parameters affect system stability, chaos, and control. This study explored a Model (1) by employing the following two numerical techniques: the MSGDTM and the JSCSM. The model incorporates memory-dependent Caputo fractional derivatives, allowing for more accurate simulation of real biological processes that exhibit hereditary

and nonlocal characteristics. Fractional-order glucose-insulin regulation is highlighted in this study. The model captures nonlocal and memory-dependent glucose-insulin interactions by incorporating fractional derivatives. This feature provides a more realistic representation of glucose regulation than traditional integer-order models. The behavior of the system is highly dependent on fractional orders and parameter variations. In healthy physiological states, fractional orders close to $\alpha = 1$ stabilize near equilibrium points. However, for $\alpha < 1$, the system exhibits oscillatory or chaotic behaviors, potentially mimicking pathological conditions like insulin resistance or glucose instability. This study provides valuable insights into how deviations in physiological conditions can lead to metabolic disorders and how fractional parameters influence system stability. The MSGDTM provides superior numerical accuracy, faster convergence, and greater computational efficiency compared to the JSCSM. It is particularly effective at handling nonlinear and memory-dependent characteristics of fractional glucose-insulin systems. As a result of lower approximation errors, MSGDTM is a more reliable method for solving fractional differential equations. Furthermore, this study explores how control mechanisms influence chaotic glucose-insulin dynamics. A controlled system exhibits significant improvements in stability, suggesting therapeutic interventions to prevent metabolic disorders. By using LE analysis and bifurcation diagrams, diabetes management strategies can be developed. Due to this, fractional-order modeling is becoming more important in biomedicine. Furthermore, it improves glucose-insulin dynamics to design therapeutic strategies for diabetes management. To improve real-world application, stochastic effects, environmental influences, or adaptive control strategies might be incorporated. Furthermore, integrating patient-specific data could enhance predictive modeling and optimize diabetes treatment.

7. Conclusion

In this work, we investigated a Model (1) incorporating Caputo fractional derivatives to capture memory effects and hereditary characteristics inherent in biological systems, particularly glucose-insulin interactions. Two advanced numerical techniques—the MSGDTM and the JSCSM—were employed to solve the model and analyze its dynamic behavior. Through comprehensive stability, bifurcation, and chaos analyses, we identified key parameters (a_{16} to a_{21}) that govern transitions between equilibrium, oscillatory, and chaotic dynamics, providing insights into mechanisms such as β-cell stress, insulin production, and glucose feedback. Numerical simulations demonstrated that MSGDTM outperforms JSCSM and other classical schemes in terms of accuracy, convergence speed, computational stability, and efficient handling of nonlocal memory terms, particularly in capturing nonlinear and oscillatory behaviors over long time intervals and near chaotic regimes. The bifurcation and Lyapunov analyses further confirmed that fractional-order models reflect more realistic physiological behavior compared to their integer-order counterparts, with graphical results emphasizing system sensitivity to fractional order variations ($\alpha = 0.97$ to 1.0) and validating the effectiveness of linear control strategies in stabilizing chaotic fluctuations. Based on these findings, fractional modeling is important in reproducing realistic glucose-insulin dynamics and informing improved diabetes treatment interventions. Although limitations remain—such as the restricted range of simulated fractional orders—the overall model remains biologically consistent, with negative parameters interpreted as inhibitory or decay processes. Looking ahead, we plan to extend the analysis to broader ranges of fractional orders, incorporate stochastic perturbations and time-delay effects, and integrate patient-specific clinical data to enhance the model's applicability for personalized treatment planning. This study highlights the value of fractional calculus and the robustness of MSGDTM as a powerful, adaptable tool for solving complex nonlinear biomedical systems.

Acknowledgments

The authors extend their appreciation to Umm Al-Qura University, Saudi Arabia, for supporting this research under Grant No. 25UQU4340608GSSR02.

Funding

This research work was funded by Umm Al-Qura University, Saudi Arabia, under Grant No. 25UQU4340608GSSR02.

Conflict of interest

The authors declare they have no competing interests.

Author contributions

Conceptualization: Sayed Saber, Brahim Dridi
Investigation: Sayed Saber, Abdullah Alahmari, Mohammed Messaoudi

Methodology: Sayed Saber
Formal analysis: Sayed Saber, Brahim Dridi
Writing–original draft: Abdullah Alahmari, Mohammed Messaoudi
Writing–review & editing: All authors

Availability of data

Not applicable.

AI tools statement

All authors confirm that no AI tools were used in the preparation of this manuscript.

References

1. Zabidi NA, Majid ZA, Kilicman A, et al. Numerical solution of fractional differential equations with Caputo derivative by using numerical fractional predict–correct technique. *Adv Cont Discr Mod.* 2022;2022:1-23.
2. Podlubny I. *Fractional Differential Equations.* San Diego: Academic Press; 1999.
3. Arena P, Caponetto R, Fortuna L, and Porto M. *Nonlinear Noninteger Order Circuits and Systems – An Introduction.* Singapore: World Scientific; 2000.
4. Nisar KS, Farman M, Abdel-Aty, Ravichandran C. A review of fractional-order models for plant epidemiology. *Prog Fract Differ Appl.* 2024;10:489-521.
5. Ahmed E, Elgazzar AS. On fractional order differential equations model for nonlocal epidemics. *Physica A.* 2007;379(2):607-614.
6. Li W, Wang Y, Cao J, Abdel-Aty M. Dynamics and backward bifurcations of SEI tuberculosis models in homogeneous and heterogeneous populations. *J Math Anal Appl.* 2025;543:128924.
7. Nisar KS, Farman M, Abdel-Aty M, Ravichandran C. A review of fractional order epidemic models for life sciences problems: past, present and future. *Alexandria Eng J.* 2024;95:283-305.
8. Bagley RL, Calico RA. Fractional order state equations for the control of viscoelastically damped structures. *J Guid Control Dyn.* 1991; 14:304-311.
9. Heaviside O. *Electromagnetic Theory.* New York: Chelsea Publishing Company; 1971.
10. Kusnezov D, Bulgac A, Dang GD. Quantum Lévy processes and fractional kinetics. *Phys Rev Lett.* 1999;82:1136-1139.
11. Almutairi N, Saber S. Existence of chaos and the approximate solution of the Lorenz–Lü–Chen system with the Caputo fractional operator. *AIP Adv.* 2024;14:015112.
12. Hilfer R. *Applications of Fractional Calculus in Physics.* Singapore: World Scientific; 2000:87-130.
13. Saber S. Control of chaos in the Burke-Shaw system of fractal-fractional order in the sense of Caputo-Fabrizio. *J Appl Math Comput Mech.* 2024;23(1):83-96.
14. Ahmed K, Adam H, Almutairi N, Saber S. Analytical solutions for a class of variable-order fractional Liu system under time-dependent variable coefficients. *Results Phys.* 2024;56:107311.
15. Almutairi N, Saber S. On chaos control of nonlinear fractional Newton-Leipnik system via fractional Caputo-Fabrizio derivatives. *Sci Rep.* 2023;13:22726.
16. Almutairi N, Saber S, and Ahmad H. The fractal-fractional Atangana-Baleanu operator for pneumonia disease: stability, statistical and numerical analyses. *AIMS Math.* 2023;8(12):29382-29410.
17. Almutairi N, Saber S. Chaos control and numerical solution of time-varying fractional Newton-Leipnik system using fractional Atangana-Baleanu derivatives. *AIMS Math.* 2023;8(11):25863-25887.
18. Petras I. *Fractional-Order Nonlinear Systems: Modeling, Analysis and Simulation.* Berlin: Springer; 2011.
19. Ahmed KIA, Adam HDS, Almutairi N, et al. Analytical solutions for a class of variable-order fractional Liu system under time-dependent variable coefficients. *Results Phys.* 2024;56:107311.
20. Alhazmi M, Dawalbait F, Aljohani A, et al. Numerical approximation method and chaos for a chaotic system in sense of Caputo-Fabrizio operator. *Thermal Sci.* 2024;28(6B):5161-5168.
21. Almutairi N, Saber S. Chaos control and numerical solution of time-varying fractional Newton-Leipnik system using fractional Atangana-Baleanu derivatives. *AIMS Math.* 2023;8:25863-25887.
22. Alsulami A, Alharb RA, Albbogami TM, et al. Controlled chaos of a fractal–fractional Newton-Leipnik system. *Thermal Sci.* 2024;28(6B).
23. Alshehri MH, Saber S, and Duraihem FZ. Dynamical analysis of fractional-order of IVGTT glucose–insulin interaction. *Int J Nonlin Sci Numer Simul.* 2023;24:1123-1140.
24. Alshehri MH, Duraihem FZ, Alalyani A, et al. A caputo (discretization) fractional-order model of glucose-insulin interaction: numerical solution and comparisons with experimental data. *J Taibah Univ Sci.* 2021;15:26-36.
25. Sayed Saber, Eihab Bashier, Alzahrani S., Noaman IA. A mathematical model of glucose-insulin interaction with time delay. *J. Appl Comput Math.* 2018;7(3):1-5.
26. Ahmed KIA, Adam HDS, Yousiff MY, et al. Different strategies for diabetes by mathematical modeling: applications of fractal-fractional derivatives in the sense of Atangana-Baleanu. *Results Phys.* 2023;26: 106892.
27. Ahmed KIA, Adam HDS, Yousiff MY, et al. Different strategies for diabetes by mathematical

modeling: modified minimal model. *Alexandria Eng J.* 2023;80:74-87.
28. Derouich M, Boutayeb A. The effect of physical exercise on the dynamics of glucose and insulin. *J Biomech.* 2002;35(7): 911–917.
29. Mukhopadhyay A, DeGaetano A, Arino O. Modeling the intravenous glucose tolerance test: a global study for a single-distributed-delay model. *Discrete Contin Dyn Syst Ser B.* 2004;228(4):407-417.
30. Tornheim K. Are metabolic oscillations responsible for normal oscillatory insulin secretion? *Diabetes.* 1997;46(9):1375-1380.
31. Dalla Man C, Caumo A, Basu R, Rizza R, Toffolo G, and Cobelli C. Minimal model estimation of glucose absorption and insulin sensitivity from oral test: Validation with a tracer method. *Am J Physiol Endocrinol Metab.* 2004;287(4):E637-E643.
32. Ahmed KIA, Mirgani SM, Seadawy A, et al. A comprehensive investigation of fractional glucose-insulin dynamics: existence, stability, and numerical comparisons using residual power series and generalized Runge–Kutta methods. *J Taibah Univ Sci.* 2025;19(1):1-15.
33. Naik PA, Yeolekar BM, Qureshi S, et al. Global analysis of a fractional-Order hepatitis B virus model under immune response in the presence of cytokines. *Adv Theory Simul.* 2024;7:2400726.
34. Saber S, Alalyani A. Stability analysis and numerical simulations of IVGTT glucose-insulin interaction models with two time delays. *Math Model Anal.* 2022;27:383-407.
35. Haroon DS, Mohammed A, Safa MM, et al. An application of Newton's interpolation polynomials to the zoonotic disease transmission between humans and baboons system based on a time-fractal fractional derivative with a power-law kernel. AIP Adv. 2025;15(4):045217.
36. Danca MF. Lyapunov exponents of a discontinuous 4D hyperchaotic system of integer or fractional order. *Entropy.* 2018;20(5):337.
37. Zhuang P, Liu F, Anh V, and Turner I. Numerical methods for the variable-order fractional advection-diffusion equation with a nonlinear source term. *SIAM J Numer Anal*, 2009;47(3):1760-1781.
38. Almutairi N, Saber S. Application of a time-fractal fractional derivative with a power-law kernel to the Burke-Shaw system based on Newton's interpolation polynomials. *MethodsX.* 2024;12:102510.
39. Gómez-Aguilar JF. Chaos in a nonlinear Bloch system with Atangana–Baleanu fractional derivatives. *Numer Methods Partial Differ Equ.* 2018;34(5):1716-1738.
40. Atangana A, Baleanu D. New fractional derivatives with non-local and non-singular kernel: theory and application to heat transfer model. *Thermal Sci.* 2016;20:763-769.
41. Caputo M, Fabrizio M. A new definition of fractional derivative without singular kernel. *Prog Fract Differ Appl.* 2015;1:73-85.
42. Nosrati K, Volos C. Bifurcation analysis and chaotic behaviors of fractional-order singular biological systems. In: Pham VT, Vaidyanathan S, Volos C, Kapitaniak T, eds.*Nonlinear Dynamical Systems with Self-Excited and Hidden Attractors* Studies in Systems, Decision and Control, vol. 133. Cham:Springer; 2018.
43. Odibat ZM, Momani S. Modified homotopy perturbation method: application to quadratic Riccati differential equation of fractional order. *Chaos Solitons Fractals.* 2008;36:167-174.
44. Tsai P, Chen CK. An approximate analytic solution of the nonlinear Riccati differential equation. *J Franklin Inst.* 2010;347: 1850-1862.
45. Zeng DQ, Qin YM. The Laplace-Adomian-Padé technique for the seepage flows with the Riemann–Liouville derivatives. *Commun Fract Calc.* 2012;3:26-29.
46. Khan Y, Diblík J, Faraz N, Smarda Z. An efficient new perturbative Laplace method for space-time fractional telegraph equations. *Adv Differ Equ.*, 2012;2012:204.
47. Khan NA, Ara A, Khan NA. Fractional-order Riccati differential equation: analytical approximation and numerical results. *Adv Differ Equ.*, 2013;2013:185.
48. Odibat Z, Momani S. An algorithm for the numerical solution of differential equations of fractional order. *J Appl Math Inform.* 2008;26:15-27.
49. Kataria KK, Vellaisamy P. Saigo space–time fractional Poisson process via Adomian decomposition method. *Stat Probab Lett.* 2017;129:69-80
50. Haq F, Shah K, Rahman GU, Shahzad M. Numerical solution of fractional-order smoking model via Laplace-Adomian decomposition method. *Alexandria Eng J.* 2018;57:1061-1069.
51. Sirisubtawee S, Kaewta S. New modified Adomian decomposition recursion schemes for solving certain types of nonlinear fractional two-point boundary value problems. *Int J Math Math Sci.* 2017;2017:1–20.
52. Liu Q, Liu J, Chen Y. Asymptotic limit cycle of fractional Van der Pol oscillator by homotopy analysis method and memory-free principle. *Appl Math Model.* 2016;40(4): 3211-3220.
53. Freihat A, Momani S. Application of multistep generalized differential transform method for the solutions of the fractional-order Chua's system. *Discrete Dyn Nat Soc.* 2012;2012:1–13.
54. Wang H, Yang D, Zhu S. A Petrov–Galerkin finite element method for variable-coefficient fractional diffusion equations. *Comput Methods Appl. Mech Eng.* 2015;290:45-56.

55. Song H, Yi M, Huang J, Pan Y. Numerical solution of fractional partial differential equations by using Legendre wavelets. *Eng Lett.* 2016;24(3):358-364.
56. Lu H, Bates PW, Chen W, Zhang M. The spectral collocation method for efficiently solving PDEs with fractional Laplacian. *Adv Comput Math.* 2017;44(6):861–878.
57. Odibat Z, Momani S, Erturk VS. Generalized differential transform method: Application to differential equations of fractional order. *Appl Math Comput.* 2008;197(2):467-477.
58. Momani S, Odibat Z. A novel method for nonlinear fractional partial differential equations: Combination of DTM and generalized Taylor's formula. *J Comput Appl Math.* 2008;220(1–2):85-95.
59. Odibat Z, Momani S. A generalized differential transform method for linear partial differential equations of fractional order. *Appl Math Lett.* 2008;21(2):194-199.
60. Erturk VS, Momani S, Odibat Z. Application of generalized differential transform method to multi-order fractional differential equations. Commun Nonlinear Sci Numer Simulat. 2008;13(8):1642-1654.
61. Odibat ZM, Bertelle C, Aziz-Alaoui MA, Duchamp GHE. A multi-step differential transform method and application to non-chaotic or chaotic systems. Comput $\mathcal{E}$ Math Appl. 2010;59(4):1462-1472.
62. Ertürk VS, Odibat ZM, Momani S. An approximate solution of a fractional order differential equation model of human T-cell lymphotropic virus I (HTLV-I) infection of CD4 4^{+}T-cells. Comput E Mathem Appl 2011;62(3):996-1002.
63. Odibat ZM, Bertelle C, Aziz-Alaoui MA, Duchamp GHE. A multistep differential transform method and application to non-chaotic or chaotic systems. Comput Mathemat Appl. 2010;59(4):1462-1472.
64. Erturk VS, Odibat ZM, Momani S. An approximate solution of a fractional order differential equation model of human T-cell lymphotropic virus I (HTLV-I) infection of CD4 T-cells. Comput Math Appl. 2011;62(3):996– 1002.
65. Asad Freihat A, Momani S. Application of multistep generalized differential transform method for the solutions of the fractional-order chua's system. Discrete Dyn Nat Soc. 2012; 2012:427393.
66. Liu C-S. Counterexamples on Jumarie's three basic fractional calculus formulae for non-differentiable continuous functions. Chaos Solit Fract. 2018;109:219-222.
67. . Odibat Z, Momani S, Erturk VS. Generalized differential transform method: application to differential equations of fractional order. Appl Math Comput. 2008;197(2):467–477.
68. Joshi H, Yavuz M, Taylan O, Alkabaa A. Dynamic analysis of fractal-fractional cancer model under chemotherapy drug with generalized Mittag-Leffler kernel. Comput Methods Programs Biomed. 2025;260:108565.
69. Gundogdu H, Joshi H. Numerical analysis of time-fractional cancer models with different types of net killing rate. Mathemat. 2025; 13:536.
70. Hardik J. Mechanistic insights of COVID-19 dynamics by considering the influence of neurodegeneration and memory trace. Physica Scrip. 2024;99(3):35254.
71. Joshi H, Jha BK. Generalized diffusion characteristics of Calcium model with concentration and memory of cells: a spatiotemporal approach. Iran J Sci Technol Trans Sci. 2022;46:309–322.
72. Yavuz M, Mur R, Yildiz M, Joshi H. Mathematical modeling of middle east respiratory syndrome coronavirus with bifurcation analysis. Contemp Math [Internet]. 2024;5(3):3997-4012.
73. Erturk V, Zaman G, Momani S. A numeric analytic method for approximating a giving up smoking model containing fractional derivatives. Comput $\mathcal{E}$ Math Appl. 2012;64(10):3065-3074.
74. Elsadany AEA, El-Metwally HA, Elabbasy EM, et al. Chaos and bifurcation of a nonlinear discrete preypredator system. Comput Ecol Softw. 2012; 2(3):169-180.
75. Shabestari PS, Panahi S, Hatef B, et al. A new chaotic model for model (1). Chaos Sol Fract. 2018;112:44-51.

Sayed Saber *Sayed Saber is a Professor of Mathematics at Al-Baha University, Saudi Arabia, and Beni-Suef University, Egypt. His research interests span several complex variables, fractional calculus, chaos theory, and advanced computational methods with a focus on biomedical systems. He has published extensively in the areas of complex analysis and applied mathematics, with a particular emphasis on nonlinear dynamics and fractional differential equations. Prof. Dr. Saber has made significant contributions to the development and analysis of advanced techniques for solving D-bar equations on complex manifolds and investigating complex systems behavior. He is also recognized for his pioneering work in chaos control and fractional-order modeling, especially in biomedical and epidemiological applications.*

https://orcid.org/0000-0002-5790-3222

Brahim Dridi *Brahim Dridi is an Associate Professor of Mathematics at Umm Al-Qura University in Makkah, Saudi Arabia. His research centers on partial differential equations, with a focus on nonlinear problems involving exponential and logarithmic weights, as well as Kirchhoff-type equations. He has published extensively in peer-reviewed journals such as Mediterranean Journal of Mathematics, Mathematische Nachrichten, and Acta Applicandae Mathematicae. His recent work explores critical exponential growth, N-Laplacian equations, and sign-changing solutions in weighted frameworks. Dr. Dridi actively*

collaborates with researchers internationally.
https://orcid.org/0000-0001-5863-029X

Abdullah Alahmari *Dr. Abdullah Alahmari is a faculty member in the Mathematics Department at Umm Al-Qura University, Saudi Arabia. His research focuses on operator theory and functional analysis, with a growing interest in complex analysis. In functional analysis, his central interests are the study of spaces of functions, and more generally of topological vector spaces and their associated structures by means of topological, analytical and geometric methods, the study of Banach algebras, and the calculus of variations, especially variational convergence.*
https://orcid.org/0000-0002-9596-910X

Mohammed Messaoudi *Dr Mohammed Messaoudi holds a PhD degree in computer science from the University of Durham, United Kingdom. He has extensive experience in both industry and academia in UK, Canada and Saudi Arabia. He is currently working as an assistant professor at Imam Mohammad Ibn Saud Islamic University. Research area: Software Requirements engineering, optimization, and Modelling and Simulation.*
https://orcid.org/0009-0005-2954-1753

An International Journal of Optimization and Control: Theories & Applications
(https://accscience.com/journal/ijocta)



This work is licensed under a Creative Commons Attribution 4.0 International License. The authors retain ownership of the copyright for their article, but they allow anyone to download, reuse, reprint, modify, distribute, and/or copy articles in IJOCTA, so long as the original authors and source are credited. To see the complete license contents, please visit http://creativecommons.org/licenses/by/4.0/.

An International Journal of Optimization and Control: Theories & Applications
ISSN: 2146-0957 eISSN: 2146-5703
Vol.15, No.3, pp.483-492 (2025)
https://doi.org/10.36922/ijocta.7118

RESEARCH ARTICLE

Trajectory controllability of integro-differential system of fractional orders in Hilbert spaces

Urvashi Arora[1], Sachin Singh[2], V. Vijayakumar[3], and Anurag Shukla[4*]

[1]Manhattan University, Manhattan College Pkwy, Bronx, New York, United States of America
[2]Department of Electrical Engineering, IET Lucknow, India
[3]Department of Mathematics, School of Advanced Sciences, Vellore Institute of Technology, Vellore, Tamilnadu, India
[4]Department of Applied Sciences and Humanities, Rajkiya Engineering College Kannauj, Kannauj, India
urvashiaroraiitr@gmail.com, sachinsingh@ietlucknow.ac.in, vijaysarovel@gmail.com, anuragshukla259@gmail.com

ARTICLE INFO

Article History:
Received: December 19, 2024
1st revised: March 22, 2025
2nd revised: April 17, 2025
3rd revised: May 6, 2025
Accepted: May 7, 2025
Published Online: May 30, 2025

Keywords:
Trajectory controllability
Fractional order system
Integrodifferential system

Subject Classification 2020:
93B05, 93C10

ABSTRACT

The trajectory controllability for fractional order semilinear integrodifferential systems of order $\nu \in (0,1]$ and $\nu \in (1,2]$ is the subject of this paper. Monotonicity is an important characteristic in many communications applications in which digital-to-analog converter circuits are used. Such applications can function in the presence of nonlinearity, but not in the presence of non-monotonicity. Therefore, it becomes quite interesting to study a problem assuming the monotonicity of the nonlinear function. With the help of fractional calculus, adequate conditions have been developed to verify the trajectory controllability for fractional order semilinear integrodifferential system using the basics of monotone nonlinearity and coercivity. Finally, some examples are presented to demonstrate the viability of the acquired results.

CC BY

1. Introduction

The principles of fractional calculus and the fractional differential equation have dominated mathematics in recent decades. Some physical problems cannot be solved using differential equations of integer order, but they can be solved using differential equations of fractional order. As a result, numerous academics have recently made significant contributions to the fields of electromagnetics, control theory, signal, porous media, viscoelasticity, biological, engineering difficulties, image processing, fluid flow, diffusion, theology, and other fields. The notation of optimal controls has performed as an important tool in analysis and design of control systems. These kinds of issues can be determined with various signification of fractional derivatives. It has different applications in separate fields, for example, economics, the control of chemical outgrowths, biology, power systems, space technology, engineering, electronics, physics, robotics, transportation, chemistry, and so on; the solution of these types of seeds has become a significant work for young scholars. Controllability research, which was conceived by Kalman, began in earnest at the beginning of the 1960s. Since then, several studies have been conducted utilizing various methodologies in the setting of finite and infinite dimensional deterministic and stochastic systems, one can refer Arora and Sukavanam,[1] Bragdi and Hazi,[2] Davison and

*Corresponding Author

Kunze,[3] Debnath,[4] George,[5] Klamka,[6–8] Lions,[9] George et al.,[10] Nandakumaran and George,[11] Miller,[12] Cardetti and Gordina[13] Muslim and Kumar,[14] Shukla et al.,[15] Shukla et al.,[16] Wang et al.,[17] Jajarmi and Baleanu,[18] Kumar and Malik,[19] Liu and Li,[20] Muslim and Kumar,[14] Dineshkumar et al.,[21] Mahmudov et al.[22] Mahmudov et al.,[23] Shukla et al.,[24] Vijayakumar.[25–27]

In the setting of fractional systems having order $\nu \in (1, 2]$, Matar,[28] Wang and Zhou,[29] Zhou and Jiao[30] established sufficient criteria for the fractional-order evolution equations in the case of fractional systems of order $\nu \in (0, 1]$. In Kumar and Sukavanam,[31] Sukavanam and Kumar, [32] the authors provided adequate conditions for the approximate controllability of fractional-order semilinear delay control systems utilizing fixed point techniques, based on existence results for mild solutions. In the setting of fractional systems having order $\nu \in (1, 2]$, Kexue et al.[33] discussed the existence and exact controllability of nonlocal fractional systems of order $\nu \in (1, 2]$ in infinite-dimensional spaces by employing Sadovskii's fixed point theorem. In[34] explored mild solutions and approximate controllability of semilinear neutral integro-differential equations in Banach spaces, utilizing resolvent families, optimal control, and sufficient conditions under Lipschitz-type assumptions. In[35] established mild solution existence, uniqueness, and trajectory controllability of conformable Hilfer fractional stochastic systems using semigroup theory, stochastic analysis, and Banach fixed-point theorem. Shukla et al.[36] recently used a sequential technique to establish approximate controllability of fractional system of order $\nu \in (1, 2]$ with indefinite delay. In recent years, a new concept of controllability known as trajectory controllability (T-controllability) has developed as a new area of research, describing the path along which our system goes while under control. There is a scarcity of the literature on T-controllability. We strive to discover a control that drives the system along a predefined trajectory rather than one that steers from a given start state to the final state in T-controllability challenges. Depending on the course chosen, it may reduce some of the costs associated with steering the system.

George introduced the concept of T-controllability for one-dimensional nonlinear systems in 1996. For example, when a rocket is launched into orbit, it may be necessary to have a precise course along with the targeted destination in order to save money and avoid collisions. It could also be used to protect the system. In principle, T-controllability ensures that an appropriate control function can be used to lead a dynamical system from an arbitrary start state to a final state with a predefined trajectory. As a result, T-controllability is a more powerful concept of controllability. The T-controllability of integer order semilinear integrodifferential systems in finite and infinite dimensional settings was established by Chalishajar et al.[37] and Chalishajar et al.[38] In[39] the authors established approximate controllability of Sobolev-type fuzzy Hilfer fractional systems using fractional calculus, Clarke subdifferentials, and Dhage's theorem.[40] This manuscript studied the optimal control problem for coupled semilinear wave systems, proved mild solution existence, optimal pairs, and time optimal control. However, because of their nonlocal nature, fractional differential equations are more efficient in representing real-life processes than classical differential equations. As a result, investigating T-controllability discussion for several types of semilinear fractional dynamical systems is fascinating. The goal of our research is to attain the T-controllability of fractional semilinear integrodifferential symmetries, which is motivated by the previous work. This study explores trajectory controllability (T-controllability) for fractional-order semilinear integro-differential systems, addressing both $\nu \in (0, 1]$ and $\nu \in (1, 2]$. By leveraging Caputo derivatives, monotone nonlinearity, and coercivity conditions, it establishes explicit control functions using Gronwall's inequality and fixed-point methods. Unlike traditional controllability, this approach ensures the system follows a predefined trajectory. The paper extends fractional control theory and provides practical examples, demonstrating its relevance in systems with memory effects and nonlinear dynamics.

The following is the outline for this paper. Under certain necessary conditions, the T-controllability of the fractional semilinear integrodifferential equations having order $\nu \in (0, 1]$ was explored in Section 2. T-controllability of the fractional semilinear integrodifferential equations having order $\nu \in (1, 2]$ was explored in Section 3. We employ the instruments of monotone nonlinearities along with coercivity property to demonstrate this. Certain examples are presented to demonstrate the applicability of the abstract theory in the final section.

2. Fractional differential systems of order $\nu \in (0, 1]$

The primary target of this section is to present the T-controllability of the fractional semilinear integrodifferential equations having order $\nu \in (0, 1]$.

We consider $\mathbb{Y}$, $\mathbb{V}$ be Hilbert spaces with $\mathbb{V}$ is a subspace of $\mathbb{Y}$ and $L_2([0,b],\mathbb{Y})$, $L_2([0,b],\mathbb{V})$ be the corresponding function spaces. We consider the fractional semilinear integrodifferential system of order $\nu \in (0,1]$:

$$\begin{aligned} {}^{c}\mathbf{D}^{\nu}_{\varrho} y(\varrho) =& Ay(\varrho) + B(\varrho, v(\varrho)) \\ &+ G\bigg(\varrho, y(\varrho), \int_0^{\varrho} g(\varrho,\alpha, y(\alpha))d\alpha\bigg), \\ & varrho \in I = [0,b], \nu \in (0,1], \end{aligned} \tag{1}$$

$$y(0) = y_0. \tag{2}$$

In the above system, ${}^{c}\mathbf{D}^{\nu}_{\varrho}$ stands for the Caputo fractional derivative of order ν. The state $y(\varrho)$ assumes its values in Hilbert space $\mathbb{Y}$ and the control $v(\varrho)$ assumes values in Hilbert space $\mathbb{V}$. $A : D(A) \subset \mathbb{Y} \to \mathbb{Y}$ is the infinitesimal generator of a strongly continuous semigroup $\{\mathcal{S}(\varrho),\ \varrho \in \mathbb{R}\}$. The operator $B : J \times \mathbb{V} \to \mathbb{Y}$ is nonlinear. Moreover, $G : J \times \mathbb{Y} \times \mathbb{Y} \to \mathbb{Y}$ and $g : \Delta \times \mathbb{Y} \to \mathbb{Y}$ are appropriate function defined later. $\Delta = \{(\varrho,\alpha) \in I : 0 \le \alpha \le \varrho \le b\}$ and $y_0 \in \mathbb{Y}$.

We assume that $C(I,\mathbb{Y}) : I \to \mathbb{Y}$ be the Banach space of all continuous functions with supremum norm given by

$$\|\psi\| = \sup_{0\le\eta\le b} \|\psi(\eta)\|, \quad \psi \in C(I,\mathbb{Y}).$$

Definition 1. [41] *"The fractional integral of order $\nu \in \mathbb{R}^+$ with the lower limit 0 for a function $f \in L^1(\mathbb{R}^+)$ is defined as*

$$I^{\nu}_t f(\varrho) = \frac{1}{\Gamma(\nu)} \int_0^{\varrho} (\varrho-\alpha)^{\nu-1} f(\alpha) d\alpha,\ \varrho > 0\ , \nu > 0$$

provided the right-hand side is point-wise defined on $[0,\infty)$, where $\Gamma(\cdot)$ is gamma function."

Definition 2. [41] *"The Riemann-Liouville (R-L) derivative of order $\nu \in \mathbb{R}^+$ with lower limit zero for a function $f : [0,\infty) \to \mathbb{R}$ can be written as*

$${}^{L}\mathbf{D}^{\nu}_{\varrho} f(\varrho) = \frac{1}{\Gamma(n-\nu)} \frac{d^n}{dt^n} \int_0^{\varrho} \frac{f(\alpha)}{(\varrho-\alpha)^{\nu+1-n}} d\alpha, \quad \varrho > 0, \quad n-1 < \nu < n."$$

Definition 3. [14] *"The Caputo fractional derivative of order ν for a function $f \in C^{n-1}((0,b);\mathbb{Y}) \cap L^1((0,b);\mathbb{Y})$ can be written as*

$${}^{c}\mathbf{D}^{\nu}_{\varrho} f(\varrho) = \frac{1}{\Gamma(n-\nu)} \int_0^{\varrho} (\varrho-\alpha)^{n-\nu-1} f^n(\alpha) d\alpha$$

where $n-1 < \nu < n$, $n = [\nu]+1$ denotes the integral part of the real number ν.

Also

$$I^{\nu}_t({}^{c}\mathbf{D}^{\nu}_{\varrho} f(\varrho)) = f(\varrho) - \sum_{r=0}^{n-1} \frac{t^r}{r!} f^r(0)."$$

where $C^{n-1}((0,b);\mathbb{Y})$ and $L^1((0,b);\mathbb{Y})$ represents the $(n-1)$ time continuously differentiable and space of Y-valued Bochner integrable functions, respectively.

Definition 4. [30] *A continuous function $x \in C(I,\mathbb{Y})$ is called the mild solution of (1)-(2) along with $u \in L_2(I;\mathbb{V})$ if it fulfills*

$$\begin{aligned} y(\varrho) =& \mathcal{S}_{\nu}(\varrho) y_0 + \int_0^{\varrho} (\varrho-\alpha)^{\nu-1} \hat{\mathcal{S}}_{\nu}(\varrho-\alpha) \\ & \bigg[B(\alpha, v(\alpha)) + G\bigg(\alpha, y(\alpha), \\ & \int_0^{\alpha} g(\alpha,\beta, y(\beta)) d\beta\bigg)\bigg] d\alpha, \end{aligned} \tag{3}$$

where

$$\mathcal{S}_{\nu}(\varrho) = \int_0^{\infty} \zeta_{\nu}(\alpha) \mathcal{S}(\varrho^{\nu}\alpha) d\alpha$$

and

$$\hat{\mathcal{S}}_{\nu}(\varrho) = \nu \int_0^{\infty} \alpha \zeta_{\nu}(\alpha) \mathcal{S}(\varrho^{\nu}\alpha) d\alpha.$$

Here

$$\zeta_{\nu}(\alpha) = \frac{1}{\nu} \alpha^{-1-\frac{1}{\nu}} \psi_{\nu}(\alpha^{-\frac{1}{\nu}})$$

is a function defined on $(0,\infty)$ satisfying $\zeta_{\nu}(\alpha) \ge 0$, $\int_0^{\infty} \zeta_{\nu}(\alpha) d\alpha = 1$ and

$$\begin{aligned} \psi_{\nu}(\alpha) =& \frac{1}{\pi} \sum_{n=1}^{\infty} (-1)^{n-1} \alpha^{-\nu n-1} \frac{\Gamma(n\nu+1)}{n!} sin(n\pi\nu), \\ & \alpha \in (0,\infty). \end{aligned}$$

Lemma 1. *[42] "For any fixed $t \ge 0$, the operators $\mathcal{S}_{\nu}(\varrho)$ and $\hat{\mathcal{S}}_{\nu}(\varrho)$ are linear and bounded, that is, for any $x \in \mathbb{Y}$, $\|\mathcal{S}_{\nu}(\varrho)y\| \le M\|y\|$ and $\|\hat{\mathcal{S}}_{\nu}(\varrho)y\| \le \frac{M\nu}{\Gamma(1+\nu)}\|y\|$, where M is a constant such that $\|\mathcal{S}(\varrho)\| \le M$, for all $\varrho \ge 0$."*

For more details on the fractional systems, refer Bazhlekova,[43] Miller,[AK12] Podlubny[45] and for the detailed study of cosine and sine families, one can relate to Travis and Webb.[46]

Before discussing the T-controllability of fractional integrodifferential system having order $\nu \in (0,1]$, we discuss the relations between T-controllability and complete controllability.

Definition 5. *The system (1)-(2) is called completely controllable provided that for every $y_0, y_1 \in \mathbb{Y}$, and fixed b, $\exists\ v(\cdot) \in L_2(I,\mathbb{V})$ such that $y(\cdot)$ fulfills $y(b) = y_1$.*

Assume that $\mathcal{P}$ be the set of all functions $z \in L_2(I, \mathbb{Y})$ determined on I with $z(0) = y_0$, $z(b) = y_1$ and the fractional derivative ${}^c\mathbf{D}_t^\nu z$ exists almost everywhere for $\nu \in (0, 1]$. Noting that $\mathcal{P}$ be the set of all feasible trajectories for (1)-(2).

Definition 6. *The system* (1)-(2) *is called* T*-controllable provided that for every* $z \in \mathcal{P}$, $\exists\ u \in L_2(I, \mathbb{V})$ *such that* $y(\varrho)$ *fulfills* $y(\varrho) = z(\varrho)$ *almost everywhere on* I.

Clearly, T-controllability $\Rightarrow$ Complete controllability.

We show that the trajectory controllability of (1)-(2) in the following two cases:

Case-I: If the control appears linearly:

Let us take a look at the linear control system, that is, $B(\varrho, v(\varrho)) = b(\varrho)v(\varrho)$, where $b : I\mathbb{R}$ and $u : I\mathbb{V}$, then the system (1)-(2) becomes

$$\begin{aligned} {}^c\mathbf{D}_\varrho^\nu y(\varrho) =& Ay(\varrho) + b(\varrho)v(\varrho) \\ &+ G\bigg(\varrho, y(\varrho), \int_0^\varrho g(\varrho, \alpha, y(\alpha))d\alpha\bigg), \\ &\varrho \in I, \nu \in (0, 1], \end{aligned} \tag{4}$$

$$y(0) = y_0. \tag{5}$$

The sufficient conditions to prove the trajectory controllability of (4)-(5) are as follows:

Assumptions [I] [38]

(1) A generates a strongly continuous semigroup $\{\mathcal{S}(\varrho) : \varrho \geq 0\}$ on $\mathbb{Y}$.

(2) $b(\varrho)$ by no means disappear on I.

(3) G is Lipschitz continuous w.r.t. (i) and (ii) argument, that is, $\exists\ \delta_1 > 0$ and $\delta_2 > 0$ such that

$$\|G(\varrho, y_1, y_1) - G(\varrho, x_2, y_2)\| \leq \delta_1\|y_1 - x_2\| + \delta_2\|y_1 - y_2\|,$$

for all $y_1, x_2, y_1, y_2 \in \mathbb{Y}$, $\varrho \in I$.

(4) g is L^1-Lipschitz continuous w.r.t. third argument, that is, $\exists\ \gamma > 0$, $\ni$,

$$\int_0^\varrho \|g(\varrho, \alpha, y(\alpha)) - g(\varrho, \alpha, z(\alpha))\|d\alpha \leq \gamma\|y(\varrho) - z(\varrho)\|, y, z \in \mathcal{P}, (\varrho, \alpha) \in \triangle.$$

Using these hypotheses, we are able to build a control function explicitly to verify T-controllability of (4)-(5). For showing this, we continue like this:

The existence and uniqueness discussion for (4)-(5) may be easily proved with the help of Lipschitz continuity of functions G and h, for each control $v \in L_2(I, \mathbb{V})$.

Assume that $z(\varrho)$ be the considered trajectory in $\mathcal{P}$. We extract admissible control $v(\varrho)$ from equation (4)-(5) by

$$v(\varrho) = \frac{{}^c\mathbf{D}_\varrho^\nu z(\varrho) - Az(\varrho) - G\Big(\varrho, z(\varrho), \int_0^\varrho g(\varrho, \alpha, z(\alpha))d\alpha\Big)}{b(\varrho)}.$$

By using this admissible control function, the state equation (4)-(5) becomes,

$$\begin{aligned} {}^c\mathbf{D}_\varrho^\nu y(\varrho) =& Ay(\varrho) + {}^c\,\mathbf{D}_\varrho^\nu z(\varrho) - Az(\varrho) \\ &- G\bigg(\varrho, z(\varrho), \int_0^\varrho g(\varrho, \alpha, z(\alpha))d\alpha\bigg) \\ &+ G\bigg(\varrho, y(\varrho), \int_0^\varrho g(\varrho, \alpha, y(\alpha))d\alpha\bigg) \\ y(0) =& y_0. \end{aligned}$$

Let us make the substitution $w(\varrho) = y(\varrho) - z(\varrho)$, Then for $w(\varrho)$, we have the subsequent fractional system

$$\begin{aligned} {}^c\mathbf{D}_\varrho^\nu w(\varrho) =& Aw(\varrho) + G\bigg(\varrho, y(\varrho), \int_0^\varrho g(\varrho, \alpha, y(\alpha))d\alpha\bigg) \\ &- G\bigg(\varrho, z(\varrho), \int_0^\varrho g(\varrho, \alpha, z(\alpha))d\alpha\bigg), \\ w(0) =& 0. \end{aligned}$$

It follows that the solution of the above system with $w(0) = 0$ is described as

$$\begin{aligned} w(\varrho) =& \int_0^\varrho (\varrho - \alpha)^{\nu-1}\hat{\mathcal{S}}_\nu(\varrho - \alpha) \\ &\bigg[G\bigg(\alpha, y(\alpha), \int_0^\alpha g(\alpha, \beta, y(\beta))d\beta\bigg) \\ &- G\bigg(\alpha, z(\alpha), \int_0^\alpha g(\alpha, \beta, z(\beta))d\beta\bigg)\bigg]d\alpha. \end{aligned}$$

Thus,

$$\begin{aligned} \|w(\varrho)\| \leq& \frac{M\nu}{\Gamma(1+\nu)}\frac{b^\nu}{\nu}\int_0^\varrho \bigg(\delta_1\|y(\alpha) - z(\alpha)\| \\ &+ \delta_2\bigg\|\int_0^\alpha g(\alpha, \beta, x(\beta))d\beta \\ &- \int_0^\alpha g(\alpha, \beta, z(\beta))d\beta\bigg\|\bigg)d\alpha \\ \leq& \frac{Mb^\nu}{\Gamma(1+\nu)}\int_0^\varrho (\delta_1\|y(\alpha) \\ &- z(\alpha)\| + \delta_2\gamma\|y(\alpha) - z(\alpha)\|)d\alpha. \end{aligned}$$

That is,

$$\|y(\varrho) - z(\varrho)\| \leq \frac{Mb^\nu}{\Gamma(1+\nu)}(\delta_1 + \delta_2\gamma) \int_0^\varrho \|y(\alpha) - z(\alpha)\|d\alpha.$$

Hence by 'Gronwall's inequality', we get

$$\|y(\varrho) - z(\varrho)\| = 0.$$

Thus, $y(\varrho) = z(\varrho)$, $\forall\ \varrho \in I$ and which concludes the T-controllability of (4)-(5).

Case-II: If the control appears nonlinearly in (1)-(2):

In this case, we need the additional assumptions on B, h, and G to prove the trajectory controllability of (1)-(2) given as:

Assumptions [II].

(1) B, h, and G fulfill Caratheadory conditions, that is, $B(\varrho,\cdot):\mathbb{V}\mapsto\mathbb{Y}$ is continuous for $\varrho\in I$ and $B(\cdot,y):I\mapsto\mathbb{Y}$ is measurable for $y\in\mathbb{V}$ and $g(\varrho,\alpha,\cdot):\mathbb{Y}\mapsto\mathbb{Y}$ is continuous $\forall(\varrho,\alpha)\in\Delta$ and $g(\cdot,\cdot,y):\Delta\mapsto\mathbb{Y}$ is measurable $\forall y\in\mathbb{Y}$ and G fulfills Caratheadory conditions identical to h.

(2) B, g, and G satisfy subsequent characteristics:

$$\|B(\varrho,v)\|_{\mathbb{Y}}\leq l_0(\varrho)+l_1\|v\|_{\mathbb{V}},\ \forall\ v\in\mathbb{V},\ \varrho\in I,$$
$$\|g(\varrho,\alpha,y)\|\leq m_0(\varrho)+m_1\|y\|_{\mathbb{Y}}\quad\forall\ \varrho\in I,y\in\mathbb{Y},$$
$$\|G(\varrho,y,z)\|_{\mathbb{Y}}\leq n_0(\varrho)+n_1\|y\|_{\mathbb{Y}}+n_2\|z\|_{\mathbb{Y}}.$$

(3) B fulfills monotonicity and coercivity conditions, i.e.,

$$\langle B(\varrho,v)-B(\varrho,w),v-w\rangle\geq 0\quad\forall\quad v,w\in\mathbb{V},\ \varrho\in I$$

and

$$\lim_{\|u\|\to\infty}\frac{\langle B(\varrho,v),v\rangle}{\|v\|}=\infty.$$

Theorem 1. *Under assumptions [I] ((i),(iii),(iv)) and [II], the nonlinear system* (1)-(2) *is T-controllable.*

Proof. The existence and uniqueness of the nonlinear system (1)-(2) can be proved by employing Lipschitz continuity of G and g for each fixed v and the solution fulfills

$$\begin{aligned}y(\varrho)=&\mathcal{S}_\nu(\varrho)y_0+\int_0^\varrho(\varrho-\alpha)^{\nu-1}\hat{\mathcal{S}}_\nu(\varrho-\alpha)\\&B(\alpha,v(\alpha))d\alpha\\&+\int_0^\varrho(\varrho-\alpha)^{\nu-1}\hat{\mathcal{S}}_\nu(\varrho-\alpha)\\&G\bigg(\alpha,y(\alpha),\int_0^\alpha g(\alpha,\beta,y(\beta))d\beta\bigg)d\alpha.\end{aligned}$$

Assume that $z\in\mathcal{P}$ is the given trajectory with $z(0)=y_0$. Our duty is to check the control v fulfilling

$$\begin{aligned}z(\varrho)=&\mathcal{S}_\nu(\varrho)y_0+\int_0^\varrho(\varrho-\alpha)^{\nu-1}\hat{\mathcal{S}}_\nu(\varrho-\alpha)\\&B(\alpha,v(\alpha))d\alpha\\&+\int_0^\varrho(\varrho-\alpha)^{\nu-1}\hat{\mathcal{S}}_\nu(\varrho-\alpha)\\&G\bigg(\alpha,z(\alpha),\int_0^\alpha g(\alpha,\beta,z(\beta))d\beta\bigg)d\alpha.\end{aligned}$$

To show this, we put $B_1(\varrho)=B(\varrho,v(\varrho))$ in (1)-(2), we get

$$\begin{aligned}{}^c\mathbf{D}^\nu_\varrho y(\varrho)=&Ay(\varrho)+B_1(\varrho)\\&+G\bigg(\varrho,y(\varrho),\int_0^\varrho g(\varrho,\alpha,y(\alpha))d\alpha\bigg),\quad(6)\\&\varrho\in I,\ \nu\in(0,1]\end{aligned}$$

$$y(0)=y_0.\quad(7)$$

We define $B_1(\varrho)$ by

$$\begin{aligned}B_1(\varrho)=&{}^c\mathbf{D}^\nu_\varrho z(\varrho)-Az(\varrho)\\&-G\bigg(\varrho,z(\varrho),\int_0^\varrho g(\varrho,\alpha,z(\alpha))d\alpha\bigg)\end{aligned}$$

for the given trajectory $z(\varrho)\in\mathcal{P}$.

Along with this control, (6) can be wriiten as,

$$\begin{aligned}{}^c\mathbf{D}^\nu_\varrho y(\varrho)=&Ay(\varrho)+{}^c\,\mathbf{D}^\nu_\varrho z(\varrho)-Az(\varrho)\\&-G\bigg(\varrho,z(\varrho),\int_0^\varrho g(\varrho,\alpha,z(\alpha))d\alpha\bigg)\\&+G\bigg(\varrho,y(\varrho),\int_0^\varrho g(\varrho,\alpha,y(\alpha))d\alpha\bigg),\\y(0)=&y_0.\end{aligned}$$

Setting $w(\varrho)=y(\varrho)-z(\varrho)$, one can get

$$\begin{aligned}{}^c\mathbf{D}^\nu_\varrho w(\varrho)=&Aw(\varrho)+G\bigg(\varrho,y(\varrho),\int_0^\varrho g(\varrho,\alpha,y(\alpha))d\alpha\bigg)\\&-G\bigg(\varrho,z(\varrho),\int_0^\varrho g(\varrho,\alpha,z(\alpha))d\alpha\bigg),\end{aligned}\quad(8)$$

$$w(0)=0.\quad(9)$$

From semigroup theory, the solution of (8)-(9) given by

$$\begin{aligned}w(\varrho)=&\int_0^\varrho(\varrho-\alpha)^{\nu-1}\hat{\mathcal{S}}_\nu(\varrho-\alpha)\\&\bigg[G\bigg(\alpha,y(\alpha),\int_0^\alpha g(\alpha,\beta,y(\beta))d\beta\bigg)\\&-G\bigg(\alpha,z(\alpha),\int_0^\alpha g(\alpha,\beta,z(\beta))d\beta\bigg)\bigg]d\alpha.\end{aligned}$$

Now taking norm on both sides and using Gronwall's inequality just in the previous case, one can attain

$$\|y(\varrho)-z(\varrho)\|=0.$$

Therefore, $y(\varrho)=z(\varrho)$, $\forall\ \varrho\in I$. Therefore, the mild solution of the given system equals the prescribed trajectory $z(\varrho)$, when the control u is given by $B_1(\varrho)=B(\varrho,v(\varrho))$. Hence to prove the trajectory controllability, it is enough to extract $v(\varrho)$ from $B_1(\varrho)$. For extracting $v(\varrho)$, we define $N:L_2(I,\mathbb{V})\to L_2(I,\mathbb{Y})$ by

$$(Nv)(\varrho)=B(\varrho,v(\varrho)).\quad(10)$$

By referring to the assumption [II(i)-(ii)], we observe that the operator N is well-defined, continuous, and bounded. Using the assumption[II(iii)], we can say that N is monotone and coercive. A hemi-continuous monotone map is of the type (M) [44]. Hence, by employing Theorem 3.6.9 of Joshi and Bose,[44] we can say that the nonlinear map N is onto. Therefore, there exists a control u fulfilling (10). Also, since $u\in L_2(I,\mathbb{V})$,

therefore u is measurable. So, we can extract $v(\varrho)$ from $B(\varrho, v(\varrho))$ so that for this control, the mild solution of the considered system equals to the prescribed trajectory $z(\varrho)$, which concludes T-controllability of (1)-(2).

3. Fractional differential systems of order $\nu \in (1, 2]$

We are primarily focusing on the trajectory controllability of the subsequent fractional semilinear integrodifferential system of order $\nu \in (1, 2]$

$$\begin{aligned} {}^{c}\mathbf{D}^{\nu}_{\varrho} y(\varrho) =& Ay(\varrho) + B(\varrho, v(\varrho)) \\ &+ G\bigg(\varrho, y(\varrho), \int_0^{\varrho} g(\varrho, \alpha, y(\alpha))d\alpha\bigg), \\ &\varrho \in I, \nu \in (1, 2], \end{aligned} \tag{11}$$

$$y(0) = y_0, y'(0) = z_0. \tag{12}$$

Here, A is the infinitesimal generator of the strongly continuous cosine family (CF) $\{C_\nu(\varrho), t \geq 0\}$ and $y_0, z_0 \in \mathbb{Y}$.

To define the mild solution of (11)-(12), we assume the subsequent system

$${}^{c}D^{\nu}_{\varrho} y(\varrho) = Ay(\varrho),\ y(0) = \eta\ y'(0) = 0. \tag{13}$$

In the above, $\nu \in (1, 2]$; $A : D(A) \subseteq \mathbb{Y} \to \mathbb{Y}$ is a closed and densely defined operator in $\mathbb{Y}$. Taking Riemann fractional integral of order ν on both sides of (13), one can attain

$$y(\varrho) = \eta + \frac{1}{\Gamma(\nu)} \int_0^{\varrho} (\varrho - \alpha)^{\nu-1} Ax(\alpha)d\alpha \tag{14}$$

Definition 7. [43] *"Let $\nu \in (1, 2]$. A family $\{C_\nu(\varrho)\}_{t\geq 0} \subset \mathbb{L}(\mathbb{Y})$ is called a solution operator (or a strongly continuous ν-order fractional CF) for (13) if the following conditions are satisfied:*

(1) $C_\nu(\varrho)$ is strongly continuous for $t \geq 0$ and $C_\nu(0) = I$;
(2) $C_\nu(\varrho)D(A) \subset D(A)$ and $AC_\nu(\varrho)\eta = C_\nu(\varrho)A\eta$ for all $\eta \in D(A)$, $t \geq 0$;
(3) $C_\nu(\varrho)\eta$ is a solution of (13),$\forall\ \eta \in D(A)$, $\varrho \geq 0$.

A is called infinitesimal generator of $C_\nu(\varrho)$. The strongly continuous ν-order fractional CF is also called ν-order CF."

Definition 8. *The sine family (SF) $S_\nu : [0, \infty) \to \mathbb{L}(\mathbb{Y})$ connected with C_ν is presented as*

$$S_\nu(\varrho) = \int_0^{\varrho} C_\nu(\alpha)d\alpha, \quad \varrho \geq 0.$$

Definition 9. *The fractional R-L family $P_\nu : [0, \infty) \to \mathbb{L}(\mathbb{Y})$ connected with C_ν is presented as*

$$P_\nu(\varrho) = J^{\nu-1}_{\varrho} C_\nu(\varrho).$$

Definition 10. [43] *"A function $x(\cdot) \in C(I; \mathbb{Y})$ is said to be the mild solution of (11)-(12) if it satisfies*

$$\begin{aligned} y(\varrho) =& C_\nu(\varrho)y_0 + S_\nu(\varrho)z_0 + \int_0^{\varrho} P_\nu(\varrho - \alpha)B(\alpha, v(\alpha))d\alpha \\ &+ \int_0^{\varrho} P_\nu(\varrho - \alpha)G\bigg(\alpha, x(s), \int_0^{\varrho} g(\varrho, \alpha, y(\alpha))d\alpha\bigg)\}ds \end{aligned} \tag{15}$$

where $S_\nu(\varrho)$ and $P_\nu(\varrho)$ are the fractional SF and fractional R-L family, respectively, associated with strongly continuous CF $C_\nu(\varrho)$ as defined above."

Assume that $\mathcal{P}$ be the set of all functions defined on I with $z(0) = y_0$, $z'(0) = z_0$, $z(b) = y_1$ and the fractional derivative ${}^{c}\mathbf{D}^{\nu}_{\varrho} z$ exists almost everywhere for $\nu \in (1, 2]$. Note that $\mathcal{P}$ be the set of all feasible trajectories for (11)-(12).

We prove the trajectory controllability of the system (11)-(12) in two cases.

Case-I: If the control appears linearly:

Consider the system (11)-(12) with the control appears linearly, i.e. , $B(\varrho, v(\varrho)) = b(\varrho)v(\varrho)$, where $b : I\mathbb{R}$ and $u : I\mathbb{V}$, then the system (11)-(12) becomes

$$\begin{aligned} {}^{c}\mathbf{D}^{\nu}_{\varrho} y(\varrho) =& Ay(\varrho) + b(\varrho)v(\varrho) \\ &+ G\bigg(\varrho, y(\varrho), \int_0^{\varrho} g(\varrho, \alpha, y(\alpha))d\alpha\bigg), \\ &\varrho \in I, \nu \in (1, 2], \end{aligned} \tag{16}$$

$$y(0) = y_0 \text{ and } y'(0) = z_0. \tag{17}$$

Assumptions [III].

(1) A generates a strongly continuous CF $\{C_\nu(\varrho) : t \geq 0\}$ on $\mathbb{Y}$.
(2) $b(\varrho)$ does not disappear on I.
(3) G and h are Lipschitz continuous in a similar manner as in Assumptions [I] of Section 2.

By referring these two assumptions, we may create the control explicitly to verify T-controllability of (16)-(17). For verifying this, we continue in the following way:

For every $v \in L_2(I, \mathbb{V})$, the existence and uniqueness of (16)-(17) follows from Assumptions [III] by employing the Lipschitz continuity of functions G and h.

Assume that $z(\varrho)$ be the given trajectory in $\mathcal{P}$. We present $v(\varrho)$ as

$$v(\varrho) = \frac{{}^{c}\mathbf{D}^{\nu}_{\varrho} z(\varrho) - Az(\varrho) - G\bigg(\varrho, z(\varrho), \int_0^{\varrho} g(\varrho, \alpha, z(\alpha))d\alpha\bigg)}{b(\varrho)}$$

By using this control, (16)-(17) becomes,

$$\begin{aligned}{}^{c}\mathbf{D}^{\nu}_{\varrho}y(\varrho) =&Ay(\varrho) +{}^{c}\mathbf{D}^{\nu}_{\varrho}z(\varrho) - Az(\varrho)\\ &- G\bigg(\varrho, z(\varrho), \int_0^{\varrho} g(\varrho,\alpha, z(\alpha))d\alpha\bigg)\\ &+ G\bigg(\varrho, y(\varrho), \int_0^{\varrho} g(\varrho,\alpha, y(\alpha))d\alpha\bigg),\\ &\nu\in(1,2]\\ y(0) =&y_0 \text{ and } y'(0) = z_0.\end{aligned}$$

Fixing $w(\varrho) = y(\varrho) - z(\varrho)$, one can get

$$\begin{aligned}{}^{c}\mathbf{D}^{\nu}_{\varrho}w(\varrho) =&Aw(\varrho)\\ &+ G\bigg(\varrho, y(\varrho), \int_0^{\varrho} g(\varrho,\alpha, y(\alpha))d\alpha\bigg)\\ &- G\bigg(\varrho, z(\varrho), \int_0^{\varrho} g(\varrho,\alpha, z(\alpha))d\alpha\bigg),\\ &\nu\in(1,2],\\ w(0) =&0 \text{ and } w'(0) = 0.\end{aligned}$$

By using the semigroup theory, the solution of the above equation may be given by

$$\begin{aligned}w(\varrho) = \int_0^{\varrho} P_{\nu}(\varrho-\alpha)\bigg[G\bigg(\alpha, y(\alpha),\\ \int_0^{\alpha} g(\alpha,\beta, y(\beta))d\beta\bigg) - G\bigg(\alpha, z(\alpha),\\ \int_0^{\alpha} g(\alpha,\beta, z(\beta))d\beta\bigg)\bigg]d\alpha\end{aligned}$$

Thus,

$$\begin{aligned}\|w(\varrho)\| \le& \frac{Mb^{\nu-1}}{\Gamma(\nu)}\int_0^{\varrho}\bigg(\delta_1\|y(\alpha)-z(\alpha)\|\\ &+\delta_2\bigg\|\int_0^{\alpha} g(\alpha,\beta,x(\beta))d\beta\\ &-\int_0^{\alpha} g(\alpha,\beta,z(\beta))d\beta\bigg\|\bigg)d\alpha\\ \le& \frac{Mb^{\nu-1}}{\Gamma(\nu)}\int_0^{\varrho}(\delta_1\|x(s)-z(s)\| + \delta_2\gamma\|x(\alpha)\\ &- z(\alpha)\|)d\alpha.\end{aligned}$$

Hence,

$$\begin{aligned}\|y(\varrho)-z(\varrho)\| \le& \frac{Mb^{\nu-1}}{\Gamma(\nu)}(\delta_1+\delta_2\gamma)\\ &\int_0^{\varrho}\|y(\alpha)-z(\alpha)\|d\alpha.\end{aligned}$$

Using "Grownwall's inequality," we get

$$\|y(\varrho)-z(\varrho)\| = 0.$$

Therefore, $y(\varrho) = z(\varrho)$ for all $\varrho\in I$. This proves T-controllability of (16)-(17).

Case-II: If the control appears nonlinearly in (11)**-**(12):

In this case, trajectory controllability of the system (11)-(12) can be verified by the same approach discussed in Theorem 1 using the Lipschitz continuity of G and h and some additional assumptions on B, g, and f given in Assumptions [II] of Section 2.

4. Examples

In this section, we present numerical examples to support and illustrate the theoretical results.

Example 1. Assume that the following nonlinear integrodifferential system with control$b(\varrho, v) = v|v|$.

$$\begin{aligned}{}^{c}\mathbf{D}^{\nu}_{\varrho}y(\varrho) =&a(\varrho)y(\varrho) + B(\varrho, v(\varrho))\\ &+\sin\bigg(y(\varrho) + 3\int_0^{\varrho} x(\alpha)d\alpha\bigg), 0<\nu\le 1,\end{aligned} \tag{18}$$

$$y(0) = y_0. \tag{19}$$

The control $B(\varrho, v)$ is continuous and coercive. It is easy to show that G and h fulfill all the requirements of the Theorem 1. Therefore, the system (18) is T-controllable.

Example 2. Assume that $\Omega = (0,1)$ be the bounded domain in $\mathbb{R}^n$ with smooth boundary $\partial\Omega$. Assume that the subsequent fractional system

$$\begin{aligned}{}^{c}\mathbf{D}^{\nu}_{\varrho}y(\varrho) =&\frac{\partial^2 y}{\partial\varrho^2} + v(y,\varrho) + \frac{1}{2}[\sin^2 y(\varrho)\\ &+\sin y(\varrho)] \text{ in } \Omega\times(0,b), 0<\nu\le 1,\end{aligned} \tag{20}$$

$$z(y,0) = 0 \text{ in } \Omega, \tag{21}$$

$$z(y,\varrho) = 0 \text{ in } \partial\Omega\times(0,b). \tag{22}$$

Let us define $A : L^2(0,1)\to L^2(0,1)$ by $Aw = w''$, where

$$\begin{aligned}D(A) = \{w\in\mathbb{Y} : w, w' &\text{ are absolutely continuous },\\ w(0) = w(1) &= 0\}\end{aligned}$$

and

$$Aw = \sum_{k=1}^{+\infty} k^2 < w, w_k > w_k, \quad w\in D(A),$$

where $w_k(\alpha) = (2/\pi)^{1/2}\sin k\alpha, \quad k = 1,2,3\cdots$ is the orthogonal set of eigenfunctions of A. Here, $< w, w_k >$ stands for the L^2 inner product. Additionally, A generates a strongly continuous semigroup $\{\mathcal{S}(\varrho), \varrho\ge 0\}$ in $\mathbb{Y}$ presented as

$$\mathcal{S}(\varrho)w = \sum_{k=1}^{+\infty}\exp(-k^2\varrho) < w, w_k > w_k, \quad w\in\mathbb{Y},$$

and $\mathbb{Y} = \mathbb{V} = L^2(\Omega)$. The control term $B(\varrho, v(\varrho)) = v(\varrho)$ is linear. Also,

$$F(\varrho, y(\varrho), z(\varrho)) = \frac{1}{2}[\sin^2 y(\varrho) + \sin z(\varrho)]$$

and $G(\varrho, \alpha, y(\alpha)) = \frac{1}{2}[\cos y(\alpha)]$, both are Lipschitz continuous and satisfy all the assumptions. Therefore, using the results of Case-I of Section 2, we get that (20) is T-controllable.

Example 3. Consider the nonlinear fractional integro-differential system represented in the sense of a Caputo fractional derivative

$$\begin{aligned} {}^c\mathbf{D}^{\nu}_{\varrho} y(\varrho) =& 4y(\varrho) + v^2(\varrho) + 10\cos y(\varrho) \\ &+ 9\int_0^{\varrho} (\varrho + \alpha^2 + \sin y(\varrho))d\alpha, \\ &\varrho \in [0,1], \\ &y(0) = y_0, \;\; y(0) = \eta_0. \end{aligned} \tag{23}$$

where $\nu \in (1,2]$. The control function $Bv(\varrho) = v^2(\varrho)$ is continuous on $[0,1] \times \mathbb{R}$ and coercive. Further, the nonlinear functions $G\left(\varrho, y(\varrho), \int_0^{\varrho} g(\varrho, \alpha, y(\alpha))d\alpha\right) = 10\cos y(\varrho) + 9\int_0^{\varrho}(\varrho + \alpha^2 + \sin y(\varrho))d\alpha$ is Lipschitz with Lipschitz constants δ_1 and δ_2. All the hypotheses of Theorem 1 are satisfied. Therefore, the nonlinear fractional integro-differential system (3.1)-(3.2) is T-controllable at any value of $\nu \in (1,2]$ and $y_0,\ \eta_0 \in \mathbb{R}$.

5. Conclusion

Future research can explore T-controllability for fractional-order systems with delays, stochastic influences, or impulsive effects, extending the current framework to more complex real-world applications. Investigating optimal control strategies (see,[47,48]) for minimizing energy or cost during trajectory tracking could enhance practical implementation. Additionally, applying machine learning or data-driven techniques to improve control accuracy in fractional systems is a promising direction. Further studies on nonlinear fractional systems in Banach spaces and their applications in robotics, biomedical engineering, and financial modeling could provide valuable advancements in the field.

Acknowledgments

None.

Funding

None.

Conflict of interest

Anurag Shukla is an Editorial Board Member of this journal, but was not in any way involved in the editorial and peer-review process conducted for this paper, directly or indirectly. Separately, other authors declared that they have no known competing financial interests or personal relationships that could have influenced the work reported in this paper.

Author contributions

Conceptualization: Urvashi Arora, Anurag Shukla
Formal analysis: Urvashi Arora, V. Vijayakumar
Investigation: Sachin Singh, Urvashi Arora
Methodology: Anurag Shukla, V. Vijayakumar
Writing -original draft: Urvashi Arora, Anurag Shukla
Writing-review & editing: V. Vijayakumar, Sachin Singh, Anurag Shukla

Availability of data

Not applicable.

References

1. Arora U, Sukavanam N. Controllability of fractional system of order with nonlinear term having integral contractor. IMA J Math Control Informat. 2019;36(1):271-283.
2. Bragdi M, Hazi M. Existence and controllability result for an evolution fractional integrodifferential systems. Int J Contemp Math Sci. 2010;5(19):901-910.
3. Davison EJ, Kunze EG. Some sufficient conditions for the global and local controllability of nonlinear time-varying systems. SIAM J Control. 1970;8(4):489-497.
4. Debnath L. Recent applications of fractional calculus to science and engineering. Int J Math Mathemat Sci. 2003;2003:3413-3442.
5. George RK. Approximate controllability of nonautonomous semilinear systems. Nonlinear Anal. 1995;24(9):1377-1394.
6. Klamka J. Constrained controllability of semilinear systems. Nonlinear Anal Theor Methods Appl. 2001;47(5):2939-2949.
7. Klamka J. Constrained exact controllability of semilinear systems. Syst Control Lett. 2002;47(2):139-147.
8. Klamka J. Constrained controllability of semilinear systems with delays. Nonlinear Dyn. 2009;56: 169-177.
9. Lions JL. Exact controllability, stabilization and perturbations for distributed systems. SIAM Rev. 1988;30(1):1-68.

10. George RK, Chalishajar DN, Nandakumaran AK. Exact controllability of the nonlinear third-order dispersion equation. J Math Anal Appl. 2007;332(2):1028-1044.
11. Nandakumaran AK, George RK. Partial exact controllability of a non-linear system. Revista Matemat Univers Complut Madrid 1995;8(N1):181-196.
12. Miller KS, Ross B. An Introduction to the Fractional Calculus and Fractional Differential Equations, A Wiley-Interscience Publication. New York: Wiley; 1993.
13. Cardetti F, Gordina M. A note on local controllability on Lie groups. Syst Control Lett. 2008; 57(12):978-979.
14. Muslim M, Kumar A. Controllability of fractional differential equation of order $\alpha \in (1, 2]$ with non-instantaneous impulses. Asian J Control. 2018;20(2):935-942.
15. Shukla A, Arora U, Sukavanam N. Approximate controllability of retarded semilinear stochastic system with non local conditions. J Appl Math Comput. 2015; 49:513-527.
16. Shukla A, Sukavanam N, Pandey DN, Arora U. Approximate controllability of second-order semilinear control system. Circ Syst Signal Process. 2016;35:3339-3354.
17. Wang J, Wei W, Yang Y. Fractional nonlocal integrodifferential equations and its optimal control in Banach spaces. J Korean Soc Ind Appl Math. 2010;14(2):79-91.
18. Jajarmi A, Baleanu D. On the fractional optimal control problems with a general derivative operator. Asian J Control. 2021;23(2): 1062-1071.
19. Kumar V, Malik M. Total controllability and observability for dynamic systems with non-instantaneous impulses on time scales. Asian J Control. 2021;23(2):847-859.
20. Liu Z, Li X. On the exact controllability of impulsive fractional semilinear functional differential inclusions. Asian J Control. 2015;17(5):1857-1865.
21. Dineshkumar C, Udhayakumar R, Vijayakumar V, Nisar KS, Shukla A. A note concerning to approximate controllability of Atangana-Baleanu fractional neutral stochastic systems with infinite delay. Chaos Solit Fract. 2022;157: 111916.
22. Mahmudov NI, Udhayakumar R, Vijayakumar V. On the approximate controllability of second-order evolution hemivariational inequalities. Results Math. 2020;75: 1-19.
23. Mahmudov NI, Murugesu R, Ravichandran C, Vijayakumar V. Approximate controllability results for fractional semilinear integro-differential inclusions in Hilbert spaces. Results Math. 2017;71:45-61.
24. Shukla A, Vijayakumar V, Nisar KS. A new exploration on the existence and approximate controllability for fractional semilinear impulsive control systems of order $r \in (1, 2)$. Chaos Solit Fract. 2022;154:111615.
25. Vijayakumar V. Approximate controllability results for non-densely defined fractional neutral differential inclusions with Hille-Yosida operators. Int J Control. 2019;92(9):2210-2222.
26. Vijayakumar V. Approximate controllability for a class of second-order stochastic evolution inclusions of Clarke's subdifferential type. Result Math. 2018a; 73(1):42.
27. Vijayakumar V. Approximate controllability results for impulsive neutral differential inclusions of Sobolev-type with infinite delay. Int J Control. 2018b;91(10): 2366-2386.
28. Matar M. Controllability of fractional semilinear mixed Volterra-Fredholm integrodifferential equations with nonlocal conditions. Int J Math Anal. 2010;4(23):1105-1116.
29. Wang J, Zhou Y. A class of fractional evolution equations and optimal controls. Nonlinear Anal Real World Appl. 2011;12(1):262-272.
30. Zhou Y, Jiao F. Existence of mild solutions for fractional neutral evolution equations. Comput Math Applicat. 2010;59(3):1063-1077.
31. Kumar S, Sukavanam N. Approximate controllability of fractional order semilinear systems with bounded delay. J Differ Equat. 2012;252(11):6163-6174.
32. Sukavanam N, Kumar S. Approximate controllability of fractional order semilinear delay systems. J Optimiz Theor Applicat. 2011;151:373-384.
33. Kexue L, Jigen P, Jinghuai G. (2013). Controllability of nonlocal fractional differential systems of order $\alpha \in (1, 2]$ in Banach spaces. Rep Math Phys. 2013;71(1):33-43.
34. Arora S, Nandakumaran A. Controllability problems of a neutral integro-differential equation with memory. arXiv preprint; 2024. arXiv:2407.07886.
35. Jalisraj A, Udhayakumar R. Existence results and trajectory controllability of conformable Hilfer fractional neutral stochastic integro-differential equations. Contemp Math. 2024;5(4):5496-5517.
36. Shukla A, Sukavanam N, Pandey DN. Approximate controllability of semilinear fractional control systems of order $\alpha \in (1, 2]$ with infinite delay. Mediterranean J Math. 2016;13:2539-2550.
37. Chalishajar D, Chalishajar H. Trajectory controllability of second order nonlinear integro-differential system: an analytical and a numerical estimation. Differ Equat Dyn Syst. 2015;23:467-481.
38. Chalishajar DN, George RK, Nandakumaran AK, Acharya FS. Trajectory controllability of nonlinear integro-differential system. J Franklin Instit. 2010;347(7):1065-1075.
39. Hariharan R, Udhayakumar R. Approximate controllability for Sobolev-type Fuzzy Hilfer fractional neutral integro-differential inclusion with Clarke subdifferential type. Qual Theor Dyn Syst. 2025;24(1):53.
40. Kumar S, Tajinder. Existence of solution and optimal control results in coupled wave system

with Lipschitz nonlinearity. Int J Dyn Control. 2025;13(1):24.
41. Balachandran K, Park JY. Controllability of fractional integrodifferential systems in Banach spaces. Nonlinear Anal Hybrid Syst. 2009;3(4):363-367.
42. Wang J, Zhou Y. Existence and controllability results for fractional semilinear differential inclusions. Nonlinear Anal Real World Appl. 2011;12(6):3642-3653.
43. Bazhlekova EG. Fractional Evolution Equations in Banach Spaces. Eindhoven: Eindhoven University of Technology; 2001.
44. Joshi MC, Bose RK. Some topics in nonlinear functional analysis. In: A Halsted Press Book. New York: Wiley; 1985.
45. Podlubny I. Fractional Differential Equations, Mathematics in Science and Engineering, vol. 198. San Diego, CA: Academic Press; 1999.
46. Travis CC, Webb GF. Cosine families and abstract nonlinear second order differential equations. Acta Math Hungarica 1978;32(1-2):75-96.
47. Baranovskii ES, Brizitskii RV, Saritskaia ZY. Optimal control problems for the reaction-diffusion-convection equation with variable coefficients. Nonlinear Anal Real World Appl. 2024;75:103979.
48. Baranovskii ES. Feedback optimal control problem for a network model of viscous fluid flows. Math Notes. 2022;112(1):26-39.

Urvashi Arora *is a Visiting Assistant Professor in the Department of Mathematics at Manhattan University, New York, USA. She earned her Ph.D. in Mathematics from the Indian Institute of Technology Roorkee, India, where she focused on the controllability of infinite-dimensional semilinear systems. She also holds an MS in Statistics and Data Science from the University of Houston, USA, where her work included developing predictive models using machine learning and advanced data analysis techniques. Dr. Arora's research spans control theory, data science, and machine learning, with a keen interest in applying mathematical tools to solve real-world problems.*
https://orcid.org/0000-0002-5764-4179

Sachin Singh *is an Assistant Professor in the Department of Electrical Engineering at the Institute of Engineering and Technology, Lucknow, Uttar Pradesh, India. He earned his Ph.D. in Electrical Engineering from the Birla Institute of Technology, India. Dr. Singh's research spans control theory, power systems, and optimization learning. He has published more than 20 research articles in reputed journals.*
https://orcid.org/0000-0002-6405-8207

V. Vijayakumar *received a B.Sc, M.Sc, M.Phil, and Ph.D. degrees in Mathematics from the Bharathiar University, Coimbatore, Tamil Nadu, India in 2002, 2004, 2006, and 2016, respectively. He was a Lecturer with the Department of Mathematics, Sri Nandhanam College of Engineering and Technology, Tirupattur, Vellore, Tamil Nadu, India, from 2006 to 2007. He was an Assistant Professor and an Associate Professor with the Department of Mathematics, Info Institute of Engineering, Coimbatore, Tamil Nadu, India, from 2007 to 2019. Since 2019, he has been an Assistant Professor at Vellore Institute of Technology, Vellore, Tamil Nadu, India. His current research interests include Fractional Calculus, Dynamical Systems, Control Theory, and Neural Networks. To his credit, he has published more than 220 research articles in reputed scientific journals. He is listed as TOP 2% Scientists in the World (All Fields) by a survey conducted by Elsevier BV and Stanford University, based on the citations, h-index, and co-authorship adjusted hm-index, for the years 2020, 2021, 2022 & 2023.*
https://orcid.org/0000-0001-5976-5794

Anurag Shukla *received M.Sc. and Ph.D. degrees in Mathematics from the IIT Roorkee, Uttarakhand, India, in 2011 and 2016, respectively. Currently, he is an Assistant Professor in the Department of Applied Sciences & Humanities, Rajkiya Engineering College, Kannauj, Uttar Pradesh, India. His current research interests include Fractional Differential Systems, Stochastic Differential Systems, and Mathematical Control Theory. To his credit, he has published more than 100 research papers in SCI Journals. He is listed as a TOP 2% Scientist in the World (All Fields) by a survey conducted by Elsevier BV and Stanford University, based on the citations, h-index, and co-authorship adjusted hm-index, for the years 2022 & 2023.*
https://orcid.org/0000-0001-5892-0342

This work is licensed under a Creative Commons Attribution 4.0 International License. The authors retain ownership of the copyright for their article, but they allow anyone to download, reuse, reprint, modify, distribute, and/or copy articles in IJOCTA, so long as the original authors and source are credited. To see the complete license contents, please visit http://creativecommons.org/licenses/by/4.0/.

An International Journal of Optimization and Control: Theories & Applications
ISSN: 2146-0957 eISSN: 2146-5703
Vol.15, No.3, pp.493-502 (2025)
https://doi.org/10.36922/IJOCTA025120056

RESEARCH ARTICLE

Investigate the solution of an initial Hilfer fractional value problem

Amol D. Khandagale[1], Arif S. Bagwan[2], Sabri T. M. Thabet[3,4,5*], and Imed Kedim[6]

[1]Department of Mathematics, Dr. Babasaheb Ambedkar Marathwada University, Chhatrapati Sambhajinagar, India
[2]Department of Applied Sciences Humanities, Pimpri Chinchwad College of Engineering, Nigdi, Pune, India
[3]Department of Mathematics, Saveetha School of Engineering, Saveetha Institute of Medical and Technical Sciences, Saveetha University, Chennai, Tamil Nadu, India
[4]Department of Mathematics, Radfan University College, University of Lahej, Lahej, Yemen
[5]Department of Mathematics, College of Science, Korea University, Seongbuk-gu, Seoul, Republic of Korea
[6]Department of Mathematics, College of Science and Humanities in Al-Kharj, Prince Sattam Bin Abdulaziz University, Al-Kharj, Saudi Arabia
kamoldsk@gmail.com, arif.bagwan@gmail.com, th.sabri@yahoo.com, i.kedim@psau.edu.sa

ARTICLE INFO

Article History:
Received: March 20, 2025
1st revised: May 7, 2025
2nd revised: May 10, 2025
Accepted: May 13, 2025
Published Online: June 3, 2025

Keywords:
Initial value problem
Hilfer fractional derivative
Fixed point theorem

AMS Classification 2010:
26A33, 34A08, 34A12, 47H09
47H10

ABSTRACT

This paper aims to investigate sufficient criteria of the existence solution for a new category of nonlinear fractional differential equation under the Hilfer fractional derivative. The primary existence results are achieved by using a modified version of the Krasnoselskii-Dhage fixed-point theorem in the weighted Banach space. Finally, an application is illustrated to test the validity of the findings.

CC BY

1. Introduction

In numerous mathematical studies, the theory of fractional calculus and its applications have been thoroughly examined. Many real-world problems in science, engineering, and economics are now mathematically modeled with the help of fractional calculus. See the books and research works[1–7] and references therein. Fractional differential equations (FDE) are undoubtedly still a popular topic among writers. The use of the fixed-point theorem approach to obtain the existence and uniqueness results for fractional differential equations is the most favored topic by several scholars. See ref.[8–21] and references therein for the recent development in this area. This motivates researchers to study various fixed-point theorems and their generalizations. See ref.[22–25] and references therein.

In ref.,[26–29] the researchers discussed some existence and optimal control results for various fractional differential equations and inclusions by means of fixed point theorems. Similarly, several scholars have demonstrated a great deal of interest in the theory of fractional differential equations with linear perturbation. See ref.[30–33] and references therein. In ref.,[25] Dhage presented a novel form of the Kransoselskii-type FPT termed the Krasnoselskii-Dhage type FPT by utilizing a nonlinear $\mathcal{D}-$contraction condition. In ref.,[30] Dhage and Lakshmikantham used fixed point theorems (FPT) of the Krasnoselskii type to study the first-order hybrid differential problem with linear perturbations:

*Corresponding Author

$$\frac{d}{dx}\left[\frac{x(t)}{f(t,x(t))}\right]=g(t,x(t)),\ \ t\in J,$$
$$x(t_0)=x_0\in\mathbb{R},$$

where $J=[t_0,t_0+a]$, for some fixed $t_0\in\mathbb{R}, a>0$ and $f:\mathcal{J}\times\mathbb{R}\to\mathbb{R}\backslash\{0\}$ and $g:\mathcal{J}\times\mathbb{R}\to\mathbb{R}$. Furthermore, Dhage et al.[31] established the existence results for hybrid differential equations with linear perturbations. In,[32] Lu et al. formulated the theory of hybrid type FDE by using linear perturbations of the second kind:

$$D^q\left[x\left(t\right)-f\left(t,x\left(t\right)\right)\right]=g\left(t,x\left(t\right)\right),\quad t\in J$$
$$x\left(t_0\right)=x_0\in\mathbb{R},$$

where $f,g:\mathcal{J}\times\mathbb{R}\to\mathbb{R}$ and $0<q<1$.

In ref.[33] Akhadkulov et al. utilized this revised version of the Krasnoselskii-Dhage type FPT to obtain the existence results for a hybrid type FDE that incorporates the differential and integral operators of Riemann–Liouville (RL) type:

$$D^{\alpha}\left[x\left(t\right)-f\left(t,x\left(t\right)\right)\right]=g\left(t,x\left(t\right),I^{\beta}\left(x\left(t\right)\right)\right),$$
$$t\in J,\ \beta>0$$
$$x\left(t_0\right)=x_0,$$

where $J=[t_0,t_0+a]$, for some fixed $t_0\in\mathbb{R}, a>0$ and $f:\mathcal{J}\times\mathbb{R}\to\mathbb{R}$ and $g:\mathcal{J}\times\mathbb{R}\times\mathbb{R}\to\mathbb{R}$.

In ref.,[34] Kiataramkul et al. discussed the existing results of the following fractional integro-differential hybrid boundary value problems for differential equations with ψ- Hilfer derivative operator:

$${}^{H}D_{a^+}^{\alpha,\rho,\psi}\left[\left(\frac{x\left(t\right)}{g\left(t,x\left(t\right)\right)}-\sum_{i=1}^{n}I_{a^+}^{\beta_i,\psi}h_i\left(t,x\left(t\right)\right)\right)\right]$$
$$=f\left(t,x\left(t\right)\right),$$
$$x\left(a\right)=0,\ x\left(b\right)=m\left(x\right),$$

where $t\in J=[a,b]$, $0<\alpha\leq 2$, $0\leq\rho\leq 1$; $\beta_i>0$, for $i=1,2,...,n$, $g:J\times\mathbb{R}\to\mathbb{R}\backslash\{0\}$, $f:J\times\mathbb{R}\to\mathbb{R}, m:J\to\mathbb{R}$, $h_i:J\times\mathbb{R}\to\mathbb{R}$ such that $h_i\left(a,0\right)=0$, $i=1,2,...,n$. Further, they obtained the existence result for inclusion ψ- Hilfer fractional integro-differential hybrid boundary value problems by means of fixed point theorem. For some recent development in the field of fractional differential equations readers are encouraged to see[35–43] and references therein.

Inspired by the aforementioned work, in this study, we examine the subsequent initial value problem (IVP) employing the Hilfer fractional derivative (HFD) operator:

$$D_{p^+}^{\sigma,\tau}\left[\varphi\left(s\right)-f\left(s,\varphi\left(s\right)\right)\right]=g\left(s,\varphi\left(s\right)\right),$$
$$s\in\mathcal{J},0<\sigma<1,0\leq\tau\leq 1,\qquad(1)$$

$$I_{p^+}^{1-\kappa}\left[\varphi\left(s\right)-f\left(s,\varphi\left(s\right)\right)\right]\left(p^+\right)=\varphi_0\in\mathbb{R},$$
$$\kappa=\sigma+\tau-\sigma\tau,\qquad(2)$$

where $\mathcal{J}=(p,q]$. The non-linear terms $f:\mathcal{J}\times\mathbb{R}\to\mathbb{R}$ and $g:\mathcal{J}\times\mathbb{R}\to\mathbb{R}$ be the given continuous functions. The operator $D_{p^+}^{\sigma,\tau}$ is a HFD operator of order σ and type τ.

The main contributions of the study are as follows:
(i) Studying the initial value problem involving the Hilfer fractional derivatives.
(ii) Investigating the applicability of the Krasnoselskii–Dhage fixed point technique to the proposed problem.
(iii) The problem being discussed in this paper is more general than in the literature, such as for $\tau=1$ it reduces to a problem in the Caputo fractional derivative, and if $\tau=0$ it returns to a problem in the Riemann-–Liouville fractional derivative.

This article is organized as follows: Section 2 presents some essential definitions and lemmas needed throughout the study. Section 3 investigates the main findings. Section 4 provides an application of the results.

2. Preliminary results

Definition 1. ([3]) *For $\sigma\in\mathbb{R}^+$, the RL-fractional integral of a function $h(u)$ is given as;*

$$\left(I_{p^+}^{\sigma}h\right)(u)=\frac{1}{\Gamma\left(\sigma\right)}\int_p^u\frac{h\left(s\right)}{\left(u-s\right)^{1-\sigma}}ds,\qquad(u>p).$$

Definition 2. ([3]) *For $\sigma\in[m-1,m)$, $m\in\mathbb{Z}^+$, the RL-fractional derivative of a function $h(u)$ is given as;*

$$\left(D_{p^+}^{\sigma}h\right)(u)=\frac{1}{\Gamma\left(m-\sigma\right)}\left(\frac{d}{du}\right)^m$$
$$\cdot\int_p^u\frac{h\left(s\right)}{\left(u-s\right)^{\sigma-m+1}}ds,\qquad(u>p).$$

Definition 3. ([1]) *The HFD of order $\sigma\in(0,1)$ and type $\tau\in[0,1]$ of a function $h(u)$ is given as;*

$$\left(D_{p^+}^{\sigma,\tau}h\right)(u)=\left(I_{p^+}^{\tau(1-\sigma)}D\left(I_{p^+}^{(1-\tau)(1-\sigma)}h\right)\right)(u),$$

where $D=\frac{d}{du}$.

Let $0<p<q<\infty$, and let $\mathcal{C}[p,q]$ denotes a Banach space of all continuous mappings from $[p,q]$ into $\mathbb{R}$ with the maximum norm

$$\|u\|_{\mathcal{C}}=\max\left\{|u\left(s\right)|:s\in[p,q]\right\}.$$

For $0\leq\kappa=\sigma+\tau-\sigma\tau<1$, we define $\mathcal{C}_{1-\kappa}[p,q]$, the weighted space of the continuous

functions ϕ as

$$\mathcal{C}_{1-\kappa}[p,q] = \{\phi(u) : [p,q] \to \mathbb{R} | \\ (u-p)^{1-\kappa}\phi(u) \in \mathcal{C}[p,q]\Big\}, \quad (3)$$

where $[p,q]$ is the finite interval.

Obviously, $\mathcal{C}_{1-\kappa}[p,q]$ is the weighted Banach space with the norm

$$\|\phi\|_{\mathcal{C}_{1-\kappa}} = \Big\|(u-p)^{1-\kappa}\phi(u)\Big\|_{\mathcal{C}}.$$

At the same time, we define a Banach space

$$\mathcal{C}_{\kappa}^{m}[p,q] := \Big\{\Theta \in \mathcal{C}^{m-1}[p,q] : \Theta^{(m)} \in \mathcal{C}_{\kappa}[p,q]\Big\},$$

with the norm

$$\|\Theta\|_{\mathcal{C}_{\kappa}^{m}} = \sum_{k=0}^{m-1}\Big\|\Theta^{(k)}\Big\|_{\mathcal{C}} + \Big\|\Theta^{(m)}\Big\|_{\mathcal{C}_{\kappa}}, \qquad m \in \mathbb{N}.$$

Also, $\mathcal{C}_{\kappa}^{0}[p,q] := \mathcal{C}_{\kappa}[p,q]$.

Lemma 1. ([3, 21]) *If $\sigma > 0$ and $\tau > 0$, there exists*

$$\Big[I_{p^+}^{\sigma}(t-p)^{\tau-1}\Big](u) = \frac{\Gamma(\tau)}{\Gamma(\tau+\sigma)}(u-p)^{\tau+\sigma-1}$$

and

$$\Big[D_{p^+}^{\sigma}(t-p)^{\sigma-1}\Big](u) = 0, \qquad 0 < \sigma < 1.$$

Lemma 2. ([3, 21]) *If $\sigma > 0, \tau > 0$, and $\phi \in \mathcal{L}^1(p,q)$, for $u \in [p,q]$, there exist the following properties,*

$$\Big(I_{p^+}^{\sigma}I_{p^+}^{\tau}\phi\Big)(u) = \Big(I_{p^+}^{\sigma+\tau}\phi\Big)(u)$$

and

$$\Big(D_{p^+}^{\sigma}I_{p^+}^{\sigma}\phi\Big)(u) = \phi(u).$$

In particular, if $\phi \in \mathcal{C}_{\kappa}[p,q]$ or $\phi \in \mathcal{C}[p,q]$, then above equalities hold at each $u \in (p,q]$ or $u \in [p,q]$, respectively.

Lemma 3. ([3, 21]) *Let $\sigma > 0$ and $0 \le \kappa < 1$. Then $I_{p^+}^{\sigma}$ is bounded from $\mathcal{C}_{\kappa}[p,q]$ into $\mathcal{C}_{\kappa}[p,q]$.*

Lemma 4. ([3, 21]) *Let $\sigma > 0$ and $0 \le \kappa < 1$. If $\phi \in \mathcal{C}_{\kappa}[p,q]$ and $I_{p^+}^{1-\sigma}\phi \in \mathcal{C}_{\kappa}^{1}[p,q]$, then*

$$I_{p^+}^{\sigma}D_{p^+}^{\sigma}\phi(u) = \phi(u) - \frac{I_{p^+}^{1-\sigma}\phi(p)}{\Gamma(\sigma)}(u-p)^{\sigma-1},$$

for all $u \in (p,q]$.

Lemma 5. ([3, 21]) *If $0 \le \kappa < 1$ and $\phi \in \mathcal{C}_{\kappa}[p,q]$, then*

$$I_{p^+}^{\sigma}\phi(p) := \lim_{u \to p^+} I_{p^+}^{\sigma}\phi(u) = 0, \qquad 0 \le \kappa < \sigma.$$

Now, we present the following weighted spaces which are required in our main result.

$$\mathcal{C}_{1-\kappa}^{\sigma,\tau} = \Big\{\phi \in \mathcal{C}_{1-\kappa}[p,q],\ D_{p^+}^{\sigma,\tau}\phi \in \mathcal{C}_{1-\kappa}[p,q]\Big\}$$

and

$$\mathcal{C}_{1-\kappa}^{\kappa} = \Big\{\phi \in \mathcal{C}_{1-\kappa}[p,q],\ D_{p^+}^{\kappa}\phi \in \mathcal{C}_{1-\kappa}[p,q]\Big\}.$$

It is obvious that

$$\mathcal{C}_{1-\kappa}^{\kappa}[p,q] \subset \mathcal{C}_{1-\kappa}^{\sigma,\tau}[p,q].$$

Lemma 6. ([3, 21]) *Let $\sigma, \tau > 0$ and $\kappa = \sigma + \tau - \sigma\tau$. If $f \in \mathcal{C}_{1-\kappa}^{\kappa}$, then*

$$I_{p^+}^{\kappa}D_{p^+}^{\kappa}f = I_{p^+}^{\sigma}D_{p^+}^{\sigma,\tau}f,$$

$$D_{p^+}^{\sigma}I_{p^+}^{\sigma}f = D_{p^+}^{\tau(1-\sigma)}f.$$

Lemma 7. ([3, 21]) *Let $h \in \mathcal{L}^1[p,q]$ and $D_{p^+}^{\tau(1-\sigma)}h \in \mathcal{L}^1[p,q]$ exists, then*

$$D_{p^+}^{\sigma,\tau}I_{p^+}^{\sigma}h = I_{p^+}^{\tau(1-\sigma)}D_{p^+}^{\tau(1-\sigma)}h.$$

Lemma 8. ([14, 21]). *Let a real-valued function ϕ defined on $(p,q] \times \mathbb{R}$ be such that, for any $\varphi \in \mathcal{C}_{1-\kappa}[p,q]$, $\phi(\cdot, \varphi(\cdot)) \in \mathcal{C}_{1-\kappa}[p,q]$. Then $\varphi \in \mathcal{C}_{1-\kappa}^{\kappa}[p,q]$ is a solution of IVP:*

$$D_{p^+}^{\sigma,\tau}\varphi(s) = \phi(s,\varphi(s)), \qquad 0 < \sigma < 1, 0 \le \tau \le 1,$$

$$I_{p^+}^{1-\kappa}\varphi(p^+) = \varphi_0, \qquad \kappa = \sigma + \tau - \sigma\tau,$$

iff φ verifies the next integral equation:

$$\varphi(s) = \frac{\varphi_0(s-p)^{\kappa-1}}{\Gamma(\kappa)} + \frac{1}{\Gamma(\sigma)} \cdot \int_p^s (s-w)^{\sigma-1}\phi(w, u(w))\,dw.$$

Now, the following are some of the concepts, which we will be employed in the main result.

Let $\mathcal{C}(\mathcal{J} \times \mathbb{R}, \mathbb{R})$ represents the category of continuous functions $\theta : \mathcal{J} \times \mathbb{R} \to \mathbb{R}$ and the kind of mappings $\phi : \mathcal{J} \times \mathbb{R} \to \mathbb{R}$, where the map

(1) $s \mapsto \phi(s,w)$ is measurable $\forall\ w \in \mathbb{R}$,
(2) $s \mapsto \phi(s,w)$ is continuous $\forall\ w \in \mathbb{R}$.

Moreover, the space $\mathcal{C}(\mathcal{J} \times \mathbb{R}, \mathbb{R})$ is referred to be the mappings of Carathéodory type on $\mathcal{J} \times \mathbb{R}$, which are Lebesgue integrable functions when bounded by a Lebesgue integrable function on $\mathcal{J}$.

Definition 4. ([22–24]) *A function $\Upsilon : \mathbb{R}_+ \to \mathbb{R}_+$ which is upper semi-continuous and non-decreasing in nature is said to be a $\mathcal{D}$-function if $\Upsilon(0) = 0$. Moreover, $\mathfrak{D}$ represents the category of each $\mathcal{D}$-functions on $\mathbb{R}_+$.*

Definition 5. ([22–24]) *For an operator $\Delta : \mathcal{C}_{1-\kappa}(\mathcal{J}, \mathbb{R}) \to \mathcal{C}_{1-\kappa}(\mathcal{J}, \mathbb{R})$, if there is a $\mathcal{D}$-function $\Upsilon_{\Delta} \in \mathfrak{D}$, where*

$$\|\Delta v - \Delta w\| \le \Upsilon_{\Delta}(\|v - w\|),$$

for all $v, w \in \mathcal{C}_{1-\kappa}(\mathcal{J}, \mathbb{R})$, where $0 < \Upsilon_{\Delta}(\alpha) < \alpha$ for all $\alpha > 0$, then the operator Δ is referred as a nonlinear $\mathcal{D}$-contraction on $\mathcal{C}_{1-\kappa}(\mathcal{J}, \mathbb{R})$.

Theorem 1. ([25, 33]) *Let $\mathcal{K} \subset \mathcal{C}_{1-\kappa}(\mathcal{J},\mathbb{R})$ be closed, convex, and bounded in nature. Let the operators $\Delta : \mathcal{C}_{1-\kappa}(\mathcal{J},\mathbb{R}) \to \mathcal{C}_{1-\kappa}(\mathcal{J},\mathbb{R})$ and $\Omega : \mathcal{K} \to \mathcal{C}_{1-\kappa}(\mathcal{J},\mathbb{R})$ satisfying:*

(1) *Δ is $\mathcal{D}$-contraction of nonlinear type,*
(2) *Ω is completely continuous and*
(3) *$u = \Delta u + \Omega w \Rightarrow u \in \mathcal{K}$ for all $w \in \mathcal{K}$.*

Then, the mapping $\Delta + \Omega$ owns a fixed point in $\mathcal{K}$.

Lemma 9. *Let a function $f : \mathcal{J} \times \mathbb{R} \to \mathbb{R}$ such that, for any $\varphi \in \mathcal{C}_{1-\kappa}[p,q]$, $f(\cdot, \varphi(\cdot)) \in \mathcal{C}_{1-\kappa}[p,q]$. Then, $\varphi \in \mathcal{C}_{1-\kappa}[p,q]$ is a solution of fractional IVP*

$$D^{\sigma,\tau}_{p^+}[\varphi(s) - f(s,\varphi(s))] = z(s), \qquad s \in \mathcal{J}, \tag{4}$$

$$I^{1-\kappa}_{p^+}[\varphi(s) - f(s,\varphi(s))]\left(p^+\right) = \varphi_0, \quad \kappa = \sigma+\tau-\sigma\tau, \tag{5}$$

if and only if $\varphi(s)$ satisfies the following VIE

$$\varphi(s) = \frac{\varphi_0(s-p)^{\kappa-1}}{\Gamma(\kappa)} + f(s,\varphi(s)) + \frac{1}{\Gamma(\sigma)}\int_p^s (s-w)^{\sigma-1} z(w)\, dw. \tag{6}$$

Proof. Let φ be a solution of (4)–(5). Consequently, by Lemma 4, we obtain

$$\begin{aligned} I^{\sigma}_{p^+} D^{\sigma,\tau}_{p^+}[\varphi(s) - f(s,\varphi(s))] &= \varphi(s) - f(s,\varphi(s)) \\ &\quad - \frac{I^{1-\kappa}_{p^+}[\varphi(s) - f(s,\varphi(s))](p^+)}{\Gamma(\kappa)}(s-p)^{\kappa-1} \\ &= I^{\sigma}_{p^+} z(s). \end{aligned}$$

Then,

$$\begin{aligned} \varphi(s) - f(s,\varphi(s)) &= I^{\sigma}_{p^+} z(s) \\ &\quad + \frac{I^{1-\kappa}_{p^+}[\varphi(s) - f(s,\varphi(s))](p^+)}{\Gamma(\kappa)}(s-p)^{\kappa-1} \\ &= I^{\sigma}_{p^+} z(s) + \frac{\varphi_0(s-p)^{\kappa-1}}{\Gamma(\kappa)}. \end{aligned}$$

So,

$$\begin{aligned} \varphi(s) &= \frac{\varphi_0(s-p)^{\kappa-1}}{\Gamma(\kappa)} + f(s,\varphi(s)) + I^{\sigma}_{p^+} z(s) \\ &= \frac{\varphi_0(s-p)^{\kappa-1}}{\Gamma(\kappa)} + f(s,\varphi(s)) \\ &\quad + \frac{1}{\Gamma(\sigma)}\int_p^s (s-w)^{\sigma-1} z(w)\, dw, \quad s \in \mathcal{J}. \end{aligned} \tag{7}$$

Thus, Equation (6) holds. Now, to demonstrate the sufficiency. Let $\varphi \in \mathcal{C}^{\kappa}_{1-\kappa}[p,q]$ satisfy Equation (6), which can be expressed as (7).

By applying $D^{\kappa}_{p^+}$ to either sides of (7), it can be deduced from Lemma 1, Lemma 6, and Definition 2 that

$$D^{\kappa}_{p^+}[\varphi(s) - f(s,\varphi(s))] = D^{\tau(1-\sigma)}_{p^+} z(s). \tag{8}$$

From (8), and the hypothesis $D^{\kappa}_{p^+}[\varphi - f(\cdot,\varphi(\cdot))] \in \mathcal{C}_{1-\kappa}[a,b]$, we have

$$DI^{1-\tau(1-\sigma)}_{p^+} z = D^{\tau(1-\sigma)}_{p^+} z \in \mathcal{C}_{1-\kappa}[a,b]. \tag{9}$$

Also, since $z \in \mathcal{C}_{1-\kappa}[a,b]$, by Lemma 3,

$$I^{1-\tau(1-\sigma)}_{p^+} z \in \mathcal{C}_{1-\kappa}[a,b]. \tag{10}$$

It follows from equations (9) and (10) that

$$I^{1-\tau(1-\sigma)}_{p^+} z \in \mathcal{C}^1_{1-\kappa}[a,b].$$

Thus, z and $I^{1-\tau(1-\sigma)}_{p^+} z$ verify the conditions of Lemma 4.

Next, applying $I^{1-\tau(1-\sigma)}_{p^+}$ to either sides of Equation (8), and using Def. 3, and Lemma 4, it implies that

$$\begin{aligned} D^{\sigma,\tau}_{p^+}[\varphi(s) - f(s,\varphi(s))] &= z(s) \\ &\quad - \frac{\left[I^{1-\tau(1-\sigma)}_{p^+} z(s)\right](p^+)}{\Gamma(\tau(1-\sigma))}(s-p)^{\tau(1-\sigma)-1}. \end{aligned} \tag{11}$$

Since, $1-\kappa < 1-\tau(1-\sigma)$, using Lemma 5, we get

$$\left[I^{1-\tau(1-\sigma)}_{p^+} z(s)\right]\left(p^+\right) = 0.$$

Hence, (11) reduces to

$$D^{\sigma,\tau}_{p^+}[\varphi(s) - f(s,\varphi(s))] = z(s), \qquad s \in \mathcal{J}.$$

Now, in order to show that equation (5) also holds, apply $I^{1-\kappa}_{p^+}$ to either sides of (7), then by means of Lemma 1 and Lemma 2, we get

$$I^{1-\kappa}_{p^+}\varphi(s) = \varphi_0 + I^{1-\kappa}_{p^+} f(s,\varphi(s)) + I^{1-\kappa}_{p^+} I^{\sigma}_{p^+} z(s).$$

Since, $1-\kappa < 1-\tau(1-\sigma)$ it follows from Lemma 5, when taking the limit as $s \to p^+$

$$I^{1-\kappa}_{p^+}[\varphi(s) - f(s,\varphi(s))]\left(p^+\right) = \varphi_0.$$

This completes the proof. □

3. Main result

Taking into account the following theories, we can demonstrate the main result:

Q1: Following weak contraction condition holds for the function $f(s,\cdot)$

$$|f(s,v) - f(s,w)| \le \psi_{\mathcal{D}}(|v-w|),$$

for all $s \in \mathcal{J}$ and $v, w \in \mathbb{R}$, where $\psi_{\mathcal{D}}(s)$ is a $\mathcal{D}-$function.

Q2: For every $s \in \mathcal{J}$ and $v \in \mathbb{R}$, there is a continuous function $\xi \in \mathcal{C}_{1-\kappa}(\mathcal{J},\mathbb{R})$,

where

$$|g(s,v)| \leq \xi(s).$$

Theorem 2. *Suppose that the assumptions (Q1) and (Q2) are fulfilled. If $(q-p)^{1-\kappa} < 1$, then the IVP (1)–(2) possesses a solution in $\mathcal{C}_{1-\kappa}(\mathcal{J},\mathbb{R})$.*

Proof. Let $\mathcal{K} = \left\{\varphi \in \mathcal{C}_{1-\kappa}(\mathcal{J},\mathbb{R}) : \|\varphi\|_{\mathcal{C}_{1-\kappa}} \leq \eta\right\}$, where

$$\eta \geq \frac{\frac{|\varphi_0|}{\Gamma(\kappa)} + \Lambda + \frac{(q-p)^{\sigma}\beta(\kappa,\sigma)}{\Gamma(\sigma)}\|\xi\|_{C_{1-\kappa}}}{1-(q-p)^{1-\kappa}},$$

$(q-p)^{1-\kappa} < 1$ and $\Lambda = \max_{t\in\mathcal{J}}(s-p)^{1-\kappa} f(s,0)$. Certainly, $\mathcal{K} \subset \mathcal{C}_{1-\kappa}(\mathcal{J},\mathbb{R})$ which is closed, convex, and bounded in nature.

Now, in order to establish the existence result for the IVP (1)–(2), let us consider the generalized IVP involving HFD operator of order σ and type τ, for $z \in \mathcal{K}$, as follows:

$$D_{p^+}^{\sigma,\tau}[\varphi(s) - f(s,\varphi(s))] = g(s,z(s)), \qquad s \in \mathcal{J}, \tag{12}$$

$$I_{p^+}^{1-\kappa}[\varphi(s) - f(s,\varphi(s))](p^+) = \varphi_0, \tag{13}$$

where $0 < \sigma < 1, 0 \leq \tau \leq 1$ and $\kappa = \sigma + \tau - \sigma\tau$, $\mathcal{J} = [p,q]$, for some fixed $p,q \in \mathbb{R}^+$ and $f,g \in \mathcal{C}(\mathcal{J}\times\mathbb{R},\mathbb{R})$.

Assume that the hypotheses (Q1) and (Q2) hold for the functions f and g. Using Lemma 9, we get the equivalent non-linear VIE to the IVP (12)–(13) as

$$\varphi(s) = \frac{\varphi_0}{\Gamma(\kappa)}(s-p)^{\kappa-1} + f(s,\varphi(s)) + \frac{1}{\Gamma(\sigma)}\int_p^s (s-w)^{\sigma-1} g(s,z(w))\,dw. \tag{14}$$

Consider the operators $\Delta : \mathcal{C}_{1-\kappa}(\mathcal{J},\mathbb{R}) \to \mathcal{C}_{1-\kappa}(\mathcal{J},\mathbb{R})$ and $\Omega : \mathcal{K} \to \mathcal{C}_{1-\kappa}(\mathcal{J},\mathbb{R})$ defined as follows:

$$(\Delta\varphi)(s) = \frac{\varphi_0}{\Gamma(\kappa)}(s-p)^{\kappa-1} + f(s,\varphi(s)), \quad s \in \mathcal{J}, \tag{15}$$

and

$$(\Omega z)(s) = \frac{1}{\Gamma(\sigma)}\int_p^s (s-w)^{\sigma-1} g(w,z(w))\,dw, \tag{16}$$

$$s \in \mathcal{J}.$$

Hence, the equation (14) can be transformed as

$$\varphi(s) = \Delta\varphi(s) + \Omega z(s), \qquad s \in \mathcal{J}. \tag{17}$$

Next, we will show that the operators Δ and Ω satisfy all the conditions of Theorem 1. The proof is divided into the following steps.

Step I: Operator Δ is non-linear $\mathcal{D}-$contraction.

Let $v, w \in \mathcal{C}_{1-\kappa}(\mathcal{J},\mathbb{R})$, by hypothesis (Q1), we have

$$\begin{aligned}\left|(s-p)^{1-\kappa}\right. &(\Delta v(s) - \Delta w(s))| \\ &= (s-p)^{1-\kappa}|f(s,v(s)) - f(s,w(s))| \\ &\leq (s-p)^{1-\kappa}\psi_D(|v(s)-w(s)|) \\ &\leq (s-p)^{1-\kappa}\psi_D \\ &\quad\cdot\left((s-p)^{\kappa-1}\|v-w\|_{\mathcal{C}_{1-\kappa}}\right).\end{aligned}$$

Applying a maximum over s gives

$$\|\Delta v - \Delta w\|_{\mathcal{C}_{1-\kappa}} \leq \psi_D\left(\|v-w\|_{\mathcal{C}_{1-\kappa}}\right).$$

Hence, the operator Δ is a non-linear contraction.

Step II: Operator Ω is a continuous and compact on $\mathcal{K}$ into $\mathcal{C}_{1-\kappa}(\mathcal{J},\mathbb{R})$.

First, to show Ω is continuous on $\mathcal{K}$, consider a sequence $\{z_n\}$ in $\mathcal{K}$ converging to $z \in \mathcal{K}$. Then, it implies from the Lebesgue-dominated convergence theorem that

$$\begin{aligned}&\lim_{n\to\infty}\Omega z_n(s) \\ &= \lim_{n\to\infty}\frac{1}{\Gamma(\sigma)}\int_p^s (s-w)^{\sigma-1} g(w,z_n(w))\,dw \\ &= \frac{1}{\Gamma(\sigma)}\int_p^s (s-w)^{\sigma-1}\lim_{n\to\infty} g(w,z_n(w))\,dw \\ &= \frac{1}{\Gamma(\sigma)}\int_p^s (s-w)^{\sigma-1} g(w,z(w))\,dw \\ &= \Omega z(s), \quad \forall s \in \mathcal{J}.\end{aligned}$$

This proves the continuity for Ω. Next, we prove that $\Omega\mathcal{K}$ is a uniformly bounded and equicontinuous set in $\mathcal{K}$ which implies the compactness of Ω on $\mathcal{K}$.

It follows from the hypothesis (Q2) that

$$\begin{aligned}&\left|(s-p)^{1-\kappa}\Omega z(s)\right| \\ &= \left|\frac{(s-p)^{1-\kappa}}{\Gamma(\sigma)}\int_p^s (s-w)^{\sigma-1} g(w,z(w))\,ds\right| \\ &\leq \frac{(s-p)^{1-\kappa}}{\Gamma(\sigma)}\int_p^s (s-w)^{\sigma-1}|g(w,z(w))|\,ds \\ &\leq \frac{(s-p)^{1-\kappa}}{\Gamma(\sigma)}\int_p^s (s-w)^{\sigma-1}\xi(w)\,ds\end{aligned}$$

$$
\begin{aligned}
&\left|(s-p)^{1-\kappa}\Omega z\left(s\right)\right| \\
&\leq \frac{(s-p)^{1-\kappa}}{\Gamma\left(\sigma\right)}\int_{p}^{s}(s-w)^{\sigma-1}(s-p)^{\kappa-1}\left\|\xi\right\|_{C_{1-\kappa}}ds \\
&\leq \frac{(q-p)^{\sigma}\beta(\kappa,\sigma)}{\Gamma\left(\sigma\right)}\left\|\xi\right\|_{C_{1-\kappa}}, \quad \forall\ s\in\mathcal{J}.
\end{aligned}
$$

Taking maximum over s, we get

$$
\left\|\Omega z\right\|_{C_{1-\kappa}} \leq \frac{(q-p)^{\sigma}\beta(\kappa,\sigma)}{\Gamma\left(\sigma\right)}\left\|\xi\right\|_{C_{1-\kappa}}.
$$

This proves the uniform boundedness of the operator Ω on $\mathcal{K}$. Let $s_1, s_2 \in \mathcal{J}$ with $s_1 < s_2$. For any $z \in \mathcal{K}$, one has

$$
\begin{aligned}
&\left|(s_1-p)^{1-\kappa}\Omega z\left(s_1\right)-(s_2-p)^{1-\kappa}\Omega z\left(s_2\right)\right| \\
&=\left|\frac{(s_1-p)^{1-\kappa}}{\Gamma\left(\sigma\right)}\int_{p}^{s_1}(s_1-w)^{\sigma-1}g\left(w,z\left(w\right)\right)dw\right. \\
&\quad\left.-\frac{(s_2-p)^{1-\kappa}}{\Gamma\left(\sigma\right)}\int_{p}^{s_2}(s_2-w)^{\sigma-1}g\left(w,z\left(w\right)\right)dw\right| \\
&\leq \frac{\left\|\xi\right\|_{C_{1-\kappa}}\beta(\kappa,\sigma)}{\Gamma\left(\sigma\right)}\left|(s_1-p)^{1-\kappa}(s_1-p)^{\sigma+\kappa-1}\right. \\
&\quad\left.-(s_2-p)^{1-\kappa}(s_2-p)^{\sigma+\kappa-1}\right| \\
&\leq \frac{\left\|\xi\right\|_{C_{1-\kappa}}\beta(\kappa,\sigma)}{\Gamma\left(\sigma\right)}\left|(s_1-p)^{\sigma}-(s_2-p)^{\sigma}\right|.
\end{aligned}
$$

Thus, there exists a $\varepsilon > 0$, for some η such that

$$
\begin{aligned}
|s_2-s_1|\leq\varepsilon \ \Rightarrow\ &\left|(s_1-p)^{1-\kappa}\Omega z\left(s_1\right)\right. \\
&\left.-(s_2-p)^{1-\kappa}\Omega z\left(s_2\right)\right|\leq\eta,
\end{aligned}
$$

for all $s_2, s_1 \in \mathcal{J}$ and $z \in \mathcal{K}$. This proves the equicontinuity of $\Omega\mathcal{K}$ in $\mathcal{C}_{1-\kappa}\left(\mathcal{J},\mathbb{R}\right)$ and hence, by Arzela–Ascoli theorem, it is compact.

Step III: There exists $\varphi \in \mathcal{K}$ such that $\varphi = \Delta\varphi + \Omega z$ for all $z \in \mathcal{K}$.

Let $\varphi \in \mathcal{C}_{1-\kappa}\left(\mathcal{J},\mathbb{R}\right)$ and $z \in \mathcal{K}$, such that $\varphi = \Delta\varphi + \Omega z$. Using Hypothesis (Q1), we can write

$$
\begin{aligned}
&\left|(s-p)^{1-\kappa}\varphi\left(s\right)\right| \\
&=\left|(s-p)^{1-\kappa}\left(\Delta\varphi\left(s\right)+\Omega z\left(s\right)\right)\right| \\
&\leq\left|(s-p)^{1-\kappa}\Delta\varphi\left(s\right)\right|+\left|(s-p)^{1-\kappa}\Omega z\left(s\right)\right| \\
&\leq\frac{|\varphi_0|}{\Gamma\left(\kappa\right)}+\left|(s-p)^{1-\kappa}f\left(s,\varphi\left(s\right)\right)\right| \\
&\quad+\left|\frac{(s-p)^{1-\kappa}}{\Gamma\left(\sigma\right)}\int_{p}^{s}(s-w)^{\sigma-1}g\left(w,z\left(w\right)\right)dw\right| \\
&\leq\frac{|\varphi_0|}{\Gamma\left(\kappa\right)}+(s-p)^{1-\kappa}\left|f\left(s,\varphi\left(s\right)\right)-f\left(s,0\right)\right| \\
&\quad+(s-p)^{1-\kappa}\left|f\left(s,0\right)\right| \\
&\quad+\left|\frac{(s-p)^{1-\kappa}}{\Gamma\left(\sigma\right)}\int_{p}^{s}(s-w)^{\sigma-1}g\left(w,z\left(w\right)\right)dw\right| \\
&\leq\frac{|\varphi_0|}{\Gamma\left(\kappa\right)}+(q-p)^{1-\kappa}\psi_D\left(\left\|\varphi\right\|_{C_{1-\kappa}}\right)+\Lambda \\
&\quad+\frac{(q-p)^{\sigma}\beta(\kappa,\sigma)}{\Gamma\left(\sigma\right)}\left\|\xi\right\|_{C_{1-\kappa}} \\
&\leq\frac{|\varphi_0|}{\Gamma\left(\kappa\right)}+(q-p)^{1-\kappa}\psi_D\left(\eta\right)+\Lambda \\
&\quad+\frac{(q-p)^{\sigma}\beta(\kappa,\sigma)}{\Gamma\left(\sigma\right)}\left\|\xi\right\|_{C_{1-\kappa}} \\
&\leq\frac{|\varphi_0|}{\Gamma\left(\kappa\right)}+(q-p)^{1-\kappa}\eta+\Lambda \\
&\quad+\frac{(q-p)^{\sigma}\beta(\kappa,\sigma)}{\Gamma\left(\sigma\right)}\left\|\xi\right\|_{C_{1-\kappa}}.
\end{aligned}
$$

Applying maximum over s, we get

$$
\begin{aligned}
\left\|\varphi\right\|_{C_{1-\kappa}} &\leq \frac{|\varphi_0|}{\Gamma\left(\kappa\right)}+(q-p)^{1-\kappa}\eta+\Lambda \\
&\quad+\frac{(q-p)^{\sigma}\beta(\kappa,\sigma)}{\Gamma\left(\sigma\right)}\left\|\xi\right\|_{C_{1-\kappa}} \\
&\leq \eta.
\end{aligned}
$$

Hence, $\varphi \in \mathcal{K}$. Thus, all the three assumptions of the Theorem 1 are hold, which implies that there exists $\varphi \in \mathcal{K}$ such that $\Delta\varphi + \Omega\varphi = \varphi$. Thus, the operator $\Delta + \Omega$ has a fixed point in $\mathcal{K}$. Hence, the IVP (1)–(2) owns a solution in $\mathcal{C}_{1-\kappa}\left(\mathcal{J},\mathbb{R}\right)$. □

Remark 1. *For $\tau = 1$ the IVP (1)–(2) reduces to a problem with the fractional derivative operator of Caputo type. Hence, the results obtained in the Theorem 2 coincide with the results published in.*[32, 33]

4. Application

Consider the following IVP:

$$
D_{0^+}^{\frac{1}{2},\frac{1}{2}}\left[\varphi\left(s\right)-\ln(1+|\varphi(s)|)\right]=\frac{1}{s^2+1}\sin(|\varphi(s)|), \tag{18}
$$

$$
s\in\mathcal{J}=(0,\frac{1}{2}],
$$

$$
I_{0^+}^{1-\frac{3}{4}}\left[\varphi\left(s\right)-\ln(1+|\varphi(s)|)\right](0^+)=2, \tag{19}
$$

Here, $\sigma=\frac{1}{2},\tau=\frac{1}{2},\kappa=\frac{3}{4},p=0,q=\frac{1}{2},\varphi_0=2$,

$$
f\left(s,\varphi\left(s\right)\right)=\ln(1+|\varphi(s)|),
$$

and

$$g\left(s,\varphi\left(s\right)\right)=\frac{1}{s^{2}+1}\sin(|\varphi(s)|).$$

Hence, we find that

$$\left|f\left(s,\varphi\right)-f\left(s,\bar{\varphi}\right)\right|\leq\left|\ln(1+|\varphi|)-\ln(1+|\bar{\varphi}|)\right|$$

$$\begin{aligned}\left|f\left(s,\varphi\right)-f\left(s,\bar{\varphi}\right)\right| &= \ln\frac{1+|\varphi|}{1+|\bar{\varphi}|}\\ &= \ln\left(1+\frac{|\varphi|-|\bar{\varphi}|}{1+|\bar{\varphi}|}\right)\\ &\leq \ln\left(1+\frac{|\varphi-\bar{\varphi}|}{1+|\bar{\varphi}|}\right)\\ &\leq \ln\left(1+|\varphi-\bar{\varphi}|\right)\\ &\leq \psi_{\mathcal{D}}\left(|\varphi-\bar{\varphi}|\right),\end{aligned}$$

for each $s\in(0,\frac{1}{2}]$, where $\psi_{\mathcal{D}}(s)=\ln(1+s)$ is a $\mathcal{D}-$function, such that $0<\psi_{\mathcal{D}}(0)=0$ and $\psi_{\mathcal{D}}(s)<s$, that is $h(s)=s-\ln(1+s)$, we have $h'(s)=1-\frac{1}{1+s}=s>0$, for $s\in(0,\frac{1}{2}]$. Also,

$$|g\left(s,\varphi\left(s\right)\right)|\leq\frac{1}{s^{2}+1}=\xi(s).$$

Additionally, $(q-p)^{1-\kappa}\approx 0.84<1$. Therefore, all assumptions of Theorem 2 are satisfied, it implies that the IVP (18)–(19) possesses a solution in $\mathcal{C}_{1-\kappa}\left(\mathcal{J},\mathbb{R}\right)$.

5. Conclusions

In this article, a Hilfer FDE with linear perturbations of the second type under a certain initial condition was discussed for the existence of the solution. An equivalent VIE is obtained for the IVP (1)–(2). The main result on the existence of the solution to IVP was established employing the Krasnoselskii–Dhage type fixed-point theorem in the weighted Banach space. At the end, an application was given to check the validity of the outcomes. The initial value problem discussed in this paper along with the fractional derivative operator considered in the IVP (1)–(2) generalizes the existing results available in the literature. In IVP (1)–(2) if we put $\tau=1$, then the results obtained in the paper coincide with the results published in.[32,33] However, it could be interesting to see the impact of the inclusion of the control term in IVP (1)–(2). This idea may be an open problem for future investigations.

Acknowledgments

This study is supported via funding from Prince Sattam bin Abdulaziz University project number (PSAU/2025/R/1446).

Fundings

None.

Conflict of interest

The authors declare no conflict of interest.

Author contributions

Conceptualization: Amol D. Khandagale, Arif S. Bagwan, Sabri T. M. Thabet
Formal analysis: Arif S. Bagwan, Sabri T. M. Thabet and Imed Kedim
Investigation: Arif S. Bagwan, Sabri T. M. Thabet, Imed Kedim
Methodology: All authors
Writing-original draft: Arif S. Bagwan, Sabri T. M. Thabet
Writing-review & editing: Arif S. Bagwan, Sabri T. M. Thabe

Availability of data

Not applicable.

AI tools statement

All authors confirm that no AI tools were used in the preparation of this manuscript.

References

1. Hilfer R. Fractional Time Evolution: Applications of Fractional Calculus in Physics. *London: World Scientific*; 2000.
2. Smart DR. Fixed Point Theorems. *Cambridge University Press*; 1973.
3. Kilbas AA, Srivastava HM, Trujillo JJ. Theory and Applications of Fractional Differential Equations. *Amsterdam:Elsevier*; 2006.
4. Miller KS, Ross B. An Introduction to the Fractional Calculus and Differential E quations. *New York: John Wiley*; 1993.
5. Abdeljawad T, Thabet STM, Kedim I, and Cortez VM. On a new structure of multi-term Hilfer fractional impulsive neutral Levin-Nohel integrodifferential system with variable time delay. AIMS Math. 2024;9(3):7372-7395.
6. Rezapour S, Thabet STM, Rafeeq AS, Kedim I, Vivas-Cortez M, Aghazadeh N. Topology degree results on a G-ABC implicit fractional differential equation under three-point boundary conditions. PLoS ONE 2024; 19(7): e0300590. https://doi.org/10.1371/journal.pone.0300590
7. Salim A, Thabet STM , Kedim I, Vivas-Cortez M. On the nonlocal hybrid (k,φ)-Hilfer inverse problem with delay and anticipation. AIMS Math. 2024;9(8): 22859–22882. https://doi.org/10.3934/math.20241112
8. Ahmad B, Ntouyas SK. Initial value problem of fractional order Hadamard-type functional differential equations. *Electron J Differ Equat.* 2015;2015:1-9.

9. Bagwan A, & Pachpatte D. Existence and stability of nonlocal initial value problems involving generalized Katugampola derivative. *Kragujevac J Math.*, 2022;46(3):443-460.
10. Bagwan A, Pachpatte D. Existence and uniqueness results for implicit fractional differential equations involving generalized Katugampola derivative. *South East Asian JMath Mathemat Sci.* 2021;17(1):77-94.
11. Bagwan A, Pachpatte D. On the existence results of a coupled system of generalized Katugampola fractional differential equations. *Prog Fract Differ Appl.*, 2023;9(2):257-269.
12. Bagwan A, Pachpatte D, Kiseľák J, Stehlík M. On existence results of boundary value problems of Caputo fractional difference equations for weak-form efficient market hypothesis. *Stoch Anal Appl.*, 2025;43(1):30-47. https://doi.org/10.1080/07362994.2024.2424343
13. Benchohra M, Lazreg JE. Existence and Ulam stability for nonlinear implicit fractional differential equations with Hadamard derivative. *Stud Univ Babes-Bolyai Math.* 2017;62:27-38.
14. Furati KM, Kassim MD, Tatar Ne. Existence and uniqueness for a problem involving Hilfer fractional derivative. *Comput Math Appl.*, 2012;64:1616-1626.
15. Hilfer R, Luckho Y, Tomovski Z. Operational method for the solution of fractional differential equations with generalized Riemann–Liouville fractional derivatives. *Fract Calc Appl Anal.* 2009;12:289-318.
16. Furati KM, Kassim MD, Tatar NE-. Nonexistence of global solutions for differential equations involving Hilfer fractional derivative. *Electron J Differ Equat.*2013;2013:1-10.
17. Khandagake AD, Hamoud AA, Ghadle KP. Existence of solutions for fractional integro-differential equations involving the Caputo type Atangana–Baleanu derivative. *Turkish J Comput Math Educ.* 2021;12(14):613-620.
18. Khandagake AD, Hamoud AA, Ghadle KP. New results on nonlocal fractional Volterra–Fredholm integro-differential equations. *J Math Comput Sci.* 2021;11(5): 6193-6204.
19. Khandagake AD, Hamoud AA, Shah R, Ghadle KP. Some new results on Hadamard neutral fractional nonlinear Volterra–Fredholm integro-differential equations. *Discontin Nonlinear Complex.* 2023;12(4):893-903.
20. Subashini R, Jothimani K, Saranya S, Ravichandran C. On the results of Hilfer fractional derivatives with nonlocal conditions. *Int J Pure Appl Math.* 2018;118:277-289.
21. Wang J, Zhang Y. Nonlocal initial value problems for differential equations with Hilfer fractional derivative. *Appl Math Comput.* 2015;266:850-859.
22. Dhage BC. Remarks on two fixed point theorems involving the sum and product of two operators. *Comput Math Appl.* 2003;46:1779-1785.
23. Dhage BC. Random fixed point theorems in Banach algebras with applications to random integral equations. *Tamkang J Math.* 2003;34:29-43.
24. Dhage BC. A fixed point theorem in Banach algebras with applications to functional integral equations. *Kyungpook Math J.* 2004;44:145-155.
25. Dhage BC. Some variants of two basic hybrid fixed point theorems of Krasnoselskii and Dhage with applications. *Nonlinear Stud.* 2018;25:559-573.
26. Mohan RM, Vijayakumar V, Veluvolu KC, Shukla A, Nisar KS. Existence and optimal control results for Caputo fractional delay Clark's subdifferential inclusions of order $r \in (1, 2)$ with sectorial operators. *Optimal Control Appl Methods.* 2024;45(4):1832-1850. doi: 10.1002/oca.3125
27. Mohan RM, Vijayakumar V, Shukla A, Nisar KS, Rezapour S. Investigating existence results for fractional evolution inclusions with order $r \in (1, 2)$ in Banach space. *Int J Nonlinear Sci Numer Simulat.* 2023;24(6): 2047-2060. https://doi.org/10.1515/ijnsns-2021-0368
28. Mohan RM, Vijayakumar V, Veluvolu KC. Higher-order Caputo fractional integro differential inclusions of Volterra–Fredholm type with impulses and infinite delay: existence results. *J Appl Math Comput.* 2025. https://doi.org/10.1007/s12190-025-02412-4
29. Mohan RM, Vijayakumar V, Veluvolu KC. Improved order in Hilfer fractional differential systems: solvability and optimal control problem for hemivariational inequalities. *Chaos Solit Fractals* 2024;188:115558. https://doi.org/10.1016/j.chaos.2024.115558
30. Dhage C, Lakshmikantham V. Basic results on hybrid differential equations. *Nonlinear Anal Real World Appl.* 2010;4:414-424.
31. Dhage BC, Jadhav NS. Basic results in the theory of hybrid differential equations with linear perturbations of second type. *Tamkang J Math.*, 2013;44:171-186.
32. Lu H, Sun S, Yang D, Teng H. Theory of fractional hybrid differential equations with linear perturbations of second type. *Bound Value Probl.*2013;23:1-16.
33. Akhadkulov H, Alsharari F, Ying TY. Applications of Krasnoselskii–Dhage type fixed-point theorems to fractional hybrid differential equations. *Tamkang J Math.* 2021;52(2):281-292.
34. Kiataramkul C, Ntouyas SK, Tariboon J. Existence results for ψ-Hilfer fractional integro-differential hybrid boundary Value problems for differential equations and inclusions. *Adv Math Phys.* 2021:12.Article Id: 9044313. https://doi.org/10.1155/2021/9044313
35. Sene N, Ndiaye A. Existence and uniqueness study for partial neutral functional fractional differential equation under Caputo derivative. *Int J Optim Control Theor Appl IJOCTA.*, 2024;14(3): 208-219. https://doi.org/10.11121/ijocta.1464

36. Houas M, Alzabut J, Khuddush M. Existence and stability analysis to the sequential coupled hybrid system of fractional differential equations with two different fractional derivatives. *Int J Optim Control Theor Appl IJOCTA*. 2023;13(2):224-235. http://doi.org/10.11121/ijocta.2023.1278
37. Mani G, Gnanaprakasam AJ, Guran L, George R, Mitrović ZD. Some results in fuzzy b-metric space with b-triangular property and applications to Fredholm Integral equations and dynamic programming. *Mathematics*2023; 11(19):4101. https://doi.org/10.3390/math11194101
38. Mani G, Gnanaprakasam AJ, Ege O, Aloqaily A, Mlaiki N. Fixed point results in C^*-algebra-valued partial b-Metric spaces with related application. *Mathematics*. 2023;11(5):1158. https://doi.org/10.3390/math11051158
39. Yavuz M. Novel solution methods for initial boundary value problems of fractional order with conformable differentiation. *Int J Optim Control Theor Appl IJOCTA*. 2018;8(1):1-7. https://doi.org/10.11121/ijocta.01.2018.00540
40. Akgül A, Inc M, Baleanu D. On solutions of variable-order fractional differential equations. *Int J Optim Control Theor Appl IJOCTA*. 2017;7(1):112-116. http://doi.org/10.11121/ijocta.01.2017.00368
41. Mani G, Haque S, Gnanaprakasam AJ, Ege O, Mlaiki N. The study of bicomplex-Valued controlled metric spaces with applications to fractional differential equations. *Mathematics*. 2023;11(12):2742. https://doi.org/10.3390/math11122742
42. Gnanaprakasam AJ, Mani G, Ege O, Aloqaily A, Mlaiki N. New fixed point results in orthogonal B-metric spaces with related applications. *Mathematics*. 2023;11(3):677. https://doi.org/10.3390/math11030677
43. Nallaselli G, Gnanaprakasam AJ, Mani G, Mitrović ZD, Aloqaily A, Mlaiki N. Integral equation via fixed point theorems on a new type of convex contraction in b-Metric and 2-Metric spaces. *Math*. 2023;11(2):344. https://doi.org/10.3390/math11020344

Amol D. Khandagale *Dr. Amol D. Khandagale is an Associate Professor at the Department of Mathematics, Dr. Babasaheb Ambedkar Marathwada University, Chhatrapati Sambhajinagar (Aurangabad), Maharashtra, India. He has been awarded a Ph.D. degree in Mathematics from Dr. Babasaheb Ambedkar Marathwada University, Chhatrapati Sambhajinagar (Aurangabad), Maharashtra, India with title "A Study on Fractional Integro-Differential Equations". His research interests span Fractional Differential and Integro-Differential Equations, Integral Transforms, Fractional Difference Equations, and Fractional Integral Inequalities. Dr. Amol has authored numerous papers in international journals and conference proceedings. He also supervised master's students for their research projects in various areas of Mathematics.*
https://orcid.org/0000-0002-8028-4335

Arif S. Bagwan *Dr. Arif S. Bagwan is an Assistant Professor and Deputy Controller of Examination at Pimpri Chinchwad College of Engineering, Nigdi, Pune. He pursued his Ph.D. in Mathematics from Dr. Babasaheb Ambedkar Marathwada University, Aurangabad, India where he studied the existence, uniqueness and stability results of some fractional differential equations by means of some fixed point theorems. Dr. Arif has published his work in some reputed international journals. His research interest is discrete and continuous fractional calculus and fixed point theory. He actively participates in international conferences.*
https://orcid.org/0000-0003-4789-7049

Sabri T. M. Thabet *Dr. Sabri T. M. Thabet is an Associate Professor and Head of the Mathematics Department at Radfan University College, University of Lahej, Yemen. He is also an adjunct professor at Korea University in South Korea and Saveetha University in India. He holds a Ph.D. in Mathematics from Dr. Babasaheb Ambedkar Marathwada University, India, with research focused on fractional differential equations. Dr. Thabet has published over 60 papers in international journals, served on editorial boards, and refereed over 50 academic journals. He has received multiple awards for research excellence and is a member of international academic societies.*
https://orcid.org/0000-0002-4568-9732

Imed Kedim *Dr. Imed Kedim is a Tunisian mathematician and Associate Professor at the College of Sciences and Humanities, Prince Sattam Bin Abdulaziz University, Saudi Arabia. He holds a Ph.D. in Mathematics from the University Louis Pasteur in Strasbourg, France, where he specialized in Schubert varieties and toric geometry. His research interests span Lie groups, representation theory, deformation theory, Fractional Calculus, and fixed point theory. Dr. Kedim has previously held academic positions at the Universities of Carthage and Gabes in Tunisia and has authored numerous papers in international journals. He also supervises Ph.D. and master's students and actively participates in international conferences.*
https://orcid.org/0000-0002-4791-9730

An International Journal of Optimization and Control: Theories & Applications
(https://accscience.com/journal/ijocta)



This work is licensed under a Creative Commons Attribution 4.0 International License. The authors retain ownership of the copyright for their article, but they allow anyone to download, reuse, reprint, modify, distribute, and/or copy articles in IJOCTA, so long as the original authors and source are credited. To see the complete license contents, please visit http://creativecommons.org/licenses/by/4.0/.

An International Journal of Optimization and Control: Theories & Applications
ISSN: 2146-0957 eISSN: 2146-5703
Vol.15, No.3, pp.503-516 (2025)
https://doi.org/10.36922/ijocta.8171

RESEARCH ARTICLE

A novel ninth-order root-finding algorithm for nonlinear equations with implementations in various software tools

Srinivasarao Thota[1], Amir Naseem[2], Thumati Gopi[3], Kashireddy Sai NandanReddy[3], Padarthi Sai Kousik[3], Thulasi Bikku[3], and Shanmugasundaram Palanisamy[4*]

[1]Department of Mathematics, Amrita School of Engineering, Amrita Vishwa Vidyapeetham, Amaravati, Andhra Pradesh, India
[2]Department of Mathematics, University of Management and Technology, Lahore, Punjab, Pakistan
[3]Department of Computer Science and Engineering, Amrita School of Computing, Amrita Vishwa Vidyapeetham, Amaravati, Andhra Pradesh, India
[4]Department of Mathematics, College of Natural Computational Sciences, MizanTepi University, Mizan-Aman, South West Ethiopia Peoples' Region, Ethiopia

t_srinivasarao@av.amrita.edu, amir.kasuri89@gmail.com, av.en.u4cse22043@av.students.amrita.edu, av.en.u4cse22020@av.students.amrita.edu, av.en.u4cse22037@av.students.amrita.edu, b_thulasi@av.amrita.edu, psserode@mtu.edu.et

ARTICLE INFO

Article History:
Received: December 24, 2024
1st revised: March 19, 2025
2nd revised: April 25, 2025
3nd revised: May 9, 2025
Accepted: May 14, 2025
Published Online: June 19, 2025

Keywords:
Root-finding algorithm
Nonlinear equations
Implementations
Halley method
Exponential method

AMS Classification:
65H05, 65Hxx

ABSTRACT

Nonlinear phenomena are prevalent in numerous fields, including economics, engineering, and natural sciences. Computational science continues to advance through the development of novel numerical schemes and the refinement of existing ones. Ideally, these numerical systems should offer both high-order convergence and computational efficiency. This article introduces a new three-step algorithm for solving nonlinear scalar equations, aiming to meet these criteria. The proposed approach requires six function evaluations per iteration and achieves ninth-order convergence. To demonstrate the efficiency of the technique, various numerical examples are shown. Implementations of the method are available in both Maple and Python, and it can be readily adapted for use in other computational environments.

CC BY

1. Introduction

Many scientific and engineering problems require nonlinear root-finding techniques for their solutions. The field of computational science is continually evolving, with ongoing development of numerical methods that offer higher-order convergence and more efficient numerical schemes. This has led to the establishment of a new ninth-order nonlinear root-finding technique aimed at improving the solution of nonlinear scalar equations. Another advantage of this method is its high converging power, which means fewer function evaluations are needed per iteration, thereby making it computationally efficient. This novel approach has the potential to be a significant breakthrough in computational science, offering accurate solutions to nonlinear problems for various areas of knowledge.

The Newton–Raphson (NR) method is one of the most widely used approaches for solving nonlinear equations, mainly because of its simplicity. As a foundational method, it serves as a basis for the development of more sophisticated numerical techniques. However, achieving an optimal rate of convergence, as conjectured by Kung–Traub, Traub[1,2] theorem may not always

*Corresponding author

be possible. Consequently, researchers have focused on developing algorithms with better convergence rates while minimizing the number of function evaluations per iteration. The efficiency index $E = p^{1/c}$ introduced as a critical measure, estimates the convergence order p relative to the number of function evaluations per step necessary for a numerical scheme. The aim is to maximize this index as larger values indicate improved efficiency. Some notable recently developed nonlinear methods include the homotopy perturbation approach,[3–5] the Adomian decomposition method,[6] the variational iteration method,[7,8] and methods based on quadrature rules.[9,10]

This paper is based on prior work and designs a new three-step numerical method with ninth-order convergence. This method combines an exponential series-based scheme (ExpM)[11–14] with the classical third-order Halley method (HM)[12,15–18] to achieve higher performance measures than existing methods. Specifically, this method minimizes the number of function evaluations while maintaining high accuracy and computational efficiency. Noor et al.[19] developed a novel two-step scheme with order p_1 p_2 by combining two schemes of orders p_1 and p_2. At each iteration, the process adds new function evaluations, but these have a higher order of convergence. However, Noor et al.[20] presented two schemes with third- and fourth-order convergence that required five and eight function evaluations per iteration, respectively. Shah et al.[21] developed a three-step scheme with third-order convergence at the cost of five function evaluations per iteration. Abro and Shaikh[21] developed a three-step sixth-order convergent technique employing seven function evaluations per iteration. Even though these methods converge at high orders, they incur extra computational costs in terms of central processing unit time. A similar method was applied in a recently published work[23] to produce an effective three-step numerical technique. The primary goal of this study is to design a novel hybrid three-step numerical approach for solving scalar and vector nonlinear equations. Inspired by these methods, we combined the classical third-order Halley scheme[24] with a modified third-order Newton scheme[25] to create a novel three-step numerical scheme. This led to the development of a ninth-order method that requires just six function evaluations per iteration: three functions, two first-order derivatives, and one second-order derivative. Several advantages are associated with the proposed scheme over previous methods. It provides improved accuracy such that fewer iterations are necessary to reach a defined accuracy threshold in less computational time. Furthermore, it is more efficient than other methods in terms of its efficiency index, demonstrating that it can effectively solve scalar and vector nonlinear equations. This paper is organized as follows: Section 2 presents an overview of various existing schemes, along with the formulation and convergence analysis for the proposed ninth-order algorithm. Theoretical comparisons and stability assessments are also discussed. Section 3 explores real-life applications and demonstrates the effectiveness of the proposed scheme through numerical experiments. Finally, Section 4 discusses key findings and highlights areas for future research development. Numerous hybrid root-finding algorithms, using different techniques, are available in the literature[26–37] and references therein.

In this article, we present a new three-step iterative method with a single parameter and memory. It is designed in a modular way, making it easier to use for solving nonlinear equations efficiently.

1.1. Previous materials and methods

We reviewed various numerical techniques applied to nonlinear models. Given the difficulty in obtaining exact analytical solutions for such models, we employed numerical methods that offer approximations. The classical NR method[1,2] is typically the first to come to mind when solving nonlinear equations numerically. NR has a second-order convergence, which is considered optimal . In simple terms, this entails one evaluation per iteration for both the function and its first derivative:

$$x_{n+1} = x_n - \frac{f(x_n)}{f'(x_n)}, \quad n = 0, 1, 2, \ldots \tag{1}$$

Halley's third-order numerical scheme, Halley3, is a precise method[16,24] that calls for three different function evaluations per iteration as follows: the function itself, its first derivative, and its second-order derivative.

$$x_{n+1} = x_n - \frac{2f(x_n)f'(x_n)}{2f'(x_n)^2 - f(x_n)f''(x_n)}, \ n = 0, 1, 2, \ldots \tag{2}$$

In a recent study, a pioneering numerical scheme called the modified Halley method (MHM) was presented. As an interpolative technique, it combines NR and HM as a correction, while also employing a finite difference approximation for estimating the second derivative. Remarkably, MHM[17] achieves fifth-order convergence and requires four function evaluations per

iteration, which consist of two function evaluations and two first-order derivatives.

$$y_n = x_n - \frac{f(x_n)}{f'(x_n)}, \quad n = 0, 1, 2, \ldots \tag{3}$$

$$x_{n+1} = y_n - \frac{2f(x_n)f(y_n)f'(y_n)}{2f(x_n)f'(y_n)^2 - f'(x_n)^2 f(y_n) + f'(x_n)f(y_n)f'(y_n)} \tag{4}$$

Another new method proposed was based on ExpM,[13] which provides faster root convergence compared to existing algorithms. The proposed algorithm ExpM is particularly useful for computing the real roots of transcendental equations (13).

$$x_{n+1} = x_n \exp\left(\frac{-f(x_n)}{x_n f'(x_n)}\right), \quad n = 0, 1, 2, \ldots \tag{5}$$

The following section presents the proposed algorithm for solving nonlinear equations.

2. Proposed algorithm

Through an extensive literature review, we identified several researchers who developed the ExpM method to improve convergence order and reduce the number of function evaluations. Nevertheless, our approach advanced beyond this by adopting the HM[16] as a starting point:

$$x_{n+1} = x_n - \frac{2f(x_n)f'(x_n)}{2f'(x_n)^2 - f(x_n)f''(x_n)}, \quad n = 0, 1, 2, \ldots \tag{6}$$

This was combined with the ExpM method Equation (5), described as follows:

$$s_n = x_n \exp\left(\frac{-f(x_n)}{x_n f'(x_n)}\right), \quad n = 0, 1, 2, \ldots, \tag{7}$$

$$x_{n+1} = x_n - \frac{f(x_n) + f(s_n)}{f'(x_n)}. \tag{8}$$

The aim was to develop a nonlinear scheme that is innovative and superior in terms of convergence order, while requiring fewer function evaluations per iteration. Hence, by combining Equations (6)–(8), a new nonlinear scheme was obtained, defined as follows for $n = 0, 1, 2, \ldots$:

$$\begin{aligned} t_n &= x_n - \frac{2f(x_n)f'(x_n)}{2f'(x_n)^2 - f(x_n)f''(x_n)}, \\ s_n &= t_n \exp\left(\frac{-f(t_n)}{t_n f'(t_n)}\right), \\ x_{n+1} &= t_n - \frac{f(t_n) + f(s_n)}{f'(t_n)}. \end{aligned} \tag{9}$$

Although the proposed method shares structural similarities with the scheme introduced by Kalantari and Hans Lee,[38] the modifications incorporated into our algorithm are both intentional and significant. Specifically, the correction step of the proposed method employed an exponential-based refinement, a distinctive enhancement absent in Kalantari and Hans Lee.[38] This refinement modifies the intermediate estimate using an exponential transformation of the residual, which contributes to a broader region of attraction, improved numerical stability, and reduced sensitivity to initial guesses. These advantages are particularly important for nonlinear problems characterized by steep gradients or closely spaced roots. The effectiveness of this modification was demonstrated through detailed polynomiographic visualizations, semi-local convergence analysis, and its application to a real-world engineering problem involving open-channel flow. Collectively, these results highlight that the novelty of the proposed method lies not only in preserving the high order of convergence and computational efficiency but also in delivering enhanced robustness, accuracy, and stability in practical scenarios.

The pseudocode for the proposed algorithm is as shown below.

Input:

```
 f(x)→ Nonlinear function
f'(x)→ First derivative of f(x)
f''(x)→ Second derivative of f(x)
x0 → Initial approximation
maxIter → Maximum number
           of iterations
```

Output:

```
 x_root → Approximate root of f(x)
```

Begin:

```
Set x ← x0
Set iter ← 0
While iter < maxIter:
 t = x-(2*f(x)*f'(x))/
      (2*(f'(x))²-f(x)*f''(x))
 s = t * exp(-f(t) / (t * f'(t)))
 x_new = t - (f(t) + f(s)) / f'(t)
 Update x ← x_new
 Increment iter ← iter + 1
 If iter == maxIter:
  Print \Max iterations reached."
End
```

The convergence of the proposed root-finding algorithm can be analyzed using both local and semi-local techniques. This ensures that the method remains robust and reliable under various conditions.

2.1. Local convergence analysis

Local convergence analysis examines how the iterative method behaves when the initial approximation is sufficiently close to the root α. The aim was to determine the order of convergence by deriving an error equation.

Let α be a simple root of (x), i.e., $f(\alpha) = 0, f'(\alpha) \neq 0$. Expanding $f(x)$ in a Taylor series around α, we obtain:

$$f(x) = f'(\alpha)(x-\alpha)+\frac{f''(\alpha)}{2}(x-\alpha)^2+O((x-\alpha)^3)$$

Similarly, the derivatives are:

$$\begin{aligned} f'(x) &= f'(\alpha) + f''(\alpha)(x-\alpha) + O((x-\alpha)^2), \\ f''(x) &= f''(\alpha) + O(x-\alpha). \end{aligned}$$

The error at the nth iteration is defined as $e_n = x_n - \alpha$. The following theorem guarantees that the nonlinear three-step scheme presented in Equation (9) for solving $f(x) = 0$ has ninth-order accuracy.

Theorem 1. *Let α be the root of a sufficiently differentiable function $f : \theta \to R$, where $\theta \subseteq R$ is an open interval. Then, the three-step scheme presented in Equation (9) has ninth-order convergence.*

Proof. The proof of this theorem is similar to that of proof of Theorem 1 in Kalantari and Hans Lee.[38] For simplicity, we include the main steps of the proof.

Let α be the root of $f(x) = 0$, x_j be the jth approximation to the root provided by Equation (IX), and

$$e_j = x_j - \alpha \tag{10}$$

be the error term after the jth iteration. Using Taylor's expansion for $f(x_j)$ about α, we obtain:

$$f(x_j) = f'(\alpha)\, e_j + \frac{1}{2} f''(\alpha)\, e_j^2 + \varphi(e_j^3). \tag{11}$$

Here, $\varphi(e_j^3)$ describes the asymptotic behavior of a function Equation (10) as $e_n \to 0$, particularly focusing on the dominant order of smallness. It represents an upper bound on the rate at which the function shrinks near the root. Expanding $f(x_j)$ using Taylor's series about α, we also have:

$$f'(x_j) = f'(\alpha) + f''(\alpha)e_j + \frac{1}{2}f'''(\alpha)e_j^2 + \varphi(e_j^3) \tag{12}$$

Multiplying Equations (11) and (12), we get:

$$\begin{aligned} f(x_j)\, f'(x_j) = {} & f'^2(\alpha)\, e_j + \frac{3}{2} f'(\alpha)\, f''(\alpha)\, e_j^2 \\ & + \frac{1}{2}\left(f'(\alpha)\, f'''(\alpha) + f''^2(\alpha)\right) e_j^3 + \varphi(e_j^4). \end{aligned}$$

Now, the Taylor expansion of the denominator in the fractional term in the first step of Equation (9), multiplied by its numerator, results in:

$$\begin{aligned} \frac{2f(x_j)\, f'(x_j)}{2f'(x_j)^2 - f(x_j)\, f''(x_j)} = {} & e_j - \frac{1}{4f'^2(\alpha)} f''^2(\alpha)\, e_j^3 \\ & - \frac{1}{4f'^3(\alpha)} f''(\alpha)\left(5f'(\alpha)\, f'''(\alpha) - 6f''^2(\alpha)\right) e_j^4 \\ & + \varphi(e_j^5), \end{aligned}$$

Following the proof of Theorem 1 in Kalantari and Hans Lee,[38] we obtain:

$$e_{j+1} = c\left(\frac{f''(\alpha)}{f'(\alpha)}\right)^8 e_j^9 + \varphi(e_j^{10}),$$

where c is a constant. Hence, the proposed algorithm has ninth-order convergence. □

Theorem 2. *Let $f : I \to R$. Suppose $\alpha \in I$ is a simple root of $f(x) = 0$ and δ is a sufficiently small neighborhood of α. Let $f''(x)$ exists and $f''(x) \neq 0$ in δ. Then the iterative Equation (9) produces a sequence of iterations $\{x_n : n = 0, 1, 2, \dots\}$ with the order of convergence nine*

Proof. Let

$$R(x) = t - \frac{f(t) + f(s)}{f'(t)},$$

where

$$s = t\exp\left(\frac{-f(t)}{tf'(t)}\right) \text{ and } t = x - \frac{2f(x)f'(x)}{2f'(x)^2 - f(x)f''(x)}.$$

As in Abbasbandy,[5] we observed that:

$$R(\alpha) = \alpha,\ R'(\alpha) = 0, \dots, R^{(8)}(\alpha) = 0, R^{(9)}(\alpha) \neq 0.$$

Hence, the proposed algorithm has convergence of order nine. □

2.2. Semi-local convergence analysis

Semi-local analysis examines the behavior of the algorithm when the initial guess is not arbitrarily close to the root. It ensures that the algorithm converges for a broader class of functions.

Kantorovich-type conditions: To ensure semi-local convergence, we verified whether the function satisfies the following:

(i) The function (x) is continuously differentiable in a neighborhood around the root,

and the first and second derivatives are well-behaved. That is, there exists a constant L such that $|f''(x)| \leq L|f'(x)|$.

(ii) The initial guess x_0 must satisfy $|f(x_0)f'(x_0)| < \frac{2}{L}$, ensuring that the error does not grow uncontrollably.

Sensitivity to initial conditions: although a higher order of convergence reduces sensitivity to initial conditions, the algorithm may still behave unpredictably for functions with closely spaced roots. Nevertheless, it tends to be more stable than Newton-type methods.

If the function satisfies smoothness and bounded derivative conditions, the method is guaranteed to converge for a broad range of initial guesses. The exponential correction step expands the region of attraction, improving robustness. The summary of the convergence properties is provided in Table 1.

The proposed root-finding algorithm exhibited *high stability* due to its rapid convergence and reduced function evaluations per iteration. Stability was analyzed using fixed-point theory and the basin of attraction, ensuring that small perturbations in the initial guess do not lead to divergence. The method's high-order accuracy allowed for faster convergence while minimizing numerical errors. Polynomiography results in Section 5 indicate that the method has wider and smoother basins of attraction, reducing sensitivity to initial conditions compared to NR and HM.

In the following section, we present several numerical examples to illustrate the proposed algorithm, and comparisons are made to show its accuracy and efficiency.

As mentioned in Section 1, the efficiency index E is defined as $E = p^{1/c}$, where is the order of convergence of the method and c is the number of function evaluations per iteration. The proposed method has ninth-order convergence ($p = 9$) and six function evaluations per iteration ($c = 6$), consisting of three function evaluations (x), two first derivative evaluations ($f'(x)$), and one second derivative evaluation ($f''(x)$). An explicit calculation gives $E = 9^{1/6} \approx 1.4422$.

The computational complexity of an iterative root-finding method is determined by the following: (i) the number of function evaluations per iteration, (ii) the arithmetic operations per iteration, and (iii) the convergence order and total iterations required. As mentioned earlier, each iteration requires six function evaluations. As each step involves only a constant number of operations, the arithmetic complexity per iteration is (1), and the number of iterations required to reach a precision ϵ is approximately $k = O(\log_9(\frac{1}{\epsilon}))$. Thus, the proposed algorithm has an optimal logarithmic complexity of $O(\log(\frac{1}{\epsilon}))$.

As discussed previously, we have proven that the semi-local convergence of the proposed method has a ninth-order rate. We assumed that: (i) $f \in C^3$ is on an open interval $D \subset R$, (ii) $\alpha \in D$ is a simple root of $f : f(\alpha) = 0,\ f'(\alpha) \neq 0$, and there exists $\delta > 0$ such that: $f'(x) \neq 0$ for all $x \in B(\alpha, \delta) \subset D$, $\left|\frac{f''(x)}{f'(x)}\right|$, and $\left|\frac{f^{(3)}(x)}{f'(x)}\right|$ are bounded in $B(\alpha, \delta)$. Now, the goal was to prove that the method converges α from an initial point $x_0 \in B(\alpha, \delta)$, under these assumptions. The key ideas in the proof consist of analyzing the error $e_n = x_n - \alpha$ and showing that

$$|e_{n+1}| \leq K|e_n|^9$$

for some constant $K > 0$, when $|e_n|$ is sufficiently small but not necessarily infinitesimal (semi-local).

In the literature, numerous root-finding algorithms exist (see, e.g., [39–43]) each with its own limitations.

3. Numerical experiments

In this section, the practical applicability of the proposed scheme is demonstrated using numerical examples.

Example 1. Consider the nonlinear equation to illustrate the proposed algorithm:

$$\sin^2(x) - x^2 + 1 = 0. \tag{13}$$

An approximate solution of Equation (13) is

$$x \approx 1.40449164821534122603508681778686807 7 \tag{14}$$

Using the proposed algorithm with the initial guess $x_0 = 1$, we obtained the following values in the first iteration:

$$t_0 = x_0 - \frac{2f(x_0)f'(x_0)}{2f'(x_0)^2 - f(x_0)f''(x_0)} = 1.352266356364,$$

$$s_0 = t_0 \exp\left(\frac{-f(t_0)}{t_0 f'(t_0)}\right) = 1.40790110417003320,$$

$$x_1 = t_0 - \frac{f(t_0) + f(s_0)}{f'(t_0)} = 1.4030669959818645244254.$$

The function value and absolute error after the first iteration are:

$$|f(x_1)| = 0.00353271303535116810231715,$$

$$\left|\frac{x_1 - x_0}{x_1}\right| = 0.28727565906416232537732 59$$

respectively. Repeating this process, we have:
Iteration 2

Table 1. Summary of convergence

Analysis type	Result
Local convergence	Ninth-order convergence (e_9^n) confirmed via Taylor expansion and error analysis
Semi-local convergence	The method is robust under smoothness conditions and has a large basin of attraction
Practical implications	Faster convergence than the Newton–Raphson; better stability for distant initial guesses

$$t_1 = 1.40449164669085474737261832721 84,$$
$$s_1 = 1.40449164821534122868351858496 37,$$
$$x_2 = 1.40449164821534122520772018543,$$
$$|f(x_2)| = 0.00000000000000000002053915,$$
$$\left|\frac{x_2 - x_1}{x_2}\right| = 0.0010143534636464643787660.$$

Iteration 3

$$t_2 = 1.40449164821534122603508681778 6868,$$
$$s_3 = 1.40449164821534122603508681778 6868,$$
$$x_4 = 1.40449164821534122603508681778 6868,$$
$$|f(x_3)| = 0.00000000000000000000000000000,$$
$$\left|\frac{x_3 - x_2}{x_3}\right| = 0.00000000000000000000589086.$$

It is evident that $f(x_3) = 0$, hence confirming the approximate root as:

$$x = 1.40449164821534122603508681778 6868$$

as stated in Equation (14).

This example demonstrates that the proposed algorithm rapidly converges to the approximate root.

Example 2. Further reinforces the applicability of the proposed method by solving a transcendental equation with an initial approximation $x_0 = 5$. The stopping conditions are $|f(x)| \leq \varepsilon$ or $\left|\frac{x_{n+1}-x_n}{x_{n+1}}\right| \leq \delta$, where $\varepsilon = 10^{-200}, \delta = 10^{-600}$.

$$x^5 + x - 10000 = 0$$

Following the proposed algorithm as demonstrated in Example 1, we obtained the following values during the iteration:

$$t_2 = 6.308777130,$$
$$s_2 = 6.308777130,$$
$$x_3 = 6.308777130,$$
$$f(x_3) = 0,$$
$$\left|\frac{x_3 - x_2}{x_3}\right| = 0.$$

The approximate solution is $x = 6.308777130$. This example further highlights the simplicity of the proposed algorithm. It can be easily applied to real-world problems involving nonlinear equations.

Expanding its utility to engineering applications, Example 3 examines the open-channel flow problem, originally discussed as Example 3 in Kalantari and Hans Lee.[38] It remains a challenge to relate water flow to elements like drainage ditches, gutters, sewers, and canals, all of which affect flow dynamics within open channels. The flow rate in such cases refers to the volume of water that passes through a certain region over a given time. A particularly problematic scenario arises when the channel is poorly maintained. The water flow in an open channel with uniform flow conditions is determined by Manning's equation:

$$Q = \frac{\sqrt{m}}{n} Wh\left[\frac{Wh}{W+2h}\right]^{2/3}, \tag{15}$$

where m is the slope of the channel, n is the Manning's roughness coefficient, W is the channel width, and h is the depth of water. The equation above can be simplified to determine the water depth (h) in the channel for a given quantity of water, as follows:

$$f(h) = \frac{\sqrt{m}}{n} Wh\left[\frac{Wh}{W+2h}\right]^{2/3} - Q. \tag{16}$$

In Kalantari and Hans Lee,[38] the authors considered the parameters: $Q = 14.15\,\mathrm{m}^3/\mathrm{s}$, $W = 4.572$ m, $n = 0.017$, and $m = 0.0015$, with the initial guess $h_0 = 8.5$ m. Substituting these values into Equation (16) yields:

$$f(h) = 28.69285373h\left[\frac{h}{4.572+2h}\right]^{2/3} - 14.15. \tag{17}$$

Applying the proposed algorithm, the following results were obtained:

Iteration 1: 1.446410377, $f(h) = 0.25324599$,

Iteration 2: 1.465091222, $f(h) = 0.2 \times 107$, and

Iteration 3: 1.465091220, $f(h) = 0$.

From this, we obtained an approximate value of $h = 1.465091220$. However, Equation (17) was also solved in Kalantari and Hans Lee,[38] where the approximate solution was obtained after four iterations using the same data. Therefore, the proposed algorithm is more efficient than the one presented by Kalantari and Hans Lee.[38]

Lastly, Example 4 presents a performance comparison between the proposed algorithm and existing methods, highlighting its efficiency. Consider the following equations:

$$Eq_1 : \sin^2(x) - x^2 + 1 = 0,$$
$$Eq_2 : x^5 + x - 10000 = 0,$$
$$Eq_3 : 28.69285373x\left[\frac{x}{4.572 + 2x}\right]^{2/3} - 14.15,$$
$$Eq_4 : e^x - 3x - 2 = 0.$$

Table 2 shows the number of iterations required to reach an approximate solution of the equation using the proposed algorithm versus various numerical methods. The stopping criterion is $\varepsilon = 10^{-200}, \delta = 10^{-600}$, as in Example 2

Table 2 shows that the proposed algorithm exhibits convergence that is equal to or faster than that of the existing methods.

The effectiveness and versatility of the proposed algorithm are demonstrated through a series of illustrative examples. Example 1 serves to elucidate the step-by-step implementation of the proposed algorithm, highlighting its computational framework and underlying logic. Example 2 emphasizes the simplicity and user-friendliness of the algorithm, showcasing its ease of understanding and applicability, even for users with limited experience. Its practical relevance is further reinforced in Example 3, which applies the algorithm to a real-world problem in civil and environmental engineering, namely open-channel flow. This example illustrates the algorithm's ability to address challenges in modeling water flow through elements such as drainage ditches, gutters, sewers, and canals, which significantly influence fluid dynamics in open channels. Finally, Example 4 offers a comparative analysis between the proposed method and several well-established algorithms, including the NR method, HM, MHM, numerical methods from refs.[38] and [1, 2] the enhanced method from ref. [44] the ninth-order root-finding method from ref. [38] and the ninth-order memory-based iterative technique from ref. [44] This comparative study underscores the superior efficiency and accuracy of the proposed algorithm in solving nonlinear equations. As observed in Table 2, the proposed algorithm demonstrates equal or superior convergence speed compared to these existing methods, showcasing its efficiency and robustness. While Table 2 demonstrates that the proposed method typically requires fewer or equal iterations compared to existing methods, it is important to note that the number of iterations alone does not fully capture an algorithm's overall effectiveness. Therefore, several additional performance metrics have been evaluated to provide a more comprehensive assessment. The proposed method not only achieved ninth-order convergence with fewer iterations but also exhibited a high-efficiency index (≈ 1.4422), low computational cost, and robust stability, confirmed through both local and semi-local convergence analyses. Its effectiveness was further supported by polynomiographic visualization (Section 5), real-world application (Example 3) in open-channel flow, and favorable comparisons with established methods across multiple performance metrics. These comprehensive results affirm the practical utility and numerical superiority of the proposed method.

4. Implementation

In this section, we discuss the implementation of the proposed algorithm using various software tools such as Maple and Python, along with sample computations.

4.1. Maple implementation

```
Prop_Alg := proc (a, Eq, max_iter)
 local i, a1, f, r, y1, z1;
 i := 0; a1 := evalf(a);
 f := unapply(lhs(Eq), x);
 if f(a1) = 0 then return a1 end if;
 i := 0;
 do
  i := i+1;
  y1 := a1-
  2*f(a1)*(D(f))(a1)/(2*(D(f))(a1)^2
  -f(a1)*((D@@2)(f))(a1));
  z1 := y1*exp(
         -f(y1)/(y1*(D(f))(y1)));
   r := y1-(f(y1)+f(z1))/(D(f))(y1);
   printf(\Iteration %a  =  %a.
      f(x) = %a,  AbsError = %a \n",
      i, r, f(r), abs((r-a1)/r));
   if max_iter == i then return r
   else a1 := r
   end if
 end do
end proc
```

Example 5. Recall Example 1 for sample computations using the Maple implementation.

Table 2. Number of iterations

Eq	Root	NR	HM	MHM	NM1	NM2	EM	Sania9	MBIT9	PM
Eq_1	1.404491648	11	7	5	5	4	5	3	3	3 (Example 1)
Eq_2	6.308777130	12	8	6	5	6	5	3	3	3 (Example 2)
Eq_3	1.465091220	10	7	5	4	4	4	3	3	3 (Example 3)
Eq_4	2.125391199	10	8	6	4	4	4	3	3	3

Notes: NM1 and NM2 represent the numerical methods proposed in refs. [38] and [1,2], respectively. EM indicates the enhanced method from reference [44]. RFM refers to the ninth-order root-finding method from ref. [37], which introduced a new three-step numerical scheme for solving nonlinear scalar and vector equations. MBIT denotes the ninth-order memory-based iterative technique from ref. [37], in which the authors proposed a novel three-step, memory-based method for solving nonlinear equations. Sania is a Ninth-order method by Sania. Abbreviations: Eq, equation; HM, Halley's method; MHM, modified Halley's method; NR, Newton Raphson method; PM, proposed method.

```
> Prop_Alg(1, sin(x)^2-x^2+1 = 0,3);
Iteration 1  =  1.403066996.
f(x) = .35327132e-2,
AbsError = .2872756591
Iteration 2  =  1.404491649.
f(x) = -.2e-8,
AbsError = .1014354910e-2
Iteration 3  =  1.404491649.
f(x) = -.2e-8,
AbsError = 0.
1.404491649
```

Example 6. Consider with x0 = 0.8.

```
> Prop_Alg(0.8, 10*x*exp(-x^2)-1 = 0, 4);
Iteration 1  =  1.531609079.
f(x) = .466791835,
AbsError = .4776735063
Iteration 2  =  1.679628729.
f(x) = .5200e-5,
AbsError = .8812640999e-1
Iteration 3  =  1.679630611.
f(x) = -.12e-8,
AbsError = .1120484461e-5
Iteration 4  =  1.679630611.
f(x) = -.12e-8,  AbsError = 0.
1.679630611
```

4.2. Python implementation

Consider the transcendental Equation (13) from Example 1 for sample computations using the Python implementation, as follows.

```
import numpy as np
import math
def f(x):
    return np.sin(x)**2-x**2+1
def df(x):
    return 2*np.sin(x)*np.cos(x)-2*x
def ddf(x):
    return 2*(np.cos(x)**2- np.sin(x)**2)-2
def ninth_order_method(x0, tol=1e-10,
max_iter=20): x = x0
    for iteration in range(1, max_iter + 1):
        t = x - (2 * f(x) * df(x)) / (2 *
        (df(x))**2 - f(x) * ddf(x))
        s = t * math.exp(-f(t) / (t * df(t)))
        if t * df(t) != 0 else t
        x_new = t - (f(t) + f(s)) / df(t)
        print(f"Iteration {iteration}:
        x = {x_new:.15f}, f(x) =
        {f(x_new):.15e}")
        if abs(x_new - x) < tol:
            print("\nConverged to root:",
            x_new)
            print("Total iterations:",
            iteration)
            return x_new
        x = x_new
    print("\nMaximum iterations reached.
    Root may not be accurate.")
    return x

# Example: Solve sin^2(x) - x^2 + 1 = 0
initial_guess = 1.0  # Start near an
expected root
root = ninth_order_method(initial_guess)
```

Output of the implementation:

```
Iteration 1: x = 1.403066995981864,
f(x) = 3.532713035351298e-03
Iteration 2: x = 1.404491648215341,
f(x) = -4.440892098500626e-16
Iteration 3: x = 1.404491648215341,
f(x) = -4.440892098500626e-16

Converged to root:
1.4044916482153413
Total iterations: 3

=== Code Execution Successful ===
```

5. Polynomiography via the proposed method

The aim of this section is to represent polynomiographs generated using our proposed method as outlined in Equation (9). A polynomiograph is an image produced through the process of polynomiography, a term coined by Kalantri in 2005. It is defined as "the art and science of visualization in approximation of the zeros of complex polynomials, via fractal and non-fractal images created using the mathematical convergence properties of iteration functions." The concept of a "fractal," introduced by Benoit Mandelbrot, describes a geometric shape in which each part has the same statistical properties as the whole. Although both polynomiographs and fractals can be created using various numerical algorithms, they differ significantly in their structural scale. A "polynomiographer" can systematically adjust the structure and pattern by applying different numerical algorithms to various complex polynomials. Generally, polynomiographs and fractals belong to different categories of graphical objects.

To create polynomiographs over the complex plane C, we begin by defining a rectangular region $\mathcal{R}$ with dimensions $[-2,2]\times[-2,2]$, setting a precision threshold of $\varepsilon = 10^{-3}$, and an iteration limit of $m = 15$. Each point z_0 within this region undergoes an iterative process, and the point corresponding to z_0 is colored based on how closely the truncated orbit converges to a root or fails to converge. The image resolution depends on the discretization of the rectangle $\mathcal{R}$. For example, a 2000×2000 grid results in a high-resolution image. The colors in polynomiographs are typically linked to the number of iterations required to approximate the zeros of the complex polynomial to a specified accuracy using a chosen numerical algorithm. The fundamental algorithm for generating polynomiographs is outlined in Algorithm 1 below.

Algorithm 1. *Polynomiograph's generation*
Input:
$p \in C$—*Polynomial*
$A \in C$—*Area*
m—$Maximumnumberofiterations$
I—$Iterationmethod$
$\in$ —$Accuracy$
$Colormap[0...C-1]$—$ColormapwithC$
$colors.$
$Output$: $Polynomiographforthecomplex$
$polynomialpinareaA$
$forz_0 \in A, do$
$i = 0$
$whileimdo$
$z_(n+1) = I(z_n)$
$if|z_(n+1) - z_n| < then$
$break$
$i = i+1$
$colorz_0bymeansofcolormap$

In iterative algorithms, a stopping criterion is crucial for determining whether the process has reached convergence or divergence. This criterion, known as a convergence test, evaluates the algorithm's progress in finding a solution. The typical form of a convergence test is

$$|z_{i+1} - z_i| < \varepsilon \tag{18}$$

where z_{i+1} and z_i are successive points in the iteration, and $\varepsilon > 0$ is a predefined accuracy threshold. The convergence test $(z_{i+1}, z_i, \varepsilon)$ indicates TRUE if the method converges to a root and FALSE otherwise. In this study, we used this convergence test Equation (18). The color variations in the polynomiographs represent the number of iterations needed to approximate the root within the specified accuracy ε. By modifying the parameter m, which limits the maximum number of iterations, it is possible to generate numerous visually appealing polynomiographs. The exploration of polynomiography and its artistic implications is covered in references.[45–47]

Here, we present some examples of the following complex polynomials using our developed algorithms and compare them with the polynomiographs obtained by using other well-known two-step iterative methods:

(i) $p_1(z) = z^3 - z^2 - z - 1$, Area$[-2,2]$
(ii) $p_2(z) = z^4 - z^3 - z^2 - z - 1$, Area [-2, 2]
(iii) $p_3(z) = z^5 - z^4 - z^3 - z^2 - z - 1$, Area [-2, 2]
(iv) $p_4(z) = z^6 - z^5 - z^4 - z^3 - z^2 - z - 1$, Area [-2, 2]

The `colormap` used for coloring the iterations in the generation of polynomiographs is presented in the following figure.



Figure 1. The colormap used for generating polynomiographs

The colormap shown in Figure 1 illustrates how points move toward the solutions of a polynomial. Different colors represent different roots, allowing one to see which point converges to which

solution. Lighter colors indicate that the point converges quickly, while darker shades denote that more steps are required. The fuzzy or mixed-color edges between regions show areas where a small change can direct a point to a different solution. This creates an image that is both complex and beautiful, with patterns that resemble fractals.

Example 7. Polynomiographs for the polynomial $z^2 - z - 1$ via the proposed method.

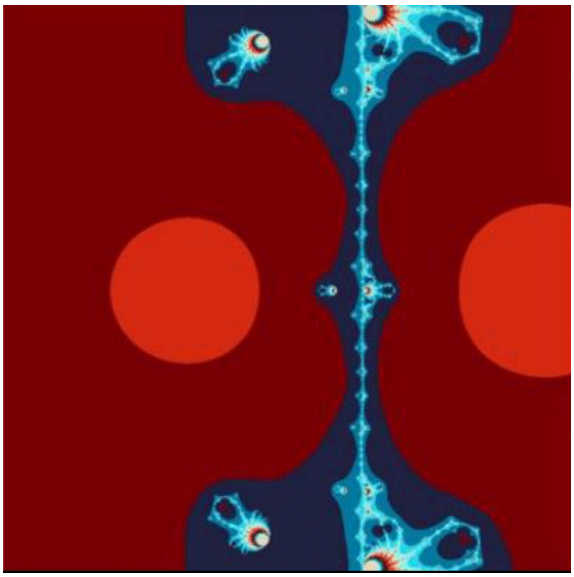


Figure 2. Polynomiograph for the polynomial $p_1(z)$ using Method IX

Example 8. Polynomiographs for the polynomial $z^3 - z^2 - z - 1$ via the proposed method.

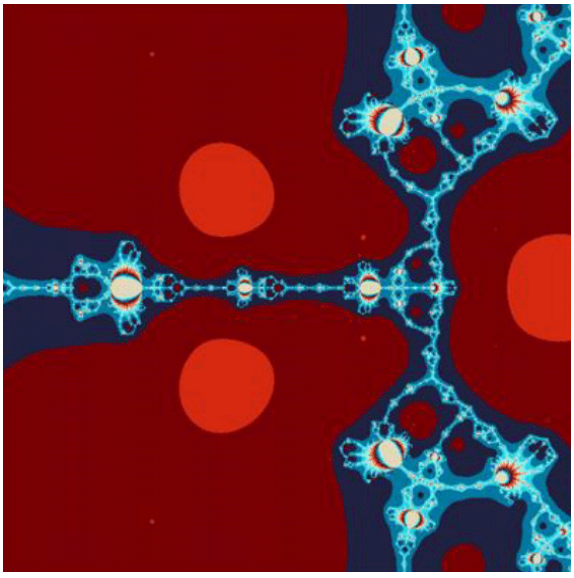


Figure 3. Polynomiograph for the polynomial $p_2(z)$ using Method IX

Example 9. Polynomiographs for the polynomial $z^4 - z^3 - z^2 - z - 1$ via the proposed method.

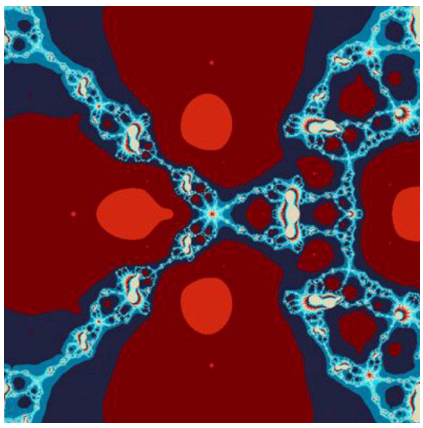


Figure 4. Polynomiograph for the polynomial $p_3(z)$ using Method IX

Example 10. Polynomiographs for the polynomial $z^5 - z^4 - z^3 - z^2 - z - 1$ via the proposed method.

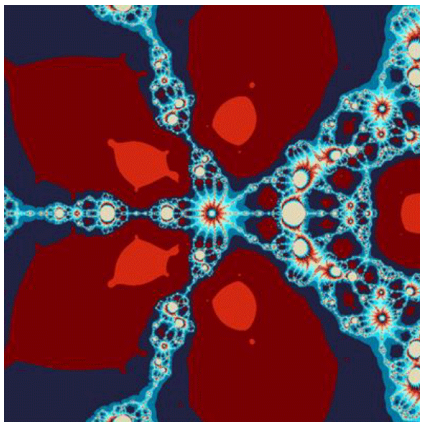


Figure 5. Polynomiograph for the polynomial $p_3(z)$ using Method IX

Example 11. Polynomiographs for the polynomial $z^6 - z^5 - z^4 - z^3 - z^2 - z - 1$ via the proposed method.

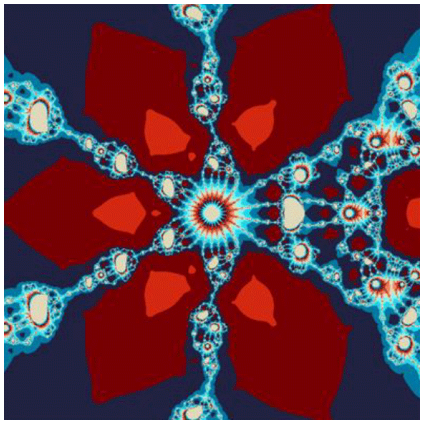


Figure 6. Polynomiograph for the polynomial $p_4(z)$ using Method IX

Table 3 presents the outstanding performance of the proposed iterative method applied to four different polynomials. The performance was evaluated based on three key metrics: average number of iterations (ANI), average area index (CAI),

and computation time (in seconds). The results clearly demonstrate that the proposed method efficiently handles increasing polynomial complexity while maintaining an exceptional balance between accuracy and computational efficiency, making it a highly reliable approach for solving polynomial equations.

Table 3. Dynamical analysis of the proposed method

Polynomial	ANI	CAI	Time
p_1	2.6811	0.9902	31.021
p_2	3.0728	0.9809	129.023
p_3	3.3573	0.9741	145.432
p_4	3.5553	0.9699	210.098

Abbreviations: ANI, average number of iterations; CAI, convergence area index.

To further highlight the advantages of the proposed method, we analyzed both numerical results and graphical representations using polynomiographs in Figures 1-6. The ANI values showed a controlled and gradual increase from 2.6811 for p_1 to 3.5553 for p_4, illustrating that the iterative method remains computationally feasible even as polynomial complexity increases. Unlike other methods that may require excessive iterations for higher-degree polynomials, the proposed method ensures stability without exponential growth in iterations. This efficiency was further confirmed by the polynomiographs, where the speed of convergence, depicted by the color of each point, highlights the method's ability to quickly approximate polynomial roots.

Moreover, the CAI values remained impressively high, with only a slight decrease from 0.9902 for p_1 to 0.9699 for p_4, proving that the method consistently delivers accurate results across all tested polynomials. These accuracy trends align with the polynomiographs, where regions with minimal color variation indicate a steady and predictable convergence pattern. The ability of the method to maintain high accuracy while efficiently converging further emphasizes its superiority over traditional iterative techniques.

Although computation time increases from 31.021 s for p_1 to 210.098 s for p_4, this is a natural consequence of the increasing complexity of the polynomial equations. Importantly, the polynomiographs further validate that the proposed method successfully converges in all cases, demonstrating its robustness and adaptability to varying polynomial structures. Compared to alternative approaches, this method ensures a favorable trade-off between computational time and accuracy, making it particularly well-suited for real-world applications that demand both precision and efficiency.

In summary, the proposed iterative method stands out as a highly effective and reliable approach for solving polynomial equations. By seamlessly integrating numerical data with graphical insights from polynomiographs, we confirm that the method maintains exceptional accuracy, exhibits a stable and controlled iteration growth pattern, and efficiently handles increasing computational demands. With further optimization, such as adaptive iteration strategies or parallel processing, the method could become even more powerful, solidifying its position as an optimal choice for complex mathematical computations.

6. Conclusion

Nonlinear phenomena appear in various fields, including economics, engineering, and scientific research. With the rapid expansion of computational science, the development of new numerical schemes and the improvement of existing ones remain crucial. These numerical methods should ideally offer higher convergence rates while being computationally efficient. In this study, we proposed a new three-step iterative algorithm for solving nonlinear scalar equations, addressing both convergence efficiency and computational cost. The proposed method was shown to have ninth-order convergence while requiring only six function evaluations per iteration. Several numerical examples were presented to demonstrate its effectiveness and superior performance over classical methods. The algorithm was implemented in Maple and Python, showcasing its practicality in widely used computational tools. Additionally, it can be extended to other software environments, making it adaptable for various applications.

Future work will focus on reducing computational cost, extending the algorithm to systems of nonlinear equations, and exploring adaptive step-size techniques to improve robustness. The proposed method provides a reliable and efficient approach to solving nonlinear equations, contributing to the advancement of numerical analysis and computational mathematics.

Acknowledgments

None.

Funding

None.

Conflict of interest

The authors declare that they have no competing interests.

Author contributions

Conceptualization: Srinivasarao Thota
Formal analysis: Amir Naseem, Thumati Gopi, Kashireddy Sai Nandan Reddy, Padarthi Sai Kousik
Investigation: Thulasi Bikku, Amir Naseem
Methodology: Srinivasarao Thota, Amir Naseem
Writing – original draft: Srinivasarao Thota
Writing – review & editing: Thulasi Bikku, Shanmugasundaram Palanisamy

Availability of data

The datasets generated and analyzed during the current study are presented in this manuscript.

References

1. Traub JF. Iterative Methods for the Solution of Equations, vol. 312. Providence, RI, USA: American Mathematical Society; 1982.
2. Rafiullah M. A fifth-order iterative method for solving nonlinear equations. *Numer Anal Appl.* 2011; 4: 239-243. https://doi.org/10.1134/S1995423911030062
3. Ganji DD. The application of He's homotopy perturbation method to nonlinear equations arising in heat transfer. *Phys Lett A*. 2006;355:337-341. https://doi.org/10.1016/j.physleta.2006.02.056
4. Thota S, Shanmugasundaram P. On new sixth and seventh order iterative methods for solving non-linear equations using homotopy perturbation technique. *BMC Res Notes.* 2022;15:267. https://doi.org/10.1186/s13104-022-06154-5
5. Abbasbandy S. Improving Newton–Raphson method for nonlinear equations by modified Adomian decomposition method. *Appl Math Comput.* 2003; 145:887-893. https://doi.org/10.1016/S0096-3003(03)00282-0
6. He JH, Wu XH. Variational iteration method: new development and applications. *Comput Math Appl* 2007;54:881-894. https://doi.org/10.1016/j.camwa.2006.12.083
7. Tari H, Ganji DD, Babazadeh H. The application of He's variational iteration method to nonlinear equations arising in heat transfer. *Phys Lett A*. 2007;363:213-217. https://doi.org/10.1016/j.physleta.2006.11.005
8. Noor MA, Waseem M. Some iterative methods for solving a system of nonlinear equations. *Comput Math Appl.* 2009;57:101-106. https://doi.org/10.1016/j.camwa.2008.10.067
9. Zafar F, Mir NA. A generalized family of quadrature based iterative methods. *Gen Math.* 2010;18:43-51.
10. Thota S, Awad MM, Shanmugasundaram P. A derivative-free root-finding algorithm using exponential method and its implementation. *BMC Res Notes.* 2023;16:276. https://doi.org/10.1186/s13104-023-06554-1
11. Thota S, Gemechu T, Ayoade AA. On new hybrid root-finding algorithms for solving transcendental equations using exponential and halley's methods. *Ural Math J.* 2023; 9(1):176-186. http://dx.doi.org/10.15826/umj.2023.1.016
12. Thota S, Gemechu T, Shanmugasundaram P. New algorithms for computing non-linear equations using exponential series. *Palestine J Math.* 2021; 10(1): 128-134.
13. Thota S. A new root-finding algorithm using exponential series. *Ural Math J.* 2022;5(1):83-90. https://doi.org/10.15826/umj.2019.1.008
14. Thota S. A New Hybrid Halley-False Position type Root Finding Algorithm to Solve Transcendental Equations. Istanbul International Modern Scientific Research Congress-III, 06-08 May 2022, Istanbul Gedik University, Istanbul, Turkey.
15. Chen D, Argyros IK, Qian QS. A note on the Halley method in Banach spaces. *Appl Math Comput.* 1983;58:215-224.
16. Noor MA, Khan WA, Hussain A. A new modified Halley method without second derivatives for nonlinear equation. *Appl Math Comput.* 2007;189:1268-1273. https://doi.org/10.1016/j.amc.2006.12.011
17. 'Cordero A, Hueso JL, Martínez E, Torregrosa JR. A modified Newton–Jarratt's composition. *Numer Algorithms.* 2010; 55:87–99. https://doi.org/10.1007/s11075-009-9359-z
18. Thota S, Ayoade AA. A new numerical algorithm to compute a root of non-linear equations using exponential method. interplay of fractals and complexity in mathematical modelling and physical patterns. In: ISMAFDS 2023. Cham: Springer; 2025. https://doi.org/10.1007/978-3-031-58641-5$_2$8
19. Noor MA, Noor KI, Al-Said E, Waseem M. Some new iterative methods for nonlinear equations. *Math Probl Eng* . 2010; 198943. https://doi.org/10.1155/2010/198943
20. Noor MA, Noor KI. Three-step iterative methods for nonlinear equations. *Appl Math Comput.* 2006; 183:322-327. https://doi.org/10.1016/j.amc.2006.05.055
21. Shah FA, Noor MA, Waseem M. Some second-derivative-free sixth-order convergent iterative methods for non-linear equations. *Maejo Int J Sci Technol.* 2016; 10(01):79-87. https://doi.org/10.14456/mijst.2016.7
22. Abro HA, Shaikh MM. A new time-efficient and convergent nonlinear solver. *Appl Math Comput.* 2019; 355:516-536. https://doi.org/10.1016/j.amc.2019.03.012
23. Torregrosa JR, Argyros IK, Chun C, Cordero A, Soleymani F. Iterative methods for nonlinear equations or systems and their applications 2014.

J Appl Math. 2014; 2014: 293263.
https://doi.org/10.1155/2014/293263
24. Darvishi MT, Barati A. A third-order Newton-type method to solve systems of nonlinear equations. *Appl Math Comput.* 2007; 187:630-635.
https://doi.org/10.1016/j.amc.2006.08.080
25. Qureshi S, Ramos H, Soomro AK. A new nonlinear ninth-order root-finding method with error analysis and basins of attraction. *Mathematics.* 2021;9(16):1996.
https://doi.org/10.3390/math9161996
26. Okawa H, Fujisawa K, Yamamoto Y, et al. The W4 method: a new multi-dimensional root-finding scheme for nonlinear systems of equations. *Appl Numer Math.* 2023; 183: 157-172.
https://doi.org/10.1016/j.apnum.2022.08.019
27. Thota S, Gopisairam T. On a symbolic method for second-order boundary value problems over algebras. *Int J Appl Math.* 2024;37(6):577-590.
http://dx.doi.org/10.12732/ijam.v37i6.1
28. Srivastav VK, Thota S, Kumar M. A new trigonometrical algorithm for computing real root of nonlinear transcendental equations. *Int J Appl Comput Math.* 2019; 5:44.
https://doi.org/10.1007/s40819-019-0600-8
29. Thota S, Krishna CB, Ayoade AA, Bikku T. On a new hybrid root-finding algorithm for solving nonlinear equations with implementation in excel and maple. *J Basic Sci.* 2024; 24(7): 270-277.
https://doi.org/10.37896/JBSV24.7/3250
30. Naseem A, Rehman MA, Abdeljawad T. A novel root-finding algorithm with engineering applications and its dynamics via computer technology. *IEEE Access.* 2022;10:19677-19684.
https://doi.org/10.1109/ACCESS.2022.3150775
31. Thota S, Srivastav VK. Quadratically convergent algorithm for computing real root of nonlinear transcendental equations. *BMC Res Notes.* 2018;11:909.
https://doi.org/10.1186/s13104-018-4008-z
32. Etesami R, Madadi M, Mashinchi M, Ganjoei RA. A new method for rooting nonlinear equations based on the Bisection method. *MethodsX* 2021;8:101502.
https://doi.org/10.1016/j.mex.2021.101502
33. Thota S. A numerical algorithm to find a root of non-linear equations using householder's method. *Int J Adv Appl Sci.* 2021; 10(2): 141-148.
http://doi.org/10.11591/ijaas.v10.i2.pp141-148
34. Chueca-Díez F, Gañán-Calvo AM. A fast numerical algorithm for finding all real solutions to a system of N nonlinear equations in a finite domain. *Numer Algor* 2024.
https://doi.org/10.1007/s11075-024-01908-7
35. Naseem A, Rehman MA, Abdeljawad T. Real-world applications of a newly designed root-finding algorithm and its polynomiography. *IEEE Access.* 2021;9: 160868-160877.
https://doi.org/10.1109/ACCESS.2021.3131498
36. Aggarwal A, Pant S. Beyond newton: a new root-finding fixed-point iteration for nonlinear equations. *Algorithms.* 2020;13(4):78.
https://doi.org/10.3390/a13040078
37. Mittal SK, Panday S, Jäntschi L. Enhanced ninth-order memory-based iterative technique for efficiently solving nonlinear equations. *Mathematics.* 2024;12(22): 3490.
https://doi.org/10.3390/math12223490
38. Kalantari B, Hans Lee E. Newton–ellipsoid polynomiography. *J Mathnd the Arts.* 2019;13(4): 336-352.
https://doi.org/10.1080/17513472.2019.1600959
39. Iliev A, Kyurkchiev N. Nontrivial Methods in Numerical Analysis: Selected Topics in Numerical Analysis. Saarbrucken: LAP LAMBERT Academic Publishing; 2010: 256. ISBN:978-3-8433-6793-6.
40. Ignatova B, Kyurkchiev N, Iliev A. Multipoint algorithms arising from optimal in the sense of Kung-Traub iterative procedures for numerical solution of nonlinear equations. *Gen Math Notes.* 2012;6(2): 45-79.
41. Kyurkchiev N, Iliev A. On some multipoint methods arising from optimal in the sense of Kung-Traub algorithms. *Int J Math Methods Models Biosci.* 2013; 2(1):12-18.
42. Hristov V, Iliev A, Kyurkchiev N. A note on the convergence of nonstationary finite–difference analogues. *Comput Math Math Phys.* 2005; 45:194-201.
43. S. Thota, Krishna CB, Ayoade AA, Bikku T. On A New Hybrid Root-Finding Algorithm for Solving Nonlinear Equations with Implementation in Excel and Maple. *J Basic Sci.* 2024;24(7):270-277.
https://doi.org/10.37896/JBSV24.7/3250
44. Petkovic M, Neta B, Petkovic L, Dzunic J. Multipoint Methods for Solving Nonlinear Equations. Oxford, UK: Academic press; 2013.
45. Gdawiec K. Fractal patterns from the dynamics of combined polynomial root finding method s. *Nonlinear Dyn.* 2017;90(4):2457-2479.
https://doi.org/10.1007/s11071-017-3813-6
46. Kang SM, Naseem A, Nazeer W, Munir M, Yong C. Polynomiography via modified Abbasbanday's method. *Int J Math Anal.* 2017;11(3):133-149.
https://www.researchgate.net/publication/299535865_POLYNOMIOGRAPHY_VIA_MODIFIED_GOLBABAI_AND_JAVIDI'S_METHOD
47. Thota S, Krishna CB. A root finding algorithm for transcendental equations using hyperbolic tangent function. *AIP Conf Proc.* 2024;2971:060012.
https://doi.org/10.1063/5.0195773

Srinivasarao Thota *completed his M.Sc. in Mathematics from the Indian Institute of Technology (IIT) Madras, India, and Ph.D. in Mathematics from Motilal Nehru National Institute of Technology (NIT) Allahabad, India. Dr. Thota's areas of research interest*

are Computer Algebra (symbolic methods for differential equations), Numerical Analysis (root finding algorithms), and Mathematical Modelling (ecology). Dr. Thota has published more than 50 research papers in several international journals and presented his work in different national and international conferences as an oral presenter and an expert/invited speaker. He is also an editorial board member of various international journals and has received several awards for academic/research work. Presently, he is working as an Associate Professor at the Department of Mathematics, Amrita Vishwa Vidyapeetham, Amaravati, Andhra Pradesh, India.
https://orcid.org/0000-0002-3265-5656

Amir Naseem *received the M.S. degree in mathematics from Lahore Leads University, Lahore, Pakistan. He is currently a Ph.D. Scholar at the Department of Mathematics, University of Management and Technology, Lahore. He has published more than 35 research articles in different well-known journals. His current research interests include numerical analysis, iterative methods, and polynomiography.*
https://orcid.org/0000-0001-7010-6810

Thumati Gopi *is a bachelor of technology (B.Tech.) student in Computer Science and Engineering (CSE). He secured more than 8.6 CGPA in his first two years. Presently, he is in the final year of his B.Tech. Degree.*

Kashireddy Sai Nandan Reddy *is a bachelor of technology (B.Tech.) student in Computer Science and Engineering (CSE). He secured more than 8.8 CGPA in his first two years. Presently, he is in the final year of his B.Tech. Degree.*

Padarthi Sai Kousik *is a bachelor of technology (B.Tech.) student in Computer Science and Engineering (CSE). He secured more than 8.9 CGPA in his first two years. Presently, he is in the final year of his B.Tech. Degree.*

Thulasi Bikku *is an accomplished Associate Professor holding a Ph.D. in Computer Science and Engineering from JNTUA, Anantapur, in 2018, with a distinguished career characterized by significant contributions to academia. Her expertise spans various domains, including Unsupervised Machine Learning, Deep Learning, and Natural Language Processing, reflecting her broad knowledge base. In May 2023, she successfully concluded her Postdoctoral Fellowship (PDF) at the University of Santiago de Chile, situated in the capital city of Santiago, Chile. Her academic career features significant roles, including serving as an Associate Professor at Vignan's Institute in Guntur. Beyond her roles in academia, she has made significant contributions to the field as an editorial member for prestigious journals, a conference chair, and a respected reviewer. Additionally, she holds patents for innovative inventions (3), further highlighting her commitment to pushing the boundaries of knowledge. Her dedication to knowledge-sharing is evident through her involvement in guest lectures, active participation in workshops, and her contributions to faculty development programs. Her passion for fostering education and research is truly commendable. She has an impressive record of scholarly achievements, with a publication history that includes over 50+ research articles published in highly regarded and indexed academic journals. In summary, Dr. Bikku embodies a well-rounded academician with an unwavering commitment to education, research, and professional growth. Her remarkable contributions to the field of Computer Science and Engineering make her a valuable asset to the academic community.*
https://orcid.org/0000-0001-6202-1438

P. Shanmugasundaram *was born and studied in Tamil Nadu, India. Presently, I am working as a Professor at the Department of Mathematics, Mizan-Tepi University, Ethiopia, and also looking at the K.S.R. College of Engineering, Tiruchengode, Namakal District, India. My research interest includes Fuzzy Logic, Topology, Differential Equations, and Optimization.*
https://orcid.org/0000-0003-1176-0411

This work is licensed under a Creative Commons Attribution 4.0 International License. The authors retain ownership of the copyright for their article, but they allow anyone to download, reuse, reprint, modify, distribute, and/or copy articles in IJOCTA, so long as the original authors and source are credited. To see the complete license contents, please visit http://creativecommons.org/licenses/by/4.0/.

An International Journal of Optimization and Control: Theories & Applications
ISSN: 2146-0957 eISSN: 2146-5703
Vol.15, No.3, pp.517-534 (2025)
https://doi.org/10.36922/IJOCTA025080034

RESEARCH ARTICLE

Proportional integral derivative plus control for nonlinear discrete-time state-dependent parameter: Industrial applications

E. M. Shaban[1,2*]

[1]Department of Mechanical Engineering Technology, College of Applied Industrial Technology, Jazan University, Jazan, Saudi Arabia
[2]On leave from Faculty of Engineering (Mataria), Helwan University, Cairo, Egypt
eeshaban@jazanu.edu.sa

ARTICLE INFO

Article History:
Received: February 21, 2025
1st revised: March 2, 2025
2nd revised: March 20 , 2025
Accepted: April 11, 2025
Published Online: July 16, 2025

Keywords:
Proportional-integral-derivative control
State-dependent parameter models
Non-minimal state space
State variable feedback

AMS Classification:
37H05, 37M05, 37M10, 37M15, 37N35, 37N40, 65P40, 70Q05, 70K70

ABSTRACT

In modern industrial automation, control of nonlinear systems with complex dynamics poses significant challenges, especially when dealing with discrete-time models that incorporate state-dependent parameters. Addressing this need, this paper explores the Proportional-integral-derivative-plus (PID+) control approach applied to nonlinear systems characterized by state-dependent parameter (SDP) discrete-time models. Two industrial applications are demonstrated as follows: a bitumen tank system and a reeling/packing machine used in a bitumen membrane sheet production line. Both systems are modeled using discrete-time transfer functions with SDP structures. The present work extends the novel SDP-PID+ approach by formulating its control algorithms and integrating additional proportional and input compensators. This enhancement enables effective and intuitive handling of processes characterized by discrete-time transfer functions with any order and sampling time delay. The approach enables a straightforward implementation of the SDP-PID+ algorithm across two distinct industrial applications, considering their varying response times. The approach reduces the time required to design the SDP-PID+ method for the selected applications while also demonstrating enhanced robustness and performance. It effectively mitigates disturbances and accommodates nonlinearities, higher-order dynamics, and delays.

CC BY

1. Introduction

Proportional integral derivative (PID) controllers have been widely used in industrial processes since their development in the mid-1950s.[1,2] Today, they remain the most prevalent method for controlling process variables due to their simplicity and reliability.[3] Research has continually refined PID tuning methods, introducing approaches such as auto-tuning,[4,5] genetic tuning,[5,6] robust tuning,[7] and optimal tuning.[8] However, significant challenges arise when addressing processes with high-order transfer functions (TFs), $n \geq 3$, time delays greater than unity, $\delta \geq 2$, or nonlinearities.[9] The proportional integral derivative plus (PID+) control approach was developed to address these challenges as an extension of conventional PID methods. It integrates additional dynamic feedback and input compensators to handle processes with higher-order dynamics or pure time delays exceeding unity.[10] Unlike traditional PID control, PID+ employs state variable feedback (SVF) techniques, replacing manual tuning with pole assignment or linear quadratic (LQ) optimization strategies.[11] These enhancements improve control performance in systems that conventional PID tuning often struggles to manage effectively.[10,12]

*Corresponding Author

Previous research on PID+ controllers has demonstrated their applicability across many practical systems. Notable applications include robot arm control,[11,12] industrial temperature regulation of bitumen tank systems,[13] liquid storage tank loading/unloading control,[14] and speed control in reeling/packing machines equipped with field programmable gate array (FPGA) modules.[15] These applications cover systems with varying response times, from slow thermal processes to fast electric motors, and have shown consistent on-site success.

The theoretical foundation of PID+ control is built upon state-dependent parameter (SDP) models, which represent nonlinear systems using quasi-linear structures. These models describe system parameters as functions of state variables, allowing nonlinear dynamics to be approximated as linear systems at each sampling instant.[16] Such SDP-TF models facilitate the design of nonlinear control laws using well-established linear techniques.[17–21] Additionally, incorporating non-minimal state space (NMSS) representations enables direct SVF control without observers or reconstructors, simplifying implementation.[22,23]

Conventional PID designs often fail to provide robust performance for high-order processes with significant delays. For example, Chien–Hrones–Reswick and Ziegler–Nichols tuning have produced noisy control actions in systems such as bitumen temperature regulation.[10] To address these limitations, the novel SDP-PID+ control strategy was introduced and applied in previous studies,[11,13–15] incorporating additional input/output compensators to address sampling delays and higher-order dynamics. Building upon this foundation, the present work further enhances the approach by formulating its control algorithms to regulate processes characterized by discrete-time TFs of any order effectively and with arbitrary sampling time delays. This refinement facilitates the seamless implementation of the SDP-PID+ algorithm across two distinct industrial applications,[13,15] in regards to their varying response times. Additionally, the approach streamlines the design process, reducing computational effort while enhancing robustness and closed-loop control performance. The two practical applications are as follows:

(i) Industrial bitumen tank system. Temperature regulation to ensure product quality and safety during mixing.[13]
(ii) Industrial reeling/packing machine. Speed control of a pulling motor on the bitumen membrane sheet production line using FPGA technology.[15]

The first demonstrator introduces a slow thermal dynamic system, focusing on temperature control of bitumen within a tank before it is mixed with additives such as polymers and fillers.[13] In contrast, the second demonstrator represents a fast response dynamic of an electric motor, specifically the speed control of the pulling motor in the reeling/packing machine used in the production line of bitumen membrane sheets.[15] FPGAs are leveraged to optimize performance in this application, taking advantage of their inherent parallel processing capabilities.[15]

Sections 2 and 3 outline the identification methodology and the extension of the SDP-PID+ approach, which facilitates the intuitive handling of processes characterized by discrete-time TFs of any order and sampling time delays. Sections 4 and 5 describe the seamless implementation of the approach for each demonstrator. Finally, conclusions are presented in Section 6.

2. System identification

2.1. Model structure

The deterministic form of the SDP-TF for single-input, single-output (SISO) models may be defined as[16,23] in Equation (1),

$$y_k = \Pi^T \Phi_k \tag{1}$$

where Π is a vector of lagged input and output variables and Φ_k is a vector of SDP parameters, defined in Equation (2).

$$\begin{aligned} \Pi^T &= \begin{bmatrix} -y_{k-1} & \dots & -y_{k-n} & u_{k-1} & \dots & u_{k-m} \end{bmatrix} \\ \Phi_k &= \begin{bmatrix} a_1\{\chi_k\} & \dots & a_n\{\chi_k\} & b_1\{\chi_k\} & \dots & b_m\{\chi_k\} \end{bmatrix}^T \end{aligned} \tag{2}$$

Here, y_k and u_k represent the system's output and control input, respectively, while $a_i\{\chi_k\}$ for $i = 1, \dots, n$ and $b_j\{\chi_k\}$ for $j = 1, \dots, m$ are SDPs for which they are assumed to be functions of a non-minimal state vector, χ_k, not necessarily y_{k-i}. or u_{k-j}. However, for the SDP-PID+ control system design in the current paper, it is sufficient to limit the model in Equation (1) to $\chi_k = \Pi$. It is worth noting that any time delay, i.e. $\delta \geq 1$, is accounted for by setting the leading terms $b_1\{\chi_k\} \dots b_{\delta-1}\{\chi_k\}$ to zero. Finally, n and m are integers representing the maximum lag associated with the output and input variables, respectively. Therefore, the SDP-TF in

Equation (1) may be expressed in discrete form as in Equation (3).

$$y_k = -\sum_{i=1}^{n} a_i\{\chi_k\}\, y_{k-i} + \sum_{j=1}^{m} b_{j+\delta-1}\{\chi_k\}\, u_{k-(j+\delta-1)} \tag{3}$$

The incremental form in Equation (3) can be expressed in a discrete-time SDP-TF representation using the backward shift operator z^{-1} as follows in Equation (4).

$$y_k = \frac{\sum_{j=1}^{m} b_{j+\delta-1}\{\chi_k\}\,\mathrm{z}^{-(j+\delta-1)}}{1+\sum_{i=1}^{n} a_i\{\chi_k\}\,\mathrm{z}^{-i}} u_k = \frac{B\left(\chi_k,\mathrm{z}^{-1}\right)}{A(\chi_k,\mathrm{z}^{-1})} u_k \tag{4}$$

Here, the output parameters, $a_1\{\chi_k\}, \ldots, a_n\{\chi_k\}$, determine the order of the SDP-TF in Equation (4), denoted as n, while the number of input parameters, $b_\delta\{\chi_k\}, \ldots, b_{m+\delta-1}\{\chi_k\}$, is denoted as m. The polynomials $A\left(\chi_k,\mathrm{z}^{-1}\right)$ and $B\left(\chi_k,\mathrm{z}^{-1}\right)$ represent the output and input parameters, respectively, using the backward shift operator z^{-i}, where n and $m+\delta-1$ are the orders of these polynomials.

Numerous recent publications have outlined an approach for identifying and estimating the SDP-TF in Equation (3) and its application to a wide range of dynamic systems.[10–17,23] This approach typically consists of model identification and parameter estimation, as discussed below.

2.2. Model identification

The model structure and its potential state variables are initially identified through statistical estimation of discrete-time linear TF models. These models follow a similar structure to Equation (1), with time-invariant parameters, i.e., a_i ($i = 1, \ldots, n$), and b_j ($j = 1, \ldots, m$) are constant coefficients. These coefficients are estimated using the simplified refined instrumental variable algorithm. The appropriate linear model structure, i.e., triad $\{n, m, \delta\}$, is determined based on two statistical measures: (i) the coefficient of determination R_T^2, which evaluates the fit based on the response error, and (ii) Young's identification criterion, a hybrid measure that combines model fit and parametric efficiency.[24–29]

Following linear model identification, stochastic time-varying parameter models are estimated using recursive Kalman filtering and fixed interval smoothing algorithms.[23] These methods capture parameter variations driven by state variables or other dynamics, enabling nonlinear or chaotic behavior modeling. The recursive Kalman filtering/fixed interval smoothing approach employs iterative "back fitting" with reordered time-series data to refine the parameter estimates in Equation (1). The approach exists in MATLAB® as a computer-aided program for time series analysis and identification of noisy systems toolbox.[24–32]

2.3. Parameter estimation

Each element of Φ_k in the SDP-TF model in Equation (1) represents a nonparametric estimate, varying at every sampling instant and visualized as a graph. To achieve a more compact representation, these nonlinearities can be parameterized in terms of their associated dependent variable[23] using functions or neural networks and optimized via deterministic least squares or statistically efficient methods. However, for the applications considered here, linear functions of the state variables suffice for control design.[16]

3. Control methodology

3.1. State-dependent parameter-proportional-integral-derivative-plus control

The typical structure of a discrete PID controller is illustrated in Figure 1. It employs three compensators as follows: proportional ($k_{P1,k}$), integral ($k_{I,k}$), and derivative ($k_{D,k}$), of which all act on the error signal $e_k = r_k - y_k$, where r_k is the reference signal, and y_k is the system output. This structure provides an SVF formulation for PID control (SVF/PID) as in Equation (5).

$$\begin{aligned} u_k &= k_{I,k}\,\frac{e_k}{1-\mathrm{z}^{-1}} + k_{P1,k}\,e_k + k_{D,k}\left(1-\mathrm{z}^{-1}\right)e_k \\ &= \begin{bmatrix} k_{I,k} & k_{P1,k} & k_{D,k} \end{bmatrix} \begin{bmatrix} z_k \\ e_k \\ \Delta e_k \end{bmatrix} \end{aligned} \tag{5}$$

Here, $\begin{bmatrix} z_k & e_k & \Delta e_k \end{bmatrix}^T$ is the feedback state vector, given that e_k is the error state, Δe_k is the difference of error state and $z_k = z_{k-1} + e_k$ is the integral of the error state. The SDP-TF model in Equation (4) within the PID control methodology, as depicted in Figure 1, typically results in state-dependent compensators that justify the term SDP-PID control. The subscript k in the elements of the control vector $\begin{bmatrix} k_{I,k} & k_{P1,k} & k_{D,k} \end{bmatrix}$ in Equation (5) indicates the time-varying state feedback compensators, which are inherently state-dependent.

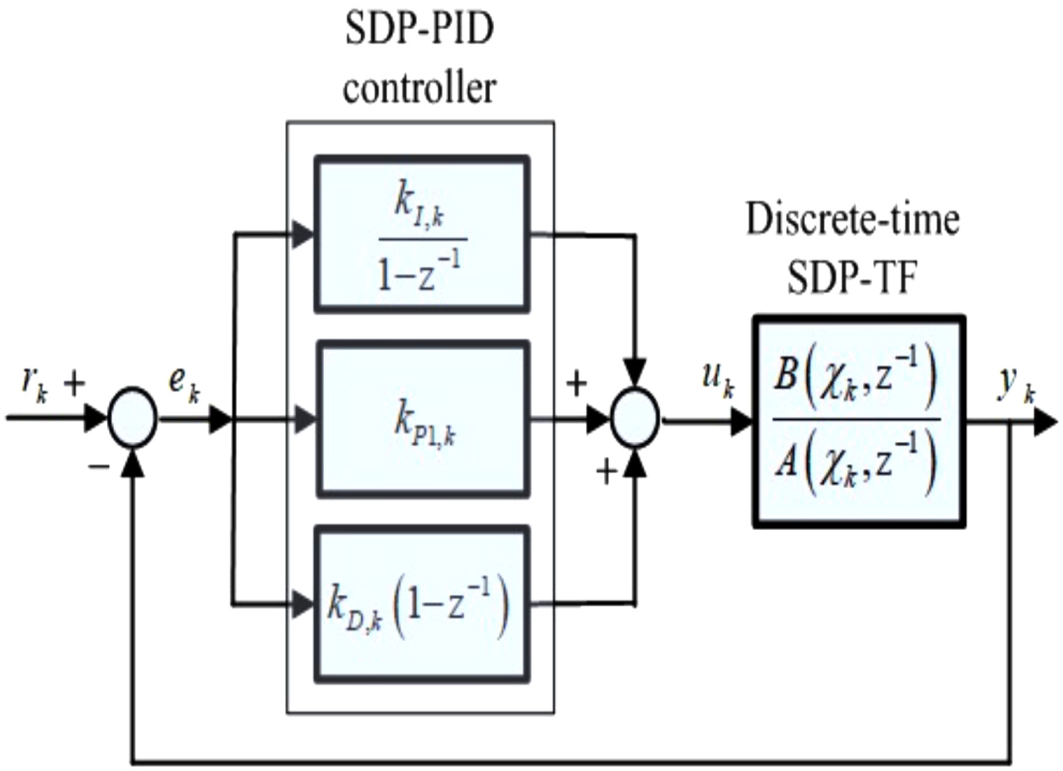


Figure 1. Typical structure of the discrete SDP-PID controller
Abbreviations: PID, proportional integral derivative; SDP, state-dependent parameter; TF, transfer function.

The PID structure, shown in Figure 1, is best suited for systems with discrete time SDP-TF of at most second order ($n \leq 2$), and unity sample time delays ($\delta = 1$). To extend its applicability, the regulator structure is employed, where the reference signal is set to zero, i.e. $r_k = 0$, making the error signal $e_k = -y_k$, and treating external disturbances as changes in the reference signal, r_k, [11–15,17] as depicted in Figure 2. This is possible because the external set point does not affect the control process .[33,34] This regulator form modifies Equation (4) to the following form in Equation (6).

$$e_k = \frac{-\sum_{j=1}^{m} b_{j+\delta-1}\{\chi_k\}\, z^{-(j+\delta-1)}}{1+\sum_{i=1}^{n} a_i\{\chi_k\}\, z^{-i}} u_k = \frac{-B\left(\chi_k, z^{-1}\right)}{A\left(\chi_k, z^{-1}\right)} u_k \tag{6}$$

To accommodate higher-order processes ($n > 2$) and numerator polynomials of order greater than unity ($m + \delta - 1 > 1$), the SDP-PID+ approach introduces additional compensators, called *plus* gains, that decelerate control actions and enhance stability. These innovative *plus* gains mirror the term SDP-PID+. Given the regulator SDP-PID+ structure, as depicted in Figure 2, the NMSS representation for SDP-PID+ control is given in Equation (7).

$$\begin{aligned} \mathbf{x}_k &= \mathbf{F}_k\, \mathbf{x}_{k-1} + \mathbf{g}_k\, u_{k-1} \\ y_k &= \mathbf{h}\, \mathbf{x}_k \end{aligned} \tag{7}$$

Equation (7) enables the direct implementation of full SVF control using the measured input and output signals of the controlled system without requiring the design of a state reconstructor.[16] Here, the k^{th} sample of the non-minimal feedback state vector is defined in Equation (8).

$$\mathbf{x}_k = \left[\begin{array}{c} \underbrace{z_k \quad e_k \quad \Delta e_k}_{\substack{\text{Typical PID feedback states} \\ n \leq 2}} \\ \underbrace{e_{k-2} \quad e_{k-3} \quad \cdots \quad e_{k-(n-2)} \quad e_{k-(n-1)}}_{\substack{\text{Extra proportional feedback states if} \\ n>2}} \\ \underbrace{u_{k-1} \quad u_{k-2} \quad \cdots \quad u_{k-(m+\delta-3)} \quad u_{k-(m+\delta-2)}}_{\substack{\text{Extra input feedback states} \\ \text{if } m \geq 1 \text{ and/or } \delta>1}} \end{array}\right]^T \tag{8}$$

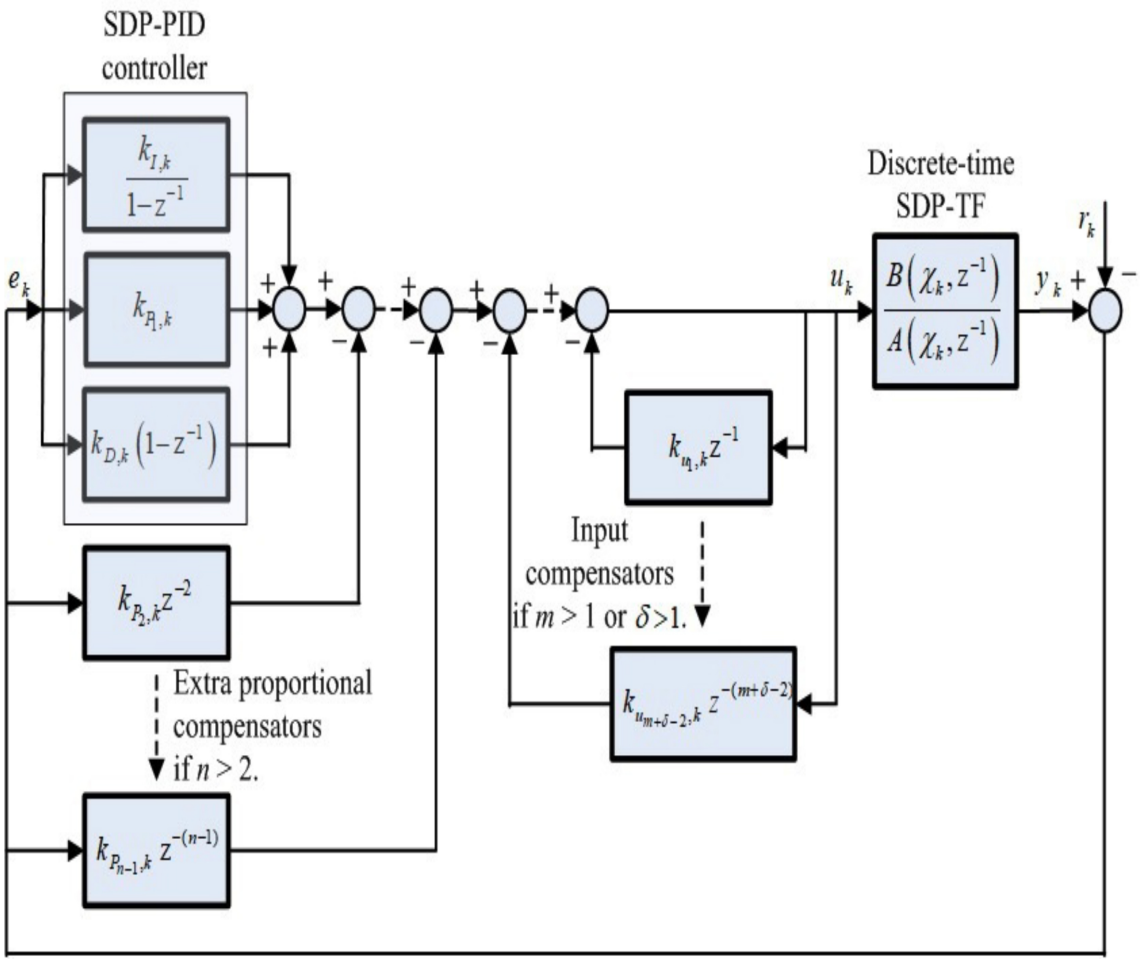


Figure 2. Regulator structure of the discrete SDP-PID+ controller, where the reference signal, r_k, is treated as a disturbance applied to the control system. Abbreviations: PID, proportional integral derivative; SDP, state-dependent parameter; TF, transfer function

The integral of error state, $z_k = z_{k-1} + e_k$, is exploited for NMSS design to introduce the inherent type 1 servomechanism performance .[35]

Given the SDP-TF model in Equation (6), the error state depicted in Equation (8), e_k, can be evaluated as in Equation (9).

$$\begin{aligned} e_k = -y_k = &-(a_{1,k} + a_{2,k})\, e_{k-1} + a_{2,k}\, \Delta e_{k-1} \\ &- a_{3,k}\, e_{k-3} - \ldots - a_{n-1,k}\, e_{k-(n-1)} \\ &- a_{n,k}\, e_{k-n} \\ &- b_{1,k}\, u_{k-1} - \ldots - b_{m-1,k}\, u_{k-(m-1)} \\ &- b_{m,k}\, u_{k-m} \end{aligned} \tag{9}$$

For the sake of generalization, the time delay in Equation (9) is assumed to be unity ($\delta = 1$), and the SDP-TF in Equation (4) is considered with at least second order ($n \geq 2$). Additionally, the terms $a_i\{\chi_k\}$ and $b_j\{\chi_k\}$ have been replaced by $a_{i,k}$ ($\forall\ i = 1, \ldots, n$) and $b_{j,k}$ ($\forall\ j = 1, \ldots, m$) respectively, for brevity. The integral of the error state, z_k, and the difference in the error state, Δe_k, can be evaluated from Equation (9) as follows in Equations (10) and (11).

$$\begin{aligned} z_k = z_{k-1} &- (a_{1,k} + a_{2,k})\, e_{k-1} + a_{2,k}\, \Delta e_{k-1} \\ &- a_{3,k}\, e_{k-3} - \ldots - a_{n-1,k}\, e_{k-(n-1)} - a_{n,k}\, e_{k-n} \\ &- b_{1,k}\, u_{k-1} - \ldots - b_{m-1,k}\, u_{k-(m-1)} - b_{m,k}\, u_{k-m} \end{aligned} \tag{10}$$

$$\begin{aligned} \Delta e_k = &-(a_{1,k} + a_{2,k} + 1)\, e_{k-1} + a_{2,k}\, \Delta e_{k-1} \\ &- a_{3,k}\, e_{k-3} - \ldots - a_{n-1,k}\, e_{k-(n-1)} - a_{n,k}\, e_{k-n} \\ &- b_{1,k}\, u_{k-1} - \ldots - b_{m-1,k}\, u_{k-(m-1)} - b_{m,k}\, u_{k-m} \end{aligned} \tag{11}$$

The set of Equations (9-11) can be used to derive the NMSS/SDP-PID+ form in Equation (7), considering the state feedback vector defined in Equation (8). The general form of the state transition square matrix $\mathbf{F}_k$ of order $n + m + \delta - 1$ ($\forall\ n \geq 2$), the input vector $\mathbf{g}_k$, and the time-invariant observation vector $\mathbf{h}$, at the k^{th} sample, are defined as follows in Equation (12).

$$\mathbf{F}_k = \begin{bmatrix} \underbrace{\mathbf{F}_{1,k}}_{(n+m+\delta-1)\times 3} & \underbrace{\mathbf{F}_{2,k}}_{(n+m+\delta-1)\times(n-2)} & \underbrace{\mathbf{F}_{3,k}}_{(n+m+\delta-1)\times(m+\delta-2)} \end{bmatrix}_{(n+m+\delta-1)\times(n+m+\delta-1)} \tag{13}$$

$$\mathbf{g}_k = \begin{bmatrix} \underbrace{-b_{1,k} \quad -b_{1,k} \quad -b_{1,k}}_{3} & \underbrace{0 \quad 0 \quad \dots \quad 0 \quad 0}_{n-2} & \underbrace{1 \quad 0 \quad \dots \quad 0 \quad 0}_{m+\delta-2} \end{bmatrix}^T \tag{12}$$

$$\mathbf{h} = \begin{bmatrix} \underbrace{0 \quad -1 \quad 0}_{3} & \underbrace{0 \quad 0 \quad \dots \quad 0 \quad 0}_{n-2} & \underbrace{0 \quad 0 \quad \dots \quad 0 \quad 0}_{m+\delta-2} \end{bmatrix}$$

The submatrices $\mathbf{F}_{1,k}$, $\mathbf{F}_{2,k}$, and $\mathbf{F}_{3,k}$ are defined as follows in Equation (13).

$$\mathbf{F}_{1,k} = \begin{bmatrix} 1 & 0 & 0 & 0 & 0 & \dots & 0 & 0 & 0 & 0 & \dots & 0 & 0 \\ -(a_{1,k}+a_{2,k}) & -(a_{1,k}+a_{2,k}) & -(a_{1,k}+a_{2,k}+1) & 0 & 0 & \dots & 0 & 0 & 0 & 0 & \dots & 0 & 0 \\ a_{2,k} & a_{2,k} & a_{2,k} & 0 & 0 & \dots & 0 & 0 & 0 & 0 & \dots & 0 & 0 \end{bmatrix}^T \quad \leftrightarrow n = 2$$

$$\mathbf{F}_{2,k} = \begin{bmatrix} -a_{3,k} & -a_{3,k} & -a_{3,k} & 0 & 1 & \dots & 0 & 0 & 0 & 0 & \dots & 0 & 0 \\ -a_{4,k} & -a_{4,k} & -a_{4,k} & 0 & 0 & \ddots & 0 & 0 & 0 & 0 & \dots & 0 & 0 \\ \vdots & \vdots & \vdots & \vdots & \vdots & \vdots & \ddots & \vdots & \vdots & \vdots & \dots & \vdots & \vdots \\ -a_{n-2,k} & -a_{n-2,k} & -a_{n-2,k} & 0 & 0 & \dots & 0 & 1 & 0 & 0 & \dots & 0 & 0 \\ -a_{n-1,k} & -a_{n-1,k} & -a_{n-1,k} & 0 & 0 & \dots & 0 & 0 & 0 & 0 & \dots & 0 & 0 \end{bmatrix}^T \quad \leftrightarrow n > 2$$

$$\mathbf{F}_{3,k} = \begin{bmatrix} -b_{2,k} & -b_{2,k} & -b_{2,k} & 0 & 0 & \dots & 0 & 0 & 0 & 1 & \dots & 0 & 0 \\ -b_{3,k} & -b_{3,k} & -b_{3,k} & 0 & 0 & \dots & 0 & 0 & 0 & 0 & \ddots & 0 & 0 \\ \vdots & \vdots & \vdots & \vdots & \vdots & \dots & \vdots & \vdots & \vdots & \vdots & \dots & \ddots & \vdots \\ -b_{m+\delta-2,k} & -b_{m+\delta-2,k} & -b_{m+\delta-2,k} & 0 & 0 & \dots & 0 & 0 & 0 & 0 & \dots & 0 & 1 \\ -b_{m+\delta-1,k} & -b_{m+\delta-1,k} & -b_{m+\delta-1,k} & 0 & 0 & \dots & 0 & 0 & 0 & 0 & \dots & 0 & 0 \end{bmatrix}^T \quad \leftrightarrow m+\delta > 2 \tag{13}$$

As depicted in Equation (13), the submatrices $\mathbf{F}_{2,k}$ and $\mathbf{F}_{3,k}$ exist if and only if $n > 2$ and $m + \delta > 2$, respectively. Therefore, in case of $n = 2$ and $m + \delta = 2$, there is no plus, and the definition in Equation (12) is downgraded to the NMSS/SDP-PID form as follows in Equation (14).

$$\begin{aligned} \mathbf{F}_k &= \begin{bmatrix} 1 & -(a_{1,k}+a_{2,k}) & a_{2,k} \\ 0 & -(a_{1,k}+a_{2,k}) & a_{2,k} \\ 0 & -(a_{1,k}+a_{2,k}+1) & a_{2,k} \end{bmatrix}, \\ \mathbf{g}_k &= \begin{bmatrix} -b_{1,k} \\ -b_{1,k} \\ -b_{1,k} \end{bmatrix}, \\ \textit{and } \mathbf{h} &= \begin{bmatrix} 0 & -1 & 0 \end{bmatrix} \end{aligned} \tag{14}$$

Here, the state feedback vector is as presented in Equation (15),

$$\mathbf{x}_k = \begin{bmatrix} z_k & e_k & \Delta e_k \end{bmatrix}^T \tag{15}$$

for which the states are given as in Equation (16).

$$\begin{aligned} e_k &= -(a_{1,k}+a_{2,k})\, e_{k-1} + a_{2,k}\, \Delta e_{k-1} - b_{1,k}\, u_{k-1} \\ z_k &= z_{k-1} - (a_{1,k}+a_{2,k})\, e_{k-1} + a_{2,k}\, \Delta e_{k-1} - b_{1,k}\, u_{k-1} \\ \Delta e_k &= -(a_{1,k}+a_{2,k}+1)\, e_{k-1} + a_{2,k}\, \Delta e_{k-1} - b_{1,k}\, u_{k-1} \end{aligned} \tag{16}$$

Also, in the case of the discrete-time SDP-TF model with unity order, i.e. $n = 1$, and $m+\delta > 2$, the submatrix $\mathbf{F}_{2,k}$ vanishes, and the third column in the submatrix $\mathbf{F}_{1,k}$ becomes zero-valued. Consequently, this results in the NMSS/SDP-PI+ representation without a *derivative* component, as the third column vector of the submatrix $\mathbf{F}_{1,k}$, associated with the derivative state, Δe_{k-1}, is zero.[17] Under this condition, the states defined in Equations (9-11) are reduced to Equation (17).

$$\begin{aligned} e_k =& -a_{1,k}\, e_{k-1} - b_{1,k}\, u_{k-1} - \dots \\ & - b_{m-1,k}\, u_{k-(m-1)} - b_{m,k}\, u_{k-m} \\ z_k =& z_{k-1} - a_{1,k}\, e_{k-1} - b_{1,k}\, u_{k-1} - \dots \\ & - b_{m-1,k}\, u_{k-(m-1)} - b_{m,k}\, u_{k-m} \end{aligned} \tag{17}$$

Thus, for $n = 1$ and $m + \delta > 2$, the set of Equation (17) represents the NMSS/SDP-PI+ form using the following state feedback vector in Equation (18).

$$\mathbf{x}_k = \begin{bmatrix} z_k & e_k & u_{k-1} & u_{k-2} & \dots, \\ u_{k-(m+\delta-3)} & u_{k-(m+\delta-2)} \end{bmatrix}^T \tag{18}$$

The state transition square matrix $\mathbf{F}_k$ (order $m + \delta$), the input vector $\mathbf{g}_k$, and the observation vector $\mathbf{h}$ are now defined as Equation (19).

$$\mathbf{F}_k = \begin{bmatrix} 1 & -a_{1,k} & -b_{2,k} & -b_{3,k} & \dots & -b_{m+\delta-2,k} & -b_{m+\delta-1,k} \\ 0 & -a_{1,k} & -b_{2,k} & -b_{3,k} & \dots & -b_{m+\delta-2,k} & -b_{m+\delta-1,k} \\ 0 & 0 & 0 & 0 & \dots & 0 & 0 \\ 0 & 0 & 1 & 0 & \dots & 0 & 0 \\ \vdots & \vdots & \vdots & \ddots & \vdots & \vdots & \vdots \\ 0 & 0 & 0 & 0 & \ddots & 0 & 0 \\ 0 & 0 & 0 & 0 & 0 & 1 & 0 \end{bmatrix}$$

$$\leftrightarrow \begin{cases} n = 1 \\ m + \delta > 2 \end{cases}$$

$$\mathbf{g}_k = \begin{bmatrix} -b_{1,k} & -b_{1,k} & 1 & 0 & \dots & 0 & 0 \end{bmatrix}^T$$

$$\mathbf{h} = \begin{bmatrix} 0 & -1 & 0 & 0 & \dots & 0 & 0 \end{bmatrix} \tag{19}$$

It is always possible to derive the NMSS/SDP-PID+ for the discrete-time SDP-TF model with the first order, $n = 1$, and $m + \delta > 2$. This is achieved by assuming that, as the controlled process approaches a steady state, i.e. $e_k \to 0$, the second difference of the error state also tends to zero, i.e., $\Delta^2 e_k \to 0$. Consequently, the first difference of the error state can be considered constant, i.e., $\Delta e_k \cong c$.[13] In this case, the states in Equation (17) may be rewritten as Equation (20).

$$\begin{aligned} e_k &= -a_{1,k}\, e_{k-1} - b_{1,k}\, u_{k-1} - \dots \\ &\quad - b_{m-1,k}\, u_{k-(m-1)} - b_{m,k}\, u_{k-m} \\ z_k &= z_{k-1} - a_{1,k}\, e_{k-1} - b_{1,k}\, u_{k-1} - \dots \\ &\quad - b_{m-1,k}\, u_{k-(m-1)} - b_{m,k}\, u_{k-m} \\ \Delta e_k &= \frac{\Delta e_k + \Delta e_{k-1}}{2} \\ &\quad - (a_{1,k} + 1)\; e_{k-1} - b_{1,k}\, u_{k-1} - \dots \\ &= \frac{-b_{m-1,k}\, u_{k-(m-1)} - b_{m,k}\, u_{k-m} + \Delta e_{k-1}}{2} \end{aligned} \tag{20}$$

The state definition in Equation (20) restores the NMSS/SDP-PID+ form for the first-order SDP-TF model using the following state feedback vector in Equation (21).

$$\mathbf{x}_k = \begin{bmatrix} z_k\; e_k \Delta e_k\; u_{k-1}\; u_{k-2}\; ..., \\ u_{k-(m+\delta-3)}\; u_{k-(m+\delta-2)} \end{bmatrix}^T \tag{21}$$

The square matrix $\mathbf{F}_k$ of order $m + \delta + 1$ ($\forall\; n = 1$), the input vector $\mathbf{g}_k$, and the observation vector $\mathbf{h}$ are defined as Equation(22).

$$\mathbf{F}_k = \begin{bmatrix} 1 & -a_{1,k} & 0 & -b_{2,k} & -b_{3,k} & \dots & -b_{m+\delta-2,k} & -b_{m+\delta-1,k} \\ 0 & -a_{1,k} & 0 & -b_{2,k} & -b_{3,k} & \dots & -b_{m+\delta-2,k} & -b_{m+\delta-1,k} \\ 0 & \frac{-a_{1,k}}{2} & \frac{1}{2} & \frac{-b_{2,k}}{2} & \frac{-b_{3,k}}{2} & \dots & \frac{-b_{m+\delta-2,k}}{2} & \frac{-b_{m+\delta-1,k}}{2} \\ 0 & 0 & 0 & 0 & 0 & \dots & 0 & 0 \\ 0 & 0 & 0 & 1 & 0 & \dots & 0 & 0 \\ \vdots & \vdots & \vdots & \vdots & \ddots & \dots & \vdots & \vdots \\ 0 & 0 & 0 & 0 & 0 & \ddots & 0 & 0 \\ 0 & 0 & 0 & 0 & 0 & \dots & 1 & 0 \end{bmatrix}$$

$$\leftrightarrow \begin{cases} n = 1 \\ m + \delta > 2 \end{cases}$$

$$\mathbf{g}_k = \begin{bmatrix} \frac{-b_{1,k}}{2} & \frac{-b_{1,k}}{2} & \frac{-b_{1,k}}{2} & 1 & 0 & \dots & 0 & 0 \end{bmatrix}^T$$

$$\mathbf{h} = \begin{bmatrix} 0 & -1 & 0 & 0 & 0 & \dots & 0 & 0 \end{bmatrix} \tag{22}$$

The methodology for deriving the SDP-PID+ and its variants is summarized in Table 1 for clarity and to disentangle the equations.

3.2. Controllability

The linear-like structure of the SDP-TF model in Equation (4) facilitates the design of the nonlinear SDP-PID+ control law using the strategies of the linear system design, such as suboptimal LQ or pole assignment approaches.[10–15] However, using these basic methods, some SDP-TF model structures may not be fully controllable.[38]

In control theory, controllability refers to the ability to drive a system's state to any desired state within a finite time, starting from any initial condition. For the SDP-TF model in Equation (4), discrete controllability at each sample k means the system can be controlled at each sampling instance. This, necessarily, leads to a system $\mathbf{F}_k$, $\mathbf{g}_k$, and $\mathbf{h}$ of NMSS/SDP-PID+, which is controllable over each sampling period.[38,39] The controllability conditions can be stated as:[39] Given a discrete-time SISO system described by Equation (4), the NMSS/SDP-PID+ form in Equation (7), characterized by the pair [$\mathbf{F}_k$ and $\mathbf{g}_k$], is locally controllable over each sampling period if and only if, the polynomials $A\left(\chi_k, \mathrm{z}^{-1}\right)$ and $B\left(\chi_k, \mathrm{z}^{-1}\right)$ are co-prime, and Equation (23) is met.

$$\sum_{j=1}^{m} b_{j+\delta-1}\left\{\chi_k\right\} \mathrm{z}^{-(j+\delta-1)} \neq 0 \tag{23}$$

Due to the time-varying nature of the parameters in the SDP case, it is important to note that these conditions may not always be met in every sample period. As a result, challenges may emerge during the control design process for the SDP-PID+ controller.

Although deriving comprehensive results for the controllability and stability of the nonlinear SDP system remains an area of ongoing research,[38,39] the practical approach described

Table 1. State-dependent parameters-proportional integral derivative plus methodology for the non-minimal state space representation in Equation (7)

Parameter	Control scheme	Description
$n \geq 2$ $m+\delta > 2$	This is the general SDP-PID+	• The state vector is defined in Equation (8) • The states are defined at Equations (9-11) • The matrices, $\mathbf{F}_k$, $\mathbf{g}_k$, and $\mathbf{h}$, of the order, $n+m+\delta-1$ are defined in Equations (12) and (13).
$n = 2$ $m+\delta = 2$	There are no plus gains SDP-PID+ switches to conventional SDP-PID	• The state vector is defined in Equation (15) • The states are defined in Equation (16) • The matrices, $\mathbf{F}_k$, $\mathbf{g}_k$, and $\mathbf{h}_k$, of the order $n+m+\delta-1$ are defined in Equation (14)
$n = 1$ $m+\delta > 2$	Special case: No derivative gain SDP-PID+ downgrades to SDP-PI+	• The state vector is defined in Equation (18) • The states are defined in Equation (17) • The matrices, $\mathbf{F}_k$, $\mathbf{g}_k$, and $\mathbf{h}$, of the order $m+\delta$ are defined in Equation (19)
$n = 1$ $m+\delta > 2$	Special case: Restoring derivative gain SDP-PI+ is upgraded back to SDP-PID+	• The state vector is defined in Equation (21) • The states are defined in Equation (20) • The matrices, $\mathbf{F}_k$, $\mathbf{g}_k$, and $\mathbf{F}_k$, of the order are $m+\delta+1$ defined in Equation (22)

Abbreviations: PI+: Proportional integral plus; PID: Proportional integral derivative; SDP: State-dependent parameter; TF: Transfer function.

above has been sufficient for the two demonstrators in this paper. This is because, in real-world applications, system variables are constrained and consistently remain within known boundaries.

3.3. Control algorithm

The SVF control is introduced in Equation (5) and can be expressed in its general form as follows in Equation (24).

$$u_k = -\mathbf{k}_k^+ \mathbf{x}_k \tag{24}$$

In Equation (24), the vector of the control gain, denoted as $\mathbf{k}_k$, is defined as

$$K_K{}^+ = \left[\begin{array}{c} \underbrace{k_{I,k} \quad k_{P_1,k} \quad k_{D,k},}_{\text{Typical PID gains, } n\leq 2} \\ \underbrace{k_{P_2,k} \quad k_{P_3,k} \quad \dots \quad k_{P_{n-2},k}, \quad k_{P_{n-1},k},}_{\text{Extra proportional gains, } n>2} \\ \underbrace{k_{u_1,k} \quad k_{u_2,k} \quad \dots \quad k_{u_{m+\delta-3},k}, \quad k_{u_{m+\delta-2},k}}_{\text{Extra input gains, } m+\delta\geq 2} \end{array}\right]^T \tag{25}$$

The SVF control vector in Equation (25) is computed at every sampling interval using either the pole placement technique or by minimizing an LQ cost function. In the latter method, the system is treated as a "frozen parameter" system, representing a specific instant of the family of the NMSS model [$\mathbf{F}_k$ and $\mathbf{g}_k$]. Alternatively, the discrete-time algebraic Riccatti equation is solved for each sampling interval.[33,36] For the pole placement approach, linear techniques are commonly employed to determine control gains, as demonstrated in .[11,12]

3.3.1. SDP-PID+/LQ tuning approach

The optimal SVF/SDP-PID+ control gain vector, as defined in Equation (25), can be determined by minimizing the following infinite-time optimal LQ cost function in Equation (26).

$$J = \sum_{k=0}^{\infty} \left[\mathbf{x}_k^T \, \mathbf{Q} \, \mathbf{x}_k + R \, u_k^2\right] \tag{26}$$

In Equation (26), R is a positive scalar that weights the input u_k and Q is a symmetric positive definite matrix that assigns weights to the states, as defined in Equation (8). For SISO systems, Q may be defined as in Equation (27).

$$\mathbf{Q} = \text{diag}\left\{\begin{array}{c} q_z \quad q_{e_1} \quad q_{\Delta e}, \\ q_{e_2} \; q_{e_3} \quad \cdots \quad q_{e_{n-2}} \quad q_{e_{n-1}}, \\ q_{u_1} \quad q_{u_2} \quad \cdots \quad q_{u_{m+\delta-3}} \quad q_{u_{m+\delta-2}} \end{array}\right\} \tag{27}$$

Based on the NMSS/SDP-PID+ form in Equation (7) with the description $\mathbf{F}_k$ and $\mathbf{g}_k$ as provided in Table 1, the time-varying SVF compensator vector, $\mathbf{k}_k^+$, of the nonlinear SDP-PID+ control, can be recursively determined as the steady state solution of the algebraic Riccati equation.[37] This equation is derived from the standard LQ cost function in Equation (26) at the k^{th} sample as follows in Equation (28),

$$\begin{aligned} \mathbf{k}_k^+ &= \left[\mathbf{g}_k^T \mathbf{P}^{(i+1)} \mathbf{g}_k + R\right]^{-1} \mathbf{g}_k^T \mathbf{P}^{(i+1)} \mathbf{F}_k \\ \mathbf{P}^{(i)} &= \mathbf{F}_k^T \mathbf{P}^{(i+1)} \left[\mathbf{F}_k - \mathbf{g}_k \, \mathbf{k}_k^+\right] + \mathbf{Q} \end{aligned} \tag{28}$$

where P is a symmetric positive definite matrix with the initial value $\mathbf{P}^{(i+1)} = \mathbf{Q}$ and $\mathbf{k}_k^+$ is the

SVF/SDP-PID+ control gain vector, as defined in Equation (25).

For simplicity, a frozen parameter system $\{\mathbf{F}'_k,\ \mathbf{g}'_k\}$ can be employed, where the frozen system is defined as a single sample instance from the family of $\{\mathbf{F}_k,\ \mathbf{g}_k\}$.[36,37] In this scenario, the matrix $\mathbf{P}$ becomes time-invariant, and Equation (28) is simplified to

$$\mathbf{P}^{(i)} = \mathbf{F'}_k^T \mathbf{P}^{(i+1)} \left[\mathbf{F'}_k - \mathbf{g}_k \left(\mathbf{g'}_k^T \mathbf{P}^{(i+1)} \mathbf{g'}_k + R\right)^{-1} \mathbf{g'}_k^T \mathbf{P}^{(i+1)} \mathbf{F'}_k\right] + \mathbf{Q} \tag{29}$$

After obtaining the matrix P from Equation (29), the SDP gain vector $\mathbf{k}_k^+$ can be derived from Equation (28) as follows:

$$\mathbf{k}_k^+ = \left[\mathbf{g}_k^T \mathbf{P}\ \mathbf{g}_k + R\right]^{-1} \mathbf{g}_k^T \mathbf{P}\ \mathbf{F}_k \tag{30}$$

Note that the system matrices $\{\mathbf{F}_k,\ \mathbf{g}_k\}$ remain unfrozen when implementing Equation (30). A straightforward trial and error approach is employed to evaluate the gain vector in Equation (30). The process begins with unity weights to ensure a balanced influence of each parameter, preventing any single parameter from dominating the others. This approach allows for consistent and logical experimentation.

3.3.2. SDP-PID+/pole placement tuning approach

The design methodology for discrete SDP-PID+/pole placement was introduced by Shaban et al.[11] It has been shown that the process is relatively straightforward, provided the performance of the closed-loop control system is predictable, i.e., if the SDP-TF in Equation (4) is controllable. Here, the nonlinear SDP-PID+ compensators, as defined in Equation (25), can be evaluated by modifying the location of the poles of the closed-loop SDP-PID+ control system. In this regard, the regulator structure of the SDP-PID+ controller, depicted in Figure 2, needs to be reduced to the unity feedback closed-loop SDP-PID+ control system in TF form, as illustrated in Figure 3 as follows in Equation (31),

$$y_k = \frac{K_k^+\left(\mathrm{z}^{-1}\right) B\left(\chi_k, \mathrm{z}^{-1}\right)}{\Delta\, K_{u,k}(\mathrm{z}^{-1})\, A(\chi_k, \mathrm{z}^{-1}) + K_k^+(\mathrm{z}^{-1})\, B(\chi_k, \mathrm{z}^{-1})}\, r_k \tag{31}$$

given that $\Delta = 1 - \mathrm{z}^{-1}$ represents the difference operator. The characteristic equation for the SDP-PID+ control system is extracted from Equation (31) as Equation (32).

$$\Delta\, K_{u,k}\left(\mathrm{z}^{-1}\right)\ A\left(\chi_k, \mathrm{z}^{-1}\right) + K_k^+\left(\mathrm{z}^{-1}\right)\ B\left(\chi_k, \mathrm{z}^{-1}\right) \tag{32}$$

This equation is used to determine the SDP-PID+ compensators, $\mathbf{k}_k^+$, in Equation (25). It is worth noting that the order of characteristic Equation (32) is $n + m + \delta - 1,\ \forall\ n \geq 2$, with a minimum order of three for a discrete-time SDP-TF of triad $\{\leq 2,\ 1,\ 1\}$. The polynomials corresponding to the proportional *plus* compensator, $K_k^+\left(\mathrm{z}^{-1}\right)$, and input *plus* compensator, $K_{u,k}\left(\mathrm{z}^{-1}\right)$, are defined as in Equation (33),

$$\begin{aligned} K_k^+\left(\mathrm{z}^{-1}\right) &= k_{1,k} - k_{2,k}\mathrm{z}^{-1} + k_{3,k}\mathrm{z}^{-2} + \sum_{i=4}^{n+1} k_{i,k}\, \mathrm{z}^{-(i-1)} \\ K_{u,k}\left(\mathrm{z}^{-1}\right) &= 1 + \sum_{j=1}^{m+\delta-2} k_{u_j,k}\mathrm{z}^{-j} \end{aligned} \tag{33}$$

where,

$$\begin{aligned} k_{1.k} &= k_{P_1,k} + k_{I,k} + k_{D,k} \\ k_{2.k} &= k_{P_1,k} + 2k_{D,k} \\ k_{3.k} &= k_{D,k} + k_{P_{i-1},k} \qquad i = 3 \text{ if } n \geq 3 \\ &\vdots \\ k_{i,k} &= -k_{P_{i-2},k} + k_{P_{i-1},k} \quad 4 \leq i \leq n+1 \end{aligned} \tag{34}$$

The *plus* compensators, $k_{P_{i-1}}$ $(i = 3, ...,\ n{+}1)$ for $n \geq 3$ and k_{u_j} $(j = 1,\ \ldots m + \delta - 2)$ for $m{+}\delta > 2$, in Equations (33) and (34) allow for exploiting additional poles to suit the discrete-time SDP-TF in Equation (4) that exceeds second-order dynamics, i.e. $n \geq 3$, and has time delay and/or numerator order greater than unity, i.e. $m + \delta > 2$. Applying polynomial algebra to the characteristic Equation (32) as Equation (35)

$$\begin{aligned} &\Delta\, K_{u,k}\left(z^{-1}\right) A_k\left(\chi_k, z^{-1}\right) + K_k^+\left(z^{-1}\right)\ B_k\left(\chi_k, z^{-1}\right) \\ =&(1 - p_1\, \mathrm{z}^{-1})\,(1 - p_2\, \mathrm{z}^{-1}) \\ &(1 - p_3\, \mathrm{z}^{-1}) \ldots (1 - p_i\, \mathrm{z}^{-1}) \\ &\begin{array}{ll} i = 4, \ldots, n + m + \delta - 1 & \forall\, n \geq 2 \\ i = 4, \ldots, n + m + \delta & \forall\, n = 1 \end{array} \end{aligned} \tag{35}$$

gives SDP-PID+ gains $\{k_{1,k},\ k_{2,k}, k_{3,k}, ..., k_{i,k}$ $(i = 4, ..., n + 1), k_{u_j,k} (j = 1, ..., m + \delta - 2)\}$ at pre-determined pole locations $\{p_1,\ p_2,\ p_3, ...,\ p_i$ $(i = 4, ..., n + m + \delta - 1\ \forall\, n \geq 2)\}$ in the complex z-plane. The control law can subsequently be extracted from Figure 3 in Equation (36).

$$\begin{aligned} u_k =& u_{k-1} + k_{1,k}\, e_k - k_{2,k}\, e_{k-1} + k_{3,k}\, e_{k-2} \\ &+ \sum_{i=4}^{n+1} k_{i,k}\, e_{k-(i-1)} \\ &- \sum_{j=1}^{m+\delta-2} k_{u_j,k} \left(u_{k-j} - u_{k-(j+1)}\right) \end{aligned} \tag{36}$$

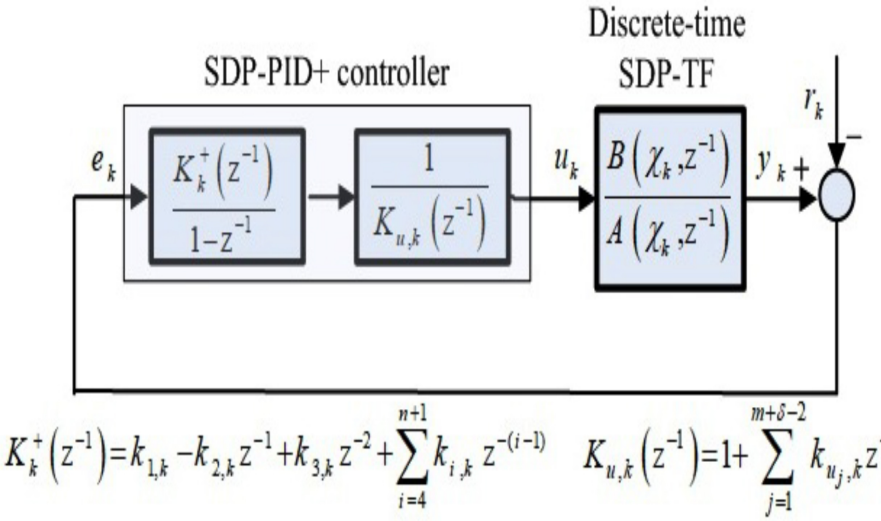


Figure 3. The regulator structure of the unity feedback closed loop SDP-PID+ control system.
Abbreviations: PID: Proportional integral derivative; SDP: State-dependent parameter; TF: Transfer function

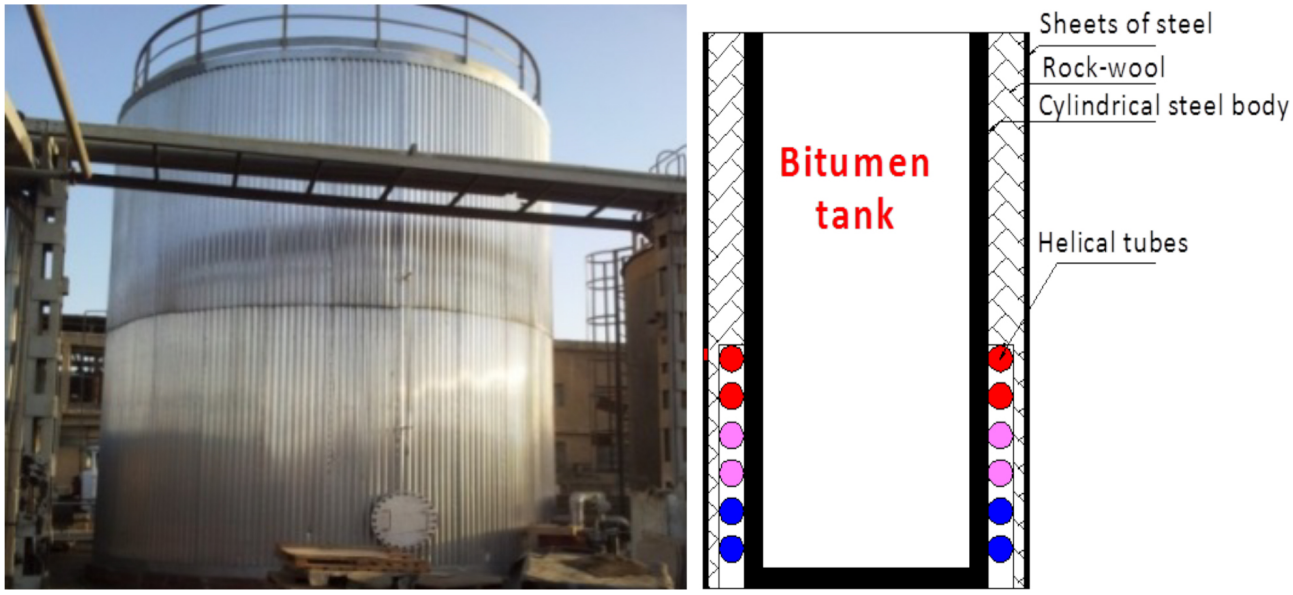


Figure 4. Bitumen tank at INSUMAT company, Tamouh, Giza, Egypt

Alternatively, the SVF/SDP-PID+ control action in Equation (24) can be directly used, where the parameters of the SVF/SDP-PID+ control vector, defined in Equation (25), are derived from Equation (34). It is worth noting that a systematic trial and error experiment is applied to analyze the closed-loop poles in the complex z-plane ($0 < p_i < 1$), aiming to determine appropriate gains that ensure a satisfactory tracking response.

4. Industrial bitumen tank

This tank, located at INSUMAT Company in Tamouh, Giza, Egypt, is used to heat raw liquid bitumen ($\sim 90°$C) before mixing to produce bitumen products. The properties of the final product depend significantly on the mixing temperature ($90 - 180°$C), which must remain within a $\pm 5\%$ range of the set value, as well as the quantity of additives used. To prevent overheating, the temperature must never reach the self-ignition point ($\sim 220°$C) of the vapor inside the tank.[10]

The bitumen tank is a closed steel reservoir enclosed by helical tubes filled with hot oil ($\sim 265°$C). Raw liquidized bitumen is fed into the tank via an inlet pipe at the top, and the heated bitumen is discharged to a blender through an outlet pipe near the base, as in Figure 4.

Rockwool blocks insulate the tank's exterior to minimize heat loss and reduce power consumption.

A motorized three-way valve and a PT100 temperature sensor are integrated into this thermal process and connected to a data acquisition unit (LabJack UE9) interfaced with a LabVIEW™ program. The valve's opening is normalized from 0 (fully closed) to 100 (fully open) to regulate the flow rate of the hot oil, functioning as an actuator. The PT100 provides temperature feedback for the control system. A LabVIEW™ module was developed to manage the hardware components (three-way valve and PT100 sensor) and apply the selected controller. Additional hardware/software interfacing details can be found in Hamed et al.[40]

4.1. State-dependent parameter model for bitumen tank

The bitumen tank's process exhibits a relatively slow dynamic response, prompting the selection of a sampling rate of one sample every four minutes, i.e., $\Delta t = 240$.[40] The analysis of the experimental data for Bitumen temperature produces an SDP-TF model with triad $\{1,\ 1,\ 3\}^{13}$, as shown below in Equation (37)

$$\begin{aligned} y_k &= -a_1(\chi_k)\, y_{k-1} + b_3\, u_{k-3} && \text{(i)} \\ a_1(\chi_k) &= 0.1 \times 10^{-5}\, y_{k-3}^2 - 0.00135\, y_{k-3} - 0.995 && \text{(ii)} \\ b_3 &= 0.063 \end{aligned} \tag{37}$$

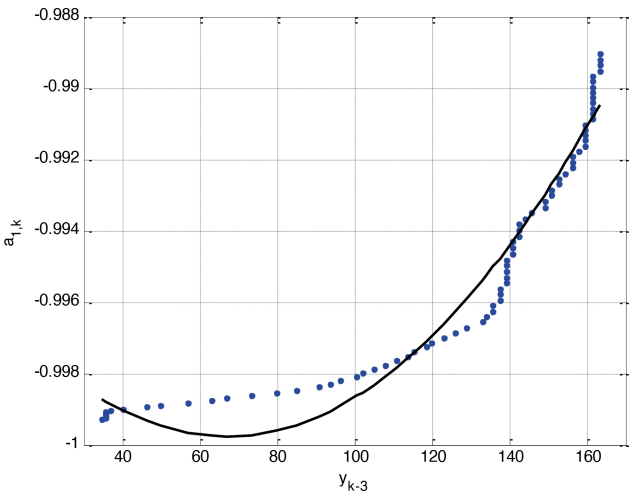


Figure 5. Estimated state-dependent parameter, $a_{1,k}$, versus its state variable y_{k-3}, i.e. $a_{1,k} = f\,(y_{k-3})$

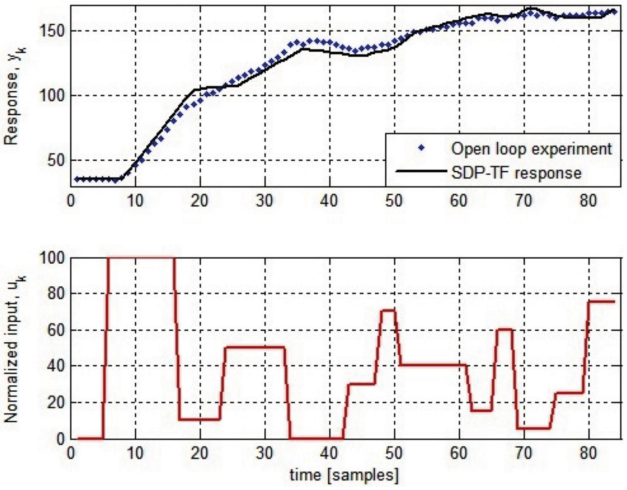


Figure 6. Open loop experiment and simulation results for the estimated SDP-TF model for bitumen temperature. Abbreviations: SDP, State-dependent parameter; TF, transfer function

where y_k represents the temperature of the bitumen, and u_k denotes the percentage of the three-way valve opening. The state-dependent output parameter $a_1(\chi_k)$, denoted as $a_{1,k}$, is time-variant, as shown in Figure 5, while the input parameter, denoted as b_3, is time-invariant. Figure 6 illustrates the simulation results for the estimated SDP-TF model in Equation (37).

4.2. Controller design and implementation for Bitumen temperature

Model in Equation (37) can be represented by using the operator z^{-1} as follows in Equation (38).

$$y_k = \frac{b_3\, \mathrm{z}^{-3}}{1 + a_1\,(\chi_{k+1})\ \mathrm{z}^{-1}}\, u_k \tag{38}$$

Using Equation (38) and Table 1, the nonlinear NMSS/SDP-PID+ form in Equation (7) can be constructed. As a result, the time-variant transition matrix $\mathbf{F}_k$ (5×5) at the k^{th} sample, and the time-invariant input vector $\mathbf{g}$ (5×1) and observation vector $\mathbf{h}$ (1×5) are defined using Equation (22) as follows in Equation (39).

$$\mathbf{F}_k = \begin{bmatrix} 1 & -a_1(y_{k-3}) & 0 & 0 & -b_3 \\ 0 & -a_1(y_{k-3}) & 0 & 0 & -b_3 \\ 0 & \dfrac{-a_1(y_{k-3}) - 1}{2} & \dfrac{1}{2} & 0 & \dfrac{-b_3}{2} \\ 0 & 0 & 0 & 0 & 0 \\ 0 & 0 & 0 & 1 & 0 \end{bmatrix},$$

$$\mathbf{g} = \begin{bmatrix} 0 \\ 0 \\ 0 \\ 1 \\ 0 \end{bmatrix}, \quad \mathbf{h} = \begin{bmatrix} 0 & 1 & 0 & 0 & 0 \end{bmatrix} \tag{39}$$

Here, the state vector, $\mathbf{x}_k$, for the bitumen system is defined as $\mathbf{x}_k = \begin{bmatrix} z_k & e_k & \Delta e_k & u_{k-1} & u_{k-2} \end{bmatrix}^T$. In this industrial example, SDP-PID+/LQ control was applied by freezing the parameters of $\{\mathbf{F}'_k,\ \mathbf{g}\}$ at ambient temperature, i.e. $y_{k-3} = 30^{\text{o}}$. Simulation trials showed that the weights $R = 1$ and $\mathbf{Q} = \text{diag}\{5\,1\,20000\,1\,1\}$ were appropriate for obtaining the time-invariant $\mathbf{P}$ matrix. Equation (30) was then used to calculate the SDP-PID+ gain vector, $\mathbf{k}_k^+$. Finally, the control law in Equation (24) was implemented for real-time bitumen temperature control, as depicted in Figure 7. This figure illustrates the practical implementation and simulation results of the SDP-TF model in Equation (38). It is worth noting that satisfactory rejection of the disturbances is shown when controlling the temperature of the bitumen.[13]

The nonlinear SDP-PID+/LQ control achieved suitable closed-loop performance, maintaining the response within the ±5% permissible range without overshooting. Negligible differences were observed between the practical and the SDP-TF model responses in Equation (38). This demonstration marks the first successful onsite application of SDP-PID+ control in an industrial bitumen system, providing robust temperature tracking and control performance.

5. Industrial reeling/packing machine

The industrial reeling/packing machine used in the bitumen membrane sheet production line at INSUMAT company, Sadat City, Egypt, incorporates nonlinear SDP-PID+ control methodology integrated into FPGAs. This control system manages the pulling motor that regulates the velocity of the floating drum. Its primary function is to maintain the bitumen sheet within the accumulator at an acceptable range (15–85%) by adjusting the motor's reference speed (Figure 8). The SDP/PID+ control system dynamically counteracts disturbances detected through a feedback encoder mounted on the floating drum. The FPGA-based control strategy uses the LabVIEW-FPGA module to enable simultaneous control operations. Detailed hardware and software interfacing is provided in Shaban *et al.*[15]

The system's primary objective is to prevent productivity losses caused by excessive infoldings of bitumen sheets around the reeling drum or interruptions due to emergency shutdowns. This would reduce reliance on operator skills and decrease workload, enhancing productivity and minimizing production costs.

5.1. State-dependent parameter model for reeling/packing machine

A SIEMENS's AC three-phase servo motor drives the reeling drum (7 kW/2000 rpm) through an analog input signal of 0-10 VDC. The encoder AUTONICS (2048 PPR/5-24 VDC) is installed on the floating drum to monitor its speed from 0 to 1500 rpm, as shown in Figure 9.

Open-loop experiments identified an optimal sampling rate, $\Delta t = 0.5$ sec, balancing accurate response measurement without redundant encoder reads. The experiments yielded an SDP-TF model with a triad $\{1,\ 1,\ 3\}$ as follows in Equation (40),

$$\begin{aligned} y_k &= -a_1(\chi_k)\, y_{k-1} + b_3(\chi_k)\, u_{k-3} \quad \text{(i)} \\ a_1(\chi_k) &= -0.0564\, u_{k-2} + 0.2836 \quad \text{(ii)} \\ b_3(\chi_k) &= -0.0675\, y_{k-1} + 192.0957 \end{aligned} \tag{40}$$

where y_k represents the floating drum's speed (rpm) and u_k is the voltage input to the AC three-phase servo motor of 0 to 10 VDC. The SDPs $a_1(\chi_k)$ and $b_3(\chi_k)$, denoted as $a_{1,k}$ and $b_{3,k}$ respectively, are time-variant and depicted in Figure 10. The model fit of the estimated SDP-TF in Equation (40) to experimental data achieved a satisfactory coefficient of determination, $R_T^2 = 0.95$, as illustrated in Figure 11.

5.2. Controller design and implementation for reeling/packing machine

By merging and rearranging Equation (40), the updated SDP-TF model is expressed as follows in Equation (41).

$$\begin{aligned} y_k = &-\left(0.0675\, u_{k-3} - 0.0564\, u_{k-2} + 0.2836\right) y_{k-1} \\ &+ 192.0957 u_{k-3} \end{aligned} \tag{41}$$

The SDPs may be further refined as Equation (42).

$$\begin{aligned} a_1(\chi_k) &= 0.0675\, u_{k-3} - 0.0564\, u_{k-2} + 0.2836 \\ b_3 &= 192.0957 \end{aligned} \tag{42}$$

The SDP-TF model in Equation (41) may be reformulated using the operator, z^{-1}, as Equation (43).

$$y_k = \frac{b_3\, \text{z}^{-3}}{1 + a_1\left(\chi_{k+1}\right) \text{z}^{-1}}\, u_k \tag{43}$$

Here, the output parameter $a_1\left(\chi_k\right)$, defined in Equation (42), is state-dependent on the lagged input $\chi_k = f\left(u_{k-3},\ u_{k-2}\right)$, while the input parameter b_3, is time-invariant.

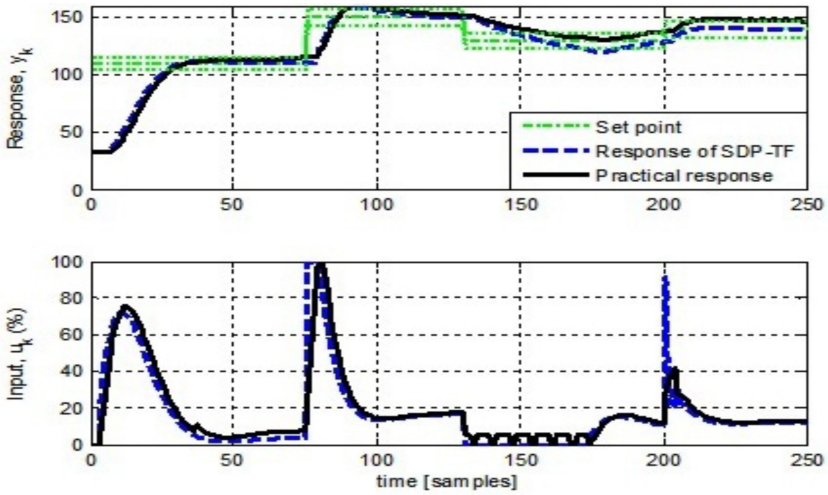


Figure 7. Onsite implementation of the SDP-PID+/LQ control for the bitumen tank, with the command input shown alongside its ±5% tolerance. Abbreviations: LQ, linear quadratic; PID+, proportional integral derivative plus; SDP, state-dependent parameter; TF, transfer function

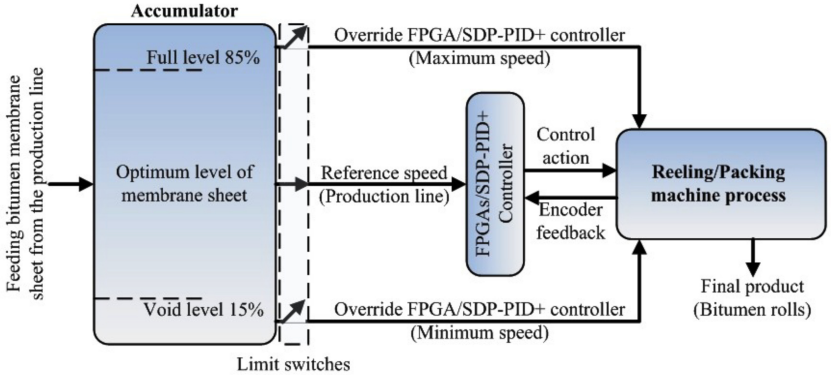


Figure 8. The control process of the reeling/packing machine for Bitumen membrane sheets employs the SDP-PID+ methodology, integrated in FPGAs, at INSUMAT company, Sadat City, Egypt. Abbreviations: FPGA, Field programmable gate array; PID+, Proportional integral derivative plus; SDP, State-dependent parameter.

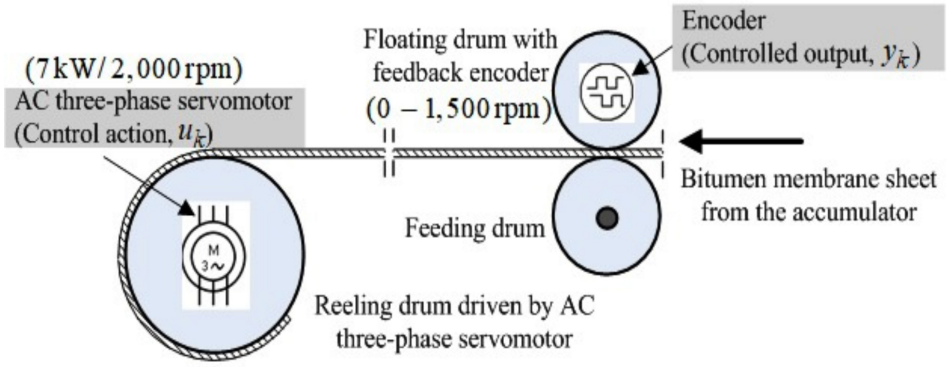


Figure 9. Schematic of the reeling/packing process for bitumen membrane sheets at INSUMAT company, Sadat City, Egypt. Abbreviation: AC, alternating current.

Using the model in Equation (43) and Table 1, the NMSS framework for nonlinear SDP-PID+ control is constructed, similar to the structure in Equation (39). The time-variant transition matrix $\mathbf{F}_k$, time-invariant input vector $\mathbf{g}$, and observation vector $\mathbf{h}$ remain consistent with the state vector $\mathbf{x}_k = \begin{bmatrix} z_k & e_k & \Delta e_k & u_{k-1} & u_{k-2} \end{bmatrix}^T$.

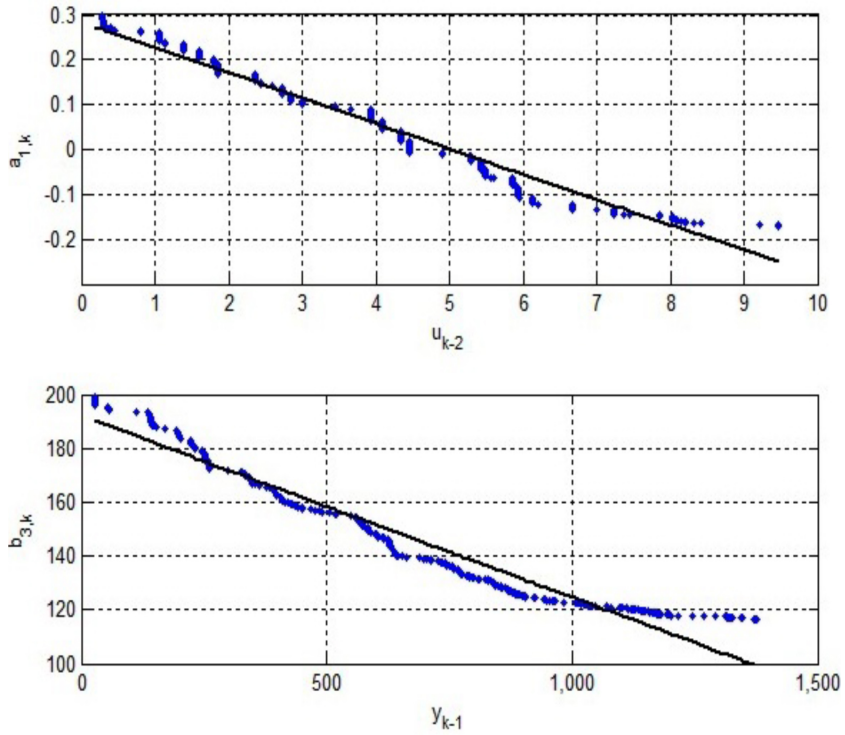


Figure 10. SDPs $a_1\,(u_{k-2})$ and $b_3\,(y_{k-1})$ of the SDP-TF model in Equation (40) versus their state variables. Abbreviations: SDP, State-dependent parameter; TF, transfer function.

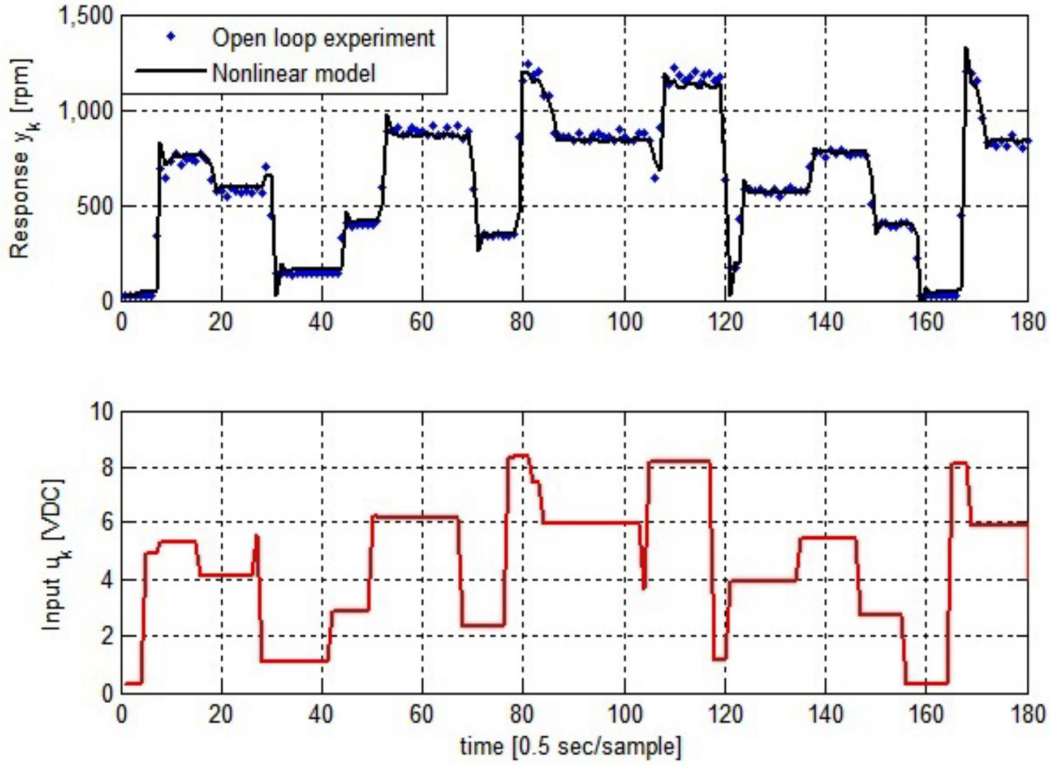


Figure 11. Open-loop experiment for the reeling/packing process with the simulation fit of the SDP-TF model in Equation (40). Abbreviations: SDP, State-dependent parameter; TF, transfer function; VDC, Volts direct current.

The time-invariant $\mathbf{P}$ matrix can be obtained by freezing $\mathbf{F}_k$ at a specific operating point $u_{k-2} = u_{k-3} = 0$. The weights $R = 1$ and $\mathbf{Q} = \text{diag}\ \{1\,1\,1\,1\,1\}$ were selected to obtain the time-invariant $\mathbf{P}$ matrix using algebraic Riccatti equation as defined in Equation (29). The time-variant SDP-PID+ gain vector, $\mathbf{k}_k^+$ is then computed using Equation (30). The control law in Equation (24) is employed to control the drum's reeling/packing machine speed, as shown in Figure 12.

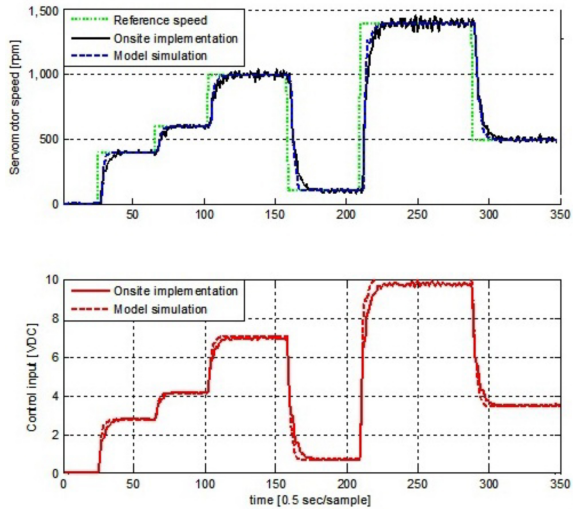


Figure 12. Onsite application of FPGAs/SDP-PID+ control for the industrial reeling/packing machine. Abbreviations: FPGA: Field programmable gate array; PID+: Proportional integral derivative plus; SDP: State-dependent parameter; VDC: Volts direct current.

The onsite implementation demonstrates that the FPGAs/SDP-PID+ control ensures acceptable performance with significant noise suppression and negligible differences between practical and SDP-TF model in Equation (40) responses. No overshoot or severe oscillations were observed, confirming robust control for the reeling/packing process. It is worth noting that the feasibility of FPGA implementation for real-scale industrial systems, including processing power and memory constraints, is detailed in Shaban et al.,[15] where all relevant hardware features are analyzed.

6. Conclusion

This paper presented the expansion and practical implementation of SDP-PID+ control systems across two distinct demonstrators: an industrial bitumen tank system and an industrial reeling/packing machine used in the bitumen membrane sheet production line. This enhancement enables efficient and intuitive control of these systems, which are characterized by discrete-time TFs of any order and sampling time delays.

The selected demonstrators represent the first industrial implementations of the SDP-PID+ control methodology, showcasing its applicability across systems with varying response times, 240 and 0.5 s, respectively, providing a comprehensive evaluation of their performance.

In all cases, the systems were modeled using the quasi-linear SDP model structure, where parameters depend on other system variables. This model structure allowed for designing an SDP-PID+ control law to leverage linear system design strategies such as suboptimal LQ optimization or pole placement. Importantly, the control gains were made state-dependent, enhancing adaptability and performance. Notably, the time-invariant numerator parameter in models in Equations (38) and (43) satisfies the two controllability conditions discussed in Section (3.2).

The proposed control strategy markedly improved temperature regulation for the industrial bitumen tank system, maintaining it consistently within the $\pm 5\%$ permissible range while avoiding overshoot. This enhanced performance minimized the risk of vapor self-ignition inside the tank, ensuring greater operational safety and improved quality of the bitumen mixture.

Finally, implementing the FPGAs/SDP-PID+ control for the industrial reeling/packing machine demonstrated robust closed-loop performance. The system exhibited no overshoot, no severe oscillations, and effective noise reduction, attributed to the advanced real-time processing capabilities of FPGA technology.

The results from these diverse demonstrators confirm the effectiveness of the extended SDP-PID+ control in optimizing design time, enhancing practicality, and improving adaptability and robustness. Its ability to accommodate systems with varying dynamics while ensuring superior performance and operational reliability highlights its potential as a versatile control strategy for industrial applications. Future work may extend this approach to more complex multivariable systems and optimize its implementation for improved computational efficiency.

Acknowledgments

The author gratefully acknowledges the support of the Deanship of Graduate Studies and Scientific Research, Jazan University, Saudi Arabia.

Funding

None.

Conflict of interest

The author has no relevant financial or non-financial interests to disclose.

Author contributions

This is a single-authored article.

Availability of data

Data will be made available upon request to corresponding author.

References

1. Borase RP, Maghade DK, Sondkar SY, Pawar SN. A review of PID control, tuning methods, and applications. *Int J Dyn Control.* 2021;9:818–827. http://dx.doi.org/10.1007/s40435-020-00665-4.
2. Bennett S. Development of the PID controller. *IEEE Control Syst Mag.* 1993;13(6):58–62. https://doi.org/10.1109/37.248006.
3. Liu L, Lv W, Liu J, et al. Performance of active-quenching SPAD array based on the tri-state gates of FPGA and packaged with bare chip stacking. *Sensors*, 2023;23(9):4314. https://doi.org/10.3390/s23094314
4. Vega P, Prada C, Aleixandre V. Self-tuning predictive PID controller. *IEE Proc D: Control Theory Appl.* 1991;138:303–312. http://dx.doi.org/10.1049/ip-d.1991.0041
5. Porter B, Jones AH. Genetic tuning of digital PID controllers. *Electron Lett.* 1992;28(9):843–844. IET Digital Library.
6. Åström KJ, Hägglund T, Hang CC, Ho WK, Automatic tuning and adaptation for PID controllers: a survey. *Control Eng Pract.* 1993;1(4):699–714. http://dx.doi.org/10.1016/0967-0661(93)91394-C.
7. Leva A. PID autotuning algorithm based on relay feedback. *IEEE Proc D Control Theory Appl.* 1993;140:328–338. http://dx.doi.org/10.1049/ip-d.1993.0044.
8. Khodadadi H, Ghadiri H. Self-tuning PID controller design using fuzzy logic for half-car active suspension system. *Int J Dyn Control.* 2018;6(1):224–232. http://dx.doi.org/10.1007/s40435-016-0291-5.
9. Loiseau J-J, Boudana M, Ladaci S. Fractional order PIDμ control design for a Class of cyber-physical systems with fractional order time-delay models. *Int J Cyber Phys Syst.* 2019;1(2):1–18. http://dx.doi.org/10.4018/IJCPS.2019070101.
10. Hamed AR, Shaban EM, Darwish RR, Abdel Ghany AM. Design and implementation of discrete PID control applied to Bitumen tank based on a new approach of pole placement technique. *J of Dyn Control.* 2017;5(3):604–613. https://doi.org/10.1007/s40435-015-0199-
11. Shaban EM, Sayed H, Abdelhamid A. A novel discrete PID+ controller applied to higher-order/time-delayed nonlinear systems with practical implementation. *J Dyn Control.* 2019;7(3):888–900. https://doi.org/10.1007/s40435-018-0472-5
12. Sayed H, Shaban EM, Abdelhamid A. State dependent parameter PID+ control applied to a nonlinear manipulator arm. In: *RAEMP 2019 International Conference on Recent Advances in Engineering Mathematics and Physics*, Dec 24–26. Springer, Cairo, Egypt; 2019. http://dx.doi.org/10.1007/978-3-030-39847-7$_1$
13. Hamed AR, Shaban EM, Abdelhaleem, Abdel Ghany AM. Industrial implementation of state dependent parameter PID+control for nonlinear time-delayed Bitumen tank system. *Iran J Sci Technol - Trans Electr.* 2022;46(11):743–751. https://doi.org/10.1007/s40998-022-00488-3
14. Bashiri AH. Empirical study of robust/developed PID control for nonlinear time-delayed dynamical system in discrete time domain. *Heliyon*, 2024;10(9). http://dx.doi.org/10.1016/j.heliyon.2024.e11935
15. Shaban EM, Hamed AR, Bassiuny AM, Abdelghany AM. On implementation of nonlinear PID+controller embedded on FPGA module for industrial system. *Int J Dyn Contr.* 2023;12(7):2331–2340. https://doi.org/10.1007/s40435-023-01338-8
16. Taylor CJ, Young PC, Chotai A. State-space control system design based on non-minimal state-variable feedback: further generalization and unification results. *Int J Control.* 2000;73:1329–1345. http://dx.doi.org/10.1080/00207170010004698.
17. Shaban EM, Hamed AR, Darwish RR, Abdel Ghany AM. New tuning approach of discrete PI/PID controller applied to Bitumen system based on non-minimal state-space formulation. In: *ICCTA 2015, IEEE 25th International Conference*, Oct 24–26, Alexandria, Egypt. IEEE Xplore Digital Library; 2015:52–57.
18. Shaban EM, Ako S, Taylor CJ, Seward DW. Development of an automated verticality alignment system for a vibro-lance. *Autom Constr.* 2008;17(5):645–655. http://dx.doi.org/10.1016/j.autcon.2007.08.001
19. Taylor CJ, Shaban EM, Stables MA, Ako S. Proportional-integral-plus control applications of state-dependent parameter models. Part I: *J Syst Control Eng.* 2007;221(7):1019–1031. https://doi.org/10.1243/09596518JSCE366
20. Stables MA, James CJ. Non-linear Control of Ventilation Rate using State-dependent Parameter Models. *Biosyst Eng.* 2006;95(1):7–18, ISSN 1537–5110. https://doi.org/10.1016/j.biosystemseng.2006.05.015
21. Taylor CJ, Robertson D. State-dependent control of a hydraulically actuated nuclear decommissioning robot. *Control Eng Pract.*

2013;21(12):1716–1725.
http://dx.doi.org/10.1016/j.conengprac.2013.06.003
22. Deepa SN, Sugumaran G. Design of PID controller for higher-order continuous systems using MPSO-based model formulation technique. *Int J Electr Electron Eng.* 2011;5(4):289–295.
http://dx.doi.org/10.5281/zenodo.1056472
23. Young PC. Stochastic, dynamic modelling and signal processing: Time variable and state dependent parameter estimation. In: Fitzgerald WJ, ed. *Nonlinear and Nonstationary Signal Processing*. Cambridge University Press; 2000.
http://dx.doi.org/10.1016/B978-0-7506-7359-4.50015-9
24. Shaban EM, James CJ, Chotai A. State dependent parameter, proportional-Integral-Plus (SDP-PIP) control of a Nonlinear Robot Digger Arm. In: *UKACC Control 2004, University of Bath*, Bath, UK, ID–059. 2004;
http://dx.doi.org/10.1016/j.ifacol.2005.10.053
25. Dixon R, Taylor CJ, Shaban EM. Comparison of classical and modern control applied to an excavator-arm. International Federation of Automatic Control 16th Triennial World Congress (IFAC-05), Prague, Czech Republic. 2005;38(1):589–594.
http://dx.doi.org/10.3182/20050703-6-CZ-1902.01368
26. Shaban EM, Zied K, Taylor CJ, Seward DW. Nonlinear control system design for construction robots: estimation, partial linearization by feedback and state-dependent-parameter control, 22nd International Symposium on Automation and Robotics in Construction (ISARC-05), Ferrara, Italy; 2005.
https://doi.org/10.22260/ISARC2005/0041.
27. Shaban EM, Nada AA. On linearization of nonlinear dynamic systems described by state-dependent-Parameter (SDP) Discrete-Time Model. In: *5th European Conference on Computational Mechanics (ECCM V)*, Barcelona, Spain. CIMNE - ECCM V Proceedings; 2014: 538–547.
28. Young PC. Recursive Estimation and Time Series Analysis. Springer-Verlag; 1984.
http://dx.doi.org/10.1007/978-3-642-21981-8
29. Young PC. Simplified Refined Instrumental Variable (SRIV) estimation and True Digital Control (TDC): A tutorial introduction. 1st European Control Conference: Grenoble, France.1991;1295–1306.
30. Janot A, Young PC, Gautier M. Identification and control of electro-mechanical systems using state dependent parameter estimation. *Int J Control.* 2017;90(4):643–660.
http://dx.doi.org/10.1080/00207179.2016.1209565
31. Taylor CJ, Pedregal DJ, Young PC, Tych W. Environmental time series analysis and forecasting with the Captain Toolbox. *Environ Model Softw.* 2007;22:797–814.
http://dx.doi.org/10.1016/j.envsoft.2006.06.002
32. Young PC, Taylor CJ, Tych W, Pedregal DJ. The Captain Toolbox. Center for Research on Environmental Systems and Statistics, Lancaster University:UK. 2007.
http://www.es.lancs.ac.uk/cres/captain
33. He J-B, Wang Q-G, Lee T-H. PI/PID controller tuning via LQR approach. *Chem Eng Sci.* 2000;55(13):2429–2439.
http://dx.doi.org/10.1016/S0009-2509(99)00512-6
34. Das S, Pan I, Halder K, Das S, Gupta A. Optimum weight selection-based LQR formulation for the design of fractional-order PID controllers to handle a class of fractional-order systems. In: *International Conference on Computer Communication and Informatics (ICCCI)*, Jan 4, IEEE; 2013: pp. 1–6;
http://dx.doi.org/10.1109/ICCCI.2013.6466137
35. Young PC, Behzadi MA, Wang CL, Chotai A. Direct digital and adaptive control by input-output, state-variable feedback pole assignment. *Int J Control.* 1987;46:1867–1881.
http://dx.doi.org/10.1080/00207178708934274
36. McCabe AP, Young PC, Chotai A, Taylor CJ. Proportional-Integral-Plus (PIP) control of nonlinear systems.*Syst Sci.* 2000;26:25–46.
http://dx.doi.org/10.1002/sys.10004
37. Åström KJ, Wittenmark B. Computer Controlled Systems: Theory and Design. *Prentice-Hall Information and System Sciences Series*. 1984.
38. Shaban EM. Deadbeat response of nonlinear systems described by discrete-time state dependent parameter using exact linearization by local coordinate transformation. *J Am Sci.* 2012;8(10):355–366.
http://dx.doi.org/10.7537/j.issn.1545-1003.2012.10.053
39. Shaban EM, Taylor CJ. Proportional-Integral-Plus control of a class of nonlinear systems using exact and partial linearization by feedback. *ICGST Int J Autom Control Syst Eng.* 2006;6:55–70.
http://dx.doi.org/10.1109/ICCCI.2013.6466137
40. Hamed AR, Darwish RR, Shaban EM, Abdel Ghany AM. Hardware synthesis and dynamic modeling of Bitumen tank. *J Am Sci.* 2014;10(12):183–189.
http://dx.doi.org/10.7537/j.issn.1545-1003.2014.12.021

E. M. Shaban *was born on July 15, 1967, in Cairo, Egypt. He earned his Ph.D. in True Digital Control (TDC) and System Dynamics from Lancaster University, Lancaster, UK, in 2006. Currently, Dr. Shaban is an Associate Professor in the Mechanical Engineering Technology Department at the College of Applied Industrial Technology, Jazan University (KSA), while on leave from the Faculty of Engineering (Mattaria), Helwan University. His research focuses on the control of highly nonlinear systems, with an emphasis on improving controller robustness.*

 https://orcid.org/0000-0002-5678-6183

An International Journal of Optimization and Control: Theories & Applications
(https://accscience.com/journal/ijocta)



This work is licensed under a Creative Commons Attribution 4.0 International License. The authors retain ownership of the copyright for their article, but they allow anyone to download, reuse, reprint, modify, distribute, and/or copy articles in IJOCTA, so long as the original authors and source are credited. To see the complete license contents, please visit http://creativecommons.org/licenses/by/4.0/.

An International Journal of Optimization and Control: Theories & Applications
ISSN: 2146-0957 eISSN: 2146-5703
Vol.15, No.3, pp.535-548 (2025)
https://doi.org/10.36922/IJOCTA025110048

RESEARCH ARTICLE

A numerical method for solving distributed-order multi-term time-fractional telegraph equations involving Caputo and Riesz fractional derivatives

Safar Irandoust Pakchin[1*], Mohammad Hossein Derakhshan[1], and Shahram Rezapour[2,3*]

[1]Department of Applied Mathematics, Faculty of Mathematics, Statistics and Computer Sciences, University of Tabriz, Tabriz, East Azerbaijan, Iran
[2]Department of Mathematics, Faculty of Basic Sciences, Azarbaijan Shahid Madani University, Tabriz, East Azerbaijan, Iran
[3]Department of Medical Research, China Medical University Hospital, China Medical University, Taichung, Taiwan
s.irandoust@tabrizu.ac.ir, m.h.derakhshan.20@gmail.com, sh.rezapour@azaruniv.ac.ir

ARTICLE INFO

Article History:
Received: March 10, 2025
Revised: April 27, 2025
Accepted: April 30, 2025
Published Online: July 23, 2025

Keywords:
Distributed-order
Finite difference method
Fractional derivative
Riesz fractional derivative
Stability analysis
Telegraph equations

Subject Classification:
26A33; 65M06; 65M12; 35R11; 47B06; 65R20

ABSTRACT

This paper introduces a robust distributed-order time-fractional telegraph model, incorporating Caputo time- and Riesz space-fractional derivatives. The spatial Riesz derivative is discretized using an optimized finite difference method. For the distributed-order fractional operator, the midpoint rule was first used to approximate the integral with respect to the order distribution, followed by the application of a finite difference scheme to approximate the Caputo time-fractional derivative. The method's flexibility and high accuracy make it a valuable tool for modeling and simulating these systems, providing insights into the behavior of fractional-order systems with both temporal and spatial fractional effects. Additionally, the proposed approach outperforms existing numerical methods in terms of both precision and computational efficiency, making it highly applicable for real-world problems requiring accurate and efficient solutions. A comprehensive analysis of convergence and stability was conducted to validate the proposed numerical method. To demonstrate its effectiveness, several numerical simulations were performed, revealing the method's exceptional accuracy and computational efficiency. Furthermore, a comparison with existing numerical approaches from the literature is provided, highlighting the proposed method's superior performance in both precision and practical applicability.

CC BY

1. Introduction

Over the past few decades, there has been growing interest among researchers in modeling and analyzing complex physical phenomena using fractional-order operators, particularly in the fields of mathematical sciences and engineering.[1–7] The significant advantage of fractional models, viewed as generalizations of classical integer-order models, lies in their ability to more accurately capture anomalous transport processes, especially those involving memory effects and spatial heterogeneity.[8–15] Many complex physical systems, such as diffusion in multifractal media, cannot be effectively described by single-order differential equations. Therefore, it becomes essential to explore fractional-order and, particularly, distributed-order differential models to account for the inherent complexities of such phenomena. The study of distributed-order time-fractional models began

*Corresponding Author

with Caputo,[16] who investigated their application in describing stress–strain relationships in viscoelastic media. Subsequently, Caputo further expanded on these models to include applications in dielectric relaxation and anomalous diffusion phenomena.[17,18] Building upon this foundation, Chechkin et al.[19] introduced and analyzed distributed-order time-fractional models in greater depth, further highlighting their effectiveness in representing physical systems that exhibit a broad spectrum of dynamical behaviors.

Sokolov et al.[20] studied and introduced distributed-order time-fractional models, also referred to as diffusion-like models, to provide a kinetic interpretation of anomalous diffusion and to describe relaxation phenomena.[21–24] Among these models, the fractional telegraph equation has garnered significant attention due to its versatility in modeling various physical and mathematical phenomena. It has been effectively used in the study of diffusive processes, elastic manifold structures, and wave-like anomalous behaviors. Furthermore, this class of equations has a broad application across different fields, including mathematical sciences, engineering, and physics.[25–27] The classical time-fractional diffusion-wave model of distributed order can be extended to the distributed-order time-fractional telegraph model by simultaneously considering the fractional derivatives of distributed order over the intervals (0,1) and (1,2). This formulation allows for a more comprehensive description of systems that exhibit both diffusive and wave-like characteristics, capturing a wider range of dynamic behaviors observed in complex media.

Obtaining analytical solutions for distributed-order fractional models is often a challenging task due to the complexity of the underlying operators and the nonlocal nature of fractional derivatives. Consequently, numerical methods have become essential tools for solving such models effectively. A wide range of numerical techniques has been developed in the literature, each tailored to specific types of fractional equations and boundary conditions. These include different schemes,[28,29] the fractional-centered difference method,[30] fast second-order implicit difference methods,[31] and Petrov–Galerkin as well as spectral collocation techniques.[32] Other methods, such as direction implicit difference approaches,[33] the operational matrix method,[34] and hybrid function-based techniques[35] have also been explored. Additionally, meshless methods,[36] compact difference schemes,[37] and finite difference-spectral methods[38] offer alternative strategies. More advanced frameworks, such as the alternating direction implicit-Galerkin finite element method,[39] finite element approximations,[40] and the shifted fractional Jacobi spectral algorithm[41] have further expanded the toolbox for solving these models. Some studies have combined the finite difference method with the matrix transfer technique to handle the space-fractional derivative in distributed-order models,[42] while others have employed the shifted Legendre method[43] or introduced novel matrix representations of fractional models.[44] Collectively, these methods reflect the rich and diverse landscape of numerical strategies developed to tackle the inherent difficulties in distributed-order fractional differential equations.

In this work, we propose an efficient and high-performance numerical method for solving the distributed-order time-fractional telegraph model, formulated as follows in Equation (1):

$$\int_0^1 b_1(\mu)\,{}^C D_t^{\mu} u d\mu + \int_1^2 b_2(\nu)\,{}^C D_t^{\nu} u d\nu = \mathbb{H}(x,t,u) \tag{1}$$

in which $\mathbb{H}(x,t,u) = -\kappa(-\Delta)^{\frac{\alpha}{2}}u + f(x,t,u)$, subject to the initial and boundary conditions in Equation (2):

$$\begin{aligned} &u(x,0) = \psi(x),\ 0 \le x \le L, \\ &u(0,t) = \varphi_0(t),\ u(L,t) = \varphi_L(t)\ 0 < t \le T \end{aligned} \tag{2}$$

Here, $\mu \in (0,1]$, $\nu \in (1,2]$, and ${}^C D_t^{\mu}$, ${}^C D_t^{\nu}$ are defined as in Equation (3):

$$\begin{aligned} &{}^C D_t^{\beta} u(x,t) = (\Gamma(n-\beta))^{-1} \\ &\times \int_0^t u^{(n)}(x,\tau)\frac{1}{(t-\tau)^{\beta-n+1}}d\tau, \\ &n-1 < \beta \le n,\ n \in \mathbb{N} \end{aligned} \tag{3}$$

Here, $-(-\Delta)^{\frac{\alpha}{2}}u$ denotes the Riesz fractional operator in Equation (4)

$$-(-\Delta)^{\frac{\alpha}{2}}u = C_\alpha({}_x D_+^{\alpha}u + {}_x D_-^{\alpha}u) \tag{4}$$

in which $c_\alpha = -\frac{1}{2\cos(\frac{\pi\alpha}{2})}$, and ${}_x D_+^{\alpha}$, ${}_x D_-^{\alpha}$ are displayed by Equation (5)[34]:

$$\begin{aligned} &{}_x D_+^{\alpha} u(x,t) = \frac{d^2}{dx^2}({}_x \mathbb{I}_+^{2-\alpha} u(x,t)) \\ &= \frac{u(a,t)}{\Gamma(1-\alpha)(x-a)^{\alpha}} + \frac{u'(a,t)}{\Gamma(2-\alpha)(x-a)^{\alpha-1}} \\ &+ \frac{1}{\Gamma(2-\alpha)}\int_a^x u^{(2)}\frac{1}{(\xi,t)(x-\xi)^{\alpha-1}}d\xi \end{aligned} \tag{5}$$

and Equation (6):

$$
\begin{aligned}
&{}_xD_-^{\alpha}u(x,t) = \frac{d^2}{dx^2}({}_x\mathbb{I}_-^{2-\alpha}u(x,t)) \\
&= \frac{u(b,t)}{\Gamma(1-\alpha)(b-x)^{\alpha}} - \frac{u'(b,t)}{\Gamma(2-\alpha)(b-x)^{\alpha-1}} \\
&+ \frac{1}{\Gamma(2-\alpha)}\int_x^b u^{(2)}(\xi,t)\frac{1}{(\xi-x)^{\alpha-1}}d\xi
\end{aligned} \tag{6}
$$

where ${}_x\mathbb{I}_+$ and ${}_x\mathbb{I}_-$ are as defined by Ahmed and Hashem.[44] This class of fractional differential equations is characterized by the incorporation of distributed-order derivatives, which allow for a more nuanced modeling of memory and hereditary properties inherent in complex physical and engineering systems. Specifically, the model under investigation incorporates time-fractional derivatives of distributed order in the Caputo sense, which are particularly advantageous for initial value problems due to their physically interpretable initial conditions.

To numerically solve the equation introduced above, the combined approach of the midpoint method and finite differences was used. To estimate the integral term, we applied the midpoint method and then used the finite differences method to approximate the Caputo fractional operator in the time direction. For the Riesz space-fractional derivative with respect to the space variable, we used the finite difference approach.[45] The implications of the proposed method are significant in solving complex distributed-order multi-term time-fractional telegraph equations, which are commonly encountered in various scientific and engineering fields. These equations arise in phenomena such as anomalous diffusion, wave propagation in heterogeneous media, and modeling complex materials with memory effects. In this paper, we introduced a novel numerical method for solving the distributed-order time-fractional telegraph model, which incorporates Caputo time derivatives and Riesz space-fractional derivatives. The primary contribution of this work lies in the development of a robust and efficient numerical scheme that combines an optimized finite difference method for the spatial Riesz derivative and a midpoint rule for discretizing the integral in the distributed-order fractional operator. This approach is followed by a finite difference scheme to approximate the Caputo time-fractional derivative. The novelty of the proposed method lies in its ability to accurately handle the complexity of the distributed-order and multi-term fractional operators simultaneously, ensuring both high accuracy and computational efficiency. To the best of our knowledge, this is one of the first approaches that directly addresses the challenges of solving such equations with both spatial and temporal fractional derivatives in a unified framework. We also provide a comprehensive analysis of the method's convergence and stability, establishing its robustness for practical applications. Several numerical experiments are conducted to demonstrate the effectiveness of the method in solving real-world problems. The proposed approach is then benchmarked against existing numerical methods in the literature, highlighting its superior performance in terms of both precision and computational efficiency. This method has broad implications for applications in fields such as anomalous diffusion, wave propagation in heterogeneous media, and modeling of complex materials with memory effects, where distributed-order time-fractional equations play a key role in accurately describing underlying physical processes.

In Section 2, we present a numerical approach based on finite differences for approximating the Caputo fractional operator. In Section 3, we introduce an implicit numerical method for approximating the solution to Equation (1). Section 4 provides the convergence and stability analyses of the proposed numerical method, ensuring its reliability. In Section 5, we present several numerical examples to validate the efficiency and effectiveness of the proposed method. Finally, Section 6 offers the concluding remarks, summarizing the key findings and potential future directions.

2. A description of the numerical approach for the fractional operator

Suppose that $\Delta t = \frac{b-a}{N}$, $t = t_k = a + k\Delta t$, $u^0 = u(x,a) = u(x,t-k\Delta t), u^1 = u(x,a+\Delta t) = u\left(x,t-(k-1)\Delta t\right),\ldots,u^{k-j} = u(x,t-j\Delta t),\ldots,$ *and* $u^k = u(x,t) = u(x,a+k\Delta t)$, then it can be presented as in Equation (7):

$$
\begin{aligned}
D_t^{\nu}u(x,t_k) &= \frac{1}{\Gamma(2-\nu)}\int_a^t u^{(2)}(x,\tau)(t-\tau)^{1-\nu}d\tau \\
&= \frac{1}{\Gamma(2-\nu)}\int_0^{t-a} u^{(2)}(x,t-\tau)\tau^{1-\nu}d\tau \\
&= \frac{1}{\Gamma(2-\nu)}\sum_{j=0}^{k-1}\int_{j\Delta t}^{(j+1)\Delta t} u^{(2)}(x,t-\tau)\tau^{1-\nu}d\tau \\
&= \frac{(\Delta t)^{-2}}{\Gamma(2-\nu)}\sum_{j=0}^{k-1}(u(x,t+k_1)-2u(x,t+k_2) \\
&\quad + u(x,t+k_3)\int_{j\Delta t}^{(j+1)\Delta t}\frac{1}{\tau^{\nu-1}}d\tau
\end{aligned}
$$

$$= \frac{(\Delta t)^{-\nu}}{\Gamma(3-\nu)} \sum_{j=0}^{k-1} b_j^{\nu} (u(x, t_{k-j+1}) - 2u(x, t_{k-j}) + u(x, t_{k-j-1})) \tag{7}$$

in which $k_1 = (1-j)\Delta t$, $k_2 = -j\Delta t$, $k_3 = (-j-1)\Delta t$ and $b_j^{\nu} = ((j+1)^{2-\nu} - j^{2-\nu})$.

Also, by applying a similar technique, we get Equation (8):

$$\begin{aligned} D_t^{\mu} u(x,t) &= \frac{1}{\Gamma(1-\mu)} \int_a^t u^{'}(x,\tau)(t-\tau)^{-\mu} d\tau \\ &= \frac{1}{\Gamma(1-\mu)} \int_0^{t-a} u^{'}(x, t-\tau)\tau^{-\mu} d\tau \\ &= \frac{1}{\Gamma(1-\mu)} \sum_{j=0}^{k-1} \int_{j\Delta t}^{(j+1)\Delta t} u^{'}(x, t-\tau)\tau^{-\mu} d\tau \\ &= \frac{1}{\Gamma(1-\mu)} \sum_{j=0}^{k-1} \frac{u(x, t+k_1) - u(x, t+k_2)}{\Delta t} \\ &\quad \times \int_{j\Delta t}^{(j+1)\Delta t} \frac{1}{\tau^{\mu}} d\tau \\ &= \frac{(\Delta t)^{-\mu}}{\Gamma(2-\mu)} \sum_{j=0}^{k-1} b_j^{\mu} (u(x, t_{k-j+1}) - u(x, t_{k-j})) \end{aligned} \tag{8}$$

in which $b_j^{\mu} = ((j+1)^{2-\mu} - j^{2-\mu})$. For $1 < \alpha < 2$, the Riesz fractional operator can be estimated as in Equation (9)[45]:

$$\begin{aligned} &-(-\Delta)^{\alpha/2} u(x,t) = -\frac{(\Delta x)^{-\alpha}}{2\Gamma(\alpha)\Gamma(3-\alpha)\cos\left(\frac{\pi\alpha}{2}\right)} \\ &\times \left\{ \frac{(1-\alpha)(2-\alpha)u_0}{q^{\alpha}} + \frac{(2-\alpha)}{q^{\alpha-1}}(u_1 - u_0) \right. \\ &+ \sum_{i=0}^{q-1} (u_{q-i+1} - 2u_{q-i} + u_{q-i-1}) \left[(i+1)^{2-\alpha} - i^{2-\alpha}\right] \\ &+ \frac{(1-\alpha)(2-\alpha)u_M}{(M-q)^{\alpha}} - \frac{(2-\alpha)}{(M-q)^{\alpha-1}}(u_M - u_{M-1}) \\ &\left. + \sum_{i=0}^{M-q-1} (u_{q+i-1} - 2u_{q+i} + u_{q+i+1}) \left[(i+1)^{2-\alpha} - i^{2-\alpha}\right] \right\} \end{aligned} \tag{9}$$

in which $\Delta x = \frac{b-a}{M}$, $x = x_q = a + q\Delta x$, $u_0 = u(a,t) = u(x - q\Delta x, t), u_1 = u(a + \Delta x, t) = u(x - (q-1)\Delta x, t), \ldots, u_{q-i} = u(x - i\Delta x, t), \ldots, u_q = u(x,t) = u(a + q\Delta x, t)$

3. Description of the numerical method

In this section, we present the discretization method used for approximating the integral terms in the distributed-order fractional operator. The proposed method utilized a quadrature rule to evaluate these integrals. This choice was motivated by the fact that quadrature methods provide a flexible and accurate approach to numerical integration, especially when dealing with functions that are difficult to handle analytically. Furthermore, quadrature methods are widely used for handling fractional integrals due to their ability to approximate the integrals over complex domains with high precision. Therefore, we have Equation (10):

$$\int_a^b b(\gamma)\, {}^{C}D_t^{\gamma} u(x,t) d\gamma = h \sum_{p=0}^{L} b(\gamma_p)\, {}^{C}D_t^{\gamma_p} u(x,t) - \frac{h^2}{24} F''(\gamma),\ \gamma \in (a,b) \tag{10}$$

where $\gamma_p = \frac{\eta_{p-1} + \eta_p}{2}$, $p = 1, \ldots, L$, $\gamma_p \in [\eta_{p-1}, \eta_p]$, and the interval $[\eta_{p-1}, \eta_p]$ is a partition of the L subintervals of $[a,b]$ with equal amplitude $h = \frac{b-a}{L}$. Here F is $F = b(\gamma)\, {}^{C}D_t^{\gamma} u(x,t)$.

Then, using Equation (10), we have Equation (11):

$$\int_0^1 b_1(\mu)\, {}^{C}D_t^{\mu} u(x,t) d\mu = \frac{1}{L} \sum_{p=0}^{L} b_1(\mu_p)\, {}^{C}D_t^{\mu_p} u(x,t) - \frac{h^2}{24} F''_1(\mu),\ \mu \in (0,1) \tag{11}$$

where $\mu_p = \frac{\eta_{p-1} + \eta_p}{2}$ for $p = 1, \ldots, L$. We consider the interval $[\eta_{p-1}, \eta_p]$ with equal amplitude $h = \frac{b-a}{L}$ such that $[\eta_{p-1}, \eta_p] \subseteq [0,1]$, $F_1 = b_1(\mu)\, {}^{C}D_t^{\mu} u(x,t)$. Similar to the procedures in Equation (11), we have Equation (12):

$$\int_1^2 b_2(\nu)\, {}^{C}D_t^{\nu} u(x,t) d\nu = \frac{1}{L} \sum_{p=0}^{L} b_2(\nu_p)\, {}^{C}D_t^{\nu_p} u(x,t) - \frac{h^2}{24} F''_2(\nu),\ \nu \in (1,2) \tag{12}$$

where $\nu_p = \frac{\eta'_{p-1} + \eta'_p}{2}$ for $p = 1, \ldots, L$ and considering the interval $[\eta'_{p-1}, \eta'_p]$ with equal amplitude $h = \frac{b-a}{L}$ such that $[\eta'_{p-1}, \eta'_p] \subseteq [1,2]$ and $F_2 = b_2(\nu)\, {}^{C}D_t^{\nu} u(x,t)$

Neglecting $\circ(h^2)$ in Equations (11) and (12), Equation (1) can be approximated as Equation (13):

$$\frac{1}{L} \sum_{p=0}^{L} b_1(\mu_p)\, {}^{C}D_t^{\mu_p} u(x,t) + \frac{1}{L} \sum_{p=0}^{L} b_2(\nu_p)\, {}^{C}D_t^{\nu_p} u(x,t) = -\kappa(-\Delta)^{\frac{\alpha}{2}} u(x,t) + f(x,t,u(x,t)) \tag{13}$$

By putting ${}^{C}D_t^{\mu_p}u(x,t)$, ${}^{C}D_t^{\nu_p}u(x,t)$, and $-(-\Delta)^{\frac{\alpha}{2}}u(x,t)$ into Equation (1), and showing by $U_q^k \approx u(x_q,t_k)$, we acquire Equation (14):

$$\begin{aligned}
&\frac{1}{L}\sum_{p=0}^{L} b_1(\mu_p)\left(\frac{(\Delta t)^{-\mu_p}}{\Gamma(2-\mu_p)}\sum_{j=0}^{k-1}(U_q^{k-j+1}-U_q^{k-j})\right)\\
&\times((j+1)^{1-\mu_p}-j^{1-\mu_p}))+\frac{1}{L}\sum_{p=0}^{L} b_2(\nu_p)\left(\frac{(\Delta t)^{-\nu_p}}{\Gamma(3-\nu_p)}\right.\\
&\times\sum_{j=0}^{k-1}(U_q^{k-j+1}-2U_q^{k-j}+U_q^{k-j-1})((j+1)^{2-\nu_p}-j^{2-\nu_p}))\\
&=-\frac{\kappa(\Delta x)^{-\alpha}}{2\Gamma(\alpha)\Gamma(3-\alpha)\cos(\frac{\pi\alpha}{2})}\left\{\frac{(1-\alpha)(2-\alpha)U_0^k}{q^\alpha}\right.\\
&+\frac{(2-\alpha)}{q^{\alpha-1}}(U_1^k-U_0^k)+\sum_{i=0}^{q-1}(U_{q-i+1}^k-2U_{q-i}^k\\
&+U_{q-i-1}^k)[(i+1)^{2-\alpha}-i^{2-\alpha}]+\frac{(1-\alpha)(2-\alpha)U_M^k}{(M-q)^\alpha}\\
&-\frac{(2-\alpha)}{(M-q)^{\alpha-1}}(U_M^k-U_{M-1}^k)+\sum_{i=0}^{M-q-1}(U_{q+i-1}^k-2U_{q+i}^k\\
&\left.+U_{q+i+1}^k)[(i+1)^{2-\alpha}-i^{2-\alpha}]\right\}+f(x_q,t_k,U_q^k)
\end{aligned}\tag{14}$$

under the conditions as in Equation (15):

$$\begin{aligned}
&U_q^0=\psi(q\Delta x),\ q=0,1,\ldots,M,\\
&U_0^k=\varphi_0(k\Delta t),\ U_M^k=\varphi_L(k\Delta t)\ k=0,1,\ldots,N
\end{aligned}\tag{15}$$

4. Convergence and stability

The stability analysis, along with convergence, is obtained by the proposed numerical method, which is presented in **Section 3**. For simplicity, we can rewrite Equation (14) as follows in Equation (16):

$$T_1(U_q^{k+1})=T_2(U_q^k)+f(x_q,t_k,U_q^k)\tag{16}$$

where it can be expanded as in Equation (17):

$$\begin{aligned}
&T_1\left(U_q^{(k+1)}\right)=\frac{1}{L}\sum_{p=0}^{L}\left[\frac{b_1(\mu_p)(\Delta t)^{-\mu_p}}{\Gamma(2-\mu_p)}\right.\\
&+\frac{b_2(\nu_p)(\Delta t)^{-\nu_p}}{\Gamma(3-\nu_p)}U_q^{(k+1)}+\frac{\kappa(\Delta x)^{-\alpha}}{2\Gamma(\alpha)\Gamma(3-\alpha)\cos\left(\frac{\pi\alpha}{2}\right)}\\
&\times\left\{\sum_{i=0}^{q-1}\left(U_{q-i+1}^{(k)}-2U_{q-i}^{(k)}+U_{q-i-1}^{(k)}\right)\left[(i+1)^{2-\alpha}-i^{2-\alpha}\right]\right.\\
&\left.\left.+\sum_{i=0}^{M-q-1}\left(U_{q+i-1}^{(k)}-2U_{q+i}^{(k)}+U_{q+i+1}^{(k)}\right)\left[(i+1)^{2-\alpha}-i^{2-\alpha}\right]\right\}\right.
\end{aligned}\tag{17}$$

and Equation (18):

$$\begin{aligned}
&T_2(U_q^k)=\frac{1}{L}\sum_{p=0}^{L}\left[b_1(\mu_p)\frac{(\Delta t)^{-\mu_p}}{\Gamma(2-\mu_p)}+b_2(\nu_p)\frac{(\Delta t)^{-\nu_p}}{\Gamma(3-\nu_p)}\right]U_q^k\\
&+\frac{1}{L}\sum_{p=0}^{L}b_2(\nu_p)(\frac{(\Delta t)^{-\nu_p}}{\Gamma(3-\nu_p)}(U_q^k-U_q^{k-1})\\
&-\frac{1}{L}\sum_{p=0}^{L}b_1(\mu_p)(\frac{(\Delta t)^{-\mu_p}}{\Gamma(2-\mu_p)}\sum_{j=1}^{k-1}(U_q^{k-j+1}-U_q^{k-j}))((j+1)^{1-\mu_p}\\
&-j^{1-\mu_p}))-\frac{1}{L}\sum_{p=0}^{L}b_2(\nu_p)(\frac{(\Delta t)^{-\nu_p}}{\Gamma(3-\nu_p)}\sum_{j=1}^{k-1}(U_q^{k-j+1}-2U_q^{k-j}\\
&+U_q^{k-j-1})((j+1)^{2-\nu_p}-j^{2-\nu_p}))-\frac{\kappa(\Delta x)^{-\alpha}}{2\Gamma(\alpha)\Gamma(3-\alpha)cos(\frac{\pi\alpha}{2})}\\
&\times\left\{\frac{(1-\alpha)(2-\alpha)U_0^k}{q^\alpha}+\frac{(2-\alpha)}{q^{\alpha-1}}(U_1^k-U_0^k)\right.\\
&\left.+\frac{(1-\alpha)(2-\alpha)U_M^k}{(M-q)^\alpha}-\frac{(2-\alpha)}{(M-q)^{\alpha-1}}(U_M^k-U_{M-1}^k)\right\}
\end{aligned}\tag{18}$$

Suppose the initial data has an error e_q^0 as in Equation (19)

$$\widetilde{\psi}_q^0=\psi(x_q)+e_q^0,\ q=1,\ldots,M\tag{19}$$

Let U_q^k and $\widetilde{U}_q^k$ are the solutions of Equations (14) and (15). Therefore, it can be depicted as in Equation (20)

$$T_1(e_q^{k+1})=T_2(e_q^k)+f(x_q,t_k,U_q^k)-f(x_q,t_k,\widetilde{U}_q^k)\tag{20}$$

in which $e_q^k=U_q^k-\widetilde{U}_q^k$. Also, let $E^k=[e_1^k,e_2^{k+1},\ldots,e_M^k]$, $k=0,1,2,\ldots,N$ and $\|E^k\|_\infty=\max_{1\le m\le M}|e_m^k|$. In proving the main theorems of this manuscript, we consider the following symbols in Equation (21):

$$\begin{aligned}
&\xi_1(L,\Delta t)=\frac{1}{L}\sum_{p=0}^{L}\frac{b_1(\mu_p)}{\Gamma(2-\mu_p)}(\Delta t)^{-\mu_p},\\
&\xi_2(L,\Delta t)=\frac{1}{L}\sum_{p=0}^{L}b_1(\mu_p)\frac{b_2(\nu_p)}{\Gamma(3-\nu_p)}(\Delta t)^{-\nu_p}
\end{aligned}\tag{21}$$

4.1. Theorem

Let $f(x,t,u)$ be a Lipschitz map. Then, the numerical method given by Equation (14) with initial boundary conditions Equation (15) is unconditionally stable, that is

$$\|E^n\|_\infty\le\varrho\,\|E^0\|_\infty,\ n=0,1,\ldots,N\tag{22}$$

where $\varrho>0$ and independent of the step sizes.

According to the conditions Equation (15), the inequality Equation (22) is satisfied for $n=0$. Suppose Equation (22) satisfies $n=1,\ldots,k$, assuming that $z\in\{1,2,\ldots,M\}$ such that $|e_z^{k+1}|=$

$\max_{0\le m\le M}|e_m^{k+1}| = \| E_z^{k+1} \|_\infty$, then, we have Equation (23):

$$
\begin{aligned}
&(\xi_1(L,\Delta t)+\xi_2(L,\Delta t)) \parallel E^{k+1} \parallel_\infty \\
&= (\xi_1(L,\Delta t)+\xi_2(L,\Delta t))|e_z^{k+1}| + \frac{\kappa(\Delta x)^{-\alpha}}{2\Gamma(\alpha)\Gamma(3-\alpha)cos(\frac{\pi\alpha}{2})} \\
&\times \left\{ \sum_{i=0}^{q-1} (2|e_{z-i}^k| - 2|e_{z-i}^k|)[(i+1)^{2-\alpha} - i^{2-\alpha}] \right. \\
&+ \left. \sum_{i=0}^{M-q-1} (2|e_{z+i}^k| - 2|e_{z+i}^k|)[(i+1)^{2-\alpha} - i^{2-\alpha}] \right\} \\
&\le (\xi_1(L,\Delta t)+\xi_2(L,\Delta t))|e_z^{k+1}| + \frac{\kappa(\Delta x)^{-\alpha}}{2\Gamma(\alpha)\Gamma(3-\alpha)cos(\frac{\pi\alpha}{2})} \\
&\times \{ \sum_{i=0}^{q-1} (2|e_{z-i}^k| - |e_{z-i-1}^k - |e_{z-i+1}^k|[(i+1)^{2-\alpha} - i^{2-\alpha}]) \\
&+ \sum_{i=0}^{M-q-1} (2|e_{z+i}^k| - |e_{z+i-1}^k| - |e_{z+i+1}^k|) \times [(i+1)^{2-\alpha} - i^{2-\alpha}] \} \\
&\le |(\xi_1(L,\Delta t)+\xi_2(L,\Delta t))|e_z^{k+1}| - \frac{\kappa(\Delta x)^{-\alpha}}{2\Gamma(\alpha)\Gamma(3-\alpha)cos(\frac{\pi\alpha}{2})} \\
&\times \{ \sum_{i=0}^{q-1} (|e_{z-i+1}^k| - 2|e_{z-i}^k| + |e_{z-i-1}^k|)[(i+1)^{2-\alpha} - i^{2-\alpha}] \\
&+ \sum_{i=0}^{M-q-1} (|e_{z+i+1}^k| - 2|e_{z+i}^k| + |e_{z+i-1}^k|)[(i+1)^{2-\alpha} - i^{2-\alpha}] \}| \\
&\le |(\xi_1(L,\Delta t)+\xi_2(L,\Delta t))|e_z^{k+1}| + \frac{\kappa(\Delta x)^{-\alpha}}{2\Gamma(\alpha)\Gamma(3-\alpha)cos(\frac{\pi\alpha}{2})} \\
&\times \left| \left\{ \sum_{i=0}^{q-1} (|e_{z-i+1}^k| - 2|e_{z-i}^k| + |e_{z-i-1}^k|) \times [(i+1)^{2-\alpha} - i^{2-\alpha}] \right. \right. \\
&+ \left. \left. \sum_{i=0}^{M-q-1} (|e_{z+i+1}^k| - 2|e_{z+i}^k| + |e_{z+i-1}^k|) \times [(i+1)^{2-\alpha} - i^{2-\alpha}] \right\} \right| \\
&= |T_1(e_z^{k+1})| = |T_2(e_z^k) + f(x_z,t_k,U_z^k) - f(x_z,t_k,\widetilde{U}_z^k)| \\
&\le |T_2(e_z^k)| + |f(x_z,t_k,U_z^k) - f(x_z,t_k,\widetilde{U}_z^k)|
\end{aligned}
\tag{23}
$$

Then, we have Equation (24)

$$
(\xi_1(L,\Delta t)+\xi_2(L,\Delta t)) \parallel E^{k+1} \parallel_\infty \le |T_2(e_z^k)| + L_f|U_z^k - \widetilde{U}_z^k)| \tag{24}
$$

where $L_f \in (0,1)$. Substituting Equation (18) into Equation (24) yields Equation (25)

$$
\begin{aligned}
&(\xi_1(L,\Delta t)+\xi_2(L,\Delta t)) \parallel E^{k+1} \parallel_\infty \le \sum_{j=1}^{k-1} a \parallel E^{k-j+1} \parallel_\infty \\
&+ b \parallel E^{k-j} \parallel_\infty + c \parallel E^{k-j-1} \parallel_\infty
\end{aligned}
\tag{25}
$$

where for $j=1$, we have Equation (26):

$$
\begin{aligned}
&a = (\xi_1 k^{1-\mu_p} + \xi_2 k^{2-\nu_p} + \xi_1 + 2\xi_2 + W(M,\alpha,z)), \\
&W(M,\alpha,z) = \left| \frac{\kappa(\Delta x)^{-\alpha}}{2\Gamma(\alpha)\Gamma(3-\alpha)cos(\frac{\pi\alpha}{2})} \right| \\
&\left\{ \frac{(1-\alpha)(2-\alpha)}{q^\alpha} + \frac{2(2-\alpha)}{q^{\alpha-1}} + \frac{(1-\alpha)(2-\alpha)}{(M-q)^\alpha} \right. \\
&\left. - \frac{2(2-\alpha)}{(M-q)^{\alpha-1}}, b = (\xi_1 k^{1-\mu_p} + 2\xi_2 k^{2-\nu_p} + \xi_2 + L_f), \right. \\
&c = \xi_2 k^{2-\nu_p}
\end{aligned}
\tag{26}
$$

and for $j = 2,\dots,k-1$, we have Equation (27):

$$
\begin{aligned}
a &= \xi_1 k^{1-\mu_p} + \xi_2 k^{2-\nu_p}, \\
b &= \xi_1 k^{1-\mu_p} + 2\xi_2 k^{2-\nu_p}, \\
c &= \xi_2 k^{2-\nu_p}
\end{aligned}
\tag{27}
$$

Equation (25) can also be rewritten as follows Equation (28)

$$
\begin{aligned}
&\parallel E^{k+1} \parallel_\infty \le \frac{1}{\xi_1(L,\Delta t)+\xi_2(L,\Delta t)} \sum_{j=1}^{k-1} a \parallel E^{k-j+1} \parallel_\infty \\
&+ b \parallel E^{k-j} \parallel_\infty + c \parallel E^{k-j-1} \parallel_\infty \\
&\le \frac{1}{\xi_1(L,\Delta t)+\xi_2(L,\Delta t)} (ak\delta_1 + bk\delta_2 + ck\delta_3) \parallel E^0 \parallel_\infty
\end{aligned}
\tag{28}
$$

From Equation (28), we get Equation (29):

$$
\parallel E^{k+1} \parallel_\infty \le \varrho \parallel E^0 \parallel_\infty \tag{29}
$$

where $\varrho = \max\{\frac{1}{\xi_1(L,\Delta t)+\xi_2(L,\Delta t)}(ak\delta_1 + bk\delta_2 + ck\delta_3)\}$. Thus, for each arbitrary initial rounding error E^0, there exists $\varrho > 0$, independent of L, Δt, and Δx, such that in Equation (30):

$$
\parallel E^n \parallel_\infty \le \varrho \parallel E^0 \parallel_\infty \tag{30}
$$

Therefore, our numerical method is unconditionally stable.

Suppose that the exact and approximate solutions of Equation (1) are U_q^k and $\widetilde{U}_q^k$, respectively. Then, we consider the error function at $(x_q,t_k$ by the following formula in Equation (31):

$$
e_q^k = U_q^k - \widetilde{U}_q^k,\ k = 1,\dots,N,\ q = 1,\dots,M \tag{31}
$$

in which $e^k = [e_1^k, e_2^k, \dots, e_M^k]$. Due to Equations (2) and (15), we have $e^0 = [0,0,\dots,0]$. Then, from Equation (14), we have Equation (32):

$$\frac{1}{L}\sum_{p=0}^{L} b_1(\mu_p)(\frac{(\Delta t)^{-\mu_p}}{\Gamma(2-\mu_p)}\sum_{j=0}^{k-1}(U_q^{k-j+1}-U_q^{k-j}))$$
$$\times((j+1)^{1-\mu_p}-j^{1-\mu_p})+b_1^{\mu_p}(\Delta t)^{2-\mu_p}\frac{\partial^2 U(x_q,\eta_k)}{\partial t^2})$$
$$-\frac{h^2}{24}F''_1(\mu)+\frac{1}{L}\sum_{p=0}^{L} b_2(\nu_p)(\frac{(\Delta t)^{-\nu_p}}{\Gamma(3-\nu_p)}\sum_{j=0}^{k-1}(U_q^{k-j+1}$$
$$-2U_q^{k-j}+U_q^{k-j-1})((j+1)^{2-\nu_p}-j^{2-\nu_p})$$
$$+b_2^{\nu_p}\frac{(\Delta t)^{4-\nu_p}}{24}\frac{\partial^4 U(x_q,\eta'_k)}{\partial t^4})-\frac{h^2}{24}F''_2(\nu))$$
$$=-\frac{\kappa(\Delta x)^{-\alpha}}{2\Gamma(\alpha)\Gamma(3-\alpha)cos(\frac{\pi\alpha}{2})}\{\frac{(1-\alpha)(2-\alpha)U_0^k}{q^\alpha}$$
$$+\frac{(2-\alpha)}{q^{\alpha-1}}(U_1^k-U_0^k)+\sum_{i=0}^{q-1}(U_{q-i+1}^k-2U_{q-i}^k$$
$$+U_{q-i-1}^k)[(i+1)^{2-\alpha}-i^{2-\alpha}]+\frac{(1-\alpha)(2-\alpha)U_M^k}{(M-q)^\alpha}$$
$$-\frac{(2-\alpha)}{(M-q)^{\alpha-1}}(U_M^k-U_{M-1}^k)+\sum_{i=0}^{M-q-1}(U_{q+i-1}^k$$
$$-2U_{q+i}^k+U_{q+i+1}^k)[(i+1)^{2-\alpha}-i^{2-\alpha}]\}$$
$$+b^\alpha\frac{(\Delta t)^{4-\alpha}}{24}\frac{\partial^4 U}{\partial x^4}(\theta_q,\eta_k)$$
$$+f(x_q,t_k,U_q^k)+\Delta t[\frac{\partial f}{\partial t}(x_q,\zeta_{k+1},U(x_q,\zeta_{k+1}))$$
$$+\frac{\partial f}{\partial U}(x_q,\zeta_{k+1},U(x_q,\zeta_{k+1}))\frac{\partial U}{\partial t}(x_q,\zeta_{k+1})] \tag{32}$$

in which $\eta_k \in (0,t_k)$, $\eta'_k \in (0,t_k)$, $\theta_q \in (x_{q-1},x_q)$ and $\zeta_k \in (t_k,t_{k+1})$. We can rewrite Equation (14) as follows in Equation (33):

$$\frac{1}{L}\sum_{p=0}^{L} b_1(\mu_p)(\frac{(\Delta t)^{-\mu_p}}{\Gamma(2-\mu_p)}\sum_{j=0}^{k-1}(U_q^{k-j+1}-U_q^{k-j}))$$
$$\times((j+1)^{1-\mu_p}-j^{1-\mu_p})+\frac{1}{L}\sum_{p=0}^{L} b_2(\nu_p)(\frac{(\Delta t)^{-\nu_p}}{\Gamma(3-\nu_p)}$$
$$\times\sum_{j=0}^{k-1}(U_q^{k-j+1}-2U_q^{k-j}+U_q^{k-j-1})((j+1)^{2-\nu_p}-j^{2-\nu_p})$$
$$+\frac{\kappa(\Delta x)^{-\alpha}}{2\Gamma(\alpha)\Gamma(3-\alpha)\cos(\frac{\pi\alpha}{2})}\{\frac{(1-\alpha)(2-\alpha)U_0^k}{q^\alpha}+\frac{(2-\alpha)}{q^{\alpha-1}}$$
$$\times(U_1^k-U_0^k)+\sum_{i=0}^{q-1}(U_{q-i+1}^k-2U_{q-i}^k+U_{q-i-1}^k)$$
$$\times[(i+1)^{2-\alpha}-i^{2-\alpha}]+\frac{(1-\alpha)(2-\alpha)U_M^k}{(M-q)^\alpha}-\frac{(2-\alpha)}{(M-q)^{\alpha-1}}$$
$$\times(U_M^k-U_{M-1}^k)+\sum_{i=0}^{M-q-1}(U_{q+i-1}^k-2U_{q+i}^k+U_{q+i+1}^k)$$
$$\times[(i+1)^{2-\alpha}-i^{2-\alpha}]\}=-\frac{1}{L}\sum_{p=0}^{L} b_1(\mu_p)b_1^{\mu_p}(\Delta t)^{2-\mu_p}$$
$$\times\frac{\partial^2 u(x_q,\eta_k)}{\partial t^2}+\frac{h^2}{24}F''_1(\mu)-\frac{1}{L}\sum_{p=0}^{L} b_2(\nu_p)b_2^{\nu_p}\frac{(\Delta t)^{4-\nu_p}}{24}$$
$$\times\frac{\partial^4 U(x_q,\eta'_k)}{\partial t^4}+\frac{h^2}{24}F''_2(\nu)+b^\alpha\frac{(\Delta t)^{4-\alpha}}{24}\frac{\partial^4 U}{\partial x^4}(\theta_q,\eta_k)$$
$$+f(x_q,t_k,U_q^k)+\Delta t[\frac{\partial f}{\partial t}(x_q,\zeta_{k+1},U(x_q,\zeta_{k+1}))$$
$$+\frac{\partial f}{\partial U}(x_q,\zeta_{k+1},U(x_q,\zeta_{k+1}))\frac{\partial U}{\partial t}(x_q,\zeta_{k+1})] \tag{33}$$

Applying the definition of T_1 and T_2, we can rewrite Equation (33) as in Equation (34):

$$T_1(U_q^{k+1})=T_2(U_q^k)+f(x_q,t_k,U_q^k)$$
$$-\frac{1}{L}\sum_{p=0}^{L} b_1(\mu_p)b_1^{\mu_p}(\Delta t)^{2-\mu_p}\frac{\partial^2 u(x_q,\eta_k)}{\partial t^2}$$
$$+\frac{h^2}{24}F''_1(\mu)-\frac{1}{L}\sum_{p=0}^{L} b_2(\nu_p)b_2^{\nu_p}\frac{(\Delta t)^{4-\nu_p}}{24}$$
$$\times\frac{\partial^4 U(x_q,\eta'_k)}{\partial t^4}+\frac{h^2}{24}F''_2(\nu)$$
$$+b^\alpha\frac{(\Delta x)^{4-\alpha}}{24}\frac{\partial^4 U}{\partial x^4}(\theta_q,\eta_k)$$
$$+\Delta t[\frac{\partial f}{\partial t}(x_q,\zeta_{k+1},U(x_q,\zeta_{k+1}))$$
$$+\frac{\partial f}{\partial U}(x_q,\zeta_{k+1},U(x_q,\zeta_{k+1}))\frac{\partial U}{\partial t}(x_q,\zeta_{k+1})] \tag{34}$$

Thus, the error e_q^k for $q=1,\ldots,M$ and $k=1,\ldots,N$ satisfies Equation (35)

$$\begin{cases} e_q^0=0, \\ T_1\left(U_q^{(k+1)}\right)=T_2\left(U_q^k\right)+\mathbb{R}_q^{(k+1)}+f(x_q,t_k,U_q^k)-f(x_q,t_k,\tilde{U}_q^k) \end{cases} \tag{35}$$

in which it can be defined as in Equation (36)

$$\mathbb{R}_q^{k+1}=-\frac{1}{L}\sum_{p=0}^{L} b_1(\mu_p)b_1^{\mu_p}(\Delta t)^{2-\mu_p}\frac{\partial^2 u(x_q,\eta_k)}{\partial t^2}$$
$$+\frac{h^2}{24}F''_1(\mu)-\frac{1}{L}\sum_{p=0}^{L} b_2(\nu_p)b_2^{\nu_p}\frac{(\Delta t)^{4-\nu_p}}{24}\frac{\partial^4 U(x_q,\eta'_k)}{\partial t^4}$$
$$+\frac{h^2}{24}F''_2(\nu)+b^\alpha\frac{(\Delta x)^{4-\alpha}}{24}\frac{\partial^4 U}{\partial x^4}(\theta_q,\eta_k)$$
$$+\Delta t[\frac{\partial f}{\partial t}(x_q,\zeta_{k+1},U(x_q,\zeta_{k+1}))$$
$$+\frac{\partial f}{\partial U}(x_q,\zeta_{k+1},U(x_q,\zeta_{k+1}))\frac{\partial U}{\partial t}(x_q,\zeta_{k+1})] \tag{36}$$

Consider $R^{k+1}=[\mathbb{R}_1^{k+1},\mathbb{R}_2^{k+1},\ldots,\mathbb{R}_M^{k+1}]$, $k=0,1,\ldots$. From Equation (37), we get

$$
\begin{aligned}
|\mathbb{R}_q^{k+1}| &\le P_1\frac{1}{L}\sum_{p=0}^{L} b_1(\mu_p)b_1^{\mu_p}(\Delta t)^{2-\mu_p} + P_2h^2 \\
&+ P_3\frac{1}{L}\sum_{p=0}^{L} b_2(\nu_p)b_2^{\nu_p}(\Delta t)^{4-\nu_p} + P_4h^2 \\
&+ P_5 b^{\alpha}(\Delta t)^{4-\alpha} + P_6\Delta t \\
&\le \bar{b}_1P_1 \max_{\mu\in(0,1)}\{b_1(\mu)\}(\Delta t)^{2-\mu_L} + P_2h^2 \\
&+ \bar{b}_2P_3 \max_{\nu\in(1,2)}\{b_2(\nu)\}(\Delta t)^{4-\nu_L} + P_4h^2 \\
&+ P_5\bar{b}^{\alpha}(\Delta t)^{4-\alpha} + P_6\Delta t
\end{aligned} \tag{37}
$$

in which it can be defined as in Equation (38):

$$
\begin{aligned}
&P_1 = \max_{t\in[0,T]}|\frac{\partial^2 u(x_q,t)}{\partial t^2}|, \quad P_2 = \max_{\mu\in(0,1)}|F''_1|, \\
&P_3 = \max_{t\in[0,T]}|\frac{1}{24}\frac{\partial^4 U(x_q,t)}{\partial t^4}|, \quad P_4 = \max_{\nu\in(1,2)}|F''_2|, \\
&P_5 = \frac{1}{24}\max_{x\in[0,L]}|\frac{\partial^4 U}{\partial x^4}(x,t_k)|, \\
&P_6 = \max_{\zeta_{k+1}\in[t_k,t_{k+1}]}|\{\frac{\partial f}{\partial t}(x_q,\zeta_{k+1},U(x_q,\zeta_{k+1})) \\
&\quad + \frac{\partial f}{\partial U}(x_q,\zeta_{k+1},U(x_q,\zeta_{k+1}))\frac{\partial U}{\partial t}(x_q,\zeta_{k+1})\}|, \\
&\bar{b}_1 = \max_p\{b_1^{\mu_p}\}, \quad \bar{b}_2 = \max_p\{b_2^{\nu_p}\}
\end{aligned} \tag{38}
$$

and $\bar{b}_\alpha = \max_\alpha\{b^\alpha\}$. Then, we get Equation (39):

$$
\begin{aligned}
&\| \mathbb{R}^{k+1} \|_\infty \le \mathbb{C}((\Delta t)^{2-\mu_L} + h^2 + (\Delta t)^{4-\nu_L} \\
&+ (\Delta t)^{4-\alpha} + (\Delta t))
\end{aligned} \tag{39}
$$

where $\mathbb{C} = \max\{\bar{b}_1P_1, P_2, \bar{b}_2P_3, P_4, \bar{b}^\alpha P_5, P_6, \}$.

5. Illustrative examples

Some numerical examples are demonstrated in this part to show the effectiveness of the studied numerical approach. The absolute errors for these illustrative examples at different points (x,t) are computed as follows in Equation (40):

$$
\begin{aligned}
&|e(x_q,t_k)| = |u(x_q,t_k) - u_q^k|, \\
&k = 1,\dots,N,\ q = 1,\dots,M,
\end{aligned} \tag{40}
$$

in which $u(x_q,t_k)$ and u_q^k show the exact and approximate solutions, respectively. Additionally, all numerical simulations presented in this study were conducted using Mathematica software (version 11). The computations were performed on a laptop equipped with an Intel Core i5 processor (2.40 GHz) and 16.00 GB of RAM. Moreover, the following formula Equation (41) was used to calculate the convergence order:

$$
\begin{aligned}
Rate_h &= \log_2(\frac{e(h,\Delta t)}{e(\frac{h}{2},\Delta t)}), \\
Rate_{\Delta t} &= \log_2(\frac{e(h,\Delta t)}{e(h,\frac{\Delta t}{2})}).
\end{aligned} \tag{41}
$$

5.1. Example 1

Consider Equation (42):

$$
\begin{aligned}
&\int_0^1 \Gamma(5-\mu)\,{}^C D_t^\mu u(x,t)d\mu \\
&+ \int_1^2 \Gamma(5-\nu)\,{}^C D_t^\nu u(x,t)d\nu = \\
&- (-\Delta)^{\frac{\alpha}{2}}u(x,t) + u^2(x,t) + g(x,t)
\end{aligned} \tag{42}
$$

where in Equation (43):

$$
\begin{aligned}
&g(x,t) = 24(x(1-x))^3\frac{(t^4-t^2)}{\ln t} - t^8(x(1-x))^6 \\
&+ g_1(x,t)g_1(x,t) = (2\cos(\frac{\alpha\pi}{2}))^{-1}t^4 \\
&\times\Bigg[\frac{\Gamma(4)}{\Gamma(4-\alpha)}(x^{3-\alpha}+(1-x)^{3-\alpha}) \\
&- \frac{3\Gamma(5)}{\Gamma(5-\alpha)}(x^{4-\alpha}+(1-x)^{4-\alpha}) \\
&+ \frac{3\Gamma(6)}{\Gamma(6-\alpha)}(x^{5-\alpha}+(1-x)^{5-\alpha}) \\
&-\frac{\Gamma(7)}{\Gamma(7-\alpha)}(x^{6-\alpha}+(1-x)^{6-\alpha})\Bigg]
\end{aligned} \tag{43}
$$

with conditions in Equation (44):

$$
\begin{aligned}
&u(x,0) = 0,\ x\in(0,1), \\
&u(0,t) = 0,\ u(1,t) = 0,\ t\in(0,1]
\end{aligned} \tag{44}
$$

The exact solution is $u(x,t) = t^4(x(1-x))^3$. We solved this problem using the numerical method developed in this study. The method was applied with $L = 20$, $M = N = 30$, and various values of α. Figure 1 presents the approximate solutions obtained by our method for these parameter values and different choices of α. This figure provides a visual representation of how the solution evolves across the spatial domain and time for different choices of α, offering insight into the influence of the fractional order on the overall behavior of the solution. Figure 2 compares the exact solution with the approximate solution at $L = 20$, $M = N = 30$, and various choices of α in $u(x,0.5)$. Figure 3 illustrates the absolute error functions for $L = 20$, $M = N = 30$, and various choices of α. These graphs illustrate the

discrepancy between the approximate and exact solutions, providing a clear indication of the accuracy of the numerical method. The absolute error is an essential metric for evaluating the effectiveness of the approximation, and these graphs help to assess how errors vary as α changes. Figure 4 shows the absolute error functions at $t = 0.5$ for the same values of L, M, and N with different choices of α. This figure focuses on the error at a specific time, offering more detailed insight into the temporal behavior of the numerical approximation. It is particularly useful for understanding how the error behaves at different fractional orders at a fixed point in time. Tables 1 and 2 provide the maximum errors and convergence orders for the numerical method in space and time, respectively. These tables are essential for understanding the accuracy and convergence behavior of the method. Specifically, the convergence order indicates how quickly the numerical solution approaches the exact solution as the grid resolution increases, and the maximum errors give a measure of the overall deviation from the true solution.

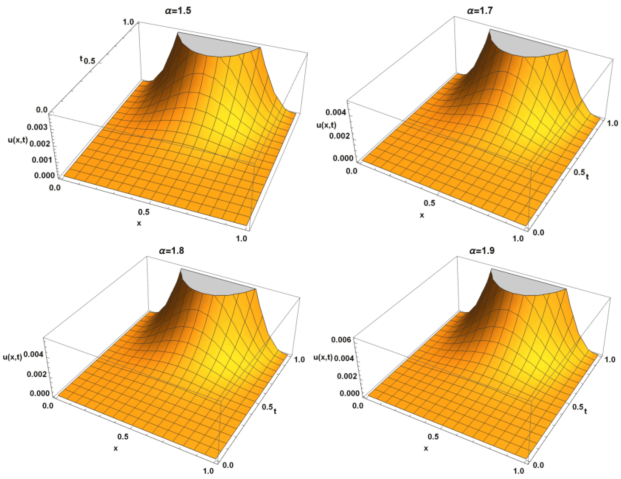


Figure 1. The plot of the approximate solution $u(x,t)$ with $L = 20$, $M = N = 30$, and various choices of α for Example 1

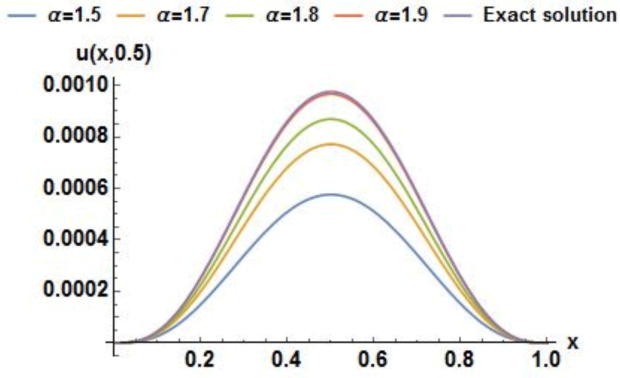


Figure 2. Approximate and exact solutions with $L = 20$, $M = N = 30$ and various choices of α for Example 1 when $t = 0.5$

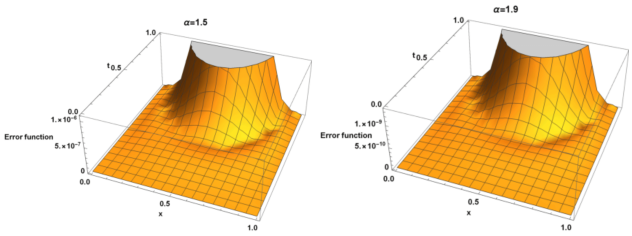


Figure 3. The absolute error functions with $L = 20$, $M = N = 30$ and various choices of α for Example 1

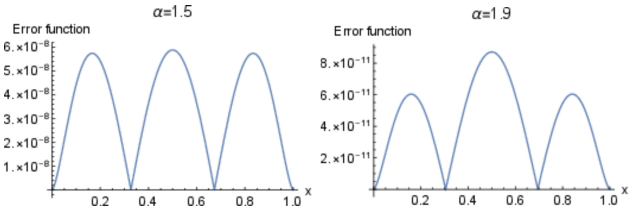


Figure 4. The absolute error functions with $L = 20$, $M = N = 30$ and various choices of α for Example 1 at $t = 0.5$

5.2. Example 2

Consider the problem in Equation (45)‘:

$$\int_0^1 \Gamma(\frac{7}{2}-\mu)\,{}^C D_t^{\mu} u(x,y,t)d\mu + \int_1^2 \Gamma(\frac{7}{2}-\nu)\,{}^C D_t^{\nu} u(x,y,t)d\nu = -(-\Delta)^{\frac{\alpha}{2}} u(x,y,t) + g(x,y,t) + \frac{15\sqrt{\pi}\sqrt{t}}{8lnt} \times (t^2-1)(x(1-x)y(1-y))^3,\ n \in \mathbb{N} \tag{45}$$

in which in Equation (46):

$$g(x,y,t) = (2cos(\frac{\alpha\pi}{2}))^{-1} t^{\frac{5}{2}}((1-y)y)^3 \times [\frac{\Gamma(4)}{\Gamma(4-\alpha)}(x^{3-\alpha}+(1-x)^{3-\alpha}) - \frac{3\Gamma(5)}{\Gamma(5-\alpha)}(x^{4-\alpha}+(1-x)^{4-\alpha}) + \frac{3\Gamma(6)}{\Gamma(6-\alpha)}(x^{5-\alpha}+(1-x)^{5-\alpha}) - \frac{\Gamma(7)}{\Gamma(7-\alpha)}(x^{6-\alpha}+(1-x)^{6-\alpha})] + (2cos(\frac{\beta\pi}{2}))^{-1} t^{\frac{5}{2}}((1-x)x)^3[\frac{\Gamma(4)}{\Gamma(4-\beta)}(y^{3-\beta} + (1-y)^{3-\beta}) - \frac{3\Gamma(5)}{\Gamma(5-\beta)}(y^{4-\beta}+(1-y)^{4-\beta})$$

Table 1. Comparison of the error function and convergence order with N= 100 for Example 1

M	$\alpha = 1.5$		$\alpha = 1.8$		$\alpha = 1.9$	
	$e(h, \Delta t)$	Rate_h	$e(h, \Delta t)$	Rate_h	$e(h, \Delta t)$	Rate_h
32	2.550426e-10	-	5.474700e-10	-	8.682241e-10	-
64	8.150868e-11	1.9820	1.558595e-10	1.9788	2.358879e-10	1.9863
128	1.205352e-11	1.9984	3.065866e-11	1.9980	5.072403e-11	1.9970
256	4.701125e-12	1.9937	1.034642e-11	1.9970	1.436730e-11	1.9972

Table 2. Comparison of the error function and convergence order with M= 100 for Example 1

N	$\alpha = 1.5$		$\alpha = 1.8$		$\alpha = 1.9$	
	$e(h, \Delta t)$	$\text{Rate}_{\Delta t}$	$e(h, \Delta t)$	$\text{Rate}_{\Delta t}$	$e(h, \Delta t)$	$\text{Rate}_{\Delta t}$
32	1.104018e-10	-	1.002382e-10	-	7.008703e-11	-
64	3.047415e-11	1.9900	2.438518e-11	1.8808	2.011908e-11	1.9931
128	6.557025e-12	1.9949	5.282357e-12	1.8845	5.045536e-12	1.9954
256	1.804933e-12	2.0007	1.500711e-12	1.8868	1.267602e-12	1.9928

$$+\frac{3\Gamma(6)}{\Gamma(6-\beta)}(y^{5-\beta}+(1-y)^{5-\beta}) - \frac{\Gamma(7)}{\Gamma(7-\beta)}(y^{6-\beta}+(1-y)^{6-\beta})] \tag{46}$$

in which $(x,t) \in [0,1]\times[0,1]$ under the conditions in Equation (47):

$$\begin{aligned} &u(x,y,0) = 0,\ (x,y) \in (0,1)\times(0,1),\\ &u(x,y,t) = 0, (x,y) \in \partial((0,1)\times(0,1)) \end{aligned} \tag{47}$$

The exact solution for this model is given by $u(x,t) = t^{\frac{5}{2}}(x(1-x)y(1-y))^3$. Applying our numerical method, taking $L = 20$ and $M = N = 30$, the numerical results for this example for different values of α are shown in Figure 5 if $t = 0.5$. The absolute error functions with $L = 20$, $M = N = 30$, and various choices of α for this example at $t = 0.5$ are demonstrated in Figure 6.

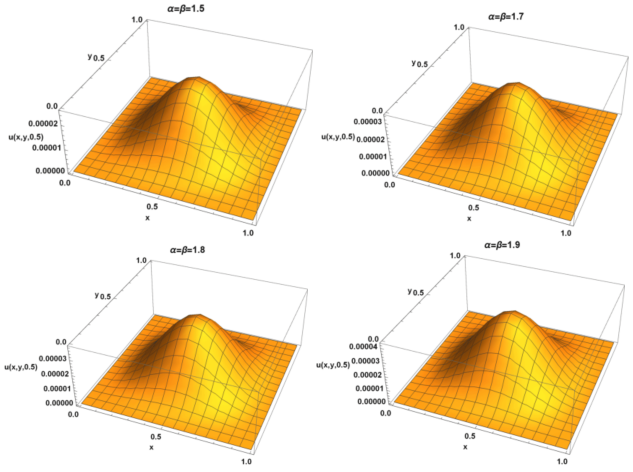


Figure 5. The plot of the approximate solution $u(x,t)$ with $L = 20$, $M = N = 30$ and various choices of α for Example 2

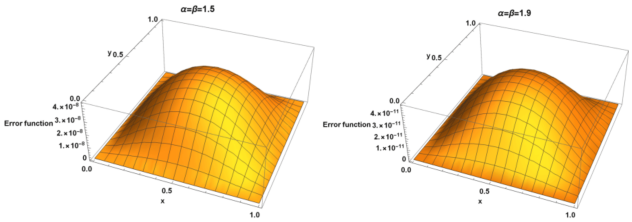


Figure 6. The absolute error functions with $L = 20$, $M = N = 30$ and various choices of α for Example 2

5.3. Example 3

Consider the time-fractional reaction-diffusion model of distributed order with$h$ $\alpha = 2$ in Equation (48):

$$\int_0^1 \Gamma(\frac{7}{2}-\mu)\,{}^C D_t^{\mu} u(x,t)d\mu = u_{xx}(x,t) + u^2(x,t) + \frac{15\sqrt{\pi}t\sqrt{t}}{8lnt}(t-1)(x(1-x)) - 2t^5 - (xt(1-x))^2 \tag{48}$$

with the following conditions in Equation (49):

$$u(x,0) = u(0,t) = u(1,t) = 0,\ x \in (0,1),\ t \in (0,1] \tag{49}$$

The exact solution for this model was calculated in previous studies [30, 31] by $u(x,t) = t^{\frac{5}{2}}x(x-1)$. We solved this model using the studied method on the domains $x \in (0,1)$ and $t \in (0,1]$ when $\Delta x = h$. Figure 7 shows the numerical results for different values of $\Delta x = h$. Figure 8 reports the error function for different values of h. Figure 9 shows the error function for different values of h with $t = 0.5$. We compared the method presented in this study with the methods discussed in previous articles[46,47] based on the error function. The comparison results are summarized in Table 3, which also includes the

Table 3. Comparison of the maximum errors and convergence orders with $\Delta t = (\Delta x)^2$ for Example 3

$\Delta x = h$	Reference[30]		Reference[31]		Proposed method	
	$e(h, \Delta t)$	$\text{Rate}_{\Delta t}$	$e(h, \Delta t)$	$\text{Rate}_{\Delta t}$	$e(h, \Delta t)$	$\text{Rate}_{\Delta t}$
0.5	7.43e-2	-	2.45e-2	-	1.34e-7	-
0.25	3.22e-2	0.60	5.47e-3	1.08	4.36e-8	1.99
0.125	8.99e-3	0.92	1.30e-3	1.04	1.21e-8	1.78
0.0625	2.31e-3	0.98	3.20e-4	1.01	2.13e-9	1.73

convergence order for the proposed method. This table provides a comprehensive overview of the performance of the proposed method in relation to those from previous studies, highlighting the accuracy and convergence behavior.

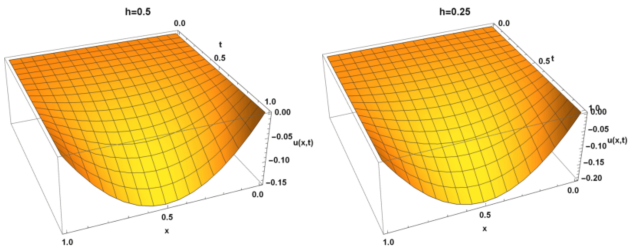


Figure 7. The surface of the approximate solution $u(x, t)$ with $L = 20$, $M = N = 30$ and various choices of α for Example 3

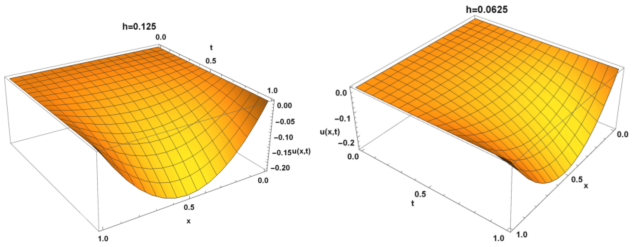


Figure 8. The absolute error functions with $L = 20$, $M = N = 30$, and various choices of α for Example 3

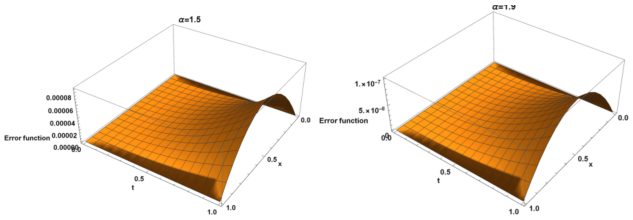


Figure 9. The absolute error functions with $L = 20$, $M = N = 30$ and various choices of α for Example 3 at $t = 0.5$

6. Conclusion

In this study, we analyzed the distributed-order multi-dimensional time-fractional telegraph equations, incorporating Caputo time- and Riesz space-fractional derivatives. The finite difference method was employed to approximate the Riesz space-fractional derivative with respect to the spatial variable. To approximate the distributed-order fractional operator, we applied the midpoint method to discretize the integral term, followed by the use of the finite difference method to approximate the Caputo fractional derivative with respect to the time variable. We have rigorously proved the convergence and stability of the proposed numerical method. To demonstrate the high efficiency and accuracy of the method, we conducted several numerical experiments, comparing the results with those obtained from other numerical methods found in the literature. The comparison clearly shows that the proposed method outperforms existing approaches in terms of both efficiency and performance, making it a highly effective tool for solving distributed-order time-fractional telegraph equations.

Acknowledgments

None.

Funding

The work was supported by the University of Tabriz, Iran (Grant No. 2070).

Conflict of interest

The authors declare that they have no competing interests.

Author contributions

Conceptualization: Safar Irandoust Pakchin, Mohammad Hossein Derakhshan
Data curation: Mohammad Hossein Derakhshan
Investigation: All authors
Methodology: All authors
Software: All authors
Writing – original draft: Shahram Rezapour
Writing – review & editing: All authors

Availability of data

All data analyzed and generated have been included in the manuscript.

AI tools statement

All authors confirm that no AI tools were used in the preparation of this manuscript.

References

1. Azroul E, Kamali N, Ragusa MA, Shimi M. Variational methods for a p(x,.)-fractional bi-nonlocal problem of elliptic type. *Rend Circ Mat Palermo, II. Ser.* 2025;74(1):1-21. https://doi.org/10.1007/s12215-024-01156-7
2. Alotaibi M, Jleli M, Ragusa MA, Samet B. On the absence of global weak solutions for a nonlinear time-fractional SchrÑ†dinger equation. *Appl Anal.* 2024;103(1):1-15. https://doi.org/10.1080/00036811.2022.2036335
3. Kilbas AA, Srivastave HM, Trujillo JJ. *Theory and Applications of Fractional Differential Equations.* Amsterdam: Elsevier B.V.; 2006. ISBN:0444518320, 9780444518323
4. Podlubny I. *Fractional Differential Equations: An Introduction to Fractional Derivatives, Fractional Differential Equations, to Methods of Their Solution and Some of their Applications*, vol. 198. New York: Academic Press; 1998. ISBN:0080531989, 9780080531984
5. Mollahasani N, Moghadam MM, Afrooz K. A new treatment based on hybrid functions to the solution of telegraph equations of fractional order. *Appl Math Model.* 2016; 40(4):2804-2814. https://doi.org/10.1016/j.apm.2015.08.020
6. Wang R, Shi L, Wang B. Asymptotic behavior of fractional nonclassical diffusion equations driven by nonlinear colored noise on R^N. *Nonlinearity.* 2019; 32(11): 4524-4556. https://doi.org/10.1088/1361-6544/ab32d7
7. Yasin F, Afzal Z, Saleem MS, Jahangir N, Shang Y. Hermite–Hadamard type inequality for non-convex functions employing the Caputo–Fabrizio fractional integral. *Res Math.* 2024;11(1):2366164. https://doi.org/10.1080/27684830.2024.2366164
8. Mohammed AA, Marasi HR, Derakhshan MH, Kumar P. An efficient numerical method for the time-fractional distributed order nonlinear Klein-Gordon equation with shifted fractional Gegenbauer multi-wavelets method. *Phys Scr.* 2023;98:084001. https://doi.org/10.1088/1402-4896/accedb
9. Umarov S. Continuous time random walk models associated with distributed order diffusion equations. *Fract Cal Appl Anal.* 2015;18:821-837. https://doi.org/10.1515/fca-2015-0049
10. Guo S, Mei L, Zhang Z. Time-fractional Gardner equation for ion-acoustic waves in negative-ion-beam plasma with negative ions and non-thermal nonextensive electrons. *Phys Plasmas.* 2015;22:052306. https://doi.org/10.1063/1.4919264
11. Ansari A, Derakhshan MH, Askari H. Distributed order fractional diffusion equation with fractional Laplacian in axisymmetric cylindrical configuration. *Commun Nonlinear Sci Numer Simul.* 2022;113:106590. https://doi.org/10.1016/j.cnsns.2022.106590
12. Derakhshan MH. Existence, uniqueness, Ulam-Hyers stability and numerical simulation of solutions for variable order fractional differential equations in fluid mechanics. *J Appl Math Comput.* 2022;68(1):403-429. https://doi.org/10.1007/s12190-021-01537-6
13. Irandoust-pakchin S, Abdi-mazraeh S, Fahimi-khalilabad I. Higher order class of finite difference method for time-fractional Liouville-Caputo and space-Riesz fractional diffusion equation. *Filomat.* 2024;38(2):505-521. https://doi.org/10.2298/FIL2402505I
14. Irandoust-Pakchin S, Abdi-Mazraeh S, Khani A. Numerical solution for a variable-order fractional nonlinear cable equation via Chebyshev cardinal functions. *Comput Math and Math Phys.* 2017;57:2047-2056. https://doi.org/10.1134/S0965542517120120
15. Fahimi-khalilabad I, Irandoust-pakchin S, Abdi-mazraeh S. High-order finite difference method based on linear barycentric rational interpolation for Caputo type sub-diffusion equation. *Math Comput Simulat.* 2022;199:60-80. https://doi.org/10.1016/j.matcom.2022.03.008
16. Caputo M. Mean fractional-order-derivatives differential equations and filters. *Ann Univ Ferrara.* 1995;41:73-84. https://doi.org/10.1007/BF02826009
17. Caputo M. Distributed order differential equations modelling dielectric induction and diffusion. *Fract Calc Appl Anal.* 2001;4:421-442. ww.math.bas.bg/fcaa, www.diogenes.bg/fcaa.
18. Caputo M. Diffusion with space memory modelled with distributed order space fractional differential equations. *Ann Geophys.* 2003;46(2). https://doi.org/10.4401/ag-3395
19. Chechkin A, Gorenflo R, Sokolov I. Retarding subdiffusion and accelerating superdiffusion governed by distributed-order fractional diffusion equations. *Phys Rev E.* 2002;66:046129. https://doi.org/10.1103/PhysRevE.66.046129
20. Sokolov I, Chechkin A, Klafter J. Distributed-order fractional kinetics. *Acta Physica Polonica B.* 2004;35:1323-1341. https://doi.org/10.48550/arXiv.cond-mat/0401146
21. Vieira N, Rodrigues MM, Ferreira M. Time-fractional telegraph equation of distributed order in higher dimensions. *Commun Nonlinear Sci Numer Simul.* 2021;102:105925. https://doi.org/10.1016/j.cnsns.2021.105925
22. Ratner V, Zeevi YY. Denoising-enhancing images on elastic manifolds. *IEEE Trans Image Process.* 2011;20(8):2099-2109. https://doi.org/10.1109/TIP.2011.2118221
23. Gorenflo R, Luchko Y, Stojanovi *M*. Fundamental solution of a distributed order time-fractional diffusion-wave equation as probability density. *Fract Calc Appl Anal.* 2013;16(2):297-316. https://doi.org/10.2478/s13540-013-0019-6

24. Mainardi F, Pagnini G. The role of the Fox-Wright functions in fractional sub-diffusion of distributed order. *J Comput Appl Math.* 2007;207(2):245-257. https://doi.org/10.1016/j.cam.2006.10.014
25. Ahmed HF, Moubarak MRA, Hashem WA. Gegenbauer spectral tau algorithm for solving fractional telegraph equation with convergence analysis. *Pramana - J Phys.* 2021;95(2):1-16. https://doi.org/10.1007/s12043-021-02113-0
26. Zhang Y, Qian J, Papelis C, Sun P, Yu Z. Improved understanding of bimolecular reactions in deceptively simple homogeneous media: from laboratory experiments to Lagrangian quantification. *Water Resour Res.* 2014;50(2):1704-1715. https://doi.org/10.1002/2013WR014711
27. Sun HG, Chen W, Li C, Chen YQ. Fractional differential models for anomalous diffusion. *Physica A: Stat Mech Appl.* 2010;389(14):2719-2724. https://doi.org/10.1016/j.physa.2010.02.030
28. Gao GH, Sun ZZ. Two difference schemes for solving the one-dimensional time distributed-order fractional wave equations. *Numer Algorithms.* 2017;74:675-697. https://doi.org/10.1007/s11075-016-0167-y
29. Wang Z, Vong S. Compact difference schemes for the modified anomalous fractional sub-diffusion equation and the fractional diffusion-wave equation. *J Comput Phys.* 2014;277:1-15. https://doi.org/10.1016/j.jcp.2014.08.012
30. Ye H, Liu F, Anh V, Turner I. Numerical analysis for the time distributed-order and Riesz space fractional diffusions on bounded domains. *IMA J Appl Math.* 2015;80(3):825-838. https://doi.org/10.1093/imamat/hxu015
31. Jian HY, Huang TZ, Gu XM, Zhao YL. Fast second-order implicit difference schemes for time distributed–order and Riesz X.L. space fractional diffusion–wave equations. *Comput Math Appl.* 2021;94:136-154. https://doi.org/10.1016/j.camwa.2021.05.003
32. Kharazmi E, Zayernouri M, Karniadakis G. Petrov-Galerkin and spectral collocation methods for distributed order differential equations. *SIAM J Sci Comput.* 2017;39:A1003-A1037. https://doi.org/10.1137/16M1073121
33. Gao G, Sun Z. Two alternating direction implicit difference schemes with the extrapolation method for the two-dimensional distributed-order differential equations. *Comput Math Appl.* 2015;69: 926-948. https://doi.org/10.1016/j.camwa.2015.02.023
34. Duong P, Kwok E, Lee M. Deterministic analysis of distributed order systems using operational matrix. *Appl Math Model.* 2016;40:1929-1940. https://doi.org/10.1016/j.apm.2015.09.035
35. Mashayekhi S, Razzaghi M. Numerical solution of distributed order fractional differential equations by hybrid functions. *J Comput Phys.* 2016;315:169-181. https://doi.org/10.1016/j.jcp.2016.01.041
36. Abbaszadeh M, Dehghan M. Meshless upwind local radial basis function-finite difference technique to simulate the time-fractional distributed-order advection-diffusion equation. *Eng Comput.* 2021;37:873-889. https://doi.org/10.1007/s00366-019-00861-7
37. Ye H, Liu F, Anh V. Compact difference scheme for distributed-order time-fractional diffusion-wave equation on bounded domains. *J Comput Phys.* 2015;298:652-660. https://doi.org/10.1016/j.jcp.2015.06.025
38. Chen H, LÃ¼ S, Chen W. Finite difference/spectral approximations for the distributed order time fractional reaction-diffusion equation on an unbounded domain. *J Comput Phys.* 2016;315:84-97. https://doi.org/10.1016/j.jcp.2016.03.044
39. Qiu W, Xu D, Chen H, Guo J. An alternating direction implicit Galerkin finite element method for the distributed-order time-fractional mobile-immobile equation in two dimensions. *Comput Math Appl.* 2020;80(12):3156-3172. https://doi.org/10.1016/j.camwa.2020.11.003
40. Yang Z, Zheng X, Wang H. A variably distributed-order time-fractional diffusion equation: analysis and approximation. Comput *Methods Appl Mech Eng.* 2020;367:113118. https://doi.org/10.1016/j.cma.2020.113118
41. Abdelkawy MA, Lopes AM, Zaky MA. Shifted fractional Jacobi spectral algorithm for solving distributed order time-fractional reaction-diffusion equations. *Comput Appl Math.* 2019;38:1-21. https://doi.org/10.1007/s40314-019-0845-1
42. Ansari A, Derakhshan MH. On spectral polar fractional Laplacian. *Math Comput Simul.* 2023;206:636-663. https://doi.org/10.1016/j.matcom.2022.12.008
43. Derakhshan MH, Aminataei A. A numerical method for finding solution of the distributed-order time-fractional forced Kortewegde Vries equation including the Caputo fractional derivative. *Math Methods Appl Sci.* 2022;45(5):3144-3165. https://doi.org/10.1002/mma.7981
44. Ahmed HF, Hashem WA. Improved Gegenbauer spectral tau algorithms for distributed-order time-fractional telegraph models in multi-dimensions. *Numer Algorithms.* 2023; 93(3):1013-1043. https://doi.org/10.1007/s11075-022-01452-2
45. Ilic M, Liu F, Turner I, Anh V. Numerical approximation of a fractional-in-space diffusion equation, I. *Fract Calc Appl Anal.* 2005;8(3):323-341. http://eudml.org/doc/11303
46. Morgado ML, Rebelo M. Numerical approximation of distributed order reaction-diffusion equations. *J Appl Math Comput.* 2015; 275:216-227. https://doi.org/10.1016/j.cam.2014.07.029
47. Moghaddam BP, Tenreiro Machado JA, Morgado ML. Numerical approach for a class of distributed

order time fractional partial differential equations. *Appl Numer Math.* 2019;136:152-162. https://doi.org/10.1016/j.apnum.2018.09.019

Safar Irandoust Pakchin*, after the completing his Ph.D. in Mathematics at the Faculty of Mathematics, Statistics and Computer Sciences, University of Tabriz, Iran, in July 2012, he engaged as an Assistant Professor at Department of Applied Mathematics, Faculty of Mathematics, Statistics and Computer Sciences, University of Tabriz, Iran, in February 2013 until now. His research areas include partial differential equations, fractional differential equations, fractional stochastic integro-differential equations, and image and signal processing. He has developed spectral methods, especially wavelets, and fractional linear multistep methods.*
http://orcid.org/0000-0001-9548-4762

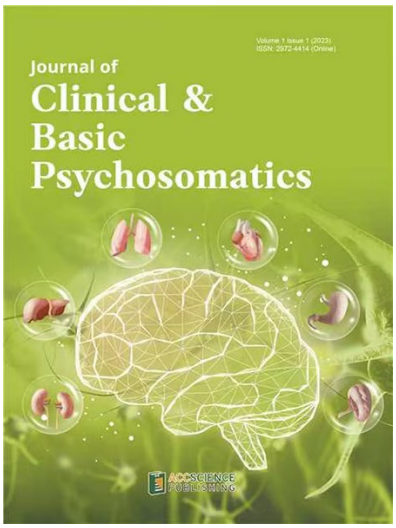
Mohammad Hossein Derakhshan *holds a Ph.D. and five postdoctoral degrees from K. N. Toosi University of Technology and University of Tabriz. His expertise lies in numerical analysis and differential equations, and he has successfully completed advanced courses in these fields. Dr. Derakhshan applies mathematical modeling, numerical methods, and differential equations, especially in fractional-order and distributed-order systems, to solve complex scientific and engineering problems.*
https://orcid.org/0000-0001-6464-7338

Shahram Rezapour *is a professor of mathematics at Azarbaijan Shahid Madani University, Tabriz, Iran, and holds a visiting professor position at China Medical University, Taichung, Taiwan. He also held an eminent scholarship position at Kyung Hee University, Seoul, Republic of Korea, in 2023.*
http://orcid.org/0000-0003-3463-2607

An International Journal of Optimization and Control: Theories & Applications
(https://accscience.com/journal/ijocta)

This work is licensed under a Creative Commons Attribution 4.0 International License. The authors retain ownership of the copyright for their article, but they allow anyone to download, reuse, reprint, modify, distribute, and/or copy articles in IJOCTA, so long as the original authors and source are credited. To see the complete license contents, please visit http://creativecommons.org/licenses/by/4.0/.

Our Journals



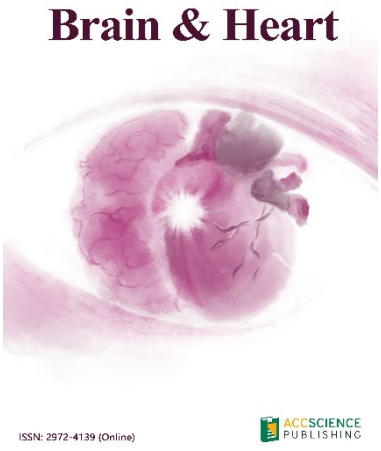
Journal of Clinical and Basic Psychosomatics (JCBP) is a quarterly journal focusing on clinical and basic research on symptoms, assessment, treatment, management, and the mechanism of psychosomatic disorders. *Journal of Clinical and Basic Psychosomatics* covers subject areas, including but not limited to the following:

- Conceptualization and classification of psychosomatic medicine
- Mechanism, biological markers, brain images, and treatment studies
- Psychosomatic reactions, syndromes, disorders, and diseases
- Psychosomatic disorders treated in general hospitals, including endocrinology, neurology, gastroenterology, dermatology, pain management, oncology, rheumatology, and other departments
- Psychological evaluation, management, rehabilitation, resilience training, and psychotherapy for general and specific populations during the pandemic
- Physiological disorders related to psychological factors (eating disorders, sleeping disorders, and sexual dysfunction)
- Somatic symptoms and related disorders and mental disorders due to somatic disease

Brain & Heart focuses on neurocardiology, a neurology and cardiology-based interdisciplinary subject that studies the circulatory mechanism of the human body, as well as the mechanisms of the interplay between the cardiovascular system and the nervous system. The journal's scope includes:

Clinical and basic research on diseases related to the circulatory and nervous systems, such as: orthostatic dizziness, orthostatic hypotension, autonomic dysfunction, and the relationship between the autonomic nervous system and the circulatory function in cerebral degeneration;

Heart-brain research on patients with syncope, autonomic dysfunction, cryptogenic stroke, and stroke with atrial fibrillation; research on the relationship between structural heart diseases and nervous system diseases, the correlation between cardiac electrophysiology and abnormal organizational structures and the pathogenesis of stroke, as well as new ways of diagnosis, treatment and prevention of unexplained stroke.



Start a new journal

Write to us via email if you are interested to start a new journal with AccScience Publishing. Please attach your CV, professional profile page and a brief pitch proposal in your email. We shall inform you of our decision whether we are interested to collaborate in starting a new journal.

Contact: info@accscience.com

https://accscience.com/journal/IJOCTA

IJOCTA
An International Journal of Optimization and Control: Theories & Applications
2010

ACCSCIENCE PUBLISHING

Contact
www.accscience.com
9 Raffles Place, Republic Plaza 1 #06-00 Singapore 048619
Email: editorial@accscience.com
Phone: +65 8182 1586